AD NUMBER
AD881332
LIMITATION CHANGES

TO:

Approved for public release; distribution is unlimited.

FROM:

Distribution authorized to U.S. Gov't. agencies and their contractors; Critical Technology; NOV 1970. Other requests shall be referred to Air Force Weapons Laboratory, Attn: DEV, Kirland AFB, NM 87117. This document contains export-controlled technical data.

AUTHORITY

AFWL ltr, 29 Apr 1985

AD 881332

AUTHORITY: *AF WL ltr, 29 Apr 85*

AFWL-TR-70-55

AFWL-TR
70-55

AD881332

EXPERIMENTAL INVESTIGATION OF SMALL SCALE LINED AND UNLINED CYLINDRICAL CAVITIES IN ROCK

I. M. Daniel

R. E. Rowlands

M. M. Singh

IIT RESEARCH INSTITUTE

TECHNICAL REPORT NO. AFWL-TR-70-55

November 1970

AIR FORCE WEAPONS LABORATORY
Air Force Systems Command
Kirtland Air Force Base
New Mexico

364

EXPERIMENTAL INVESTIGATION OF SMALL SCALE

LINED AND UNLINED CYLINDRICAL

CAVITIES IN ROCK

I. M. Daniel
R. E. Rowlands
M. M. Singh
IIT Research Institute

TECHNICAL REPORT NO. AFWL-TR-70-55

AFWL-TR-70-55

AIR FORCE WEAPONS LABORATORY
Air Force Systems Command
Kirtland Air Force Base
New Mexico

FOREWORD

This report was prepared by the IIT Research Institute, Chicago, Illinois, under Contract F29601-69-C-0016. The research was performed under Program Element 61102H, Project 5710, Subtask SC 157, and was funded by the Defense Atomic Support Agency under MIPR-515-68.

Inclusive dates of research were October 1968 through December 1969. The report was submitted 8 October 1970 by the Air Force Weapons Laboratory Project Officer, Captain Lawrence E. Browder (DEV).
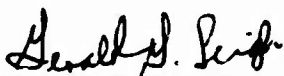
Information in this report is embargoed under the US Export Control Act of 1949, administered by the Department of Commerce. This report may be released by departments or agencies of the US Government to departments or agencies of foreign governments with which the United States has defense treaty commitments, subject to approval of AFWL (DEV), Kirtland AFB, NM, 87117.

Additional personnel who contributed to the work reported herein include Dr. T. Liber, Dr. V. G. Gregson, Jr., and Messrs. E. J. Smith, R. R. King, R. J. Nelson, T. Niiro, C. M. Palkovic, R. D. Rowe, and J. T. Staulcup.

This technical report has been reviewed and is approved.

LAWRENCE E. BROWDER
Captain, USAF
Project Officer

GERALD G. LEIGH
Major, USAF
Chief, Facility Survivability
  Branch

JEAN M. MARCHAND
Lt Colonel, USAF
Chief, Civil Engineering
  Division

ABSTRACT
(Distribution Limitation Statement No. 2)

An experimental study of the state of strain, deformation
and fracture around lined and unlined cylindrical cavities in rock
under uniaxial and biaxial static compressive loadings is discussed.
Twenty limestone and marble specimens of typical dimensions 36 in.
high, 24 in. wide and 3 in. thick with a 4 in. diameter cylindrical
hole unlined or lined with hydrostone and aluminum liners were used.
Deformation and fracture were monitored with strain gages, differen-
tial transformers and photoelastic coatings. Strain distributions
and diametral changes as a function of applied load were obtained.
Deviations from linear elastic theory were noted and discussed. Crack
initiation and propagation were monitored with all three experimental
means. Strain concentration factors were, with few exceptions, higher
and in some instances appreciably higher than theoretical factors.
The presence of the liner, even the weak hydrostone liner, had a
strengthening influence, although not always predictable. Depending
on the combination of material, geometrical and loading parameters,
several types of failure were observed: tensile cracking along the
vertical axis for the unlined specimens and those lined with hydro-
stone; tensile cracking off the axes of symmetry for specimens lined
with aluminum; fracture away from cavity boundary for the aluminum-
lined specimen; splitting along a vertical plane, or compressive
(shear) failure, or combined splitting and radial cracking for
biaxially compressed limestone specimens. The tensile stresses
computed at the point and time of fracture were much higher than the
tensile strengths determined from uniaxial tests. In limestone,
maximum tensile stresses from 1.5 to 3.5 times the uniaxial tensile
strength were computed. In marble, this factor varied from 3.7 to
5.0.

CONTENTS

CONTENTS (Cont'd.)

CONTENTS (Cont'd.)

ILLUSTRATIONS

viii

ILLUSTRATIONS (Cont'd.)

ILLUSTRATIONS (Cont'd.)

x

ILLUSTRATIONS (Cont'd.)

xi

ILLUSTRATIONS (Cont'd.)

ILLUSTRATIONS (Cont'd.)

ILLUSTRATIONS (Cont'd.)

ILLUSTRATIONS (Cont'd.)

ILLUSTRATIONS (Cont'd.)

ILLUSTRATIONS (Cont'd.)

ILLUSTRATIONS (Cont'd.)

ILLUSTRATIONS (Cont'd.)

ILLUSTRATIONS (Cont'd.)

ILLUSTRATIONS (Cont'd.)

ILLUSTRATIONS (Cont'd.)

ILLUSTRATIONS (Cont'd.)

ILLUSTRATIONS (Cont'd.)

ILLUSTRATIONS (Cont'd.)

ILLUSTRATIONS (Cont'd.)

This page intentionally left blank.

SECTION I
INTRODUCTION

The design of underground installations capable of with-
standing the effects of explosively generated pressure waves requires
knowledge of the state of stress, strain, deformation and material
response, such as yielding and failure, in the vicinity of the
structure. A great deal of theoretical and experimental work has
been performed to determine stress distributions around disconti-
nuities of varying geometry, for various loading conditions (static,
dynamic) and material response (elastic, viscoelastic). However,
the intrinsic properties of the rock media surrounding such under-
ground openings and installations have not been adequately taken
into consideration in their analysis and design.

Rocks behave as linear elastic materials when subjected to
relatively low static stress levels in relatively small sizes. At
higher stress levels beyond the elastic limit the analyses mentioned
above are not valid. Tensile and compressive properties of rock are
appreciably different. In tension, they behave nearly linearly to
failure which is of a brittle nature. Compressive failure occurs
at a much higher stress, usually an order of magnitude higher, and
is preceded by plastic flow of the material. In addition, the
inhomogeneity and anisotropy of the material and the presence of
discontinuities, such as dikes, faults, joints and the like, tend
to make the problem more complex.

In designing structures in rock, all intrinsic properties
of the medium must be determined and known, both under laboratory
and in situ conditions and account must be taken of the statistical
variability of some of these properties, especially failure properties.
Stresses, both residual and induced by subsequent loading, must be
analyzed carefully with special attention to stress concentrations
and tensile stresses, in view of the low tensile strength and brittle
behavior or rock. Shear can also be a problem especially along pre-
existing faults.

1

In view of the limitations of theoretical analysis and the difficulty in conducting field experiments an experimental laboratory approach was undertaken. A great deal of useful information can be reaped from small scale experiments with rock or rocklike specimens. This approach has been followed successfully by previous investigators such as Hiramatsu and Ika (Ref. 1), Hoek (Refs. 2,3) and Hawkes and Hollister (Ref. 4). They studied stress distributions and failure around cavities in rock specimens. In particular, Hoek (Ref. 3) proposed a modified Griffith fracture theory to explain failure around openings in rock.

The objective of this investigation is to determine experimentally the state of stress, deformation and failure around lined and unlined circular tunnels or silos in rocks subjected to static loading and compare the results with theoretical analysis. The end goal is the ability to correlate the state of strain, deformation and failure around cavities with stress-strain and ultimate properties of the material obtained from elementary laboratory tests.

Materials investigated were Limestone and Marble with aluminum and hydrostone as liner materials. Experimental techniques used were strain gages, differential transformers and photoelastic coatings. The specimens were tested under both uniaxial and biaxial loadings. Results were not always in agreement with predictions of elasticity theory but, whenever comparisons were possible, agreed well with previous experimental work. One significant result was the demonstration of the advantage of the liner in redistributing and reducing critical stresses. Subsequent sections of this report give background information on the problem and describe results and discussion of each test individually. In the closing section, results are summarized, conclusions are drawn and recommendations for future work are made.

2

SECTION II

STRESS DISTRIBUTION AND FRACTURE AROUND CYLINDRICAL
CAVITIES IN ROCK

1. _Elastic Stress Distribution Around Cylindrical Cavity_

At low stress levels, the behavior of rock is linearly elastic and the stress distribution around a cylindrical cavity can be obtained from the classical Kirsch solution (Ref. 5). The stress distribution around a cylindrical hole in an infinite plate under a homogeneous state of biaxial stress (Fig. 1) is given by

$$\sigma_r = \frac{p}{2}\left[(1+m)(1-\frac{a^2}{r^2}) + (1-m)(1-4\frac{a^2}{r^2}+3\frac{a^4}{r^4})\cos 2\theta\right]$$

$$\sigma_\theta = \frac{p}{2}\left[(1+m)(1+\frac{a^2}{r^2}) - (1-m)(1+3\frac{a^4}{r^4})\cos 2\theta\right] \qquad (1)$$

$$\sigma_{r\theta} = \frac{p}{2}\left[-(1-m)(1+2\frac{a^2}{r^2}-3\frac{a^4}{r^4})\sin 2\theta\right]$$

where

$$\sigma_r, \sigma_\epsilon, \sigma_{r\theta} = \text{radial, tangential and shear stresses, respectively}$$

$$p = \text{free-field vertical stress (in the } \theta = 0° \text{ direction)}$$

$$m = \text{ratio of free-field horizontal to vertical stress}$$

$$a = \text{radius of the hole}$$

$$r, \theta = \text{polar coordinates of point in question}$$

On the boundary of the hole, $r = a$, Eqs. (1) reduce to

$$\sigma_r = 0$$

$$\sigma_\theta = p\left[(1+m) - 2(1-m)\cos 2\theta\right] \qquad (2)$$

$$\sigma_{r\theta} = 0$$

3
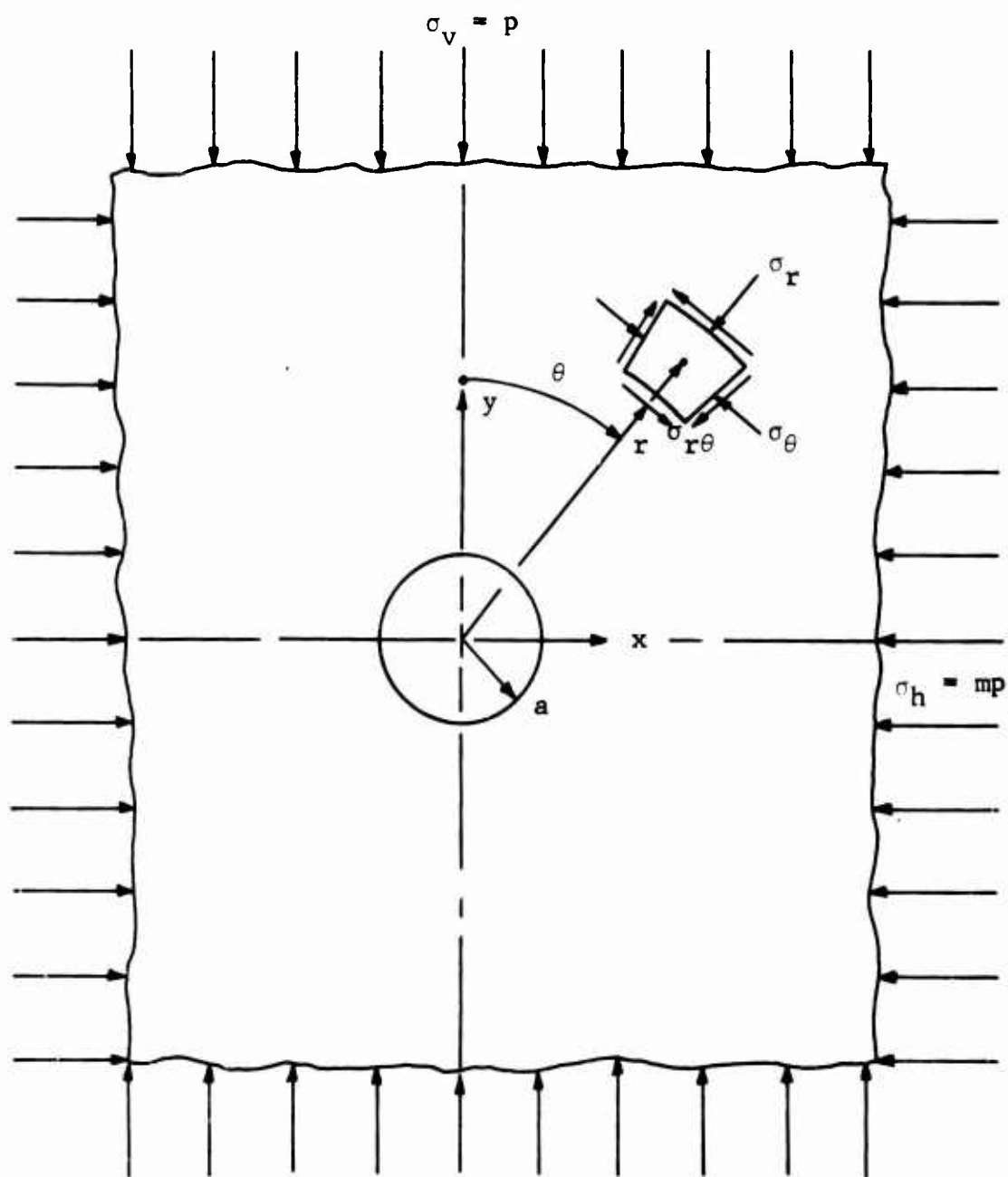
Fig. 1   CIRCULAR HOLE IN AN INFINITE PLATE UNDER A HOMOGENEOUS
STATE OF BIAXIAL STRESS

4

Two cases of biaxiality were considered in this investigation, a uniaxial (m = 0) and a biaxial case corresponding to complete lateral restraint. For the uniaxial case, Eq. (2) above gives

$$\sigma_\theta = p (1 - 2 \cos 2\theta) \tag{3}$$

For the biaxial condition corresponding to full lateral restraint, the lateral (horizontal) strain must be zero:

$$\varepsilon_x = \frac{1}{E} \left[\sigma_x - \nu \sigma_y - \nu \sigma_z \right] = 0 \tag{4}$$

For an infinite thin plate (plane stress)

$$\sigma_z = 0$$

therefore,

$$\sigma_x = m \sigma_y = \nu \sigma_y$$

and

$$m = \nu$$

For an infinite mass (plane strain) the lateral restraint is the same in all directions,

$$\sigma_x = \sigma_z = m \sigma_y \tag{5}$$

and from Eq. (4)

$$m = \frac{\nu}{1 - \nu} \tag{6}$$

For most rocks $\nu \cong 0.25$, therefore,

$$m \cong 1/3$$

The stress distributions along the two axes of symmetry for the two cases of biaxiality discussed here (m = 0 and m = 1/3) are shown in Fig. 2.

Since the original work by Kirsch (Ref. 5) many other problems dealing with finite dimensions of the medium, multiple openings, various shapes of holes, a variety of loading conditions and material properties have been solved. The solution for a finite width of plate was given by Howland (Ref. 6). Comprehensive reviews on the subject of stress distributions around holes have been given by Neuber (Ref. 7) and Savin (Ref. 8).
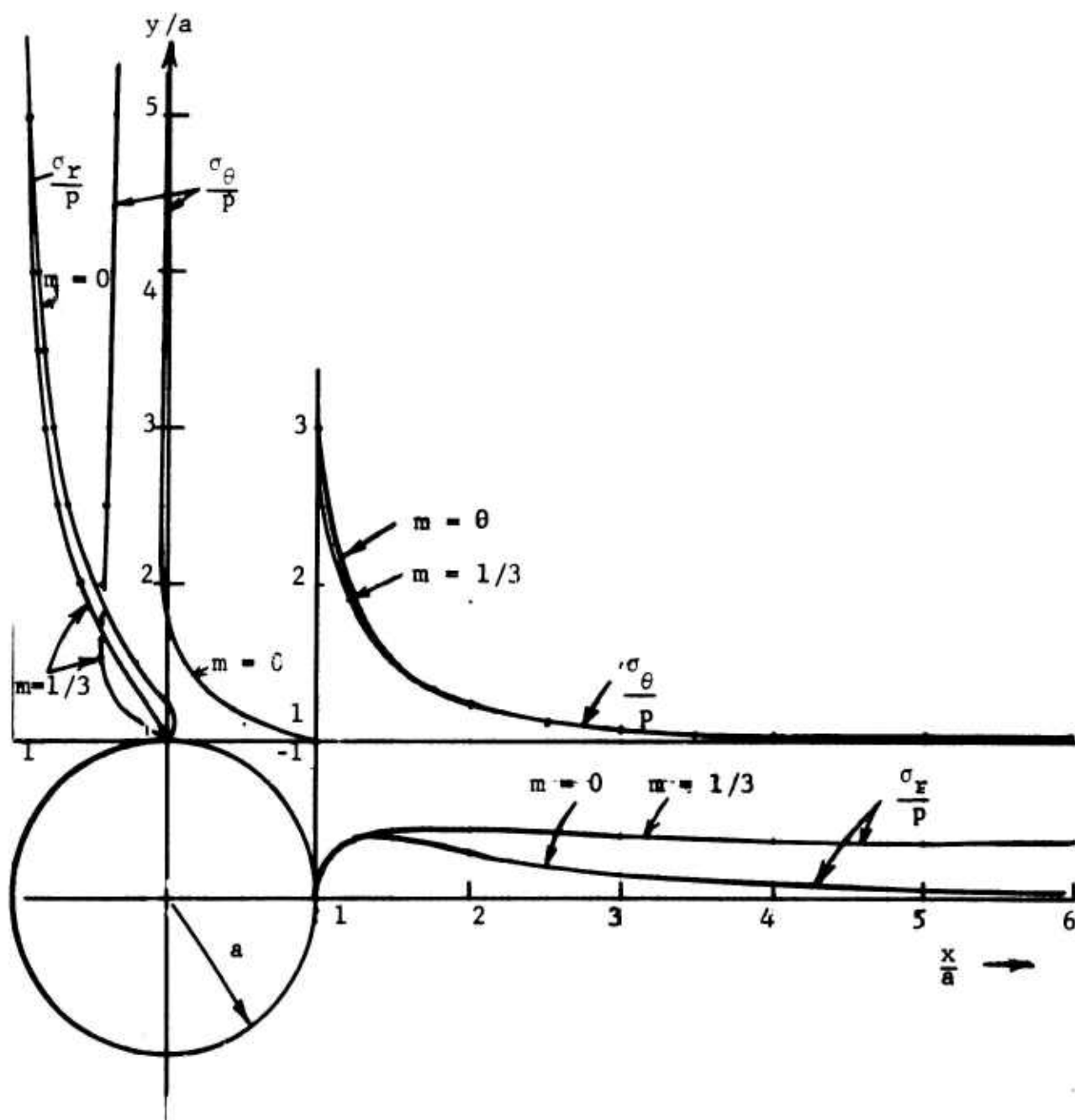
Fig. 2   STRESS DISTRIBUTIONS ALONG TWO AXES OF SYMMETRY AROUND A
CIRCULAR HOLE IN AN INFINITE PLATE UNDER A UNIAXIAL (m = 0)
AND A BIAXIAL (m = 1/3) STATE OF STRESS

6

Several aspects of this problem are of special importance in the design of protective underground structures: geometrical parameters (shape of cavity, presence and type of liner), loading parameters (dynamic loading) and material parameters (elastic, viscoelastic, elasto-plastic media). The dynamic loading aspects of the problem for an elastic medium have been treated analytically by Baron and Matthews (Ref. 9) and experimentally by Daniel and Riley (Ref. 10). One important result from these studies is the fact that the dynamic stress concentration factor exceeds the static one by no more than approximately ten percent. Further studies were conducted later by Daniel (Ref. 11) using viscoelastic media. Results show that the dynamic viscoelastic stress concentration factor can exceed the static one appreciably in the early stages of engulfment of the cavity by the stress wave.

2. Tensile Failure

For the uniaxial loading condition it can be seen in Fig. 2 that tangential tensile stresses equal to the applied vertical pressure p are developed at the crown and bottom points of the cavity. Due to the much lower tensile strength of rocks compared to the compressive strength, failure by cracking takes place at those two points of the cavity. This type of failure occurs not only under uniaxial loading but can take place for a whole range of biaxial compressive loadings, specifically, for

$$0 \leq m < 1/3$$

Hoek (Ref. 2) studied the initiation and propagation of this tensile failure both in rock and glass specimens. He found that for any particular biaxiality ratio the tensile stress at the tip of the crack decreased with increasing crack length and established an experimental relation between crack length and biaxiality ratio. Thus, the length of the crack, once formed, is a function of the biaxiality ratio only and not of the magnitude of the applied load. A similar study using photoelastic models was made by Gettel (Ref. 12).

7

It is generally accepted that tensile failure in rock follows the maximum principal stress theory, i.e., that the tensile stress at which cracking starts is equal to the tensile strength of the material (Refs. 2,3). However, Hiramatsu and Oka (Ref. 1) and the present investigators have found that the tensile stress at failure around the hole can be higher than twice the tensile strength of the material.

Once cracks are formed at the crown and bottom points of the opening, the stresses are redistributed and can only be determined experimentally. Gettel (Ref. 12) showed that the crack causes a slight increase in the compressive stresses along the horizontal axis of symmetry.

Hoek (Ref. 3) used Griffith's theory (Ref. 13) of brittle fracture modified by Mc Clintock and Walsh (Ref. 14) to account for the effects of crack closure and friction between crack surfaces in compression to study the stress distribution and failure around a circular hole. He studied the biaxial loading condition with a biaxiality ratio of 0.15 and calculated principal stress ratios and trajectories (Fig. 3) using the Kirsch solution. On the basis of fracture theory he gave critical crack orientations and fracture contours for both plane stress and plane strain conditions (Fig. 4). At a certain load cracks form at the top and bottom of the hole and propagate to a fixed length as discussed before, 0.55 of the radius for a biaxiality ratio of 0.15. Hoek (Ref. 3) obtained the redistributed principal stresses and trajectories (Fig. 5) and determined new critical crack orientations and fracture contours (Fig. 6) following tensile cracking. Contrary to Gettel (Ref. 12) a slight decrease in maximum compressive stress was observed.

3. Compressive Failure

Following the formation of tensile cracks, the stresses around the hole are redistributed and new areas become critical. One is the point of maximum compression on the boundary of the hole. Failure at this point occurs according to elastic theory, when the maximum compressive stress σ_1 exceeds the uniaxial compressive
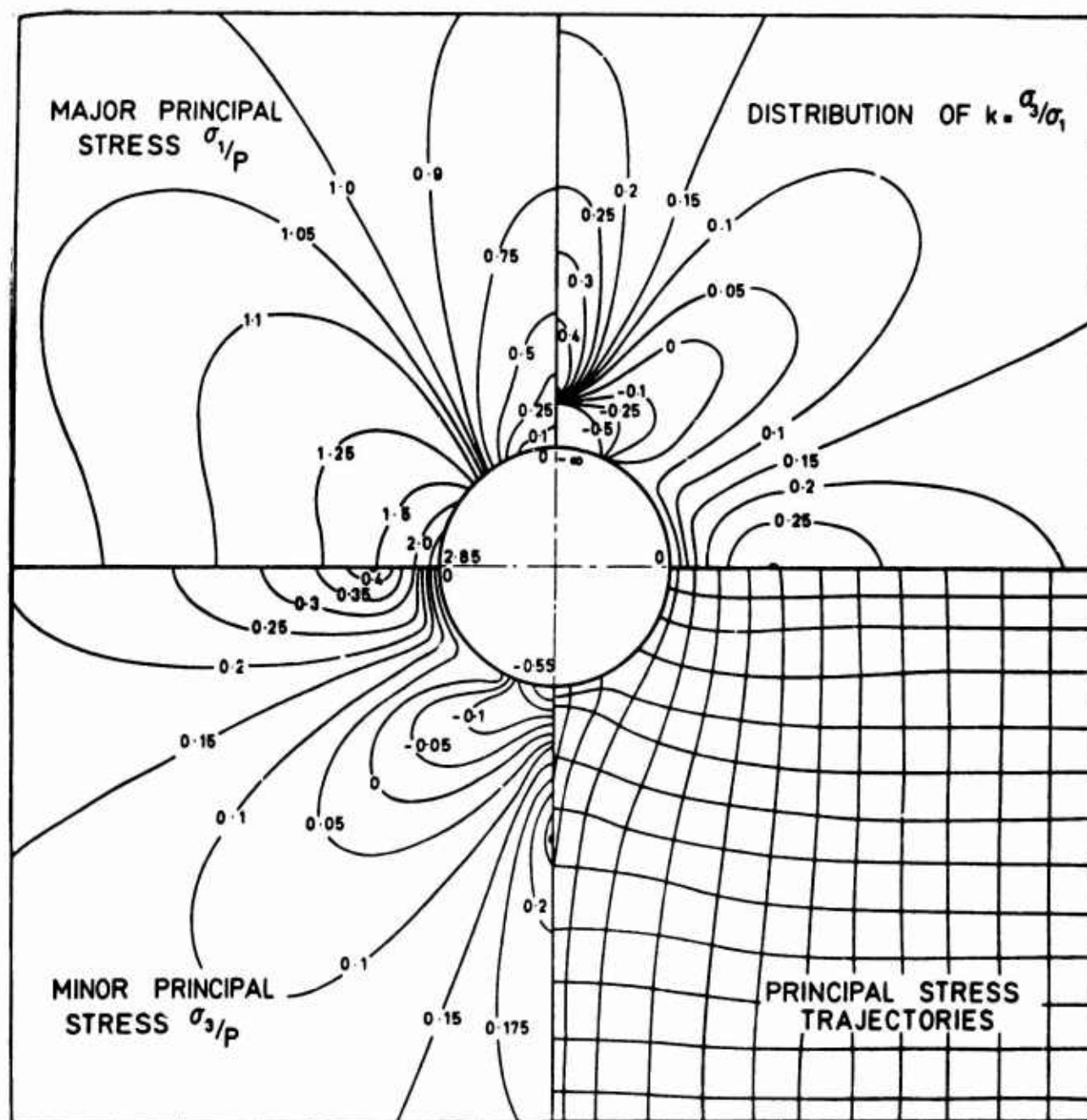
Fig. 3   DISTRIBUTION OF PRINCIPAL STRESSES AND PRINCIPAL STRESS
         TRAJECTORIES IN THE MATERIAL SURROUNDING AN UNFRACTURED
         HOLE FOR A BIAXIALITY RATIO OF m = 0.15.   (After Hoek,
         Ref. 3)

CONTOURS OF VERTICAL EXTERNAL PRESSURE (P/σ_1) REQUIRED FOR FRACTURE AROUND HOLE UNDER PLANE STRESS CONDITIONS

CONTOURS OF VERTICAL EXTERNAL PRESSURE (P/σ_1) REQUIRED FOR FRACTURE AROUND HOLE UNDER PLANE STRAIN CONDITIONS

DOTTED CONTOURS INDICATE FRACTURE IN UNIAXIAL COMPRESSION

CRITICAL CRACK ORIENTATION IN THIS REGION IS AT 18° TO THE PLANE OF THE PLATE MODEL

CRITICAL CRACK ORIENTATION (Ψ_c) WITHIN POTENTIAL FRACTURE ZONE FOR PLANE STRESS

CRITICAL CRACK ORIENTATION (Ψ_c) WITHIN POTENTIAL FRACTURE ZONE FOR PLANE STRAIN

Fig. 4   FRACTURE CONTOURS AND CRITICAL CRACK ORIENTATIONS IN THE MATERIAL SURROUNDING AN UNFRACTURED HOLE FOR A BIAXIALITY RATIO OF m = 0.15.   (After Hoek, Ref. 3)

10

Fig. 5 DISTRIBUTION OF PRINCIPAL STRESSES AND PRINCIPAL STRESS
TRAJECTORIES IN THE MATERIAL SURROUNDING A HOLE WITH CROWN
AND BOTTOM CRACKS FOR A BIAXIALITY RATIO OF m = 0.15.
(After Hoek, Ref. 3)

11

CONTOURS OF VERTICAL EXTERNAL PRESSURE (P/σ_1) REQUIRED FOR FRACTURE AROUND HOLE UNDER PLANE STRESS CONDITIONS

CONTOURS OF VERTICAL EXTERNAL PRESSURE (P/σ_1) REQUIRED FOR FRACTURE AROUND HOLE UNDER PLANE STRAIN CONDITIONS

DOTTED CONTOURS INDICATE FRACTURE IN UNIAXIAL COMPRESSION

CRITICAL CRACK ORIENTATION IN THIS REGION IS AT 16° TO THE PLANE OF THE PLATE MODEL

CRITICAL CRACK ORIENTATION (ψ_c) WITHIN POTENTIAL FRACTURE ZONE FOR PLANE STRESS

CRITICAL CRACK ORIENTATION (ψ_c) WITHIN POTENTIAL FRACTURE ZONE FOR PLANE STRAIN

Fig. 6 FRACTURE CONTOURS AND CRITICAL CRACK ORIENTATIONS IN THE MATERIAL SURROUNDING A HOLE WITH CROWN AND BOTTOM CRACKS FOR A BIAXIALITY RATIO OF m = 0.15. (After Hoek, Ref. 3)

12

strength of the material. In reality, the apparent compressive stress at failure may be somewhat higher due to inelastic effects and size effects.

Following the stress redistribution mentioned above, the maximum tensile stress σ_3 moves away from the boundary. The location and magnitude of this tensile stress is a function of the biaxiality ratio m. The Griffith theory, as modified by Hoek (Ref. 3), predicts the maximum compressive stress ratio $\frac{\sigma_1}{\sigma_t}$ or applied stress ratio $\frac{P}{\sigma_t}$ at failure as a function of the local biaxiality ratio $\frac{\sigma_3}{\sigma_1}$. Depending on the applied load biaxiality (m) the local stress biaxiality (k) may reach a critical value before compressive failure occurs on the boundary. This was the case for m = 0.15 where Hoek (Ref. 3) predicted such weak points away from the boundary (Fig. 6) and observed them experimentally.

Following compressive failure on the hole boundary, the stresses are further redistributed. Such failure has been treated as equivalent to the formation of a sharp notch with a resulting increase in stress concentration. Results of a photoelastic study following the formation of this notch were obtained by Hoek (Ref. 3) and are shown in Figs. 7 and 8.

For a certain range of load biaxiality, including the biaxiality ratios of 0.25 and 0.33 studied by Hiramatus and Oka (Ref. 1) and in the present investigation, the first and only failure observed is compressive failure at the point of maximum stress concentration. Compressive failures were observed for marble at loads approximately three times as high as those causing tensile cracking under uniaxial conditions (Ref. 1). Furthermore, compressive failure occurred at theoretical maximum stresses only slightly higher than the compressive strength of the material.

4. Elastic Stress Distribution Around a Lined Circular Hole

The stress distribution around a hole can be drastically altered by the presence of a liner of a different material. Critical stresses can be reduced appreciably and the fracture loads increased. The effect of a liner on the strength of the cavity is primarily a function of the thickness, modulus and strength of the liner material. A comprehensive analysis of stresses around lined holes has been given by Savin. (Ref. 8.) For a lined hole in an infinite plate under a

13
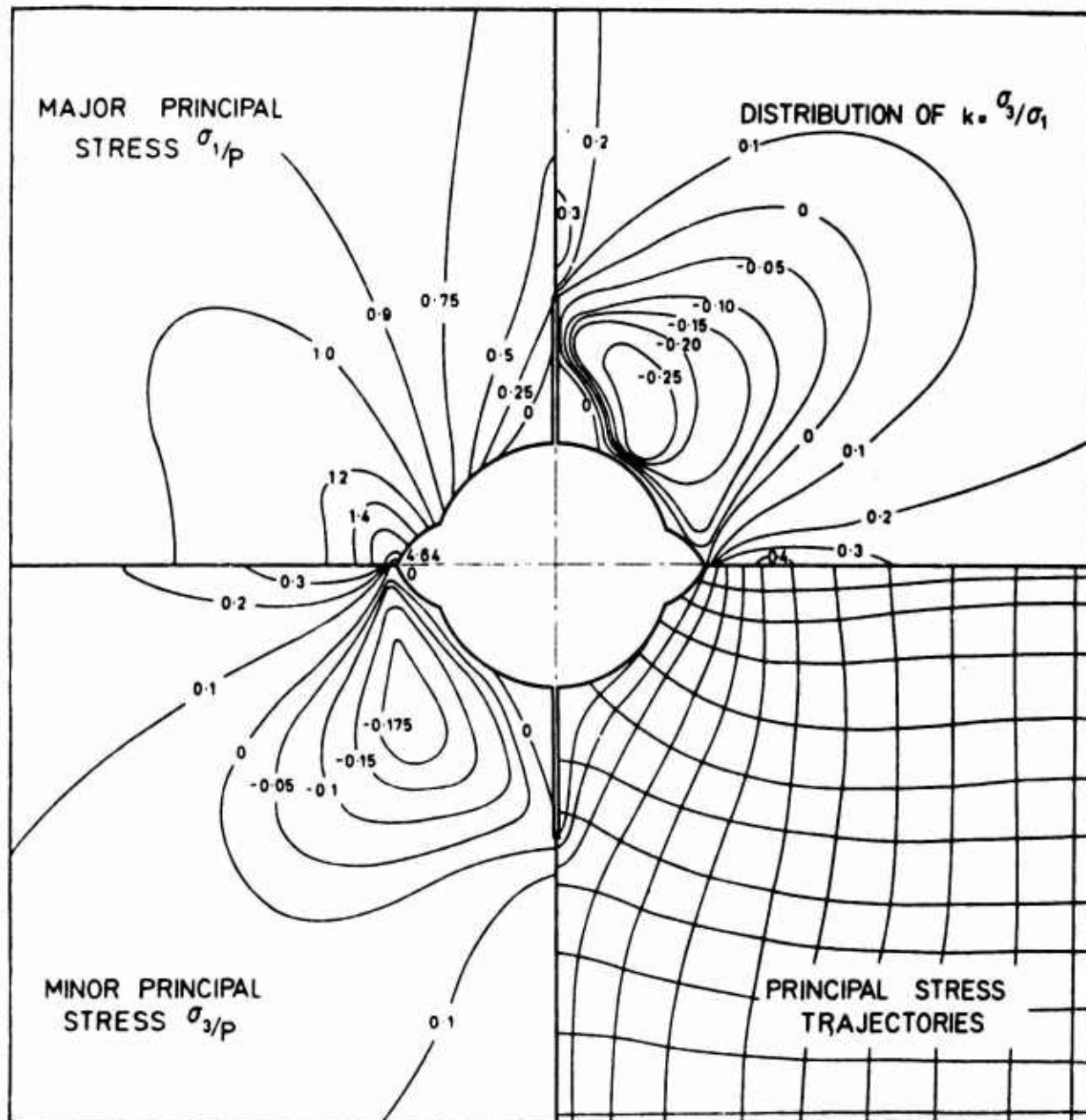
Fig. 7 DISTRIBUTION OF PRINCIPAL STRESSES AND PRINCIPAL STRESS
TRAJECTORIES IN THE MATERIAL SURROUNDING A HOLE WITH CROWN
AND BOTTOM CRACKS AND SIDE FRACTURE FOR A BIAXIALITY RATIO
OF m = 0.15. (After Hoek, Ref. 3)

14
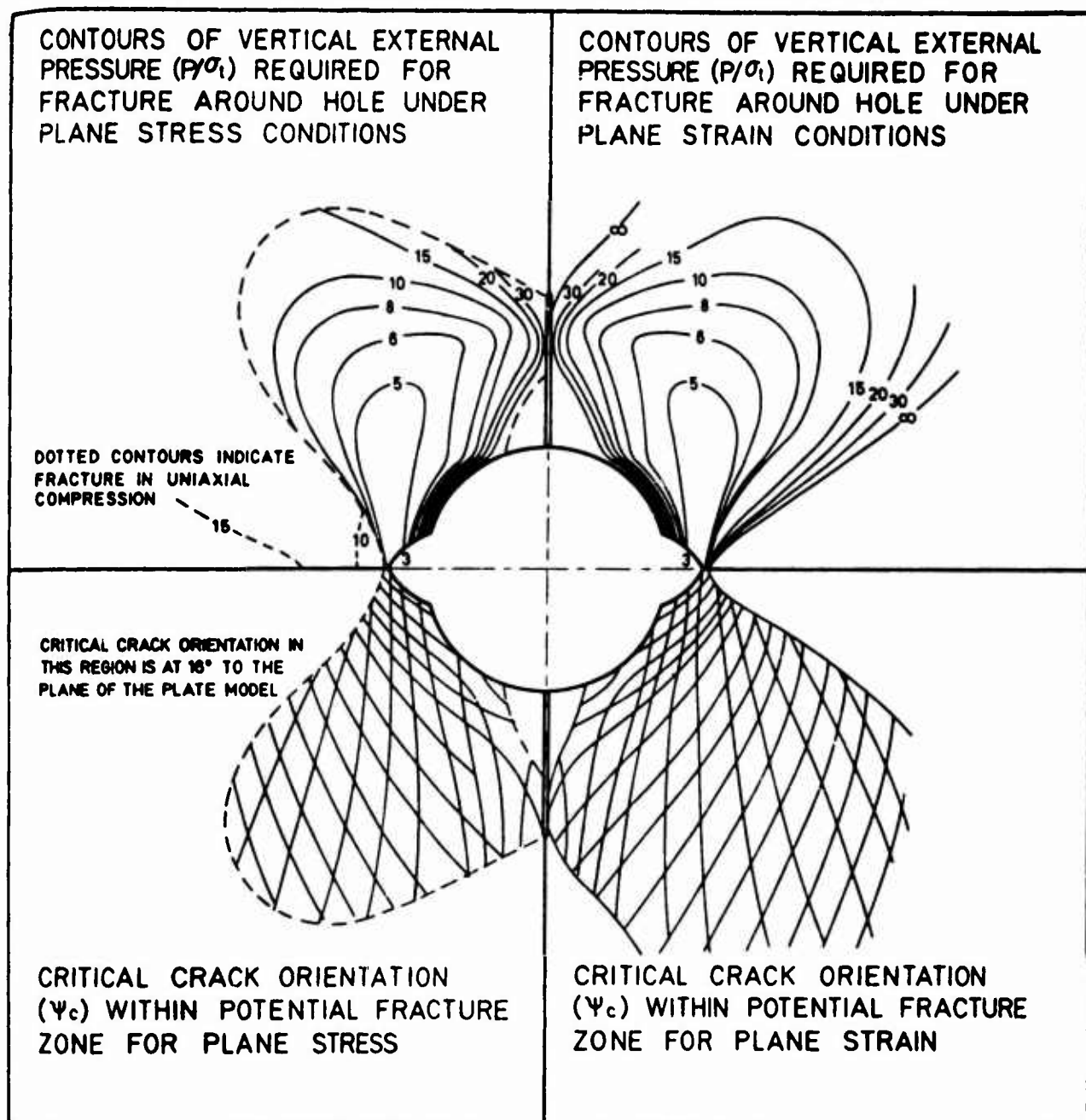
Fig. 8   FRACTURE CONTOURS AND CRITICAL CRACK ORIENTATIONS IN THE
MATERIAL SURROUNDING A HOLE WITH CROWN AND BOTTOM CRACKS
AND SIDE FRACTURE FOR A BIAXIALITY RATIO OF m = 0.15.

(After Hoek, Ref. 3)

15

homogeneous uniaxial state of stress (Fig. 9), the stresses are:

For the liner, i.e., for $R_1 \leq r \leq R$,

$$\frac{2}{p}\sigma_r = (a_1 - \frac{b_{-1}}{2} \cdot \frac{R^2}{r^2}) + (\frac{b_1}{2} - 2a_{-1} \frac{R^2}{r^2} - \frac{3}{2} b_{-3} \cdot \frac{R^4}{r^4}) \cos 2\theta$$

$$\frac{2}{p}\sigma_\theta = (a_1 + \frac{b_{-1}}{2} \cdot \frac{R^2}{r^2}) - (\frac{b_1}{2} - 6a_3 \frac{r^2}{R^2} - \frac{3}{2} b_{-3} \cdot \frac{R^4}{r^4}) \cos 2\theta \qquad (7)$$

$$\frac{2}{p}\sigma_{r\theta} = (3a_3 \cdot \frac{r^2}{R^2} - \frac{b_1}{2} - a_{-1} \cdot \frac{R^2}{r^2} - \frac{3}{2} b_{-3} \frac{R^4}{r^4}) \sin 2\theta$$

and for the plate, i.e., for $r \geq R$,

$$\frac{2}{p}\sigma_r = (1 - \frac{1}{2} \beta_{-1} \cdot \frac{R^2}{r^2}) + (1 - 2 \alpha_{-1} \cdot \frac{R^2}{r^2} - \frac{3}{2} \beta_{-3} \cdot \frac{R^4}{r^4}) \cos 2\theta$$

$$\frac{2}{p}\sigma_\theta = (1 + \frac{1}{2} \beta_{-1} \cdot \frac{R^2}{r^2}) - (1 - \frac{3}{2} \beta_{-3} \frac{R^4}{r^4}) \cos 2\theta \qquad (8)$$

$$\frac{2}{p}\sigma_{r\theta} = -(1 + \alpha_{-1} \cdot \frac{R^2}{r^2} + \frac{3}{2} \beta_{-3} \cdot \frac{R^4}{r^4}) \sin 2\theta$$

where

$$a_{-1} = \frac{2(1+\kappa)}{D_1} \left[(\frac{\mu}{\mu_1} - 1) + n^6 (1 + \kappa_1 \frac{\mu}{\mu_1}) \right]$$

$$a_1 = \frac{n^2 (1 + \kappa)}{2(\frac{\mu}{\mu_1} - 1) - n^2 \left[(\frac{\mu}{\mu_1} - 1) - (1 + \kappa_1 \frac{\mu}{\mu_1}) \right]}$$

$$a_3 = -\frac{2(1 + \kappa)}{D_1} n^4 (n^2 - 1) (\frac{\mu}{\mu_1} - 1)$$

16
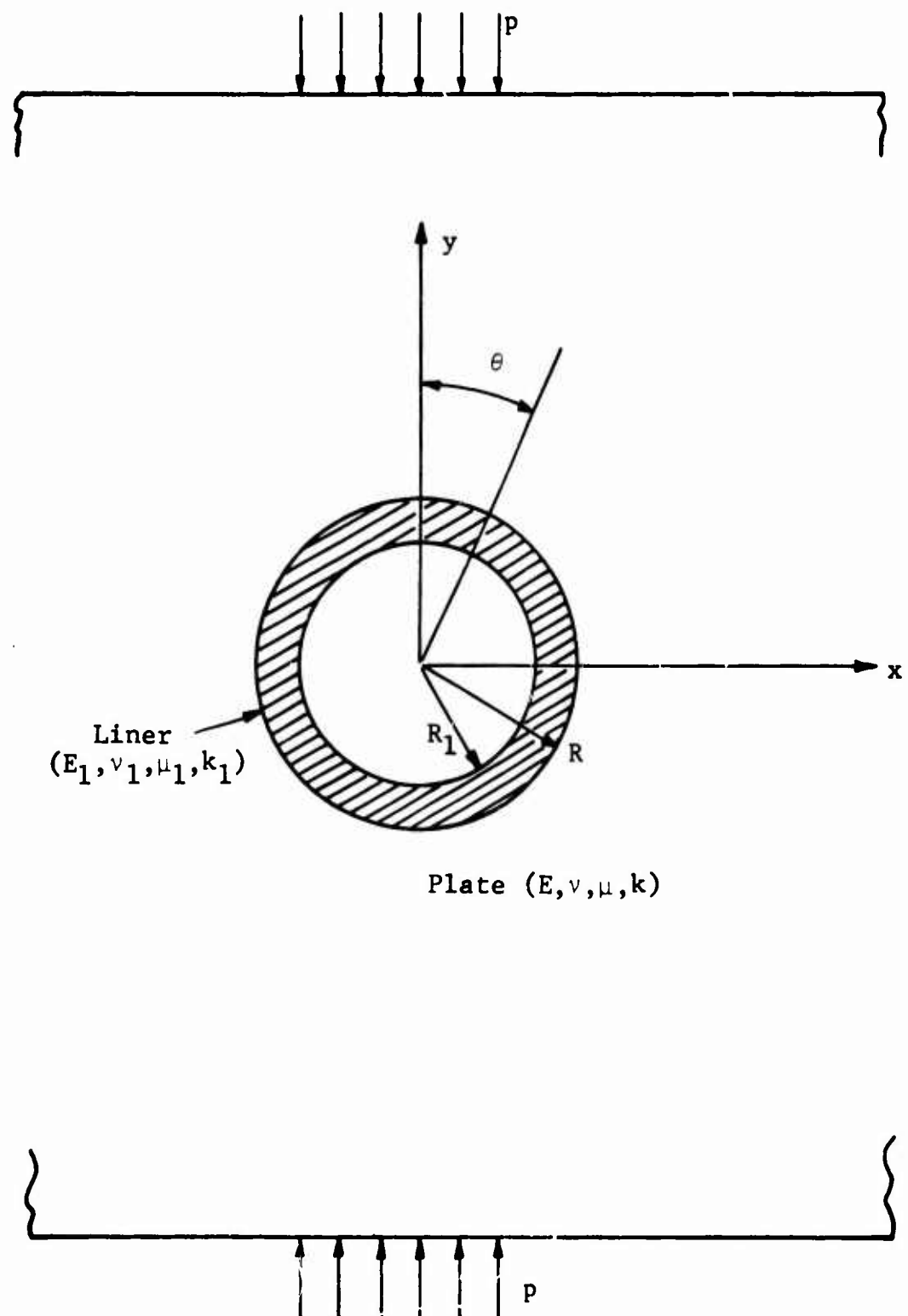
Fig. 9 GEOMETRICAL AND MATERIAL PARAMETERS ENTERING ANALYSIS
OF LINED CAVITY

17

$$b_{-3} = -\frac{2(1+\kappa)}{D_1}\left[\left(\frac{\mu}{\mu_1}-1\right) + n^4\left(1+\kappa_1\frac{\mu}{\mu_1}\right)\right]$$

$$b_{-1} = \frac{2(1+\kappa)}{2\left(\frac{\mu}{\mu_1}-1\right)-n^2\left[\left(\frac{\mu}{\mu_1}-1\right)-\left(1+\kappa_1\frac{\mu}{\mu_1}\right)\right]}$$

$$b_1 = \frac{2(1+\kappa)}{D_1}\left[\left(\frac{\mu}{\mu_1}-1\right)(4-3n^2) + n^6\left(1+\kappa_1\frac{\mu}{\mu_1}\right)\right]n^2$$

$$\beta_{-1} = 2 - \frac{2(n^2-1)(1+\kappa)}{2\left(\frac{\mu}{\mu_1}-1\right)-n^2\left[\left(\frac{\mu}{\mu_1}-1\right)-\left(1+\kappa_1\frac{\mu}{\mu_1}\right)\right]}$$

$$\beta_{-3} = -2 + \frac{2(1+\kappa)}{D_1}\left[\left(\frac{\mu}{\mu_1}-1\right)(4n^6-7n^4+4n^2-1) + \right.$$

$$\left. + n^4(n^4-1)\left(1+\kappa_1\frac{\mu}{\mu_1}\right)\right]$$

$$\alpha_{-1} = 2 - \frac{2(1+\kappa)}{D_1}\left[\left(\frac{\mu}{\mu_1}-1\right)(3n^6-6n^4+4n^2-1) + \right.$$

$$\left. + n^6(n^2-1)\left(1+\kappa_1\frac{\mu}{\mu_1}\right)\right]$$

$$n = \frac{R}{R_1} \quad \text{(see Fig. 9)}$$

$$D_1 = \left(\kappa+\frac{\mu}{\mu_1}\right)n^2\left[\left(\frac{\mu}{\mu_1}-1\right)(3n^4-6n^2+4) + n^6\left(1+\kappa_1\frac{\mu}{\mu_1}\right)\right] +$$

$$+ \left(\kappa_1\frac{\mu}{\mu_1}-1\right)\left[\left(\frac{\mu}{\mu_1}-1\right) + n^6\left(1+\kappa_1\frac{\mu}{\mu_1}\right)\right]$$

$$\mu = \frac{E}{2(1+\nu)} = \text{shear modulus}$$

18

$$\kappa = \frac{3 - \nu}{1 + \nu}$$

Subscript 1 denotes liner material.

The most critical stresses in the plate occur at the interface between the liner and the plate and the most critical stresses in the liner occur on its free surface. The stresses on the free surface of the liner are given by

$$\sigma_r = 0$$

$$2\,\frac{\sigma_\theta}{p} = (a_1 + \frac{b_{-1}}{2}\,n^2) - (\frac{b_1}{2} - 6\,a_3\,\frac{1}{n^2} - \frac{3}{2}\,b_{-3}\,n^4)\,\cos 2\theta$$

$$\sigma_{r\theta} = 0$$

and the stresses in the plate at the interface are

$$\frac{2}{p}\,\sigma_r = (1 - \frac{1}{2}\beta_{-1}) + (1 - 2\alpha_{-1} - \frac{3}{2}\beta_{-3})\,\cos 2\theta$$

$$\frac{2}{p}\,\sigma_\theta = (1 + \frac{1}{2}\beta_{-1}) - (1 - \frac{3}{2}\beta_{-3})\,\cos 2\theta \tag{10}$$

$$\frac{2}{p}\,\sigma_{r\theta} = -(1 + \alpha_{-1} + \frac{3}{2}\beta_{-3})\,\sin 2\theta$$

Stresses for a biaxial state of stress would be obtained by superposition.

Savin (Ref. 8) studied many specific cases of steel plates with copper liners and copper plates with steel liners. Suzuki (Ref. 15) conducted experiments with aluminum plates with brass, copper and mild steel liners and obtained relationships between stress concentration factors, modulus ratio and liner dimensions. Some important conclusions have been derived from the analyses above:

1. The influence of the liner dies out at a distance of 4 to 5 radii from the center of the hole.

2. Both liner and plate stresses decrease with increasing liner thickness. This decrease is sharper for liner thicknesses up to 1/10 of the hole radius.

3. For fixed liner thickness and increasing liner rigidity, the stress concentration in the plate decreases but that in the liner increases.

4. It is possible to design a liner such that the stresses in the plate are lower than in a solid plate without a cavity.

5. The condition of bond between plate and liner is extremely critical. Slight debonding can increase stress concentration appreciably.

SECTION III

EXPERIMENTAL METHODS AND PROCEDURES

1. Test Specimens

The two rock varieties selected for this program were
Indiana limestone and Vermont marble. These rocks were selected
on the basis of availability, uniformity of grain size, moderate
compressive strength (since large specimens and correspondingly
large loads to failure were required for this project), and cost.

The geometry of the typical rock specimen is shown in
Fig. 10. The height of 36 in. was selected so that end effects can
be avoided at the hole location. The width (24 in.) to hole
diameter (4 in.) ratio was judged sufficient to approximate conditions
of an infinite plate (Ref. 6). The typical thickness was 3 in., less
than the hole diameter, to obtain plane stress conditions in the
direction of the axis of the hole. A few specimens were 2-1/2 in.
thick and one was 16 in. thick. Twenty specimens were prepared
and tested altogether, ten limestone and ten marble. The material
and geometrical description of these specimens is given in Table 1.

The rock specimens were obtained as sawn 24 in. x 36 in. x
2-1/2 in. and 24 in. x 36 in. x 3 in. slabs for Indiana limestone
and 24 in. x 36 in. x 3 in. slabs for Vermont marble from the
vendors. A few Indiana limestone slabs were 16 in. thick. All
these were checked to determine if the loading edges were smooth and
parallel to within 0.001 in. When this was not the case, the speci-
mens were machined smooth to that tolerance.

The slabs were clamped in angle irons for ease of handling
in the laboratory. They were very carefully measured and marked to
locate the center of the slads and then drilled through with a
radial drill equipped with a 4 in. diameter water-cooled diamond-
tipped bit. Several precautions were necessary in this operation in

21
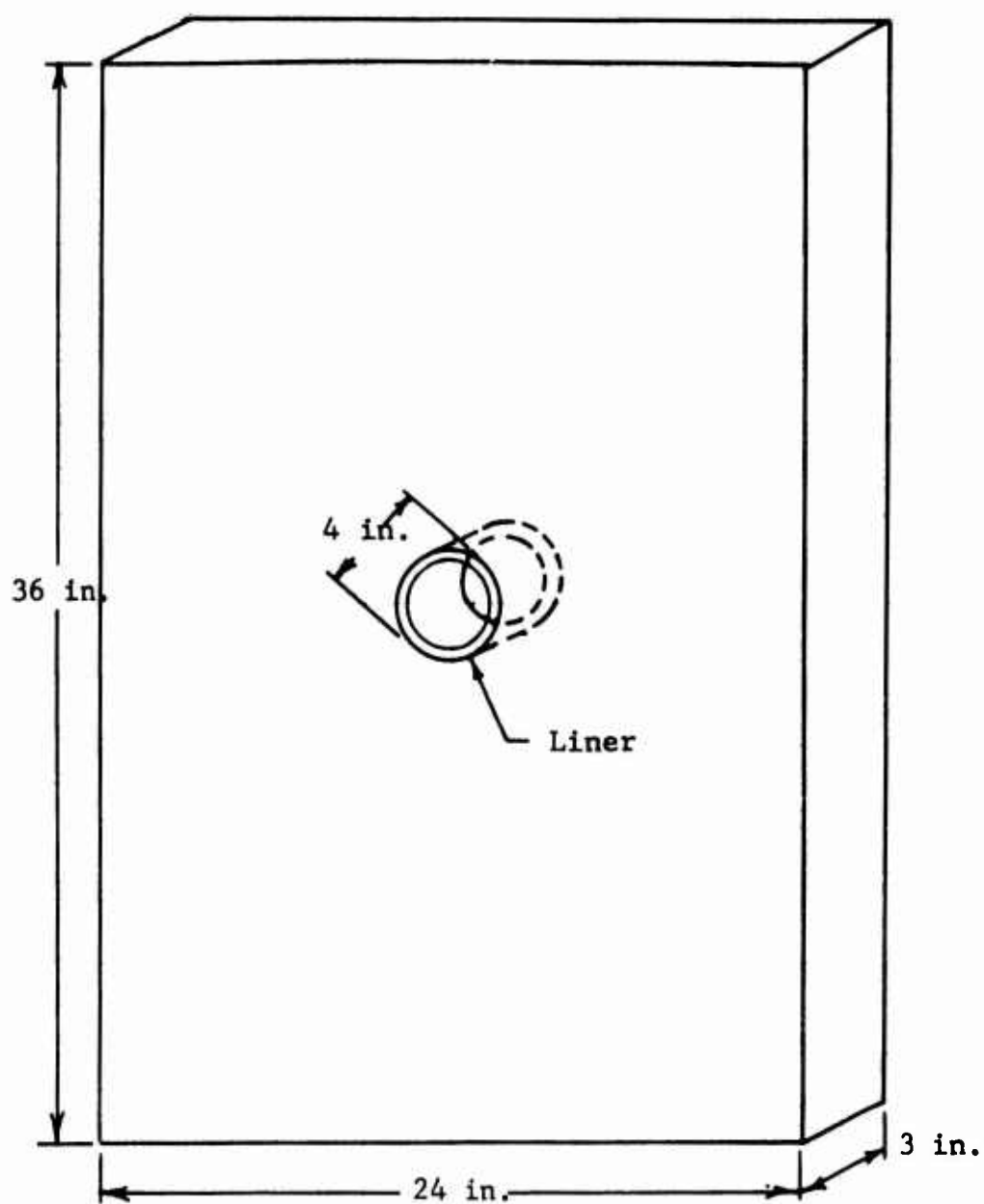
Fig. 10   SPECIMEN GEOMETRY

Table 1

DESCRIPTION OF TEST SPECIMENS

Specimen Number	Material	Loading	Specimen Dimensions	Liner	Liner Wall Thickness
1	Limestone	Uniaxial	24 in. x 36 in. x 2.50 in.	None	-
2	Limestone	Uniaxial	24 in. x 36 in. x 16 in.	None	-
3	Marble	Uniaxial	24 in. x 36 in. x 3.25 in.	None	-
4	Marble	Uniaxial	24 in. x 36 in. x 3.28 in.	None	-
5	Limestone	Uniaxial	24 in. x 36 in. x 3.0 in.	Hydrostone	0.44 in.
6	Limestone	Uniaxial	24 in. x 36 in. x 3.06 in.	Hydrostone	0.44 in.
7	Limestone	Uniaxial	24 in. x 36 in. x 2.54 in.	Aluminum	0.40 in.
8	Limestone	Uniaxial	24 in. x 36 in. x 2.53 in.	Aluminum	0.40 in.
9	Marble	Uniaxial	24 in. x 36 in. x 3.42 in.	Hydrostone	0.44 in.
10	Marble	Uniaxial	24 in. x 36 in. x 3.42 in.	Hydrostone	0.44 in.
11	Marble	Uniaxial	24 in. x 36 in. x 3.32 in.	Aluminum	0.40 in.
12	Marble	Uniaxial	24 in. x 36 in. x 3.30 in.	Aluminum	0.40 in.
13	Limestone	Biaxial	24 in. x 36 in. x 3.08 in.	None	-
14	Limestone	Biaxial	24 in. x 36 in. x 2.55 in.	None	-
15	Marble	Biaxial	24 in. x 36 in. x 3.13 in.	None	-
16	Marble	Biaxial	24 in. x 36 in. x 3.12 in.	None	-
17	Limestone	Biaxial	24 in. x 36 in. x 3.07 in.	Hydrostone	0.44 in.
18	Limestone	Biaxial	24 in. x 36 in. x 3.04 in.	Aluminum	0.40 in.
19	Marble	Biaxial	24 in. x 36 in. x 3.03 in.	Hydrostone	0.44 in.
20	Marble	Biaxial	24 in. x 36 in. x 3.26 in.	Aluminum	0.40 in.

order to avoid broken edges. The specimen was backed by a piece of masonite into which the drill bit passed on coring through the rock. The rotating drill bit was brought into contact with the rock gradually at the beginning, and not withdrawn until the operation was completed. When continuous coring was not possible, e.g. with the 16 in. thick specimen, the drill was withdrawn while rotating, but re-entered while at rest. The specimen was firmly clamped in position so as not to move during the drilling operation.

As described in Table 1, ten specimens of each material were tested under uniaxial and biaxial loading. For the case of uniaxial loading two specimens of each material were tested with unlined cavities and cavities lined with hydrostone and aluminum liners. The remaining eight specimens loaded biaxially were similarly unlined and lined with hydrostone and aluminum liners. Two of each of the unlined specimens were tested.

Specimens 7 and 8 were lined with 2024-T4, T351 aluminum ($E = 10.6 \times 10^6$ psi) while the reinforcing liners of specimens 11, 12, 18, and 20 were of 6061-T6 aluminum ($E = 10 \times 10^6$ psi). Specimens 5, 6, 9, 10, 17, and 19 contained hydrostone ($CaCO_3$) liners. The hydrostone liners were cast as thick-walled cylinders in a mylar-lined mold using a collapsible cardboard core, room temperature cured and subsequently machined to size. These liners were poured using a hydrostone-to-water ratio of three-to-one by weight. Based on uniaxial tests described further on, the hydrostone has a measured modulus of 2.2×10^6 psi, a tensile strength (σ_t) of 610 psi and a compressive strength (σ_c) of 4,400 psi.

The liners were bonded to the rock with their length machined flush with the planes of the specimen. All liners except that of specimen No. 7 were bonded to the rock with Hysol 0151 room temperature curing epoxy resin. The aluminum liner of specimen No. 7 was bonded with plastic steel type B supplied by Devcon Corporation.

24

The liners had a nominal wall thickness of 0.4 inches, the actual dimensions of the individual liners being indicated in Table 1. The radial clearance between unbonded liner and the rock was nominally 0.02 inches.

The properties of the bonding material were not determined by experiment, however, it is estimated that it has a modulus of approximately 0.5×10^6 psi and a tensile strength sufficiently higher than that of limestone and marble. Thus, it is believed that an adequate bond was provided. The effective modulus of the material in thin film form loaded normal to the surface of the film is

$$M = K + \frac{4}{3} G$$

where

$$K = \frac{E}{3(1-2\nu)}, \text{ bulk modulus}$$

$$G = \frac{E}{2(1+\nu)}, \text{ shear modulus}$$

Thus, the bonding film of epoxy has an effective modulus of approximately 10^6 psi. When such a film of 0.040 in. thickness (twice the radial clearance) is loaded by an average stress of 3000 psi it produces a deflection of 0.0001 in which is approximately one percent the maximum diametral deflection measured in the aluminum-lined specimens. Thus, it is believed that no double ring problem exists.

2. Electrical Resistance Strain Gages

The electrical resistance bonded foil strain gage is a grid of parallel miniature foil strips joined by end loops so as to form a single continuous length of metal foil. This gage is manufactured by photo etching the grid on a special alloy foil which has been precisely rolled to a thickness ranging from 0.0001 in. to 0.0002 in. For ordinary use at room temperature, the grid is

25

bonded on a thin epoxy backing to electrically insulate it from the specimen. The gage is bonded at a point of interest on the surface of a specimen with the grid oriented in a given direction. The strains which develop in the specimen due to applied loads are transmitted through the bonding cement to the gage and produce changes in the electrical resistance of the wire grid. Proper instrumentation permits this resistance change to be precisely measured and interpreted in terms of average strain over the length of the grid.

The extreme flexibility in the thin foil grid permits the gage to conform accurately to surface contours and facilitates installation on sharply curved surfaces. Foil gages with small grids (0.015 in. long x 0.020 in. wide) are commercially available for measuring the strain at a point in a strain field where the gradient is very steep; e.g., near the boundary of a hole or in a small fillet.

The electrical strain gage has its axis of greatest sensitivity in the direction of the grid. If the principal directions are known in a biaxial stress field, gages are positioned to measure the principal strains directly. If the principal strains are not known, it is necessary to measure the normal strains in three directions to completely define the state of strain at a point. In a biaxial stress field, measurements are generally made by means of a strain rosette. Rosettes are strain gages which contain two or more strain sensitive elements or grids. These grids are positioned at a given orientation relative to each other on a single backing. The most common two-gage rosettes are manufactured so that the grids are mutually perpendicular. The most common three-gage rosettes are manufactured so that the included angle between the individual grids is 45 degrees.

26

In the present investigation foil strain gages were selected compatible with the rock materials to which they were applied. High elongation gages with a strain range of $\pm$ 10 percent to $\pm$ 20 percent were used. (EP Series, Micromeasurements, Division of Vishay Intertechnology, Inc.) Single element gages selected were of the type EP-08-250AF-120 and were applied at points where the strain was uniaxial and of known direction, such as on the face of the specimen near the edge of the cavity in the tangential direction and on the inside surface of the cavity perpendicular to its axis. Two-gage rosettes selected were of the type EP-08-250TA-120 and were used at points where the principal strain directions were known such as the horizontal and vertical axes of symmetry. Three-gage rosettes of type EP-08-250YA-120 were used on the 45 degree radial lines of the specimen where the principal directions are now known a priori. These high elongation gages have an active gage length of 0.250 in. and a self-temperature compensation of 08, i.e., they are most compatibel with materials having a coefficient of thermal expansion equal to 8 μin./in./°F. Although this does not quite match the coefficients of 4 ± 1 μ in./in./°F for marble and 5 ± 2 μin./in./°F for limestone used, it was the only one available in the high elongation series. However, the errors due to such a discrepancy are negligible. Two-gage rosettes (type EA-13-062TT-120) were used on the edge of the liners. All gages except those used on the aluminum liners were bonded with a room temperature curing cement (W. T. Bean, Epoxy Cement Kit, Type RTC). A primer was applied to the back of the gage prior to bonding (W. T. Bean, EA-gage primer) and a protective coating after bonding (W. T. Bean, Gagekote No. 3).

3. Displacement Transducers

The most commonly used type of displacement transducer is the linear differential transducer. It has the form of a hollow cylinder with three windings, one primary and two secondary, potted in plastic and a movable core of magnetic material supported on a shaft of nonmagnetic material inside the cylinder. The primary winding is excited with the input voltage and the induced voltage in the secondary windings, which is proportional to the displacement of the core, is measured and related to the displacement. The simplest type of differential transformer to use is the DC Differential Transformer which contains a built-in oscillator, phase-sensitive demondulator and filter. This requires a DC input voltage and produces a DC output voltage proportional to the displacement measured. Two such transducers were used in the present investigation to measure the horizontal and vertical diametral changes in the cavity of the loaded specimen. They were linear motion transducers with a $\pm$ 0.100 in. displacement range requiring a 6v DC input voltage (G. L. Collins Corporation SS-102 and SS-103).

The DCDTs were calibrated to establish the voltage-displacement relationship and were mounted in the specimen cavity as shown in Fig. 11. The coils were inserted into specially made cups of Plexiglas and the probes were extended. The assembly of coil and probe was spring-loaded so that the coil pressed against one side of the cavity and the outer end of the probe the other. The DCDTs were carefully aligned by eye guided by the axes of symmetry marked on the face of the specimen. The DCDTs as mounted provided diametral change data for the horizontal and vertical diameters.

4. Recording Instrumentation

Strain gage and DCDT data were recorded by means of a digital data acquisition system. This is a Hewlett-Packard system capable of recording sequentially analog signals from up to 200 channels.

28
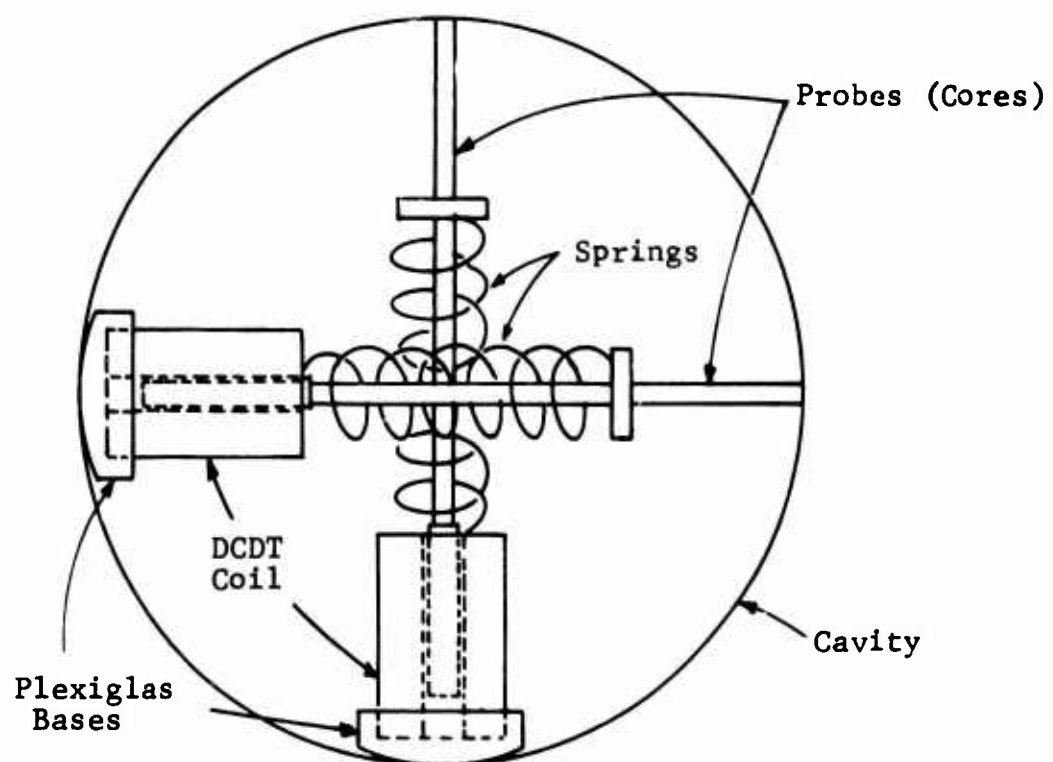
Fig. 11   MOUNTING OF DCDTs FOR MEASUREMENT OF HORIZONTAL   AND VERTICAL
DIAMETRAL CHANGES IN SPECIMEN CAVITY

The basic system consists of a guarded crossbar scanner set, an integrating digital voltmeter and a digital recorder. The scanner accepts up to 200 volts dc at its input terminals and feeds this into the digital voltmeter. The scanner control unit controls the scanning sequence and provides channel identification data to the digital recorder to identify the signal source. The digital voltmeter measures dc voltages and displays the readings together with decimal point, polarity and units on its front panel and supplies the same data to the digital recorder. The latter receives channel identification data from the scanner control unit and measurement data from the digital voltmeter and prints the data on paper tape. The system is capable of scanning and recording data to six place accuracy at a rate of up to nine channels per second.

In the case of strain gage data, the voltage signals must be conditioned before they are fed into the scanner unit. In the present case, each gage element was connected as one arm of a Wheatstone bridge having standard 120 ohm resistors as the other three arms (Fig. 12). All bridges were excited by one dc power supply. However, the excitation voltage of each individual bridge was adjusted by means of a potentiometer span control so that the voltage output of the bridge in μv would be equal to the strain in $\mu in./in.$ This excitation voltage is calculated as follows:

For an excitation voltage V across a bridge, the bridge output ΔE for a gage resistance change of ΔR_g is given by (Ref. 16).

$$\Delta E = V \frac{r}{(1 + r)^2} \frac{\Delta R_g}{R_g} \tag{11}$$

where $r = \dfrac{R_2}{R_1}$ = ratio of resistances of two adjacent arms of the bridge. Noting that

$$\frac{\Delta R_g}{R_g} = \varepsilon\, S_g \tag{12}$$

30
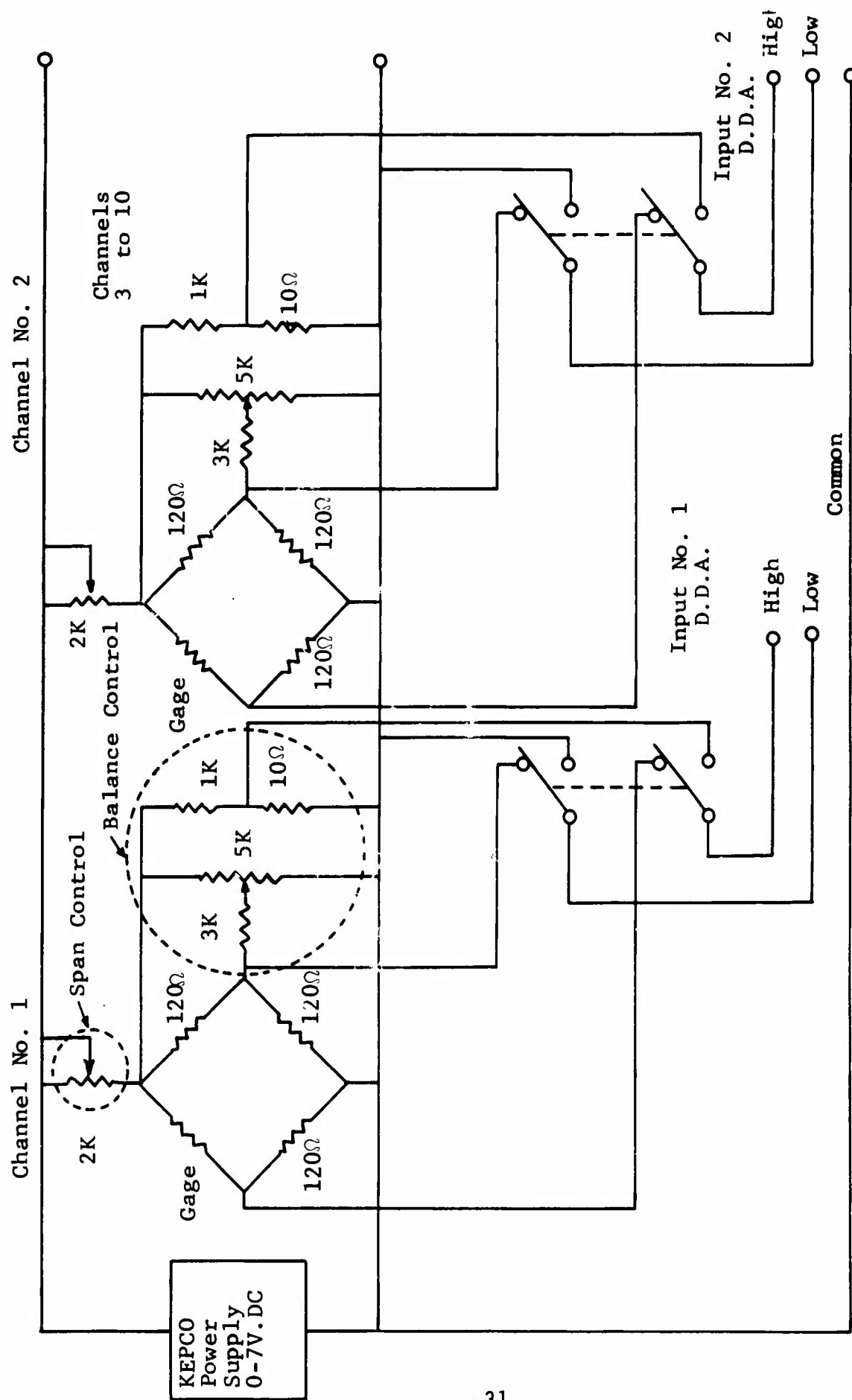
Fig. 12 SCHEMATIC DIAGRAM OF SIGNAL CONDITIONING FOR RECORDING STRAIN GAGE DATA WITH DIGITAL DATA ACQUISITION SYSTEM

31

where S_g = gage factor

ϵ = strain,

$$\Delta E = V \epsilon S_g \frac{r}{(1 + r)^2} \qquad (13)$$

The voltage output will be equal to the strain when the excitation voltage is

$$V = \frac{(1 + r)^2}{r S_g} \qquad (14)$$

In the present case, $r \cong 1$, therefore,

$$V \cong \frac{4}{S_g} \qquad (15)$$

A second potentiometer was provided for balancing of each individual bridge so that the output would be zero at zero load. (Fig. 12)

After balancing the bridge and adjusting the excitation voltage as described previously, the calibration was checked by means of a shunt calibration resistor. This is done by introducing a known resistance in parallel with the gage and comparing the bridge output with the calculated value. Thus, if for a shunt resistance R_c the equivalent resistance change across the gage arm of the bridge will be

$$\Delta R_g = \frac{R_g^2}{R_g + R_c} \qquad (16)$$

and the equivalent strain will be

$$\epsilon = \frac{\Delta R_g}{R_g S_g} = \frac{R_g}{(R_g + R_c) S_g} \qquad (17)$$

32

The voltage output from each balanced and calibrated bridge was received by the scanner unit for the scanning and recording operation. The strain output from the gages was thus obtained directly on the printed tape of the system.

5. Birefringent Coating Method

While the conventional method of transmission photoelasticity is not feasible with opaque rock materials, the birefringent coating technique is ideally suited for determining the surface strains in such materials. Knowledge of the strain field and the stress-strain response for the rock enables evaluation of the stress field. The birefringent coating method has been widely used in recent years in industrial and aerospace applications for measuring the in-plane principal stress or strain differences of metal and composite components. Numerous academic studies have also been conducted to further develop the method and to establish the accuracy of the technique under various practical conditions.

The birefringent coating technique consists of bonding a thin sheet of photoelastic material to the structure, in this case the rock. When the rock structure is loaded, the surface deformations and strains of the rock are transferred to the bonded coating and induce a birefringence in the latter. The birefringence is observed and recorded by means of a reflection polariscope, where the polarized light traverses the thickness of the coating and is reflected back from a reflective layer provided at the interface between the coating and the structure. Within the linear strain-optic range of the coating, the fringe patterns are directly related to the surface deformations (and strains) in the structure whether they are elastic or not. While strain gages provide point-by-point results, photoelastic coatings give full-field information. Moreover, coatings provide instantaneous visual observation of the strain field throughout the loading cycle.

33

At any generic point, the relative retardation fringe order n of the photoelastic coating is related to the difference in the in-plane principal strains in the rock ε_1, ε_2 by the strain-optic law:

$$\varepsilon_1 - \varepsilon_2 = \frac{n\lambda}{2tK} = \frac{nf_\varepsilon}{2t} \tag{18}$$

where

t = coating thickness

λ = wavelength of light

K = strain sensitivity coefficient

f_ε = strain fringe value of coating material

In those cases where the material response is linearly elastic, the observed birefringence in the coating is related to the principal stresses σ_1, σ_2 in the structure (rock) by

$$\sigma_1 - \sigma_2 = \frac{nf_\varepsilon}{2t} \frac{E}{(1 + \nu)} \tag{19}$$

where E and ν are the elastic modulus and Poisson's ratio of the material.

The accuracy of the coating technique is influenced by the mismatch in Poisson's ratio between the rock and coating. While the Poisson's ratio for the rock materials was smaller than that of the coating, the mismatch effect can be minimized by using thin coatings as was done here. However, thin coatings produce fewer fringes as can be seen from Eq. (18). The mismatch in Poisson's ratio becomes significant over a transition zone between a free boundary of a specimen and the internal region.

On a free boundary the tangential strains in the specimen and the coating are the same

$$\varepsilon_1^c = \varepsilon_1^s \tag{20}$$

34

where superscripts s and c refer to structure and coating, respectively.

The transverse strain in the coating, however, varies from

$$\varepsilon_2{}^c = \varepsilon_2{}^s = -\nu^s \varepsilon_1{}^s \tag{21}$$

at the interface, to

$$\varepsilon_2{}^c = -\nu^c \varepsilon_1{}^c \tag{22}$$

at the free surface. Thus, the observed fringe order, representing an average effect, is a function of both Poisson's ratios and can be expressed as

$$n = \left[\frac{1 + \nu^s + C_\nu (\nu^c - \nu^s)}{f_\varepsilon} \right] 2 t \varepsilon_1{}^s \tag{23}$$

where c_ν is a correction factor ranging in value from 1 at the boundary to zero away from it. The transition region extends for about four coating thicknesses from the boundary and the variation of the correction factor above must be established over this region in order for the analysis to be valid. This transition region of course is reduced by reducing the coating thickness and is completely eliminated when the Poisson's ratio of the rock equals that of the coating.

On a free boundary where $c_\nu = 1$ and the normal and shear stresses vanish, the only nonzero stress is the principal stress parallel to this boundary and is given by

$$\sigma_1{}^s = \frac{n}{2t} E^s \left(\frac{f}{1 + \nu^c} \right) \tag{24}$$

The choice of coating is also influenced by the magnitude of the specimen strains, the requirement being that the strain-optic response of the coating material remain linear throughout the range

35

of rock strains to be measured. In this program, commercial bire-
fringent coating type PS-1-8(0.08 in. thick) supplied by Photo-
elastic, Inc. was used. There sheets were bonded to the rock with
a commercial adhesive, PC-7, obtained from the same supplier. The
size and location of a typical sheet of photoelastic coating is
indicated in Fig. 13. In those cases in which the hole was rein-
forced by a liner, the photoelastic coating extended to the inner
boundary of the liner.

6. Method of Loading

     Of the 20 rock specimens tested, 12 were loaded in uniaxial
compression and eight in biaxial compression, the latter with a
horizontal compressive stress equal to one-third the vertical.

     The first uniaxially loaded specimen (limestone with unlined
cavity) was tested in a 120,000 lb Riehle testing machine (Fig. 14).
However, the capacity of this machine was found to be inadequate
to carry the test to complete destruction of the specimen. The
vertical load in all subsequent tests was applied by means of a
1,000,000 lb Riehle testing machine (Fig. 15). This machine is
equipped with an electro-balance load indicator with an accuraty of
within 0.5 percent and applies a constant rate of strain in five
speed ranges. The compression was transferred from the machine
crosshead to the specimen by means of a specially fabricated rein-
forced I-beam visible on top of the specimen in Fig. 14. A 1/4 in.
thick aluminum plate and a neoprene rubber sheet were placed between
the I-beam and the rock specimen with the rubber sheet in contact
with the rock. A similar rubber sheet was placed between the bottom
of the specimen and the bearing plate. Every effort was made to
grind the loaded surfaces of the rock smooth and parallel. In all
cases, preliminary low load tests were conducted and the far-field
gages were monitored to check uniformity and alignment of the load-
ing. In most cases, some shimming was necessary to insure uniform
loading.
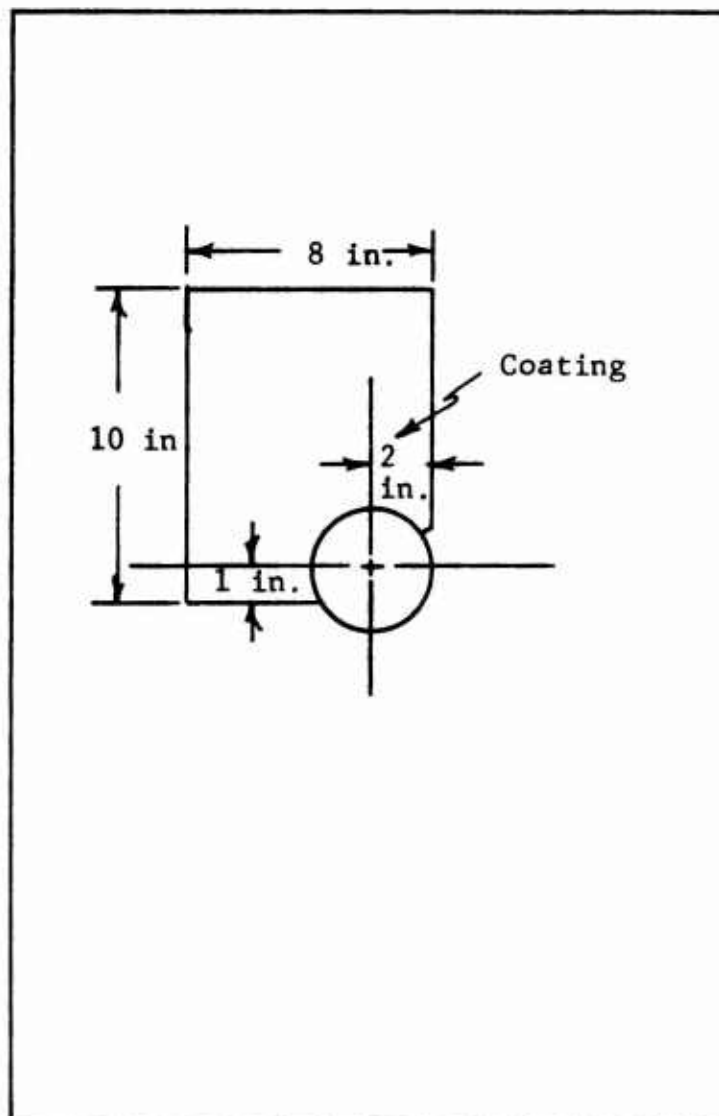
Fig. 13   SIZE AND LOCATION OF BIREFRINGENT COATING
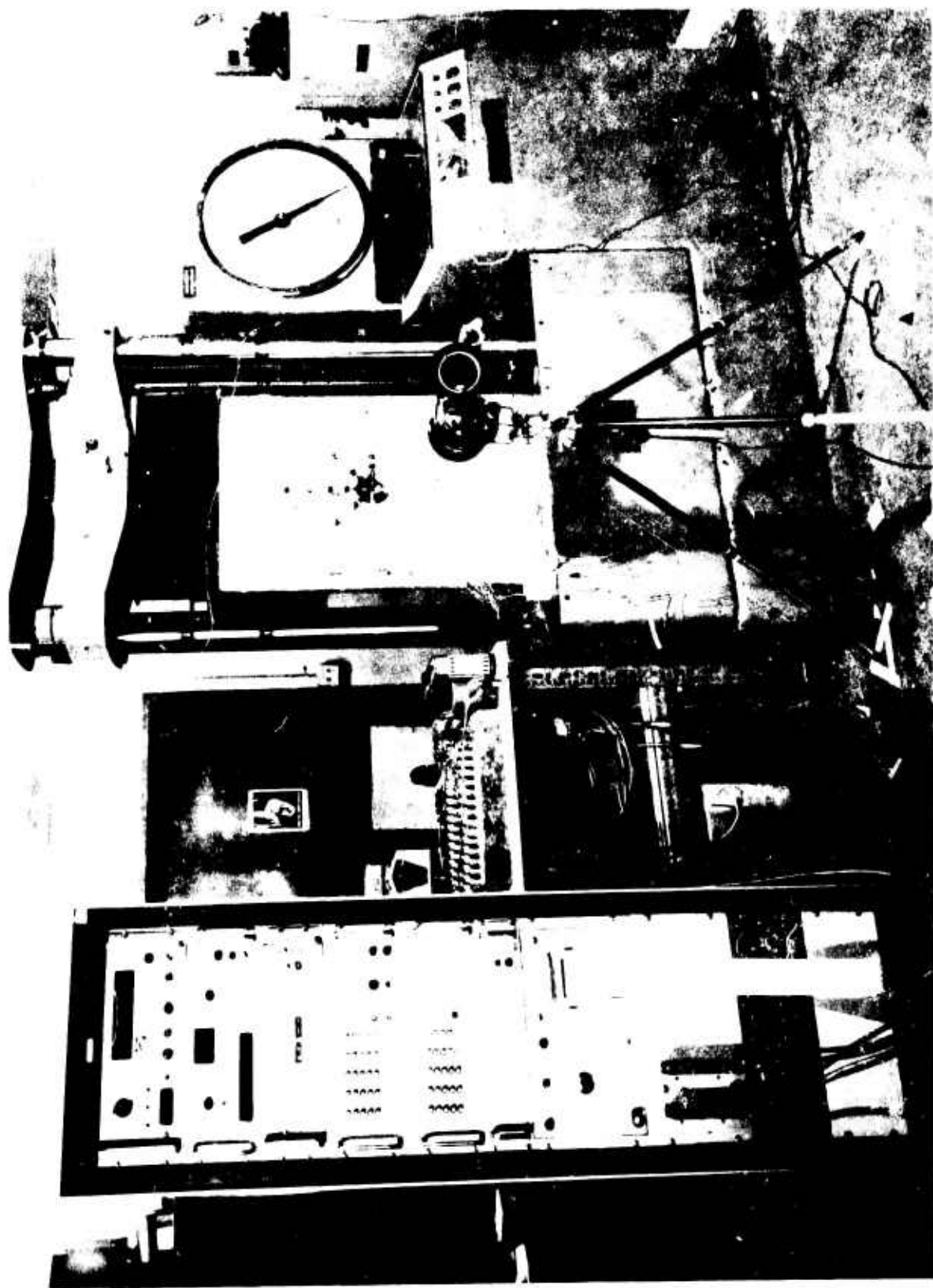
Fig. 14 SPECIMEN IN 120,000 LB TESTING MACHINE
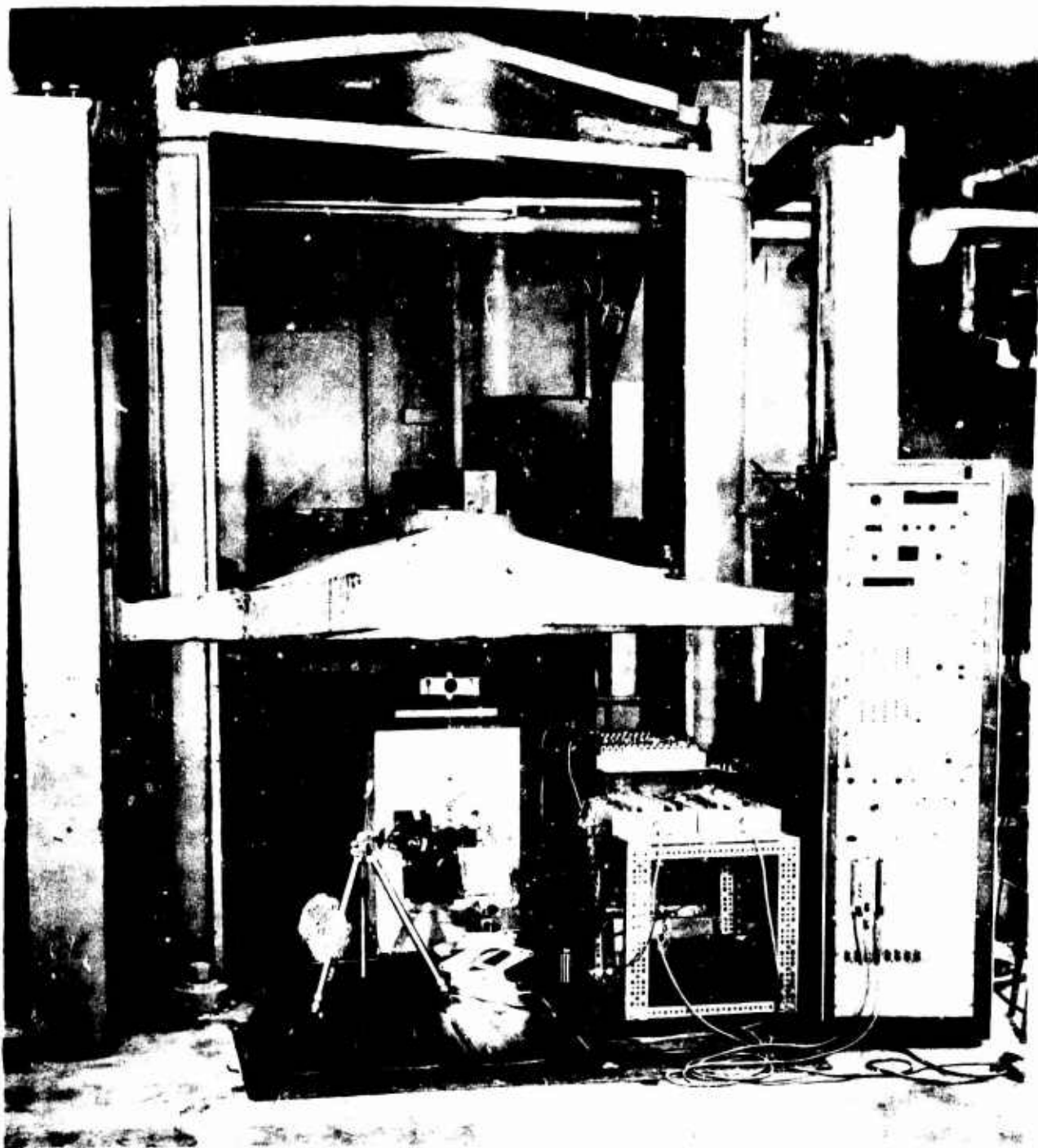
Fig. 15   EXPERIMENTAL SET-UP IN 1,000,000 LB TESTING MACHINE

The transverse (horizontal) loading in the biaxial tests was applied by means of a hydraulic fixture. Figure 16 shows two views of this fixture, the top view showing the complete fixture while in the bottom view it is partially disassembled. The fixture consists of six independent reaction frames stacked one on top of the other. Each frame consists of two parallel steel bars, 3 in. x 3 in. in cross section and 37-3/4 in. long. These steel bars were fastened at each end to short blocks, 3-1/8 in. x 6 in. x 10 in., by means of 1-1/2 in. diameter high strength bolts. One of the frames had a specially designed side member with a wide cutout to provide visibility of the photoelastic coating around the cavity. One end of each reaction frame acted against one vertical edge of the rock specimen while a hydraulic jack was located between the other end of the reaction frame and the specimen. These jacks were of 20-ton capacity, corresponding to a hydraulic pressure of 10,000 psi. (Model RC-251, Enerpac, Inc.) The force from each hydraulic ram was transferred to the specimen by means of an individual 6 in. x 3 in. x 2-1/4 in. steel block. As with the vertical loading, a neoprene rubber sheet and a 1/8 in. thick aluminum plate were placed in contact with the loaded edges to insure uniform load distribution. The rams were positioned and aligned by means of a wooden frame (Fig. 16-b) and were connected to a common manifold through high-pressure hoses. An electric hydraulic pump was used in the beginning of each test to purge the system of air. Subsequently, load increments were applied, simultaneously with the corresponding vertical load increments. This was achieved by means of a hand pump and measured with a Heise hydraulic gage.
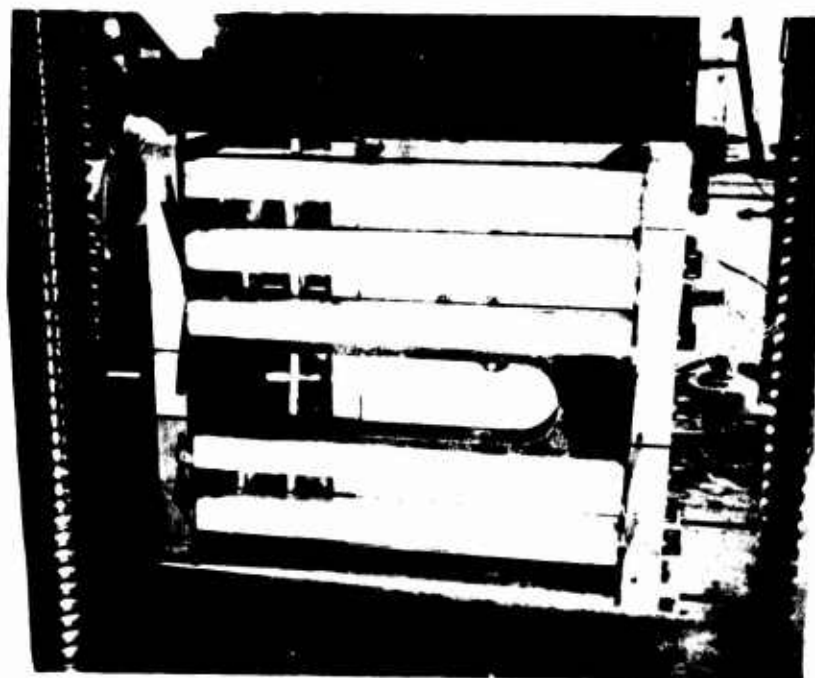
(a)
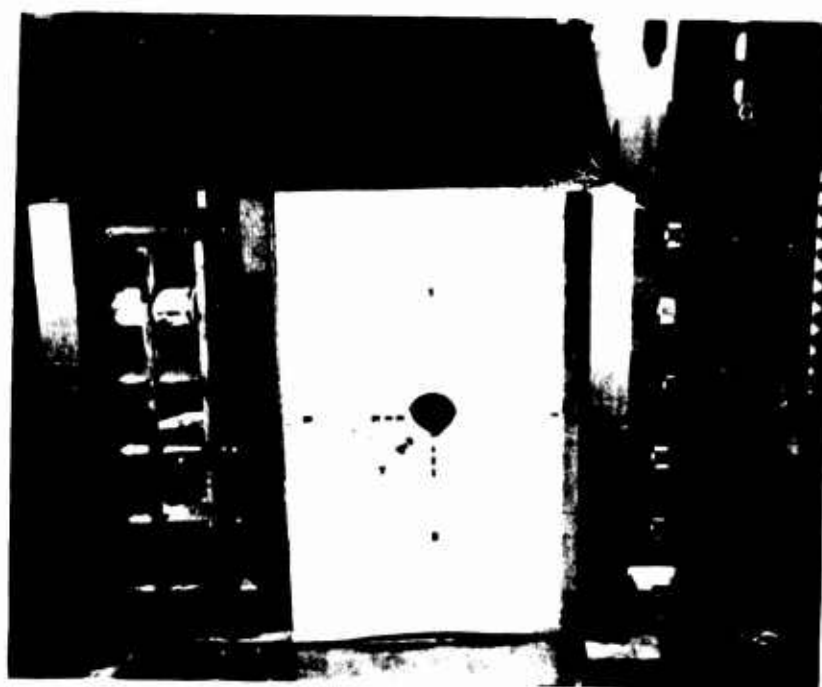
(b)

Fig. 16   FIXTURE FOR TRANSVERSE LOADING OF ROCK SPECIMENS

41

SECTION IV

PROPERTIES OF SPECIMEN MATERIALS

1. Rock Properties

Both rock materials used have some degree of anisotropy due to the nature of their formation. The limestone specimens were cut parallel to the bedding planes so that the properties are the same in the plane of the specimen. In the case of the marble, slight bedding exists in the vertical direction (direction of loading) and normal to the plane of the specimen. Properties of these rock materials were measured along all three principal directions, the direction of loading, direction perpendicular to that of loading and along the axis of the hole.

The following rock properties were determined for both rock materials:

- Tensile strength
- Compressive strength
- Static Young's modulus
- Static Poisson's ratio
- Static modulus of rigidity
- Bulk density

In addition, Mohr envelopes were developed for both materials in order to ascertain their behavior under biaxial stress.

a. Tensile Strength

This property was determined in accordance with the proposed ASTM procedure now under consideration. Since this test has not been released by ASTM, its major features may be briefly indicated.

The test was conducted on NX cores (2-1/2 in. dia) with an aspect ratio (length/diameter) of 2 to 2.5. The sides of the specimens were smooth and straight to within 0.005 in. The ends of the

core were cut parallel and at right angles to its longitudinal axis within 0.25 deg, i.e., approximately 0.01 in. in 2 in. The diameter of the specimens were measured to within 0.01 in. The cores were tested dry under ambient conditions.

Metal end caps, of the same diameter as the cores, were cemented to the specimens, ensuring alignment of the cap axes to within 0.001 in. of the longitudinal axis of the core. Link chains were then attached to these end caps and the specimen pulled in a tensile loading machine. The load was applied continuously, without shock, at a rate so that failure occurred in about 5 to 15 minutes. At lease three tests were conducted for each rock direction investigated.

b. Compressive Strength

This property was also conducted in accordance with the proposed ASTM procedure which is not yet released.

Again, the test specimens were NX cores (2-1/8 in. dia) with aspect ratios of 2 to 2.5. The sides of the specimens were smooth to within 0.005 in., and the ends parallel to each other and perpendicular to the longitudinal axis. The ends were ground and lapped to within 0.001 in., and were perpendicular to the core axis to within 0.25 deg. The diameters of the cores were measured to the nearest 0.01 in. The tests were performed on air-dry specimens, under ambient conditions.

The specimens were placed on spherically seated bearing blocks, and tested in a compression machine. The hardness of each bearing surface directly in contact with the core ends was in excess of Rockwell C58. The specimen and the ball-and-socket axes were carefully aligned prior to each test. The load was applied at a constant rate, continuously, to cause failure in 5 to 15 minutes. At least three tests were performed for each rock direction reported.

43

c. Elastic Constants

A compressometer was mounted on the rock specimen for the compressive strength tests. This instrument has DCDTs mounted in a frame so as to measure axial and radial strains. There were three DCDTs for measuring axial strains and three for radial strains. A few tests were also conducted by affixing strain gages directly on to the rock specimen. This procedure also complies with proposed ASTM requirements. About 15 points were obtained for each stress-strain curve, up to failure. Typical stress-strain plots for Indiana limestone and Vermont marble are shown in Figs. 17-19.

Young's modulus (E) is, of course, obtained directly from the slope of the axial stress (σ_a)-strain (ε_a) curve, i.e.,

$$E = \frac{\sigma_a}{\varepsilon_a} \tag{25}$$

Poisson's ratio (ν) is given by the ratio of the lateral strain (ε_r) to axial strain (ε_a), i.e.,

$$\nu = -\frac{\varepsilon_r}{\varepsilon_a} \tag{26}$$

The negative sign implies that the radial strain is tensile on applying a compressive axial strain.

Modulus of rigidity (μ) was computed from the simple ralation

$$\mu = \frac{E}{2(1+\nu)} \tag{27}$$

d. Bulk Density

This is readily determined by weighing each core specimen prepared for the tests and dividing this by the volume.

e. Mohr Envelopes

These were prepared by subjecting linear 1 in. dia x 2 in. long rock specimens to triaxial stress. The axial stress to failure for

44
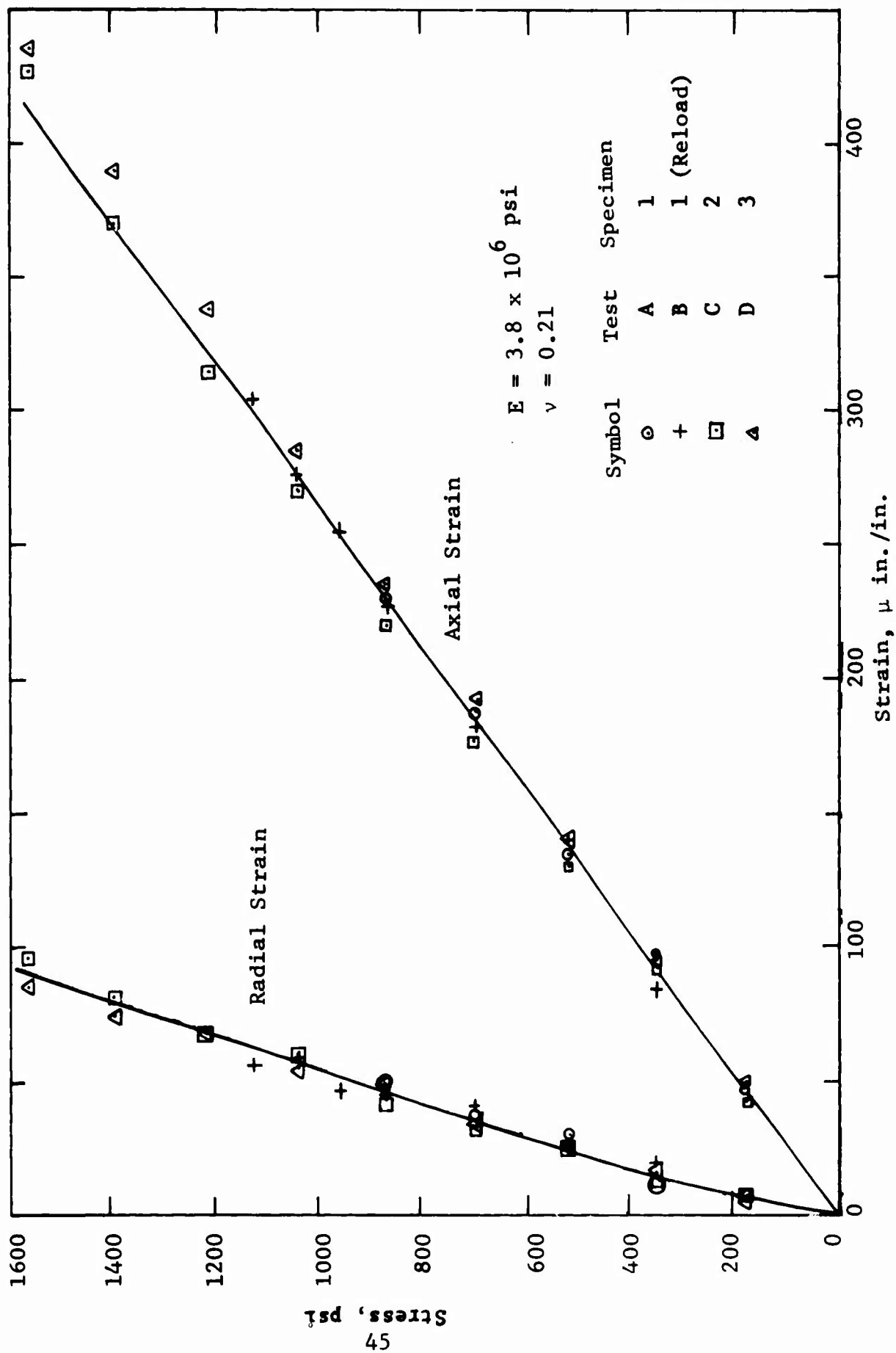
Fig. 17 TYPICAL STRESS-STRAIN CURVES FOR INDIANA LIMESTONE (ALONG DIRECTION OF LOADING)

45
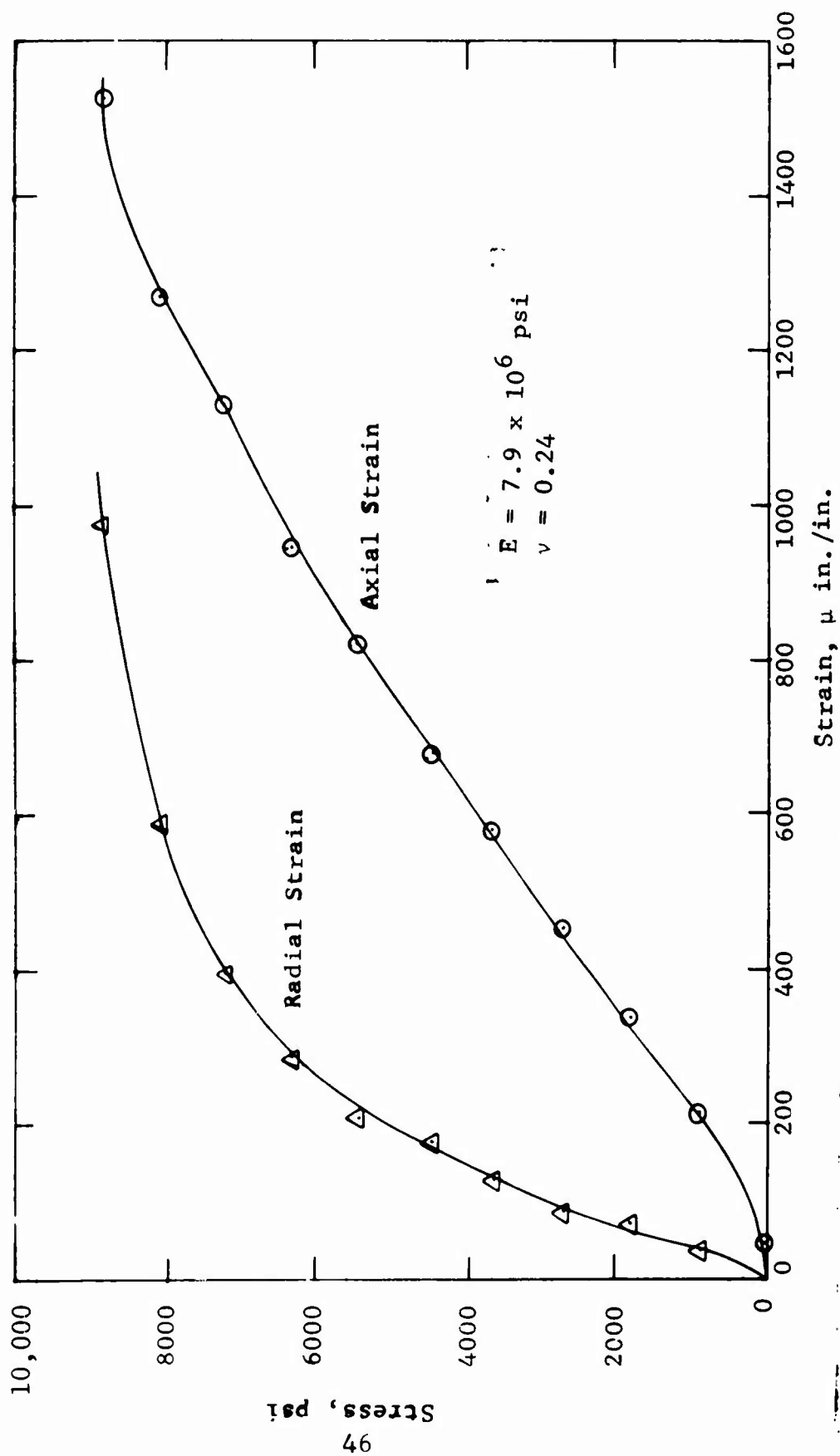
Fig. 18 TYPICAL STRESS-STRAIN CURVES FOR VERMONT MARBLE (ALONG DIRECTION OF LOADING)

$E = 7.9 \times 10^6$ psi
$\nu = 0.24$

Axial Strain

Radial Strain

Strain, μ in./in.

Stress, psi

46
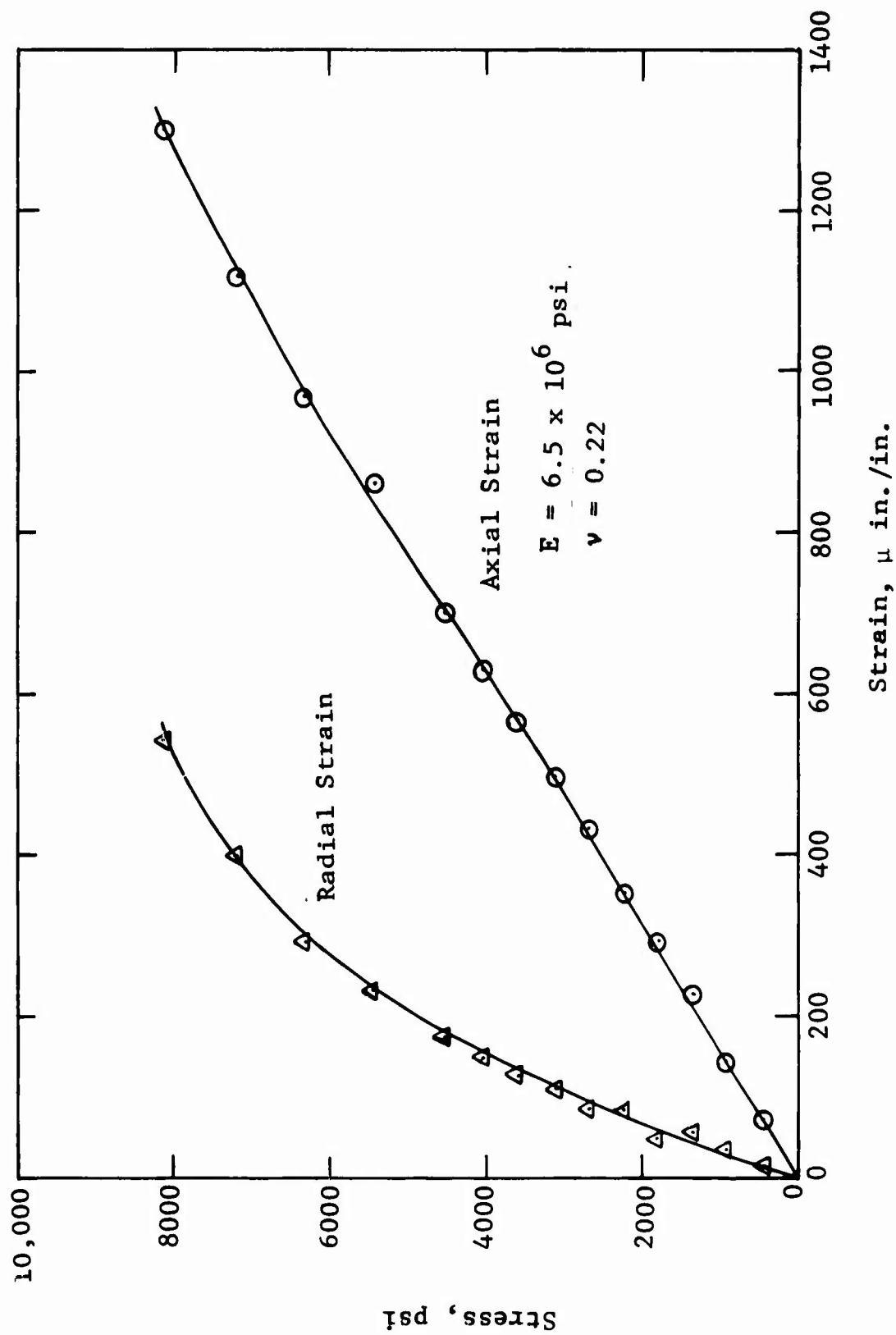
Fig. 19   TYPICAL STRESS-STRAIN CURVES FOR VERMONT MARBLE (PERPENDICULAR TO DIRECTION OF LOADING)

47

each confining pressure is noted and used to draw a Mohr circle.
In addition, Mohr circles are plotted from uniaxial tensile and
compressive strength data. The curve tangential to all these
circles is the Mohr envelope.

For any point subjected to a biaxial state of stress, the
stress conditions along any plane are given by

$$\sigma = \frac{\sigma_1 + \sigma_3}{2} + \frac{\sigma_1 - \sigma_3}{2} \cos 2\theta \tag{28}$$

and

$$\tau = -1/2(\sigma_1 - \sigma_3) \sin 2\theta \tag{29}$$

where

σ = normal stress

τ = shear stress

σ_1 = maximum principal stress

σ_3 = minimum principal stress

θ = is the angle of inclination of the plane
under consideration with respect to σ_1.

If we put $\sigma_m = (\sigma_1 + \sigma_3)/2$, $\tau_m = (\frac{\sigma_1 - \sigma_3}{2})$, and eliminate θ
between these two equations, we get

$$(\sigma - \sigma_m)^2 + \tau^2 = \tau_m^2 \tag{30}$$

This is the equation of Mohr's circle.

Mohr's failure theory postulates that a material will fail
when the shear stress τ on a fracture or slip plane increases beyond
a value dependent upon the normal stress σ on that plane, i.e., at
failure

$$\tau = f(\sigma) \tag{31}$$

or when the largest tensile principal stress (σ_1) attains a limiting
value (i.e., its tensile strength, σ_t), i.e.

$$\sigma_1 = \sigma_t$$

These relationships must be determined experimentally, and are in fact the Mohr envelopes generated as indicated earlier. Mohr's theory implies that the intermediate stress, σ_2, does not influence failure.

It can be readily shown that when the Mohr envelope is elliptical it coincides with the failure curve predicted by Griffith's criterion. When the envelope becomes a straight line, it represents the Navier-Coulomb theory.

In order to conduct the triaxial test experiments mentioned above, the ends of the rock cores are ground and lapped smooth. The specimens are then inserted in a polyethylene tube and placed in a triaxial cell. A schematic of this cell is shown in Fig. 20. Hydraulic oil is pumped into the annulus around the circumference of the specimen to provide the confining pressure. The entire cell is placed on a spherically seated block, and the core subjected to axial stress by means of a compression loading machine. Cores from at least two directions were taken from each rock type and triaxial tests run at 3 or 4 confining pressure levels.

Mohr's envelopes developed for Indiana limestone are given in Figs. 21 and 22, and those for Vermont marble are depicted in Figs. 23 and 24. Photographs of Indiana limestone cores retrieved from the triaxial tests are shown in Fig. 25, and those for Vermont marble in Fig. 26. Shear planes of failure and barreling of the cores at high confining pressures are evident in these figures, although the former are more readily observed in Fig. 25 and the latter is more pronounced in Fig. 26.

f. Mechanical Properties Data

Property data for Indiana limestone may be tabulated as follows:

1. Static Young's Modulus (E)
    (along direction of loading) 3.8×10^6 psi
    (perpendicular to direction of loading) 2.3×10^6 psi
    (along axis of hole) 3.6×10^6 psi

49
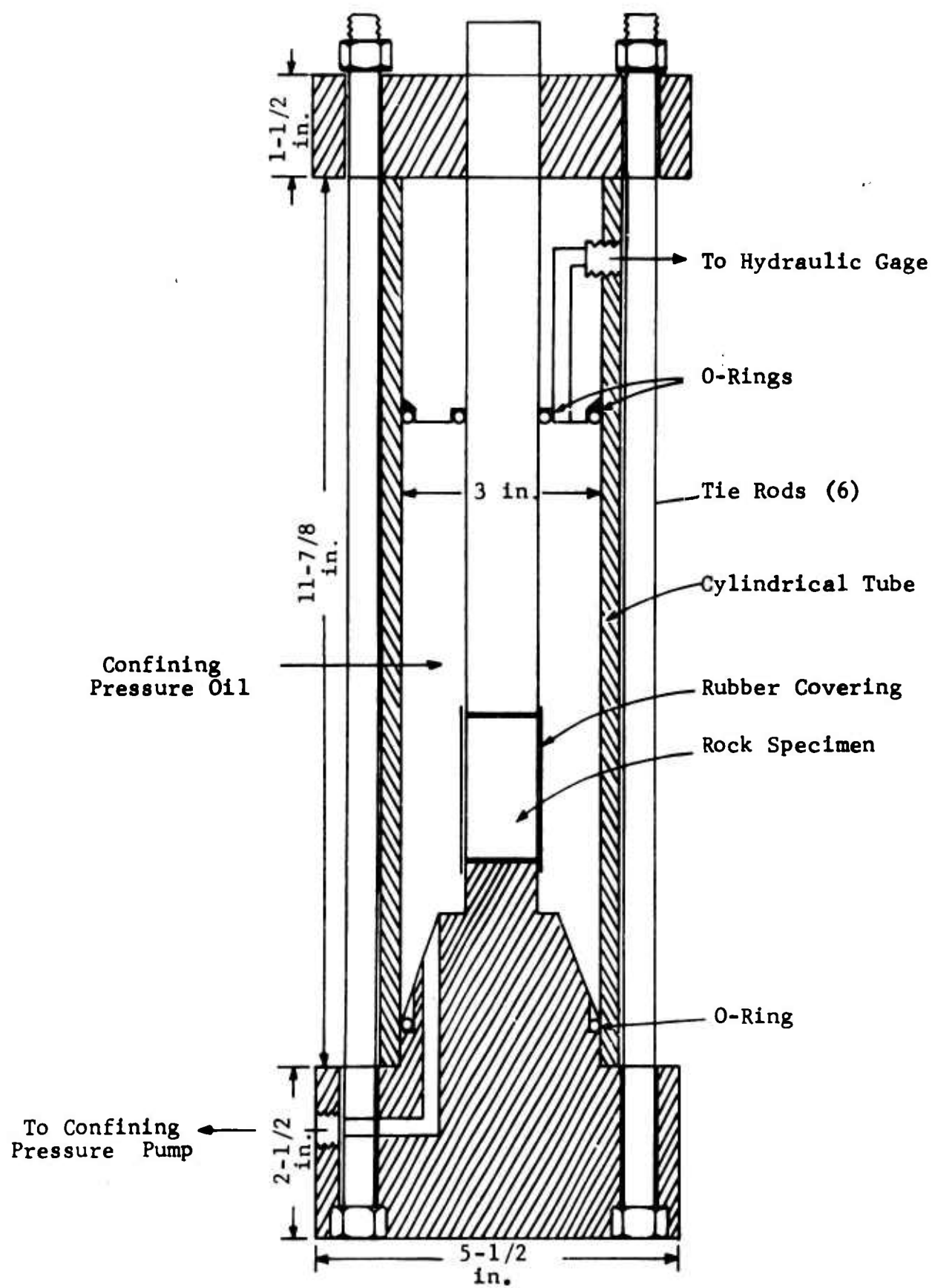
Fig. 20   TRIAXIAL TEST CELL

50
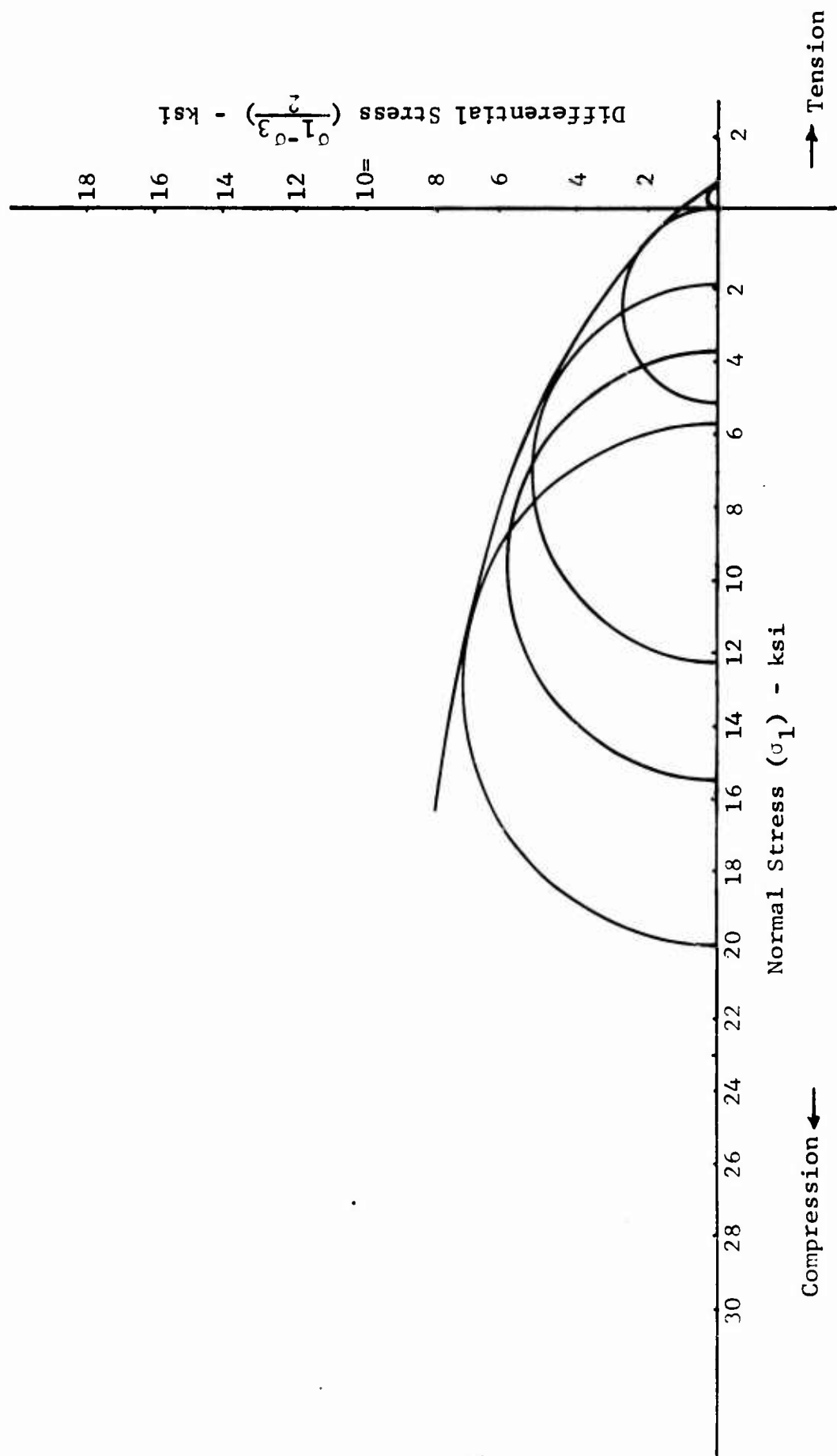
Fig. 21 MOHR'S ENVELOPE FOR INDIANA LIMESTONE PERPENDICULAR TO HOLE AXIS

51
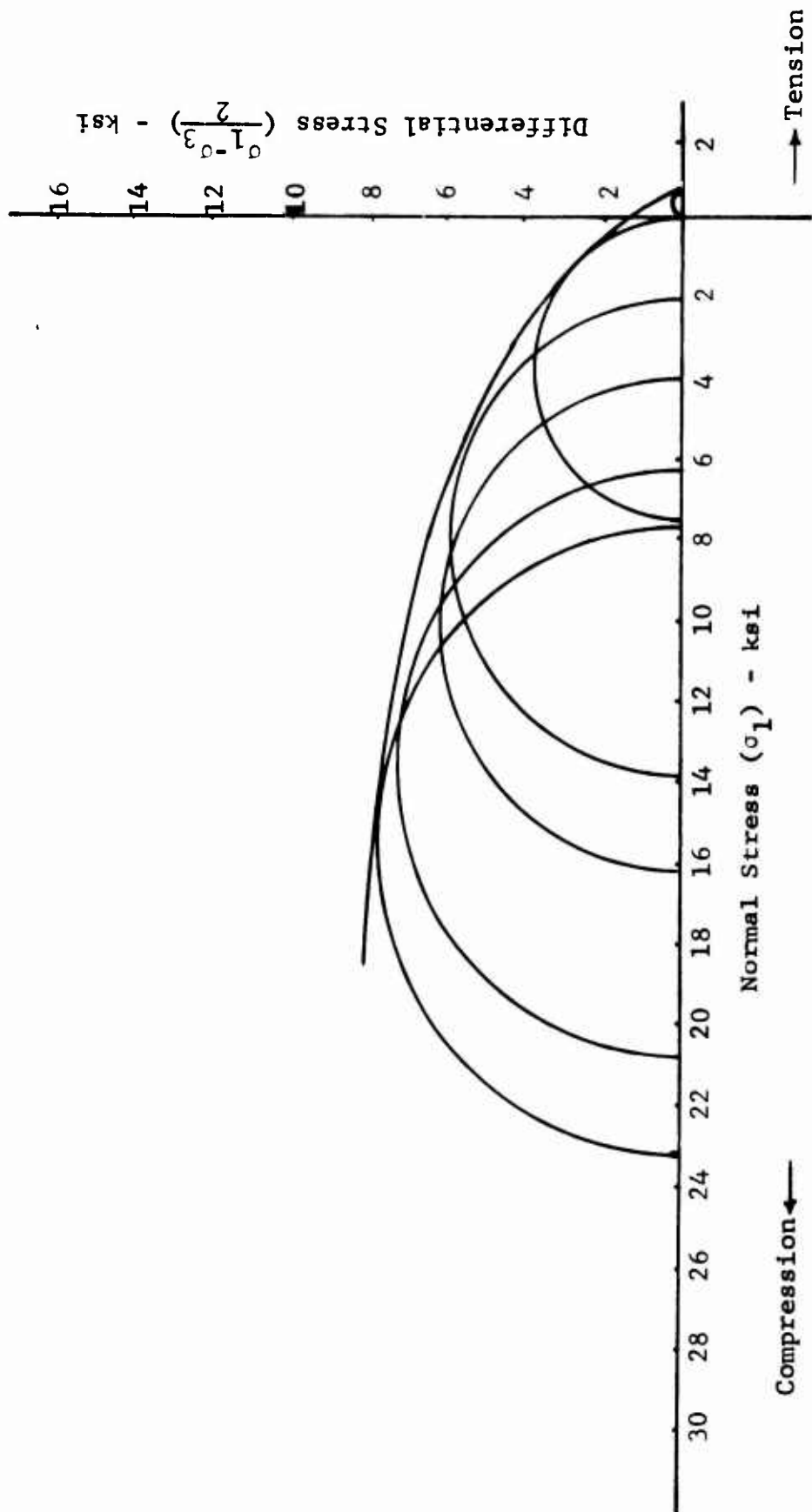
Fig. 22 MOHR'S ENVELOPE FOR INDIANA LIMESTONE ALONG HOLE AXIS

52
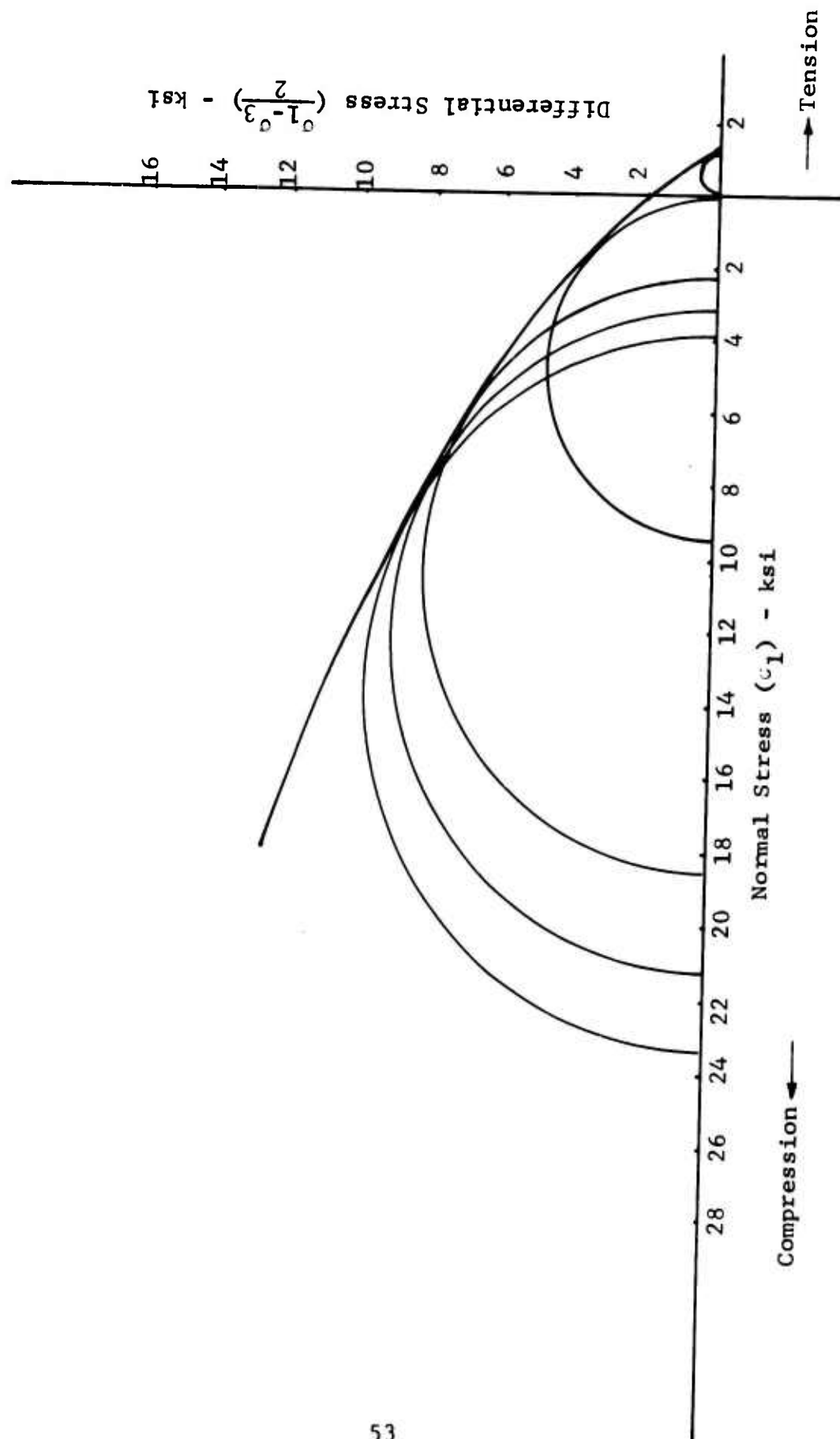
Fig. 23 MOHR'S ENVELOPE FOR VERMONT MARBLE ALONG LOADING DIRECTION

53
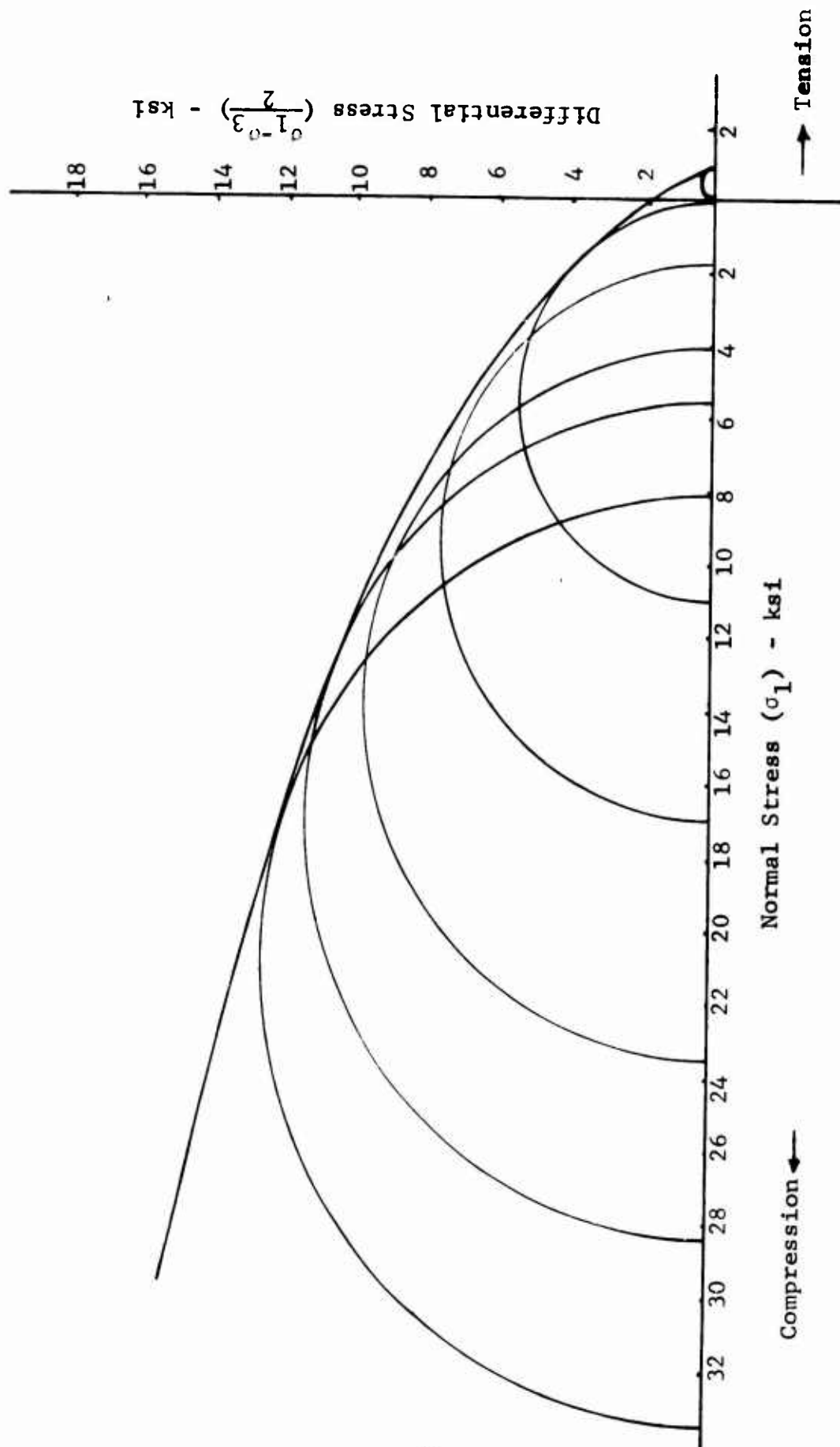
Fig. 24 MOHR'S ENVELOPE FOR VERMONT MARBLE PERPENDICULAR TO LOADING DIRECTION

a)   b)   c)

Fig.25 INDIANA LIMESTONE SPECIMENS SUBJECTED TO TRIAXIAL
COMPRESSION.

Confining pressures: a) 2000 psi
b) 4500 psi
c) 6000 psi

a)   b)   c)

Fig.26 VERMONT MARBLE SPECIMENS SUBJECTED TO TRIAXIAL
COMPRESSION.

Confining pressures: a) 4000 psi
b) 6000 psi
c) 8000 psi

2. Static Poisson's Ratio (ν)
   (along direction of loading)   0.21
   (perpendicular to direction of loading)   0.20
   (along axis of hole)   0.22

3. Static Modulus of Rigidity (μ) -
   computed from E and ν above
   (along direction of loading) 1.6×10^6 psi
   (perpendicular to direction of loading) 1.2×10^6 psi
   (along axis of hole) 1.5×10^6 psi

4. Bulk Density - 140 lb/cu ft (i.e., 2.25 gm/cc)

5. Compressive Strength (σ_c)
   (along direction of loading)   4,710 psi
   (perpendicular to direction of loading)   6,620 psi
   (along axis of hole)   7,910 psi

6. Tensile Strength (σ_t)
   (along direction of loading)   630 psi
   (perpendicular to direction of loading)   630 psi
   (along axis of hole)   600 psi

Properties data for Vermont marble were determined to be:

1. Static Young's Modulus (E)
   (along direction of loading) 7.9×10^6 psi
   (perpendicular to direction of loading) 6.5×10^6 psi

2. Static Poisson's Ratio (ν)
   (along direction of loading)   0.24
   (perpendicular to direction of loading)   0.22

3. Static Modulus of Rigidity (μ) -
   computed from E and ν above
   (along direction of loading) 3.2×10^6 psi
   (perpendicular to direction of loading) 2.7×10^6 psi

4. Bulk Density - 169 lb/cu ft (i.e., 2.71 gm/cc)

5. Compressive Strength (σ_c)
   (along direction of loading)   9,700 psi
   (perpendicular to direction of loading)   11,370 psi

6. Tensile Strength (σ_t)
   (along direction of loading)   1,010 psi
   (perpendicular to direction of loading)   700 psi

Data along the axis of the hole were not taken.

Mohr's envelopes for both rocks are given in Figs. 21 through 24, as already mentioned.

g. Petrographic and Mineralogic Descriptions

The rocks were examined both macroscopically in hand specimens and microscopically in slides.

Indiana limestone: Indiana limestone or Indiana marble is the trade name for the rock formation spergen limestone. This formation belongs to the Meramec group, is Mississippian in age and is quarried in Southern Indiana. The formation was called the Bedford limestone but is now termed the spergen limestone by the U.S. Geological Survey. The Indiana and Illinois Geological Surveys use the term Salem limestone.

The limestone is a gray, well cemented spergenite composed of

fossil fragments	30 percent
oolites	40 percent
cement	20 percent
pore space	10 percent

The fossil fragments are predominantly Globagerinia Foraminifera, ostracodes, coral stems, brachiopod shells, and crinoid stems. The oolites showed a thin outer coating but were rather homogeneous inside. Grain size of the oolites and fossil fragments ranged from 1.5 to 3mm.

The grain cement is primarily crystalline calcite (biosparite and biomicrite) with some calcite grains lining occasional vugs in the rock. The cement tends to have a "sub-poikiloblastic" texture. Some of the bioclastic fragments, which are

57

included in the grains of cementing calcite have the same optic orientation as the neighboring calcite grains, implying the existence of an equivalent environment and the action of anisotropic forces.

Vermont marble: The rock is a white marble composed of over 98 percent calcite grains 0.05 to 0.5mm long. The grains appear equant. Light green and brown streaks swirl through the rock over 8 to 12 inches. Most of the color is a result of atom impurities in the calcite crystal structure. However, less than one percent of the rock is a sericite-zoisite type mineral. The rock does not show any metamorphic lineations or remnant sedimentary bedding.

The mineralogic composition of the marble is

Calcite	98 percent
Quartz	1 percent
Black opaque minerals	1 percent

The quartz grains range from 0.04 to 0.3mm in size. The opaque minerals average 0.05mm.

2. Hydrostone

One of the liner materials chosen was hydrostone, which has a modulus lower than either rock medium used. The hydrostone powder was mixed with one-third of water by weight and cast in molds made by two concentric cylinders lined with mylar. Simultaneously with the liners, solid cylinders and dogbone specimens were cast for material property determination.

Compression properties were obtained by tesing a cylindrical specimen instrumented with strain gages. The specimen was a solid cylinder, 1.727 in. in diameter and 4 in. long, instrumented with two-gage rosettes (Micromeasurements, type EP-08-250TA-120) at three locations 120 deg apart around the circumference. The specimen was loaded in increments to failure and strain readings were recorded at each load level. The applied compressive stress was plotted versus the longitudinal and transverse strains averaged for the three locations in Fig. 27. The following results were obtained from this test.

58
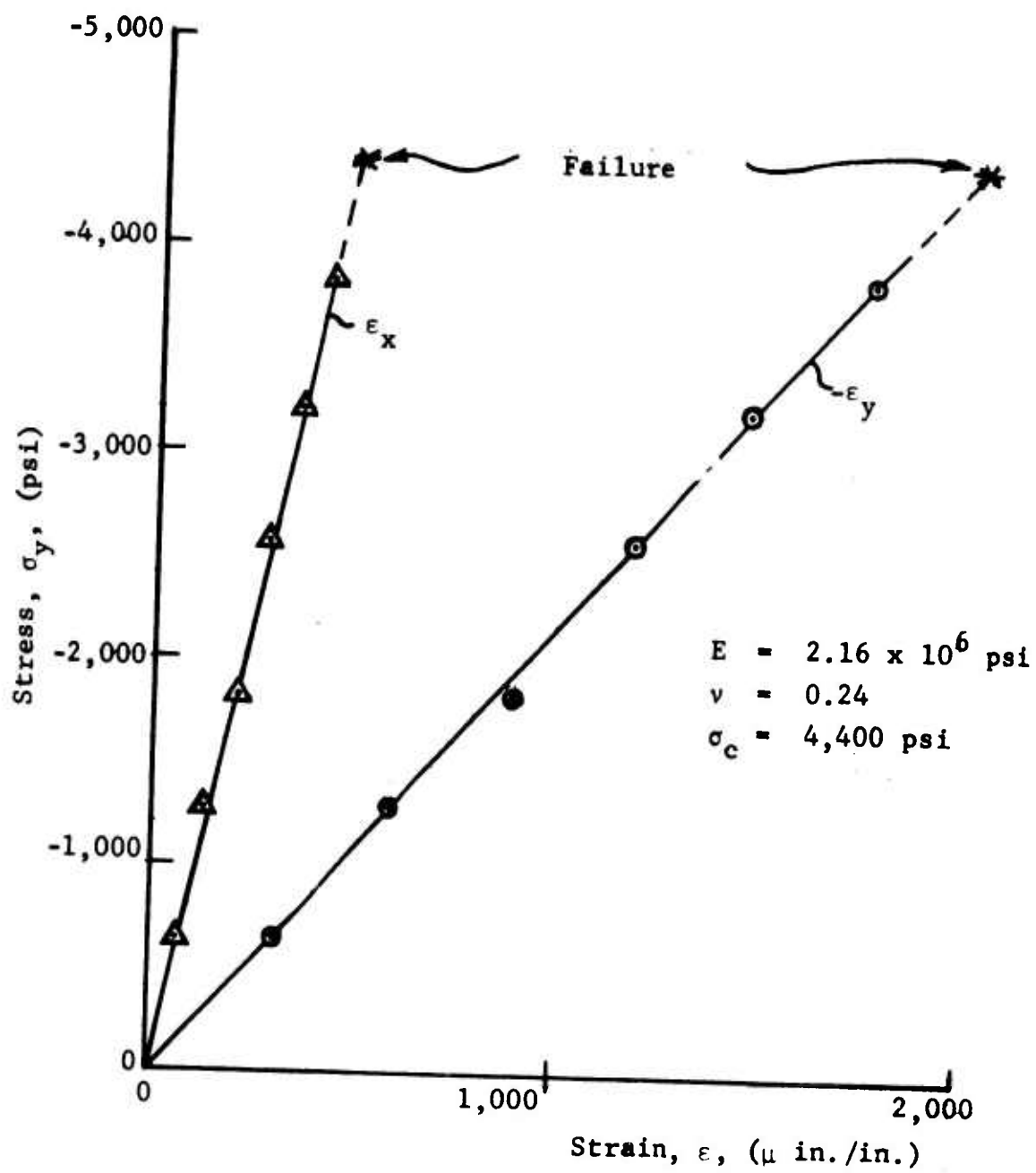
Fig. 27 LONGITUDINAL AND TRANSVERSE STRAIN VARIATION
IN HYDROSTONE COMPRESSION SPECIMEN

59

$$\text{Modulus:} \quad E = 2.16 \times 10^6 \text{ psi}$$
$$\text{Poisson's ratio:} \quad \nu = 0.24$$
$$\text{Compressive strength:} \quad \sigma_c = 4{,}400 \text{ psi}$$

Tensile properties were obtained by testing a dogbone speci-
men instrumented with strain gages. The specimen had a rectangular
cross section of 0.349 in. x 0.305 in. and was instrumented with two
rosettes on two opposite faces near the center. It was loaded in
increments to failure. The applied tensile stress was plotted versus
the longitudinal and transverse strains averaged for the two locations
in Fig. 28. The following results were obtained from this test:

$$\text{Modulus:} \quad E = 2.25 \times 10^6 \text{ psi}$$
$$\text{Poisson's ratio:} \quad \nu = 0.27$$
$$\text{Tensile strength:} \quad \sigma_t = 610 \text{ psi}$$

The Young's modulus seems to be the same in tension and
compression. The apparent difference in Poisson's ratio is rather
due to the wider scatter in the transverse strain readings in the
tension test. The strength properties are almost an order of
magnitude apart as expected. The tensile strength is almost the
same as that of Indiana limestone, and the compressive strength is
a little lower than that of limestone. Compared to the Vermont
marble used here, the strengths of hydrostone are roughly half of
the corresponding values for marble.

3. Aluminum

As mentioned earlier, two types of aluminum were used as
liner materials. Specimens 7 and 8 were lined with 2024-T4, T351
with a modulus of $E = 10.6 \times 10^6$ psi and specimens 11, 12, 18, and
20 were lined with 6061-T6 aluminum with a modulus of $E = 10.0 \times
10^6$ psi. Poisson's ratio for both types is $\nu = 0.33$.
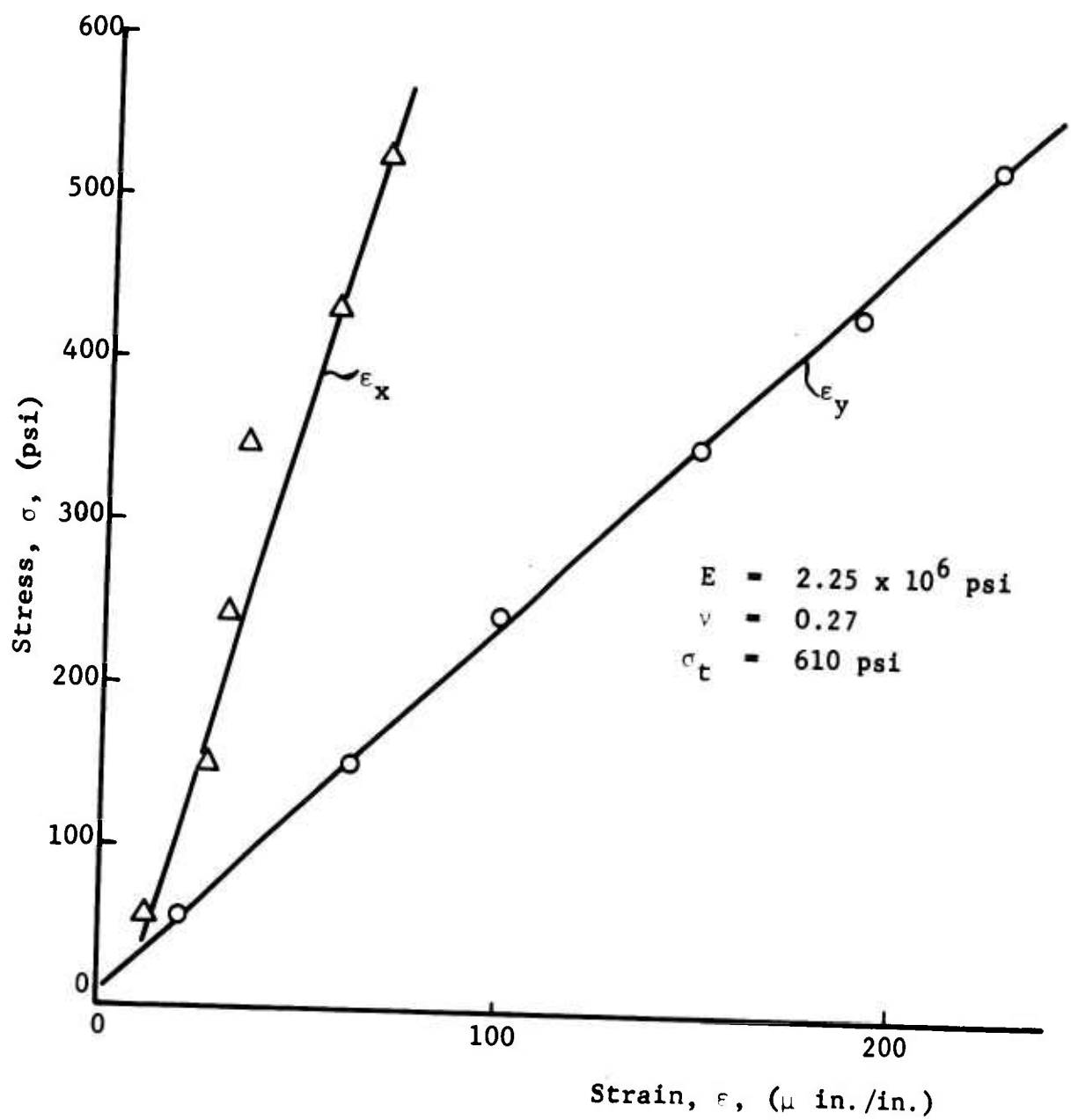
Fig. 28   LONGITUDINAL AND TRANSVERSE STRAIN VARIATION
IN HYDROSTONE TENSION SPECIMEN

61

SECTION V

STRESS DISTRIBUTION AND FRACTURE AROUND UNLINED CAVITIES
IN ROCK UNDER UNIAXIAL LOADING

1. Specimen No. 1 - Limestone Unlined Under Uniaxial Loading
    a. Experimental Procedure

·Specimen No. 1 consisted of a limestone plate of dimensions
36 in. x 24 in. x 2.50 in. thick with a 4 in. diameter centrally
located hole. The hole was unlined. Strain gages were applied
along the horizontal and vertical axes of symmetry, and along the
45-degree radii (Fig. 29). Two-element gages were employed along
the axes of symmetry while three-element gages were applied on the
45-degree radii. Strain gages were also applied to the transverse
surface of the hole both on the axes of symmetry and at the 45-
degree locations. Temperature compensation was assured by applying
gages to unloaded limestone samples located adjacent to the test
specimen. Diametral changes were monitored with two DCDTs inserted
along the horizontal and vertical directions. Full-field surface
strains were visually observed and photographically recorded
throughout part of a quadrant of the specimen by means of a bire-
fringent coating.

The instrumented specimen was loaded vertically in the
previously discussed 120,000 lb Riehle Testing machine (Fig. 14).
Alignment was checked by preliminary loadings to 10,000 lb
(p = 167 psi) and monitoring the free-field strain gages plus those
on the transverse surface of the hole. Some shimming was necessary
to insure uniformity of loading. During the actual test, the speci-
men was loaded in approximately 5,000 lb (84 psi) increments up to
120,000 lb, strain gage and DCDT outputs recorded for all load
levels. Subsequently, the specimen was unloaded and then reloaded
to 130,000 lb. At this load, failure progressed with time as
shown below. The strain gage and DCDT readings were recorded by
means of the Hewlett-Packard Digital Data Acquisition system
described previously. Unbalanced bridges were employed. Photo-
elastic patterns of the photoelastic coating were recorded at
selected load levels with a portrait camera.

62
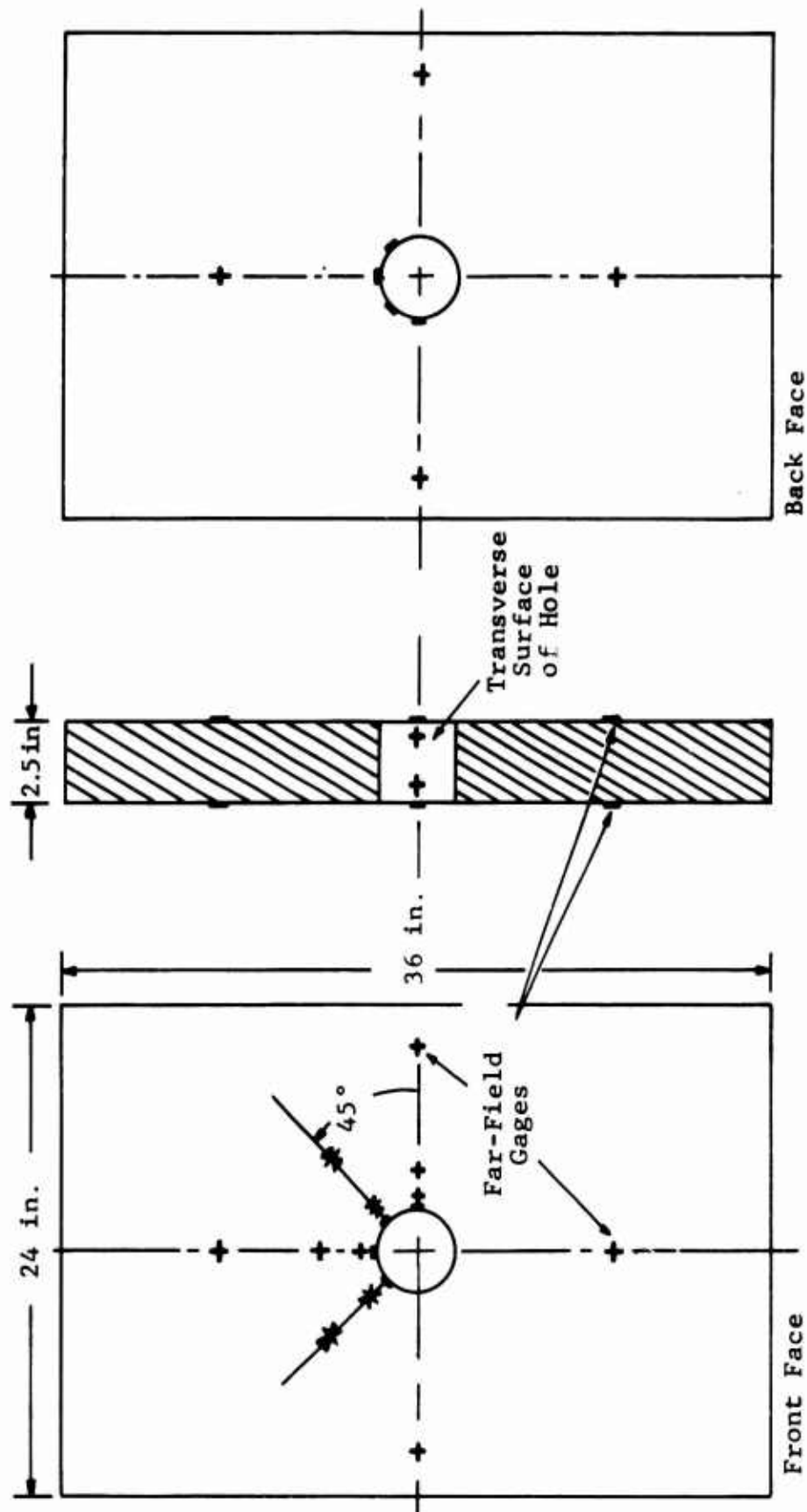
Fig. 29   STRAIN GAGE LAYOUT FOR SPECIMEN NO. 1 (UNLINED LIMESTONE UNDER UNIAXIAL LOADING)

63

b. <u>Results and Discussion</u>

Isochromatic fringe patterns for two load levels are shown in Fig. 30. The average stress (on gross area) of the bottom photograph was 1,000 psi while that at the top pattern was 2,000 psi. According to fringe patterns such as those of Fig. 30, crack initiation occurred at a vertical load of approximately 75,000 lb (1250 psi) at the tensile region at the bottom of the hole.

At the stress level of p = 2,000 psi, the following results are obtained from the photoelastic data.

At the 270 degree location, the fringe order is 2.3 which corresponds to

$$\varepsilon_1 - \varepsilon_2 = 876 \times 2.3 = 2,020 \ \mu in./in.$$

For a coating Poisson's ratio of,

$$\nu = 0.40$$

$$\varepsilon_2 = -\frac{2020}{1.40} = -1,450 \ \mu in./in.$$

At the 180 degree location, the fringe order is four which would correspond to a principal strain difference of

$$\varepsilon_1 - \varepsilon_2 = 3,500 \ \mu in./in.$$

(The resolution to individual strain components would be meaningless in this extensively cracked area.)

Upon unloading and then reloading to p = 2,170 psi the cracked region extended with the increase in load to a distance of approximately 2 in. from the boundary of the hole (Fig. 31). Under constant load then it exhibited creep fracture characteristics and the cracks extended further as shown in this figure.

64

Fig. 30 ISOCHROMATIC FRINGE PATTERNS IN PHOTOELASTIC COATING
OF SPECIMEN NO. 1 INDICATING CRACKING IN THE ROCK
ALONG VERTICAL DIAMETER OF HOLE. (TOP: AT p = 2,000 PSI;
BOTTOM: AT p = 1,000 PSI UNLOADED FROM 2,000 psi)

Fig. 31 ISOCHROMATIC FRINGE PATTERNS IN PHOTOELASTIC COATING
AROUND HOLE OF SPECIMEN NO. 1 SHOWING CRACK EXTENSION
UNDER CONSTANT LOAD (PHOTOGRAPHS WERE TAKEN AT 5 MIN
INTERVALS AFTER REACHING 2,170 PSI)

Diametral changes for specimen No. 1 measured with the DCDTs are plotted in Fig. 32 as a function of applied stress. Vertical diametral changes are linear up to approximately 1,250 psi, the stress level at which cracking initiated. The curve for the horizontal deflection does not go through zero, possibly due to an initial drift of the DCDT. However, when shifted horizontally until it passes through zero it shows the same characteristics as the curve for the vertical deflections. The deflections per unit of applied stress in the linear range are:

$$\frac{\delta_h}{p} = 1.3 \times 10^{-6} \text{ in./psi}$$

$$\frac{\delta_v}{p} = -2.7 \times 10^{-6} \text{ in./psi}$$

Strain-gage readings along the horizontal, vertical and 45-degree radii for specimen No. 1 are plotted as a function of applied stress in Figs. 33 through 38 with radial location as a parameter, while the compressive strain distribution along the horizontal axis is plotted in Fig. 39 for two load levels, 75,000 lb (p = 1,250 psi), the proportional limit and 120,000 lb (p = 2,000 psi), the maximum load at which readings were taken. Some stress and strain redistribution did take place as evidenced by the increased strain concentration ratio from 3.4 to 3.5 (Fig. 39). From Figs. 33 through 36, it is seen that the far-field strains remained linear throughout the test. (Some curves not passing through zero were shifted horizontally until they did.) On the basis of these far-field readings, both on the horizontal and vertical axes, the following modulus and Poisson's ratio were determined (Ref. 6) for the limestone

$$E = 4.8 \times 10^6 \text{ psi}$$
$$\nu = 0.22$$

The previous indications (photoelastic coating and diametral changes) that cracking initiated at approximately p = 1,250 psi is confirmed by the response of the horizontal strain on the vertical axis at the hole boundary. This strain increased linearly up to

67
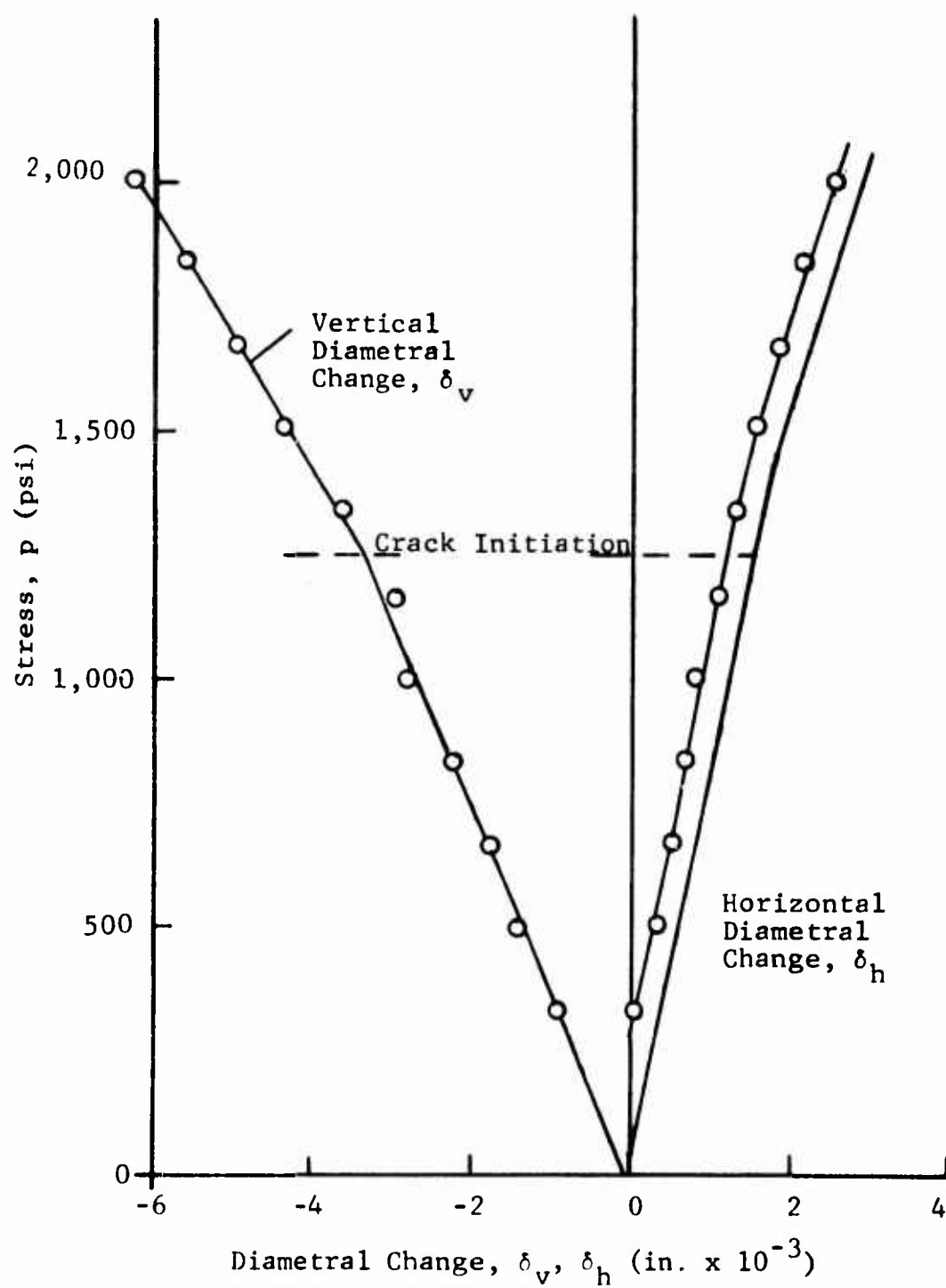
Fig. 32   DIAMETRAL CHANGES AS A FUNCTION OF APPLIED STRESS
FOR SPECIMEN NO. 1 (UNLINED LIMESTONE UNDER UNIAXIAL
LOADING)

68
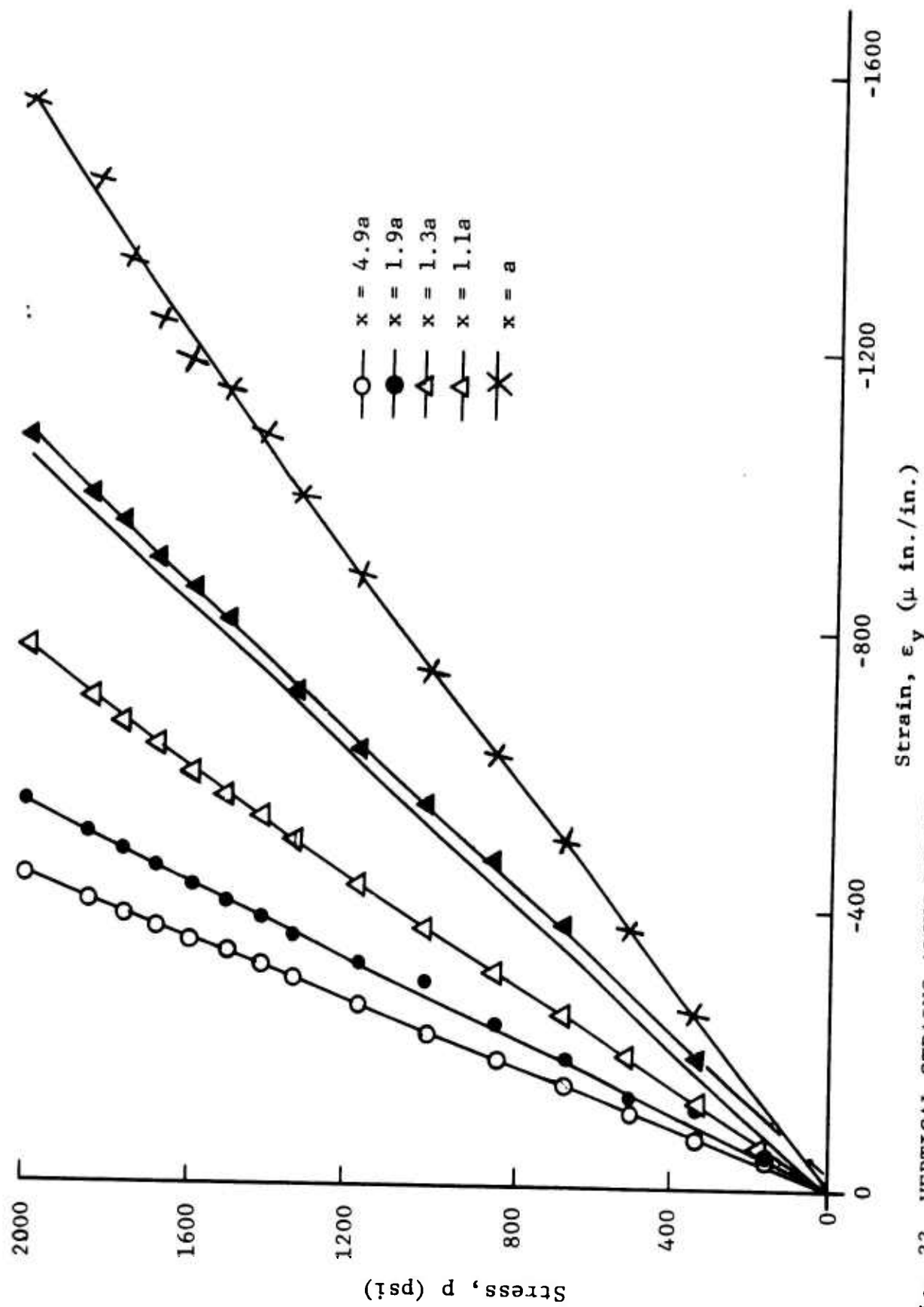
Fig. 33 VERTICAL STRAINS ALONG HORIZONTAL AXIS OF SYMMETRY AS A FUNCTION OF APPLIED VERTICAL STRESS FOR SPECIMEN NO. 1 (UNLINED LIMESTONE UNDER UNIAXIAL LOADING)

69
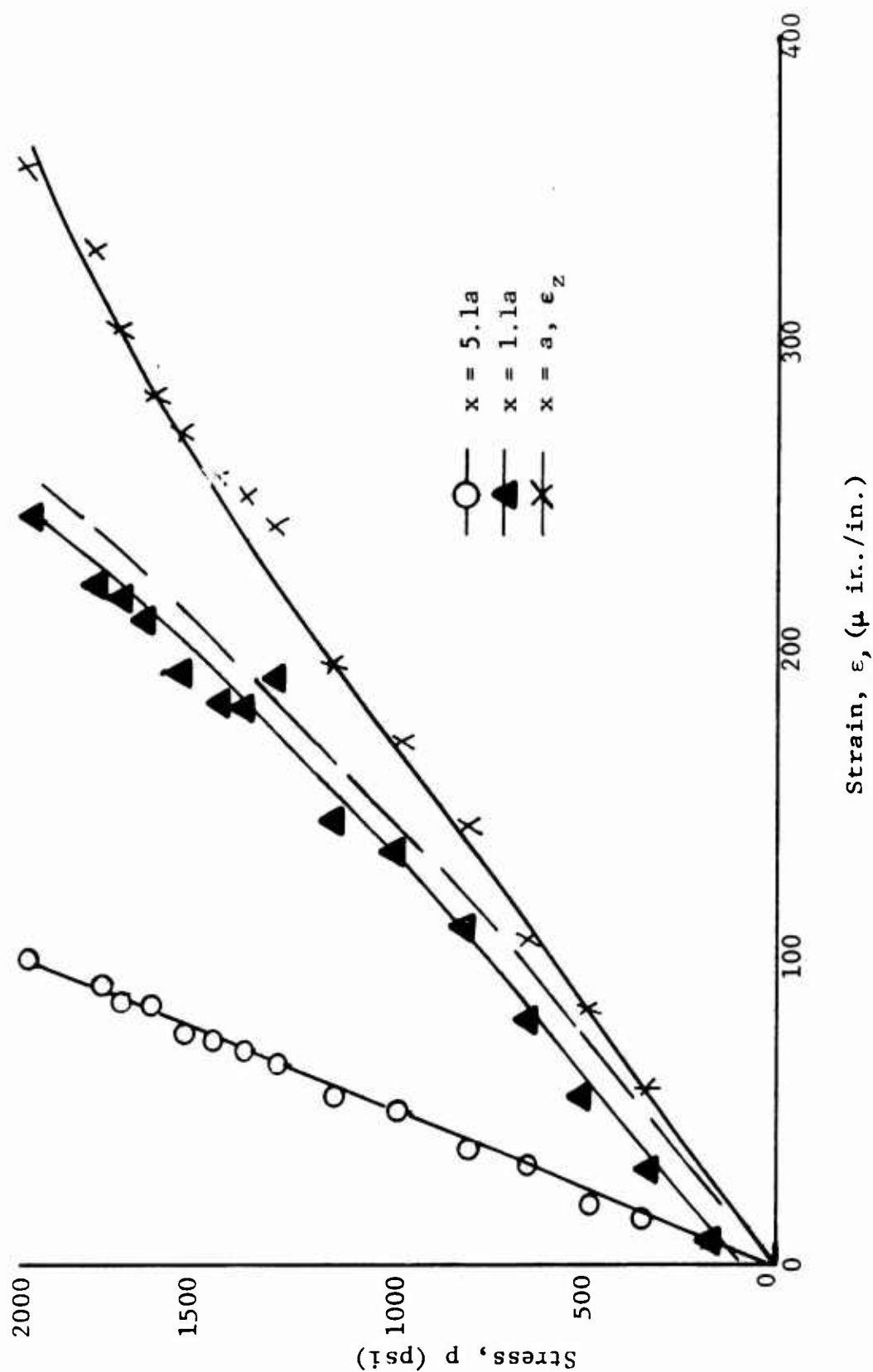
Fig. 34   HORIZONTAL STRAINS ALONG HORIZONTAL AXIS OF SYMMETRY AS A FUNCTION OF APPLIED
VERTICAL STRESS FOR SPECIMEN NO. 1 (UNLINED LIMESTONE UNDER UNIAXIAL LOADING)

70
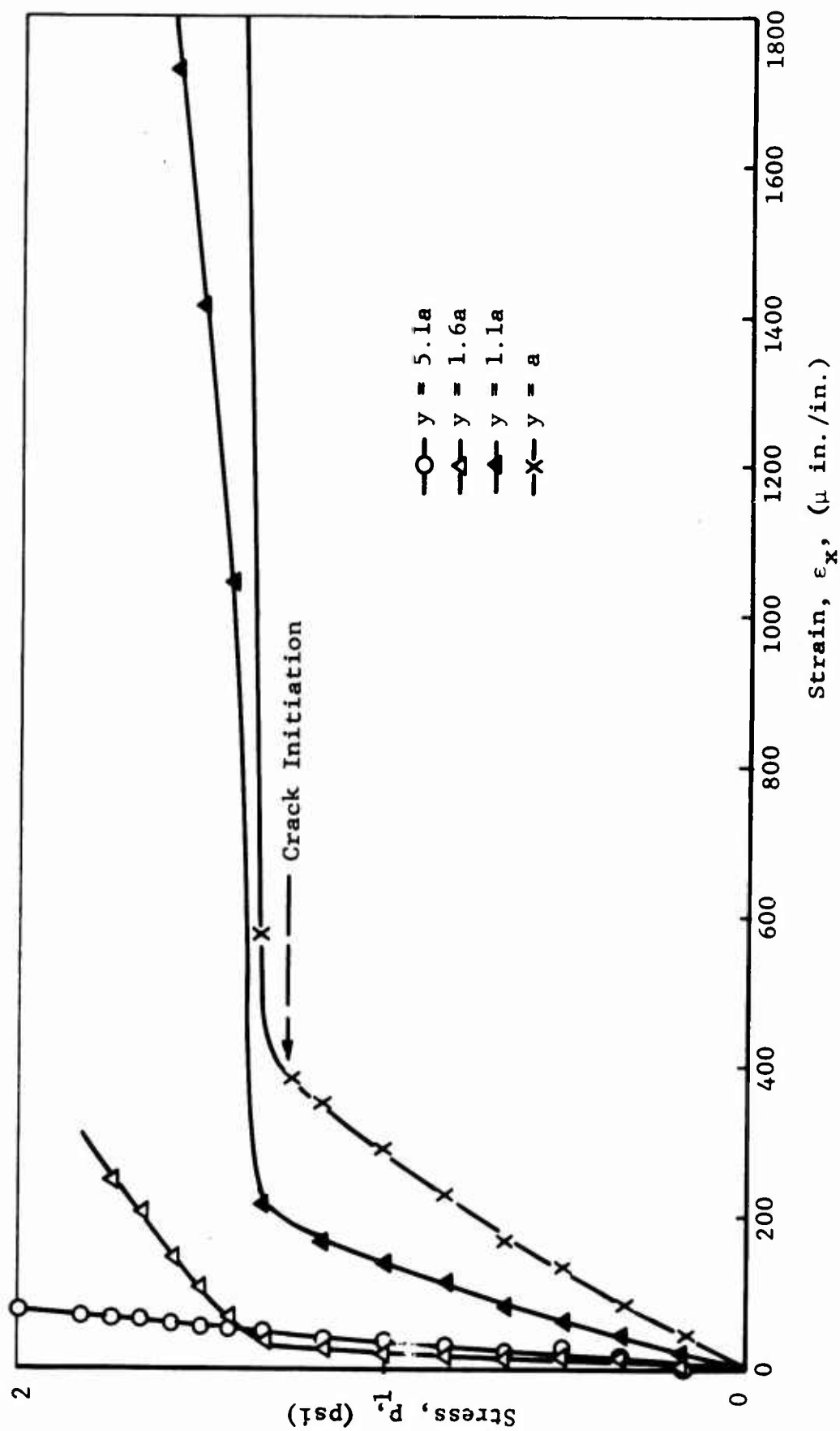
Fig. 35 HORIZONTAL STRAINS ALONG VERTICAL AXIS OF SYMMETRY AS A FUNCTION OF APPLIED VERTICAL STRESS FOR SPECIMEN NO. 1 (UNLINED LIMESTONE UNDER UNIAXIAL LOADING)

71
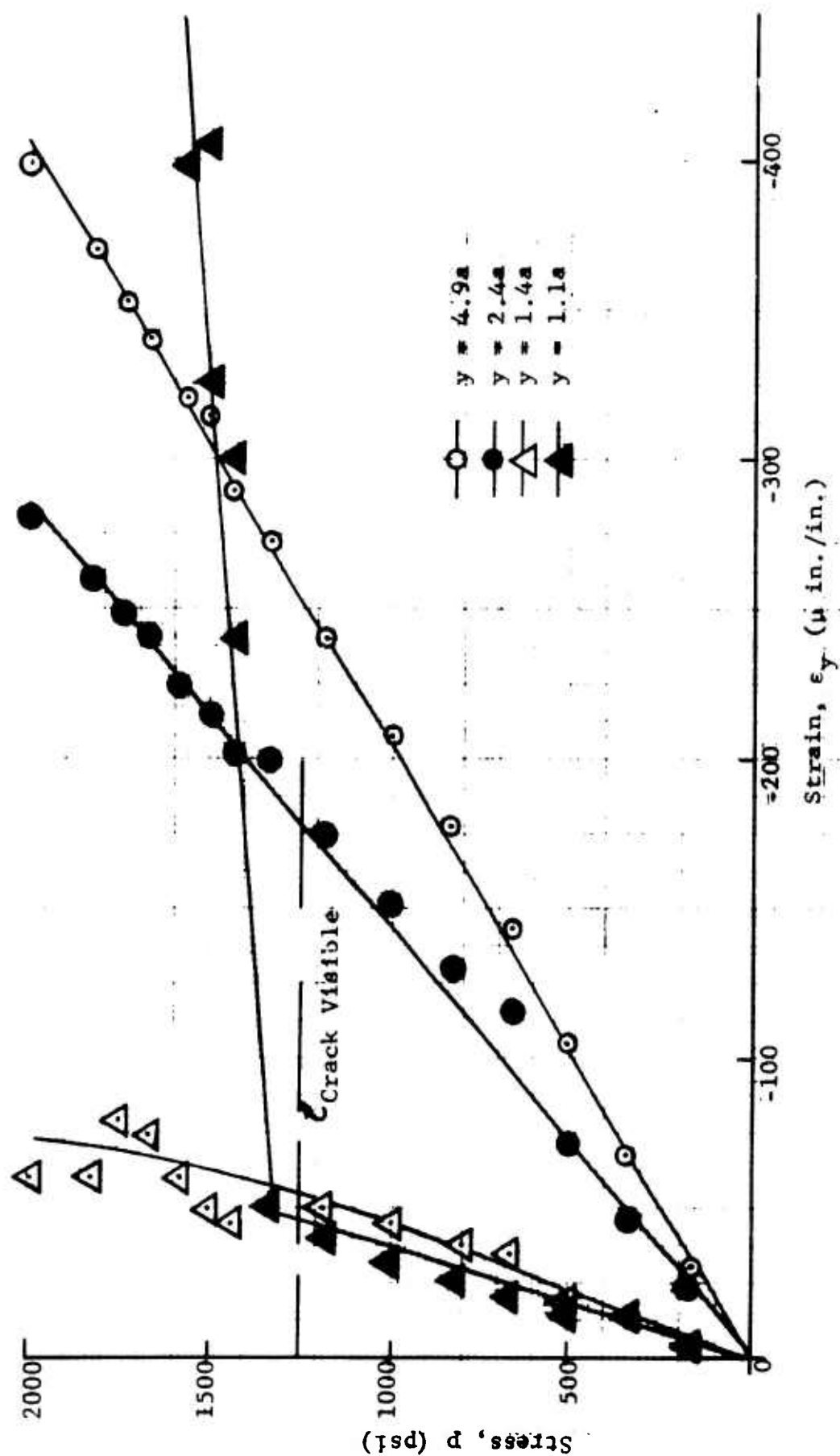
Fig. 36   VERTICAL STRAINS ALONG VERTICAL AXIS OF SYMMETRY AS A FUNCTION OF APPLIED VERTICAL STRESS FOR SPECIMEN NO. I (UNLINED LIMESTONE UNDER UNIAXIAL LOADING)
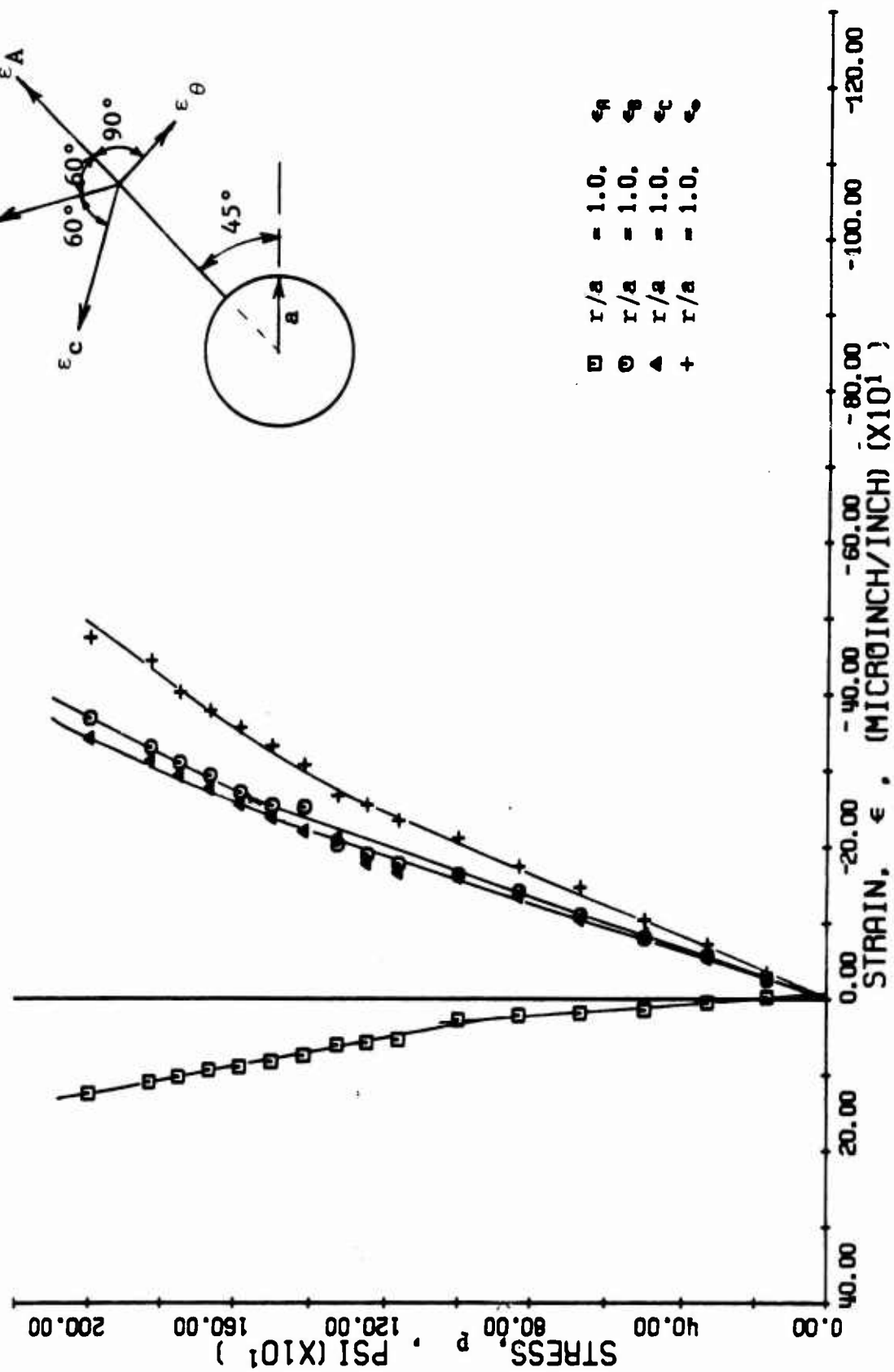
FIG. 37 STRAINS ALONG 45 DEGREE RADIUS FOR SPECIMEN NO. 1
(LIMESTONE UNLINED UNDER UNIAXIAL LOADING)

73
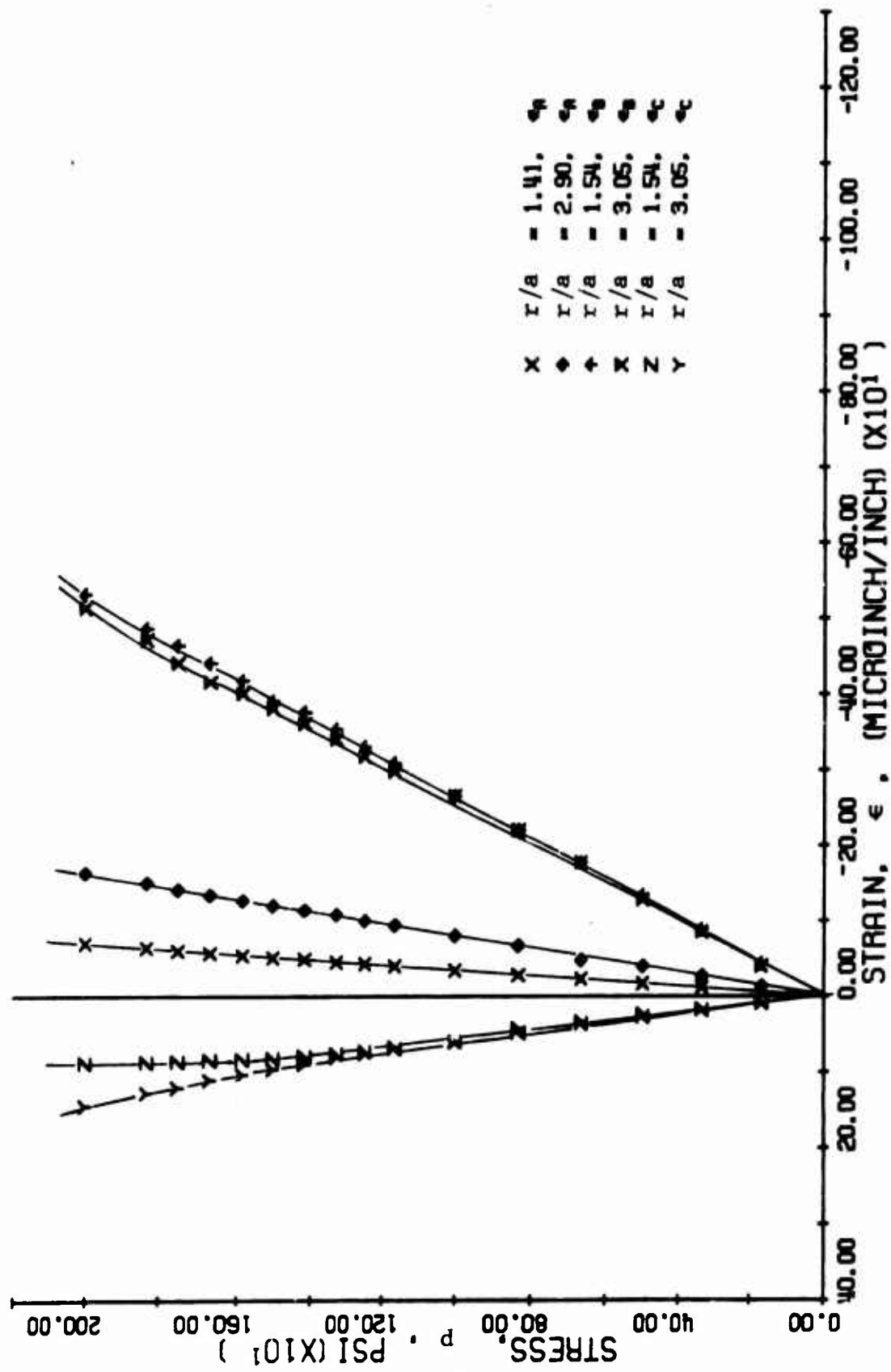
FIG. 38 STRAINS ALONG 45 DEGREE RADIUS FOR SPECIMEN NO. 1
(LIMESTONE UNLINED UNDER UNIAXIAL LOADING)

74
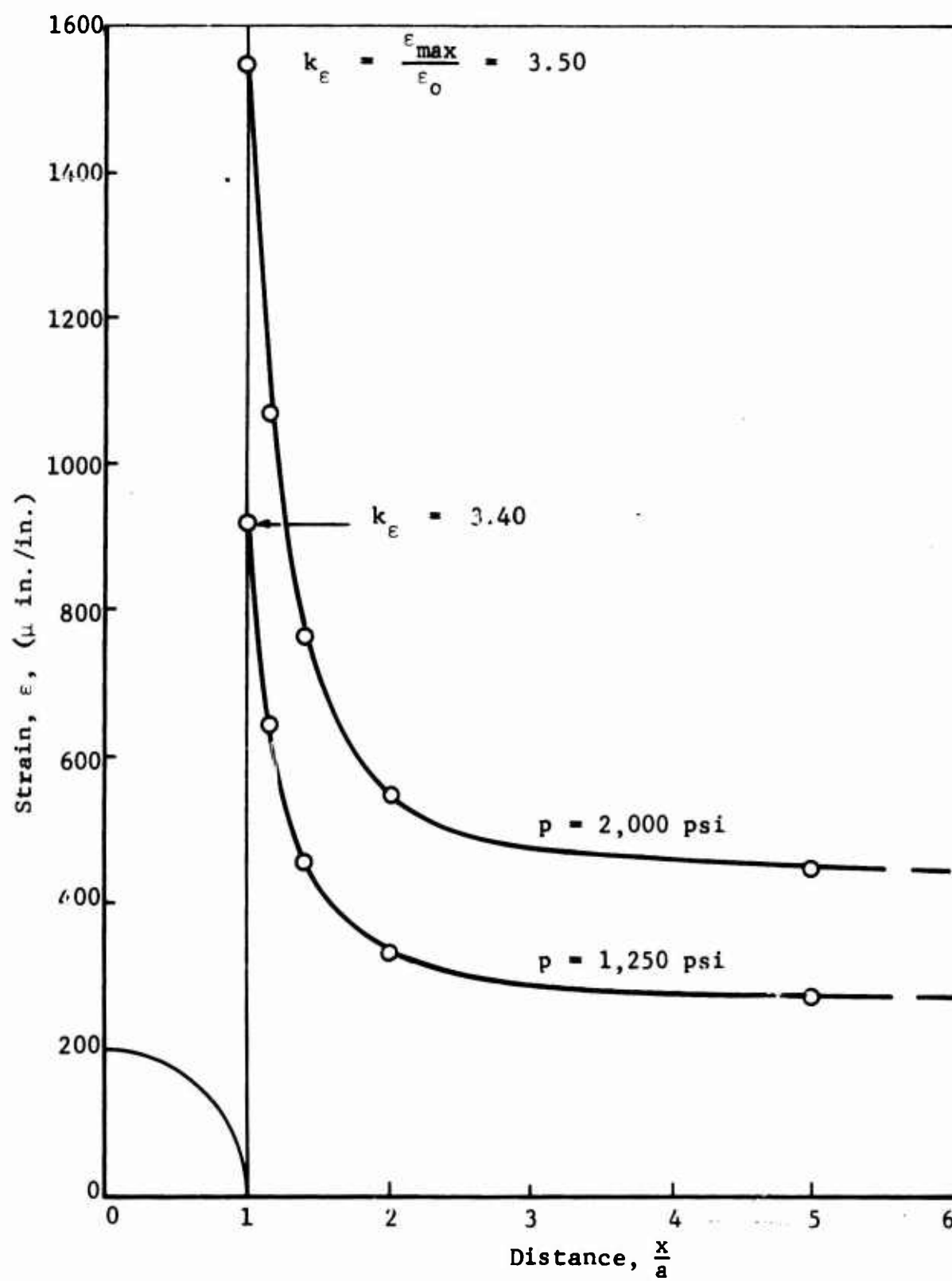
Fig. 39   COMPRESSIVE STRAIN DISTRIBUTION ALONG HORIZONTAL AXIS
FOR TWO LOAD LEVELS - SPECIMEN NO. 1

75

a stress of 800 psi, thereafter it increased at a gradually increas-
ing rate up to the crack initiation level of 1,250 psi, subsequent
to which it increased at an enormous rate. Strains along the
45-degree direction were first plotted as recorded (Figs. 37 and 38)
with ϵ_a, ϵ_b, ϵ_c designating rosette strains along the radial direction
and at 60 degree and 120-degree directions from the radius (measured
counterclockwise). Subsequently, principal strains were computed
using the rosette equations and are plotted in Fig. 40. Principal
directions were similarly computed and plotted versus stress for
two radial locations in Fig. 41. As expected, the principal
directions are constant in the linear region and deviate slightly
at the higher stress levels where some nonlinearities and redistri-
bution occur. The angle between the 45-degree radius and the principal
tensile stress direction, measured clockwise, varies from 37-1/2
degrees to 43 degrees between radial locations $r = 1.5a$ and $r = 3a$.
Of course, the principal directions will approach zero degrees at
$r = a$ and 45 degrees very far from the hole.

2. Specimen No. 2 - Limestone Unlined Under Uniaxial Loading

   a. Experimental Procedure

   Specimen No. 2 consisted of a limestone block of dimensions
36 in. x 24 in. x 16 in. thick with a 4 in. diameter centrally
located unlined hole. This is similar to the previous specimen
except for the increased thickness. As in the case of specimen 1
(Fig. 29), strain gages were applied along the horizontal and
vertical axes of symmetry, and along the 45-degree radii. Two-
element gages were employed along the axes of symmetry while three-
element gages were applied on the 45-degree radii. Strain gages were
also applied to the transverse surface of the hole both on the two

76
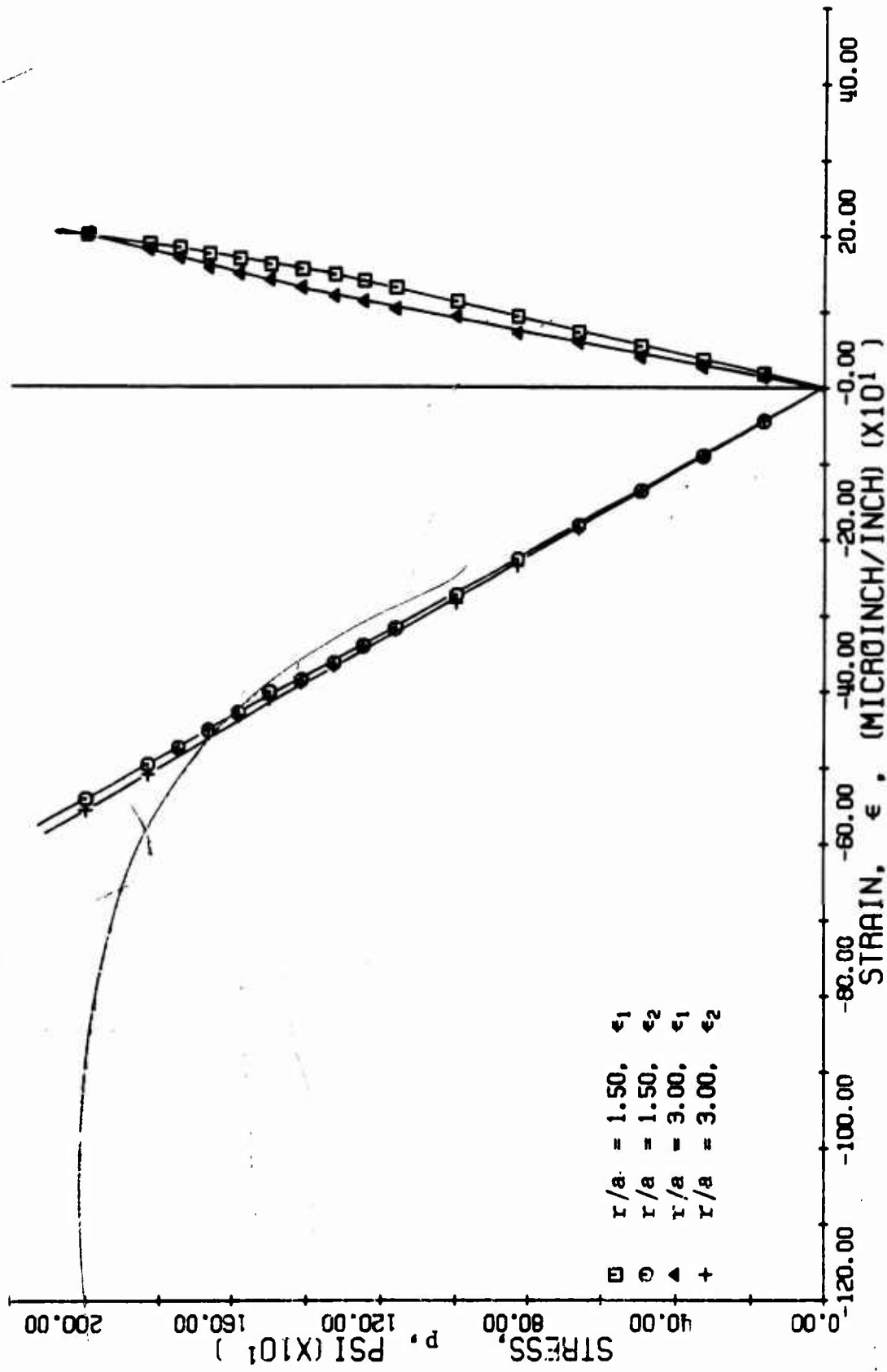
FIG. 40 PRINCIPAL STRAINS ALONG 45-DEGREE RADIUS FOR SPECIMEN NO. 1
(LIMESTONE UNLINED UNDER UNIAXIAL LOADING)

77
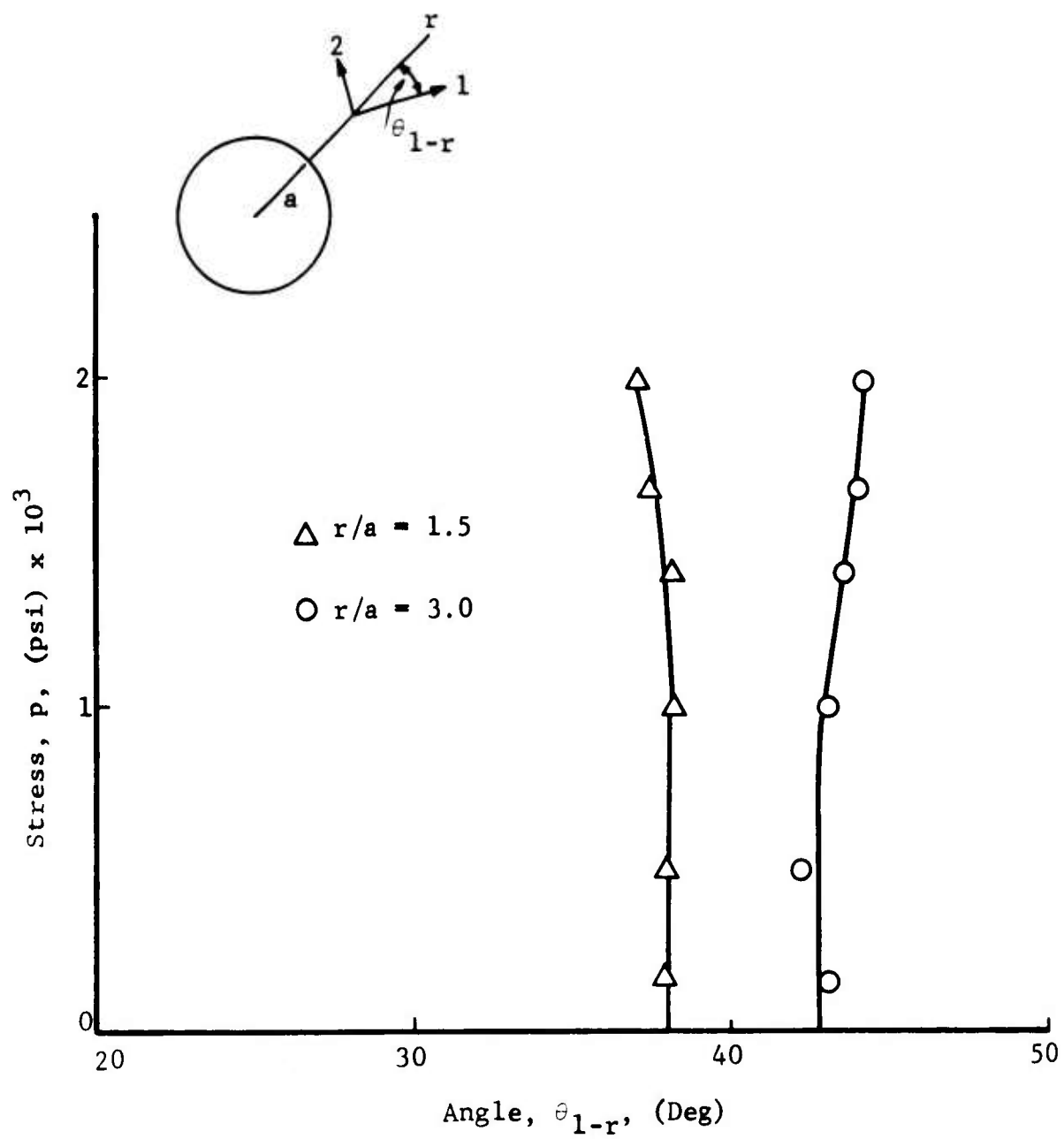
Fig. 41   PRINCIPAL DIRECTIONS ALONG 45-DEGREE RADIUS FOR SPECIMEN NO. 1

axes of symmetry and at the 45-degree locations (Fig. 42). Temperature compensation was assured by applying gages to unloaded limestone samples located adjacent to the test specimen. Diametral changes were monitored with two DCDTs inserted along the horizontal and vertical directions. Full-field surface strains were visually observed and photographically recorded throughout part of a quadrant of the specimen by means of a birefringent coating.

The instrumented specimen was loaded in the previously discussed 1,000,000 lb testing machine (Fig. 15). The specimen was aligned as was specimen No. 1. The strain gage and DCDT data were recorded using unbalanced bridges and the previously described Hewlett-Packard Digital Data Acquisition system. The specimen was loaded in increments of 50,000 lb (p = 130 psi).

b. Results and Discussion

Initial cracking of the specimen, as noted in the photoelastic fringe patterns in the coating, occurred at approximately 300,000 lbs (780 psi). The load was subsequently increased to a mean stress (based on gross area) of approximately 912 psi (350,000 lb) and maintained there. The crack initially increased only slightly and then suddenly propagated throughout the entire length of the specimen with a snap (Fig. 43). Isochromatic fringe patterns at this stress level and at a subsequently increased load of 400,000 lb (p = 1,040 psi) are shown in Fig. 44.

Diametral changes for specimen No. 2 as measured by the DCDTs are plotted in Fig. 45 as a function of applied stress. Both the horizontal and vertical diametral changes are linear up to an applied stress of approximately 640 psi, somewhat lower than 780 psi when cracking was manifested in the photoelastic coating. (Both curves have been shifted horizontally to pass through zero.) In the linear range, the deflections per unit of applied stress are

$$\frac{\delta_h}{p} = 1.5 \times 10^{-6} \text{ in./psi}$$

$$\frac{\delta_v}{p} = -2.7 \times 10^{-6} \text{ in./psi}$$

79
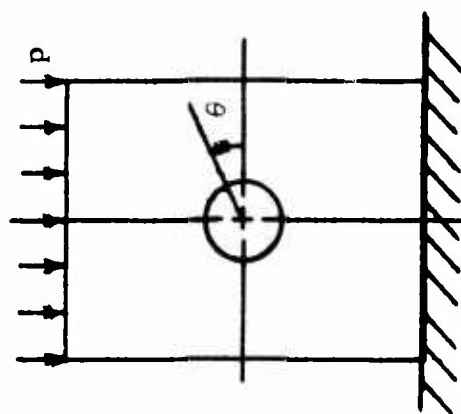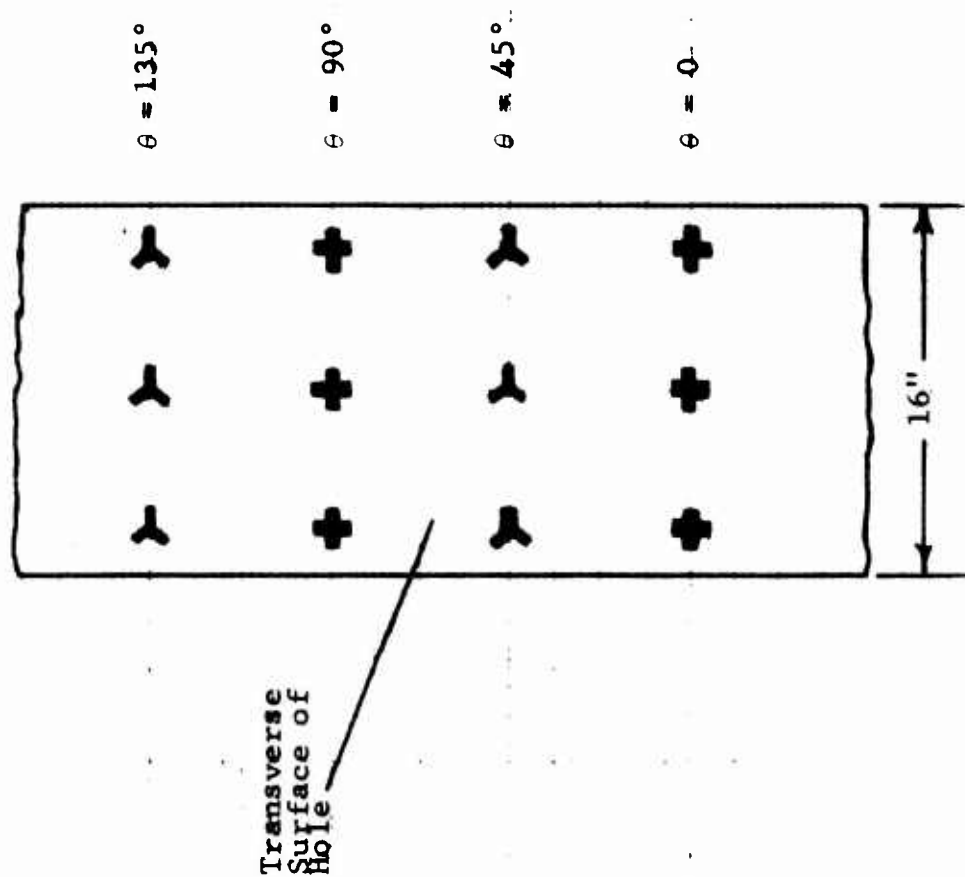
Fig. 42   STRAIN GAGE LOCATIONS ON TRANSVERSE SURFACE OF HOLE OF SPECIMEN NO. 2

80
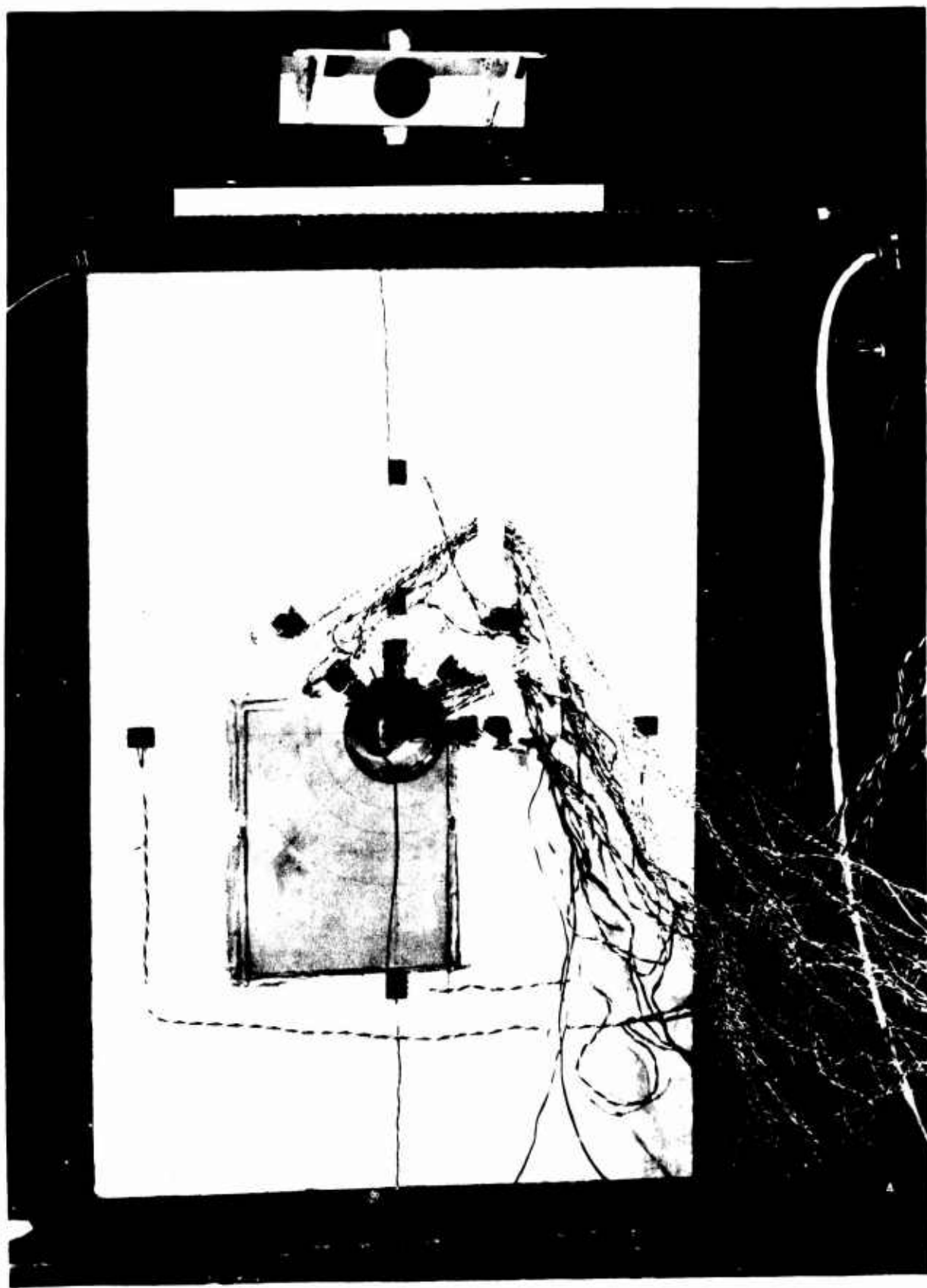
Fig. 43 LIMESTONE SPECIMEN NO. 2 AFTER CRACKING ALONG VERTICAL
AXIS OF SYMMETRY
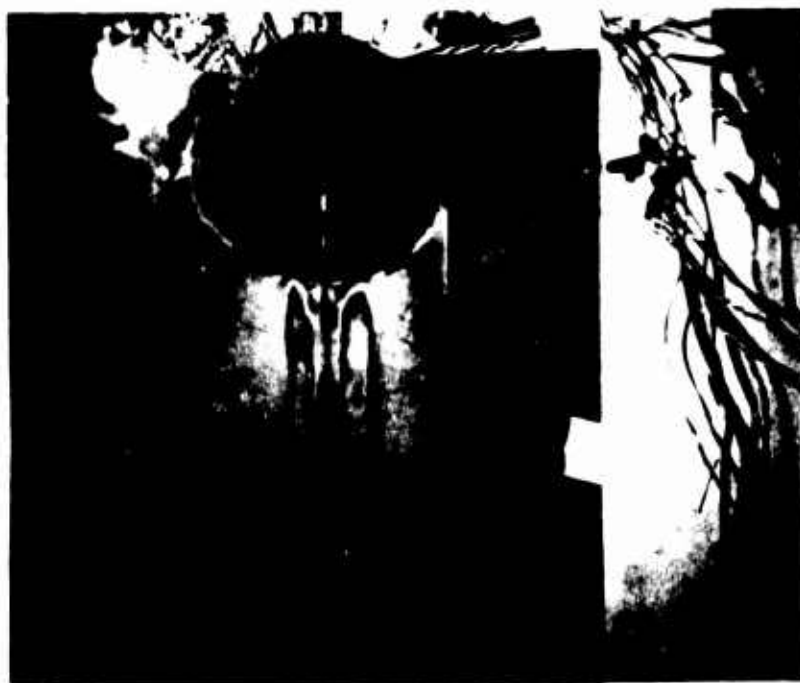
Fig. 44   ISOCHROMATIC FRINGE PATTERNS IN PHOTOELASTIC COATING
INDICATING CRACKING IN THE ROCK ALONG VERTICAL DIAMETER
OF HOLE (TOP: AT p = 912 PSI; BOTTOM: AT p = 1,040 PSI)
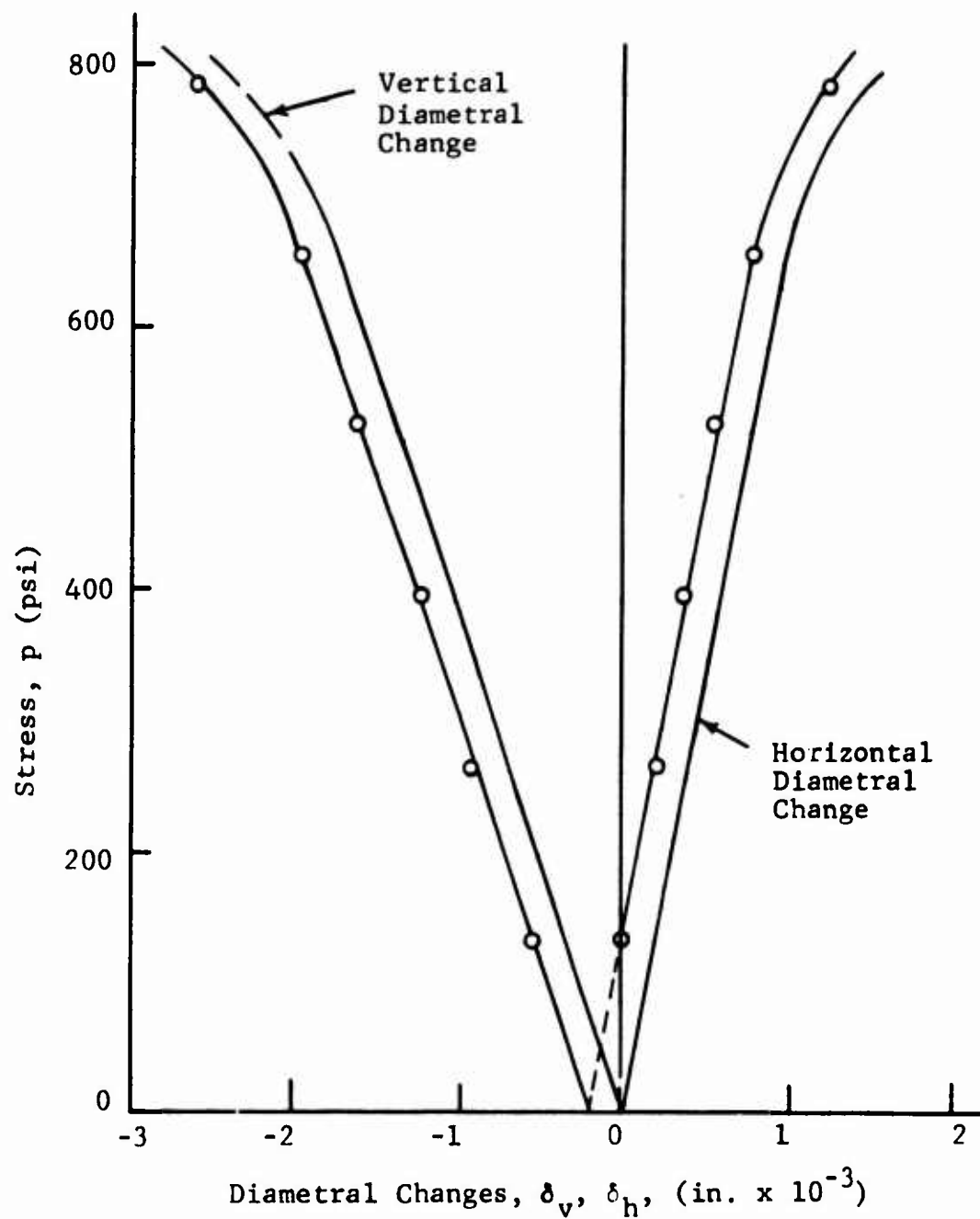
Fig. 45 DIAMETRAL CHANGES AS A FUNCTION OF APPLIED STRESS FOR SPECIMEN NO. 2 (UNLINED LIMESTONE UNDER UNIAXIAL LOADING)

83

Strain gage readings along the horizontal, vertical and 45-degree radii are plotted as a function of applied stress in Figs. 46 through 50 with radial location as a parameter, while the compressive strain distribution along the horizontal axis is plotted in Fig. 51 for applied stress levels of 520 and 780 psi, respectively. Again, some yielding occurred as indicated by the increased strain concentration factor from 4.0 to 4.2.

Figures 48 through 50 substantiate the diametral-change information that cracking initiated along the vertical axis at about the 650 psi level. The strains near the hole on the vertical axes rapidly increased at this load, particularly those measured by the gages on the flat, vertical faces of the specimen.

On the basis of the far-field strains for the linear portion (Figs. 46 through 49), the following modulus and Poisson's ratio were determined for the limestone of this test.

$$E = 5.5 \times 10^6 \text{ psi}$$

$$\nu = 0.23$$

The as-recorded strains along the 45-degree radial direction on the boundary of the hole are plotted in Fig. 50. Principal strains computed from rosette strain gage readings are plotted in Fig. 52, while Fig. 53 contains the variation of the principal directions for two radial positions. While the tensile principal strains are small and remain linear throughout the loading, the larger compressive principal strains on the 45-degree direction do become nonlinear at the higher stress levels. The principal directions are essentially constant up to the neighborhood of 600 psi at which time redistribution of load occurs, in part due to the initiation of cracking, and the principal directions rotate. As the radial distance along the 45-degree axis changes from $r = 1.5a$ to $r = 3a$, the principal direction as measured clockwise from the radial direction to the largest principal strain ε_1,

Fig. 46 VERTICAL STRAINS ALONG THE HORIZONTAL AXIS OF SYMMETRY AS A FUNCTION OF APPLIED STRESS FOR SPECIMEN NO. 2 (UNLINED LIMESTONE UNDER UNIAXIAL LOADING)

Fig. 47 HORIZONTAL STRAINS ALONG HORIZONTAL AXIS OF SYMMETRY AS A FUNCTION OF APPLIED STRESS FOR SPECIMEN NO. 2 (UNLINED LIMESTONE UNDER UNIAXIAL LOADING)

Strain, ε, (μ in./in.)

x = 5a
x = 2.2a
x = 1.5a
x = 1.1a
x = a

⊙ ● ◁ ◀ ✻

Stress, p (psi)

1000
800
600
400
200
0

0   200   400   600   800

Fig. 48 HORIZONTAL STRAINS ALONG VERTICAL AXIS OF SYMMETRY AS A FUNCTION OF APPLIED STRESS FOR SPECIMEN NO. 2 (UNLINED LIMESTONE UNDER UNIAXIAL LOADING)

87
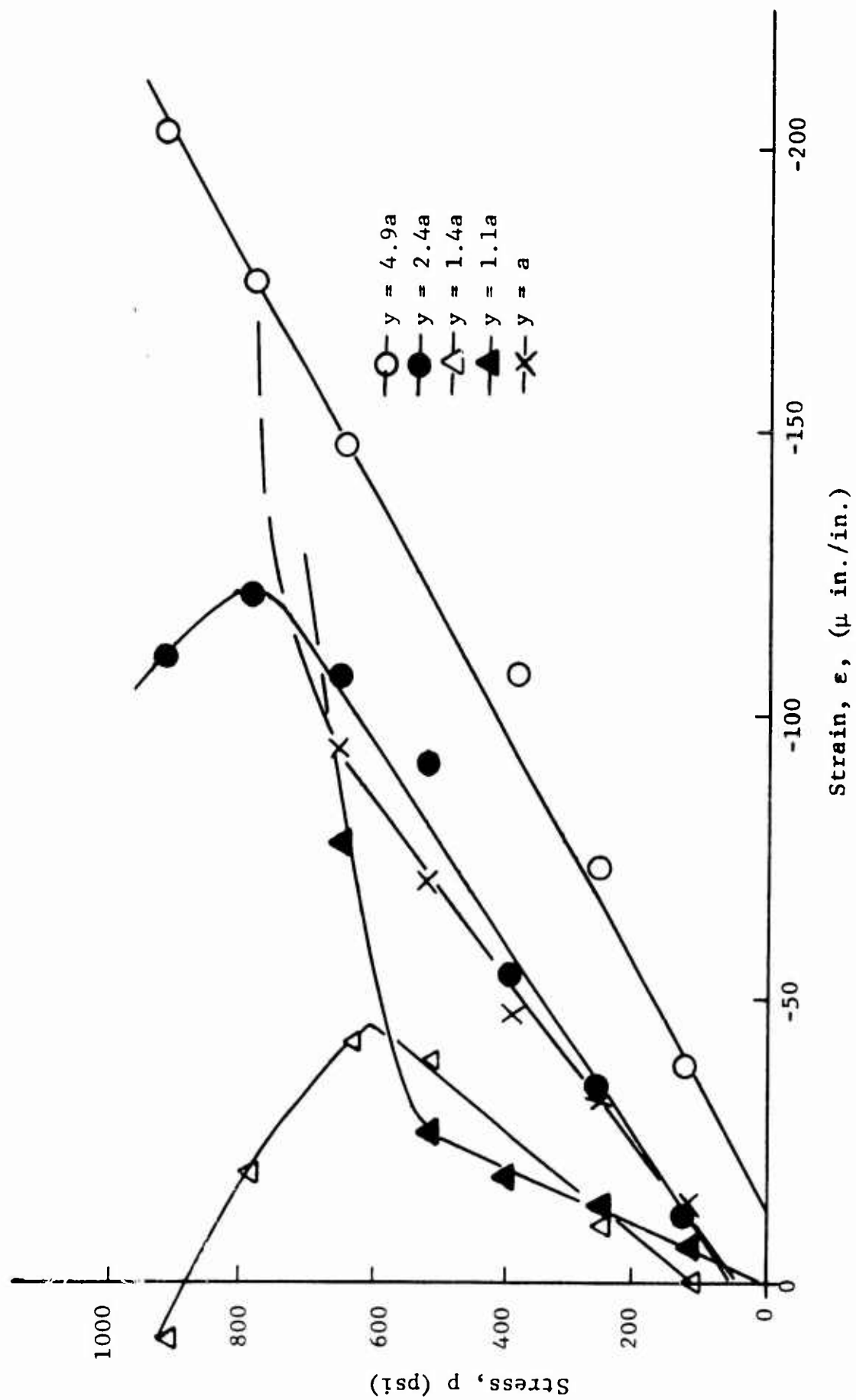
Fig. 49 VERTICAL STRAINS ALONG VERTICAL AXIS OF SYMMETRY AS A FUNCTION OF APPLIED STRESS
FOR SPECIMEN NO. 2 (UNLINED LIMESTONE UNDER UNIAXIAL LOADING)

88
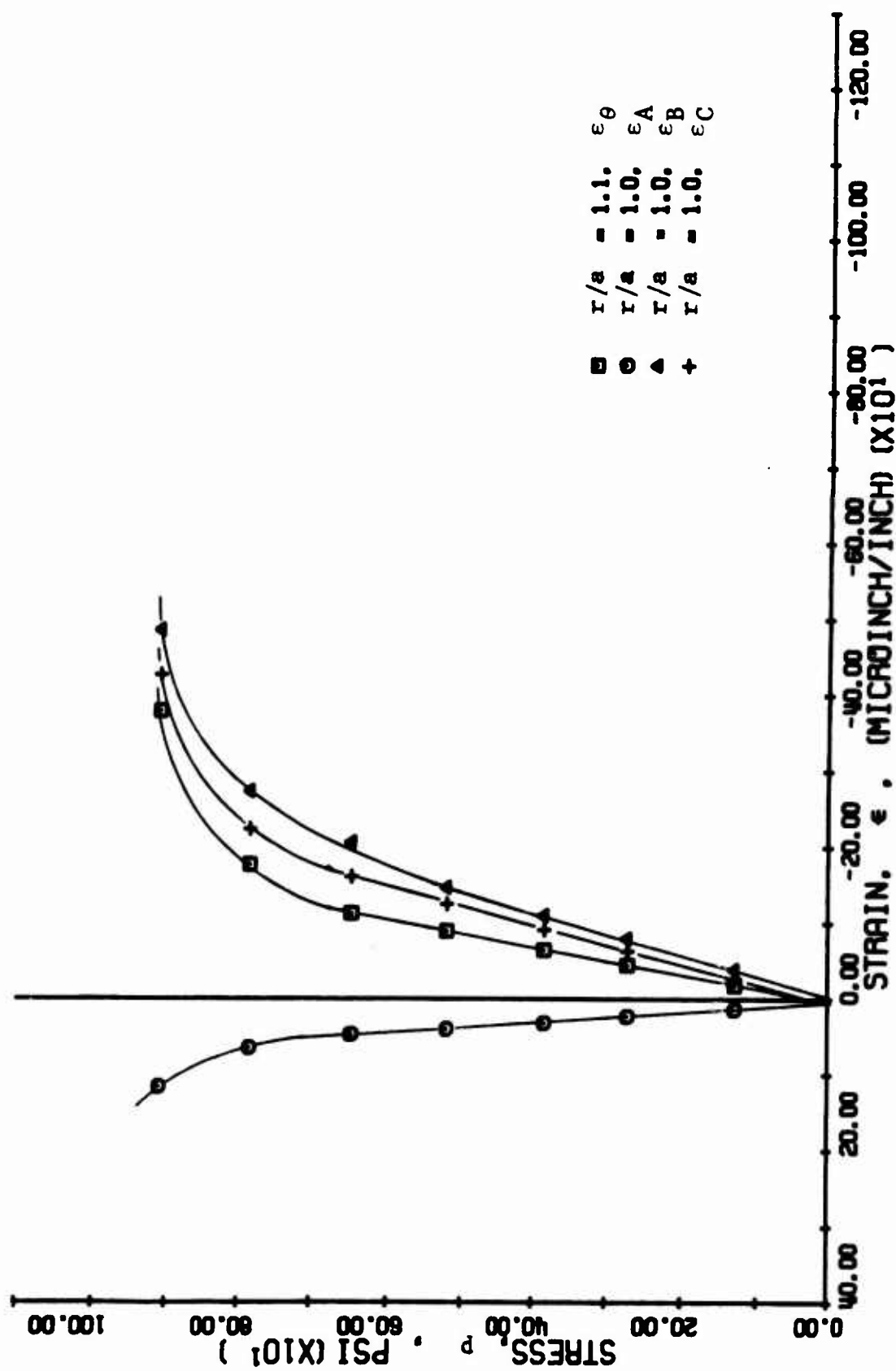
FIG. 50   STRAINS AT 45 DEGREE LOCATION FOR SPECIMEN NO. 2
(LIMESTONE UNLINED UNDER UNIAXIAL LOADING)
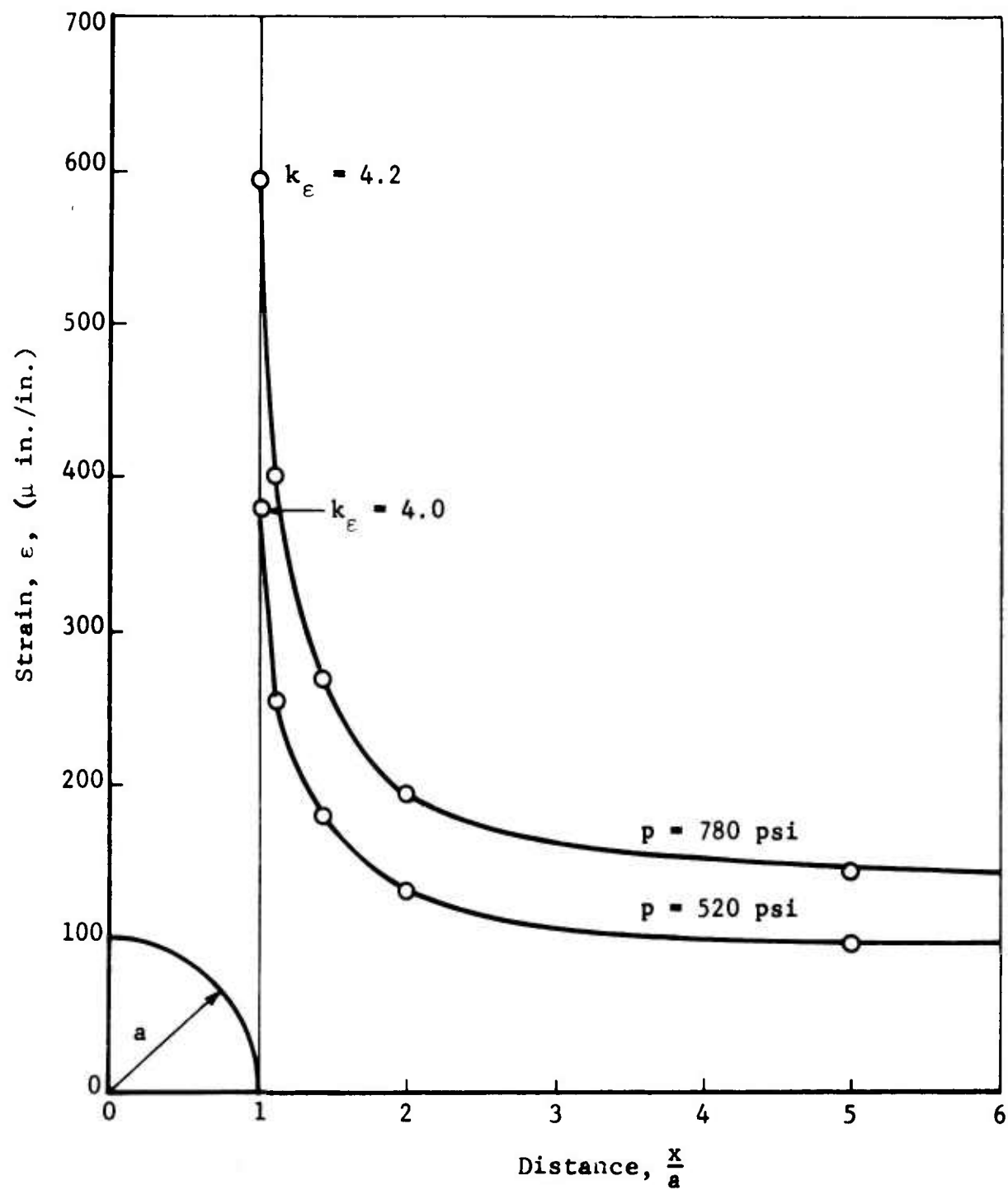
Fig. 51 COMPRESSIVE STRAIN DISTRIBUTION ALONG HORIZONTAL AXIS FOR TWO
STRESS LEVELS (UNCONFINED LIMESTONE SPECIMEN NO. 2)

90

FIG. 52 PRINCIPAL STRAINS ALONG 45-DEGREE RADIUS FOR SPECIMEN NO. 2
(LIMESTONE UNLINED UNDER UNIAXIAL LOADING)

91
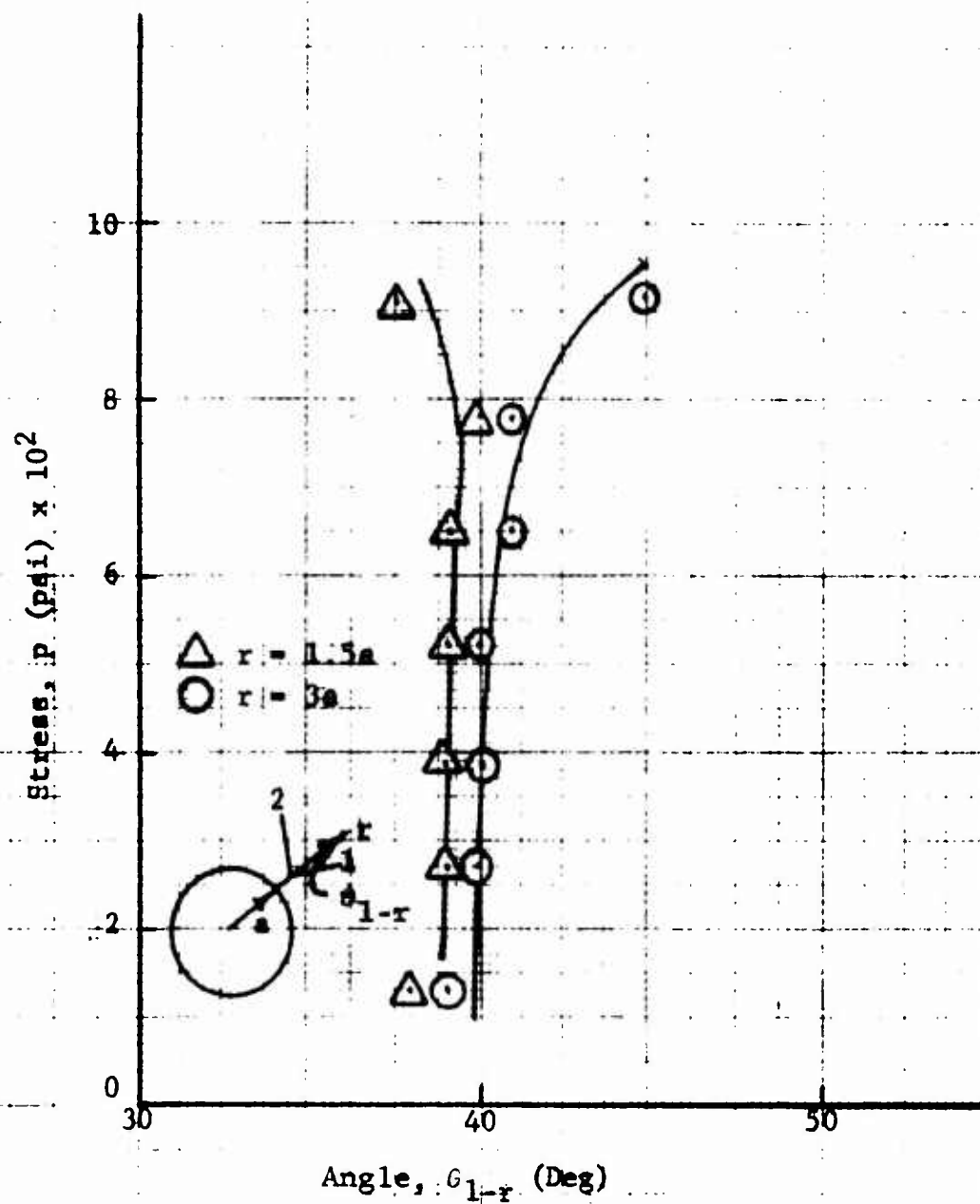
Fig. 53 PRINCIPAL DIRECTIONS ALONG 45 DEGREE RADIUS
FOR SPECIMEN NO. 2

92

increases from 39 to 40 degrees. The nature of the subsequent cracking was such as to cause the principal direction at the smaller radial distance to rotate toward the vertical whereas the tensile principal stress at $r = 3a$ rotated to eventually become horizontal, indicating that at that position the specimen was essentially a column subjected to vertical compression.

3. Comparison of Specimens No. 1 and 2

Specimens No. 1 and 2 were both unlined limestone subjected to uniaxial compressive loading. The only difference between the specimens was that while specimen No. 1 was only 2-1/2 in. thick, specimen No. 2 was 16 in. thick. Upon loading, specimen No. 1 cracked at an applied stress of approximately 1,250 psi, whereas crack initiation commenced in specimen No. 2 in the vicinity of 640 psi. This reduced fracture strength of the larger specimen is probably due to the so-called size effect in which the probability of having a catastrophic flaw in a critical location increases with increased volume at the elevated stressed regions (Ref. 17). While both the stresses and strains were much lower, an appreciably greater strain concentration factor occurred in the thicker specimen (Figs. 39 and 51), even prior to apparent cracking. The excessive size of specimen No. 2 did pose difficulties in loading uniformly. From other results, the excessively high strains at the hole resulted, in part, from slight nonuniformity in the applied loading.

For both specimens, cracking occurred vertically along the vertical axis, in both cases commencing at the hole - as predicted by the elastic analysis. At the crack initiation in specimen No. 1 at $p = 1,250$ psi, the horizontal tensile strain on the vertical axis at the boundary of the hole was $\varepsilon_x = 335$ μin./in. which based on an elastic modulus of 4.8×10^6 psi, corresponds to a computed σ_{max} at fracture of 1600 psi. This is much higher than the tensile fracture strength of 630 psi determined from uniaxial specimens

93

(Section IV). In the case of specimen No. 2, appreciable yielding in the horizontal direction occurred along the vertical axis in the vicinity of the hole before cracking ensued, hence it is not possible to evaluate the maximum tensile stress at failure using Hooke's law.

In the two unlined, uniaxially loaded limestone specimens, the computed Poisson's ratio was essentially 0.22 in both cases, in agreement with the value of 0.23 determined from uniaxially loaded specimens. The Young's moduli of 4.8×10^6 psi and 5.5×10^6 psi obtained from specimens No. 1 and 2, respectively, are somewhat higher than the value of 4×10^6 psi determined from the uniaxial specimens.

4. Specimens 3 and 4 - Marble Unlined Under Uniaxial Loading
a. Experimental Procedure

Specimens No. 3 and 4 were both 24 in. x 36 in. slabs of marble, each containing a 4 in. diameter centrally located unlined hole. Specimen No. 3 was 3.25 in. thick while specimen No. 4 was 3.28 in. thick. Both specimens were subjected to uniaxial compression using the previously described 1,000,000 lb testing machine. Two-element strain gages were applied on the faces of the specimen along the horizontal and vertical axes of symmetry, while three-element gages were applied along the 45-degree directions, similar to that in Fig. 29. As in the previous cases, far-field gages on the horizontal and vertical axes of symmetry were located on both the front and back faces of the slab, as were the single-element gages around the edge of the hole. Temperature compensation was achieved by adhering corresponding gages to unloaded marble specimens, the latter placed close to the specimen being tested. Diametral changes were monitored by DCDTs inserted into the hole along the horizontal and vertical directions. Full-field strains were observed and recorded by means of a birefringent coating adhered to the specimen surface. As with previous tests, specimen alignment was checked by low level preliminary loading and monitoring the far-field gages plus those in the vicinity of the hole. During actual testing, the instrumented specimen was loaded in

94

approximately 15,000 lb ($\approx$ 192 psi) load increments. Strain gage and DCDT readings were recorded with the Digital Data Acquisition system, using external balanced bridges. The photoelastic fringe patterns were photographed at selected load levels.

b. <u>Results and Discussion</u>

A sequence of isochromatic fringe patterns at various stress levels for specimens No. 3 and 4 is illustrated in Figs. 54 and 55, respectively. The applied average stress is indicated below each frame. According to these fringe photographs, cracking again commenced in the region of high tensile stress along the vertical axis on the boundary of the hole, as predicted by the theory. Fringe records indicate that cracking started at an applied stress of approximately 1,685 psi in specimen No. 3 and at about 1,900 psi in specimen No. 4. The extremely dense fringe patterns in the neighborhood of the propagating crack is visible in both specimens.

Diametral changes measured with the DCDT's are plotted in Figs. 56 and 57 as functions of applied stress. The curves for specimen No. 3 (Fig. 56) are linear up to about 1,600 psi, whereas those for specimen No. 4 (Fig. 57) become nonlinear at about 1,900 psi. These stress levels agree with the visible onset of cracking discussed previously. The deflections per unit of applied stress in the linear range for specimen No. 3 are

$$\frac{\delta_h}{P} = 0.6 \times 10^{-6} \text{ in./psi}$$

$$\frac{\delta_v}{P} = -1.5 \times 10^{-6} \text{ in./psi}$$

The corresponding values for specimen No. 4 are

$$\frac{\delta_h}{P} = 1.1 \times 10^{-6} \text{ in./psi}$$

$$\frac{\delta_v}{P} = -1.2 \times 10^{-6} \text{ in./psi}$$

95

P = 1885 psi   P ≑ 2160 psi   P = 2540 psi

P = 2685 psi   P = 2950 psi   P = 3100 psi

Fig. 54   SEQUENCE OF ISOCHROMATIC FRINGE PATTERNS IN PHOTOELASTIC
COATING INDICATING CRACKING IN THE ROCK ALONG THE VERTICAL
AXIS OF SYMMETRY OF SPECIMEN NO. 3 (UNLINED MARBLE UNDER
UNIAXIAL LOADING)

96

Fig. 55 SEQUENCE OF ISOCHROMATIC FRINGE PATTERNS IN PHOTOELASTIC
COATING INDICATING CRACKING IN THE ROCK ALONG THE VERTICAL
AXIS OF SYMMETRY OF SPECIMEN NO. 4 (UNLINED MARBLE UNDER
UNIAXIAL LOADING)

97
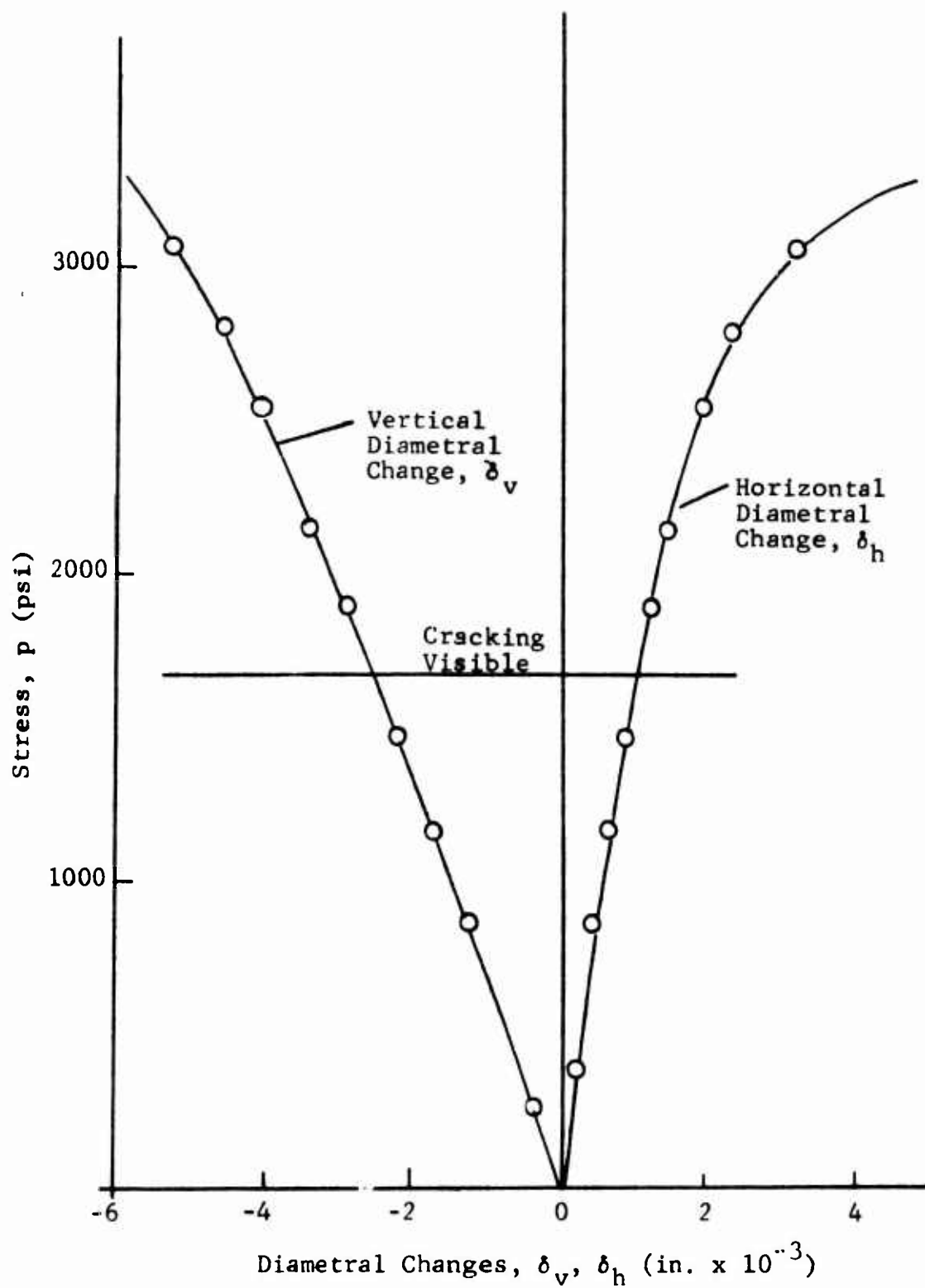
Fig. 56 DIAMETRAL CHANGES AS A FUNCTION OF APPLIED STRESS
FOR SPECIMEN NO. 3 (UNLINED MARBLE UNDER UNIAXIAL
LOADING)

98
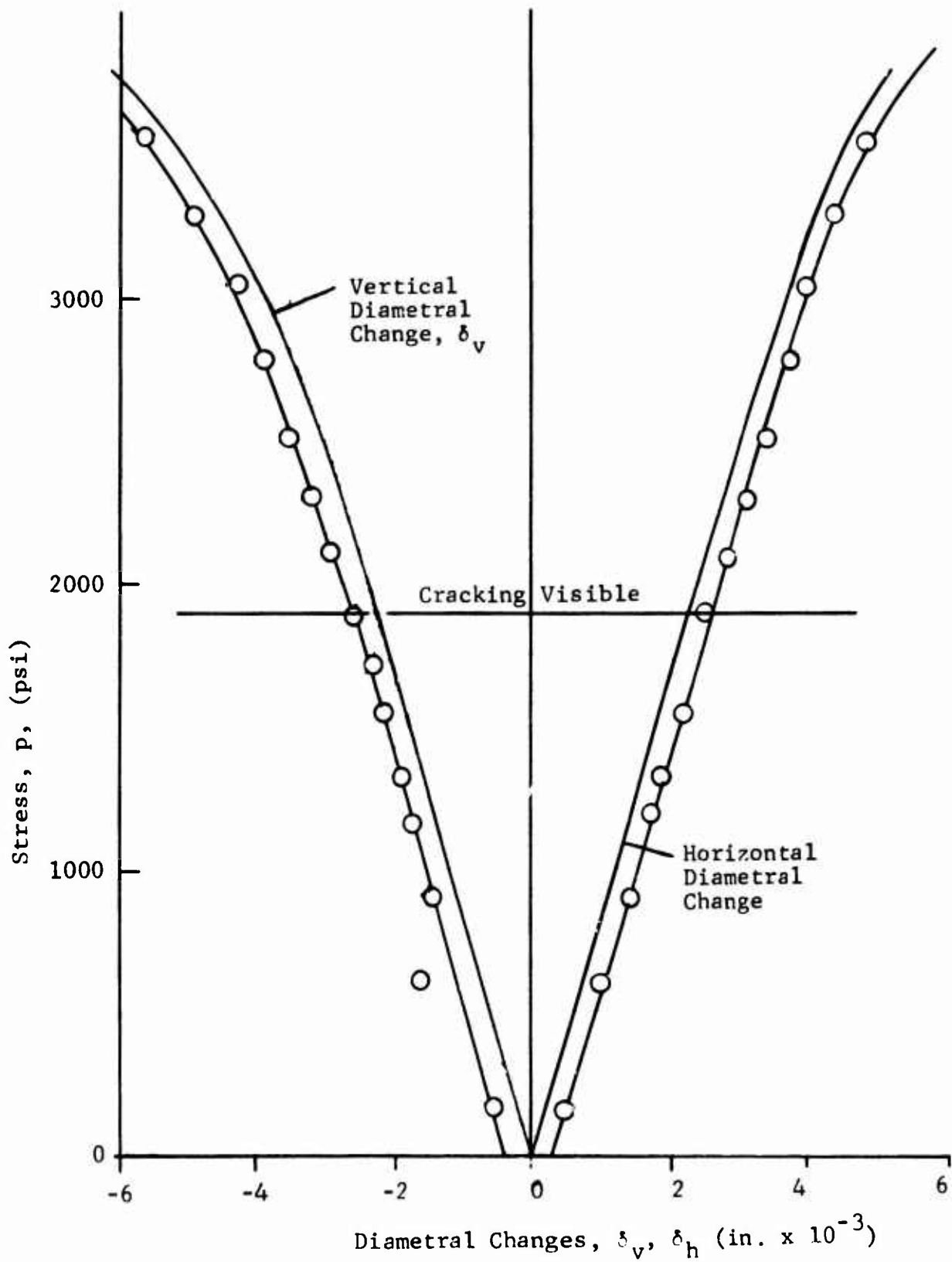
Fig. 57 DIAMETRAL CHANGES AS A FUNCTION OF APPLIED STRESS FOR SPECIMEN NO. 4 (UNLINED MARBLE UNDER UNIAXIAL LOADING)

99

While the vertical deflections for the two specimens agree well, there is some discrepancy between the horizontal deflections.

Strain gage readings along the horizontal, vertical and 45-degree directions are plotted versus applied stress for specimen No. 3 in Figs. 58 through 61, with radial location as parameter. The corresponding results for specimen No. 4 are plotted in Figs. 62 through 66. On the basis of the far-field gages on both the horizontal and vertical axis of symmetry, the following modulus and Poisson's ratio were computed for the marble of specimen No. 3.

$$E = 8.3 \times 10^6 \text{ psi}$$
$$\nu = 0.25$$

The corresponding values for specimen No. 4 are

$$E = 8.0 \times 10^6 \text{ psi}$$
$$\nu = 0.28$$

Consideration of the strains along the vertical axis of symmetry of specimen No. 3 (Figs. 60 and 61) confirms the previous indications that crack initiation occurred at an applied stress of approximately 1,600 psi. At this load level, horizontal and vertical strain profiles in the neighborhood of the hole for top and bottom of hole and front and back faces deviate (Figs. 60 and 61). Again, strains in the neighborhood of cracking increased rapidly. The strains along the horizontal axis remained linear at least up to crack initiation at 1,600 psi with the high compressive strains near the hole remaining linear well beyond this point. On the other hand, tensile nonlinearities associated with yielding did occur in the high strain region along the vertical axis in the vicinity of the hole (Fig. 60).

The vertical and horizontal strains along the horizontal axis of specimen No. 4 (Figs. 62 and 63) remain linear at least up to 1,900 psi. The horizontal (tensile) strains along the vertical

100
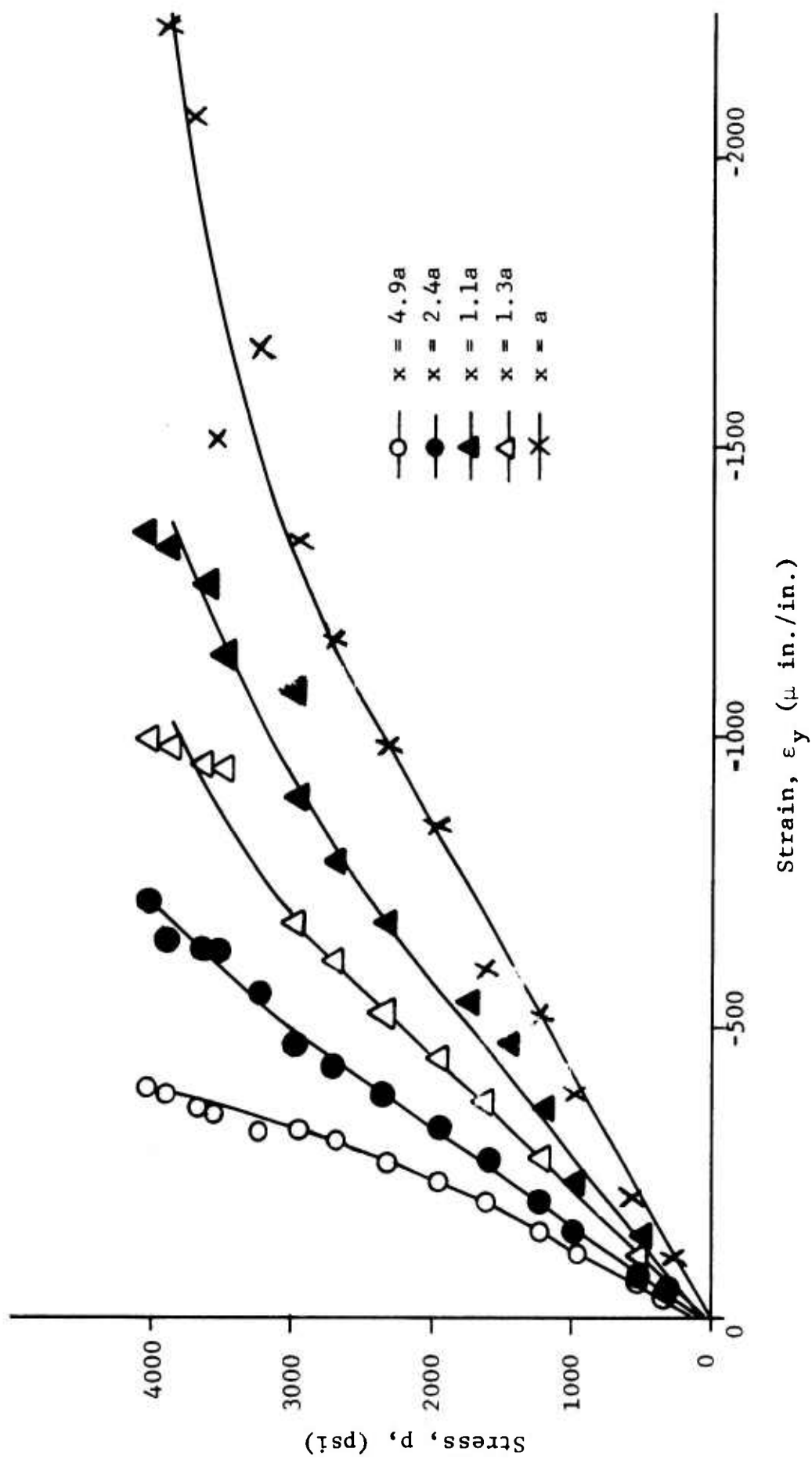
Fig. 58   VERTICAL STRAINS ALONG HORIZONTAL AXIS OF SYMMETRY AS A FUNCTION OF APPLIED STRESS
FOR SPECIMEN NO. 3 (UNLINED MARBLE UNDER UNIAXIAL LOADING)

101
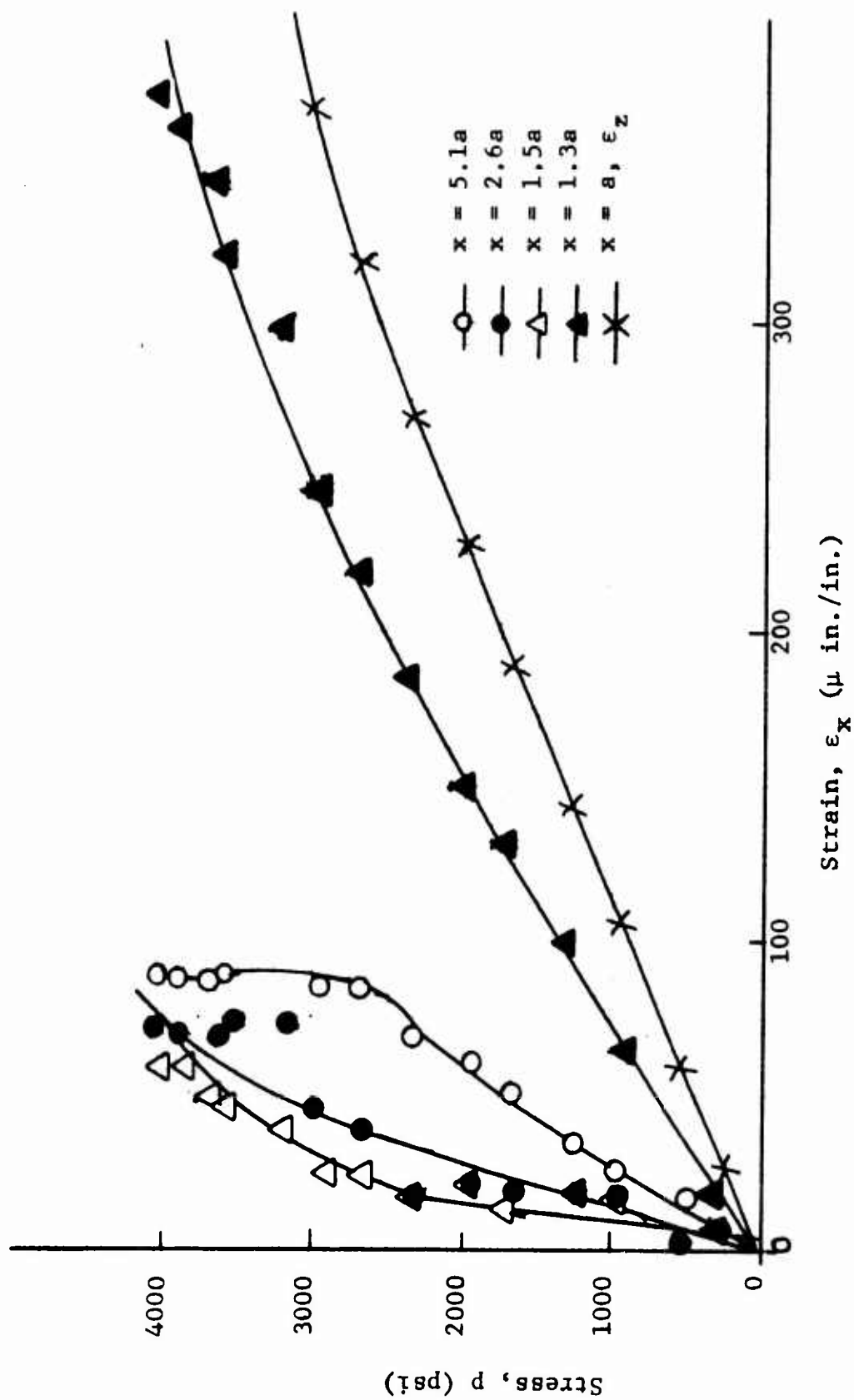
Fig. 59 HORIZONTAL STRAINS ALONG HORIZONTAL AXIS OF SYMMETRY AS A FUNCTION OF APPLIED STRESS FOR SPECIMEN NO. 3 (UNLINED MARBLE UNDER UNIAXIAL LOADING)
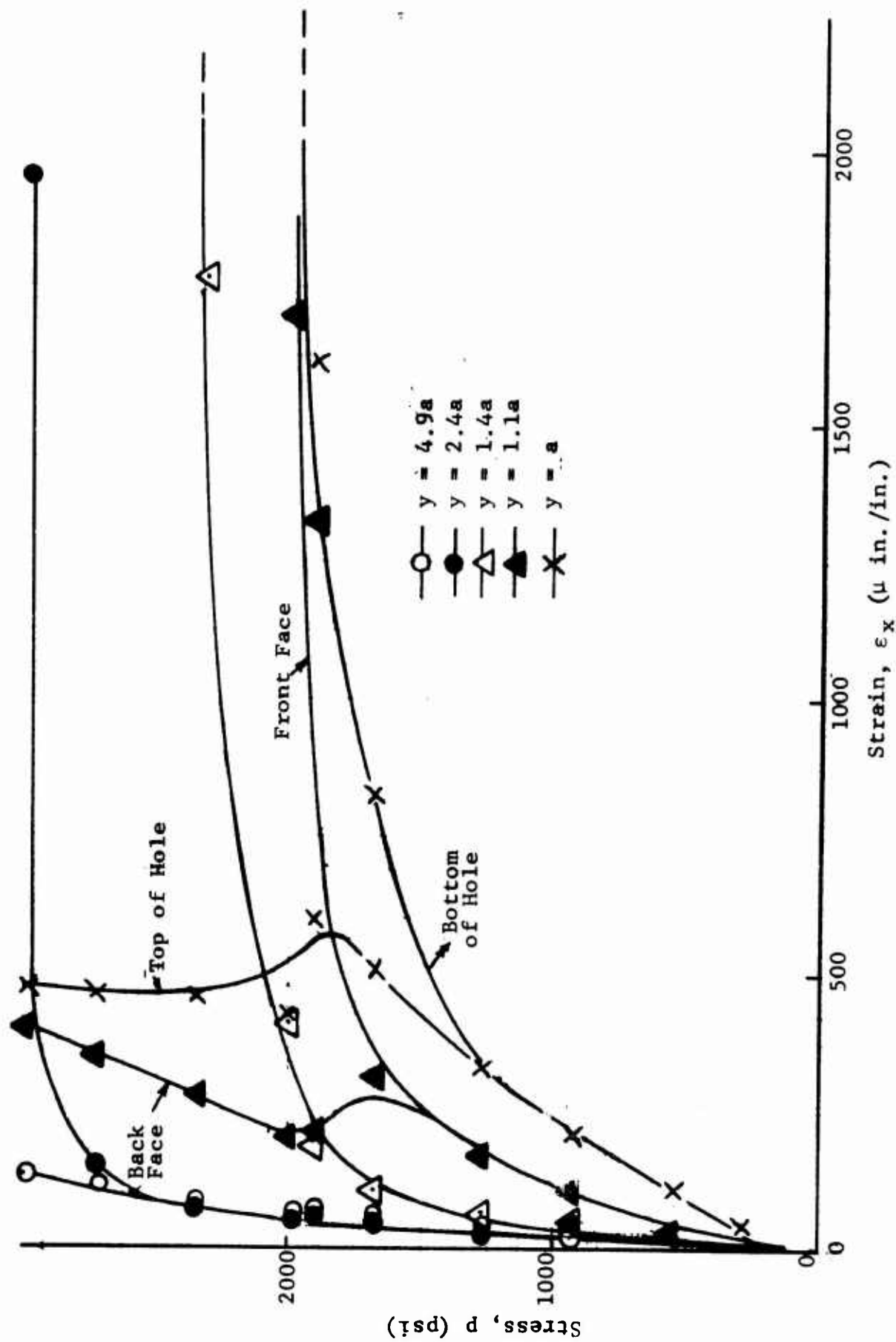
Fig. 60 HORIZONTAL STRAINS ALONG VERTICAL AXIS OF SYMMETRY AS A FUNCTION OF APPLIED STRESS FOR SPECIMEN NO. 3 (UNLINED MARBLE UNDER UNIAXIAL LOADING)

103
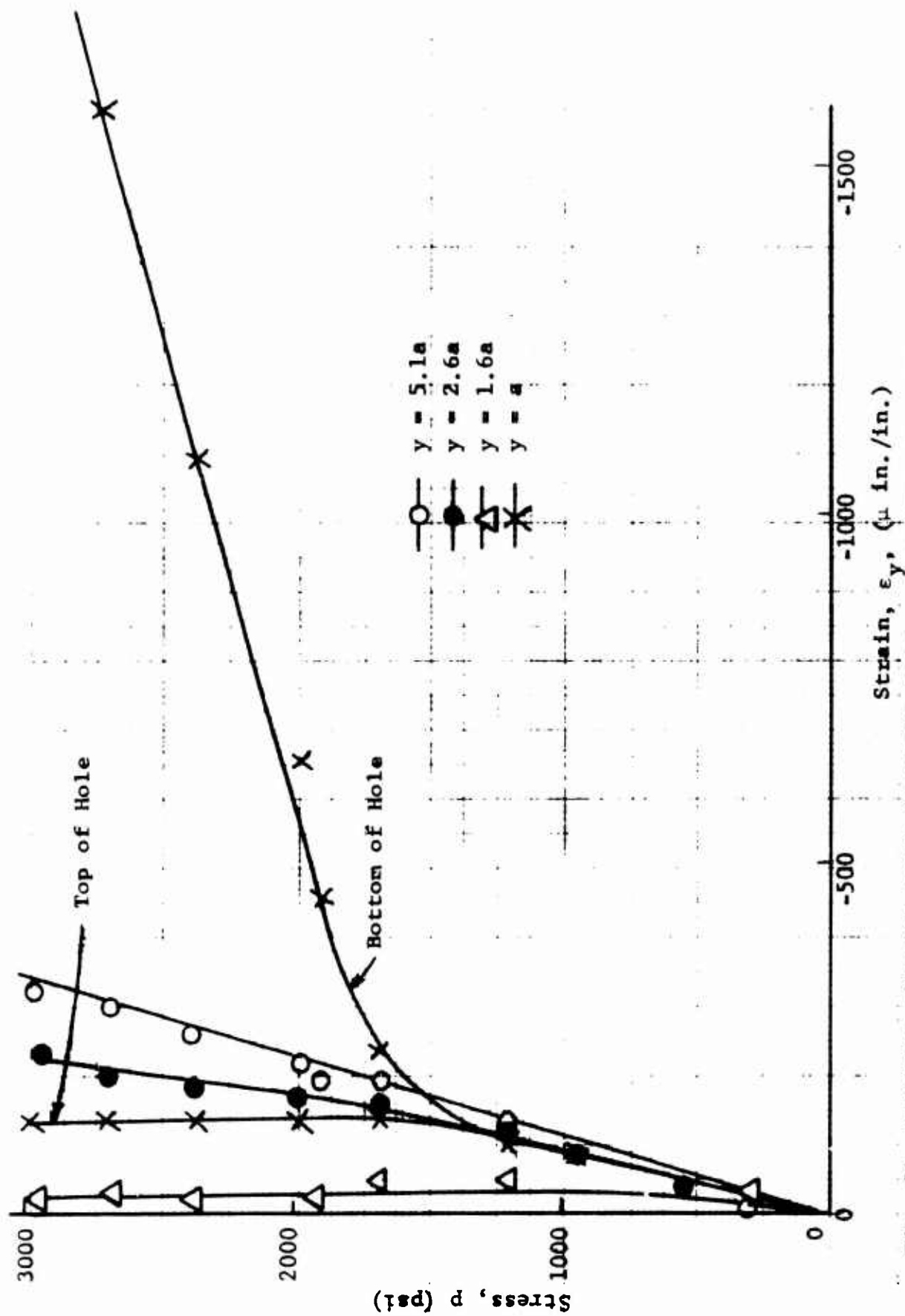
Fig. 61 VERTICAL STRAINS ALONG VERTICAL AXIS OF SYMMETRY AS A FUNCTION OF APPLIED
STRESS FOR SPECIMEN NO. 3 (UNLINED MARBLE UNDER UNIAXIAL LOADING)

104
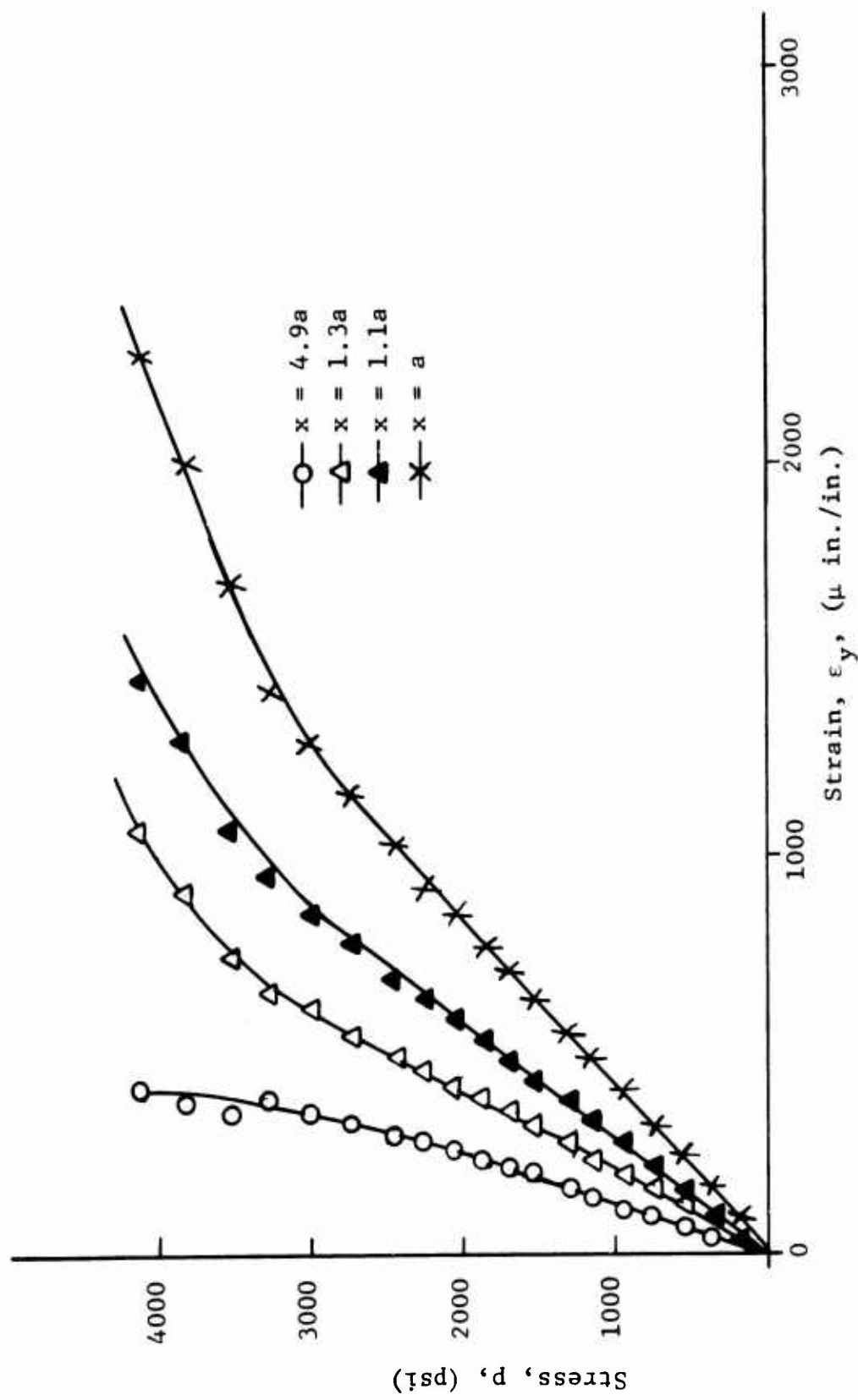
Fig. 62 VERTICAL STRAINS ALONG HORIZONTAL AXIS OF SYMMETRY AS A FUNCTION OF APPLIED STRESS
FOR SPECIMEN NO. 4 (UNLINED MARBLE UNDER UNIAXIAL LOADING)

105
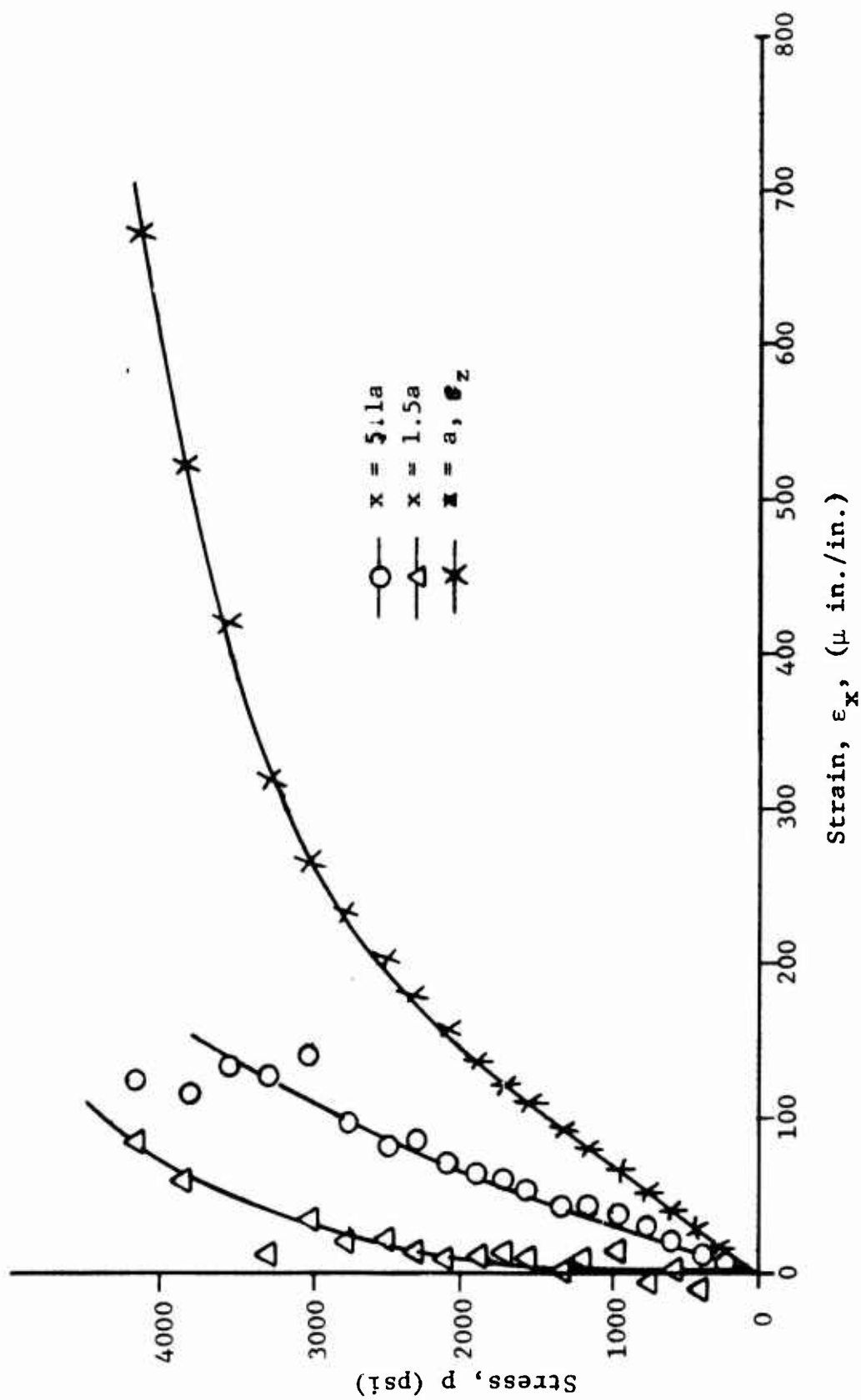
Fig. 63 HORIZONTAL STRAINS ALONG HORIZONTAL AXIS OF SYMMETRY AS A FUNCTION OF APPLIED STRESS FOR SPECIMEN NO. 4 (UNLINED MARBLE UNDER UNIAXIAL LOADING)
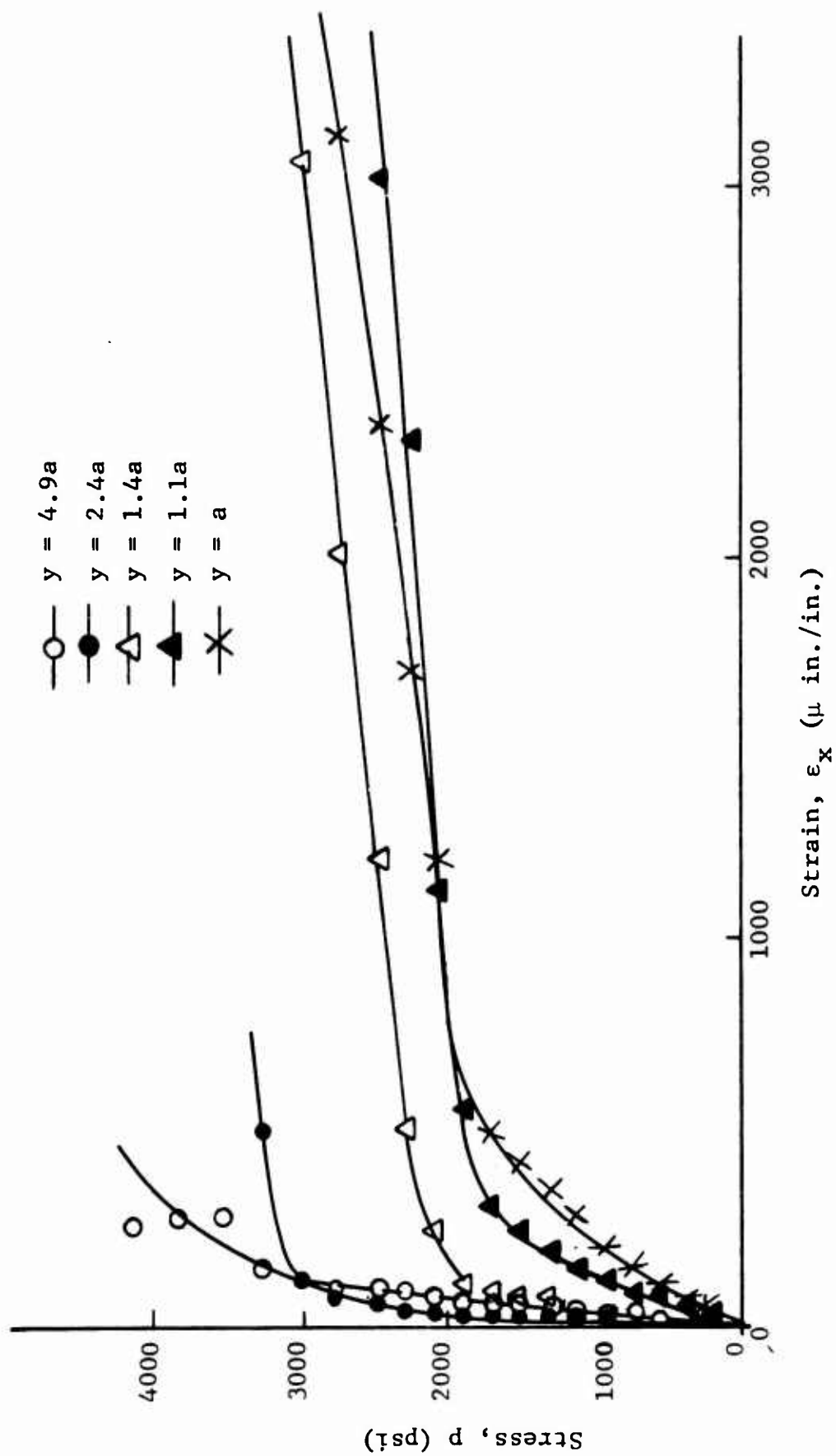
Fig. 64 HORIZONTAL STRAINS ALONG VERTICAL AXIS OF SYMMETRY AS A FUNCTION OF APPLIED STRESS
FOR SPECIMEN NO. 4 (UNLINED MARBLE UNDER UNIAXIAL LOADING)

107
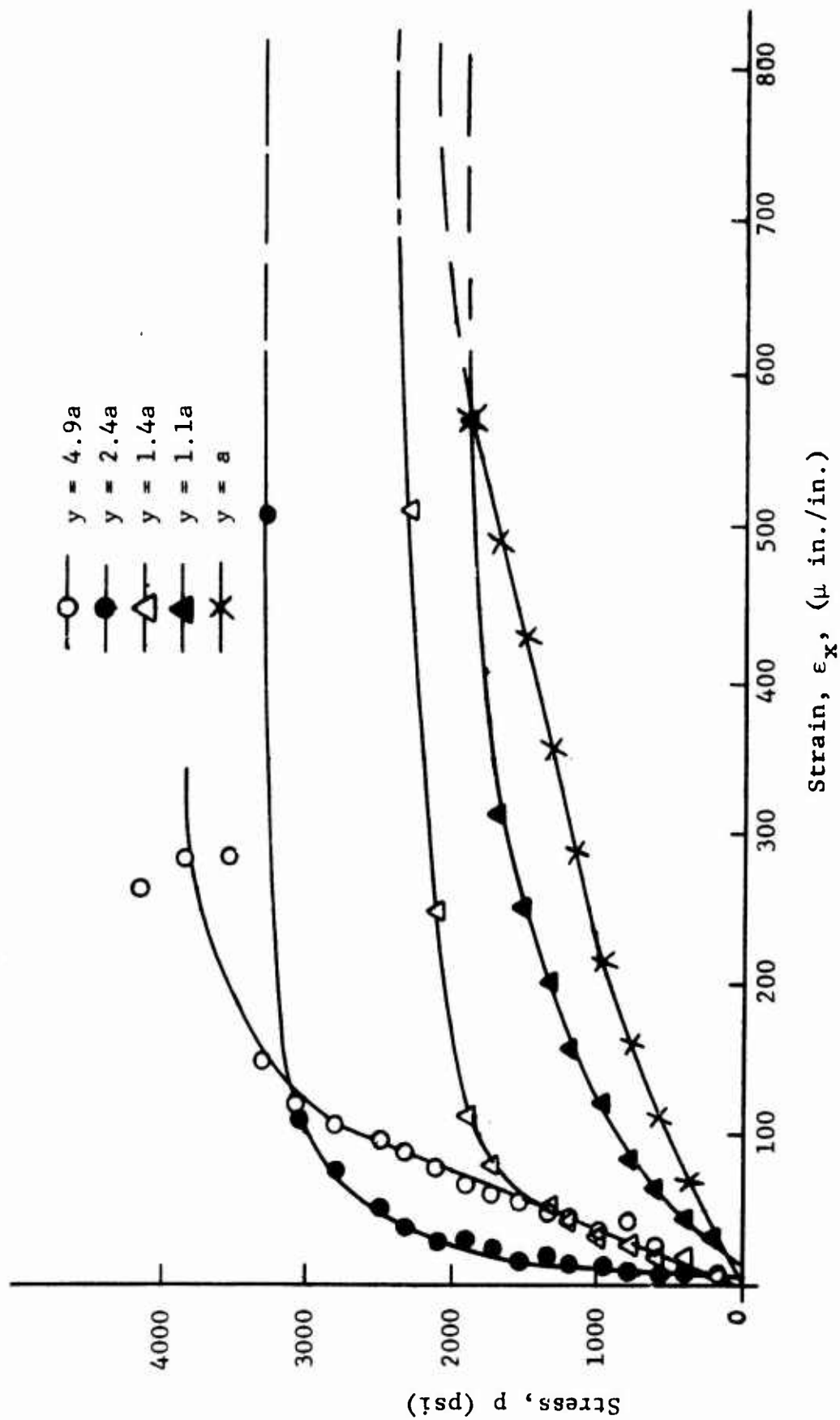
Fig. 65   HORIZONTAL STRAINS ALONG HORIZONTAL AXIS OF SYMMETRY AS A FUNCTION OF APPLIED
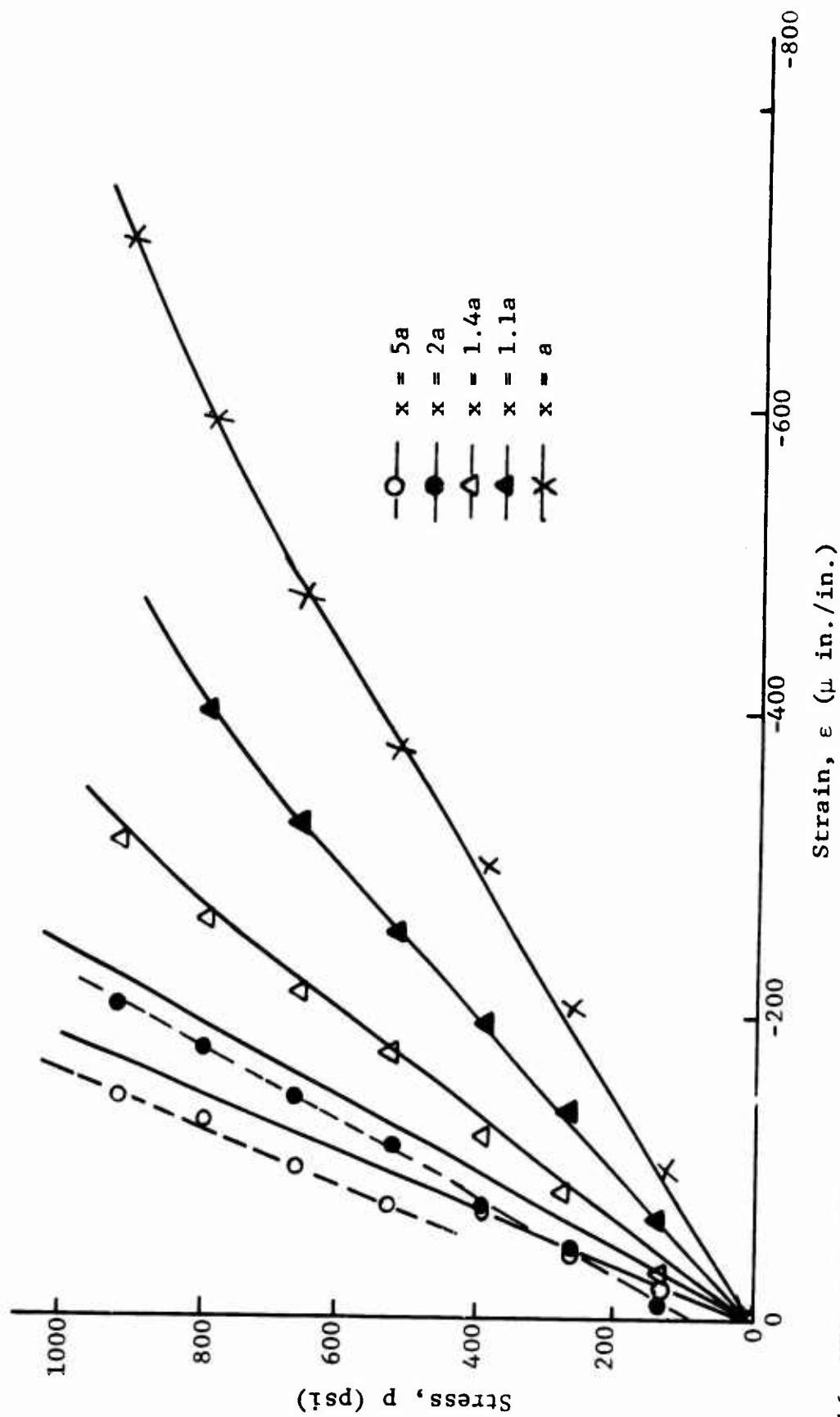STRESS FOR SPECIMEN NO. 4 - EXPANDED SCALE (UNLINED MARBLE UNDER UNIAXIAL LOADING)

108
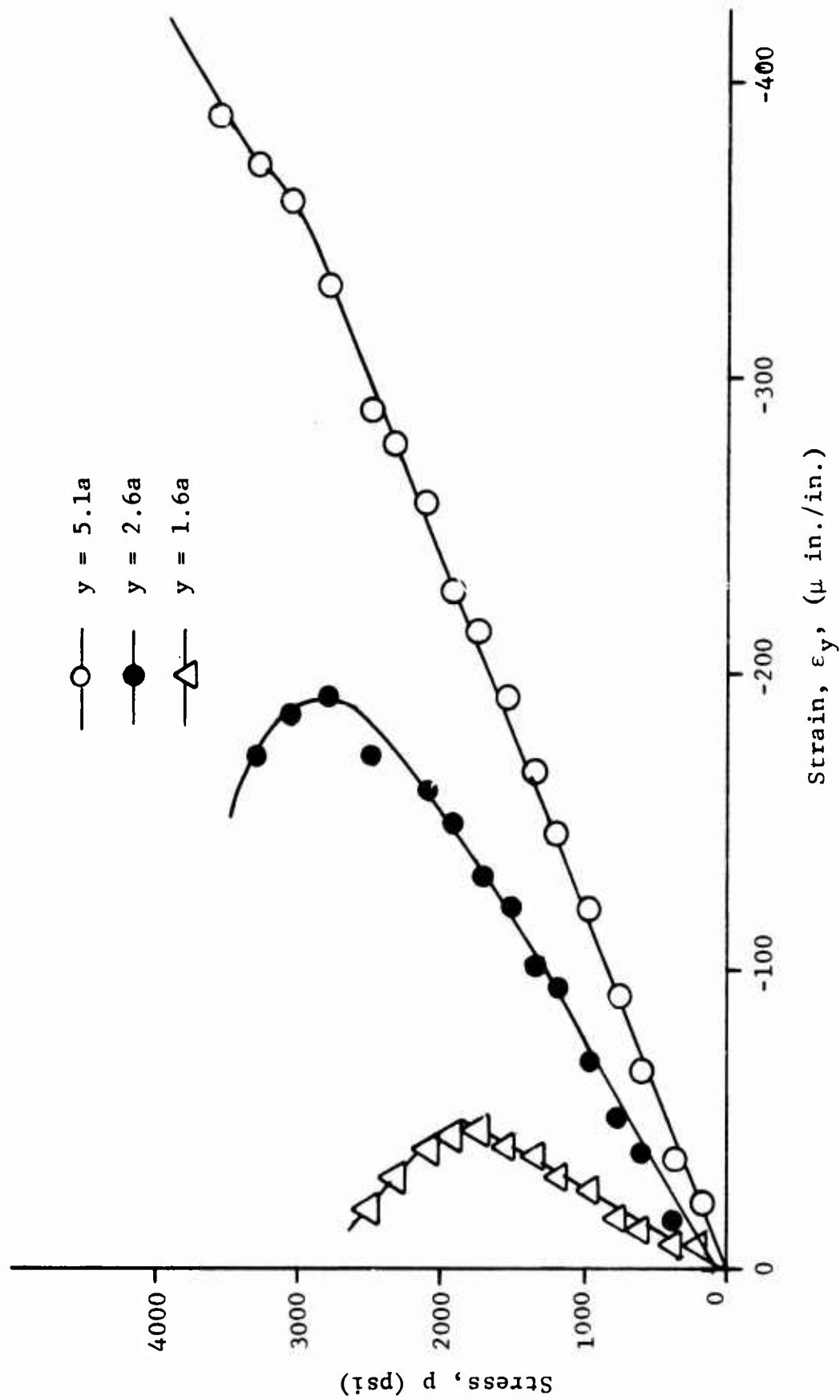
Fig. 66 VERTICAL STRAINS ALONG VERTICAL AXIS OF SYMMETRY AS A FUNCTION OF APPLIED STRESS FOR SPECIMEN NO. 4 (UNLINED MARBLE UNDER UNIAXIAL LOADING)
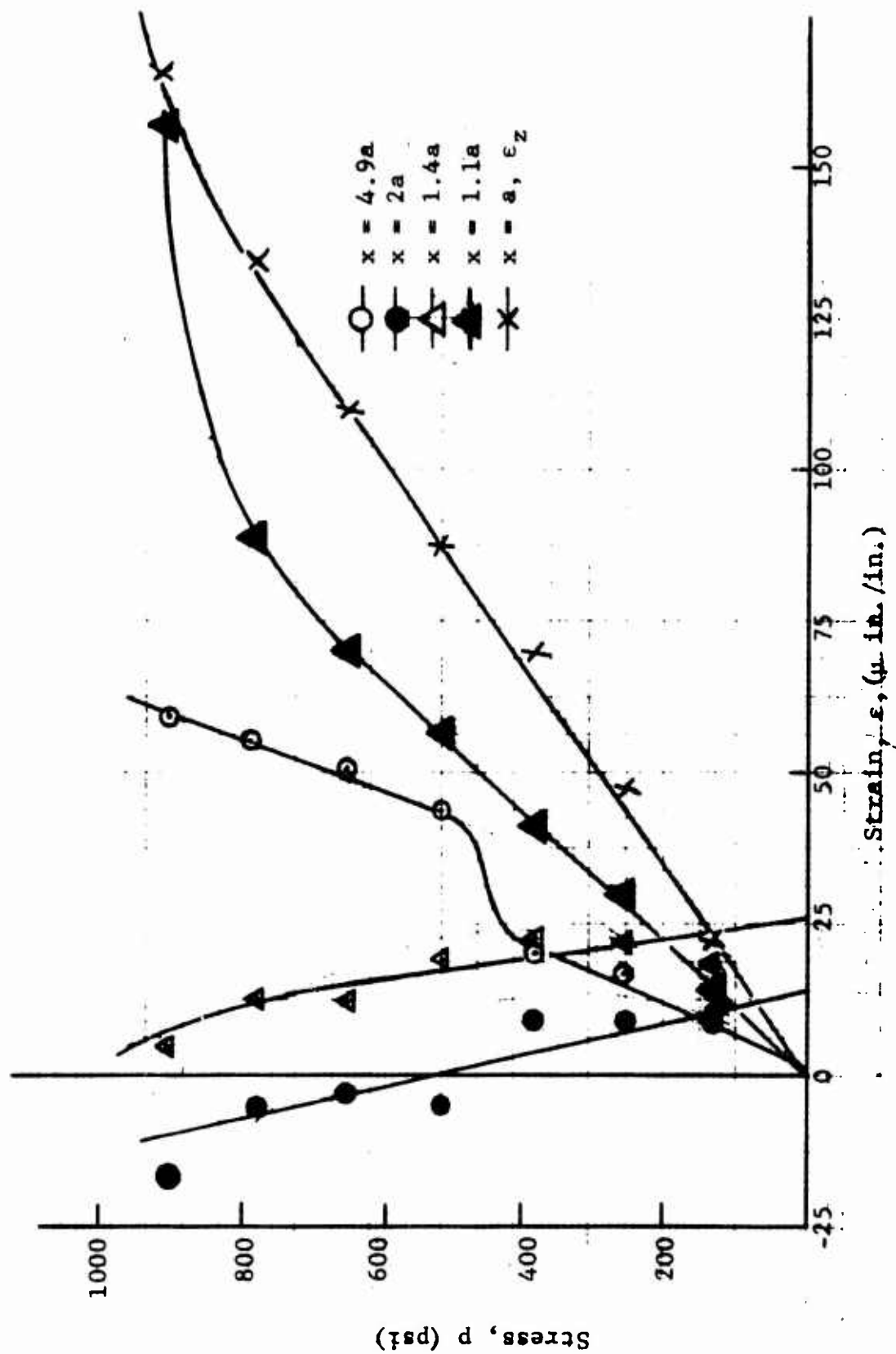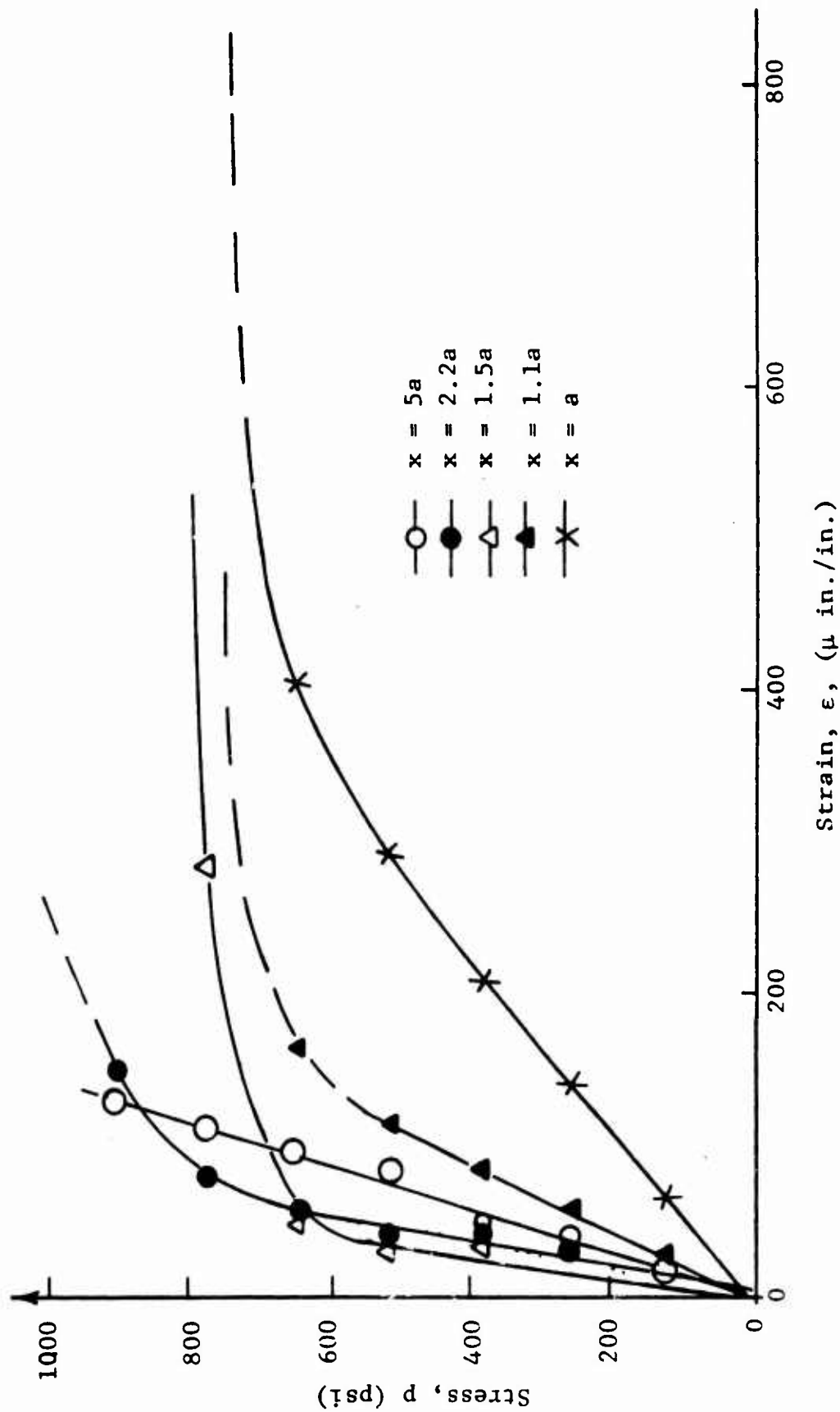
109

axis in the neighborhood of the hole increase abruptly at p = 1900 psi, confirming the previous indications that crack initiation occurred at this stress (Figs. 65 and 66). Moreover, crack growth along the vertical axis is apparent by observing how the strains at subsequent locations increase abruptly (Fig. 64). Consideration of Fig. 66 shows that upon crack initiation, redistribution of the stress and strain fields along the vertical axis are such that the vertical compressive strains in the immediate vicinity of the hole decreased with increased applied stress while those more remote from the crack continued to increase, although at a reduced rate.

From Figs. 58 and 62, the strain concentration factor (ratio between the vertical strain at the edge of the hole and the far-field vertical strain) for specimens No. 3 and 4 in the linear ranges is

$$k_\epsilon = 3.35$$

Strains along the 45-degree radius were first plotted as read (Fig. 67 for specimen No. 3) with ϵ_a, ϵ_b, ϵ_c designating rosette strains along the radial, 60-degree and 120-degree directions, respectively (measured counterclockwise from the radius). Subsequently, principal strains were computed using the rosette equations and plotted in Fig. 68. Principal directions were similarly computed and plotted versus stress for two radial locations, Fig. 69. The principal strain profiles remain linear well beyond crack initiation. The principal directions remain constant up to approximately p = 2,200 psi and start rotating thereafter. Again, the principal directions along the 45-degree radial line will be close to zero at the boundary of the hole (r = a), increasing to about 35 degrees at r = 1.5a; 44 degrees at r = 3a and close to 45 degrees far from the hole.

The corresponding rosette strains along the 45-degree radial direction are displayed for specimen No. 4 in Fig. 70, the computed principal strains in Fig. 71 and the principal directions in Fig. 72. As with specimen No. 3, the principal strains along the 45-degree direction remain linear beyond the initiation of cracking.

110
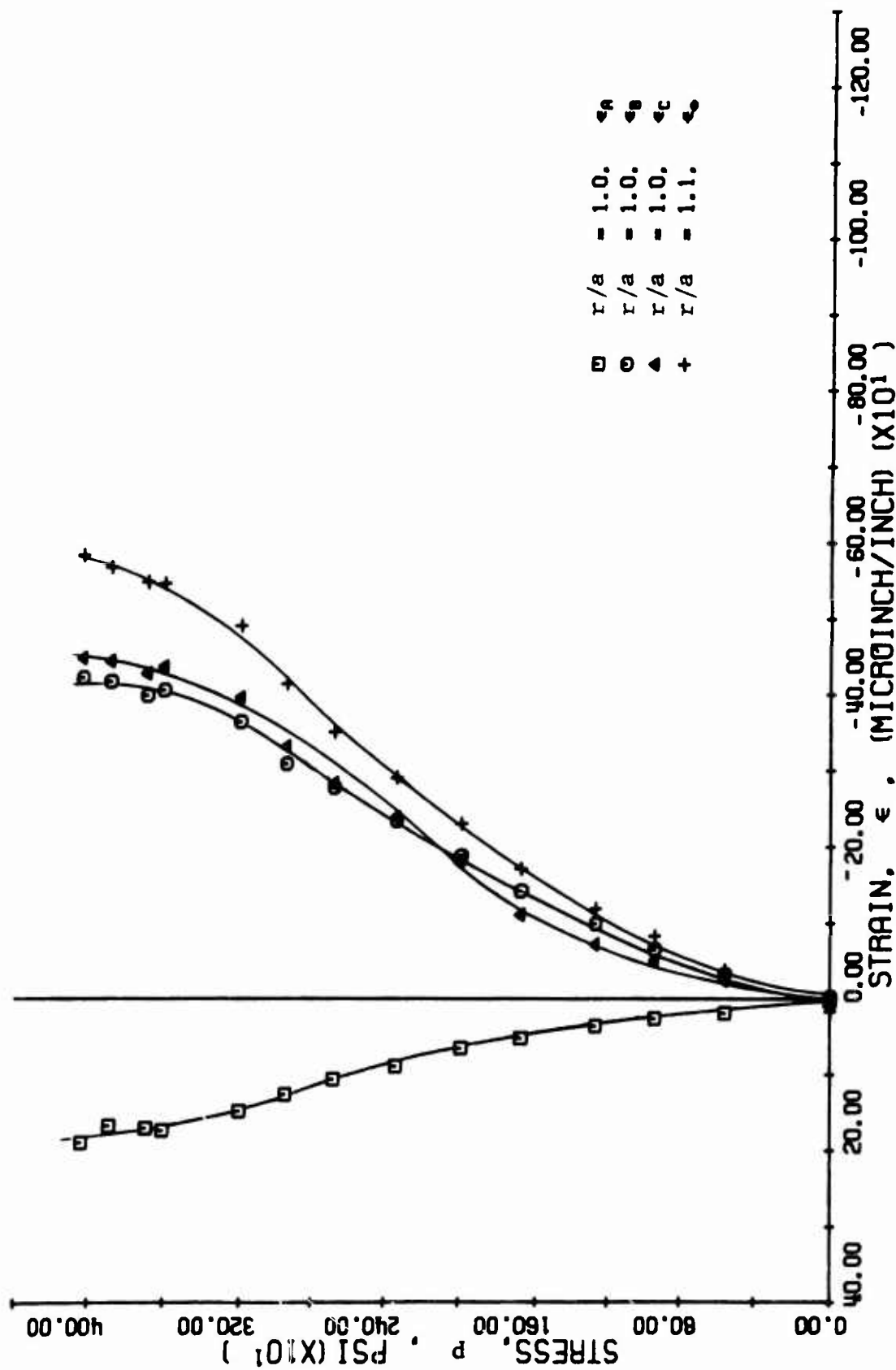
FIG. 67   STRAINS ALONG 45 DEGREE RADIUS FOR SPECIMEN NO. 3
(MARBLE UNLINED UNDER UNIAXIAL LOADING)

111
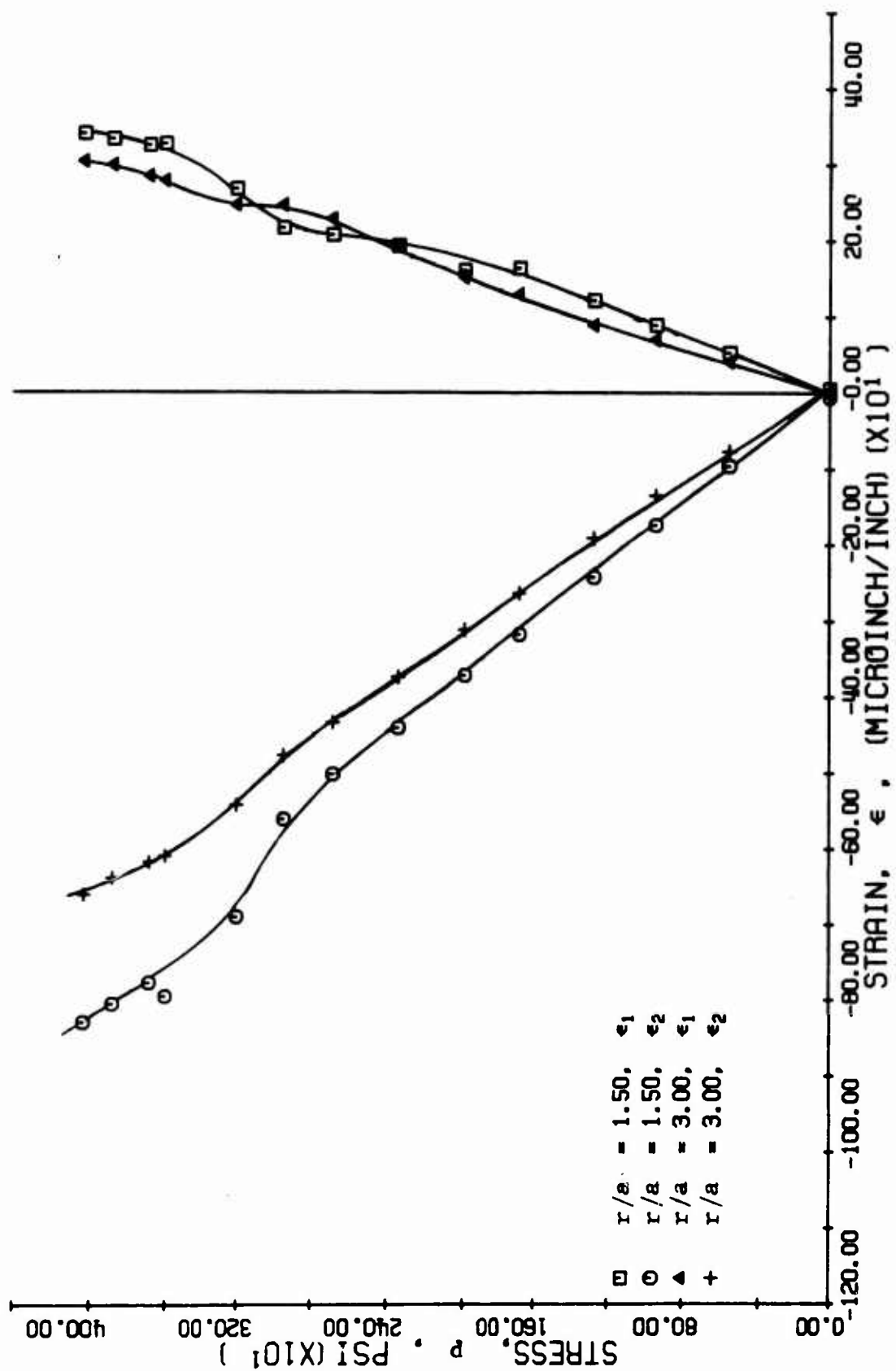
FIG. 68   PRINCIPAL STRAINS ALONG 45-DEGREE RADIUS FOR SPECIMEN NO. 3
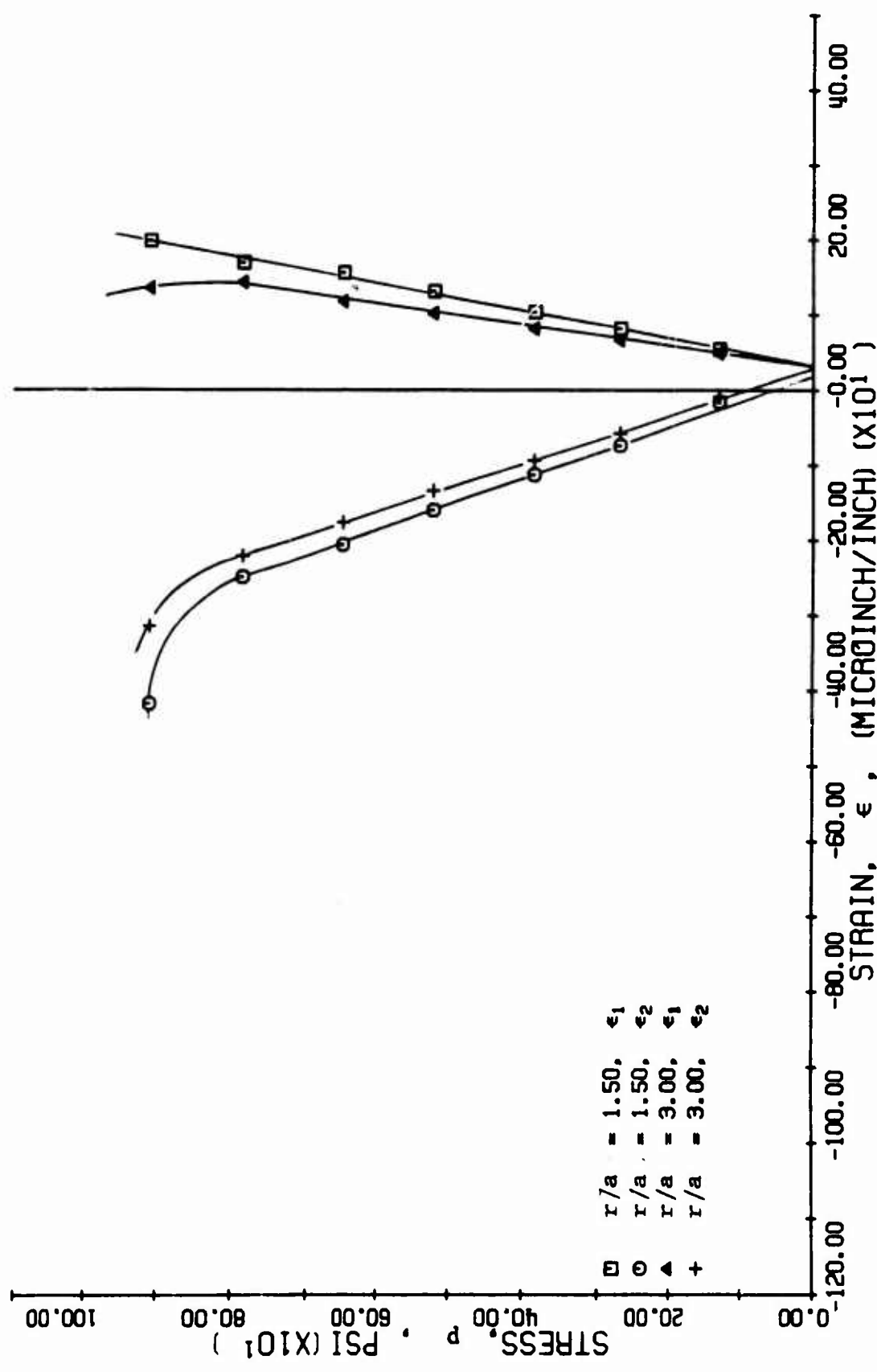(MARBLE UNLINED UNDER UNIAXIAL LOADING)

112
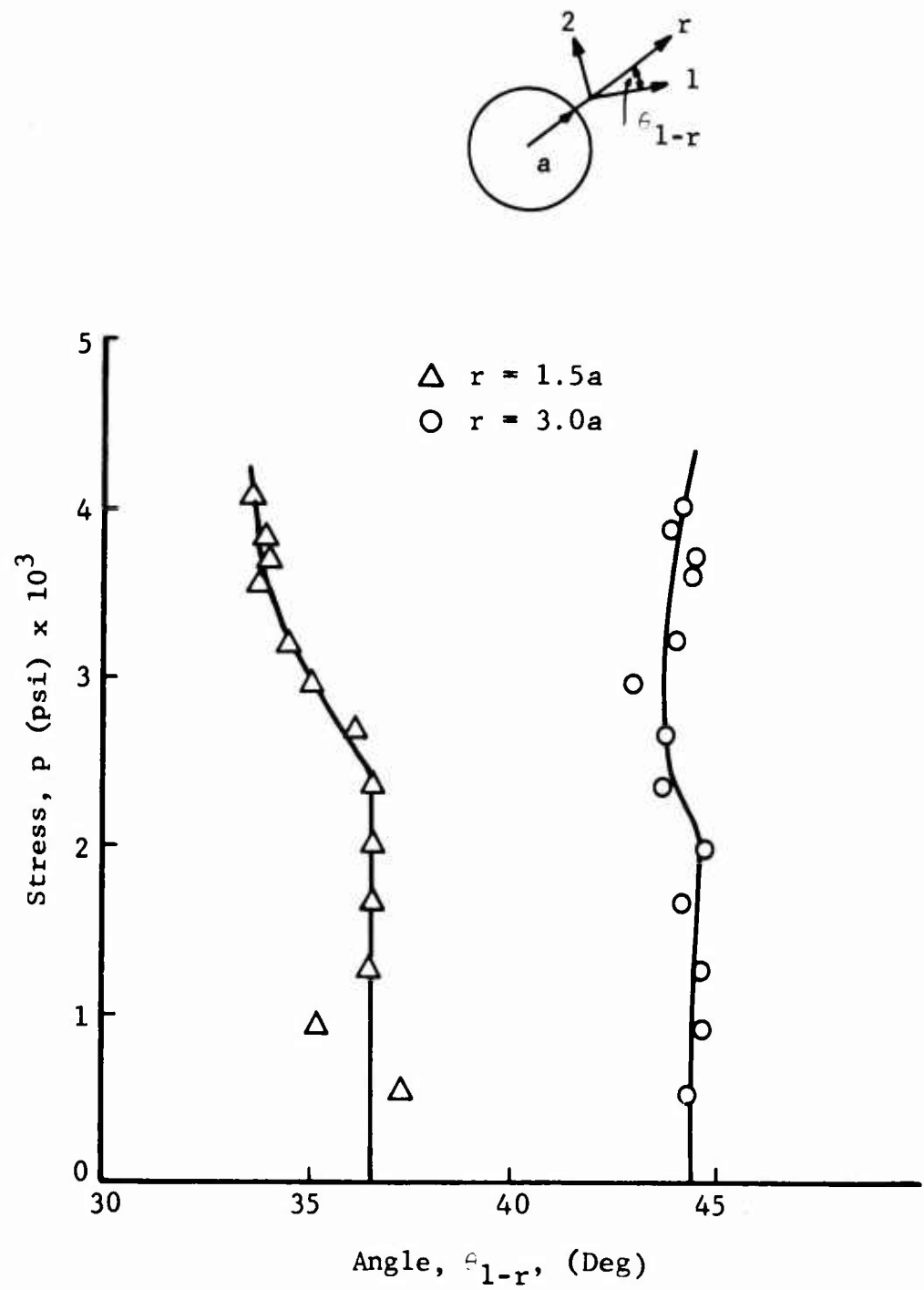
Fig. 69   PRINCIPAL DIRECTIONS ALONG 45-DEGREE RADIUS FOR SPECIMEN NO. 3

113
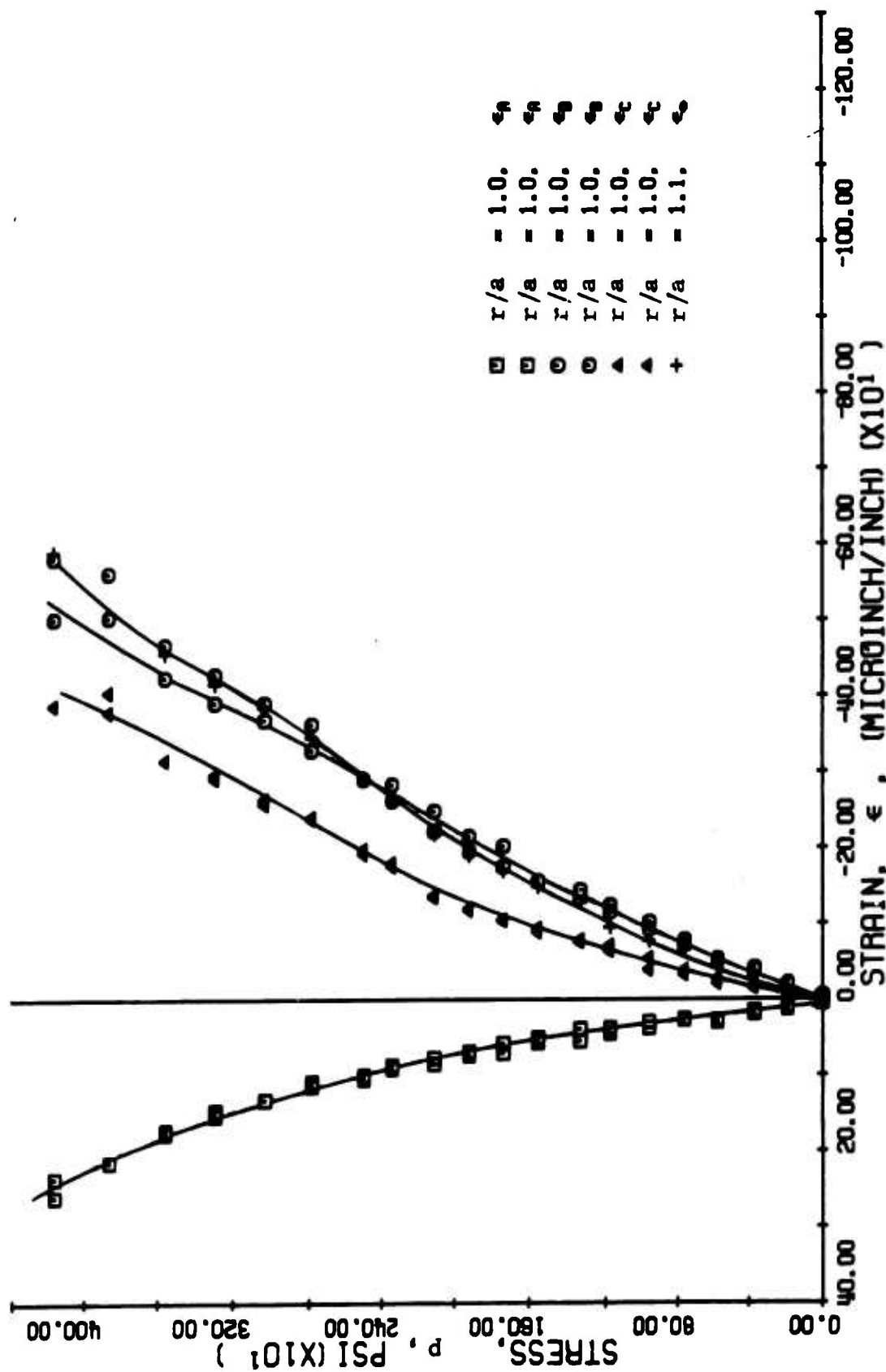
FIG. 70   STRAINS ALONG 45 DEGREE RADIUS FOR SPECIMEN NO. 4
(MARBLE UNLINED UNDER UNIAXIAL LOADING)

114
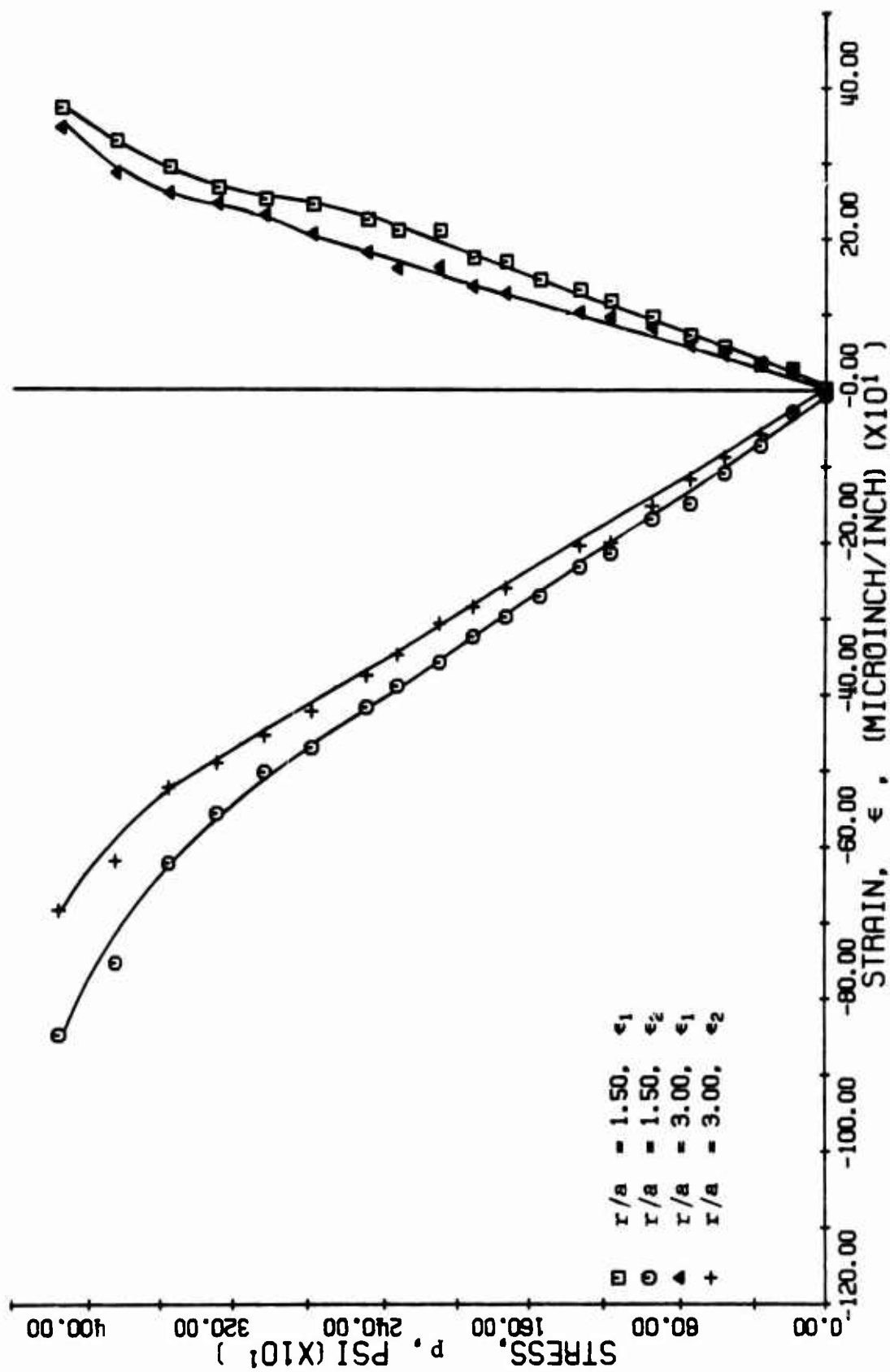
FIG. 71   PRINCIPAL STRAINS ALONG 45-DEGREE RADIUS FOR SPECIMEN NO. 4
(MARBLE UNLINED UNDER UNIAXIAL LOADING)

115
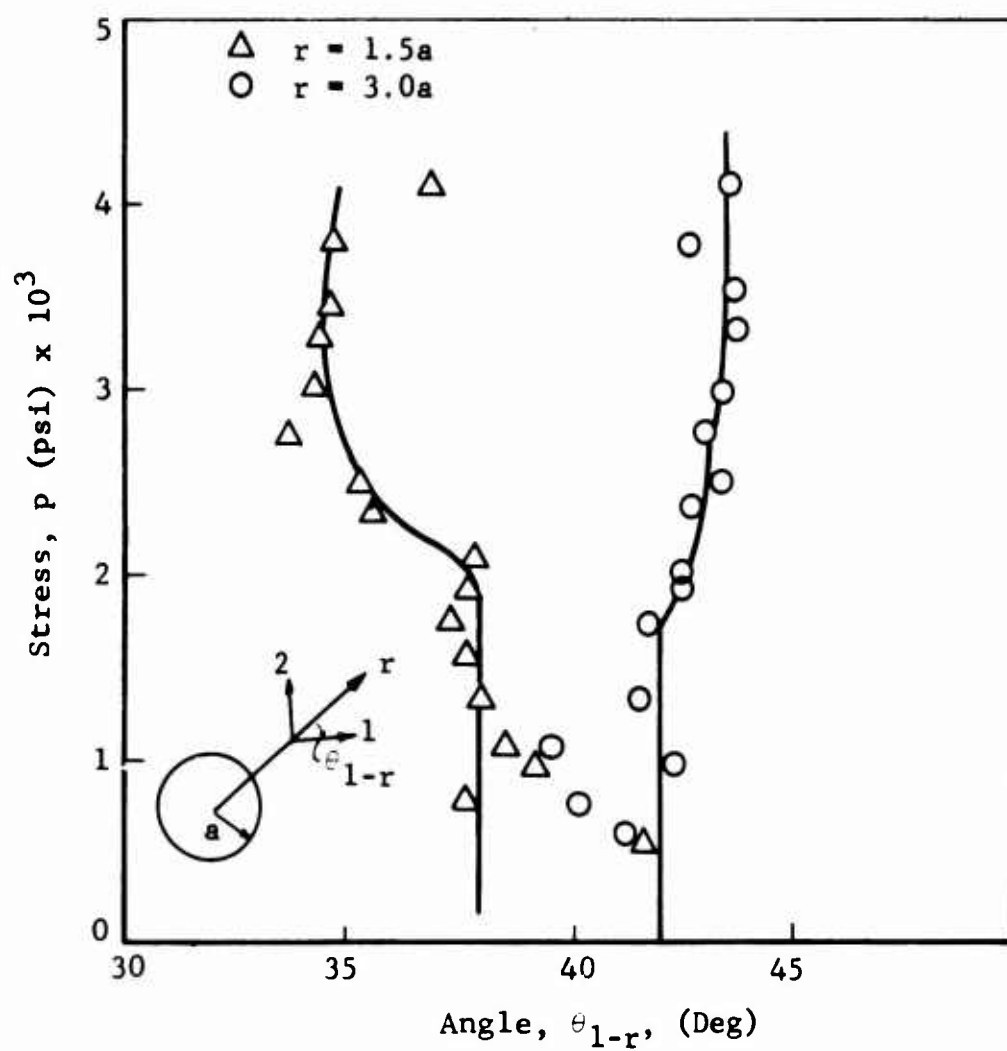
Fig. 72 PRINCIPAL DIRECTIONS ALONG 45-DEGREE RADIUS FOR SPECIMEN NO. 4

As previously noted, the principal direction (measure clockwise from the radial direction to the largest principal stress) rotates toward the horizontal as the distance from the hole increases.

SECTION VI

STRESS DISTRIBUTION AND FRACTURE AROUND LINED CAVITIES
IN ROCK UNDER UNIAXIAL LOADING

1. Specimens No. 5 and 6 - Limestone with Hydrostone Liner
   Under Uniaxial Loading

   a. Theoretical Stress Distributions

   Stresses on the free surface of the hydrostone liner and
stresses in the limestone at the interface with the liner were
calculated using Eqs. (9) and (10). The following material proper-
ties were used for the evaluation of the pertinent constants
entering these equations:

Limestone: $E = 4.0 \times 10^6$ psi

$\nu = 0.23$

$\mu = \dfrac{E}{2(1 + \nu)} = 1.63 \times 10^6$ psi

$\kappa = \dfrac{3-\nu}{1 + \nu} = 2.25$

Hydrostone: $E_1 = 2.2 \times 10^6$ psi

$\nu_1 = 0.25$

$\mu_1 = \dfrac{E_1}{2(1 + \nu_1)} = 0.88 \times 10^6$ psi

$\kappa_1 = \dfrac{3-\nu_1}{1 + \nu_1} = 2.20$

Evaluations were made for two liner thicknesses to determine
the liner's influence on critical stresses. For a liner thickness

118

t = 0.25 in., the circumferential stress on the free surface of the liner becomes

$$\frac{\sigma_\theta}{p} = 0.59 - 1.25 \cos 2\theta \tag{33}$$

which gives a maximum compressive stress

$$\left(\frac{\sigma_\theta}{p}\right)_{\theta = 90°} = 1.84 \tag{34}$$

and a maximum tensile stress

$$\left(\frac{\sigma_\theta}{p}\right)_{\theta = 0°} = -0.66 \tag{35}$$

(Positive stress ratios indicate compression and negative ones tension). Stresses in the limestone along the interface with the liner were calculated to be

$$\frac{\sigma_r}{p} = 0.07 - 0.09 \cos 2\theta \tag{36}$$

$$\frac{\sigma_\theta}{p} = 0.93 - 1.61 \cos 2\theta \tag{37}$$

The maximum tensile and compressive circumferential stresses are

$$\left(\frac{\sigma_\theta}{p}\right)_{\theta = 0°} = -0.68 \tag{38}$$

and

$$\left(\frac{\sigma_\theta}{p}\right)_{\theta = 90°} = 2.54, \text{ respectively.} \tag{39}$$

For a liner thickness t = 0.44 in. the circumferential stress on the free surface of the liner is

$$\frac{\sigma_\theta}{p} = 0.62 - 1.30 \cos 2\theta \tag{40}$$

119

with peak values

$$\left(\frac{\sigma_\theta}{p}\right)_{\theta=0°} = -0.68 \tag{41}$$

$$\left(\frac{\sigma_\theta}{p}\right)_{\theta=90°} = 1.92 \tag{42}$$

The stresses in the limestone plate at the interface are

$$\frac{\sigma_r}{p} = 0.13 - 0.11 \cos2\theta \tag{43}$$

$$\frac{\sigma_\theta}{p} = 0.88 - 1.36 \cos2\theta \tag{44}$$

$$\frac{\sigma_{r\theta}}{p} = -0.38 \sin2\theta \tag{45}$$

The peak circumferential stresses are

$$\left(\frac{\sigma_\theta}{p}\right)_{\theta=0°} = -0.48 \tag{46}$$

$$\left(\frac{\sigma_\theta}{p}\right)_{\theta=90°} = 2.24 \tag{47}$$

To illustrate the influence of thickness, the peak tangential stresses at the free surface ($r = R_1$) in the liner and at the interface ($r = R$) in the plate were plotted versus thickness-to-diameter ratio in Fig. 73. As the liner thickness approaches zero the stresses in the plate approach those predicted by the classical Kirsch solution. The stresses in the liner would approach values equal to those in the plate multiplied by the ratio of moduli. This implies that the circumferential strains are equal at the interface and that the liner stiffness approaches zero.

The liner thickness selected for the specimens was t = 0.44 in. Using the expressions for the three stress components in the limestone at the interface (Eqs. 43-45), the principal stresses at the interface were calculated and plotted versus angular position in Fig. 74. It is seen that the principal stresses reach their extreme values at the 0° and 90° positions.

120
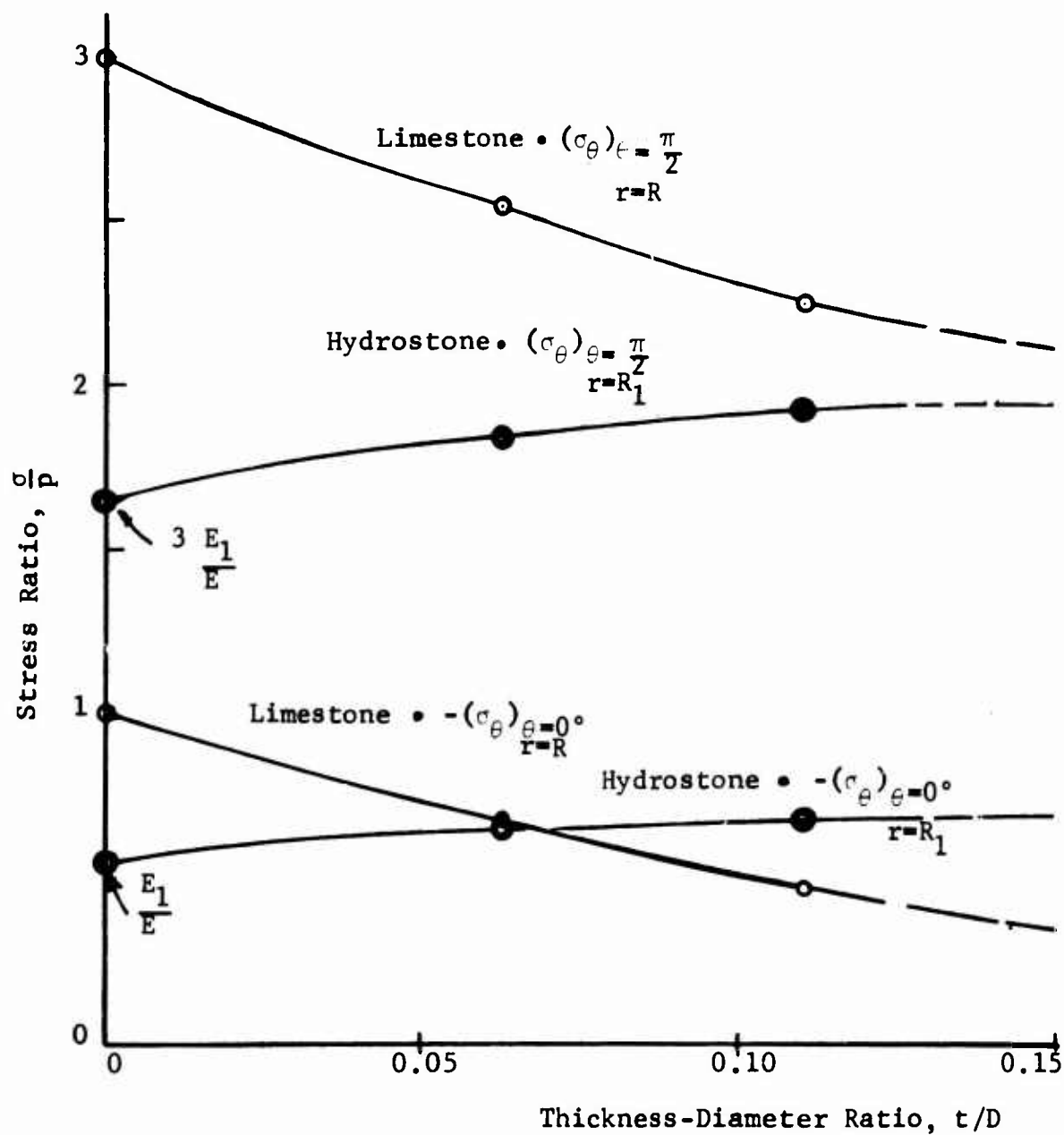
Fig. 73   VARIATION OF STRESSES IN LIMESTONE PLATE AND HYDROSTONE
LINER AS A FUNCTION OF LINER THICKNESS

121
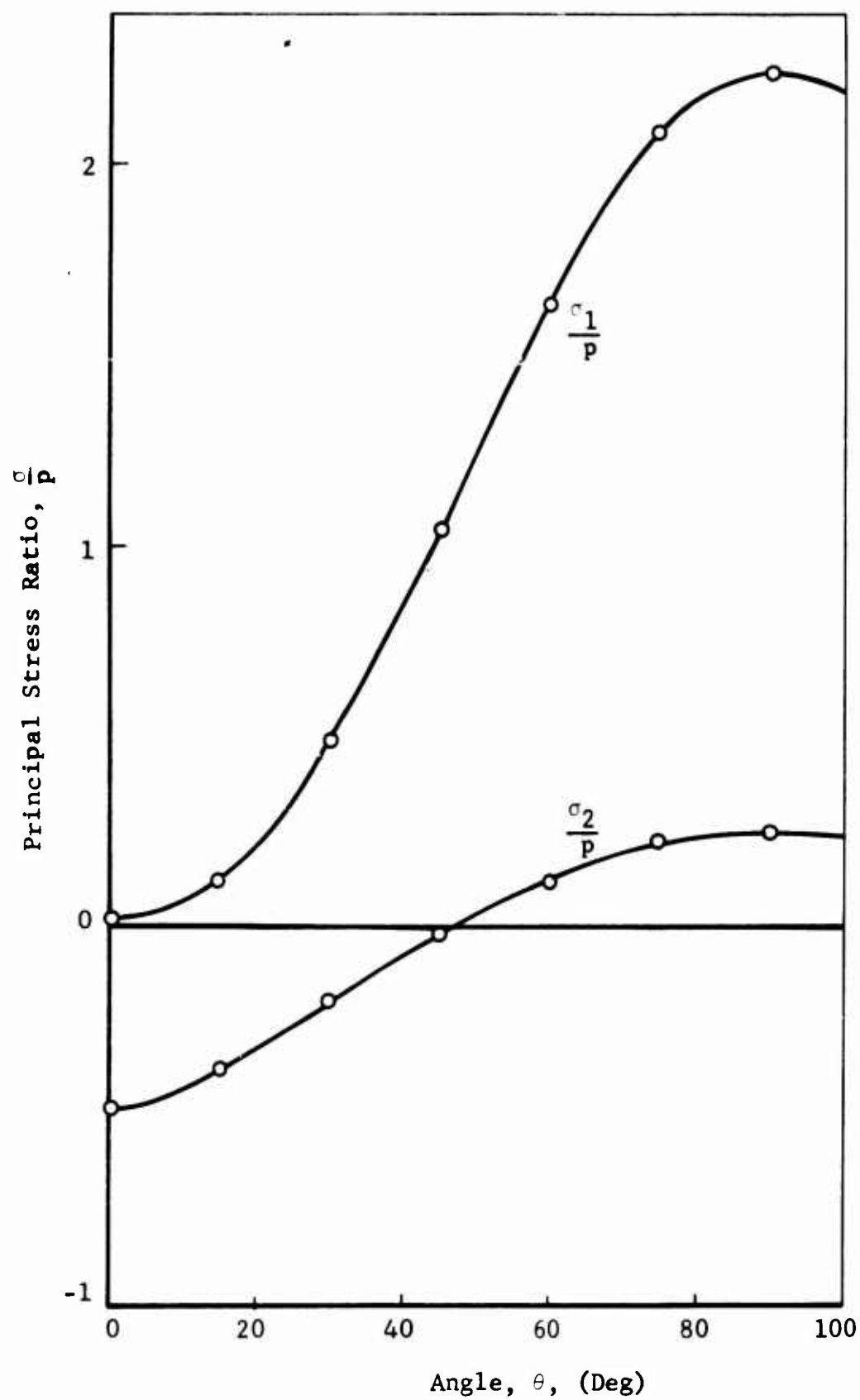
Fig. 74 VARIATION OF PRINCIPAL STRESSES IN LIMESTONE AT INTERFACE
WITH HYDROSTONE LINER

122

b. Experimental Procedure

Two limestone plates of dimensions 36 in. x 24 in. x 3 in.
with a 4 in. diameter hole and a 0.44 in. thick hydrostone liner
bonded to the cavity surface were used. Strain gages were applied
along the horizontal and vertical axes of symmetry and along a 45°
radius (Fig. 75). Five single-element gages were applied to the
inside surface of the liner in the circumferential direction at
the four points on the axes of symmetry and at the 45° location.
Twenty-eight two-gage rosettes were applied along the axes of
symmetry including the end surface of the liner and at the interface
between liner and plate. Three three-gage rosettes were used along
the 45° radius. Three single-element gages applied to an unloaded
piece of limestone were used to monitor any possible temperature
effects since these were not automatically compensated for with
compensating gages. Diametral changes were monitored with two
DCDT's inserted along the horizontal and vertical diameters. The
overall surface strain distribution was observed and recorded by
means of a photoelastic coating as described earlier.

The instrumented specimens were loaded in the 1,000,000 lb
testing machine described earlier. (Fig. 76). The specimens were
loaded in 20,000 lb increments up to 100,000 lb and in approximately
10,000 lb increments thereafter up to approximately 220,000 lb,
when total destruction occurred. Strain gage and DCDT readings
were recorded with the Digital Data Acquisition system at every
load level. Photoelastic patterns on the photoelastic coating were
photographed at each load level and also recorded with a color
movie camera.

c. Results and Discussion

Isochromatic fringe patterns for specimens No. 5 and No. 6
are shown in Figs. 77 and 78 for various levels of loading. The
applied average stress (based on gross area) is shown in each frame.
According to these patterns, cracking started in the hydrostone

123

Gage No.	r/a
1,2,3,4	5
30,31,32,33	5
10	2.3
21,29	2.3
9	1.8
20,28	1.8
8,34,36	1.35
19,27	1.35
7,23	1
5,22	0.8
16,24	0.8
11	0.8
12	1
13	1.35
14	1.8
15	3
18,26	1
6	0.9
17	0.9
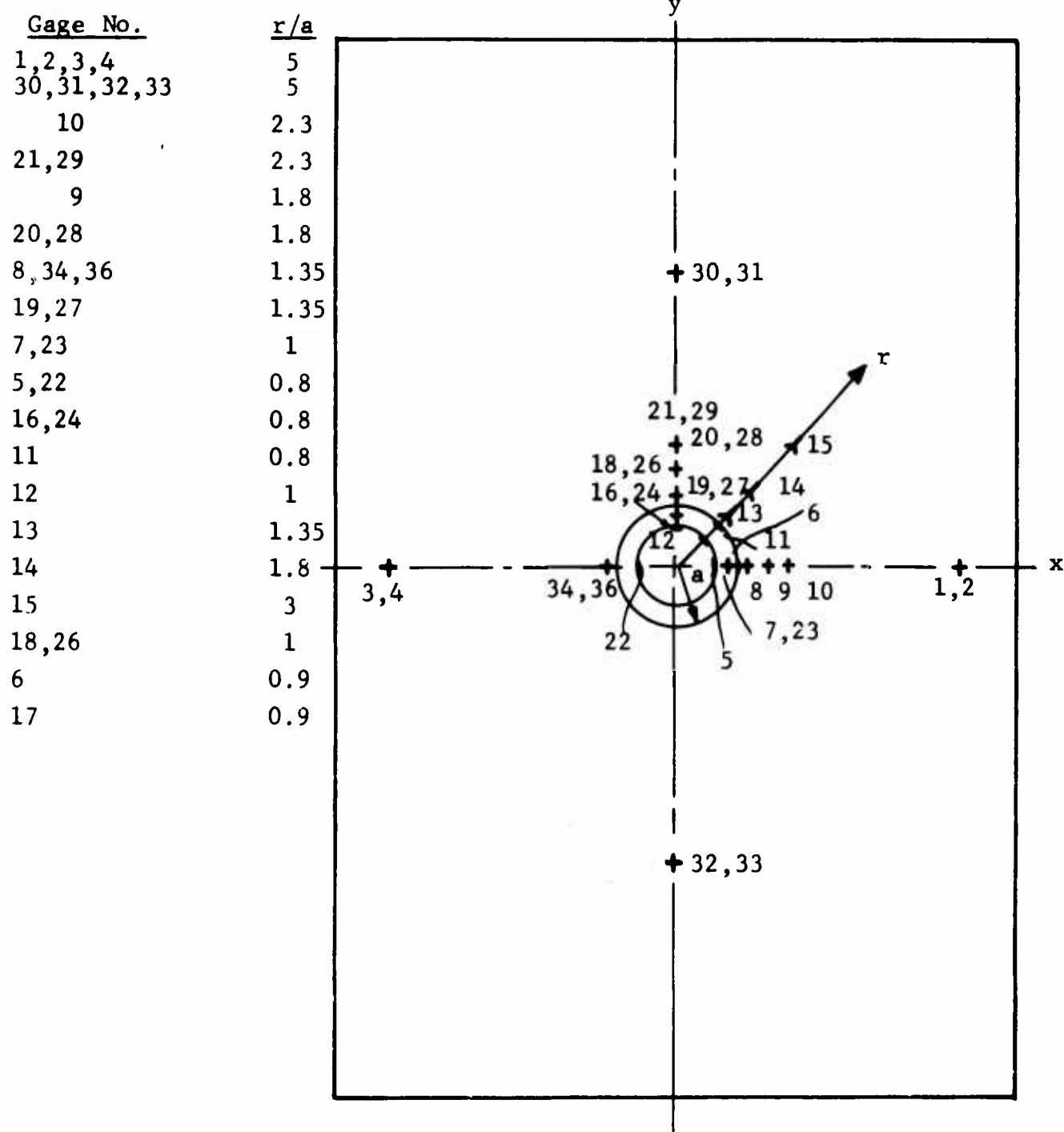
Fig. 75 STRAIN GAGE LAYOUT FOR LIMESTONE SPECIMENS WITH HYDROSTONE
LINERS

124
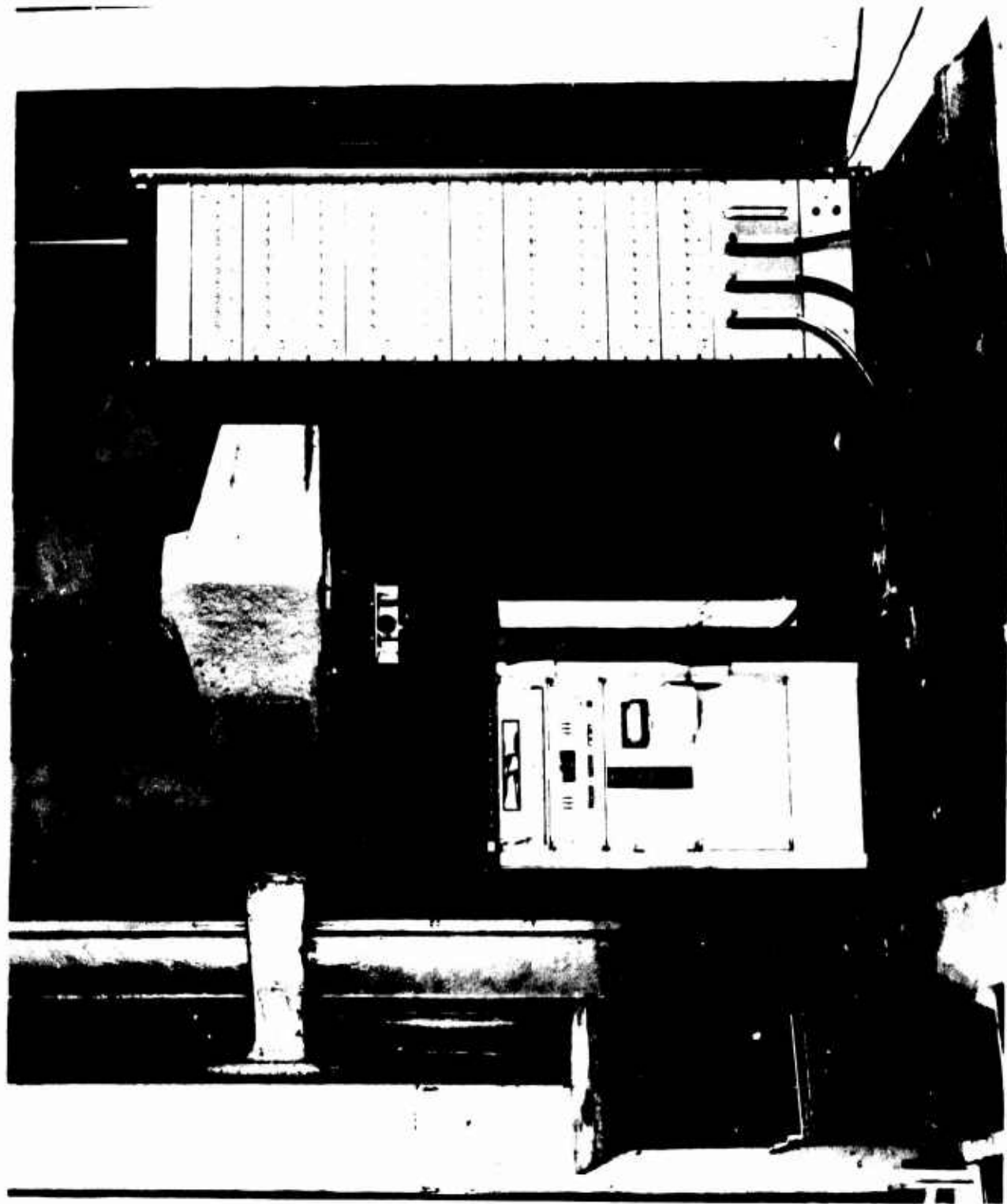
Fig. 76 EXPERIMENTAL SETUP SHOWING SPECIMEN IN 1,000,000 LB TESTING MACHINE AND DIGITAL DATA ACQUISITION SYSTEM

125
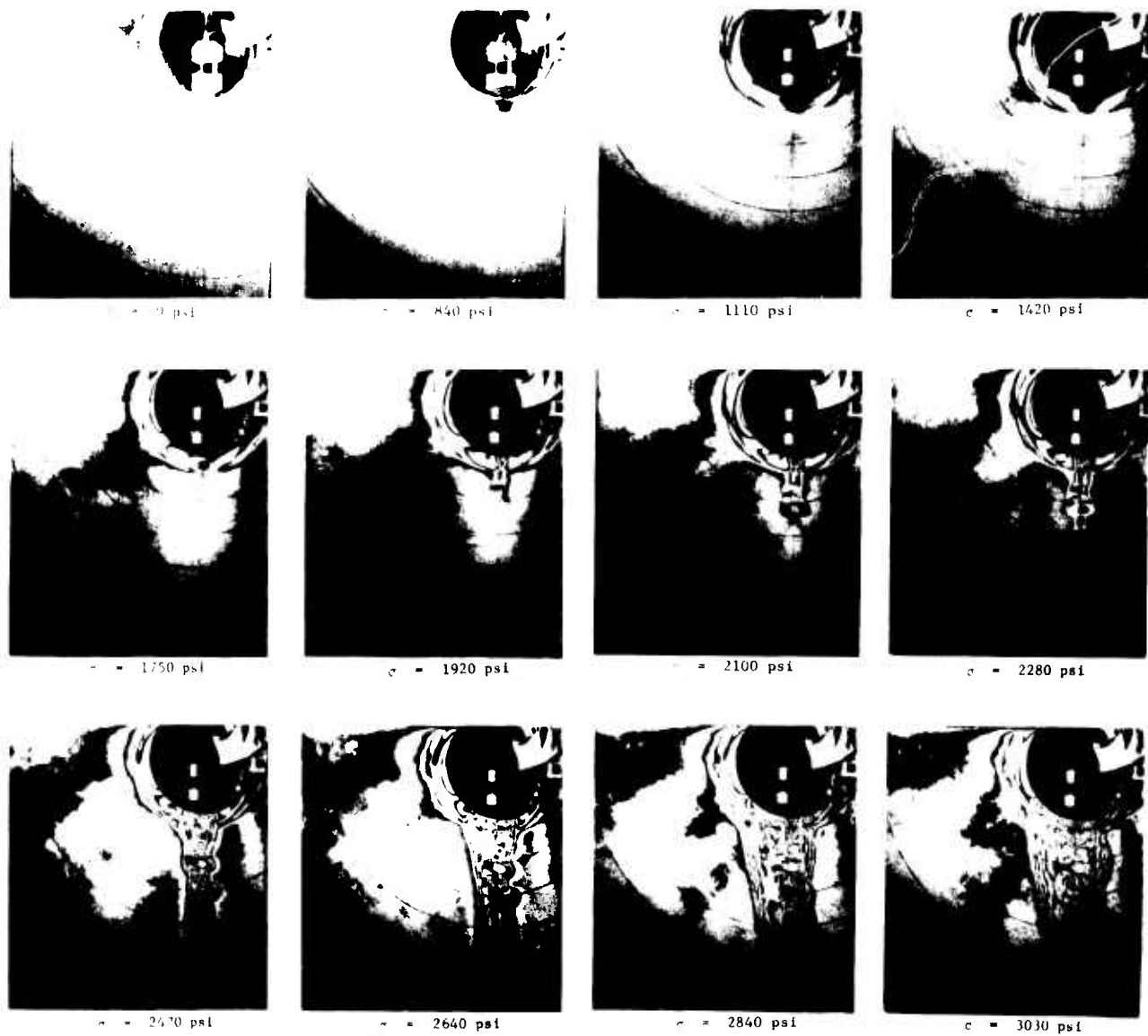
Fig. 77   ISOCHROMATIC FRINGE PATTERNS IN PHOTOELASTIC COATING
AROUND HOLE IN SPECIMEN NO. 5 (LIMESTONE WITH HYDROSTONE
LINER UNDER UNIAXIAL LOADING)

126

σ = 1670 psi

σ = 1840 psi

σ = 1990 psi

σ = 2160 psi

σ = 2360 psi

σ = 2550 psi

σ = 2800 psi

σ = 3020 psi

Fig. 78 ISOCHROMATIC FRINGE PATTERNS IN PHOTOELASTIC COATING AROUND HOLE IN SPECIMEN NO. 6 (LIMESTONE WITH HYDROSTONE LINER UNDER UNIAXIAL LOADING)

127

liner and quickly propagated into the limestone along the vertical
axis. In specimen No. 5, cracking started at an applied stress
between 1750 and 1920 psi and in specimen No. 6 at an applied
stress of between 1670 and 1840 psi. The exact load level of crack
initiation will be established below from the strain gage and DCDT
data.

The stress levels at failure are approximately 50 percent
higher than in the unlined specimen No. 1. Although hydrostone
has the same tensile strength as limestone, its lower modulus (one-
half of that of limestone) increases the overall strength of the
lined specimen. From theoretical considerations, it is possible
that in the present case cracking started in the limestone at the
interface and it quickly propagated into the hydrostone liner.
This crack propagated vertically along the specimen centerline
until complete separation at 3500 psi and 3200 psi for specimens
No. 5 and No. 6, respectively. The failure patterns are shown in
Figs. 79 and 80. Both specimens show cracking off the centerline
starting at a point near the 90° location at some angle and quickly
turning in a vertical direction. This may be a secondary failure
pattern forming after the first vertical centerline crack appears.

The photoelastic data yield the difference in principal
strains everywhere in the field according to relation (18). On
free surfaces, the fringe order is related to the tangential strain
ε_1 as follows:

$$n = \frac{2t}{f_\varepsilon} (1 + \nu^c)\varepsilon_1 \tag{48}$$

The maximum fringe order on the free boundary of the liner
on the horizontal axis was plotted versus applied stress for both
specimens in Fig. 81. Both curves are linear and have the same
slope up to a stress level of approximately 2,000 psi. At 1,000
psi the fringe order is 1.3. Then, using the following material
properties for the photoelastic coating

$$\nu^c = 0.4$$

128
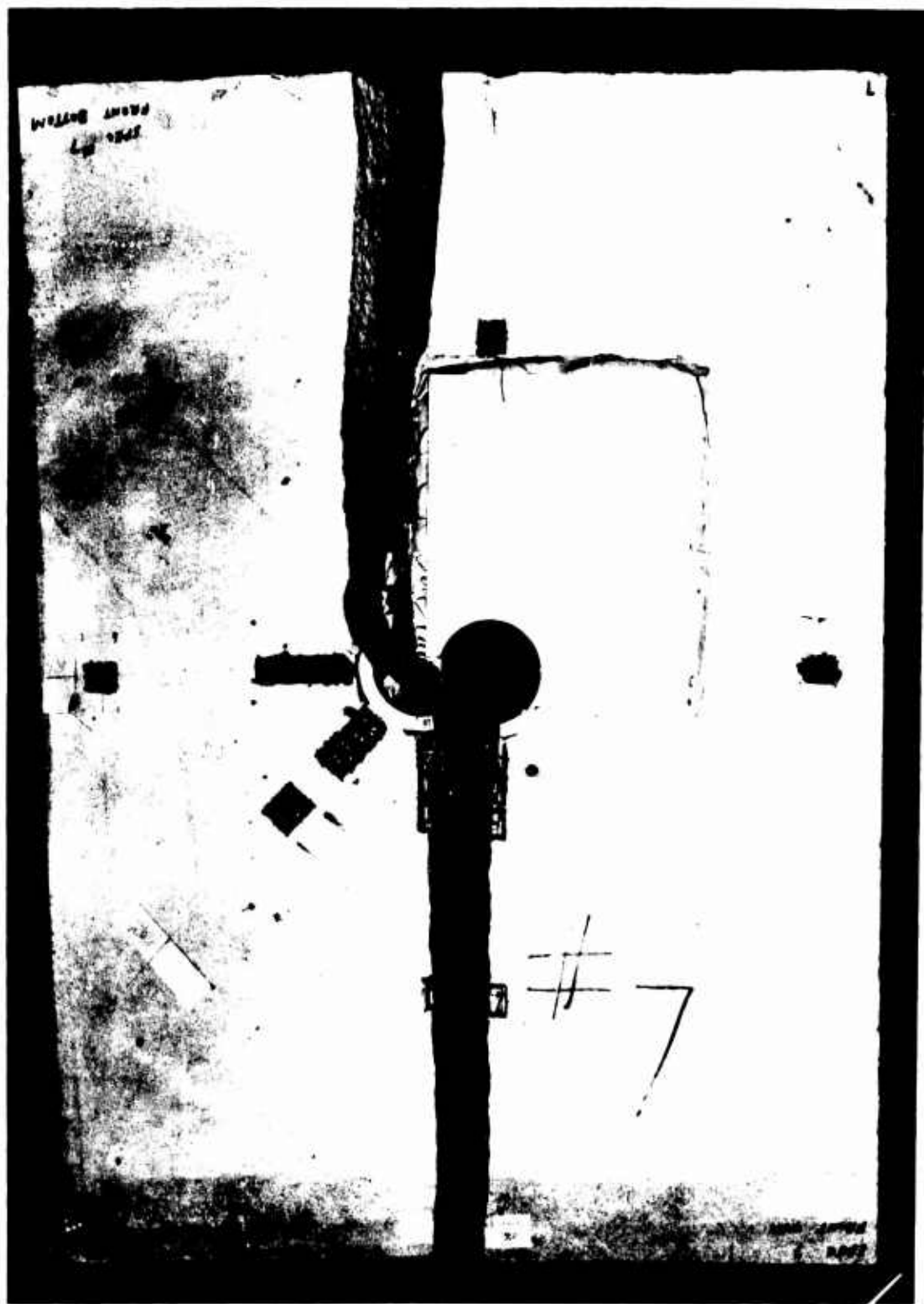
Fig. 79 FAILURE PATTERN IN SPECIMEN NO. 5 (LIMESTONE WITH
HYDROSTONE LINER UNDER UNIAXIAL LOADING)

129
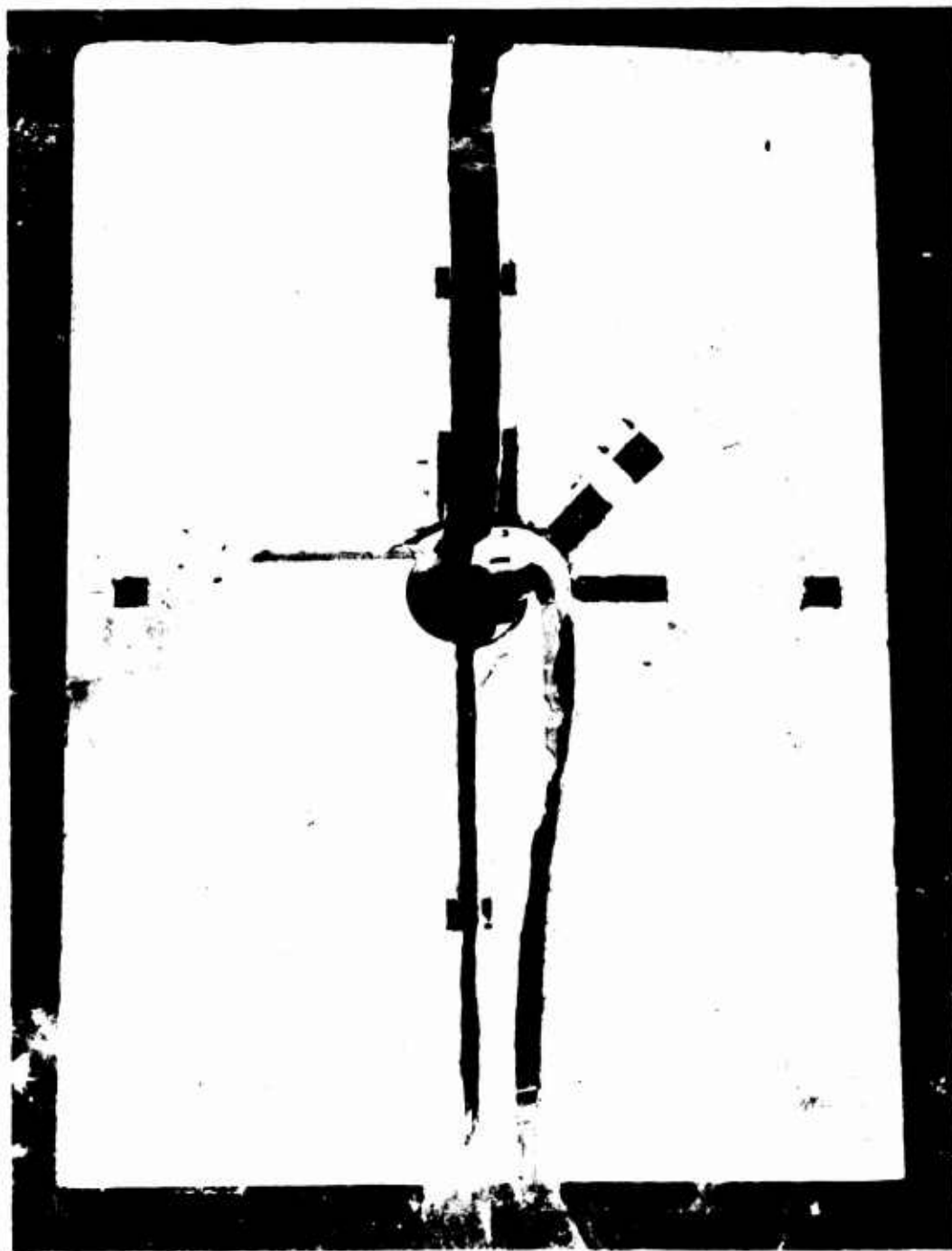
Fig. 80   FAILURE PATTERN IN SPECIMEN NO. 6 (LIMESTONE
          WITH HYDROSTONE LINER UNDER UNIAXIAL LOADING)
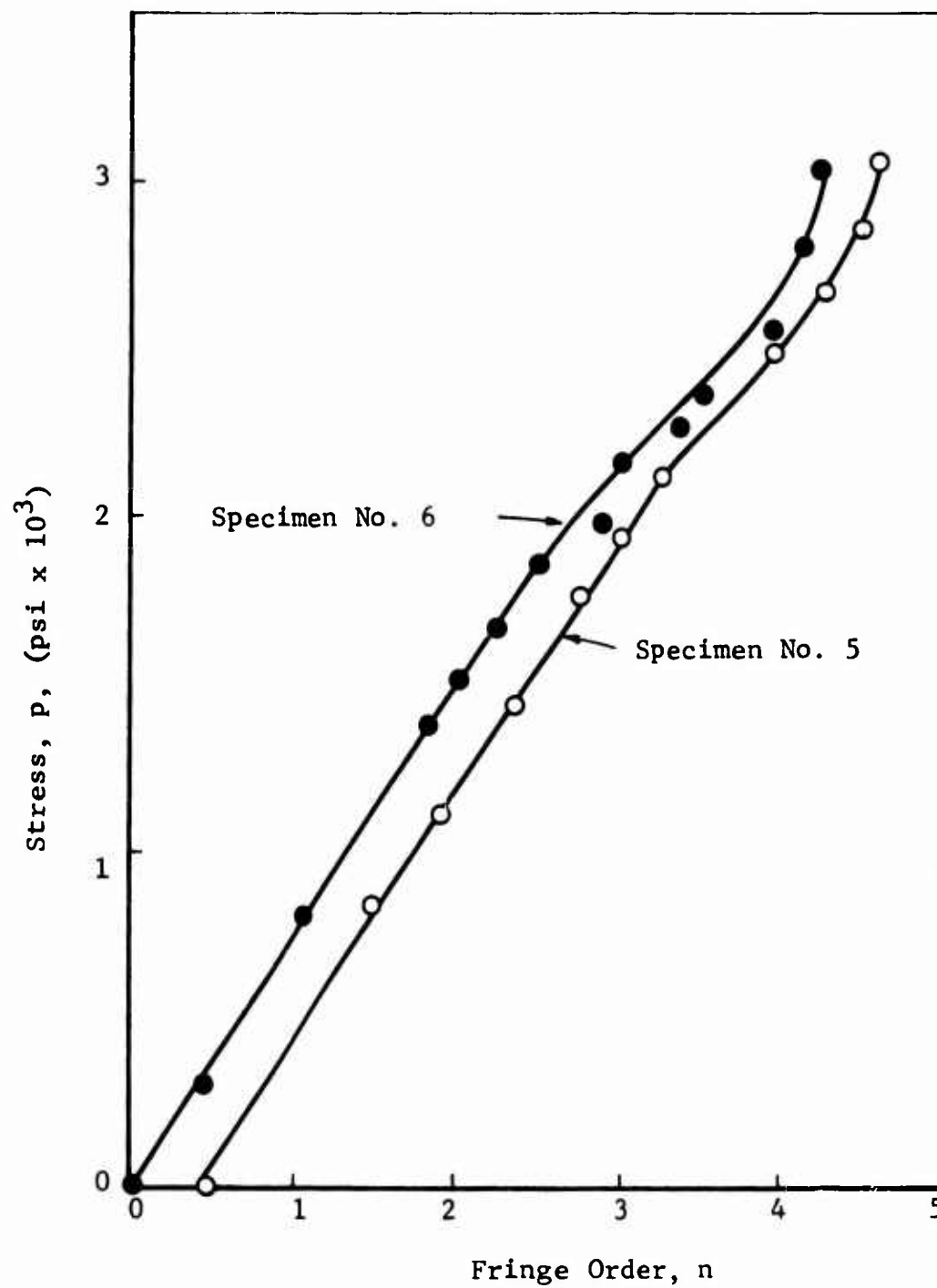
Fig. 81 FRINGE ORDER AT INNER BOUNDARY OF LINER ON HORIZONTAL AXIS
FOR SPECIMENS NO. 5 AND 6 AS A FUNCTION OF APPLIED VERTICAL
STRESS

131

$$\frac{f_\varepsilon}{2t} = 860 \quad \mu in./in./fringe$$

we obtain

$$(\varepsilon_1)_{p = 1,000 \text{ psi}} = 800 \ \mu in./in.$$

Another area of high birefringence is at the interface between the liner and the limestone at angles of 52° and 55° from the vertical axis for specimens No. 5 and 6, respectively. The birefringence at that point is of the same order as in the maximum compression region above. It is an indication of high shear strain at the interface, higher than would be predicted theoretically.

Diametral changes measured with DCDT's are plotted in Figs. 82 and 83 as a function of applied vertical stress. The curves for specimen No. 5 are linear up to approximately p = 1900 psi. The deflections per unit of applied stress in this linear range are

$$\frac{\delta_h}{p} = 1.1 \times 10^{-6} \ in./psi$$

$$\frac{\delta_v}{p} = -2.5 \times 10^{-6} \ in./psi$$

The curves for specimen No. 6 are linear up to approximately 1,600 psi and the deflections per unit stress are

$$\frac{\delta_h}{p} = 1.1 \times 10^{-6} \ in./psi$$

$$\frac{\delta_v}{p} = -3.2 \times 10^{-6} \ in./psi$$

The horizontal deflections, between one-half and one-third of the vertical, are the same for both specimens, however some discrepancy exists in the vertical deflections.

132
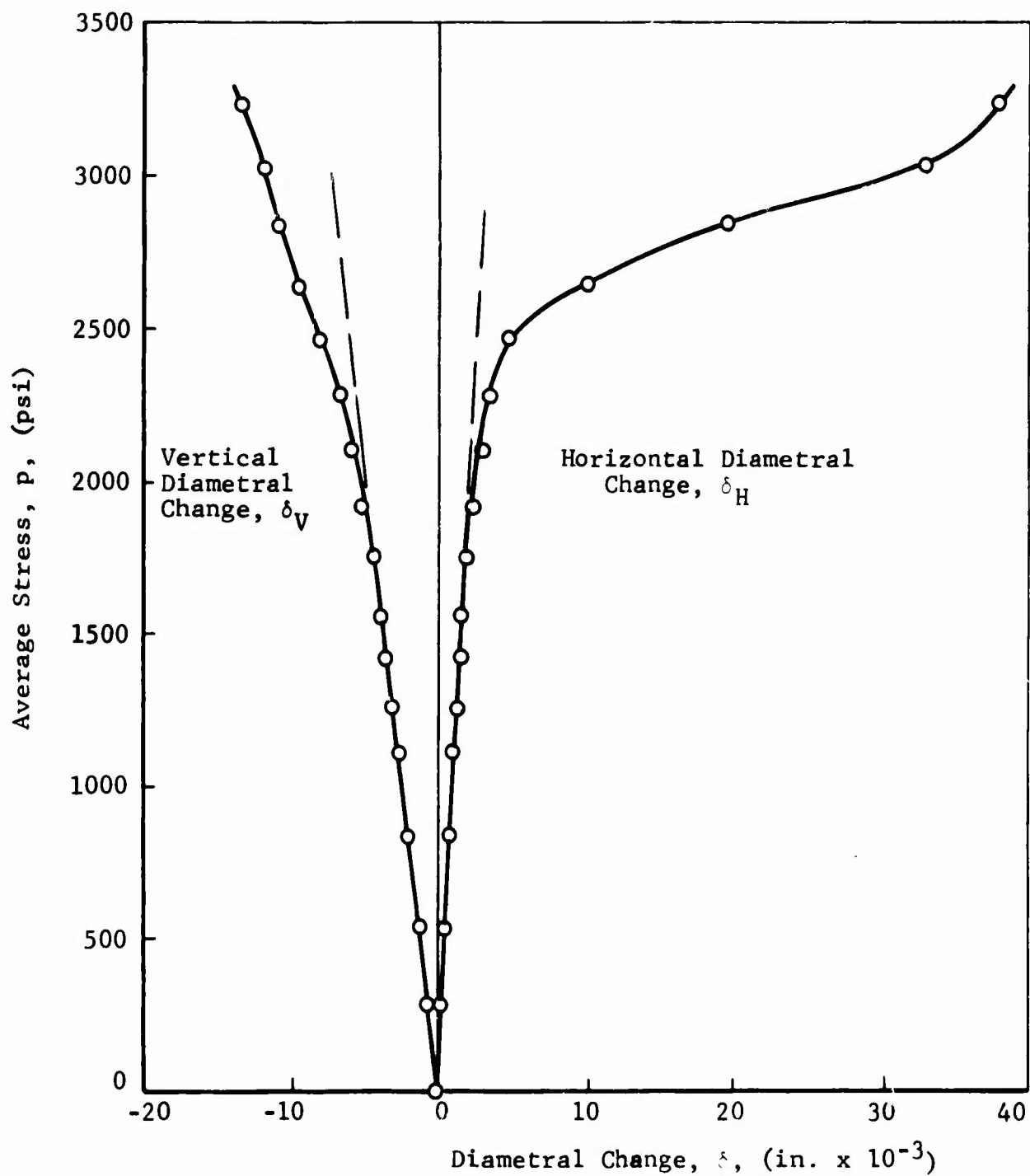
Fig. 82   DIAMETRAL CHANGES AS A FUNCTION OF APPLIED VERTICAL STRESS
FOR SPECIMEN NO. 5 (LIMESTONE WITH HYDROSTONE LINER UNDER
UNIAXIAL LOADING)

133
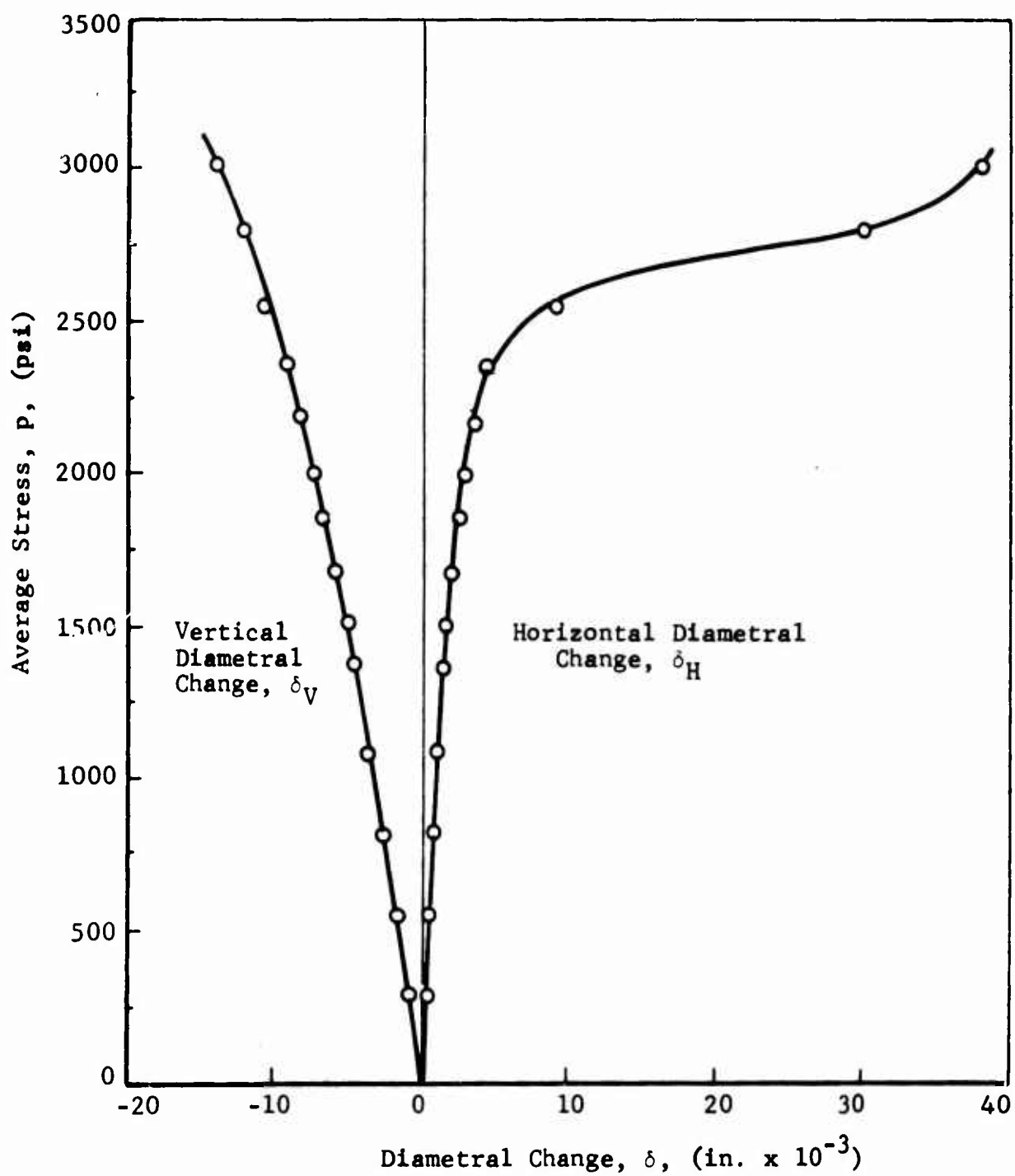
Fig. 83   DIAMETRAL CHANGES AS A FUNCTION OF APPLIED VERTICAL STRESS FOR
SPECIMEN NO. 6 (LIMESTONE WITH HYDROSTONE LINER UNDER UNIAXIAL
LOADING)

Strain gage readings along the horizontal, vertical and 45-degree radii for specimen No. 5 are plotted as a function of applied average stress in Figs. 84 to 88 with radial location as a parameter. The vertical strains along the horizontal axis are linear up to at least 1900 psi. On the basis of the far-field gage readings, both on the horizontal and vertical axes, the following modulus and Poisson's ratio were determined:

$$E = 4.2 \times 10^6 \text{ psi}$$

$$\nu = 0.23$$

The maximum strain ratio between the vertical strain at the interface and the far-field strain in the linear range is

$$k_\varepsilon = 3.15$$

The horizontal strains along the vertical axis are very significant as they indicate the progression of cracking (Fig. 86). According to the strain variation, cracking in the limestone at the interface started very early. This occurred at approximately 1100 psi which is below the level for the unlined limestone specimen. This occurred at one of the two symmetrical points only and it may be due to a local flaw. Strain variation at the symmetrical point continued linear up to 1400 psi. Cracking of the hydrostone liner occurred at a much higher stress of 1750 psi. Strains along the 45-degree radius were first plotted as read. Subsequently, principal strains were computed using the rosette equations and plotted in Fig. 89. Principal directions were similarly computed and plotted versus stress for three radial locations in Fig. 90. As expected, the principal directions are constant in the linear region and deviate slightly in the nonlinear region. The angle between the 45-degree radius and the principal tensile direction, measured clockwise, varies from 37 degrees to 45 degrees between radial locations $r = 1.35a$ and $r = 3.00a$.

135
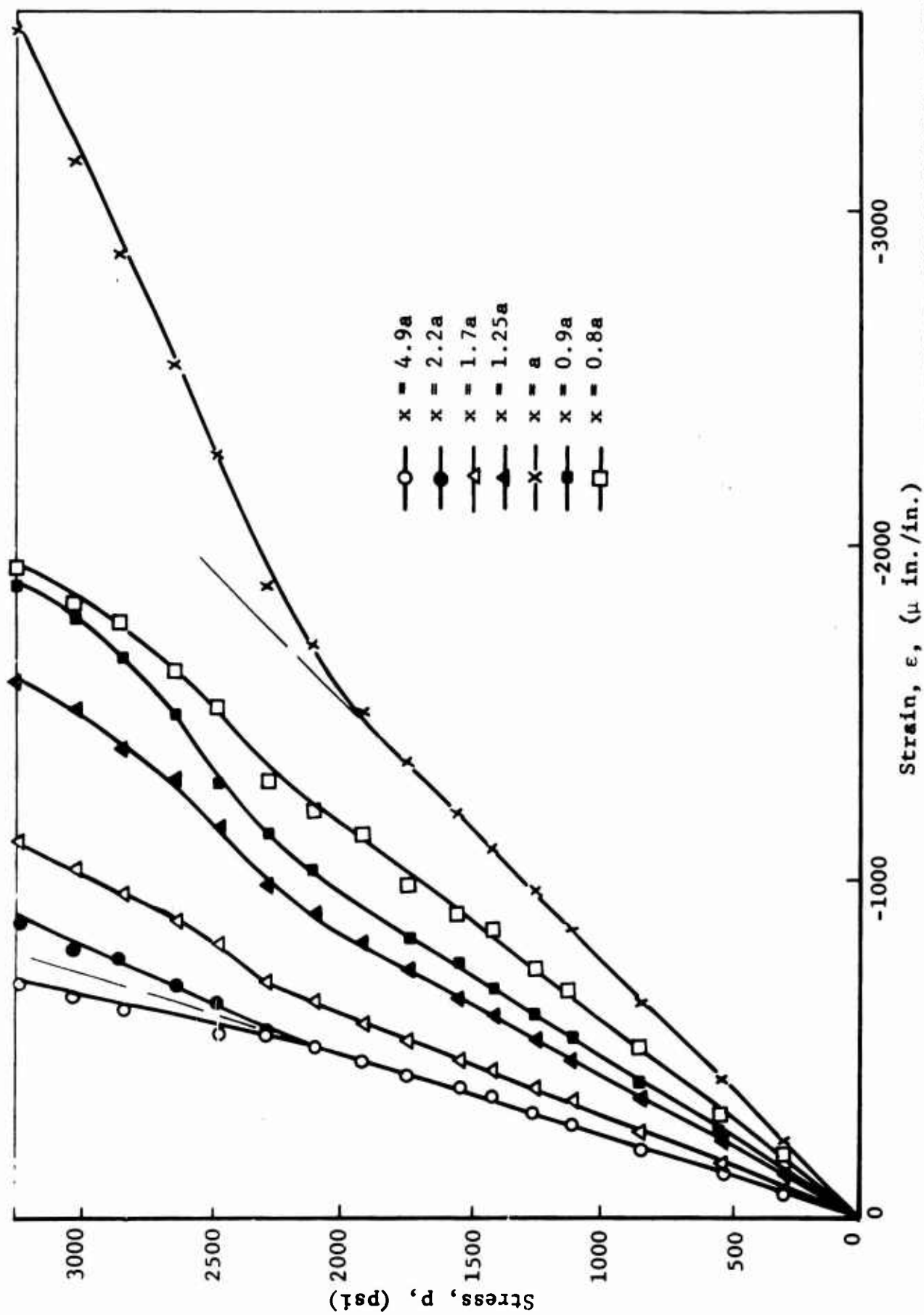
Fig. 84   VERTICAL STRAINS ALONG HORIZONTAL AXIS OF SYMMETRY AS A FUNCTION OF APPLIED VERTICAL STRESS
FOR SPECIMEN NO. 5 (LIMESTONE WITH HYDROSTONE LINER UNDER UNIAXIAL LOADING)
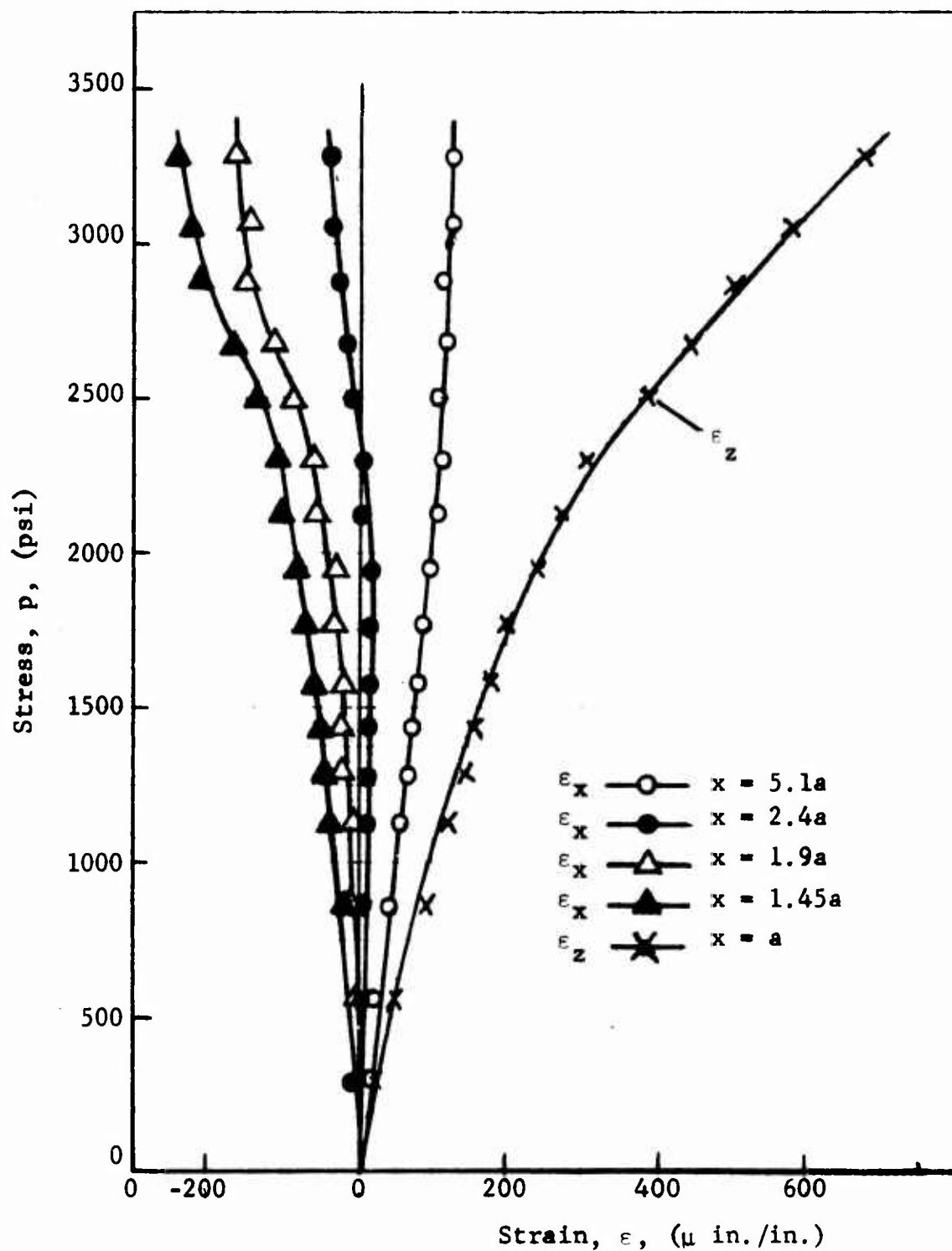
Fig. 85 HORIZONTAL STRAINS ALONG HORIZONTAL AXIS OF SYMMETRY AS A
FUNCTION OF APPLIED VERTICAL STRESS FOR SPECIMEN NO. 5
(LIMESTONE WITH HYDROSTONE LINER UNDER UNIAXIAL LOADING)

137
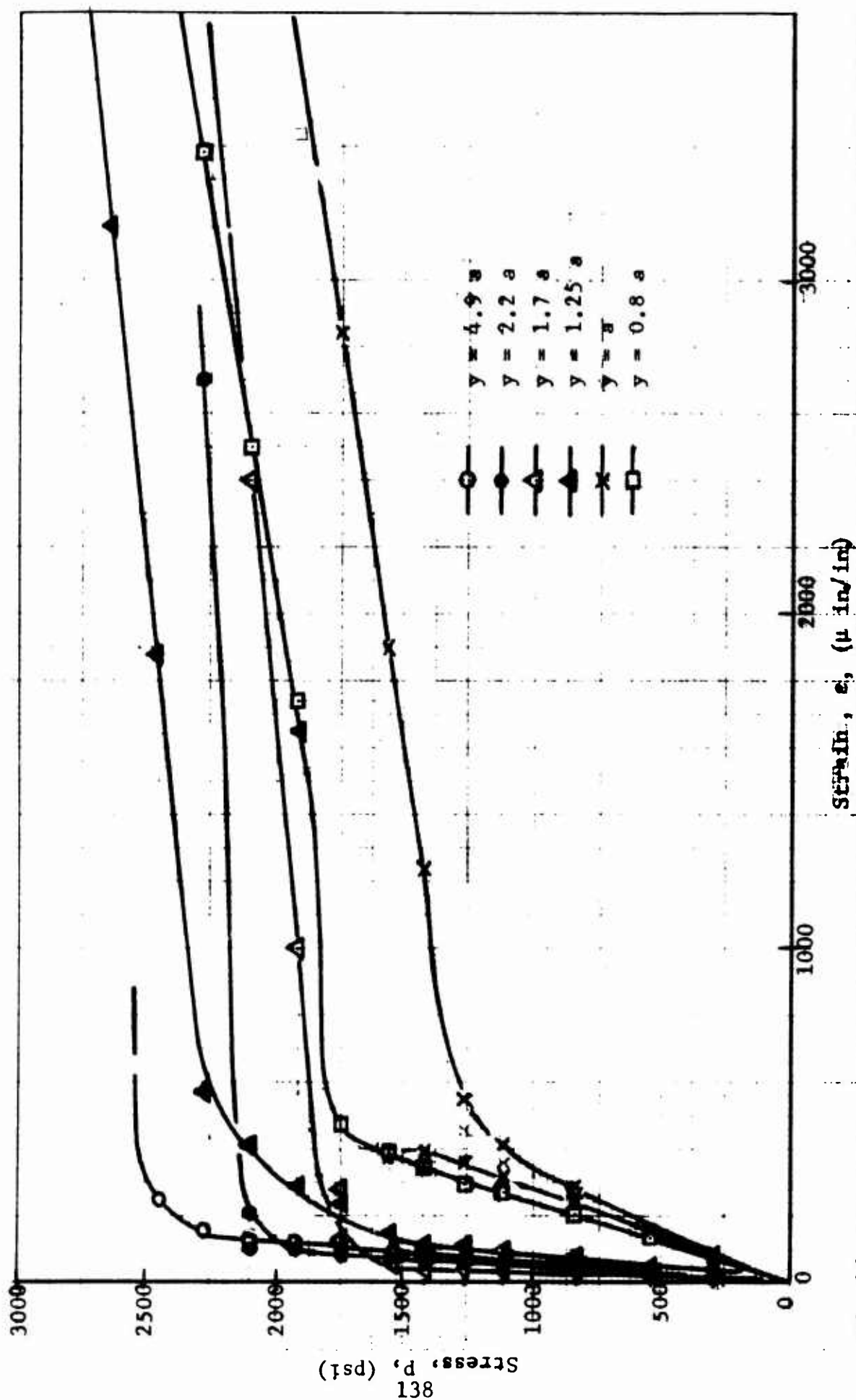
Fig. 86 HORIZONTAL STRAINS ALONG VERTICAL AXIS OF SYMMETRY AS A FUNCTION OF APPLIED VERTICAL STRESS FOR SPECIMEN NO. 5 (LIMESTONE WITH HYDROSTONE LINER UNDER UNIAXIAL LOADING)

138
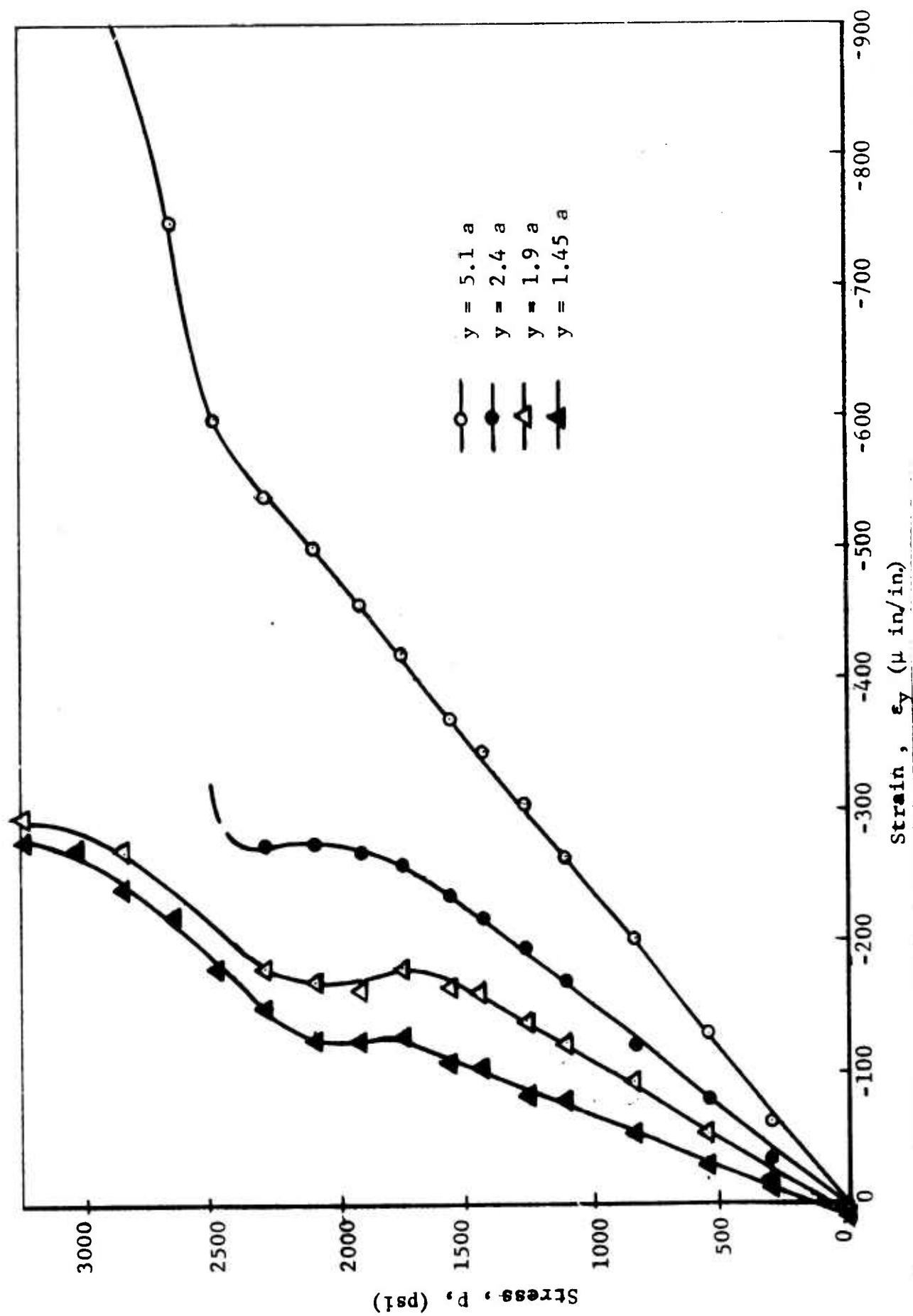
Fig. 87   VERTICAL STRAINS ALONG VERTICAL AXIS OF SYMMETRY AS A FUNCTION OF APPLIED VERTICAL STRESS
FOR SPECIMEN NO. 5 (LIMESTONE WITH HYDROSTONE LINER UNDER UNIAXIAL LOADING)

139
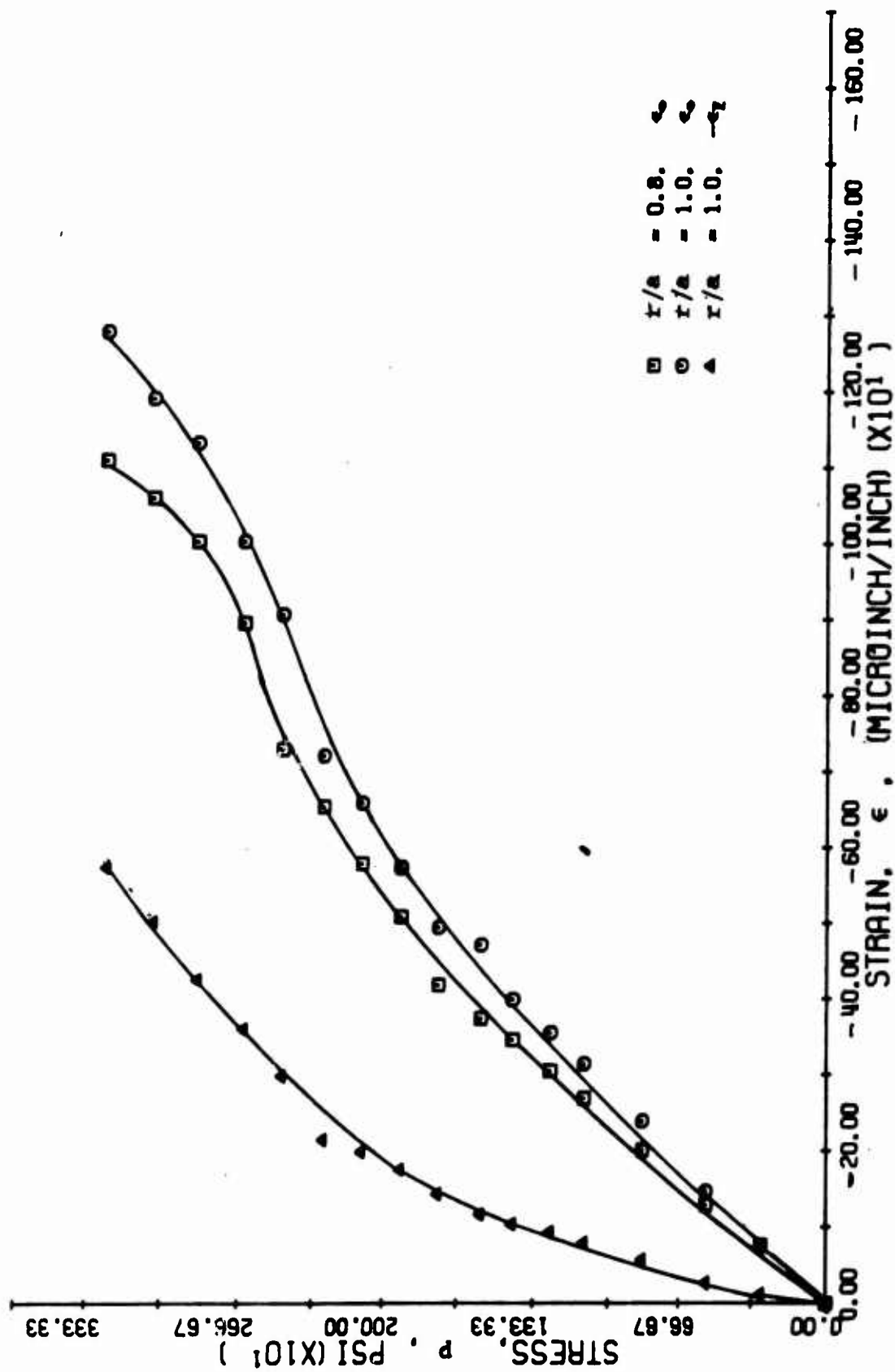
FIG. 88 STRAINS ALONG 45 DEGREE RADIUS FOR SPECIMEN NO. 5
(LIMESTONE WITH HYDROSTONE LINER UNDER UNIAXIAL LOADING)
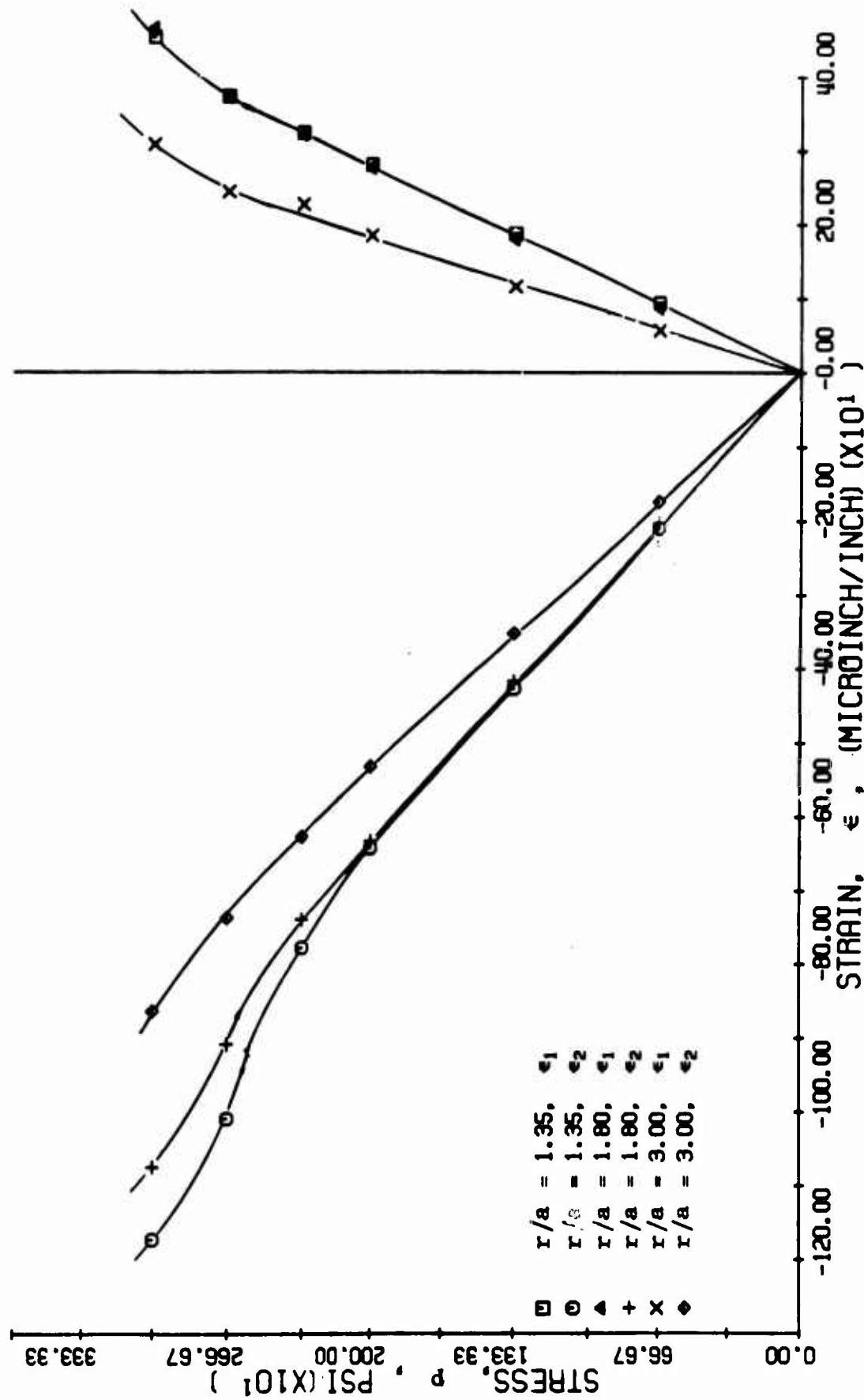
FIG. 89 PRINCIPAL STRAINS ALONG 45-DEGREE RADIUS FOR SPECIMEN NO. 5
(LIMESTONE WITH HYDROSTONE LINER UNDER UNIAXIAL LOADING)

141
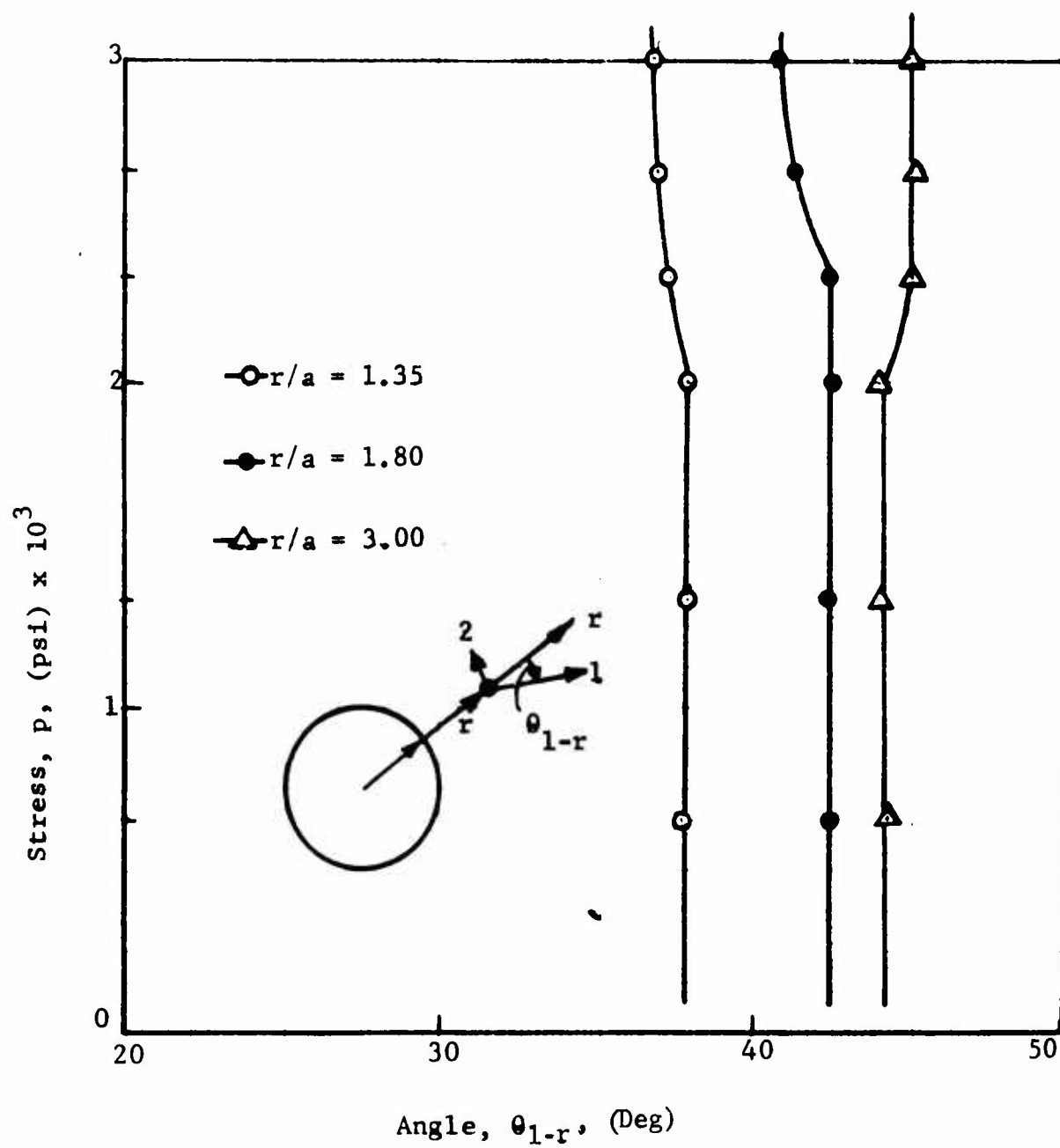
Fig. 90   PRINCIPAL DIRECTIONS ALONG 45 DEGREE RADIUS FOR SPECIMEN
            NO. 5

142

Strain-gage readings along the horizontal, vertical and
45-degree radii for specimen No. 6 are plotted as a function of
applied average stress in Figs. 91 to 95 with radial location as
a parameter. The vertical strains along the horizontal axis
(Fig. 91) are linear up to at least 1650 psi which is slightly
higher than the crack initiation level of 1500 psi. On the basis
of the far-field gages, the following modulus and Poisson's ratio
were determined:

$$E = 3.7 \times 10^6 \text{ psi}$$
$$\nu = 0.23$$

The maximum strain occurs now at the inner surface of the liner.
The stress ratio between the vertical strain at the interface and
the far-field strain in the linear range is

$$k_\varepsilon = 2.45$$

which is appreciably lower than the corresponding value for speci-
men No. 5 but higher than the theoretical value of 2.18. The
horizontal strains along the vertical axis indicate that cracking
started in the limestone at the interface with the liner at an
average stress of 1500 psi. Cracking in the hydrostone liner
occurred at a slightly higher stress. Principal strains along the
45-degree radius were computed as before and are plotted in Fig. 96.
One result worthy of notice is the small variation of principal
strains with radial location. The angle between the 45-degree
radius and the maximum tensile strain direction varies between 38
degrees and 36 degrees at $r = 1.35a$, 43 degrees and 42 degrees at
$r = 1.80a$ and 42 degrees and 43 degrees at $r = 3.00a$.

The strain variation along the axes of symmetry at given
stress levels within the linear range was plotted in Figs. 97 and 98
for specimens No. 5 and No. 6. Theoretical points for an infinite
elastic plate are also shown. On the basis of the strain distribu-
tions of Fig. 98 and the crack initiation levels obtained from

143
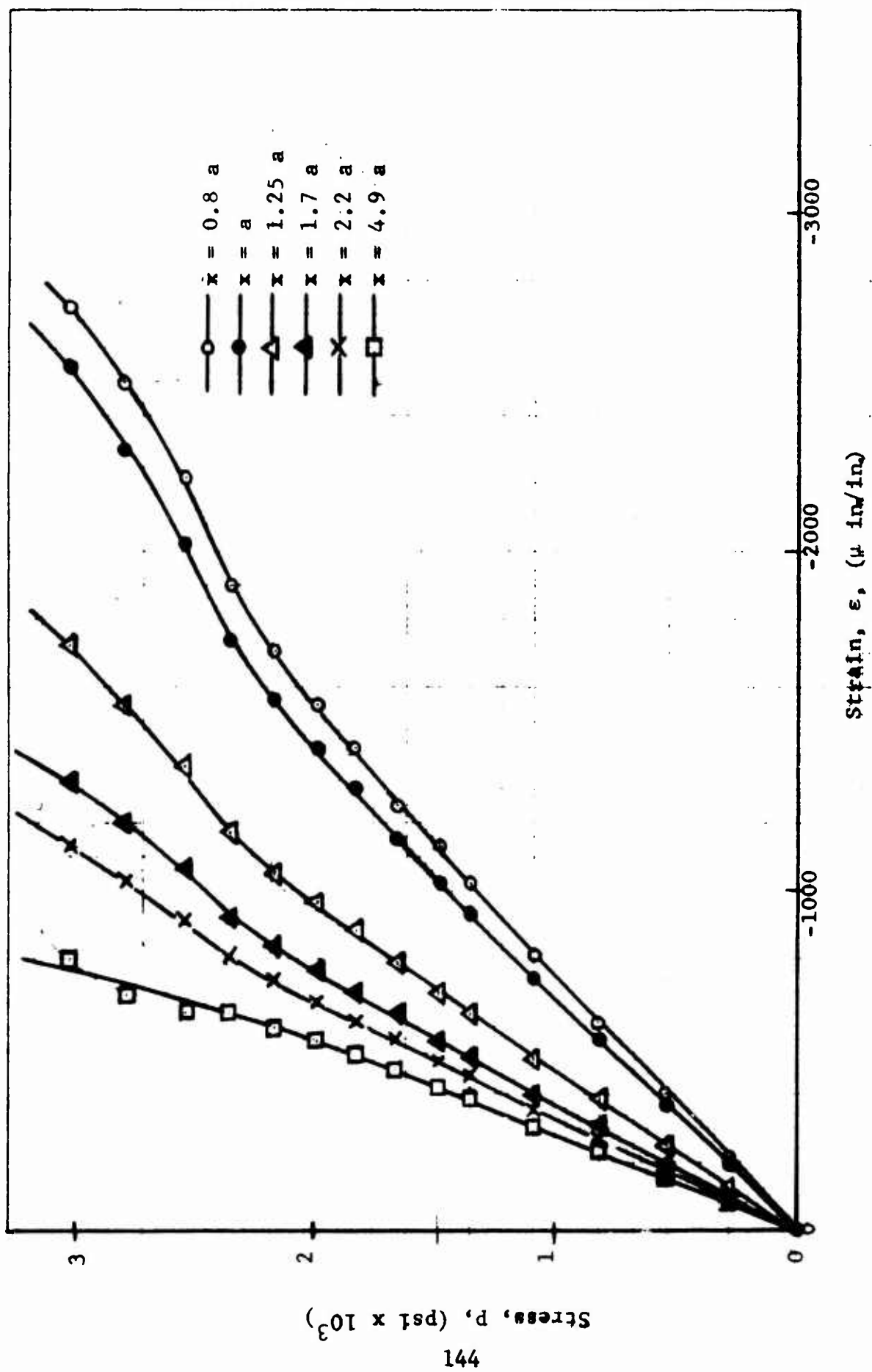
Fig. 91 VERTICAL STRAINS ALONG HORIZONTAL AXIS OF SYMMETRY FOR SPECIMEN NO. 6 (LIMESTONE LINED WITH HYDROSTONE UNDER UNIAXIAL LOADING)

144
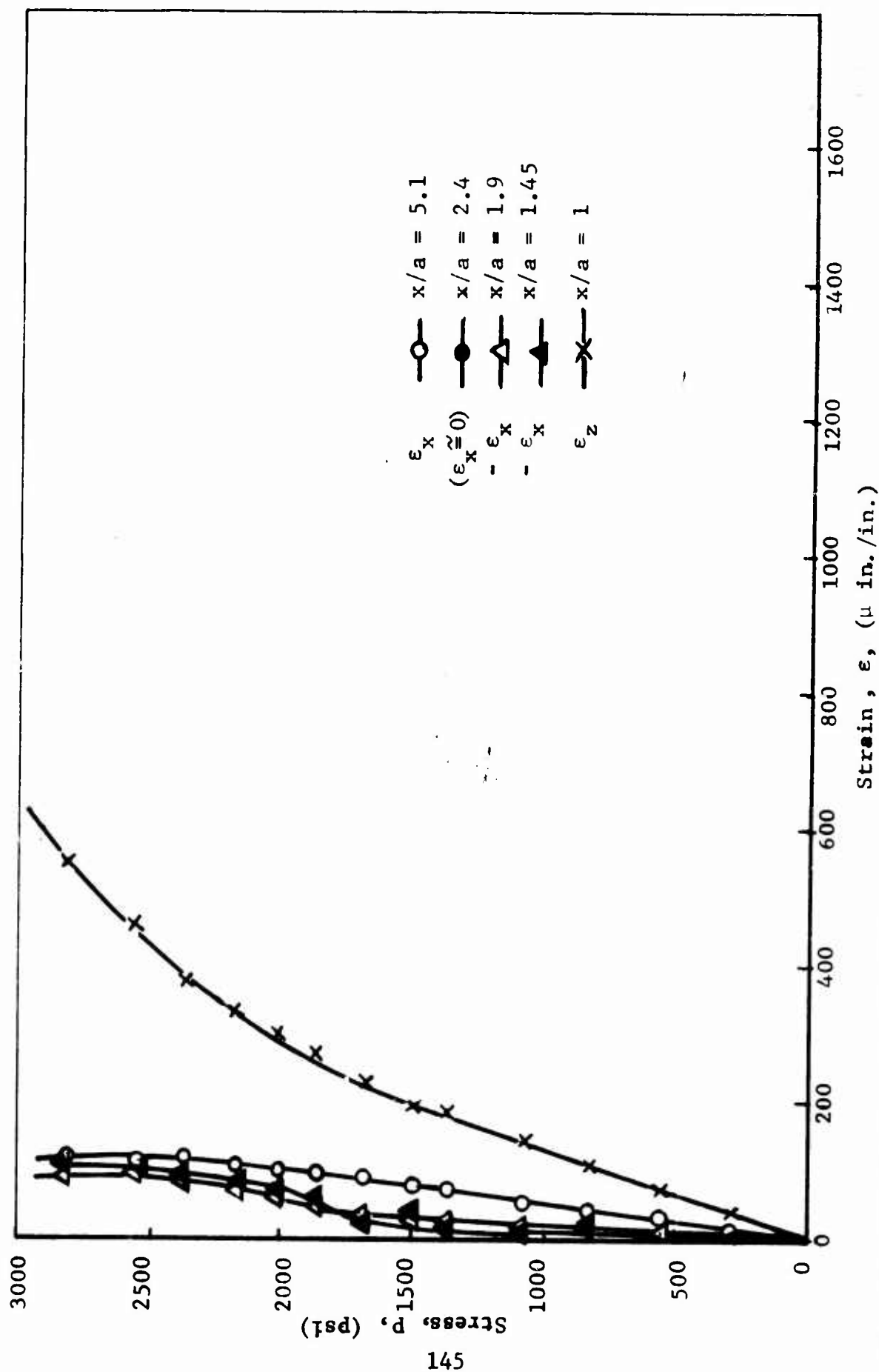
Fig. 92   HORIZONTAL STRAINS ALONG HORIZONTAL AXIS OF SYMMETRY AS A FUNCTION OF APPLIED VERTICAL
STRESS FOR SPECIMEN NO. 6 (LIMESTONE WITH HYDROSTONE LINER UNDER UNIAXIAL LOADING)
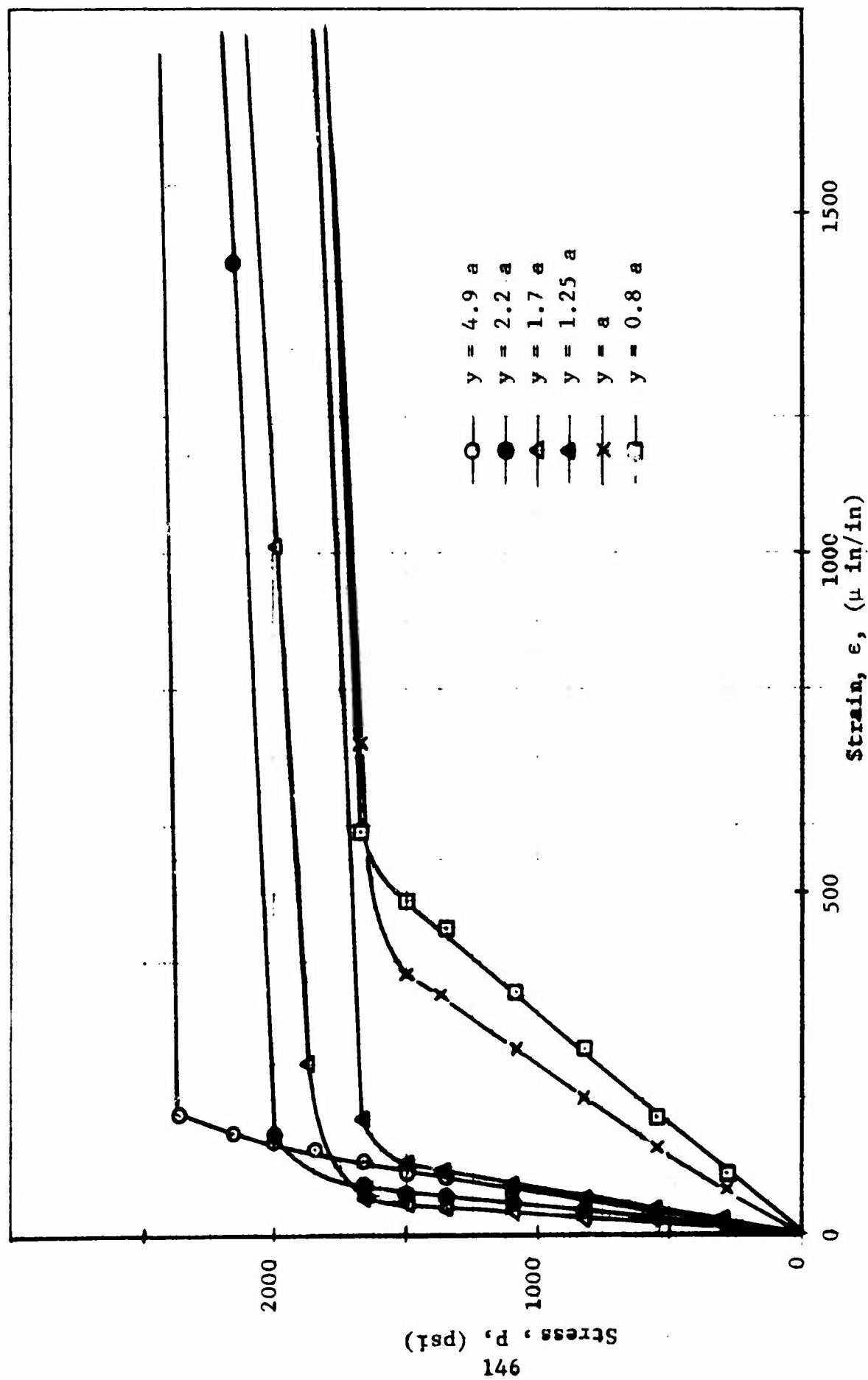
Fig. 93 HORIZONTAL STRAINS ALONG VERTICAL AXIS OF SYMMETRY AS A FUNCTION OF APPLIED VERTICAL STRESS FOR SPECIMEN NO. 6 (LIMESTONE WITH HYDROSTONE LINER UNDER UNIAXIAL LOADING)

146

Fig. 94 VERTICAL STRAINS ALONG VERTICAL AXIS OF SYMMETRY AS A FUNCTION OF APPLIED VERTICAL STRESS FOR SPECIMEN NO. 6 (LIMESTONE WITH HYDROSTONE LINER UNDER UNIAXIAL LOADING)

147
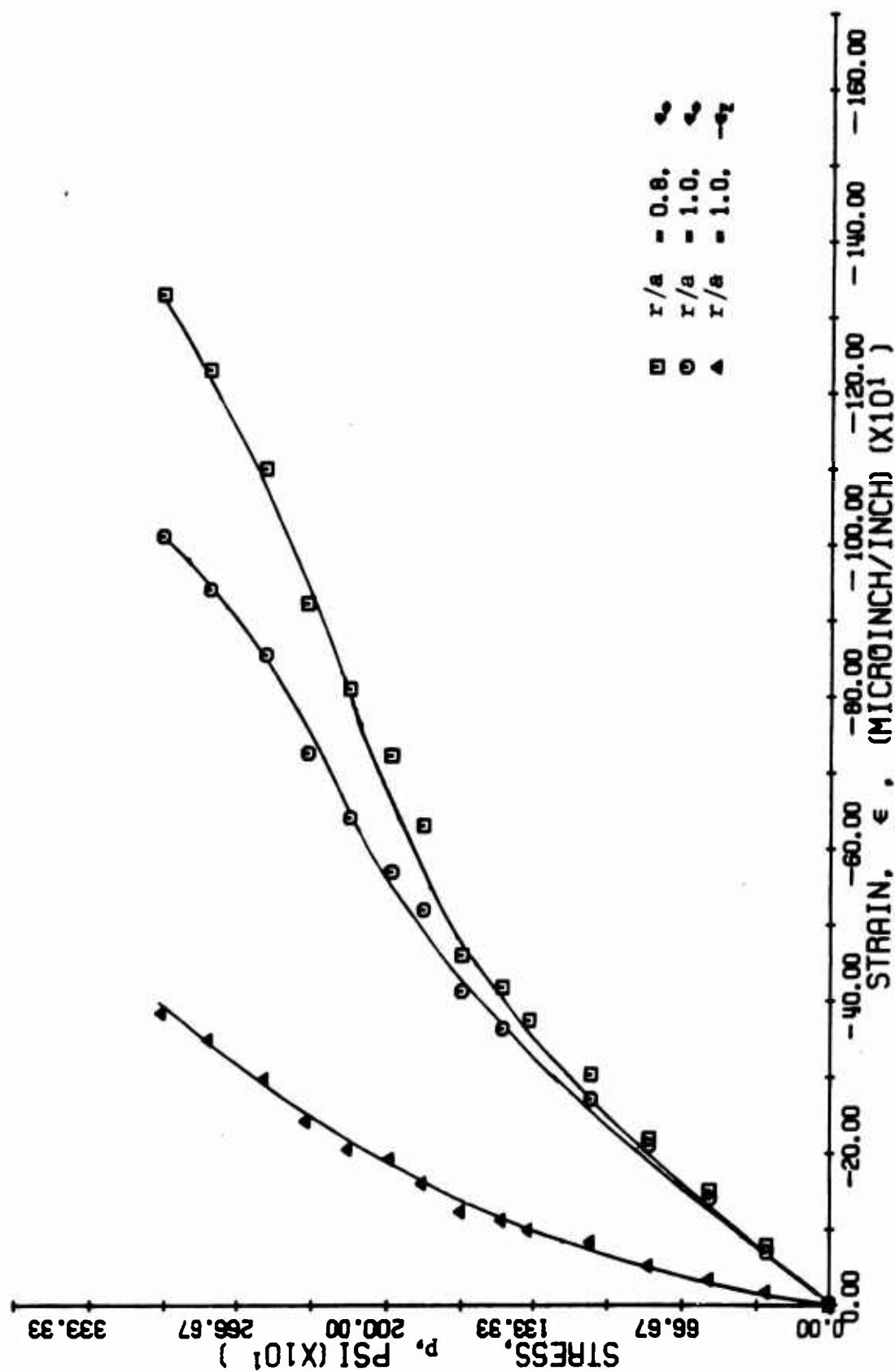
FIG. 95 STRAINS ALONG 45 DEGREE RADIUS FOR SPECIMEN NO. 6
(LIMESTONE WITH HYDROSTONE LINER UNDER UNIAXIAL LOADING)

148
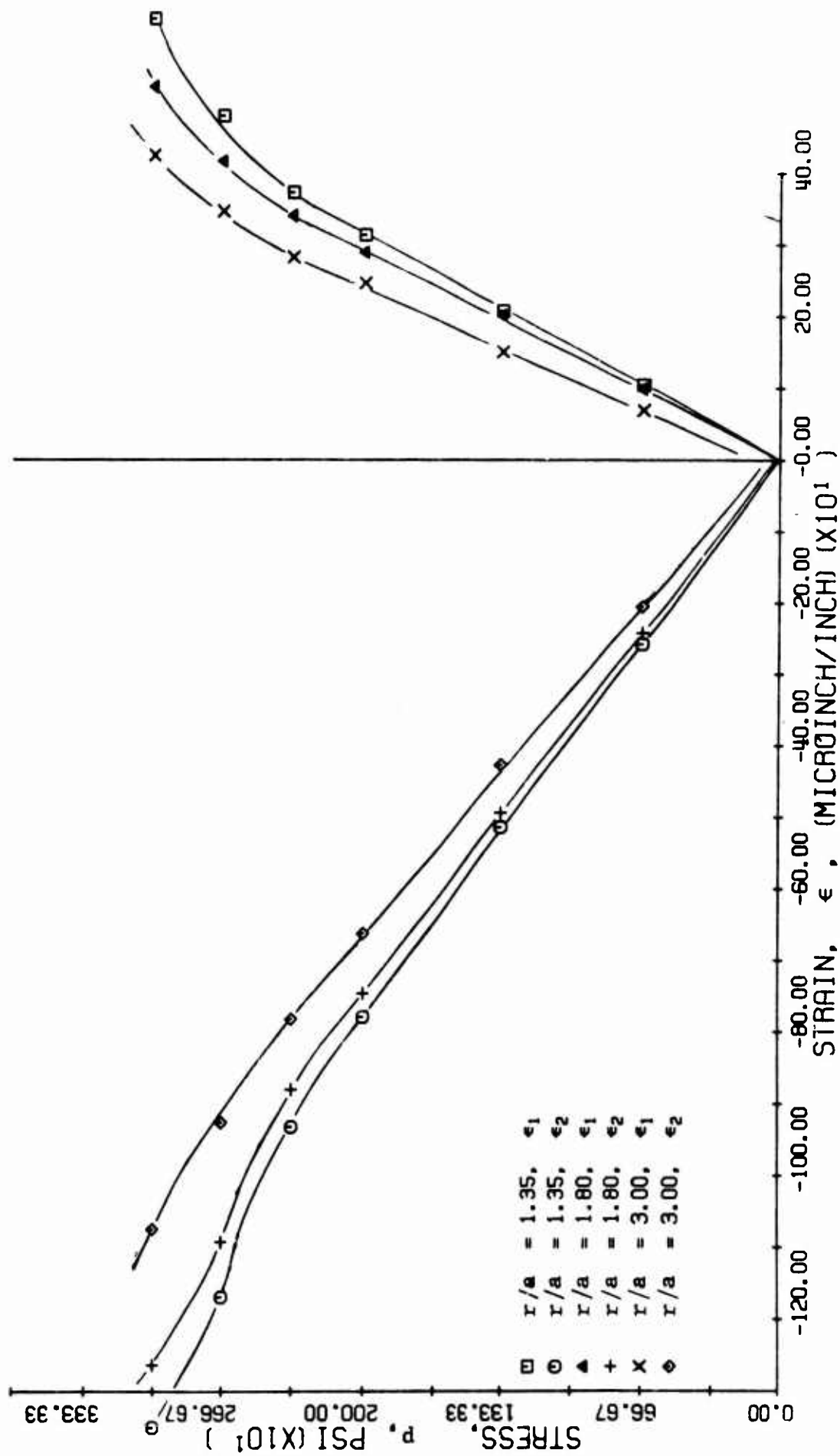
FIG. 96 PRINCIPAL STRAINS ALONG 45-DEGREE RADIUS FOR SPECIMEN NO. 6
(LIMESTONE WITH HYDROSTONE LINER UNDER UNIAXIAL LOADING)

149
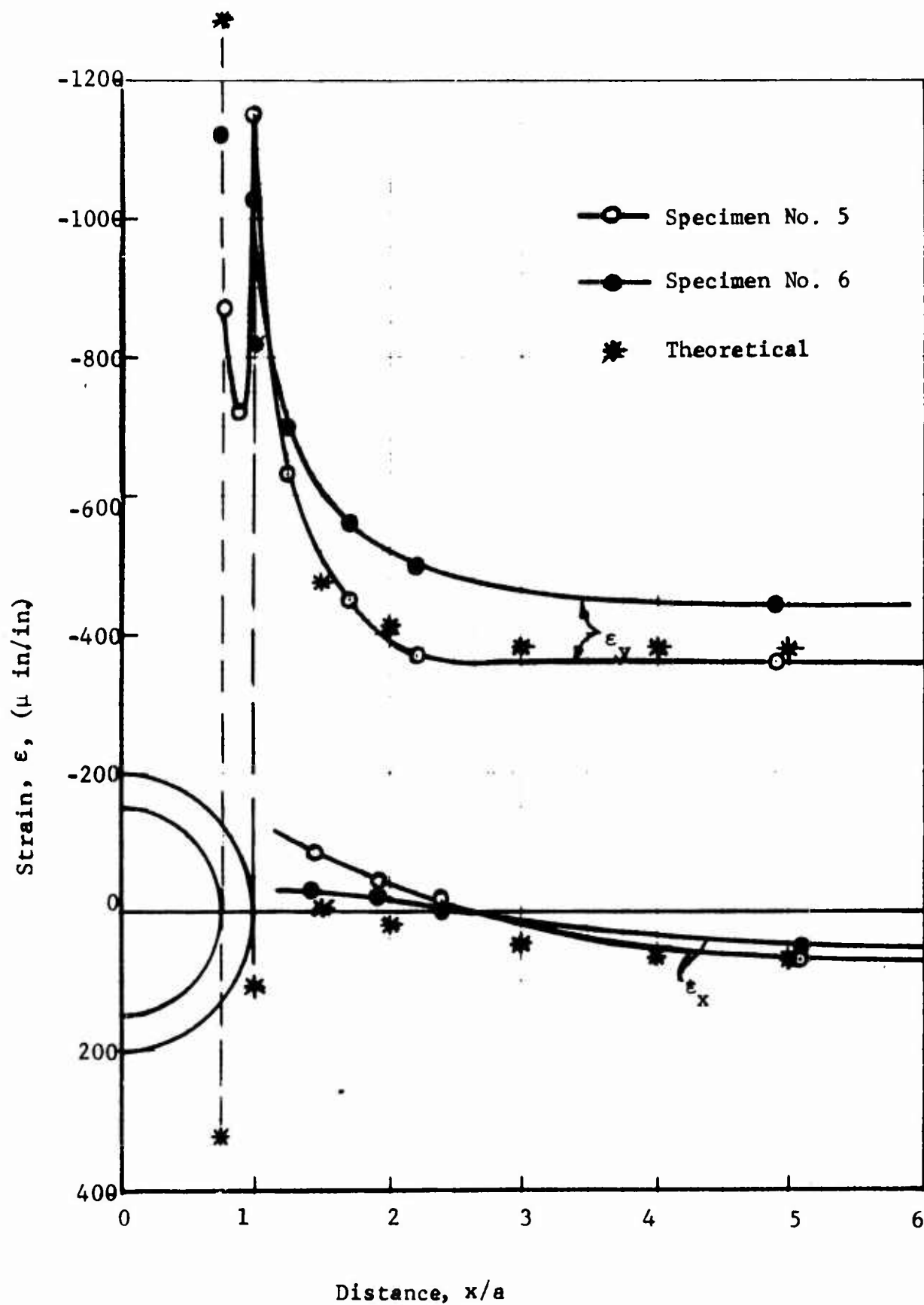
Fig. 97 STRAIN DISTRIBUTION ALONG X-AXIS FOR SPECIMENS NO. 5
AND 6 AT APPLIED STRESS OF 1500 PSI (LIMESTONE WITH
HYDROSTONE LINER UNDER UNIAXIAL LOADING)

150
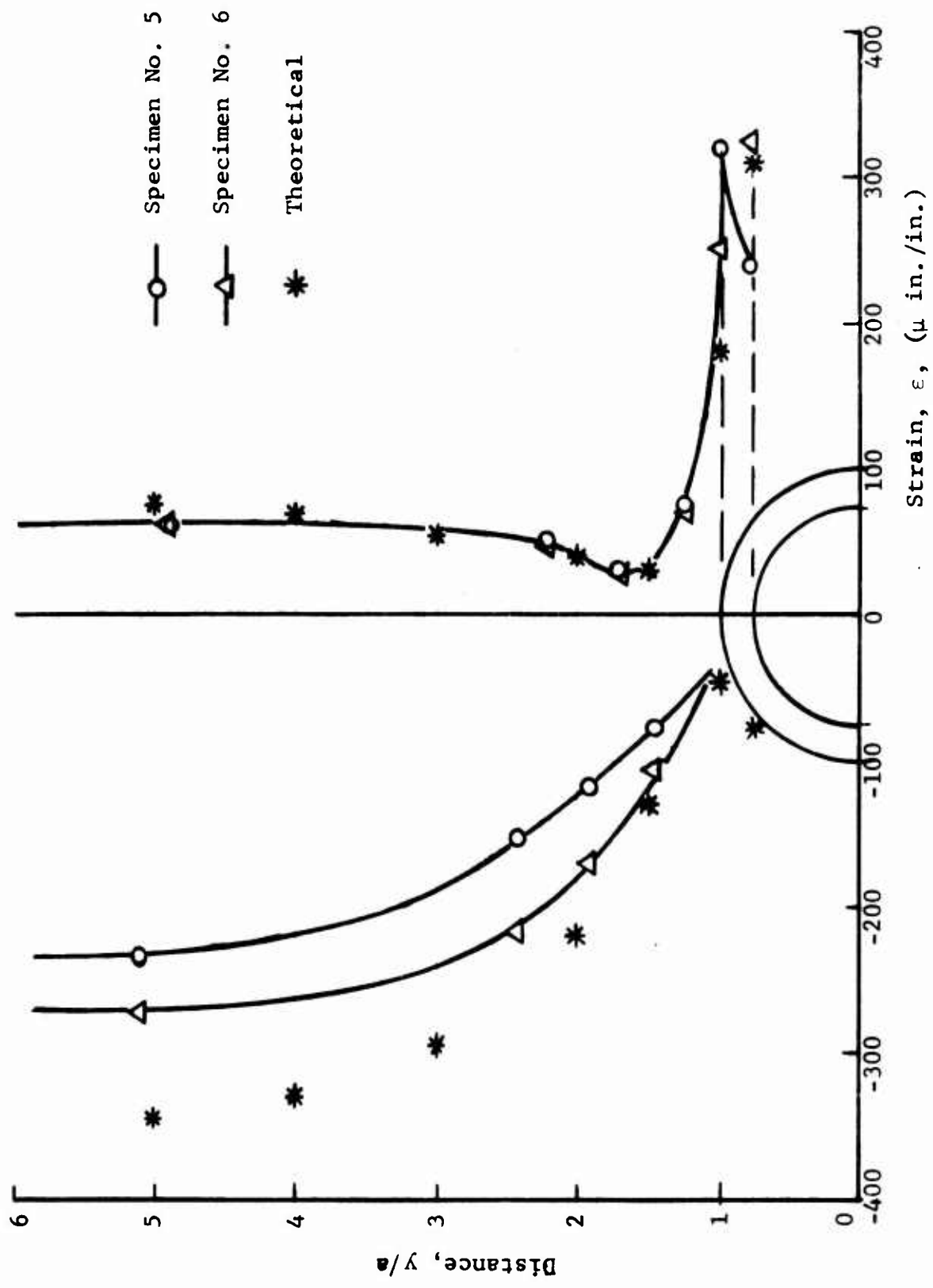
Fig. 98   STRAIN DISTRIBUTION ALONG Y-AXIS FOR SPECIMENS NO. 5 AND 6 AT APPLIED STRESS
OF 1000 PSI (LIMESTONE WITH HYDROSTONE LINER UNDER UNIAXIAL LOADING)

151

previous stress-strain curves (Figs. 86 and 93) the maximum tensile stress in the limestone was computed as follows:

For specimen No. 5, at crack initiation level of p = 1100 psi, the strains at the interface on the vertical axis are

$$\varepsilon_x = 350 \ \mu in./in.$$

$$\varepsilon_y = -27 \ \mu in./in.$$

from which the maximum tensile stress at fracture is computed as

$$\sigma_{max} = 1450 \ psi$$

A similar computation for specimen No. 6, at the crack initiation level of p = 1500 psi, gives

$$\sigma_{max} = 1550 \ psi$$

These levels of stress are appreciably higher than the tensile strength of limestone (630 psi) determined from uniaxial tension tests.

2. Specimens No. 7 and 8 - Limestone with Aluminum Liner Under Uniaxial Loading

    a. Theoretical Stress Distributions

    Stresses on the free surface of the aluminum liner and stresses in the limestone plate at the interface were calculated as before using Eqs. (9) and (10). The following material properties were used for the evaluation of the pertinent constants:

$$Limestone: \ E = 4.3 \times 10^6 \ psi$$

$$\nu = 0.23$$

$$\mu = \frac{E}{2(1+\nu)} = 1.75 \times 10^6 \ psi$$

$$\kappa = \frac{3-\nu}{1+\nu} = 2.25$$

152

Aluminum: $E_1 = 10.6 \times 10^6$ psi

$\nu_1 = 0.33$

$\mu_1 = \dfrac{E_1}{2(1+\nu_1)} = 4.00$

$\kappa_1 = \dfrac{3-\nu_1}{1+\nu_1} = 2.01$

Stress calculations were made for two liner thicknesses. For $t = 0.25$ in. the tangential stress on the free surface of the liner is given by

$$\frac{\sigma_\theta}{p} = 2.05 - 3.66 \cos2\theta \tag{48}$$

with a maximum compressive stress of

$$\left(\frac{\sigma_\theta}{p}\right)_{\theta=90°} = 5.71 \tag{49}$$

The stresses in the limestone plate at the interface are

$$\frac{\sigma_r}{p} = 0.24 - 0.27 \cos2\theta \tag{50}$$

$$\frac{\sigma_\theta}{p} = 0.76 - 0.92 \cos2\theta \tag{51}$$

$$\frac{\sigma_{r\theta}}{p} = -0.33 \sin2\theta \tag{52}$$

with peak values of the circumferential stress at

$$\left(\frac{\sigma_\theta}{p}\right)_{\theta=0°} = -0.16 \tag{53}$$

and

$$\left(\frac{\sigma_\theta}{p}\right)_{\theta=90°} = 1.68 \tag{54}$$

153

For a liner thickness of $t = 0.40$ in. the tangential stress on the free surface of the liner is

$$\frac{\sigma_\theta}{p} = 1.89 - 3.49 \cos2\theta \tag{55}$$

with a maximum compressive value of

$$(\frac{\sigma_\theta}{p})_{\theta=90°} = 5.38 \tag{56}$$

The limestone stresses at the interface are

$$\frac{\sigma_r}{p} = 0.34 - 0.25 \cos2\theta \tag{57}$$

$$\frac{\sigma_\theta}{p} = 0.66 - 0.61 \cos2\theta \tag{58}$$

$$\frac{\sigma_{r\theta}}{p} = -0.82 \sin2\theta \tag{59}$$

The influence of liner thickness on stresses on the inner surface of the liner and at the interface is illustrated by plotting the peak tangential stresses above versus the thickness diameter ratio (Fig. 99). The limiting values for zero liner thickness were obtained as explained before.

The liner thickness selected for specimens No. 7 and 8 was $t = 0.40$ in. Using the expressions for the stress components at the interface, the principal stresses were calculated and plotted versus angular location in Fig. 100. One significant result is that both tensile and compressive stresses reach maximum values at intermediate locations between 0° and 90°. The tensile stress reaches a peak at

$$(\frac{\sigma_2}{p}) = -0.43 \quad \text{at} \quad \theta = 33° \tag{60}$$

and the compressive stress reaches a peak at

$$(\frac{\sigma_1}{p}) = 1.46 \quad \text{at} \quad \theta = 60° \tag{61}$$

154
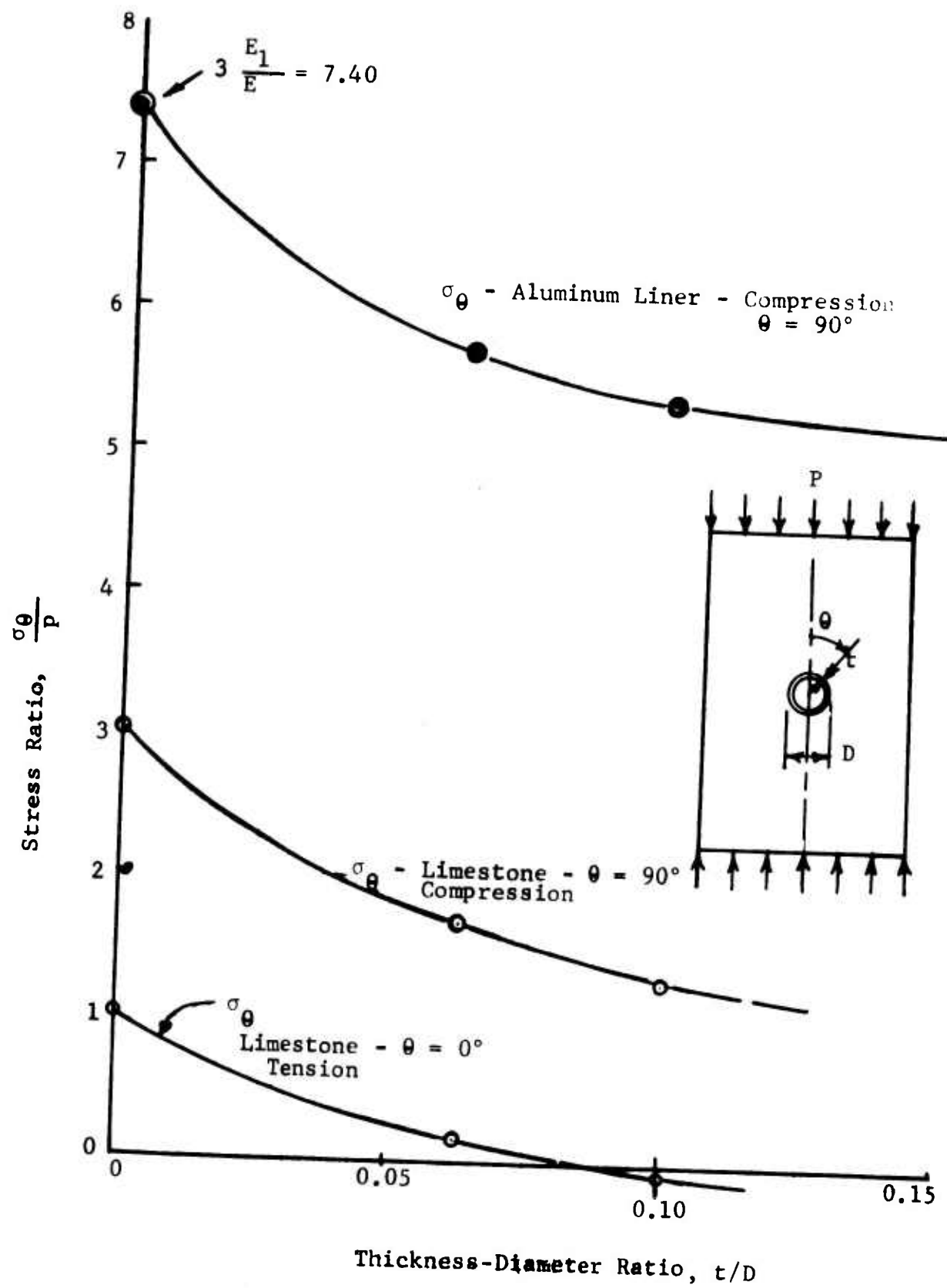
Fig. 99 VARIATION OF STRESSES IN ALUMINUM LINER AND LIMESTONE PLATE AS A FUNCTION OF LINER THICKN SS

155
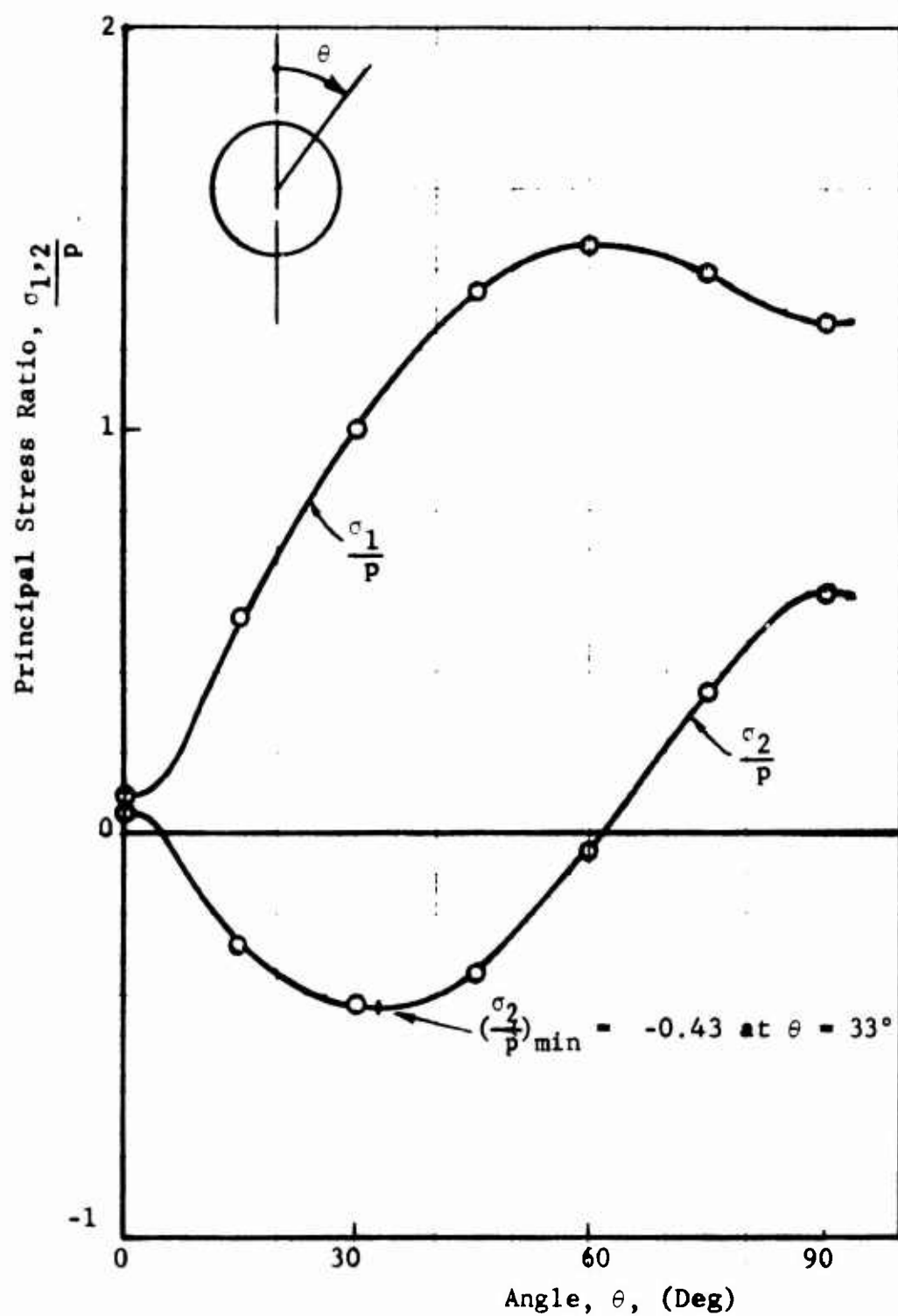
Fig. 100   VARIATION OF PRINCIPAL STRESSES IN LIMESTONE
AT INTERFACE WITH ALUMINUM LINER

156

The most significant results from the point of view of fracture are the maximum tensile stress and its direction. The latter is indicative of the direction of crack propagation at the interface. The calculated principal directions at this point on the first quadrant are

$$\varphi_{1-x} = 15° \tag{62}$$

$$\varphi_{2-x} = -75°$$

measured counterclockwise from the x-axis to the tensile and compressive principal stresses, respectively.

b. Experimental Procedure

Two limestone plates of dimensions 36 in. x 24 in. x 2.5 in. with a 4 in. diameter hole and a 0.40 in. thick aluminum liner bonded to the cavity surface were used. A flexible filled epoxy was used to bond the liner in specimen No. 7 and a hard unfilled epoxy in specimen No. 8. Strain gages were applied as before with minor modifications in the layout (Fig. 101). Diametral changes were monitored with DCDTs and the overall strain distribution on the surface was observed and recorded with a photoelastic coating. The instrumented specimens were loaded in the 1,000,000 lb testing machine at approximately 25,000 lb load increments. Strain gage and DCDT readings and isochromatic fringe patterns were recorded as before.

c. Results and Discussion

Isochromatic fringe patterns for specimens No. 7 and 8 are shown in Figs. 102 and 103 for various stress levels. The applied average stress is shown in each frame. The patterns show a high interface shear between liner and specimen at the 45° location as predicted theoretically.

In the case of specimen No. 7 (with filled epoxy cement), there is evidence of early bond failure which subsequently resulted in cracking in the rock slightly off the vertical axis at an applied stress of 1200 psi. This stress level is comparable to that at which

157

Gage No.	r/a
1,7,12,18	0.8
2,13,27	0.9
25,28,14,3,26,31,8	1.2
4,15,29	1.6
5,16,30	2
6,20,22,24	5
32,33,34	1
9	1.65
10	3
17,19,21,23	5
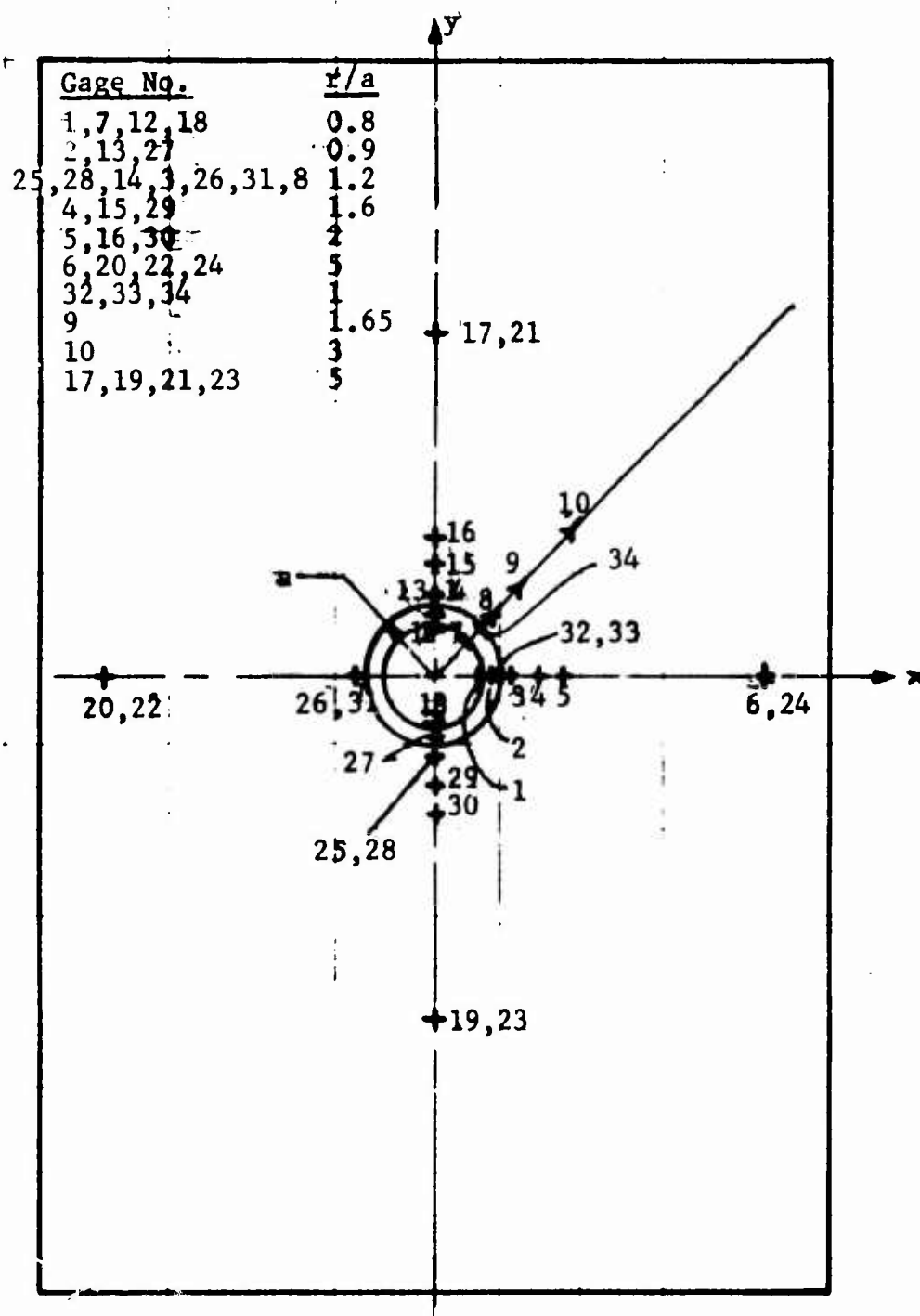
Fig. 101   STRAIN GAGE LAYOUT FOR LIMESTONE SPECIMENS WITH ALUMINUM LINERS

158
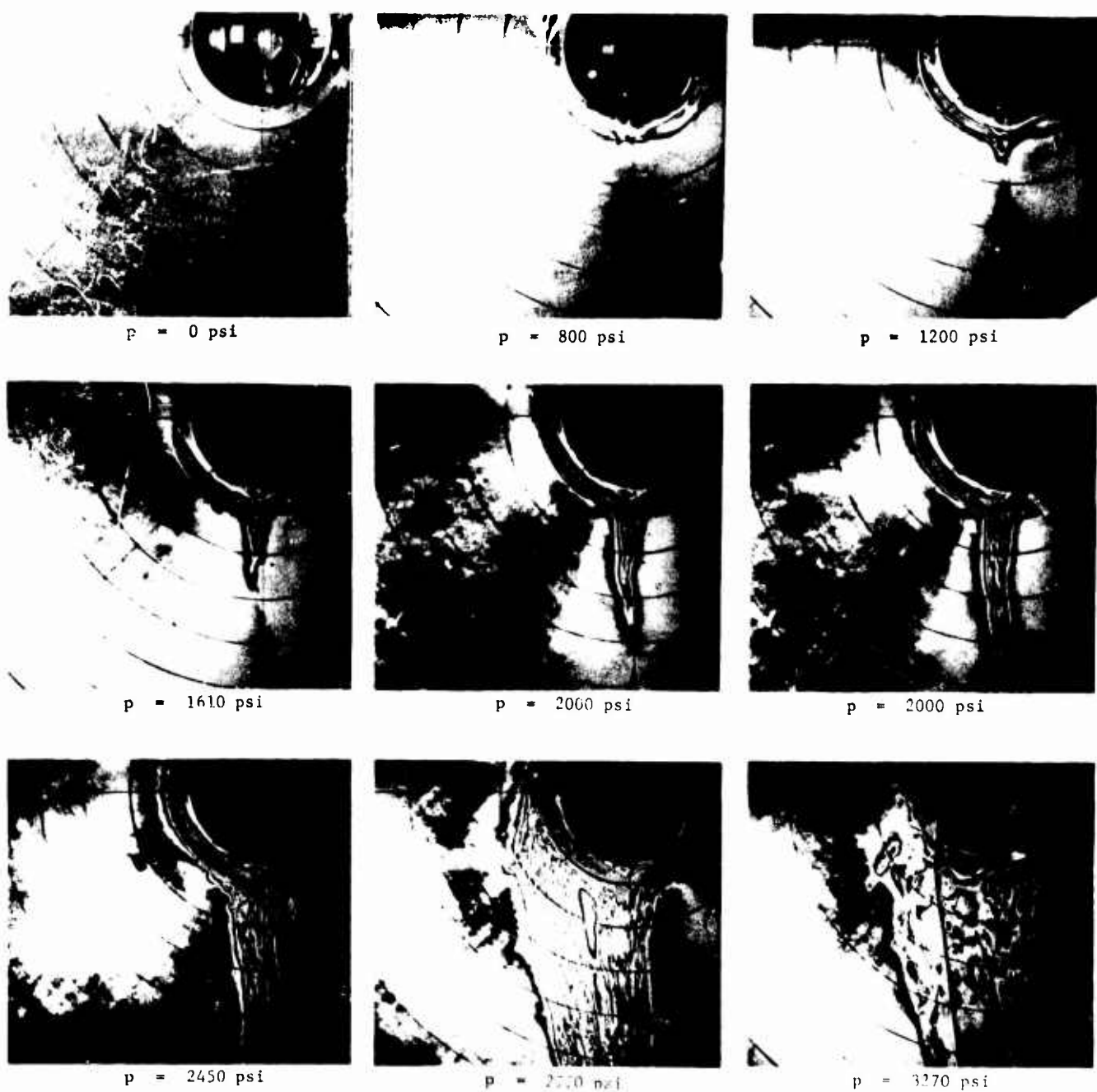
Fig. 102 ISOCHROMATIC FRINGE PATTERNS IN PHOTOELASTIC COATING AROUND HOLE IN SPECIMEN NO. 7 (LIMESTONE WITH ALUMINUM LINER UNDER UNIAXIAL LOADING)

159
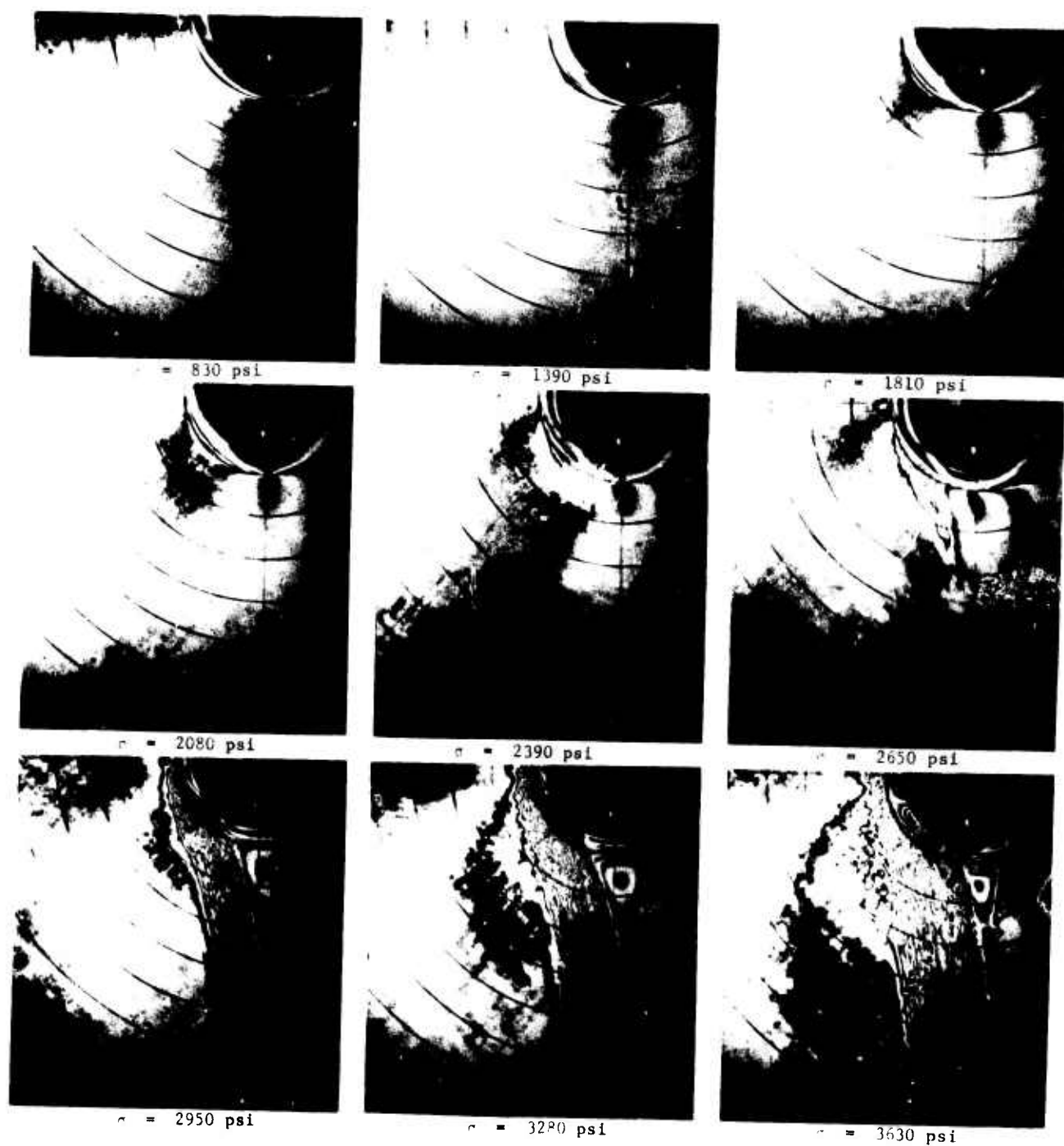
Fig. 103 ISOCHROMATIC FRINGE PATTERNS IN PHOTOELASTIC COATING AROUND HOLE IN SPECIMEN NO. 8 (LIMESTONE WITH ALUMINUM LINER UNDER UNIAXIAL LOADING)

160

cracking occurred in the unlined specimen No. 1. As the load was increased, the first crack propagated along the vertical axis and another crack developed near the 45° location. This is due to the high tensile stress existing at the interface in this region (Fig. 100). The direction of this crack as seen in the last frame of Fig. 102 is inclined toward the vertical axis at an angle of approximately 8°. An island of nearly zero stress forms as the two cracks propagate and meet on the vertical axis as indicated in frame 8 of Fig. 102. The specimen failed by spallation at an average stress of 3,270 psi. The failure pattern of this specimen is shown in Fig. 104. (In this and subsequent similar figures disregard specimen numbers marked on the specimen.)

Specimen No. 8 was identical to No. 7 except for a hard unfilled resin used in bonding the liner. High interface shear was noticed again at the 45° location. Cracking of the rock at the interface occurred at an angular location of 42° from the vertical centerline. This should be compared with the theoretical location of $\theta = 33°$ where the maximum tensile stress occurs (Fig. 100). This crack started at an applied stress of less than $p = 2390$ psi and it propagated toward the vertical axis at an angle of 28° with the vertical. The theoretical value for the principal direction at the maximum tensile stress location is 15° (Eq. 62). A second crack at a symmetrical point is noticed at a stress level of $p = 2950$ psi. This crack is inclined at an angle of 21° with the vertical axis. Complete failure by spallation of the segment between the two inclined cracks occurred at a stress of 3970 psi. The failure pattern shown in Fig. 105 clearly shows how the cracks propagated from the high tensile stress area off the vertical axis of symmetry.

Diametrical changes measured with DCDTs are plotted in Figs. 106 and 107 as a function of applied vertical stress. The curves for specimen No. 7 are linear up to the crack initiation level of 1200 psi. The deflections per unit stress in this linear range are

$$\frac{\delta_h}{p} = 1.6 \times 10^{-6} \text{ in./psi}$$

$$\frac{\delta_v}{p} = -2.3 \times 10^{-6} \text{ in./psi}$$

161
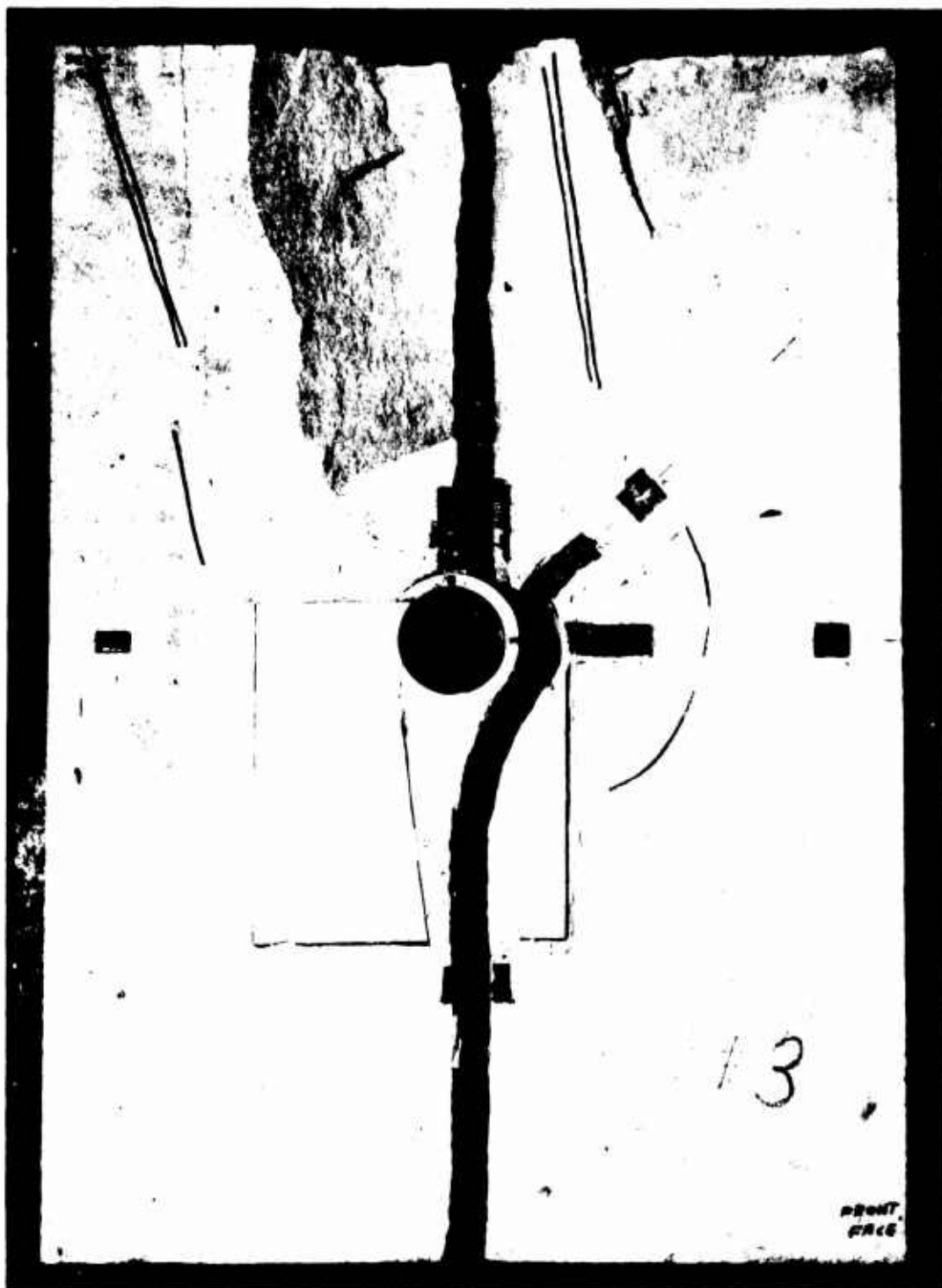
Fig. 104   FAILURE PATTERN IN SPECIMEN NO. 7 (LIMESTONE
WITH ALUMINUM LINER UNDER UNIAXIAL LOADING)
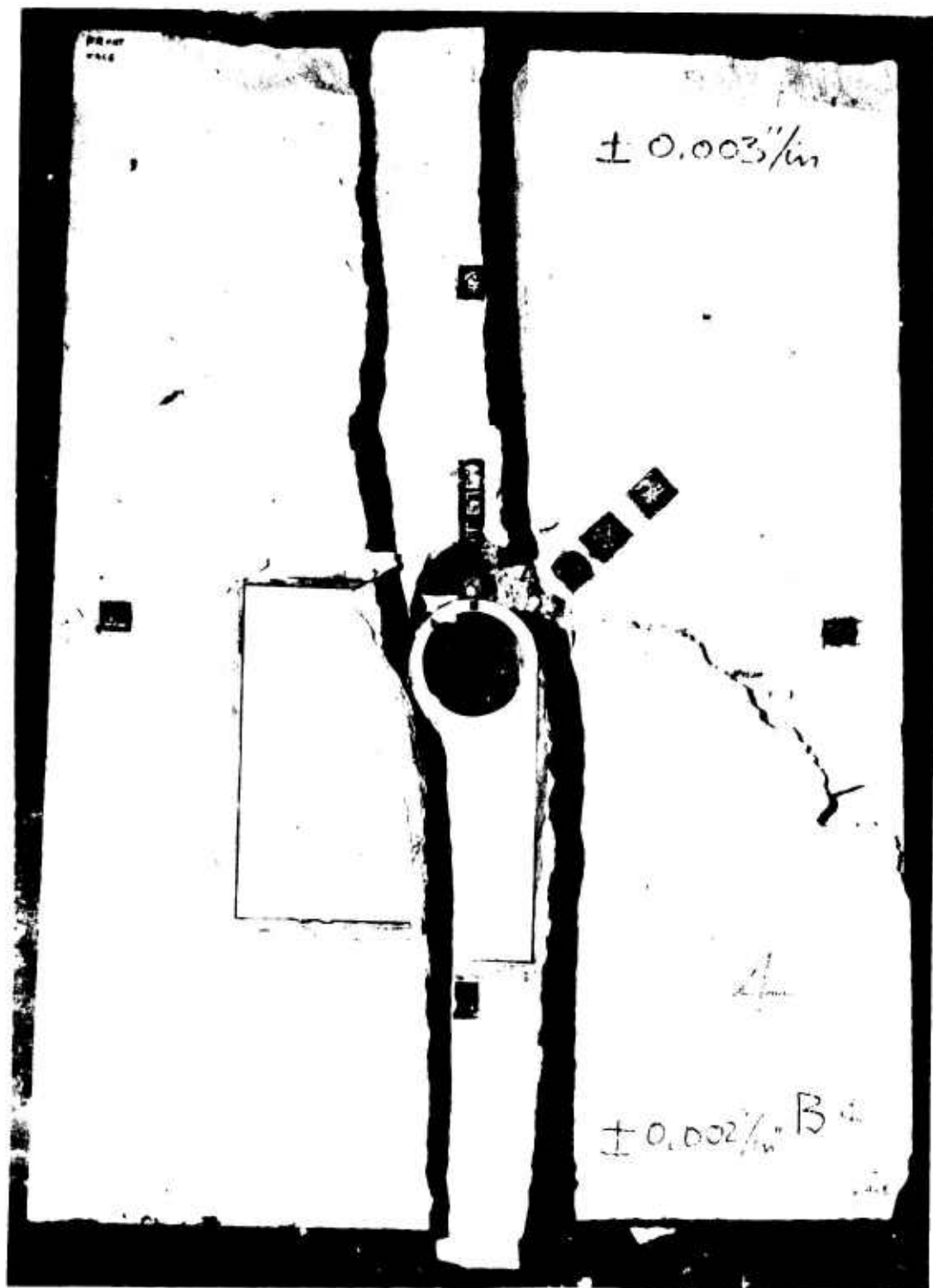
Fig. 105   FAILURE PATTERN IN SPECIMEN NO. 8   (LIMESTONE
WITH ALUMINUM LINER UNDER UNIAXIAL LOADING)

163
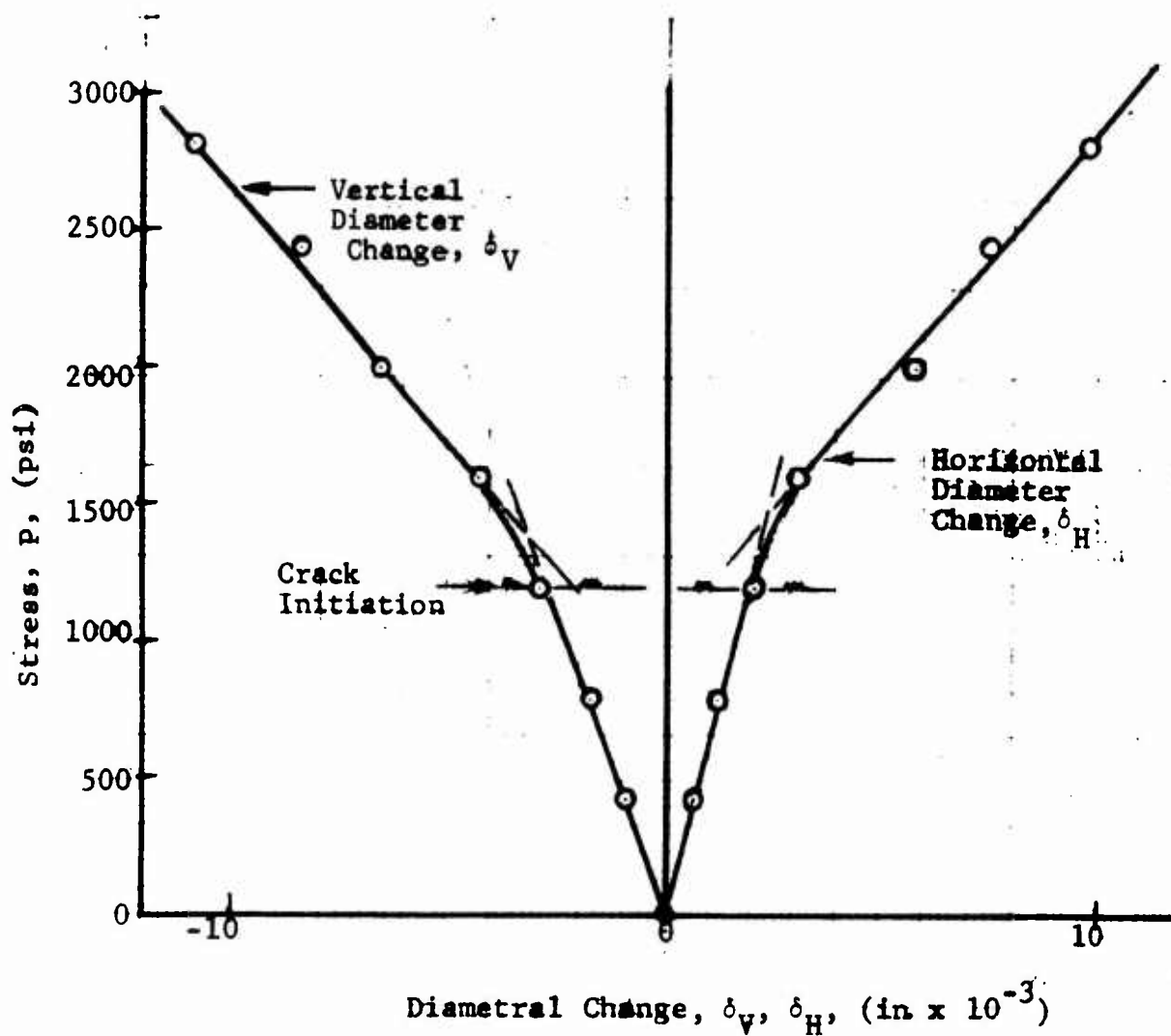
Fig. 106   DIAMETRAL CHANGES AS A FUNCTION OF APPLIED VERTICAL STRESS
FOR SPECIMEN NO. 7 (LIMESTONE SPECIMEN WITH ALUMINUM LINER
UNDER UNIAXIAL LOADING)

164
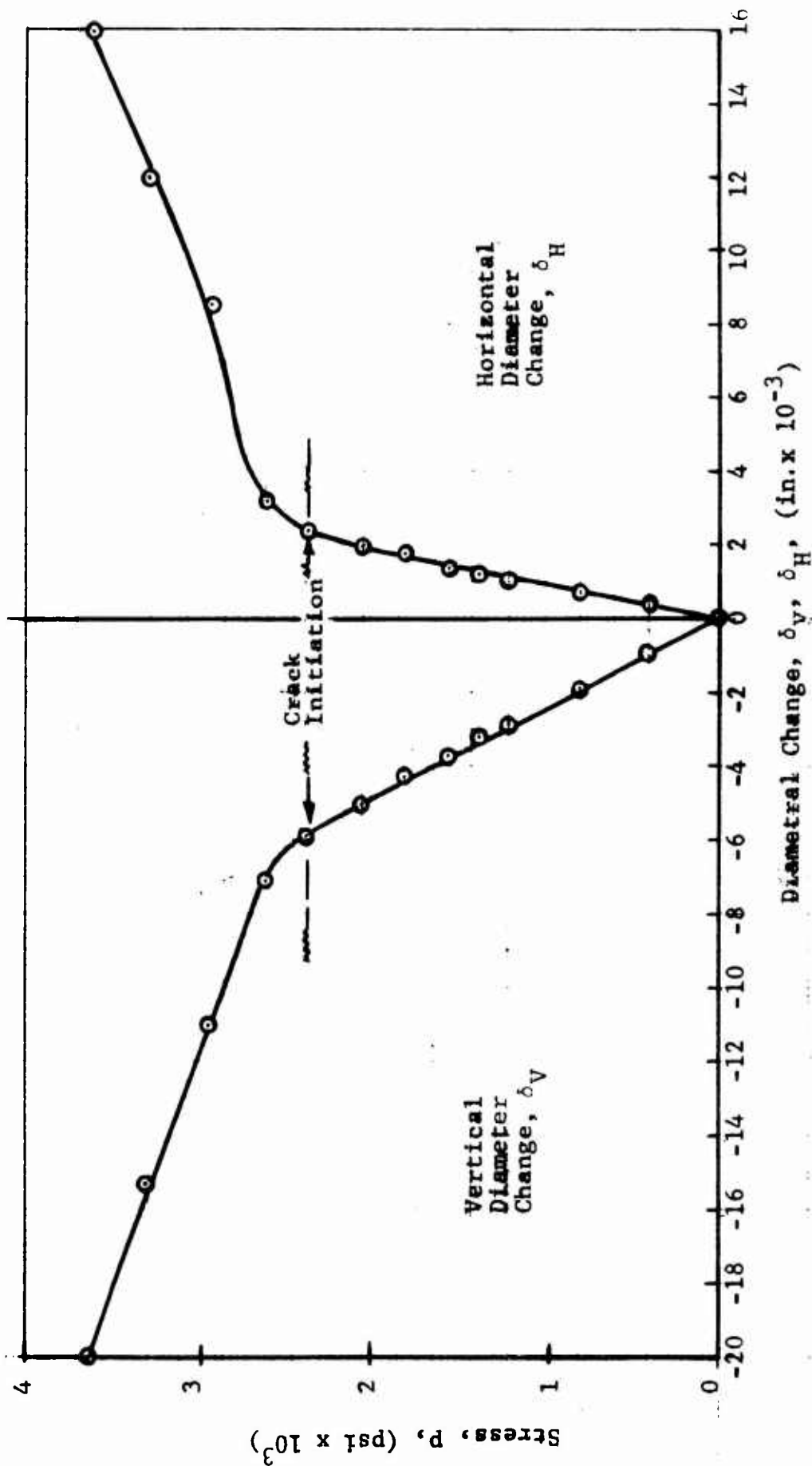
Fig. 107 DIAMETRAL CHANGES AS A FUNCTION OF APPLIED VERTICAL STRESS FOR SPECIMEN NO. 8 (LIMESTONE LINED WITH ALUMINUM UNDER UNIAXIAL LOADING)

165

The deflections for specimen No. 8 are linear up to the crack initiation level of 2,390 psi. Unit deflections in this range are

$$\frac{\delta_h}{p} = 0.9 \times 10^{-6} \text{ in./psi}$$

$$\frac{\delta_v}{p} = -2.5 \times 10^{-6} \text{ in./psi}$$

The vertical diametral changes are approximately the same for both specimens, however, some discrepancy exists in the horizontal deflections. This may be due to differences in bonding of the liner to the plate.

Strain gage readings for specimen No. 7 are plotted in Figs. 108 to 112. The vertical strains along the horizontal axis (Fig. 113) are linear up to at least 1200 psi, the crack initiation level. On the basis of the far-field strains, the following modulus and Poisson's ratio were determined.

$$E = 4.3 \times 10^6 \text{ psi}$$
$$\nu = 0.22$$

The maximum compressive strain occurs in the limestone at the interface with the aluminum liner. The ratio of this strain to the far-field strain is

$$k_\varepsilon = 3.13$$

The horizontal strains along the vertical axis indicate that cracking in the limestone started at a stress level between 1,000 and 1,200 psi. Principal stresses along the 45 degree radius were computed as before and plotted in Fig. 113. The angle between the 45-degree radius and the principal tensile direction varies between 39 degrees and 20 degrees at $r = 1.20a$, 39 degrees and 35 degrees at $r = 1.65a$, and 41 degrees and 40 degrees at $r = 3.00a$. This angle generally decreases as the strains go from the linear into the nonlinear region.
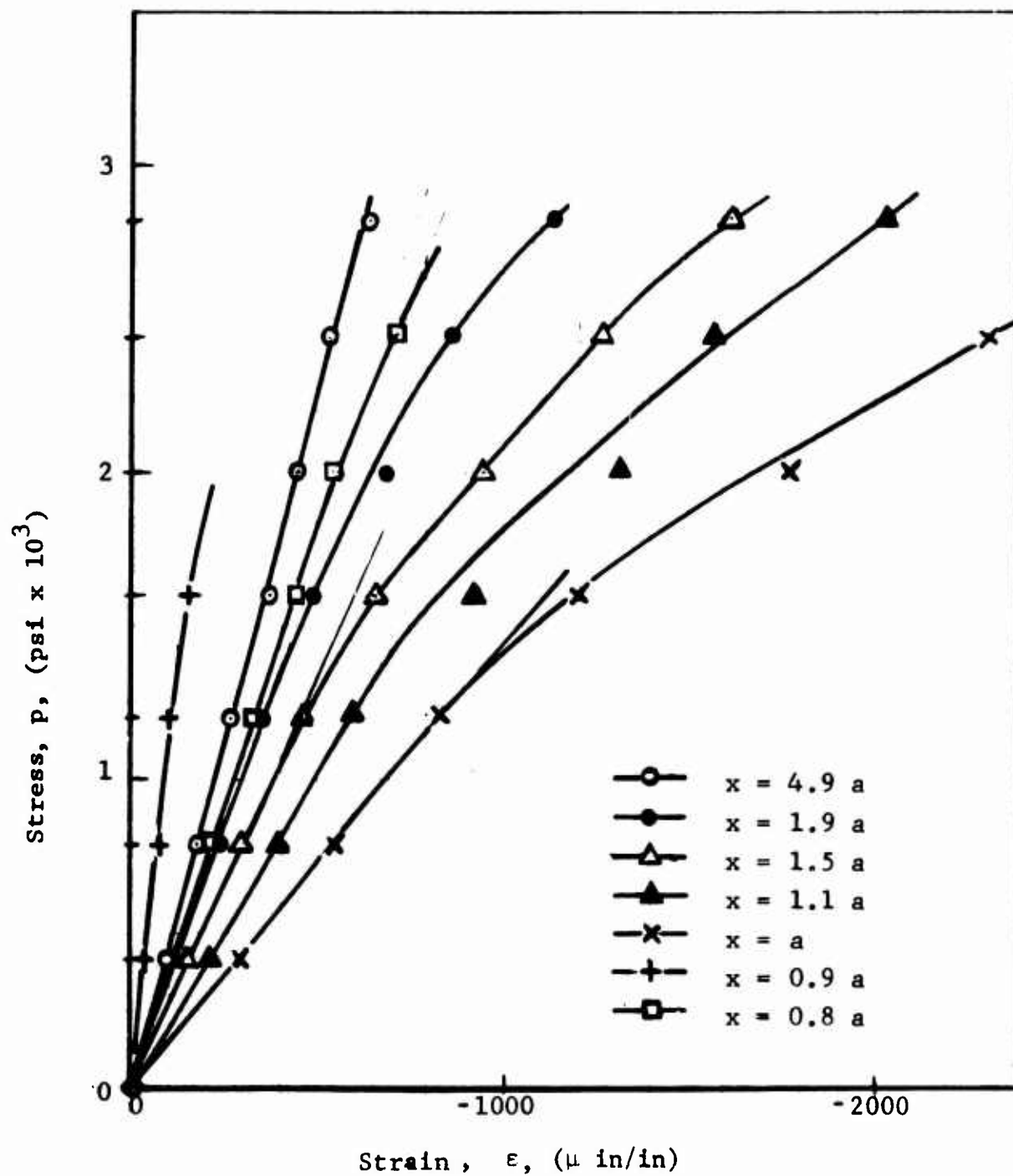
Fig.108 VERTICAL STRAINS ALONG HORIZONTAL AXIS OF SYMMETRY
AS A FUNCTION OF APPLIED VERTICAL STRESS FOR SPECIMEN
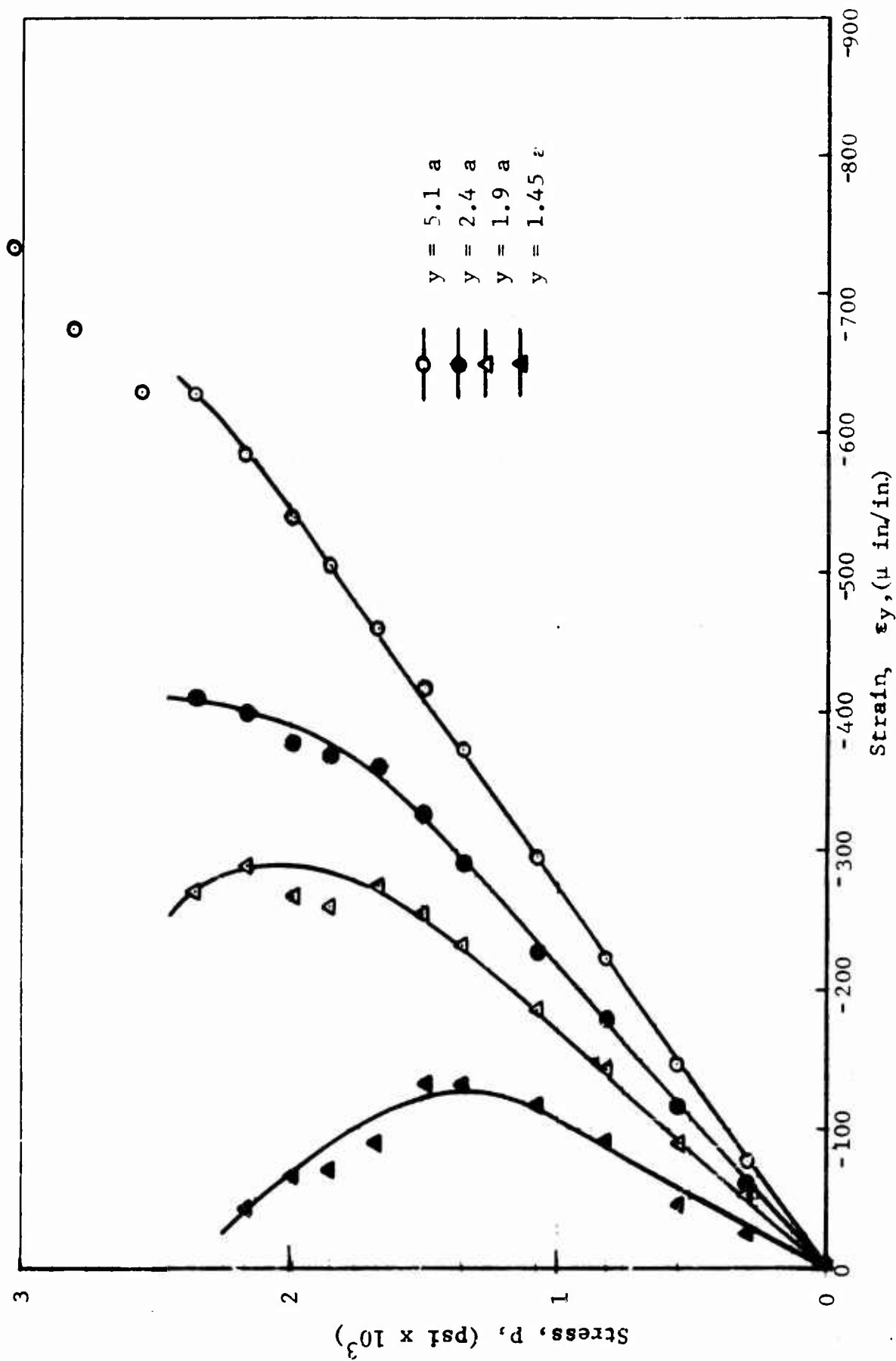NO. 7 (LIMESTONE LINED WITH ALUMINUM UNDER UNIAXIAL
LOADING)

167
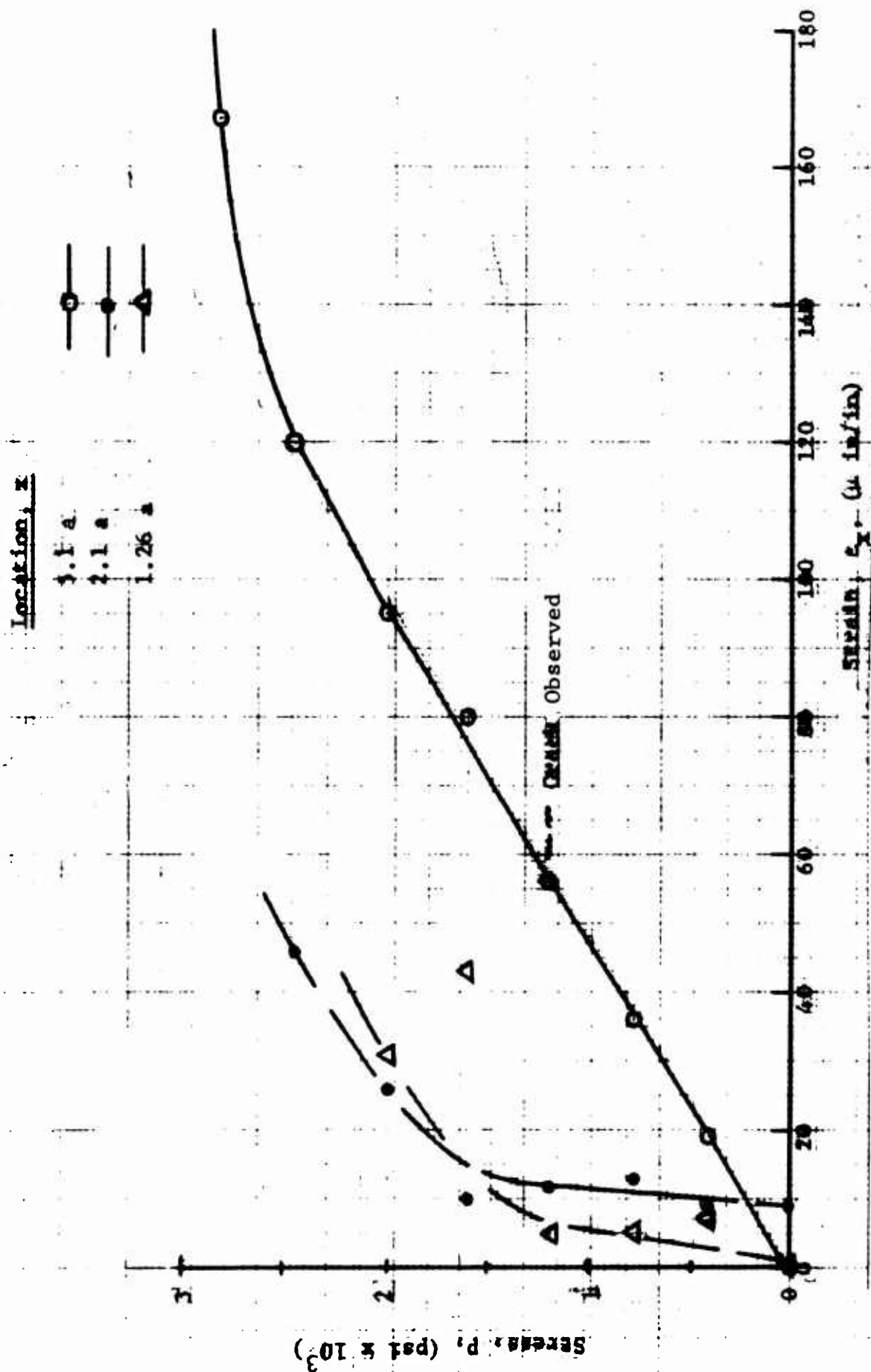
Fig. 109 HORIZONTAL STRAINS ALONG HORIZONTAL AXIS OF SYMMETRY AS A FUNCTION
OF APPLIED VERTICAL STRESS FOR SPECIMEN NO. 7 (LIMESTONE LINED
WITH ALUMINUM UNDER UNIAXIAL LOADING)

168
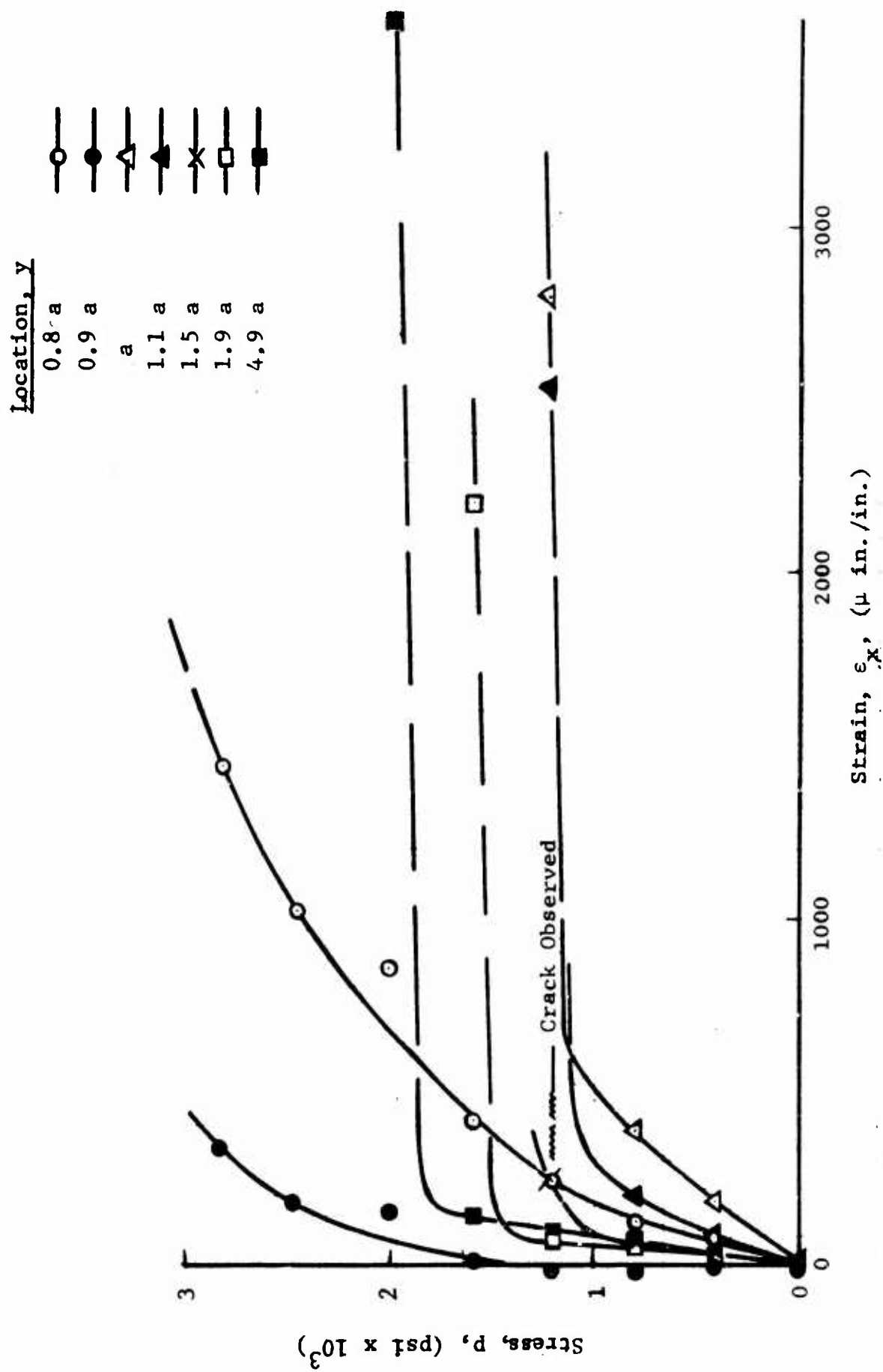
Fig. 110 HORIZONTAL STRAINS ALONG VERTICAL AXIS OF SYMMETRY AS A FUNCTION
OF APPLIED VERTICAL STRESS FOR SPECIMEN NO. 7 (LIMESTONE LINED
WITH ALUMINUM UNDER UNIAXIAL LOADING)

169
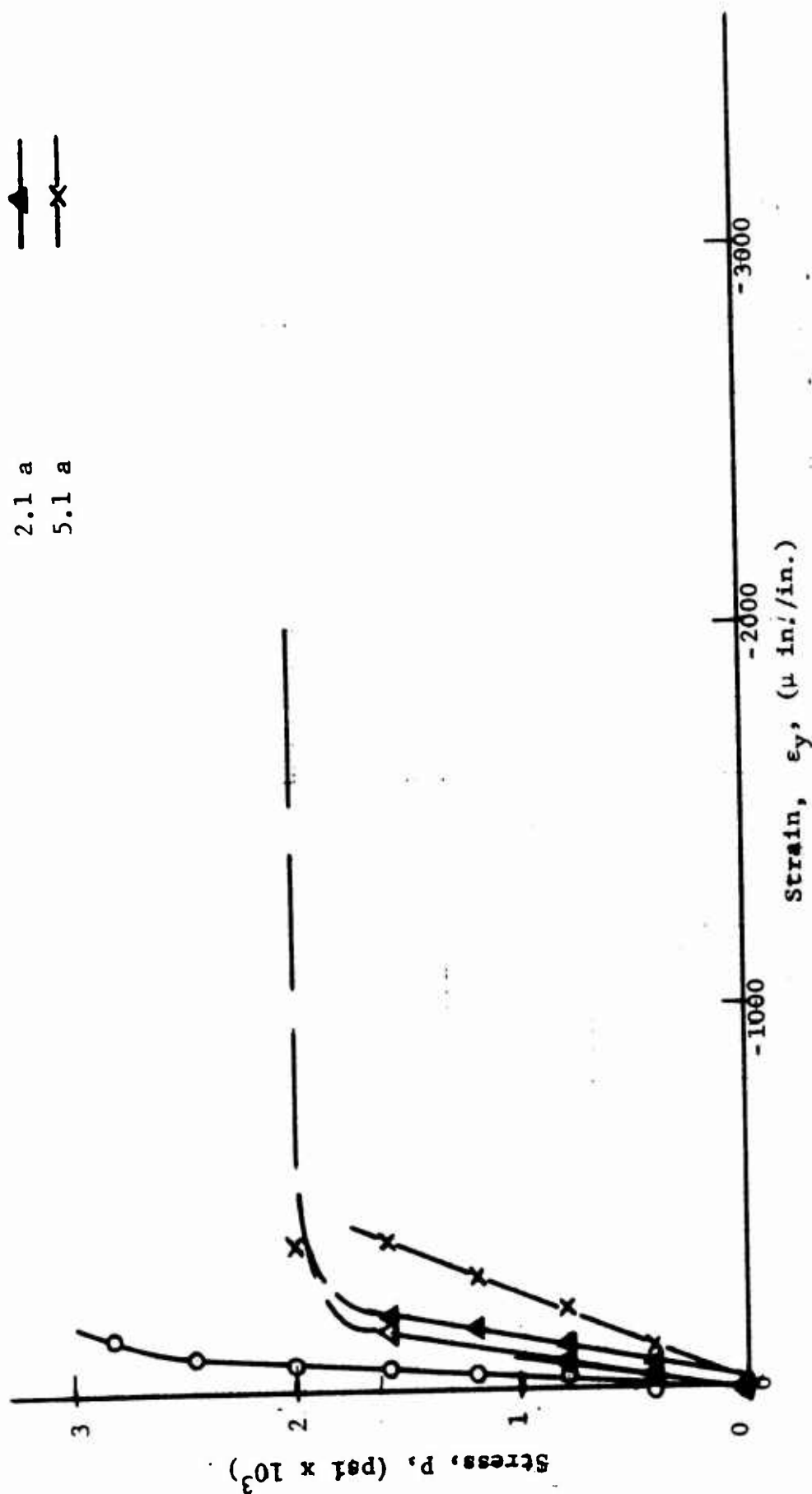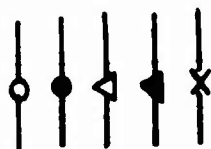
Fig. 111 VERTICAL STRAINS ALONG VERTICAL AXIS OF SYMMETRY AS A FUNCTION OF APPLIED VERTICAL STRESS FOR SPECIMEN NO. 7 (LIMESTONE LINED WITH ALUMINUM UNDER UNIAXIAL LOADING)

170
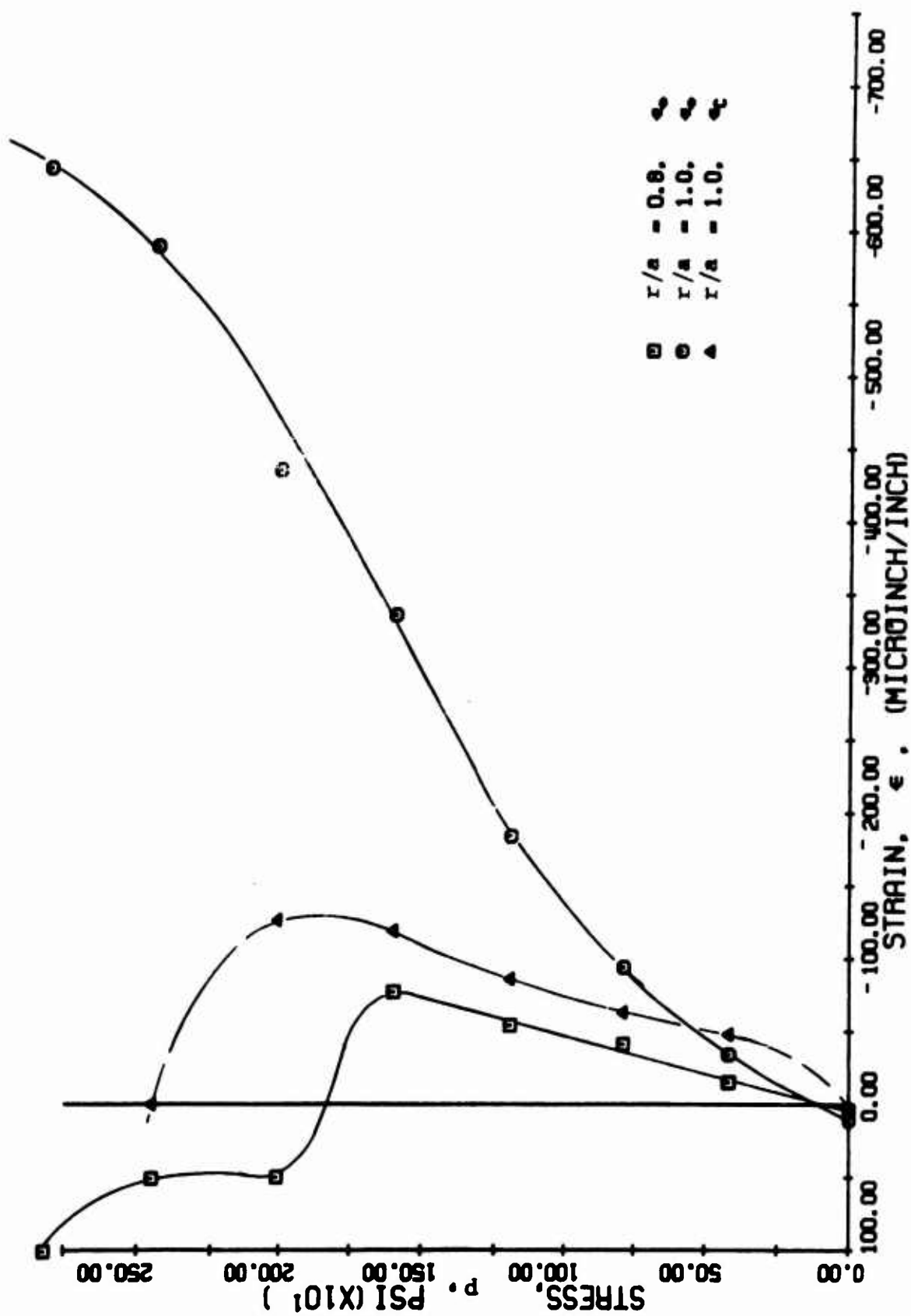
FIG. 112 STRAINS ALONG 45 DEGREE RADIUS FOR SPECIMEN NO. 7
(LIMESTONE WITH ALUMINUM LINER UNDER UNIAXIAL LOADING)
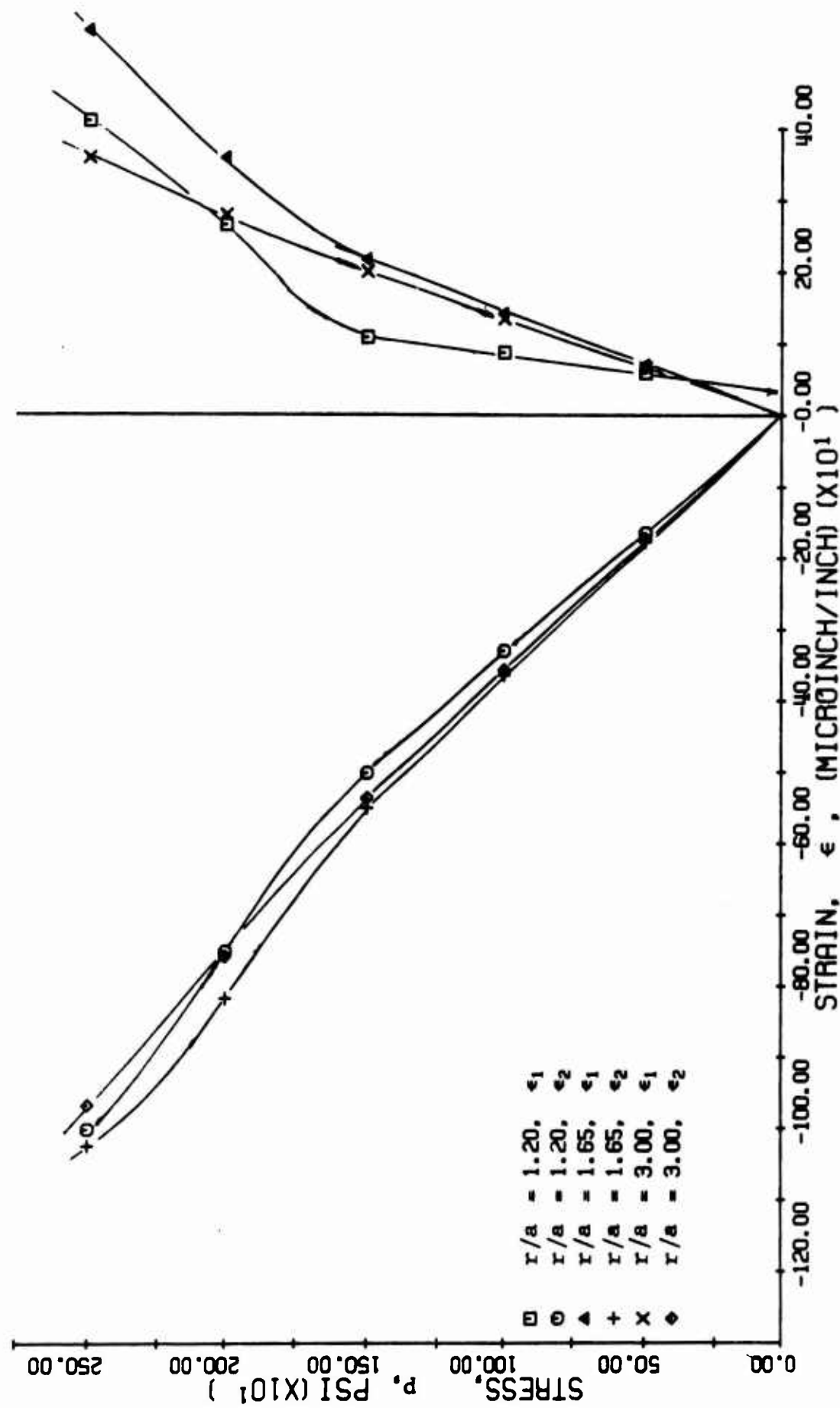
FIG. 113 PRINCIPAL STRAINS ALONG 45-DEGREE RADIUS FOR SPECIMEN NO. 7 (LIMESTONE WITH ALUMINUM LINER UNDER UNIAXIAL LOADING)

Strains for specimen No. 8 are plotted in Figs. 114 to 119.
The vertical strains along the horizontal axis (Fig. 114) appear
linear up to at least 2,000 psi. On the basis of the average of
eight far-field gages, the following modulus and Poisson's ratio
were determined:

$$E = 4.3 \times 10^6 \text{ psi}$$
$$\nu = 0.30$$

The far-field gages show a stiffening effect after crack initiation
with all the other vertical strains showing a rapid increase with
load at this point. The most rapid increase is observed at the
interface between liner and plate and resembles plastic flow. The
strain on the inside of the aluminum liner remains linear up to
approximately 3,000 psi, at which level the first crack had propa-
gated the length of the coating and the symmetric crack appeared.
It is possible that excessive debonding had occurred at this point.
The liner strain varies linearly again beyond this point but at a
much faster rate.

The ratio of the maximum compressive strain at the interface
with the liner to the far-field strain is

$$k_\varepsilon = 1.64$$

compared to the theoretically computed value of 1.14.

The variation of the tensile horizontal strains along the
vertical axis (Figs. 116 and 117) shows crack initiation (lowest
linearity limit) at approximately 2,050 psi. Most strains show
apparent and unexplained stiffening effect beyond their limit of
linearity except for the far-field strains and the strain on the
inner surface of the liner. The latter shows linearity up to 3,000
psi as in the case of the horizontal axis.

Principal strains and directions along the 45-degree radius
were computed as before and the former are plotted in Fig. 120.
The angle between the 45-degree radius and the principal tensile
direction varies between 40 degrees and 36 degrees at $r = 1.25a$,
41 degrees and 45 degrees at $r = 2.00a$, and 44 degrees and 45
degrees at $r = 3.00a$.

173
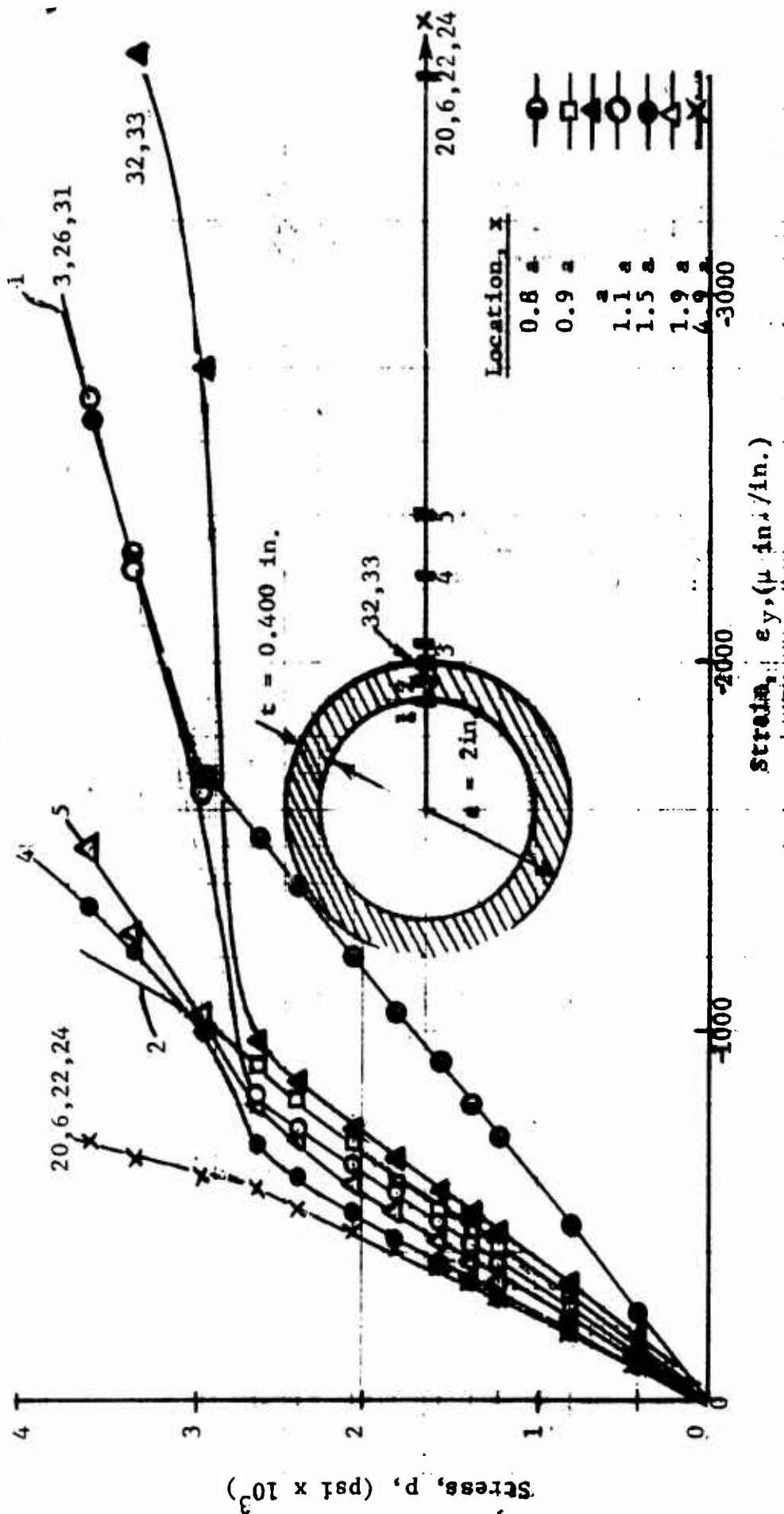
Fig. 114 VERTICAL STRAINS ALONG HORIZONTAL AXIS OF SYMMETRY AS A FUNCTION OF APPLIED VERTICAL STRESS FOR SPECIMEN NO. 8 (LIMESTONE LINED WITH ALUMINUM UNDER UNIAXIAL LOADING)

Fig. 11.5 HORIZONTAL STRAINS ALONG HORIZONTAL AXIS OF SYMMETRY AS A FUNCTION OF APPLIED VERTICAL STRESS FOR SPECIMEN NO. 8 (LIMESTONE LINED WITH ALUMINUM UNDER UNIAXIAL LOADING)

175

Fig. 116 HORIZONTAL STRAINS ALONG VERTICAL AXIS OF SYMMETRY AS A FUNCTION OF APPLIED VERTICAL STRESS FOR SPECIMEN NO. 8 (LIMESTONE LINED WITH ALUMINUM UNDER UNIAXIAL LOADING)

Fig. 117 HORIZONTAL STRAINS ALONG VERTICAL AXIS OF SYMMETRY AS A FUNCTION OF APPLIED VERTICAL STRESS FOR SPECIMEN NO. 8 (LIMESTONE LINED WITH ALUMINUM UNDER UNIAXIAL LOADING)

177

Fig. 118 VERTICAL STRAINS ALONG VERTICAL AXIS OF SYMMETRY AS A FUNCTION OF APPLIED VERTICAL STRESS FOR SPECIMEN NO. 8 (LIMESTONE LINED WITH ALUMINUM UNDER UNIAXIAL LOADING)

178
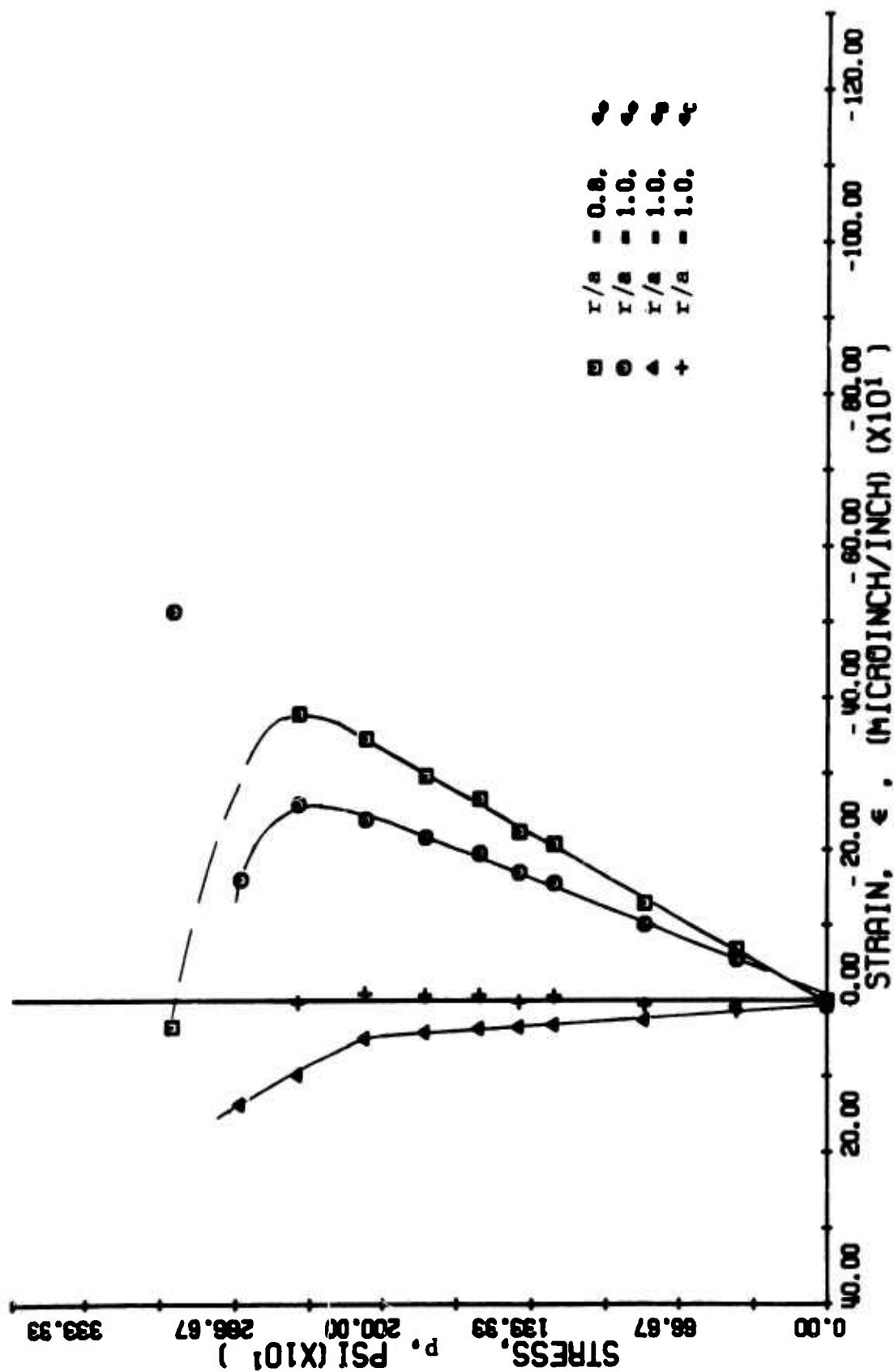
FIG. 119 STRAINS ALONG 45 DEGREE RADIUS FOR SPECIMEN NO. 8
LIMESTONE WITH ALUMINUM LINER UNDER UNIAXIAL LOADING
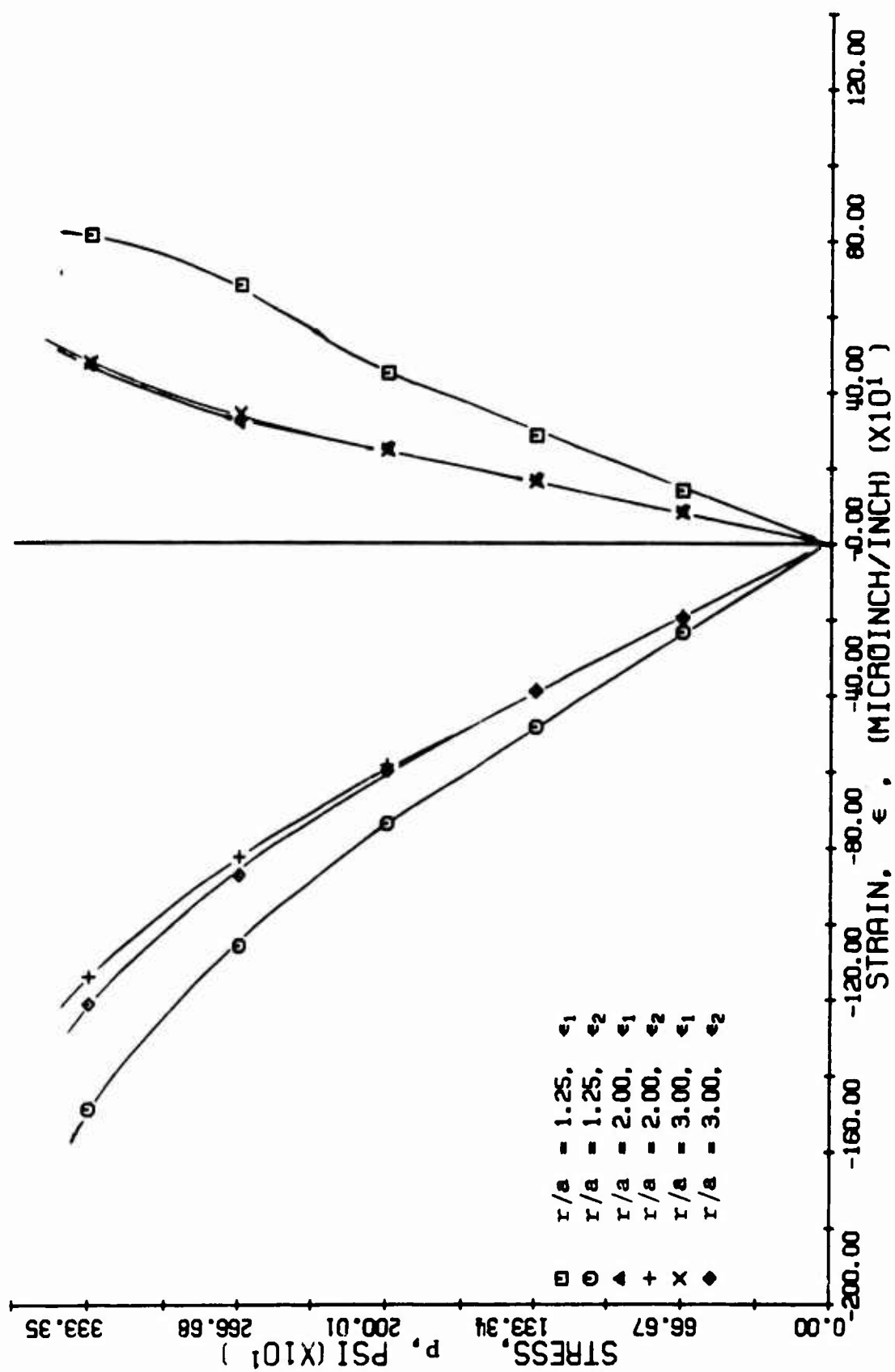
FIG. 120 PRINCIPAL STRAINS ALONG 45-DEGREE RADIUS FOR SPECIMEN NO. 8 (LIMESTONE WITH HYDROSTONE LINER UNDER UNIAXIAL LOADING)

180

The strain distribution along the two axes of symmetry at a stress level of p = 1,000 psi was plotted in Figs. 121 and 122 for specimens No. 7 and No. 8. Theoretical values for the liner and the plate have been noted. As can be seen there is appreciable discrepancy between the two specimens in the peak tensile and compressive strains at the interface, with specimen No. 7 indicating much higher strains. This difference may be due to the flexible bonding agent used with specimen No. 7. The maximum tensile stress at cracking, which occurred at p = 1,100 psi for this specimen, was computed as

$$\sigma_{max} = 2,260 \text{ psi}$$

In specimen No. 8, the tensile strain at the interface on the vertical axis was too low to cause cracking. According to the theory discussed earlier, the maximum tensile stress occurs along the interface at some point off the vertical axis. The maximum tensile stress at the crack initiation level of p = 2,050 psi is $\sigma_{max} = 0.43 \times 2050 = 880$ psi. However, based on the principal strains of Fig. 120, a tensile stress of approximately

$$\sigma_{max} \cong 1,500 \text{ psi}$$

can be computed at the 45-degree location at the interface at the crack initiation level of p = 2,050 psi.
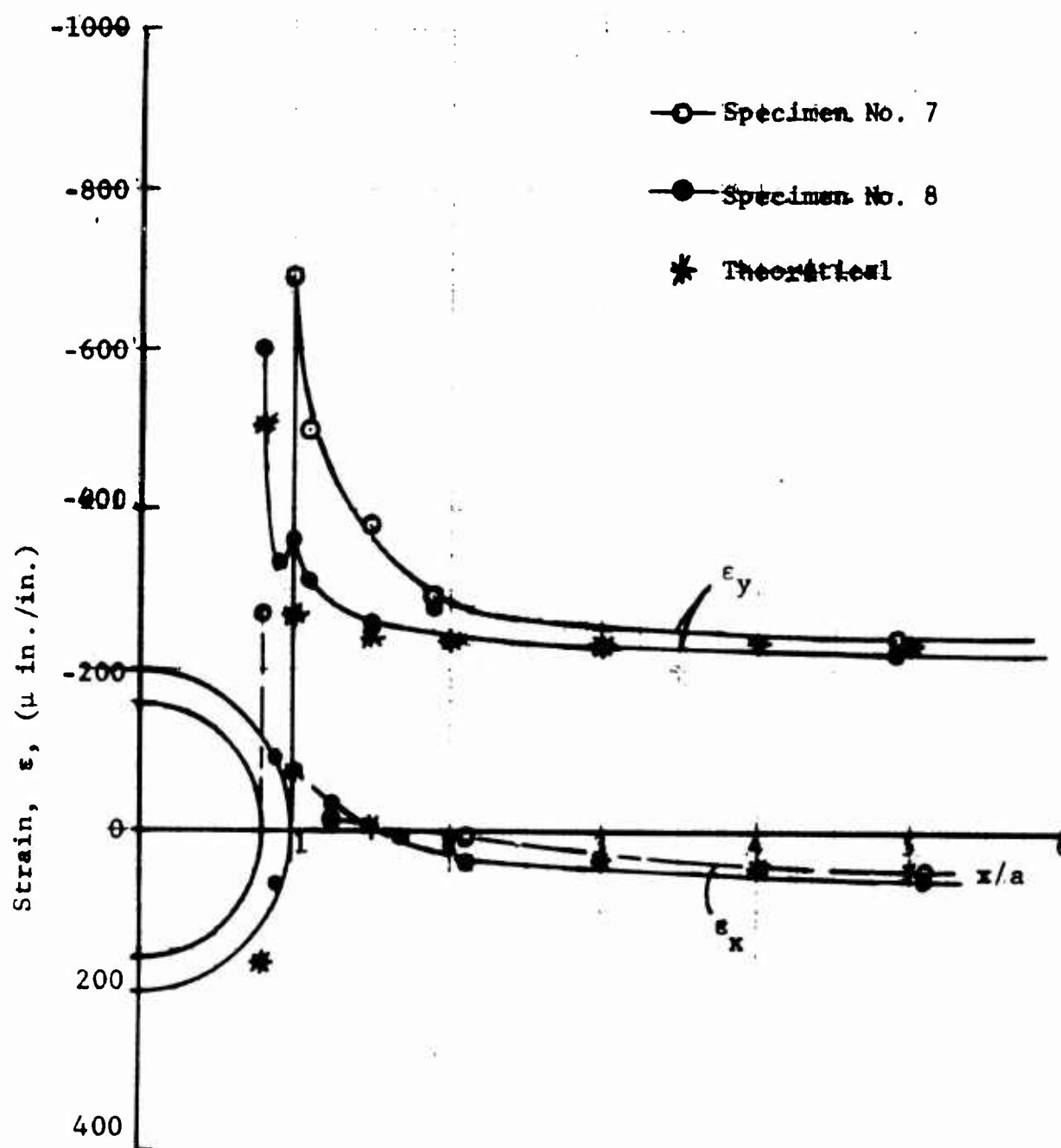
Fig. 121   STRAIN DISTRIBUTION ALONG X-AXIS FOR SPECIMENS NO. 7
AND 8 AT APPLIED STRESS OF 1,000 PSI (LIMESTONE
WITH ALUMINUM LINER UNDER UNIAXIAL LOADING)
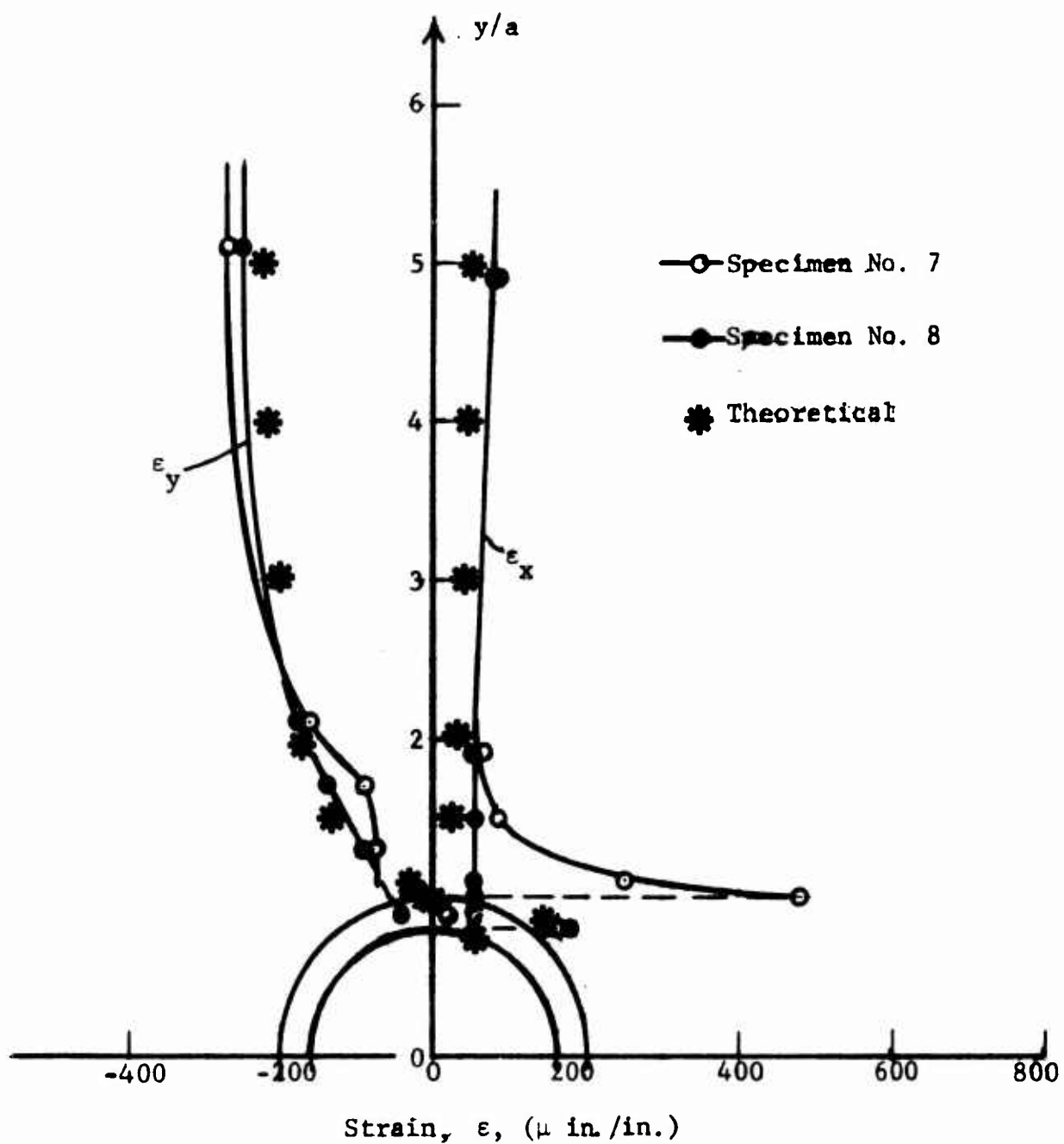
Fig. 122 STRAIN DISTRIBUTION ALONG Y-AXIS FOR SPECIMENS NO. 7
AND 8 AT APPLIED STRESS OF 1,000 PSI (LIMESTONE
WITH ALUMINUM LINER UNDER UNIAXIAL LOADING)

183

3. **Specimens No. 9 and 10 - Marble with Hydrostone Liner Under Uniaxial Loading**

    a. **Theoretical Stress Distributions**

        The following material properties were used:

        Marble: $E = 8.2 \times 10^6$ psi

                    $\nu = 0.28$

                    $\mu = \dfrac{E}{2(1+\nu)} = 3.20 \times 10^6$ psi

                    $\kappa = \dfrac{3-\nu}{1+\nu} = 2.13$

        Hydrostone: $E_1 = 2.2 \times 10^6$ psi

                    $\nu_1 = 0.25$

                    $\mu_1 = \dfrac{E_1}{2(1+\nu_1)} = 0.88 \times 10^6$

                    $\kappa_1 = \dfrac{3-\nu_1}{1+\nu_1} = 2.20$

        For the liner thickness used $t = 0.44$ in. the circumferential stress on the free surface of the liner is given by

$$\frac{\sigma_\theta}{p} = 0.33 - 1.14 \cos 2\theta \tag{62}$$

with peak values at

$$\left(\frac{\sigma_\theta}{p}\right)_{\theta=0°} = -0.81 \tag{63}$$

and

$$\left(\frac{\sigma_\theta}{p}\right)_{\theta=90°} = 1.47 \tag{64}$$

The interface stresses in the marble plate are

$$\frac{\sigma_r}{p} = 0.06 + 0.16 \cos 2\theta \tag{65}$$

$$\frac{\sigma_\theta}{p} = 0.93 - 1.70 \cos 2\theta \tag{66}$$

$$\frac{\sigma_{r\theta}}{p} = -0.07 \sin 2\theta \tag{67}$$

Because of the low radial and shear stresses, the principal stresses at the interface differ little from the radial and circumferential stresses. The latter were plotted versus angular location in Fig. 123. The peak values of the circumferential stress are

$$\left(\frac{\sigma_\theta}{p}\right)_{\theta=0°} = -0.77 \tag{68}$$

and

$$\left(\frac{\sigma_\theta}{p}\right)_{\theta=90°} = 2.63 \tag{69}$$

which shows that the hydrostone liner does not reduce stresses in the medium appreciably in this case.

b. Experimental Procedure

Two marble plates of dimensions 36 in. x 24 in. x 3.42 in. with a 4 in. diameter hole and a 0.44 in. thick hydrostone liner bonded to the cavity surface were used. Strain gages, DCDT's and a photoelastic coating were applied as described previously. The instrumented specimens were loaded vertically at 20,000 to 25,000 lb intervals to failure and the data recorded as before.

c. Results and Discussion

Isochromatic fringe patterns for specimens No. 9 and No. 10 are shown in Figs.124 and 125 for various stress levels. The applied average stress is shown in every frame. In both specimens,

185
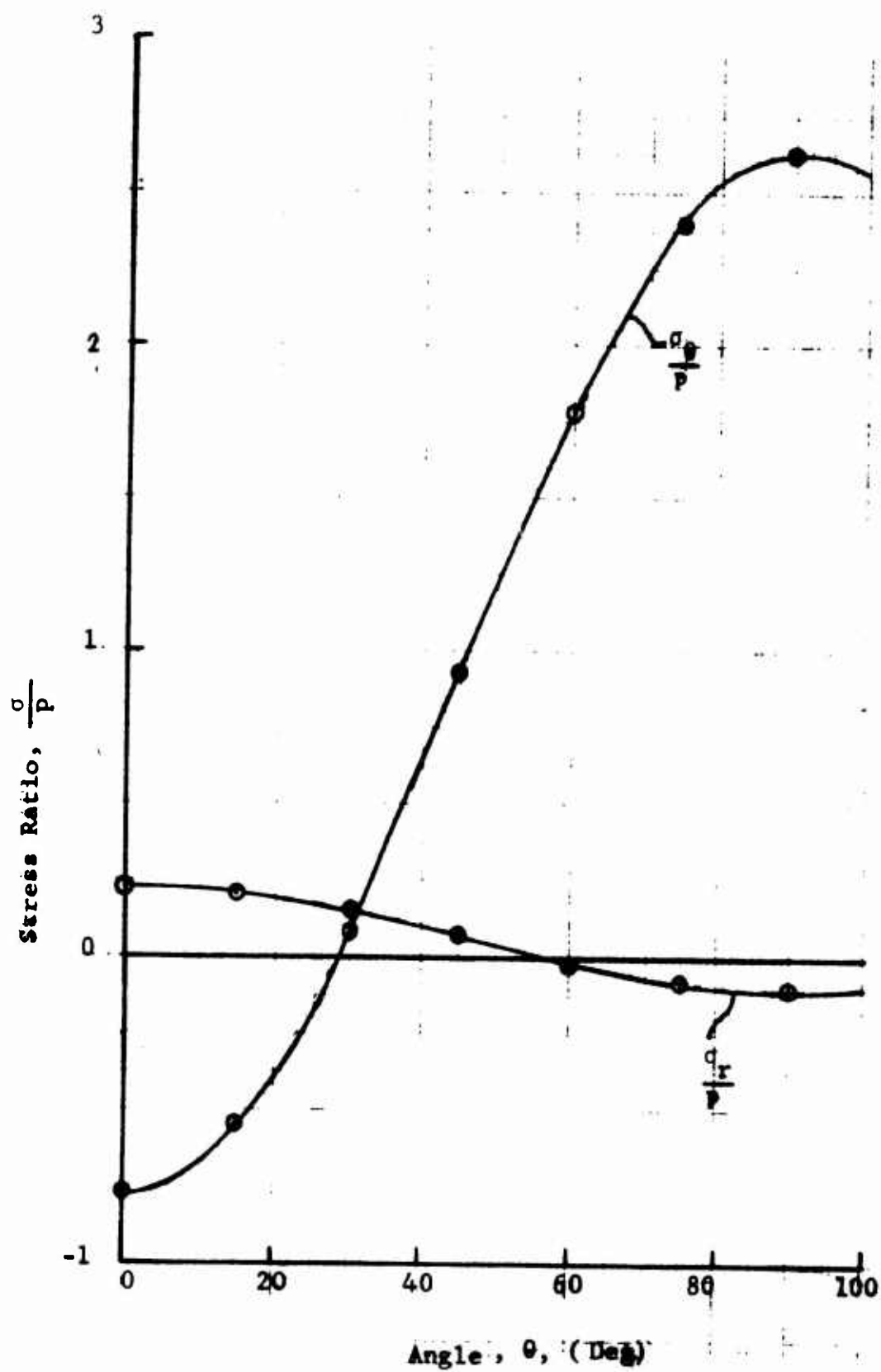
Fig. 123 VARIATION OF CIRCUMFERENTIAL AND RADIAL STRESSES IN MARBLE
AT INTERFACE WITH HYDROSTONE LINER

186

$\sigma = 0$ psi $\sigma = 1370$ psi $\sigma = 1880$ psi $\sigma = 2370$ psi

$\sigma = 2700$ psi $\sigma = 2960$ psi $\sigma = 3210$ psi $\sigma = 3510$ psi

$\sigma = 3800$ psi $\sigma = 4030$ psi $\sigma = 4330$ psi $\sigma = 4630$ psi
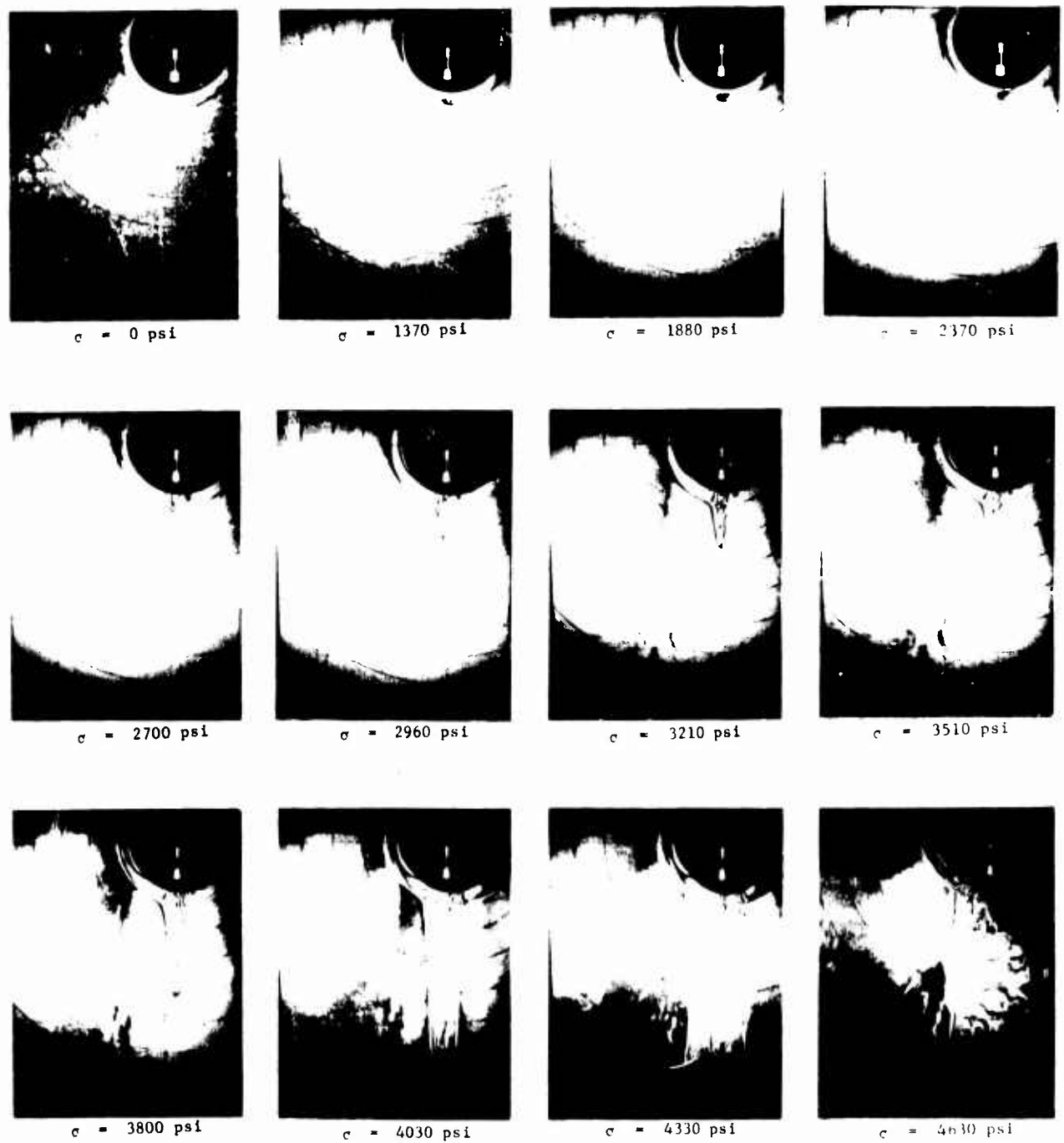
Fig. 124   ISOCHROMATIC FRINGE PATTERNS IN PHOTOELASTIC COATING AROUND HOLE IN SPECIMEN NO. 9 (MARBLE WITH HYDROSTONE LINER UNDER UNIAXIAL LOADING)

187

$\sigma = 0$ psi	$\sigma = 2500$ psi
$\sigma = 2740$ psi	$\sigma = 2980$ psi
$\sigma = 3250$ psi	$\sigma = 3490$ psi
$\sigma = 3750$ psi	$\sigma = 4070$ psi

Fig. 125   ISOCHROMATIC FRINGE PATTERNS IN PHOTOELASTIC
COATING AROUND HOLE IN SPECIMEN NO. 10 (MARBLE
WITH HYDROSTONE LINER UNDER UNIAXIAL LOADING)

188

cracking started on the inner surface of the hydrostone liner along the vertical axis and propagated into the marble at stress levels around 2,700 psi. This stress is appreciably higher than the stress levels of 1,700 to 1,900 psi at which crack initiation was induced in the unlined marble specimens No. 3 and No. 4. As the load was increased, the crack propagated along the vertical axis until complete separation resulted. The failure patterns are illustrated in Figs. 126 and 127.

The maximum fringe order on the free boundary of the liner on the horizontal axis was plotted versus applied stress for both specimens in Fig. 128. Both curves are linear with equal slopes up to a stress level of approximately 3,000 psi. The fringe order at 1,000 psi is 0.70. Then, the maximum strain at the boundary is

$$(\varepsilon_1)_{p=1,000 \text{ psi}} = 876 \times \frac{0.70}{1.40} \cong 440 \ \mu\text{in./in.}$$

The birefringence concentration at the interface between liner and marble plate off the axes of symmetry is lower than in the comparable case of limestone because of the much lower interface shear resulting from the lower modulus of the hydrostone liner.

Diametral changes measured with DCDTs are plotted in Figs. 129 and 130 as a function of applied vertical stress. The limit of linearity of these curves is a little over 2,000 psi which is below the apparent crack initiation level of 2,700 psi. The deflections per unit stress in the linear range for specimen No. 9 are

$$\frac{\delta_h}{p} = 0.6 \times 10^{-6} \text{ in./psi}$$

$$\frac{\delta_v}{p} = -1.6 \times 10^{-6} \text{ in./psi}$$

and for specimen No. 10,

$$\frac{\delta_h}{p} = 0.6 \times 10^{-6} \text{ in./psi}$$

$$\frac{\delta_v}{p} = -1.5 \times 10^{-6} \text{ in./psi}$$
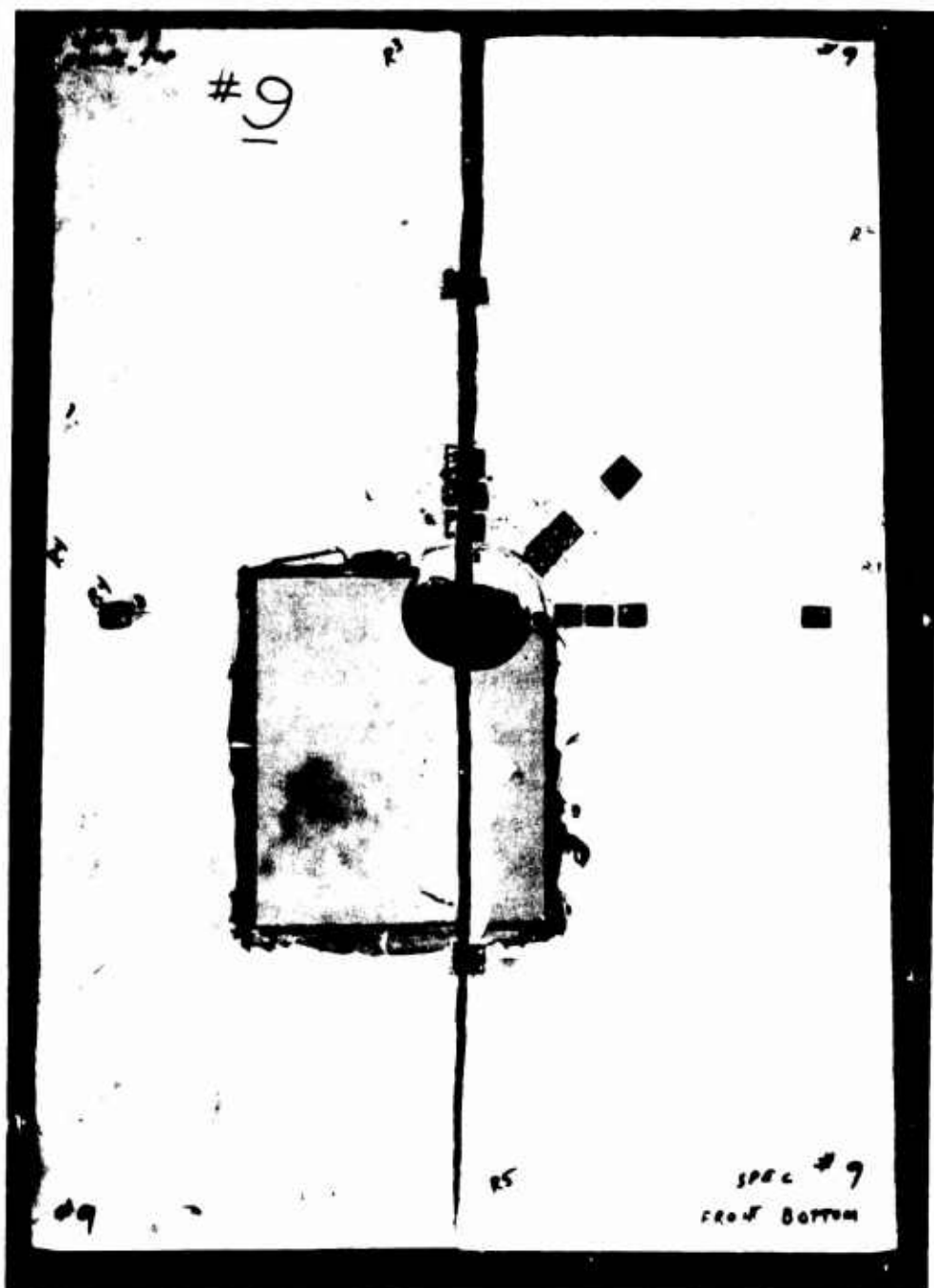
Fig. 126   FAILURE PATTERN IN SPECIMEN NO. 9   (MARBLE WITH
           HYDROSTONE LINER UNDER UNIAXIAL LOADING)
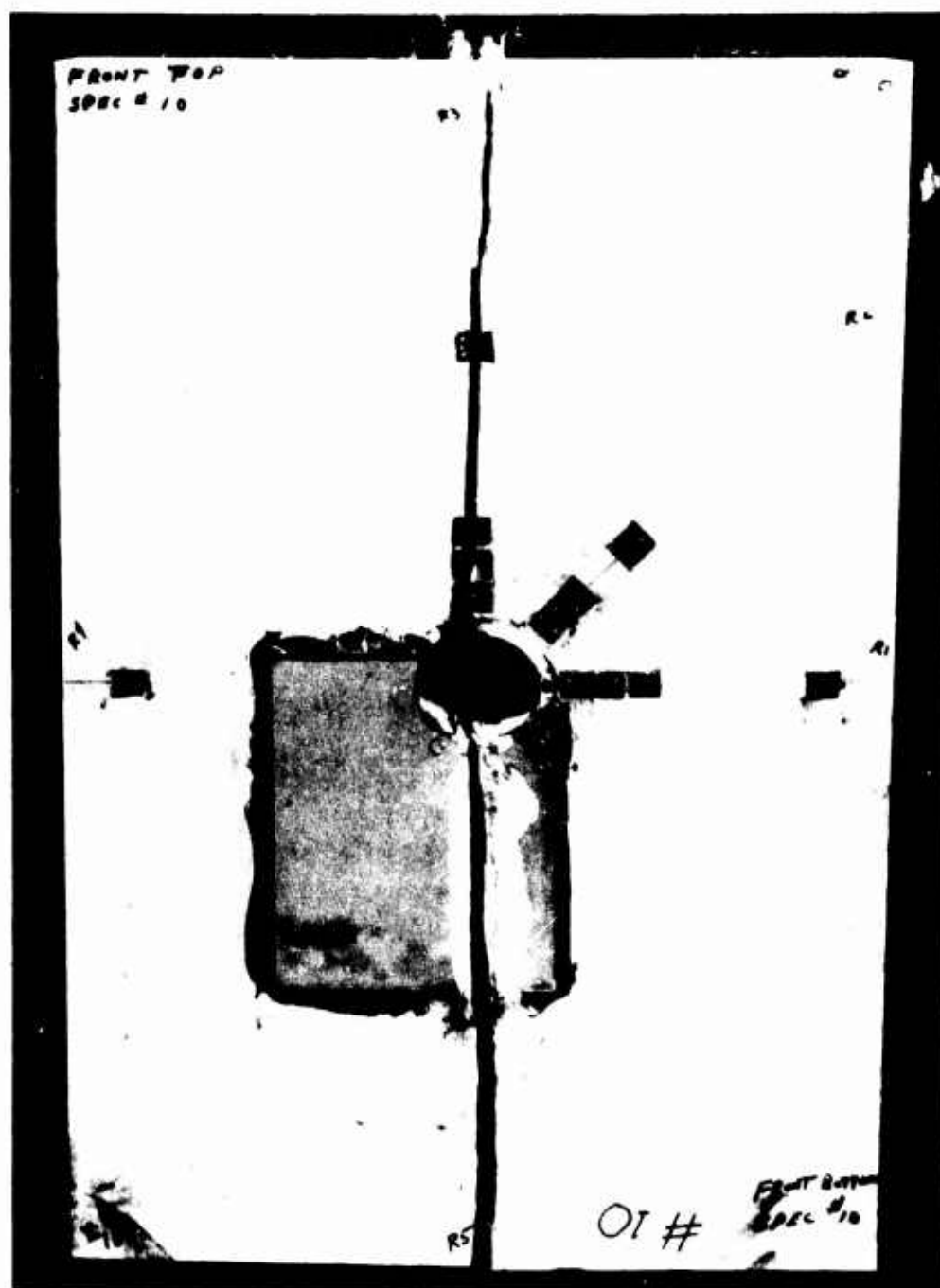
Fig. 127   FAILURE PATTERN IN SPECIMEN NO. 10   (MARBLE WITH
HYDROSTONE LINER UNDER UNIAXIAL LOADING)
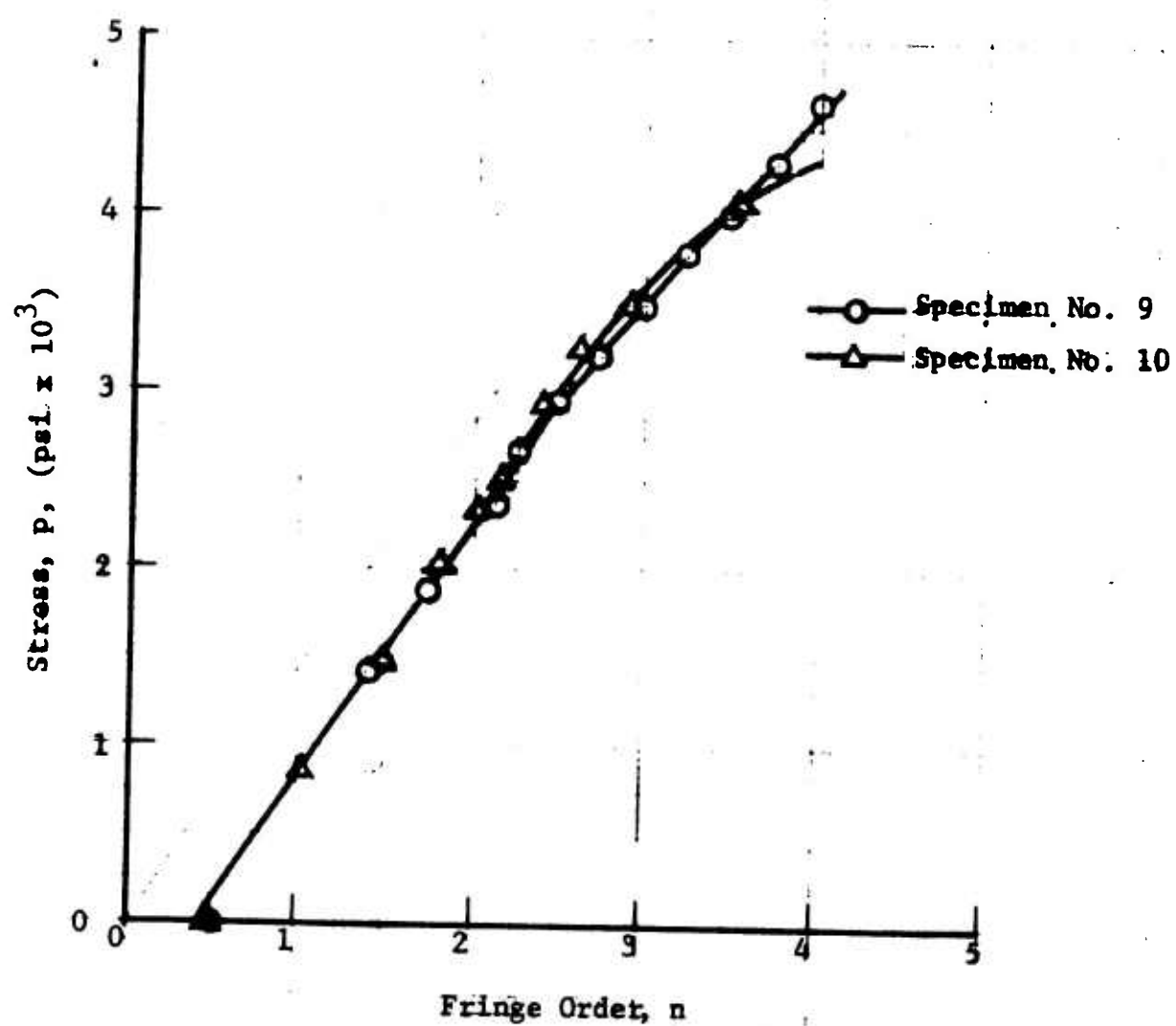
Fig. 128 FRINGE ORDER AT INNER BOUNDARY OF LINER ON HORIZONTAL
AXIS FOR SPECIMENS NO. 9 AND 10 AS A FUNCTION OF APPLIED
VERTICAL STRESS

192
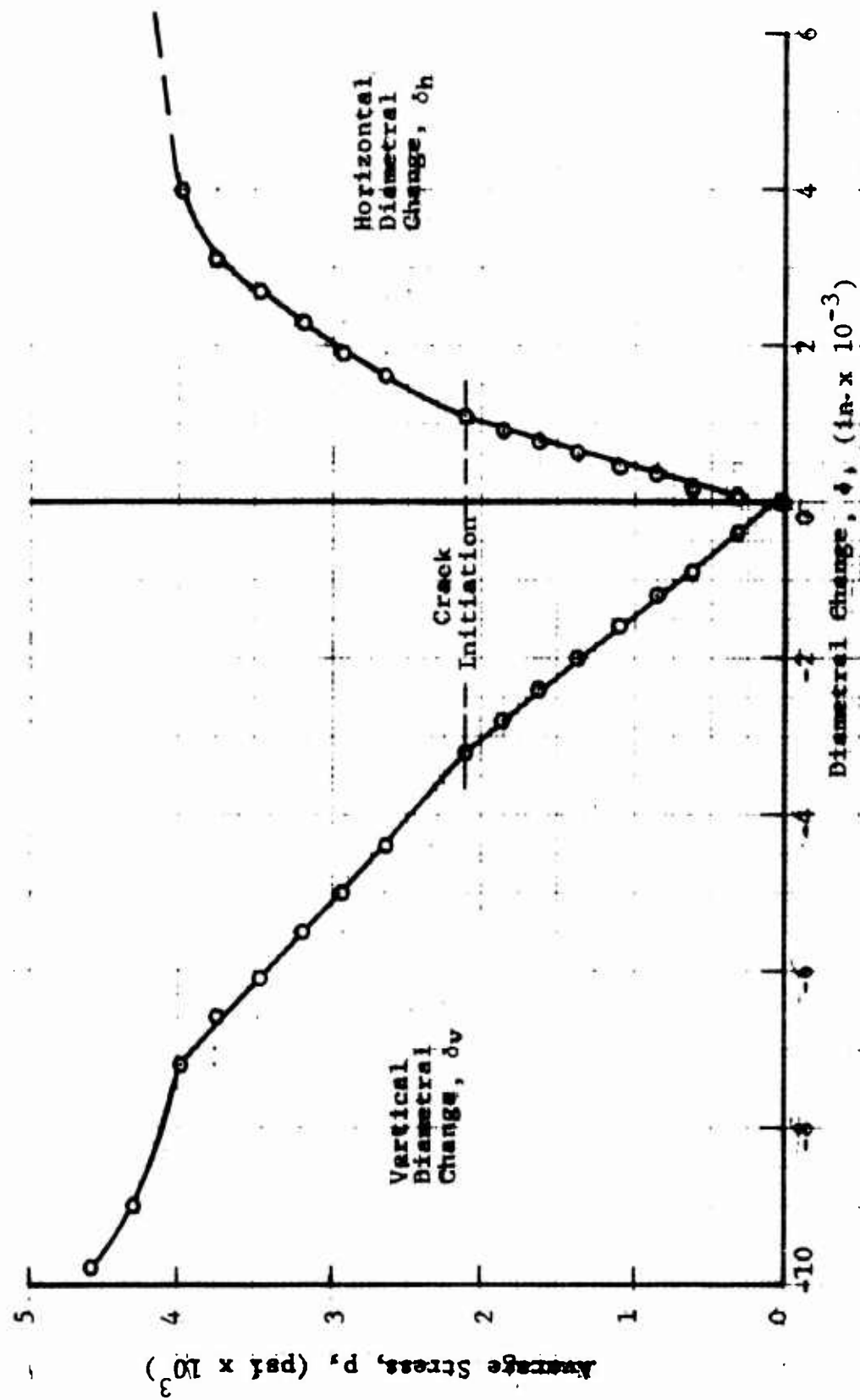
Fig. 129   DIAMETRAL CHANGES AS A FUNCTION OF APPLIED VERTICAL STRESS FOR SPECIMEN NO. 9
(MARBLE WITH HYDROSTONE LINER UNDER UNIAXIAL LOADING)

193
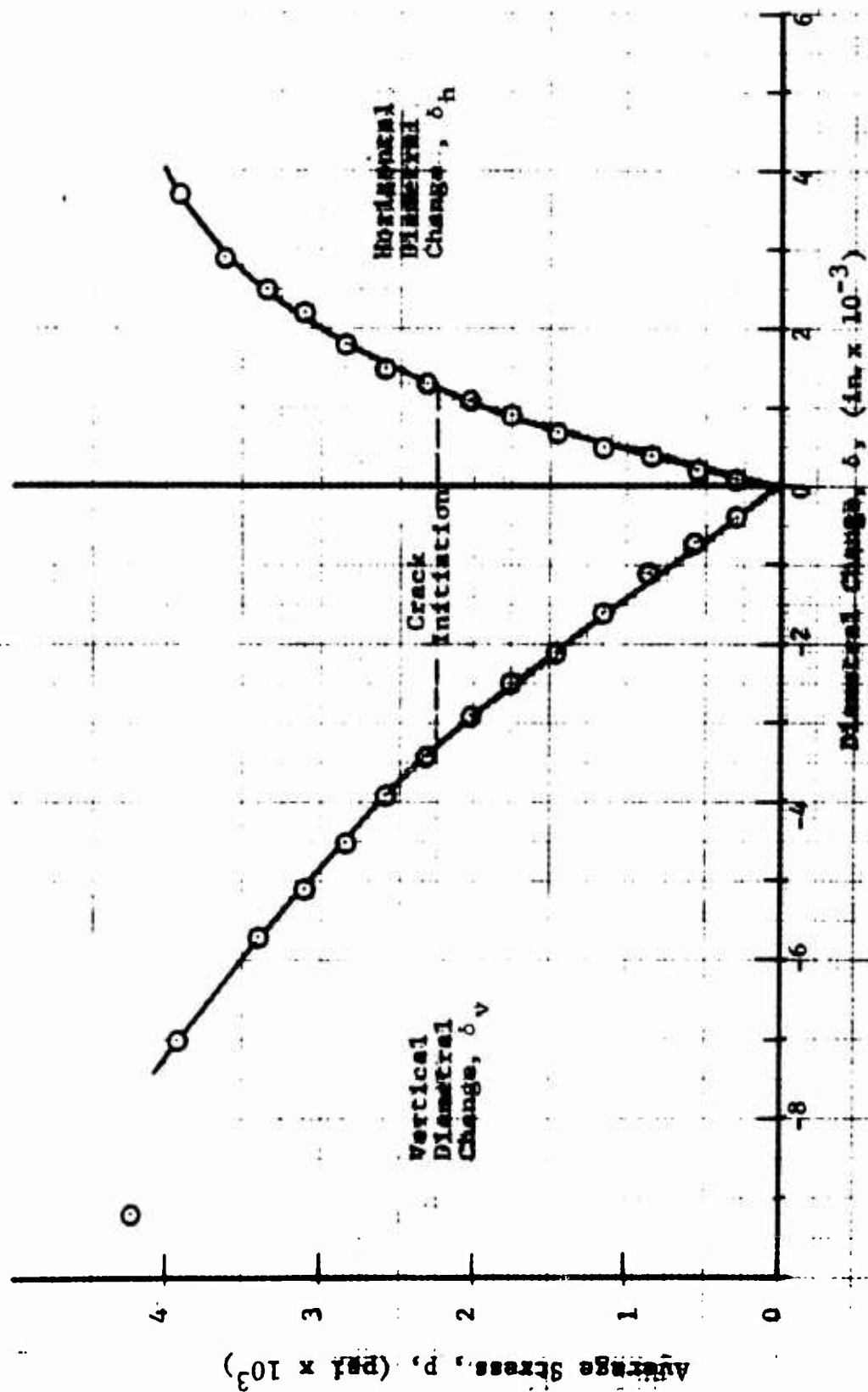
Fig. 130   DIAMETRAL CHANGES AS A FUNCTION OF APPLIED VERTICAL STRESS FOR SPECIMEN NO. 10
(MARBLE WITH HYDROSTONE LINER UNDER UNIAXIAL LOAD)

194

The values are approximately half of the corresponding values
for limestone specimens No. 5 and No. 6, since the modulus of
marble is approximately twice that of limestone.

Strain gage readings along the various axes are plotted
as a function of applied stress in Figs. 131 through 135 for
specimen No. 9. Vertical strains along the horizontal axis (Fig.
131) are linear up to approximately 3,000 psi. On the basis of
the average of the far-field strains, the following modulus and
Poisson's ratio were determined:

$$E = 8.1 \times 10^6 \text{ psi}$$
$$\nu = 0.26$$

The ratio of the maximum compressive strain at the inter-
face to the far-field strain is

$$k_\epsilon = 2.92$$

compared to the theoretically computed value of 2.66 for an infinite
plate. The maximum compressive strain at the inner surface of the
liner is 460 μin./in. at p = 1,000 psi which compares well with
the photoelastically computed strain of 440 μin./in.

The horizontal strains along the vertical axis show some
nonlinearity from the beginning. The crack initiation level is
clearly seen at approximately 2,350 psi, somewhat earlier than
evidenced in the photoelastic fringe patterns.

Principal strains along the 45-degree radius were computed
as before and plotted in Fig. 136. The angle between the 45-degree
radius and the principal tensile direction varies between 41 degrees
and 37 degrees at r = 1.35a, 42 degrees and 41 degrees at r = 1.80a
and 40 degrees and 45 degrees at r = 3.00a.

Strains for specimen No. 10 were plotted as a function of
applied vertical stress in Figs. 137 through 141. Vertical strains
along the horizontal axis (Fig. 137) are linear up to approximately
3,000 psi. The far-field strains yield the following modulus and
Poisson's ratio:

195
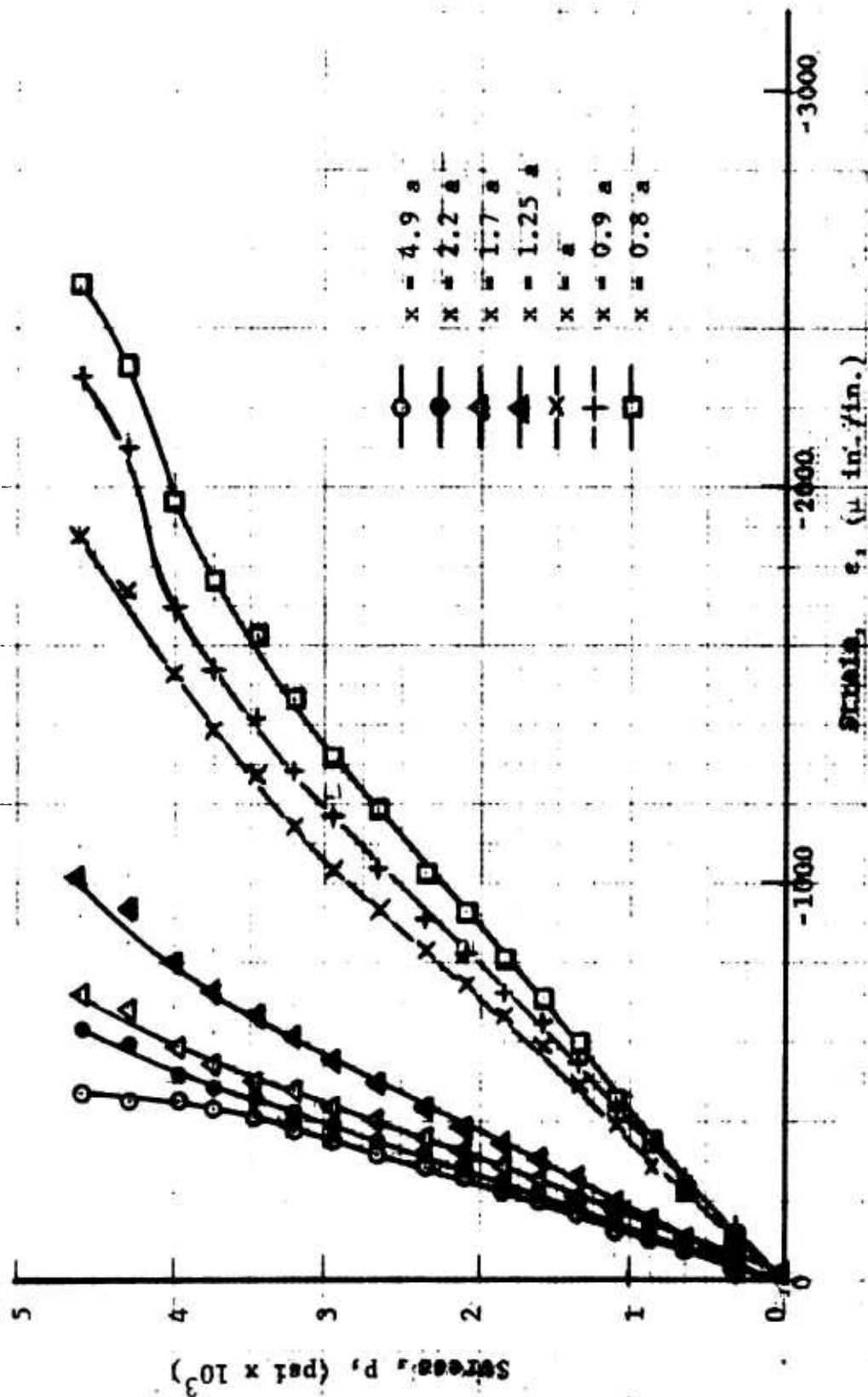
Fig. 131   VERTICAL STRAINS ALONG HORIZONTAL AXIS OF SYMMETRY AS A FUNCTION OF APPLIED
VERTICAL STRESS FOR SPECIMEN NO. 9 (MARBLE WITH HYDROSTONE LINER UNDER
UNIAXIAL LOADING)

196
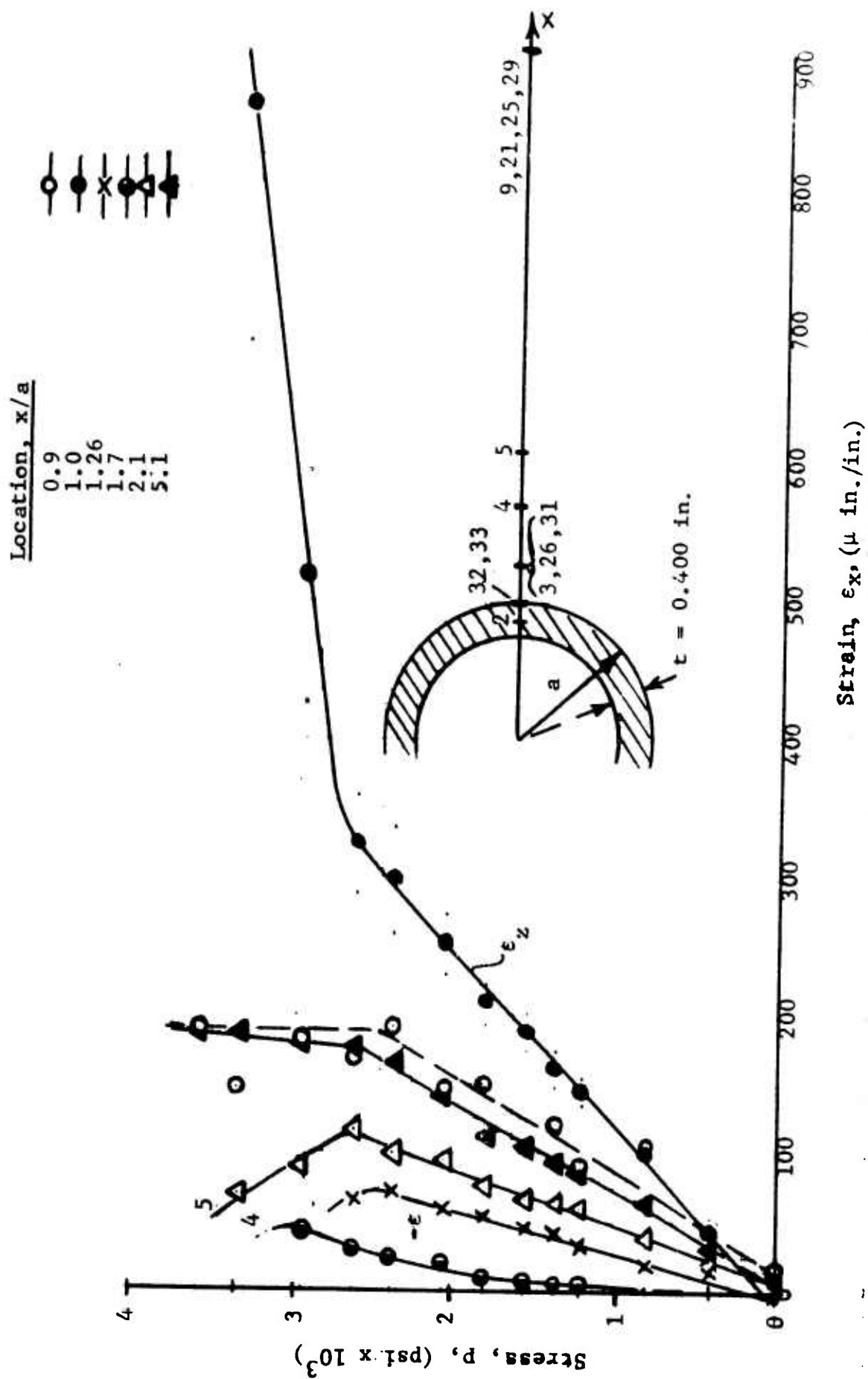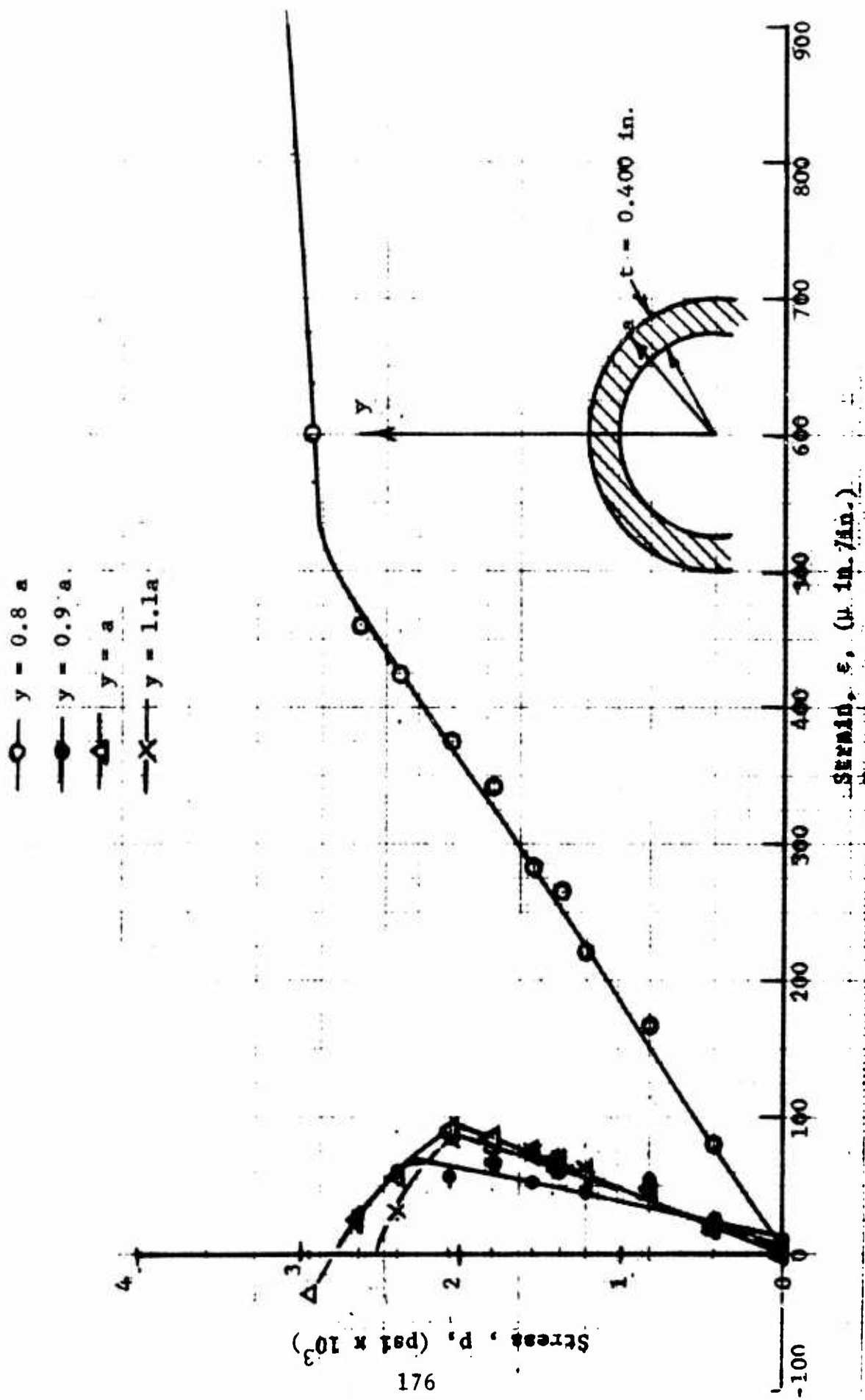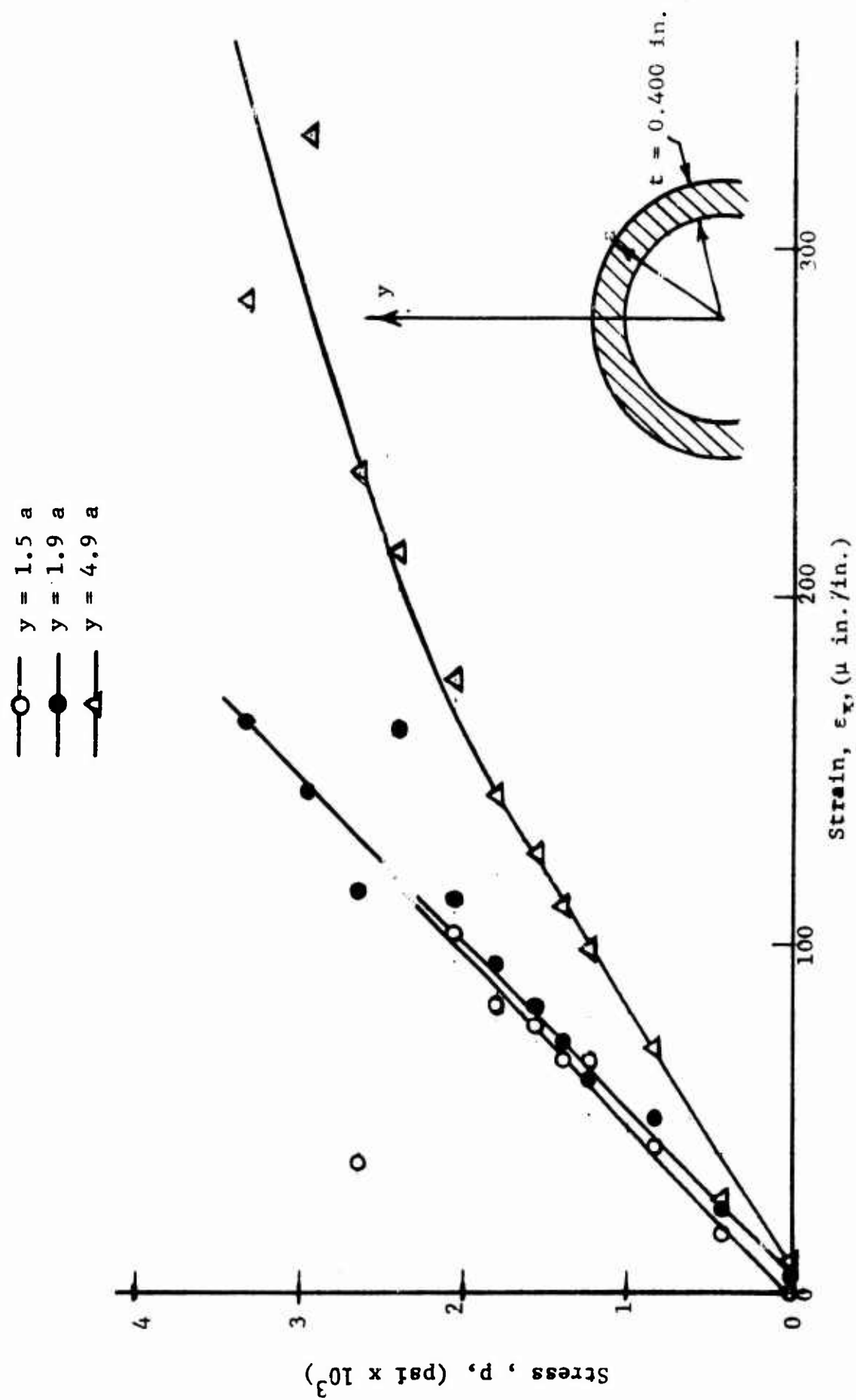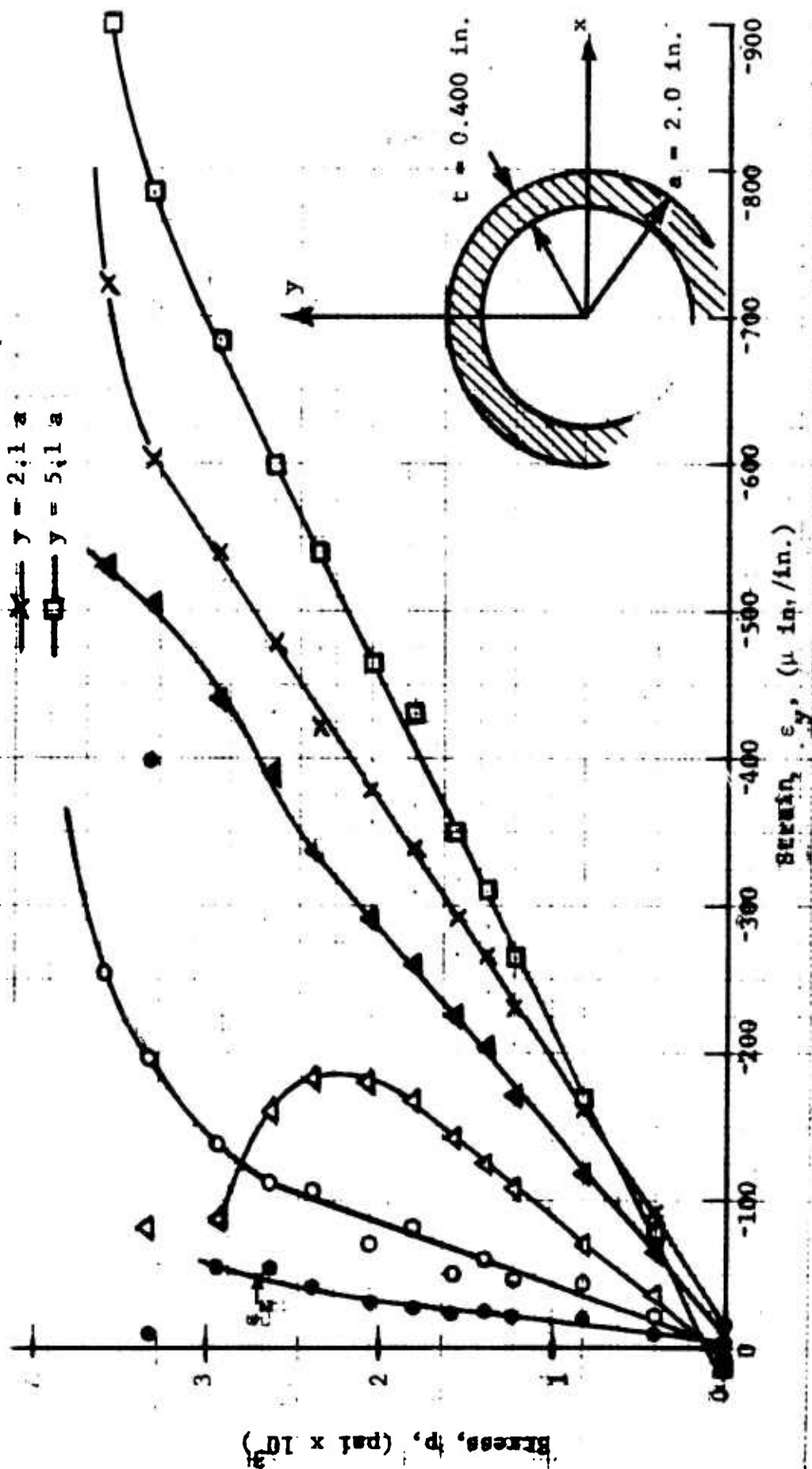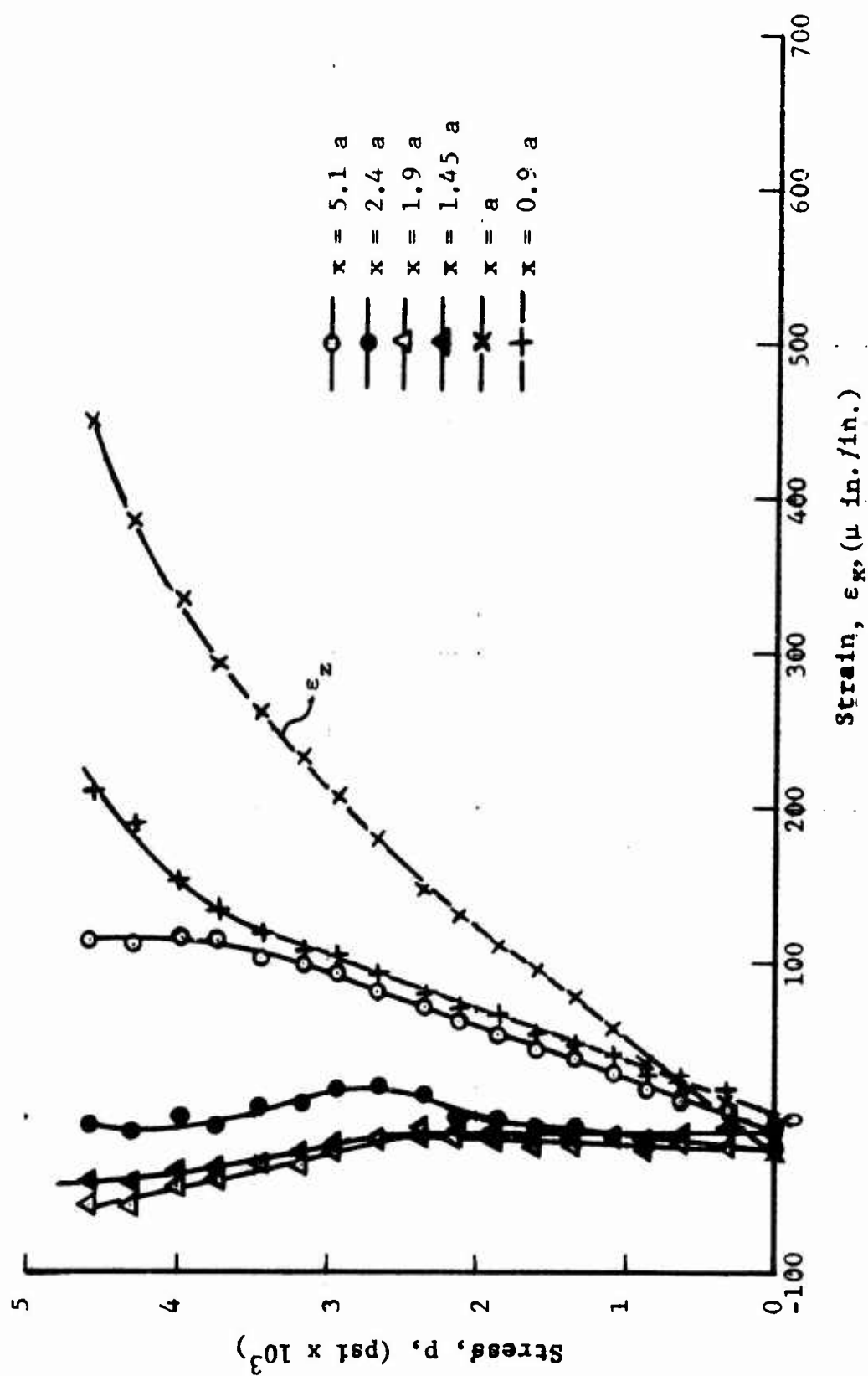
Fig. 132 HORIZONTAL STRAINS ALONG HORIZONTAL AXIS OF SYMMETRY AS A FUNCTION OF APPLIED
VERTICAL STRESS FOR SPECIMEN NO. 9 (MARBLE WITH HYDROSTONE LINER UNDER
UNIAXIAL LOADING)

197
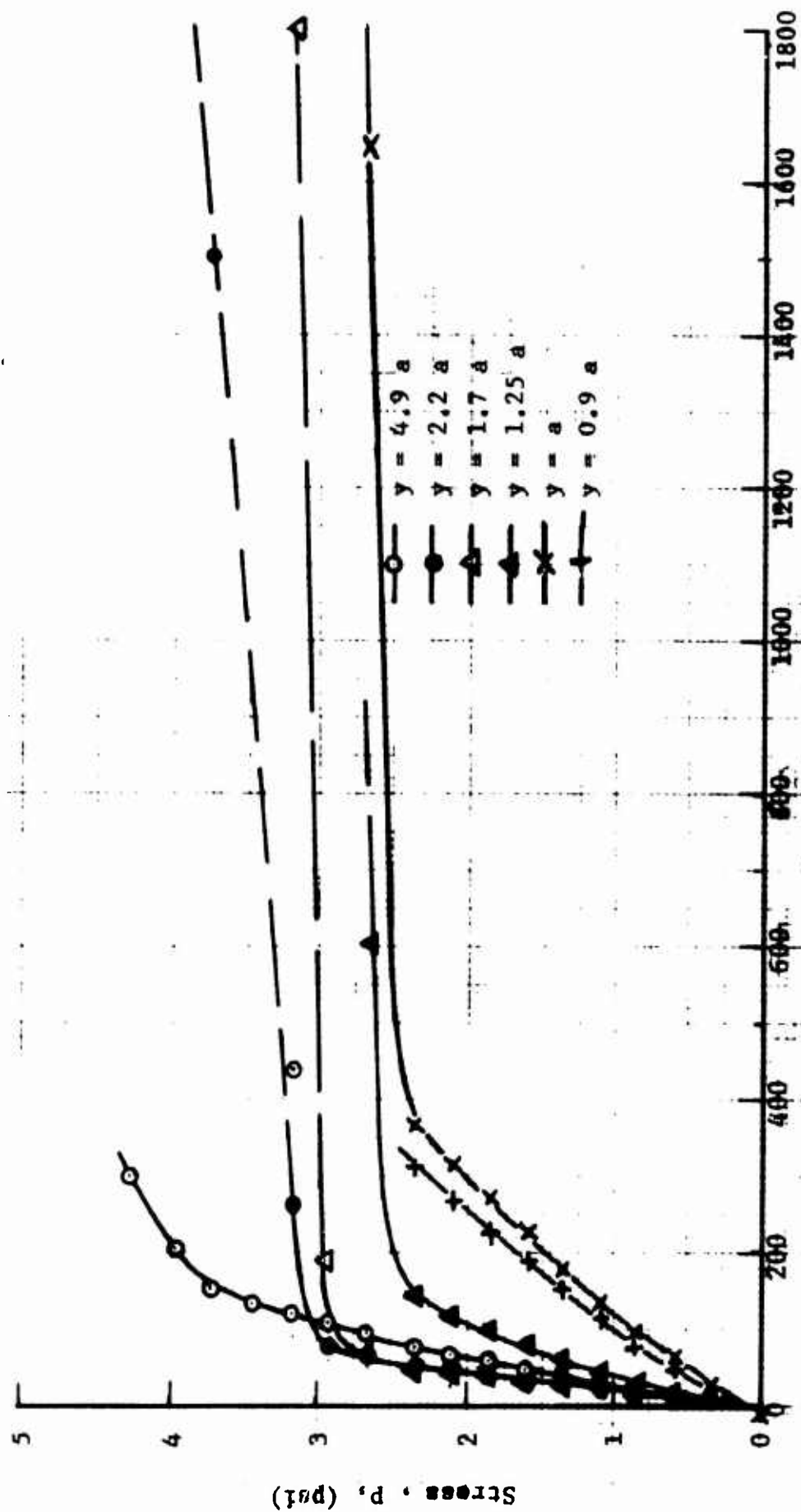
Fig. 133 HORIZONTAL STRAINS ALONG VERTICAL AXIS OF SYMMETRY AS A FUNCTION OF APPLIED VERTICAL STRESS FOR SPECIMEN NO. 9 (MARBLE WITH HYDROSTONE LINER UNDER UNIAXIAL LOADING)
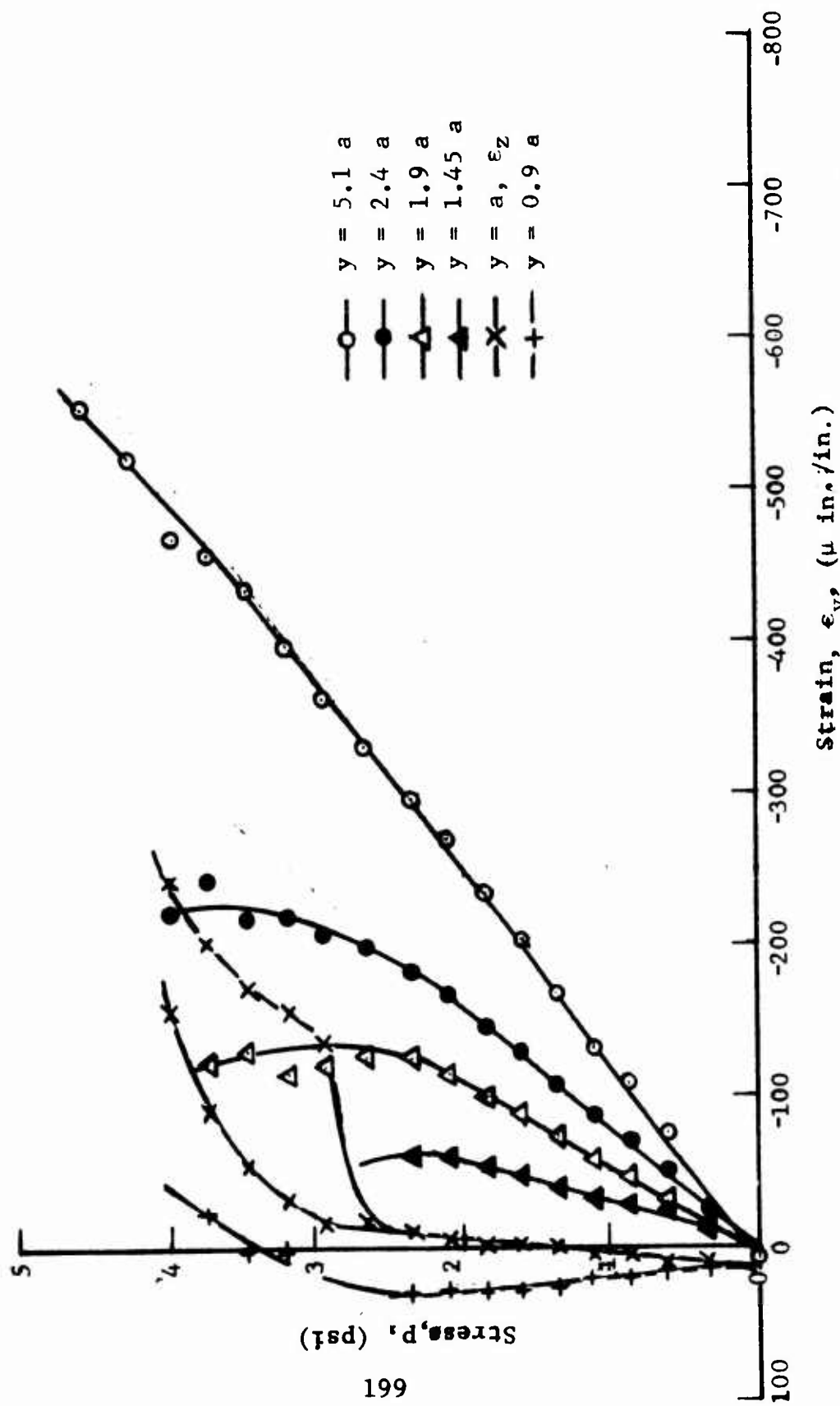
Fig. 134   VERTICAL STRAINS ALONG VERTICAL AXIS OF SYMMETRY FOR SPECIMEN NO. 9
(MARBLE WITH HYDROSTONE LINER UNDER UNIAXIAL LOADING)

199
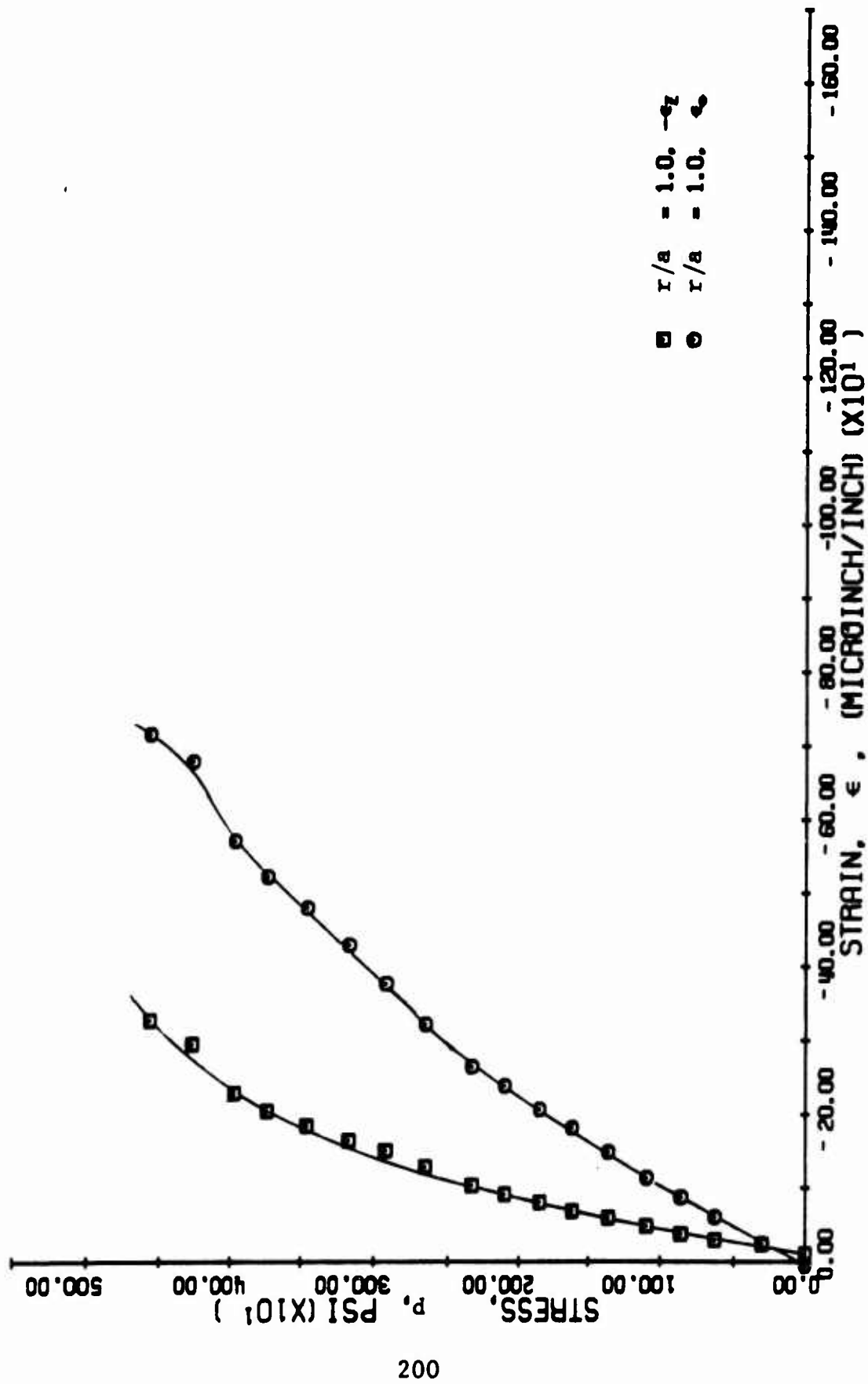
FIG. 13.5 STRAINS ALONG 45 DEGREE RADIUS FOR SPECIMEN NO. 9 (MARBLE WITH HYDROSTONE LINER UNDER UNIAXIAL LOADING)

200
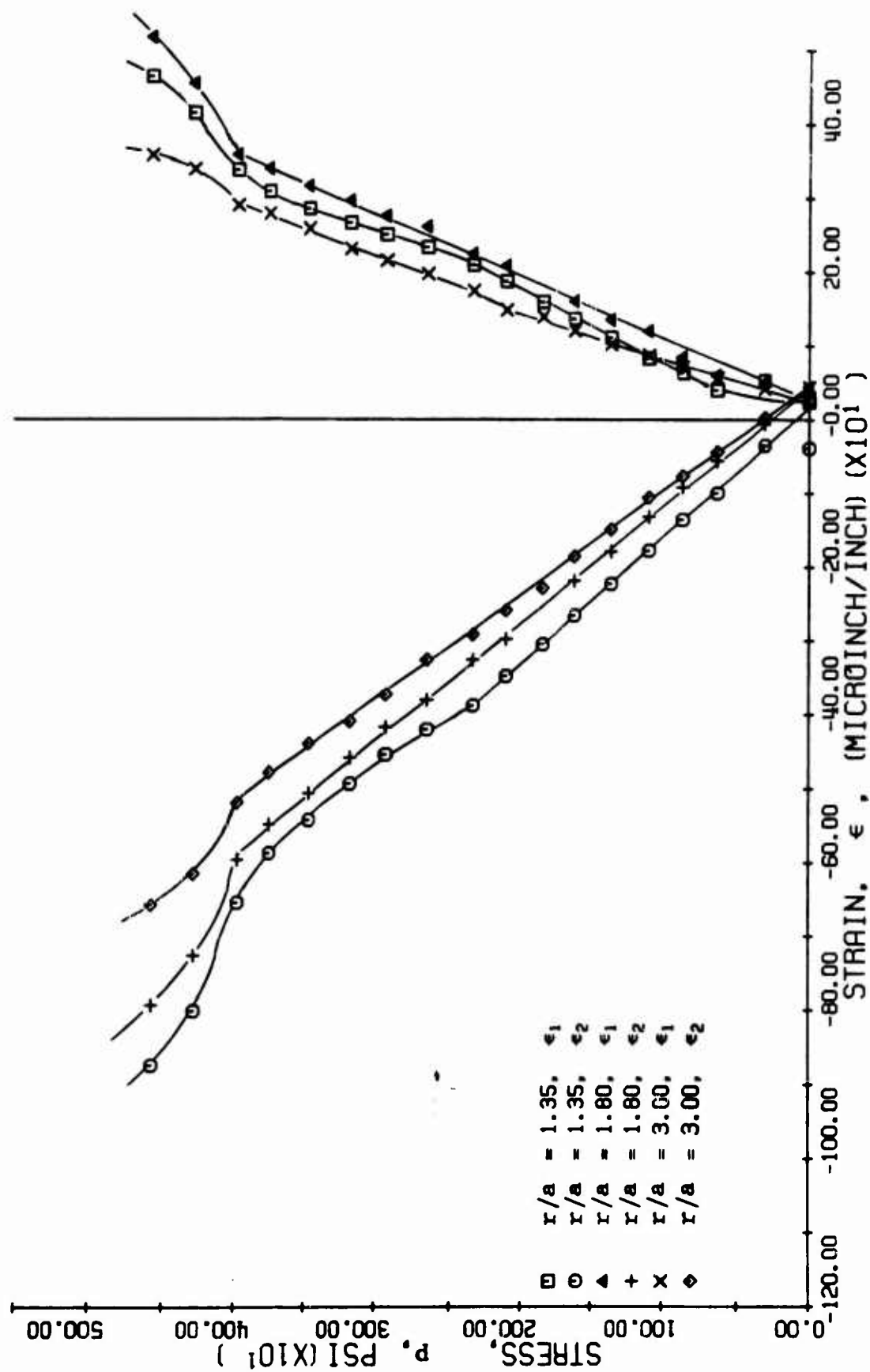
FIG. 136 PRINCIPAL STRAINS ALONG 45-DEGREE RADIUS FOR SPECIMEN NO. 9
(MARBLE WITH HYDROSTONE LINER UNDER UNIAXIAL LOADING)

201
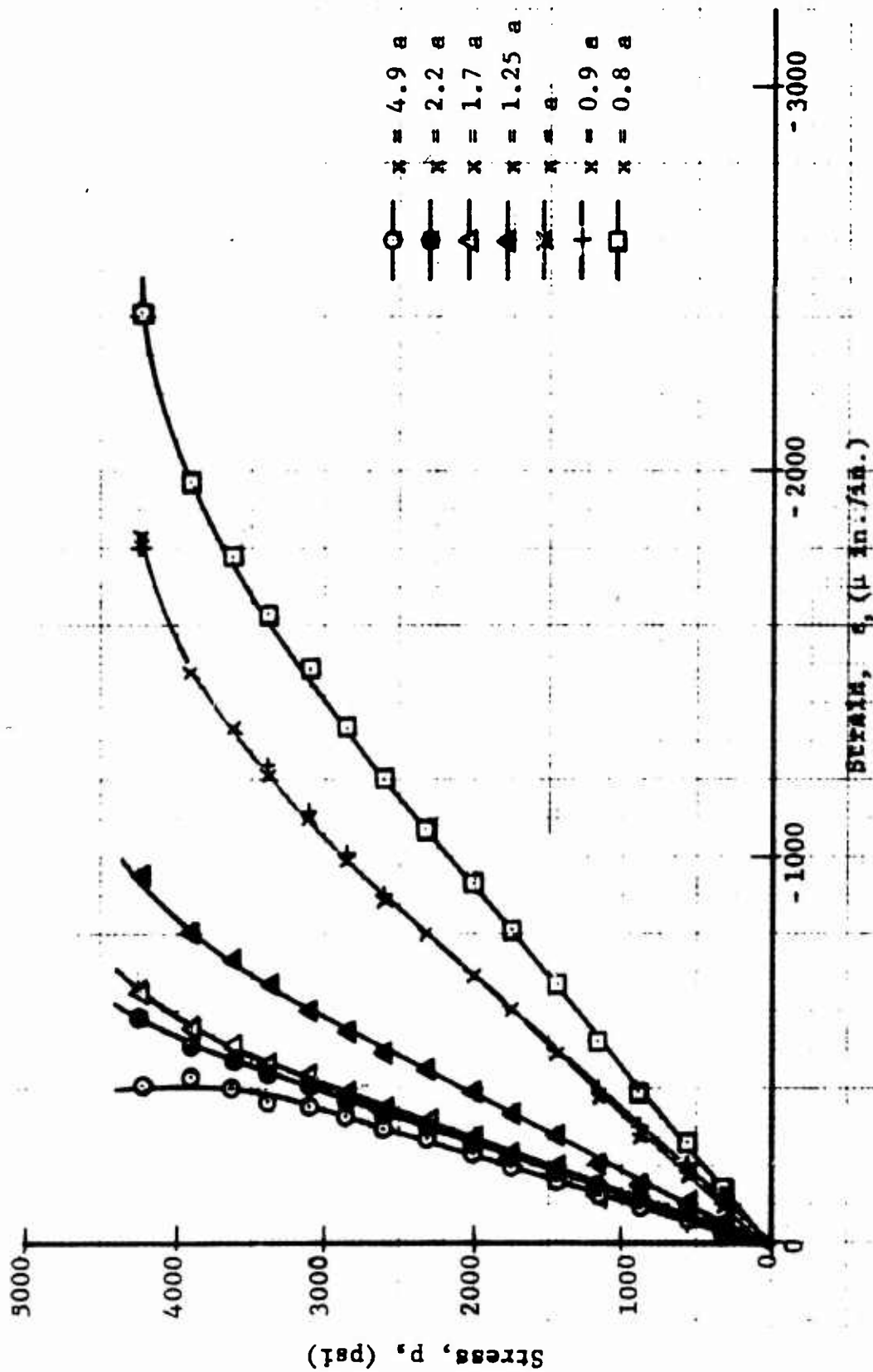
Fig.137 VERTICAL STRAINS ALONG HORIZONTAL AXIS OF SYMMETRY AS A FUNCTION OF APPLIED VERTICAL STRESS FOR SPECIMEN NO. 10 (MARBLE WITH HYDROSTONE LINER UNDER UNIAXIAL LOADING)

202
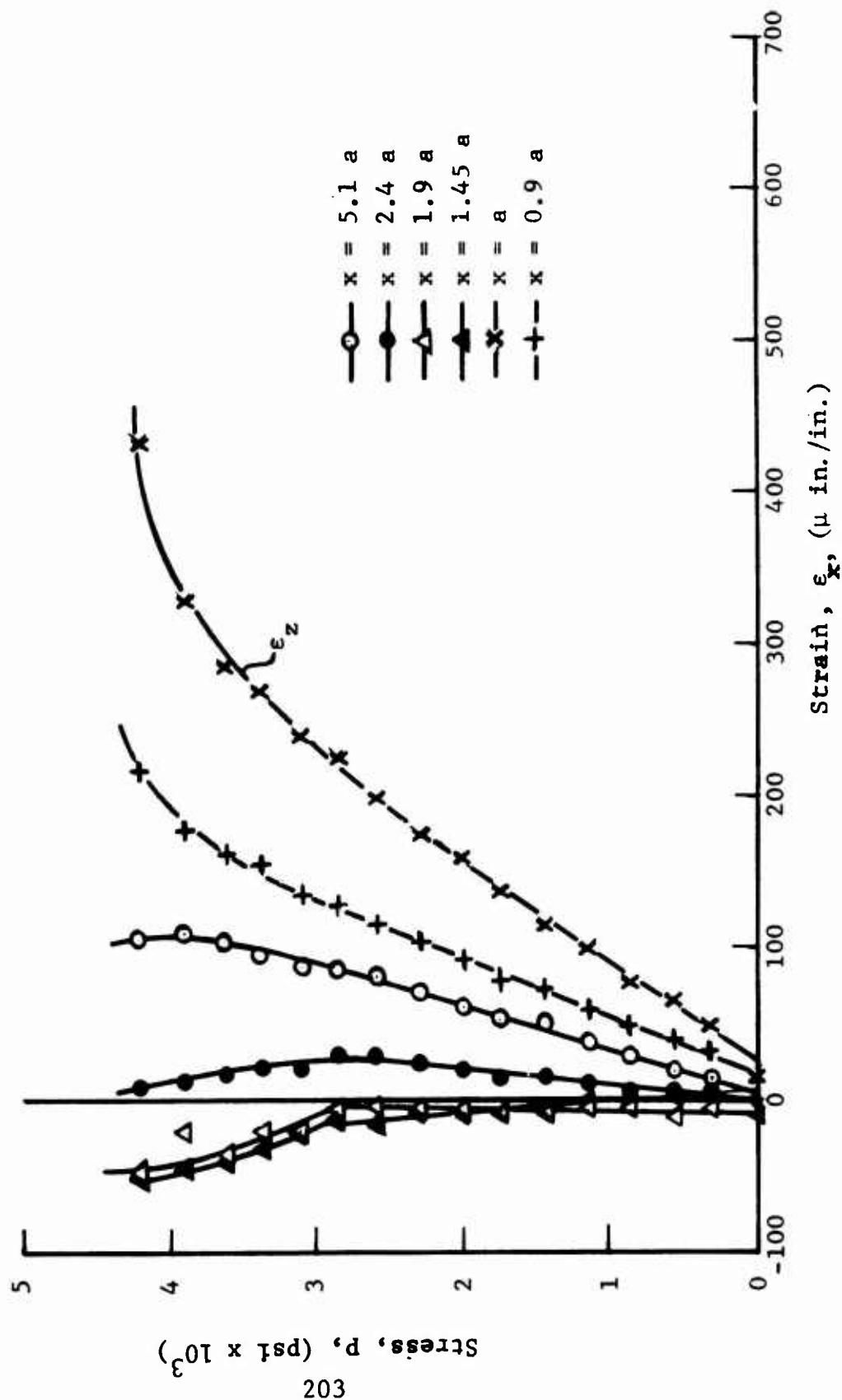
Fig. 138   HORIZONTAL STRAINS ALONG HORIZONTAL AXIS OF SYMMETRY AS A FUNCTION OF APPLIED
VERTICAL STRESS FOR SPECIMEN NO. 10 (MARBLE WITH HYDROSTONE LINER
UNDER UNIAXIAL LOADING)

203

Fig. 139 HORIZONTAL STRAINS ALONG VERTICAL AXIS OF SYMMETRY AS A FUNCTION OF APPLIED
VERTICAL STRESS FOR SPECIMEN NO. 10 (MARBLE WITH HYDROSTONE LINER
UNDER UNIAXIAL LOADING)

204

Fig. 140 VERTICAL STRAINS ALONG VERTICAL AXIS OF SYMMETRY FOR SPECIMEN NO. 10 (MARBLE WITH HYDROSTONE LINER UNDER UNIAXIAL LOADING)

205
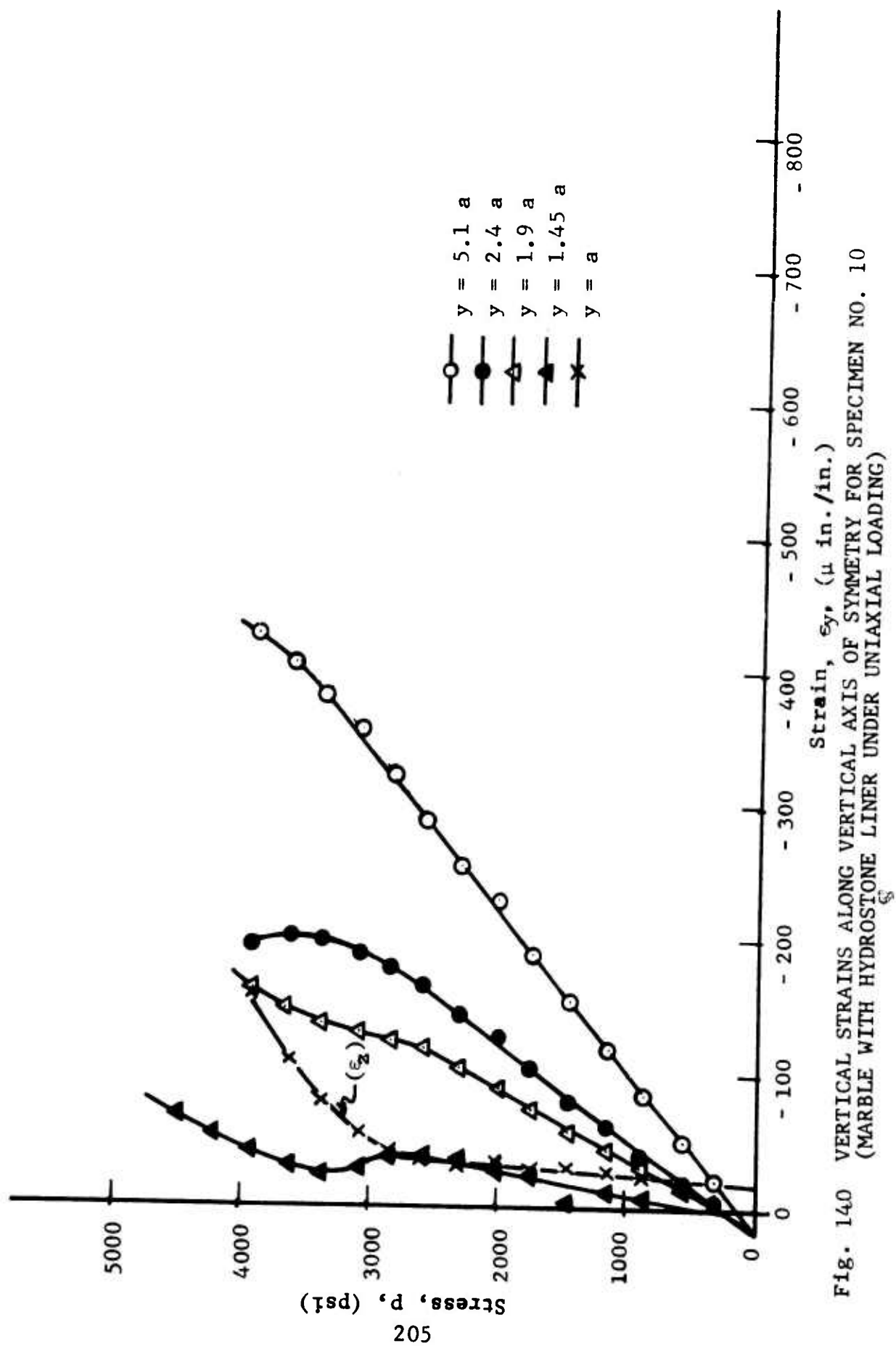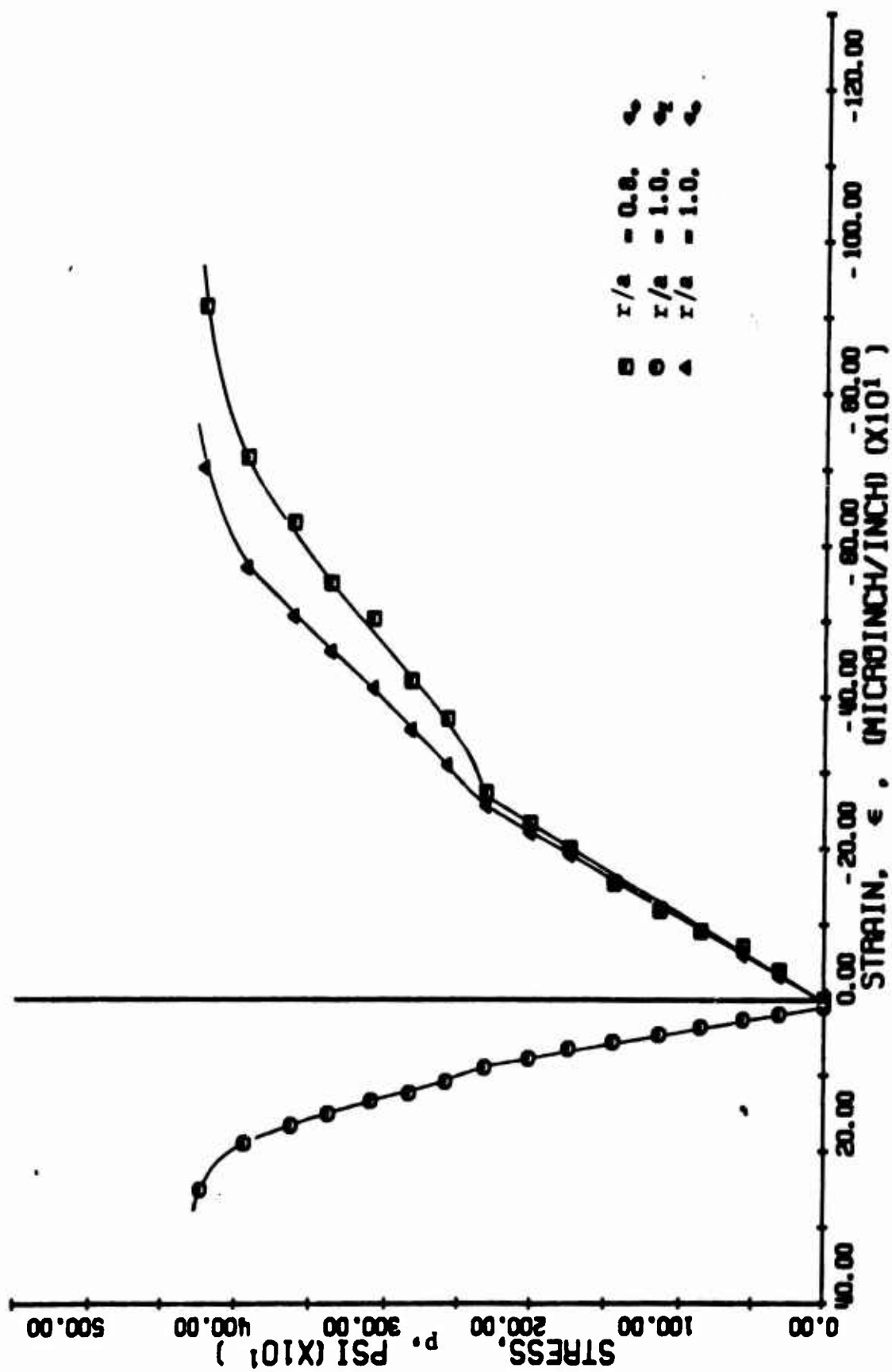
FIG. 141 STRAINS ALONG 45 DEGREE RADIUS FOR SPECIMEN NO. 10
DARBLE WITH HYDROSTONE LINER UNDER UNIAXIAL LOADING

206

$$E = 8.4 \times 10^6 \text{ psi}$$
$$\nu = 0.28$$

The ratio of the maximum compressive strain in the marble at the interface with the aluminum liner to the far-field strain is

$$k_\varepsilon = 2.90$$

which is almost the same as that for specimen No. 9 and a little higher than the theoretical value of 2.66. The maximum compressive strain on the inside of the liner is 450 μin./in. at 1,000 psi which is in excellent agreement with the photoelastic value of 440 μin./in.

The horizontal strains along the vertical axis (Fig. 139) show that cracking in the hydrostone liner occurred at around 2,100 psi and was soon followed by cracking in the marble.

Principal strains along the 45-degree radius were computed as before and plotted in Fig. 142. The angle between the 45-degree radius and the principal tensile direction varies between 29 degrees and 37 degrees at $r = 1.35a$, 32 degrees and 38 degrees at $r = 1.80a$ and 41 degrees and 47 degrees at $r = 3.00a$.

Strain distributions along the axes of symmetry at a stress level of $p = 2,000$ psi were plotted for specimens No. 9 and No. 10 in Figs. 143 and 144. Theoretical points are also shown. The agreement between the two specimens is satisfactory. The greatest discrepancy is, as noted in previously discussed results, in the peak tensile strain at the interface along the vertical axis. On the basis of the strain distributions of Fig. 144, the following maximum stresses were computed. For specimen No. 9, at $p = 2,350$ psi

$$\sigma_{max} = 3,060 \text{ psi}$$

in the marble at the interface. For specimen No. 10, at $p = 2,100$ psi

$$\sigma_{max} = 3,500 \text{ psi}$$

in the marble at the interface and

$$\sigma_{max} = 1,250 \text{ psi}$$

in the hydrostone on the inner surface. All of the stresses above are two to four times the strengths determined from uniaxial tension tests.
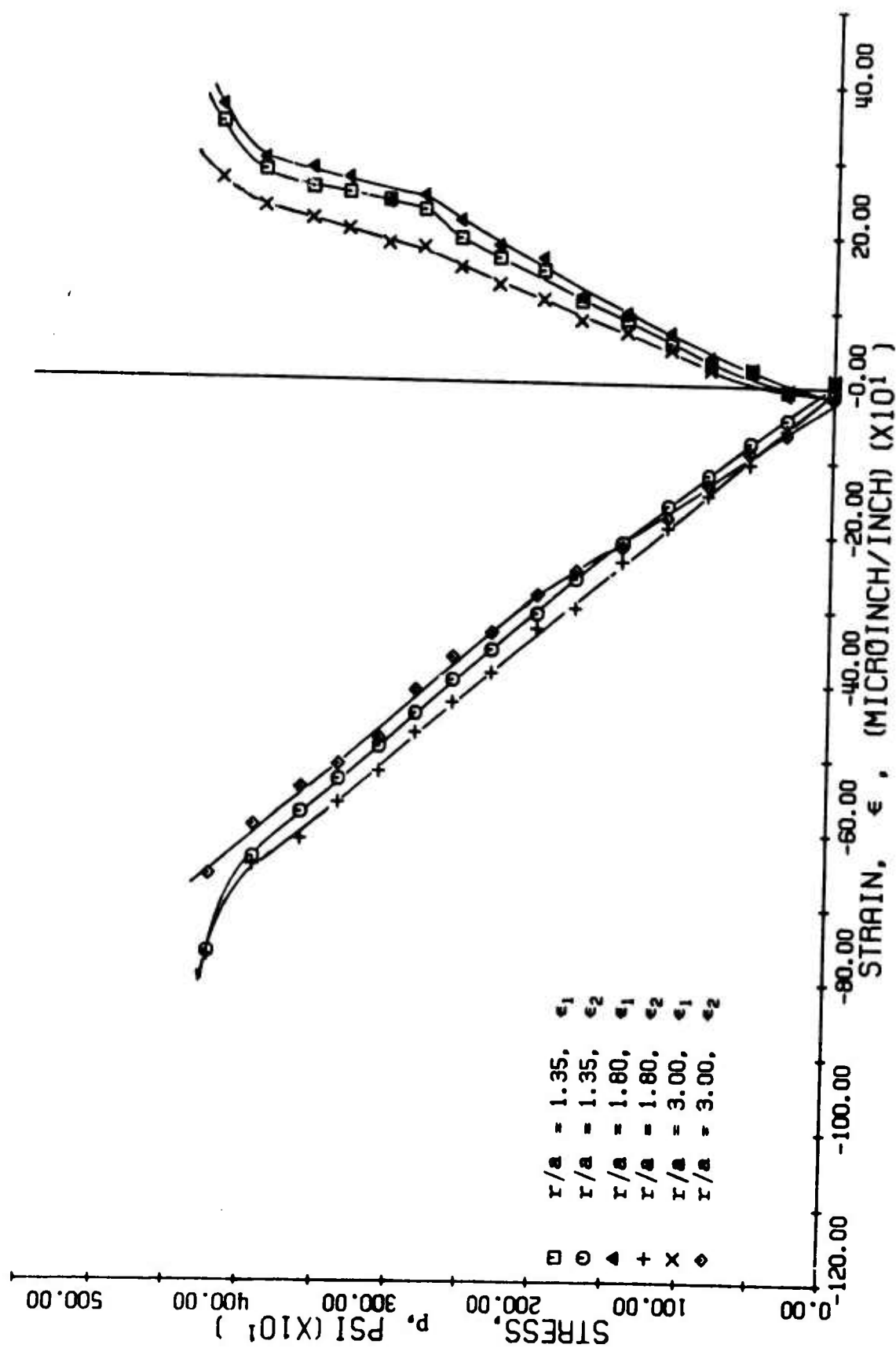
FIG. 142 PRINCIPAL STRAINS ALONG 45-DEGREE RADIUS FOR SPECIMEN NO. 10
(MARBLE WITH HYDROSTONE LINER UNDER UNIAXIAL LOADING)

208
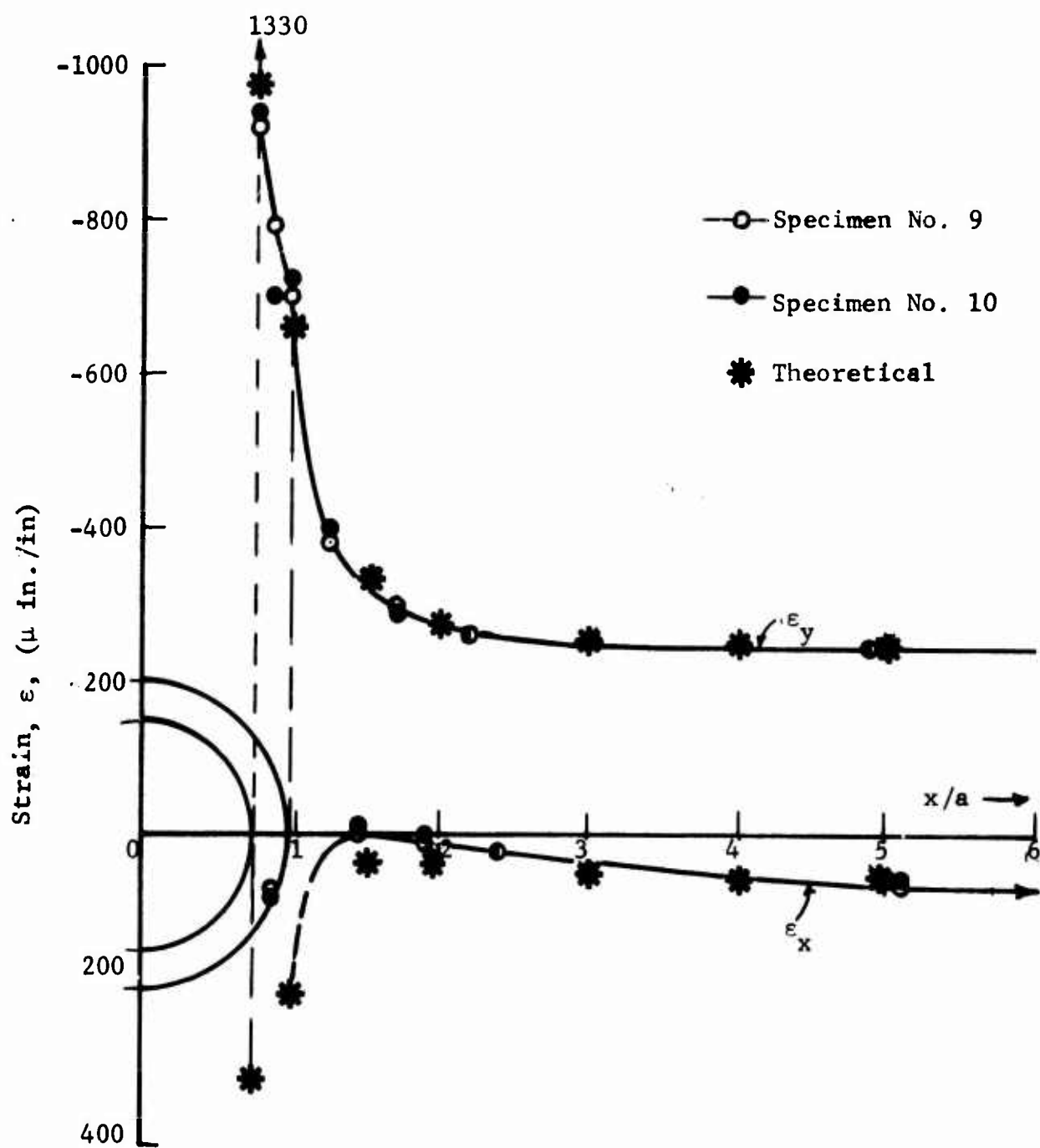
Fig. 143 STRAIN DISTRIBUTION ALONG X-AXIS FOR SPECIMENS NO.9 AND 10 AT 2,000 PSI APPLIED STRESS (MARBLE WITH HYDROSTONE LINER UNDER UNIAXIAL LOADING)
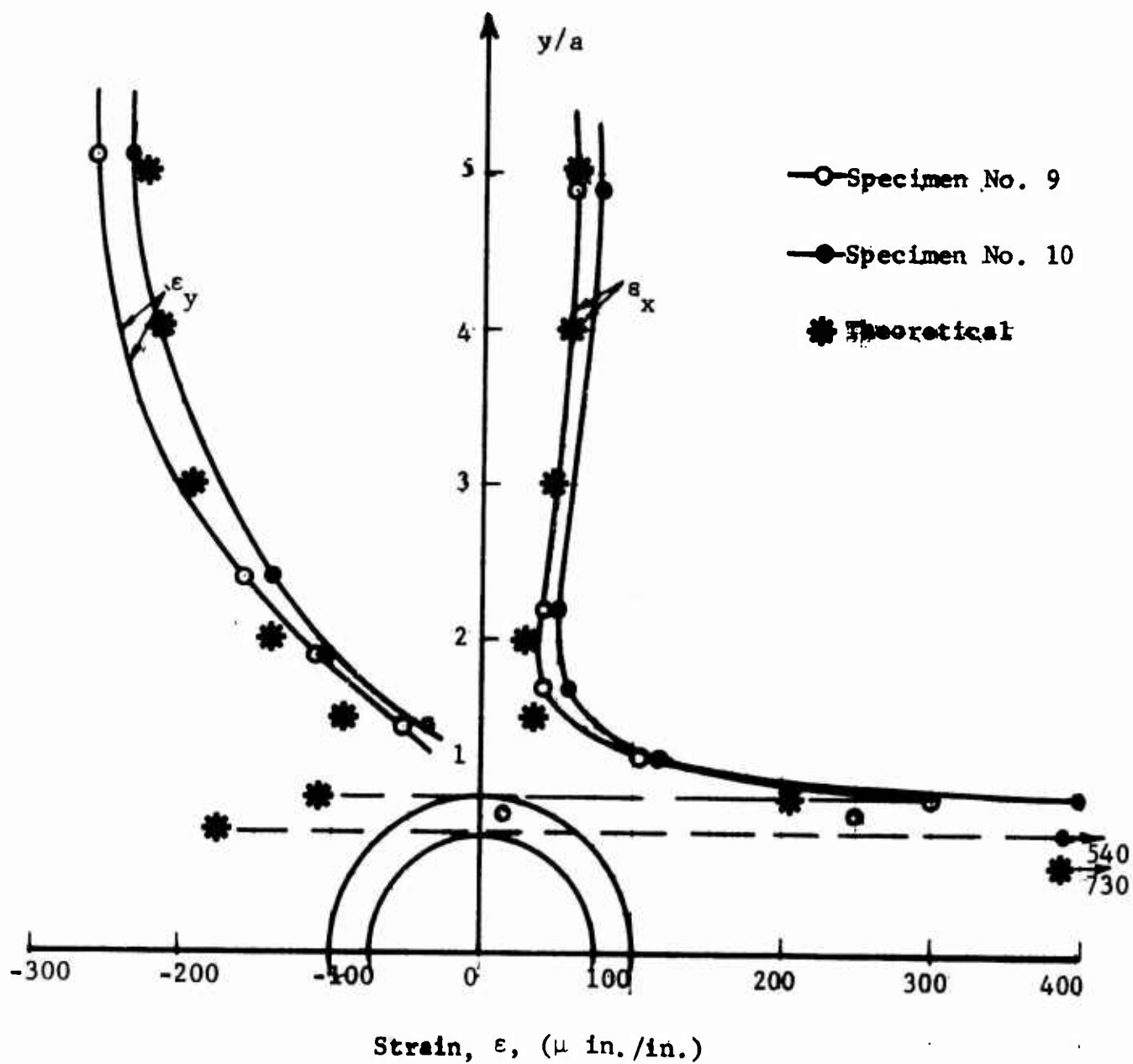
Fig. 144   STRAIN DISTRIBUTION ALONG Y-AXIS FOR SPECIMENS NO. 9
AND 10 AT 2,000 PSI APPLIED STRESS (MARBLE WITH
HYDROSTONE LINER UNDER UNIAXIAL LOADING)

4. Specimens No. 11 and 12 - Marble with Aluminum Liner
   Under Uniaxial Loading

   a. Theoretical Stress Distributions

   The following material properties were used:

   Marble: E = 8.2×10^6 psi
                 ν =   0.28
                 μ = 3.20×10^6 psi
                 κ = 2.13

   Aluminum: E_1 = 10×10^6 psi
                 ν_1 = 0.33
                 μ_1 = 3.76
                 κ_1 = 2.01

   For the liner thickness used $t = 0.40$ in. the circum-
ferential stress on the free surface of the liner is

$$\frac{\sigma_\theta}{p} = 1.17 - 2.09 \cos 2\theta \tag{70}$$

with peak values of

$$\left(\frac{\sigma_\theta}{p}\right)_{\theta=0°} = -0.92 \tag{71}$$

and

$$\left(\frac{\sigma_\theta}{p}\right)_{\theta=90°} = 3.26 \tag{72}$$

   The interface stresses in the marble are

$$\frac{\sigma_r}{p} = 0.21 + 0.50 \cos 2\theta \tag{73}$$

$$\frac{\sigma_\theta}{p} = 0.79 - 1.76 \cos 2\theta \tag{74}$$

$$\frac{\sigma_{r\theta}}{p} = -0.13 \sin 2\theta \tag{75}$$

211

Because of the low shear stress, the principal stresses differ little from the radial and circumferential ones. The latter are plotted versus angular location in Fig. 145. The peak values of the circumferential stress are

$$(\frac{\sigma_\theta}{p})_{\theta=0°} = -0.97 \tag{76}$$

and

$$(\frac{\sigma_\theta}{p})_{\theta=90°} = 2.55 \tag{77}$$

which shows that the stress reduction, especially that of the tensile stress, is even lower than in the case of the hydrostone liner. This is due to the fact that the modulus of aluminum is very close to that of marble. The main advantage would result from an increased thickness of liner which tends to move the points of critical stress in the rock farther from the cavity.

b. Experimental Procedure

Two marble plates of dimensions 36 in. x 24 in. x 3.30 in. with a 4 in. diameter hole and a 0.40 in. thick aluminum liner bonded to the cavity surface were used. Strain gages, DCDT's and photoelastic coating were applied as before. The instrumented specimens were loaded in uniaxial vertical compression at 20,000 to 25,000 lb load intervals to failure and the data recorded as before.

c. Results and Discussion

Isochromatic fringe patterns for specimens No. 11 and No. 12 are shown in Figs. 146 and 147 for various stress levels. The applied average stress is shown in every frame.

In specimen No. 11, cracking started in the marble at the interface with the liner near the vertical axis at a stress level below 2,780 psi. As the load was increased, the crack propagated nearly vertically along the centerline and it was joined by another crack initiated off the centerline to the right. This second crack

212
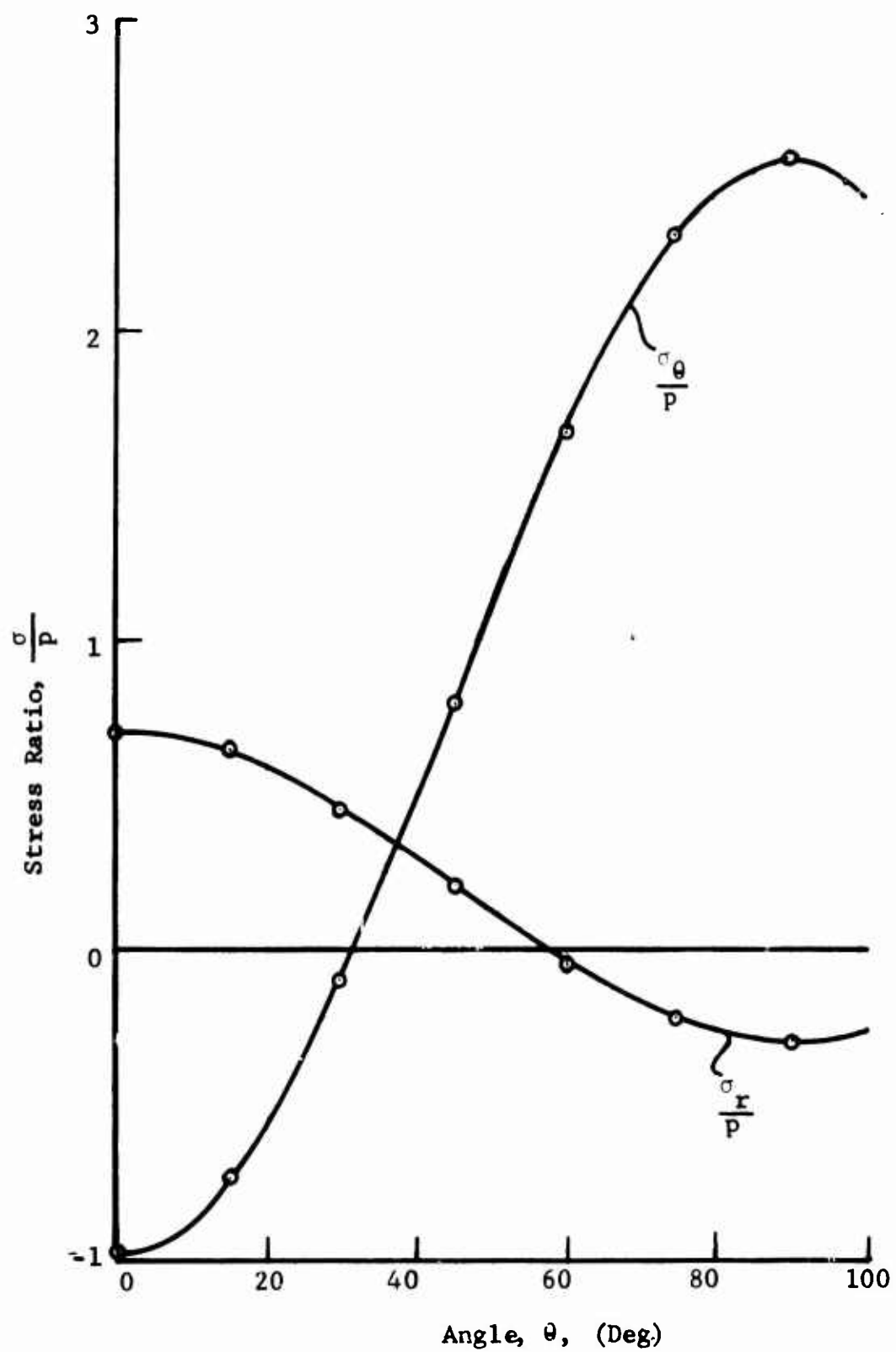
Fig. 145   VARIATION OF CIRCUMFERENTIAL AND RADIAL STRESSES
IN MARBLE AT INTERFACE WITH ALUMINUM LINER

213
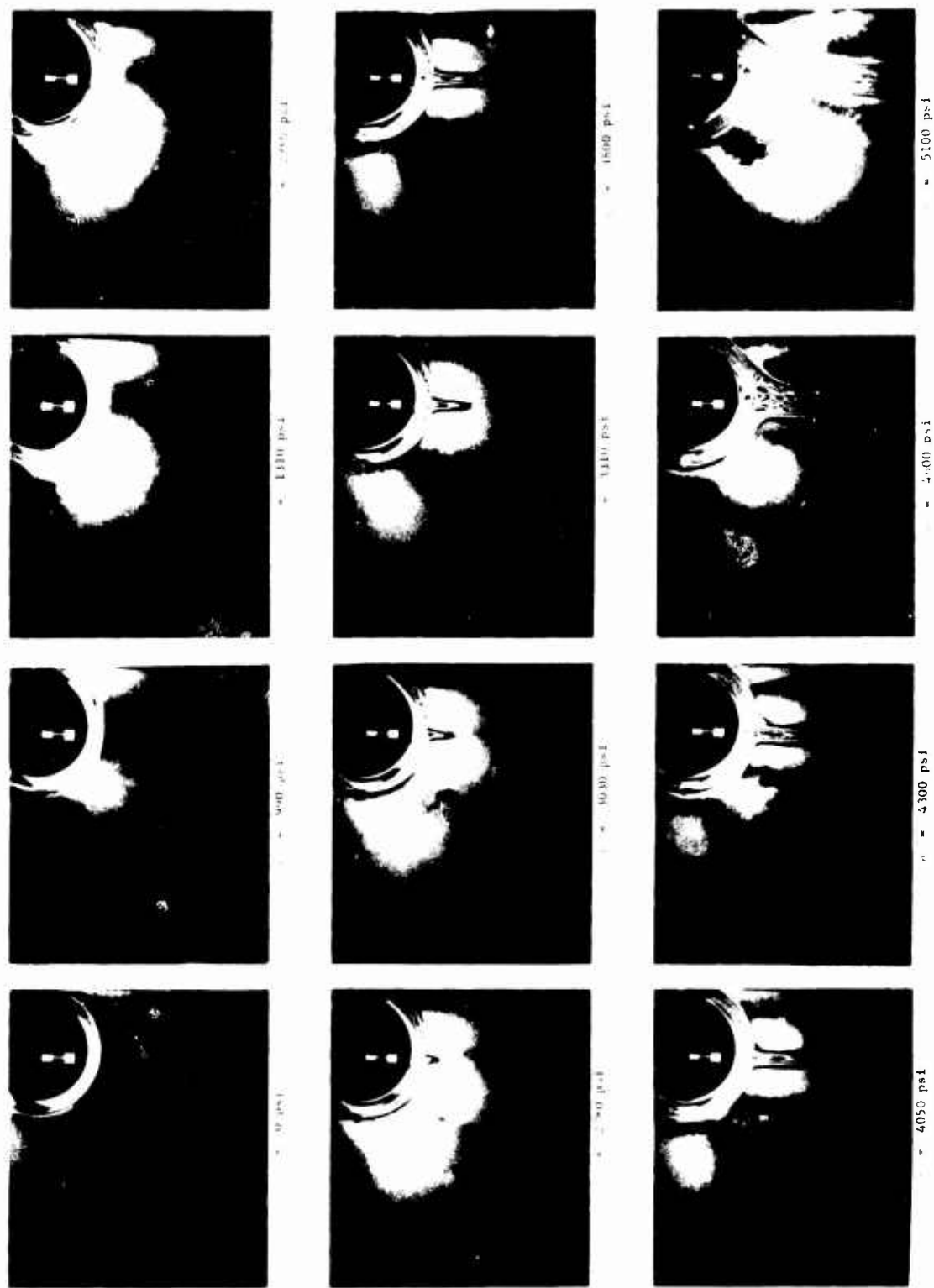
Fig. 146 ISOCHROMATIC FRINGE PATTERNS IN PHOTOELASTIC COATING AROUND HOLE IN SPECIMEN
NO. 11 (MARBLE WITH ALUMINUM LINER UNDER UNIAXIAL LOADING)

214
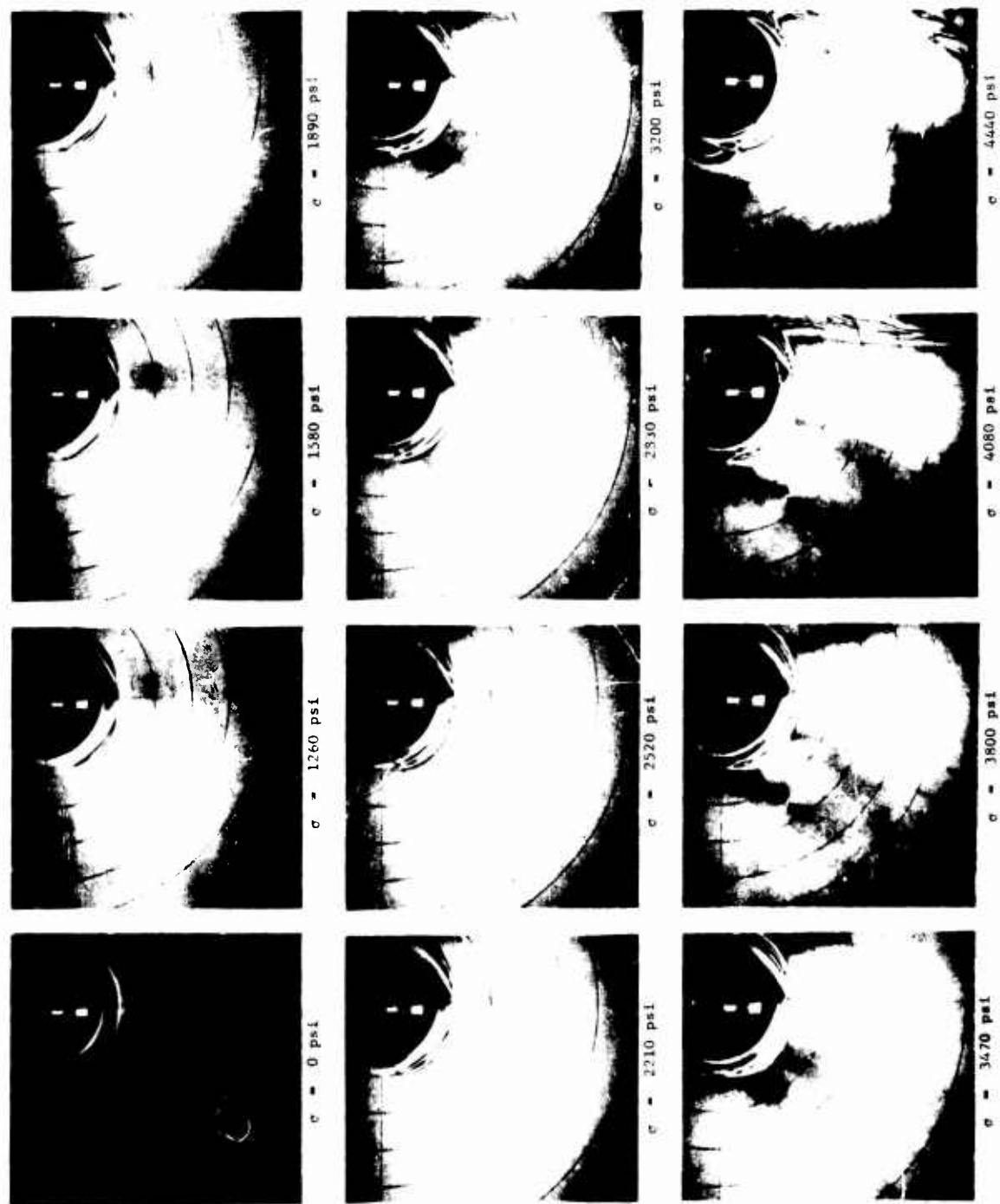
Fig. 147 ISOCHROMATIC FRINGE PATTERNS IN PHOTOELASTIC COATING AROUND HOLE IN SPECIMEN NO. 12 (MARBLE WITH ALUMINUM LINER UNDER UNIAXIAL LOADING)

215

started at approximately 4,300 psi. The load was increased up to a stress level of 5,600 psi where failure by complete separation occurred. The failure pattern is shown in Fig. 148.

In specimen No. 12, as in No. 11, the fringe concentration at the 45-degree location at the interface is very pronounced although a relatively low shear is predicted theoretically. A stress level of 4,080 psi was reached without any apparent sign of failure, however, a crack started suddenly after the specimen had been under load for 1-2 minutes. The crack appeared to the right of the vertical axis and it seems to have started at some point away from the interface. This peculiar type of fracture has been predicted theoretically by Hoek (Ref. 3) as shown in Fig. 6 and confirmed experimentally by him. It was shown that under biaxial loading with a biaxiality ratio of m = 0.15, failure away from the hole boundary occurred after vertical cracks had formed at the crown and bottom points of the cavity. The crack propagated nearly vertically off the vertical centerline in the bottom part of the specimen. Fracture in the top part was similar to that in specimen No. 11. Complete separation of the specimen occurred at p = 4,440 psi (Fig. 149).

The maximum fringe order on the free boundary of the liner on the horizontal axis was plotted versus applied stress for both specimens in Fig. 150. The maximum strain at the boundary computed from the photoelastic data is

$$(\varepsilon_1)_{p=1,000 \text{ psi}} = 900 \times \frac{0.45}{1.40} = 290 \; \mu\text{in./in.}$$

for specimen No. 11, and

$$(\varepsilon_1)_{p=1,000 \text{ psi}} = 900 \times \frac{0.52}{1.40} = 335 \; \mu\text{in./in.}$$

for specimen No. 12.

Diametral changes are plotted in Figs. 151 and 152 as a function of stress. In specimen No. 11, the vertical deflection is linear up to 4,000 psi but the horizontal becomes nonlinear at the

216
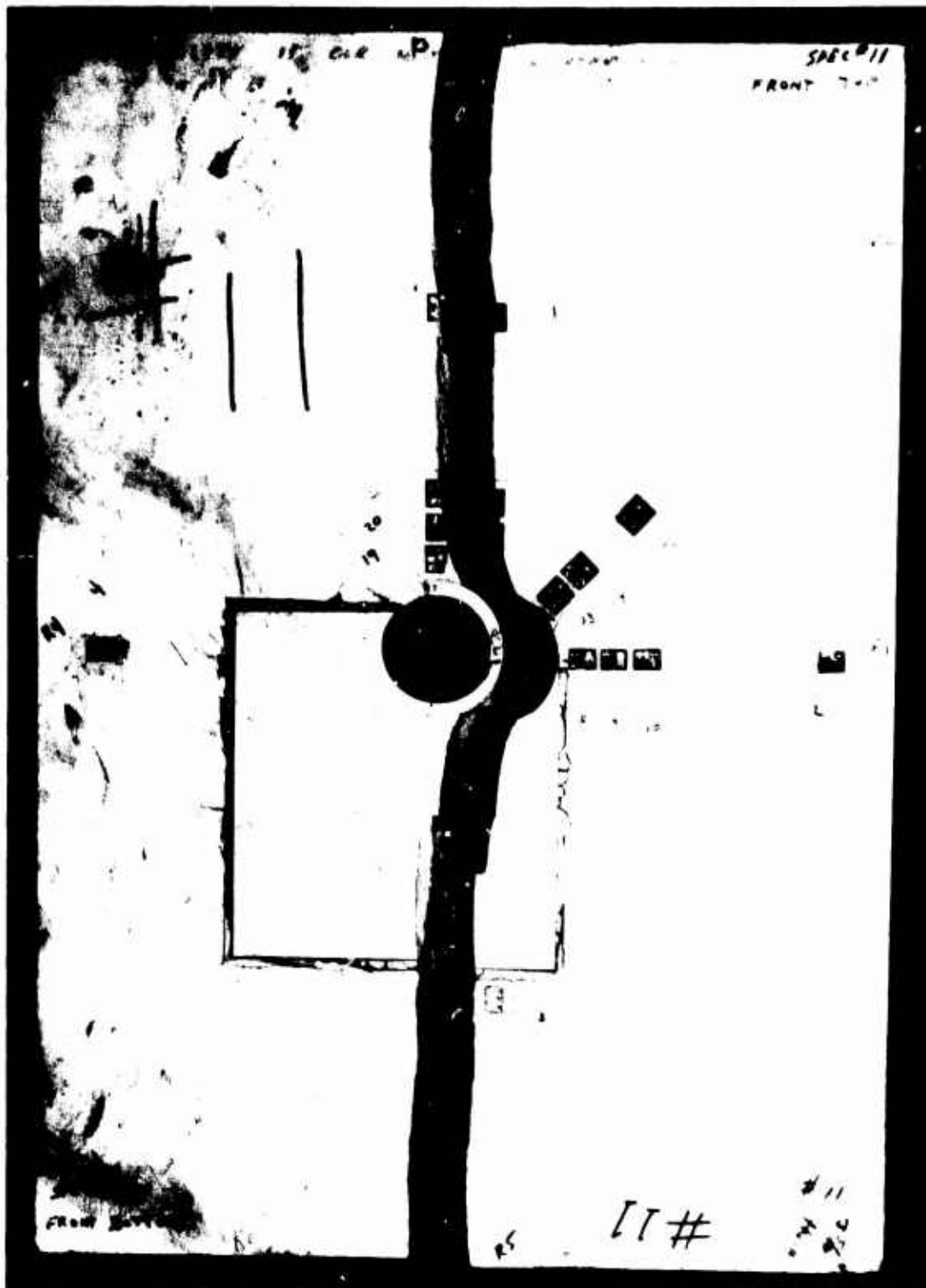
Fig. 148 FAILURE PATTERN IN SPECIMEN NO. 11 (MARBLE WITH ALUMINUM LINER UNDER UNIAXIAL LOADING)
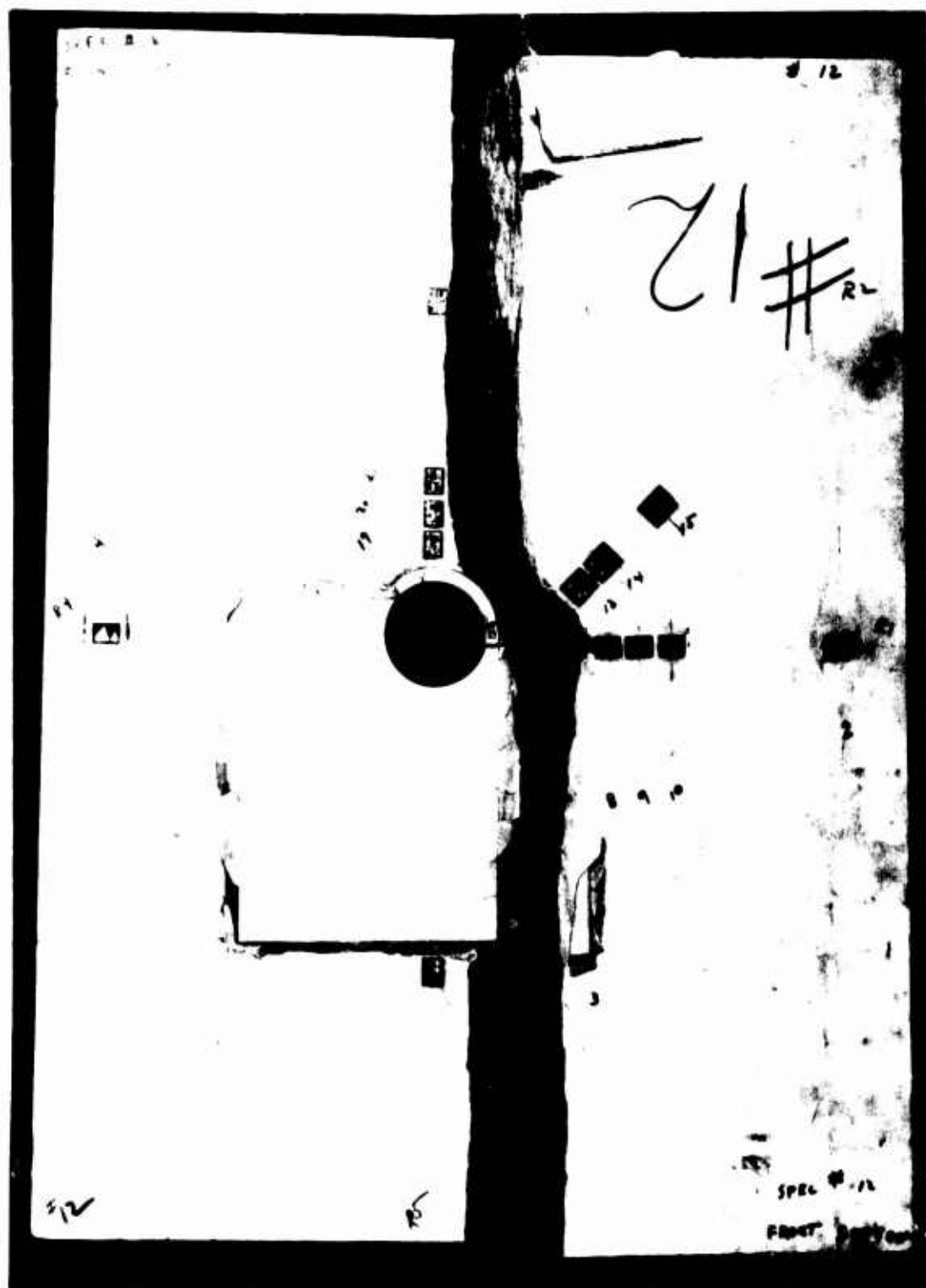
Fig. 149 FAILURE PATTERN IN SPECIMEN NO. 12 (MARBLE WITH ALUMINUM LINER UNDER UNIAXIAL LOADING)
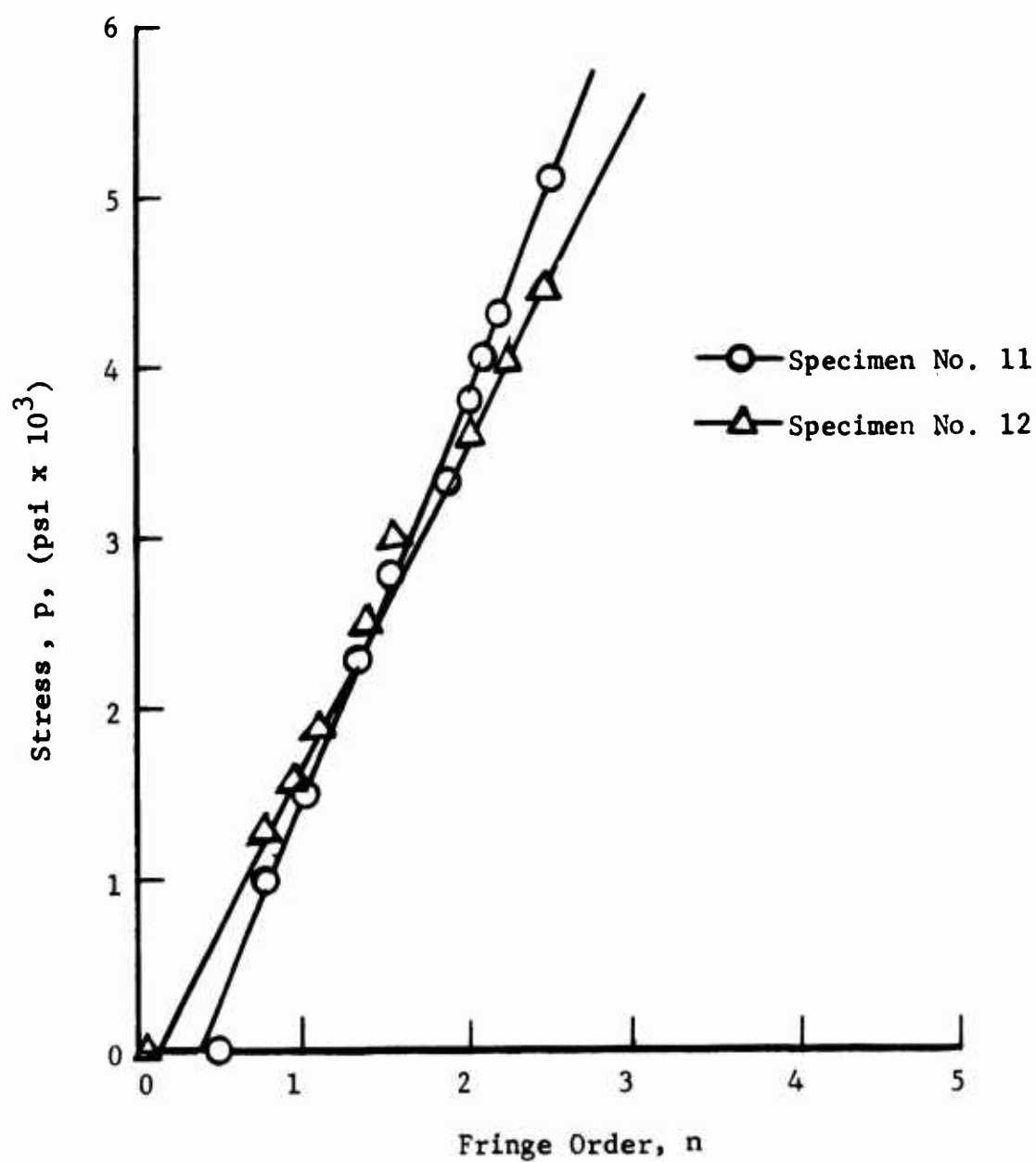
Fig. 150   FRINGE ORDER AT INNER-BOUNDARY OF LINER ON HORIZONTAL
AXIS FOR SPECIMENS NO. 11 AND 12 AS A FUNCTION OF
APPLIED VERTICAL STRESS

219
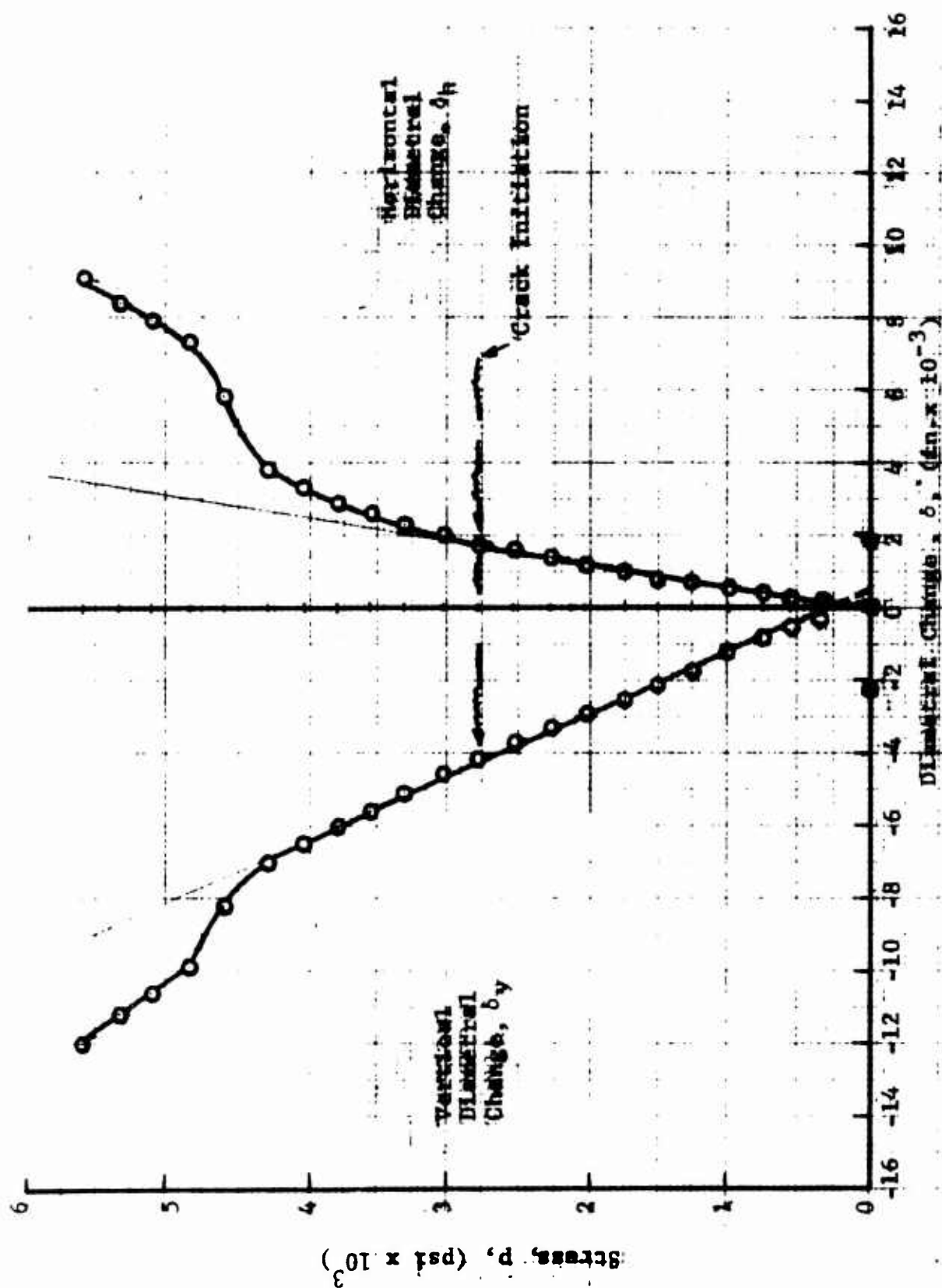
Fig. 151 DIAMETRAL CHANGES AS A FUNCTION OF APPLIED VERTICAL STRESS FOR SPECIMEN NO. 11
(MARBLE WITH ALUMINUM LINER UNDER UNIAXIAL LOADING)

220
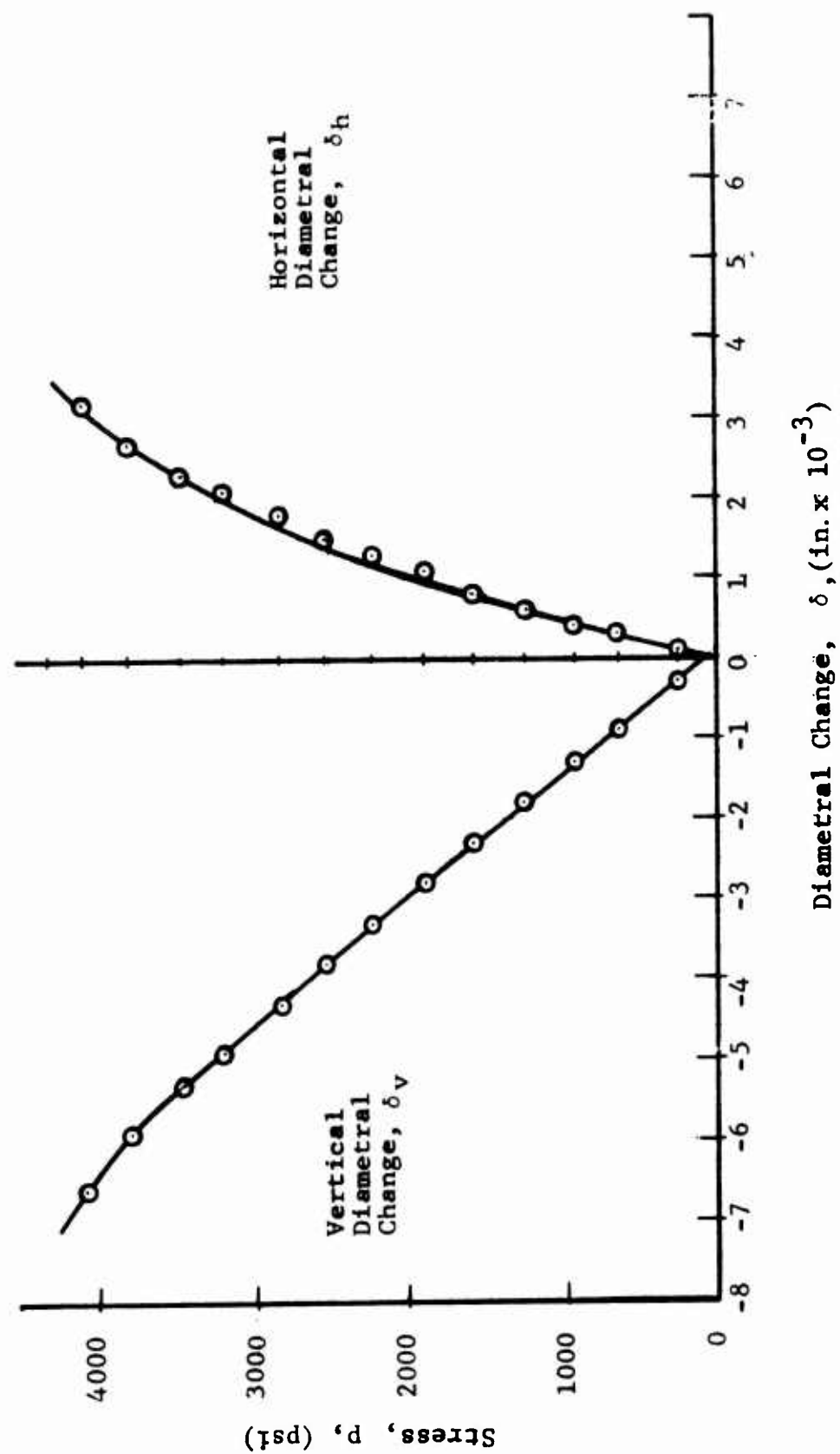
Fig. 152   DIAMETRAL CHANGES AS A FUNCTION OF APPLIED VERTICAL STRESS FOR
SPECIMEN NO. 12 (MARBLE WITH ALUMINUM LINER UNDER UNIAXIAL LOADING)

crack initiation level of 2,780 psi. The deflections per unit
stress in the linear range are

$$\frac{\delta_h}{P} = 0.6 \times 10^{-6} \text{ in./psi}$$

$$\frac{\delta_v}{P} = -1.7 \times 10^{-6} \text{ in./psi}$$

In specimen No. 12, the vertical deflection is linear up
to approximately 3,500 psi but the horizontal one becomes nonlinear
at a much lower stress, around 2,000 psi. The deflections per unit
stress in the linear range are

$$\frac{\delta_h}{P} = 0.5 \times 10^{-6} \text{ in./psi}$$

$$\frac{\delta_v}{P} = -1.6 \times 10^{-6} \text{ in./psi}$$

The values above are approximately equal to the correspond-
ing values for the hydrostone-lined marble specimens No. 9 and
No. 10. This indicates that the aluminum liner has no noticeable
stiffening effect since the modulus of aluminum is close to that of
marble.

Strains for specimen No. 11 as a function of applied stress
were plotted in Figs. 153 through 157. Vertical strains along the
horizontal axis (Fig. 153) are linear up to approximately 3,000 psi.
The modulus and Poisson's ratio computed from the average of the
far-field strains are

$$E = 8.2 \times 10^6 \text{ psi}$$
$$\nu = 0.27$$

The ratio of the maximum compressive strain at the interface
to the far-field strain is

$$k_\varepsilon = 2.85$$

222
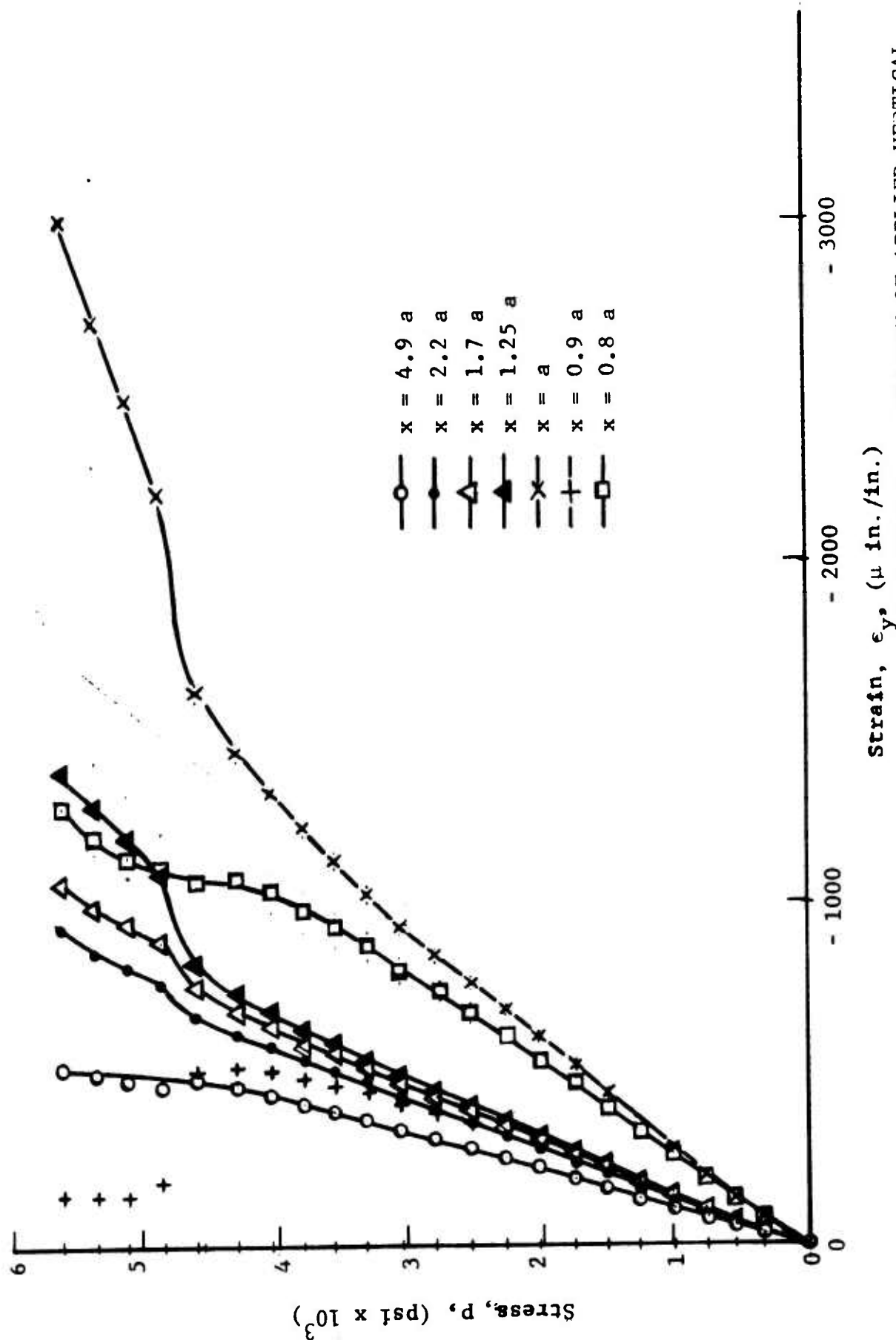
Fig. 153   VERTICAL STRAINS ALONG HORIZONTAL AXIS OF SYMMETRY AS A FUNCTION OF APPLIED VERTICAL STRESS FOR SPECIMEN NO. 11 (MARBLE WITH ALUMINUM LINER UNDER UNIAXIAL LOADING)
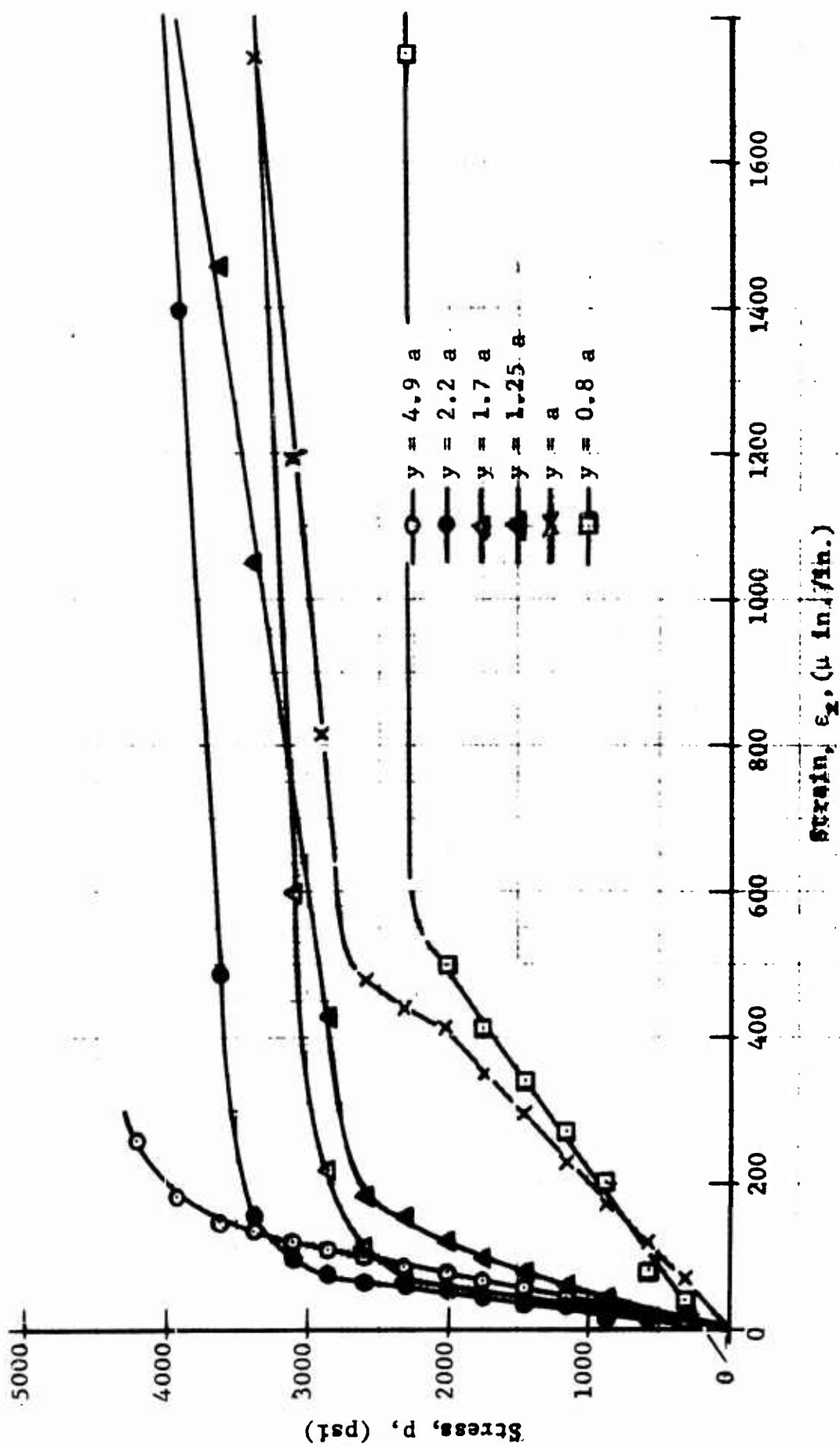
223
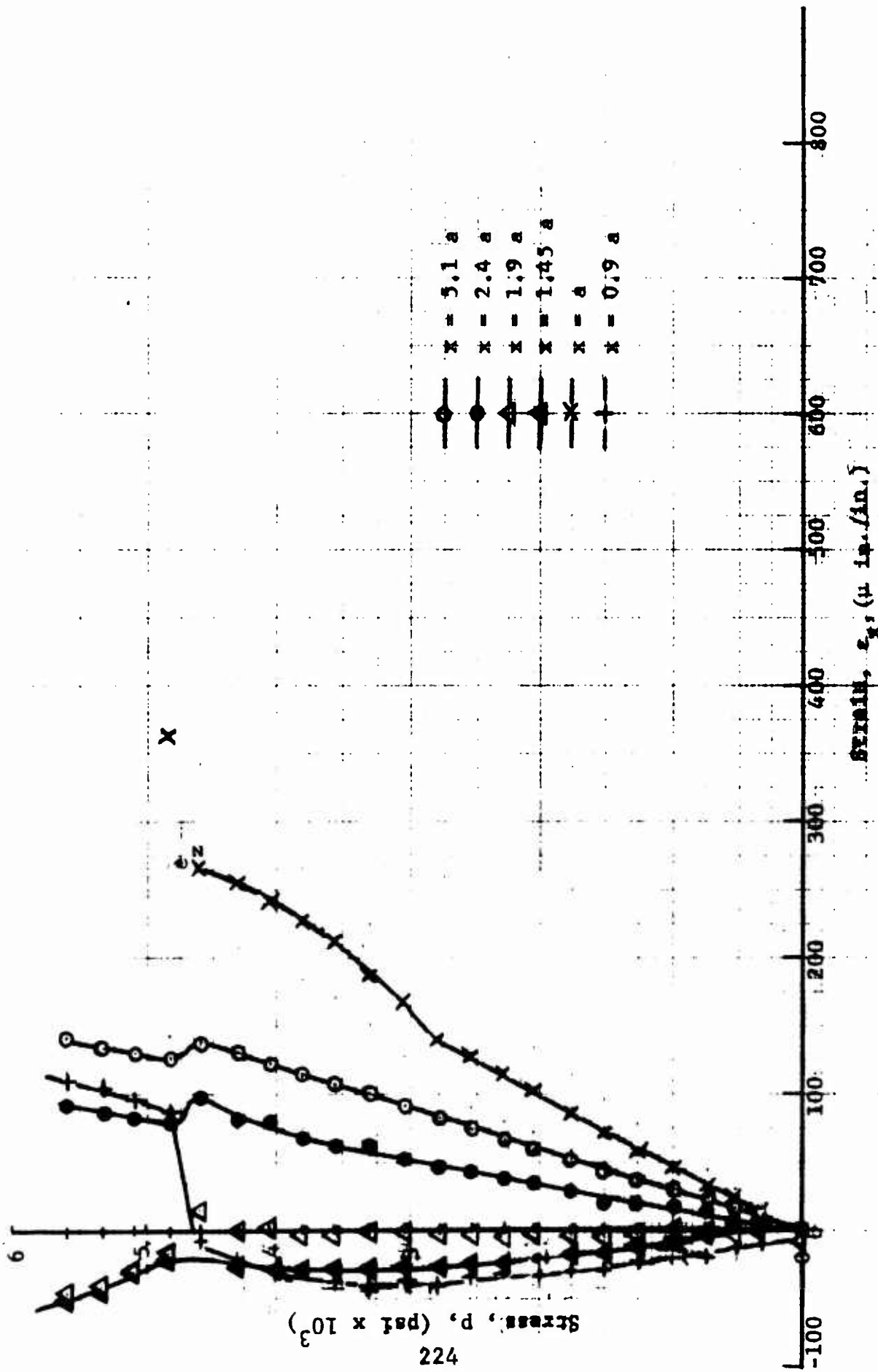
Fig. 154 HORIZONTAL STRAINS ALONG HORIZONTAL AXIS OF SYMMETRY AS A FUNCTION OF APPLIED VERTICAL STRESS FOR SPECIMEN NO. 11 (MARBLE WITH ALUMINUM LINER UNDER UNIAXIAL LOADING)

224

Fig. 155 HORIZONTAL STRAINS ALONG VERTICAL AXIS OF SYMMETRY AS A FUNCTION OF APPLIED VERTICAL STRESS FOR SPECIMEN NO. 11 (MARBLE WITH ALUMINUM LINER UNDER UNIAXIAL LOADING)

Strain, ε, (μ in./in.)

Stress, p, (psi x 10^3)

225
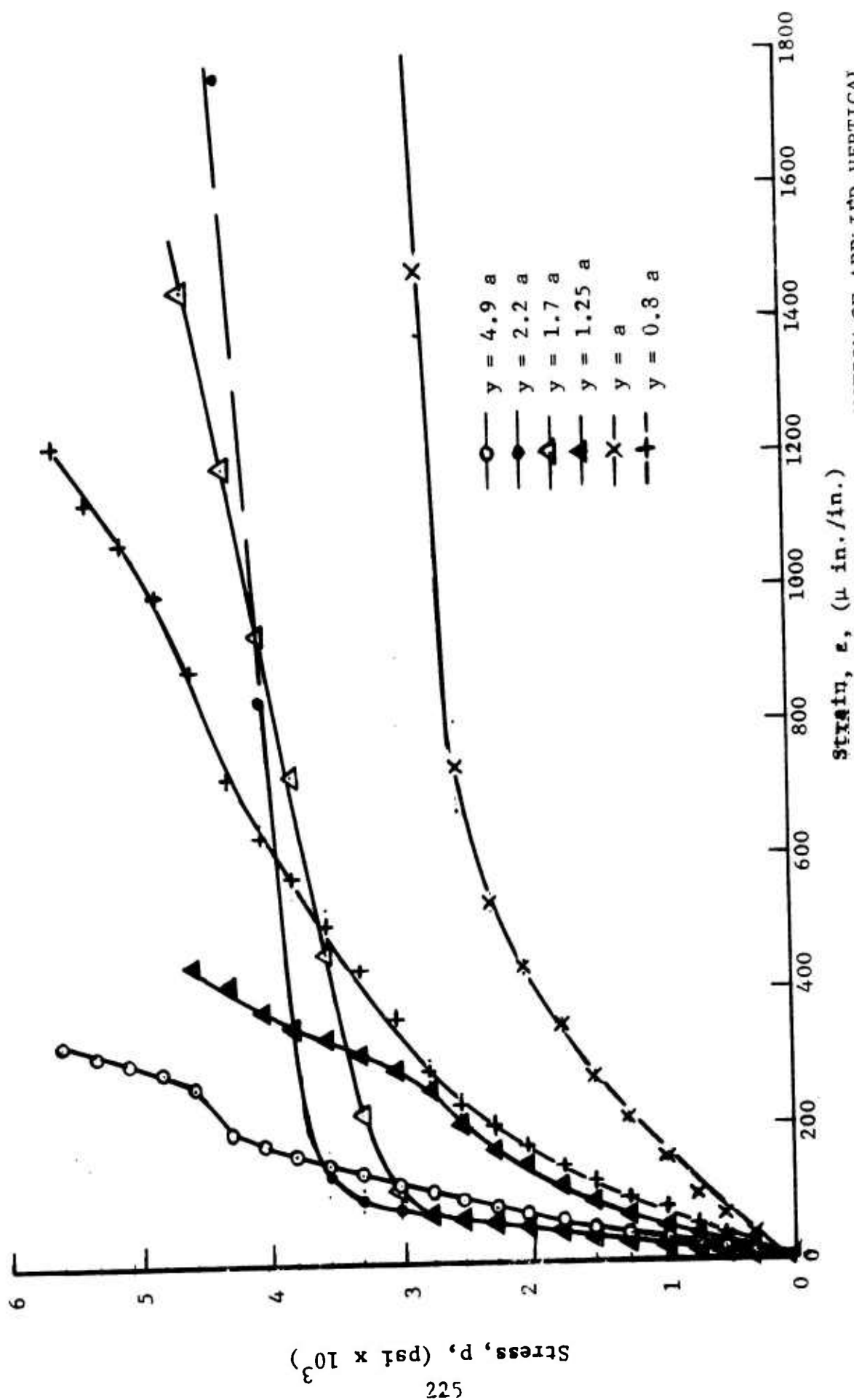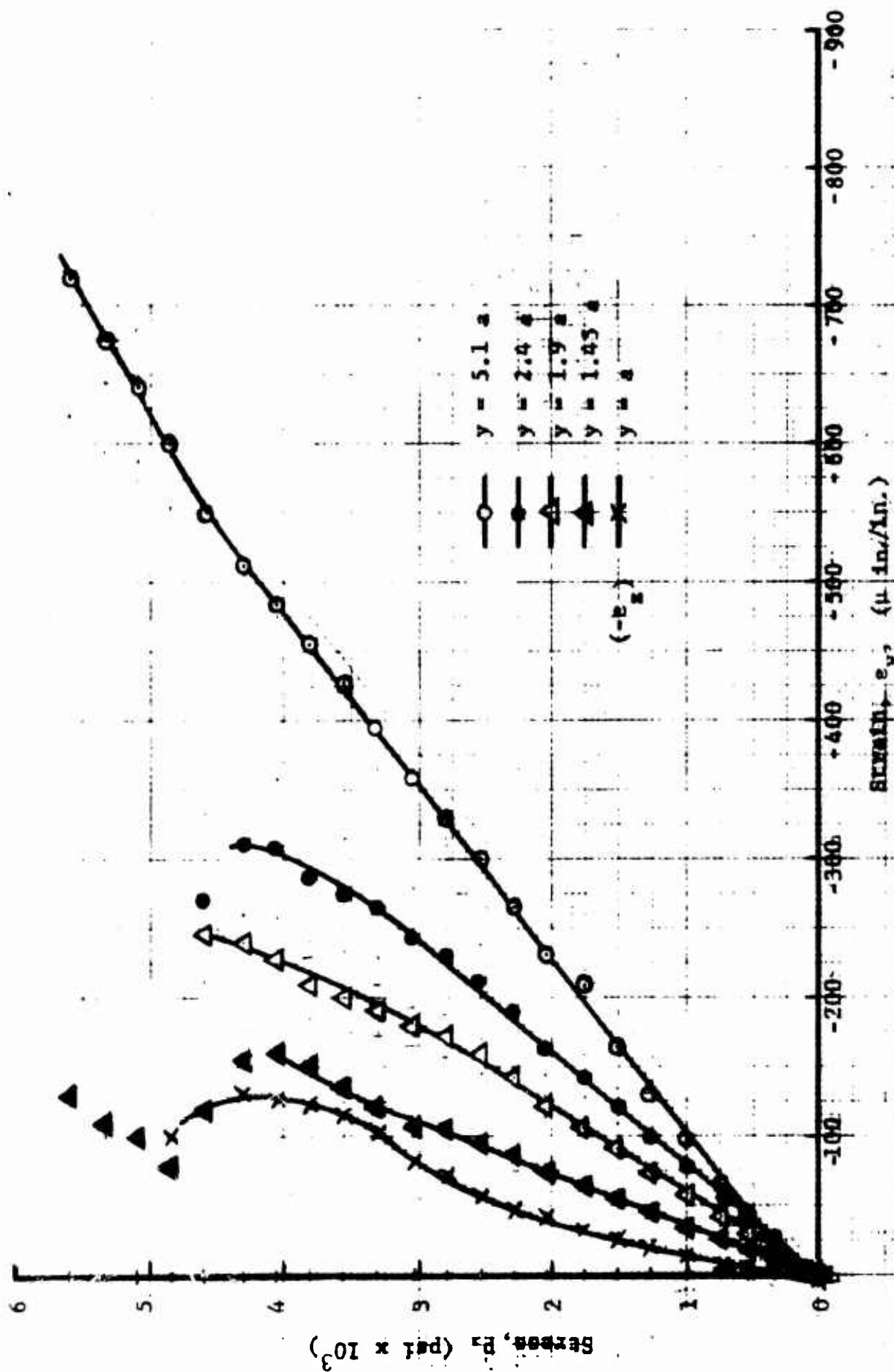
Fig. 156   VERTICAL STRAINS ALONG VERTICAL AXIS OF SYMMETRY AS A FUNCTION OF APPLIED VERTICAL STRESS FOR SPECIMEN NO. 11 (MARBLE WITH ALUMINUM LINER UNDER UNIAXIAL LOADING)
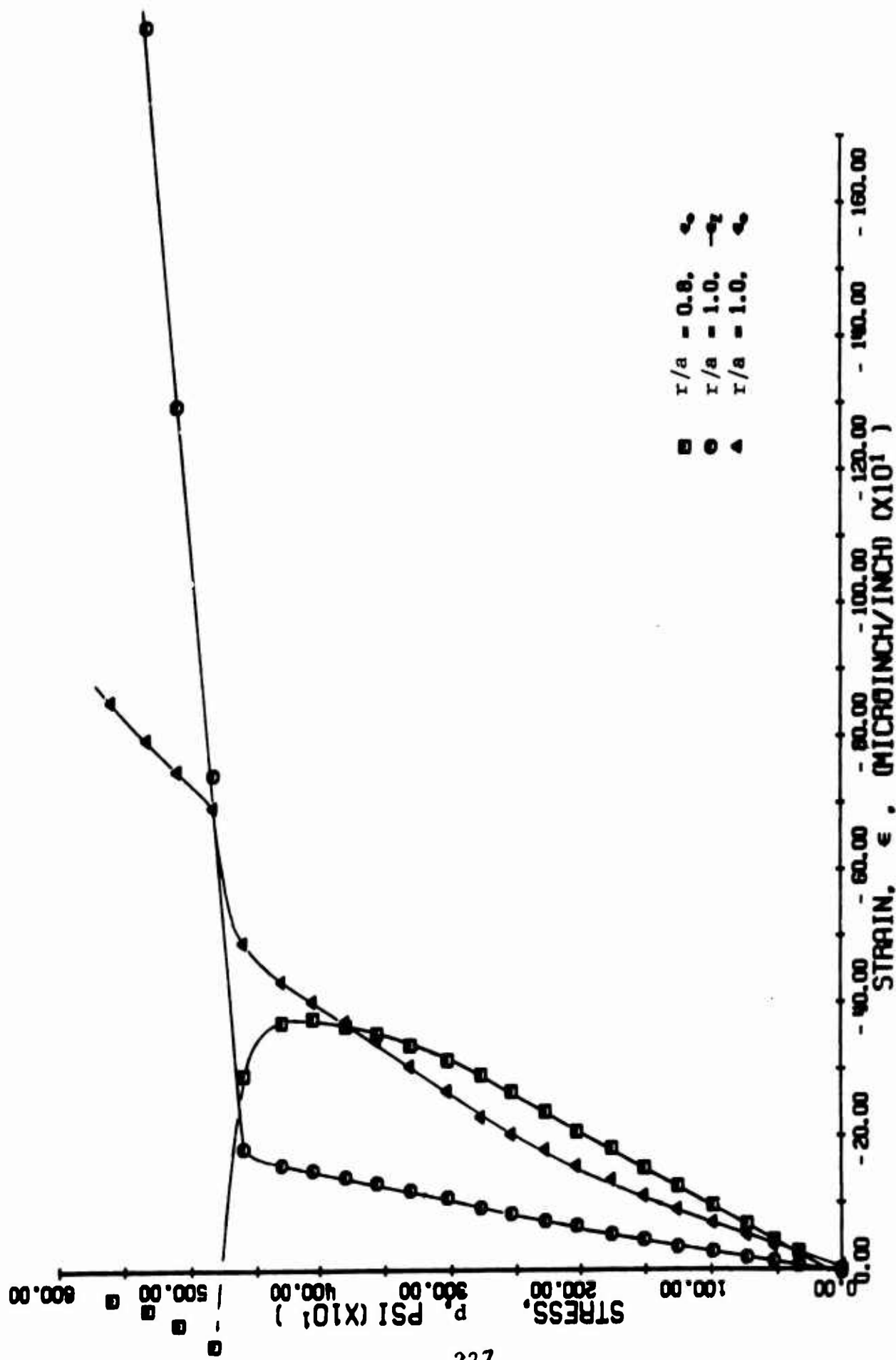
FIG. 157 STRAINS ALONG 45 DEGREE RADIUS FOR SPECIMEN NO. 11
MARBLE WITH ALUMINUM LINER UNDER UNIAXIAL LOADING

227

compared to the theoretically computed value of 2.63 for an infinite plate. The maximum compressive strain at the inside of the liner is 290 μin./in. at p = 1,000 psi which is identical to the photoelastic result.

Most of the horizontal strains along the vertical axis, especially those close to the liner, show nonlinearity from the very beginning. Crack initiation and propagation occurred at around 2,500 psi which is slightly higher than the crack initiation level in the hydrostone-lined specimens and somewhat lower than evidenced in the photoelastic patterns.

Principal strains along the 45-degree radius were computed as before and plotted in Fig. 158. The angle between the 45-degree radius and the principal tensile direction measured clockwise varies between 40 degrees and 32 degrees at _ = 1.35a, 43 degrees and 38 degrees at r = 1.80a and 45 degrees and 47 degrees at r = 3.00a.

Strains for specimen No. 12 as a function of applied stress are plotted in Figs. 159 through 163. Vertical strains along the horizontal axis (Fig. 159) are linear throughout the loading range. The modulus and Poisson's ratio determined from the far-field strains (with emphasis on those along the vertical axis) are

$$E = 8.2 \times 10^6 \text{ psi}$$
$$\nu = 0.28$$

The maximum compressive strain ratio in the marble is

$$k_\varepsilon = 2.50$$

compared to the theoretical value of 2.63. The maximum compressive strain on the liner is 310 μin./in. at p = 1,000 psi which is in good agreement with the photoelastic value of 290 μin./in.

The horizontal strains along the vertical axis show the characteristic nonlinearity from the very beginning with evidence of plastic flow at approximately 4,000 psi. This is the level at which cracking remote from the interface was initiated as seen in the photoelastic fringe patterns.
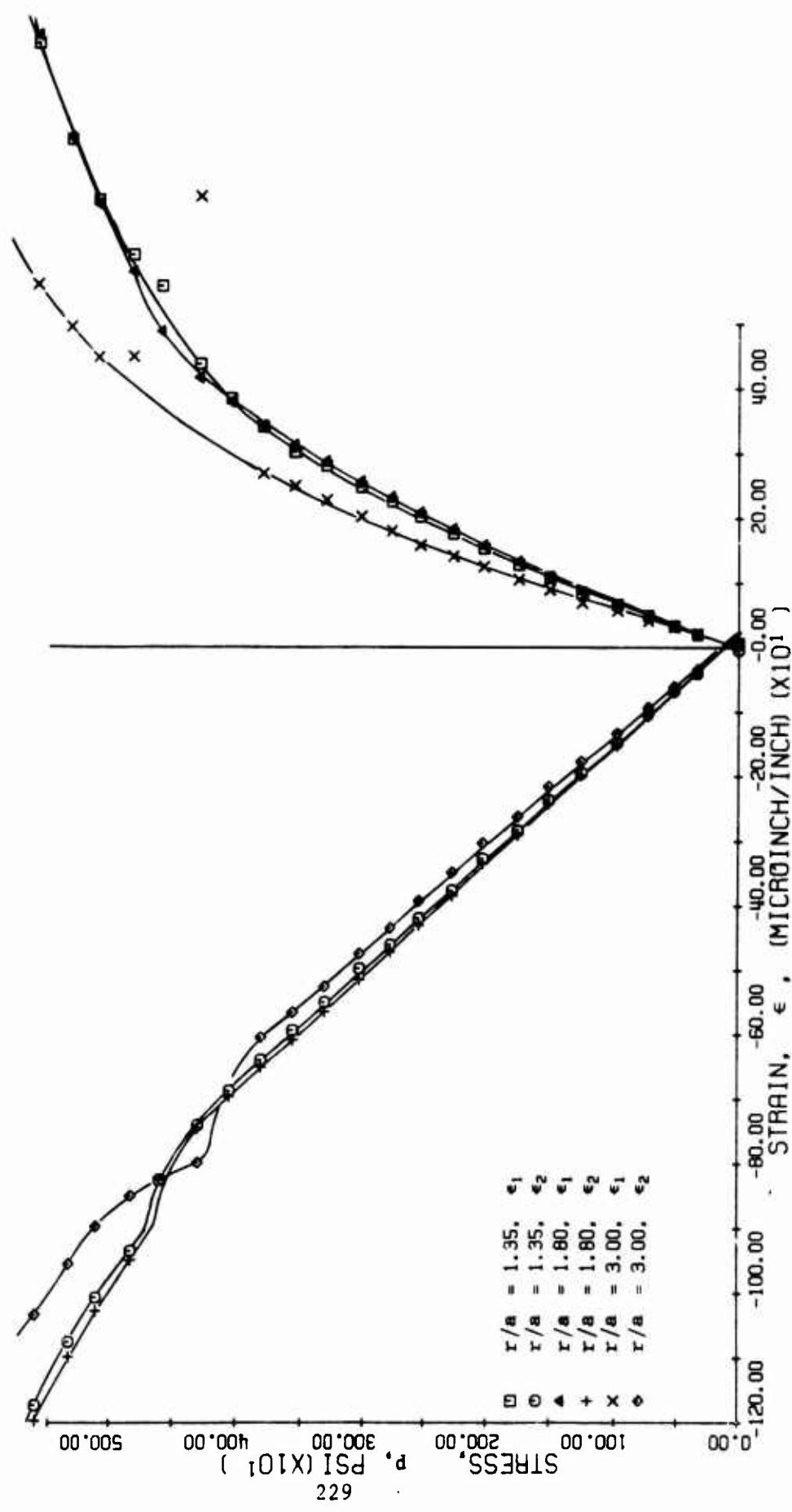
FIG. 158   PRINCIPAL STRAINS ALONG 45-DEGREE RADIUS FOR SPECIMEN NO. 11
(MARBLE WITH ALUMINUM LINER UNDER UNIAXIAL LOADING)

229

Fig. 159 VERTICAL STRAINS ALONG HORIZONTAL AXIS OF SYMMETRY AS A FUNCTION OF APPLIED VERTICAL STRESS FOR SPECIMEN NO. 12 (MARBLE WITH ALUMINUM LINER UNDER UNIAXIAL LOADING)

230

Fig. 160   HORIZONTAL STRAINS ALONG HORIZONTAL AXIS OF SYMMETRY AS A
FUNCTION OF APPLIED VERTICAL STRESS FOR SPECIMEN NO. 12
(MARBLE WITH ALUMINUM LINER UNDER UNIAXIAL LOADING)

231

Fig. 161 HORIZONTAL STRAINS ALONG VERTICAL AXIS OF SYMMETRY AS A FUNCTION OF APPLIED VERTICAL STRESS FOR SPECIMEN NO. 12 (MARBLE WITH ALUMINIM LINER UNDER UNIAXIAL LOADING)

232
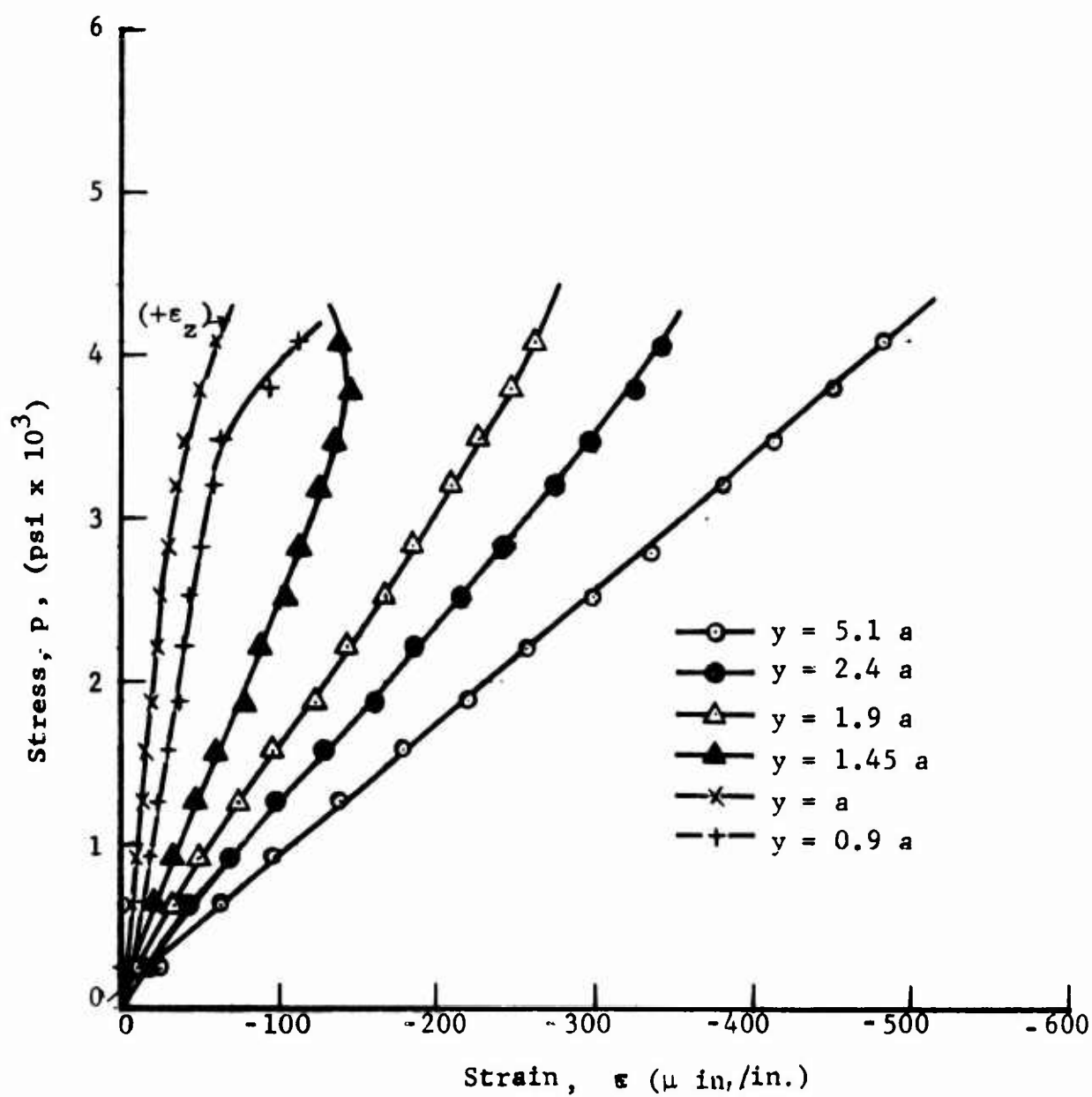
Fig.162 VERTICAL STRAINS ALONG VERTICAL AXIS OF SYMMETRY AS A
FUNCTION OF APPLIED VERTICAL STRESS FOR SPECIMEN NO. 12
(MARBLE WITH ALUMINUM LINER UNDER UNIAXIAL LOADING)

233
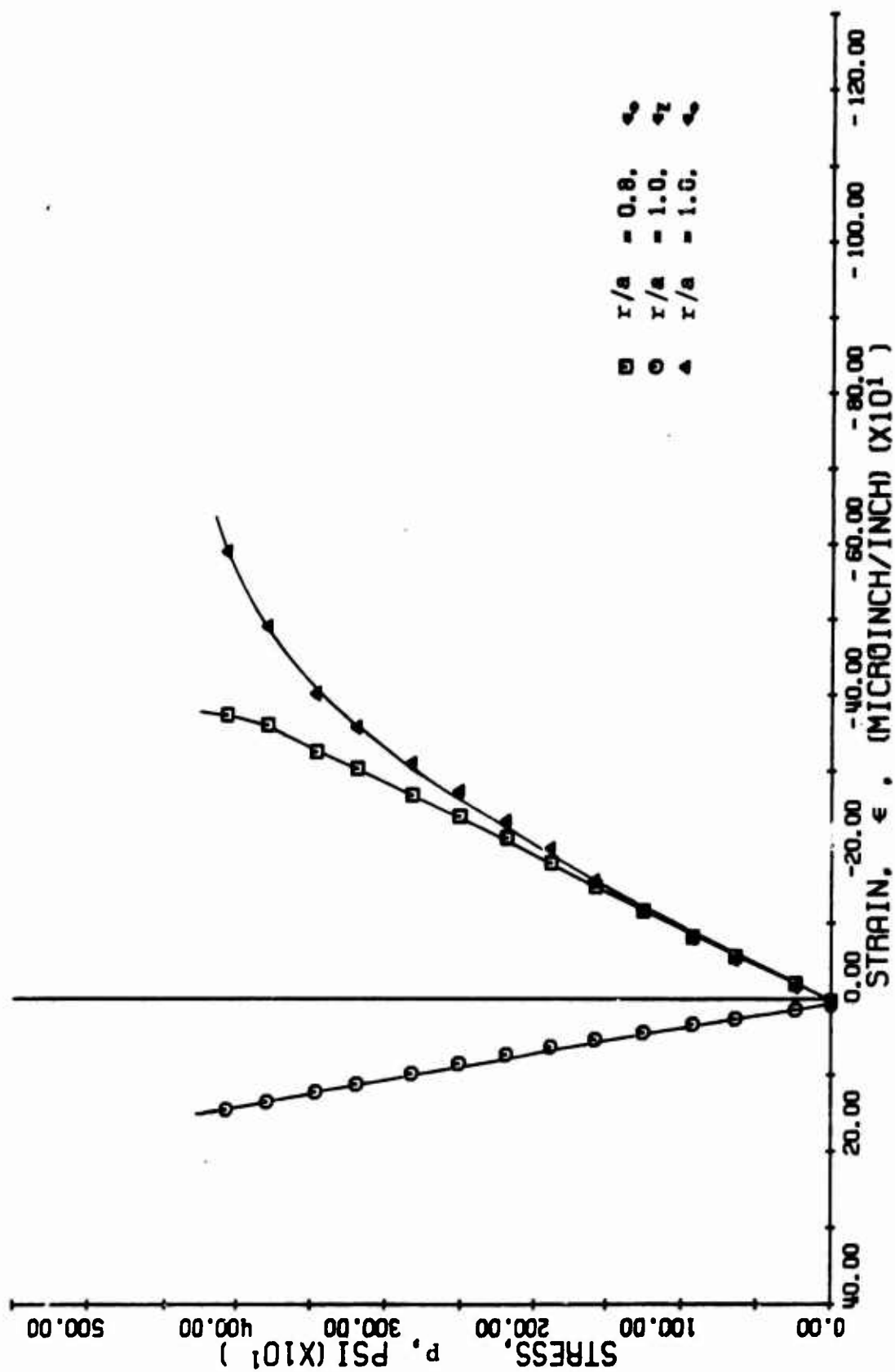
FIG. 163 STRAINS ALONG 45 DEGREE RADIUS FOR SPECIMEN NO. 12
(MARBLE WITH ALUMINUM LINER UNDER UNIAXIAL LOADING)

Principal strains along the 45-degree radius were computed as before and plotted in Fig. 164. The angle between the 45-degree radius and the principal tensile direction measured clockwise varies between 38 degrees and 40 degrees at $r = 1.35a$, 39 degrees and 43 degrees at $r = 1.80a$, and 42 degrees and 44 degrees at $r = 3.00a$.

Strain distributions along the axes of symmetry for specimens No. 11 and No. 12 at $p = 2,000$ psi were plotted in Figs. 165 and 166. Also shown are theoretical values for the interface and inside of the liner. The overall agreement between the two experiments and the theory is good. The maximum tensile stress in the marble at the interface for specimen No. 11 is

$$\sigma_{max} = 4,500 \text{ psi}$$

A similar stress calculation can not be made for specimen No. 12 in which failure started at a point remote from the interface and off the axes of symmetry. However, it can be said that a tensile stress of the order of 5,000 psi was reached at the interface on the vertical axis when cracking started. The maximum tensile stress at the point of crack initiation was of the order of 2,000 psi.

235
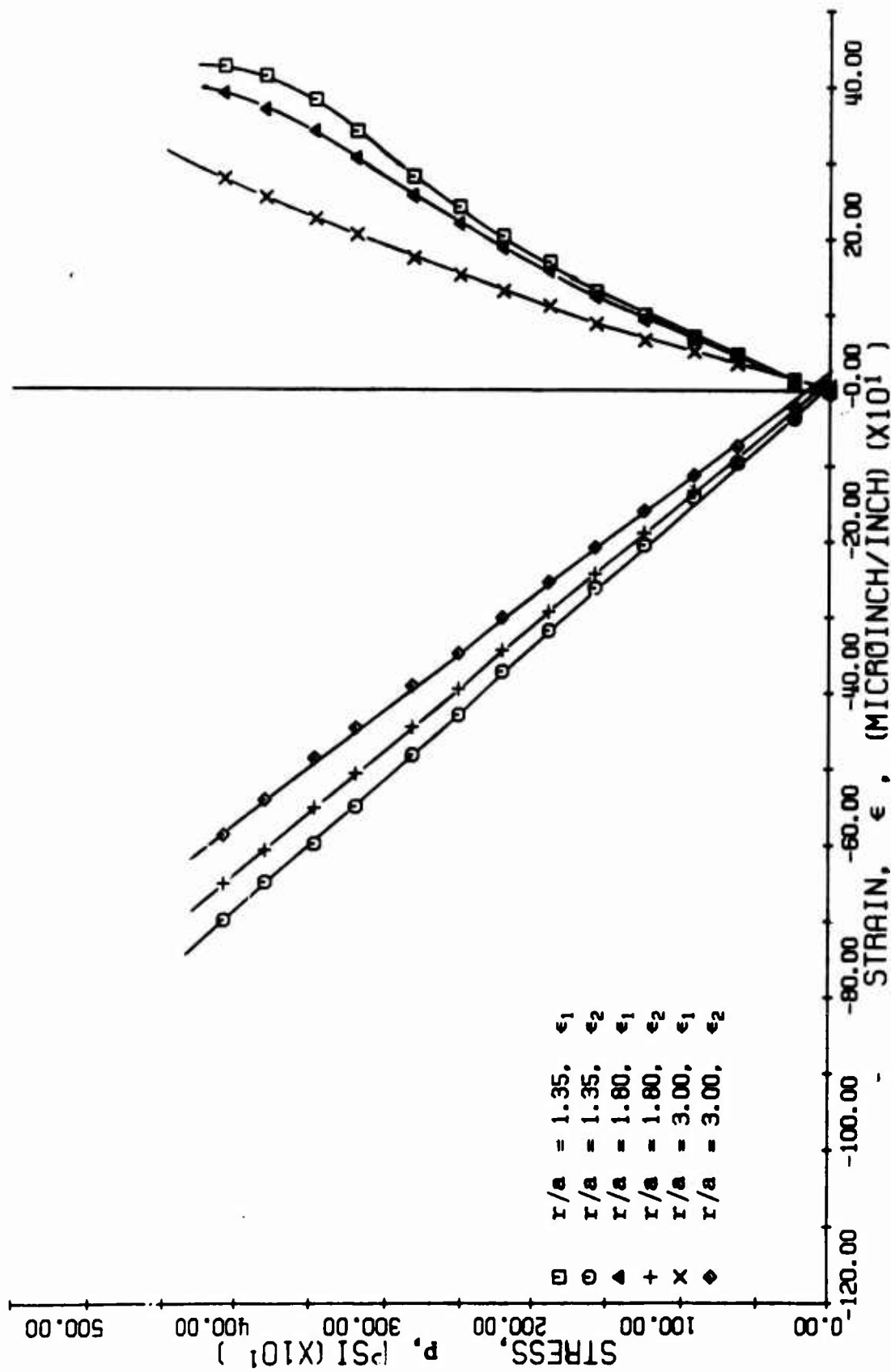
FIG. 164 PRINCIPAL STRAINS ALONG 45-DEGREE RADIUS FOR SPECIMEN NO. 12 (MARBLE WITH ALUMINUM LINER UNDER UNIAXIAL LOADING)

236
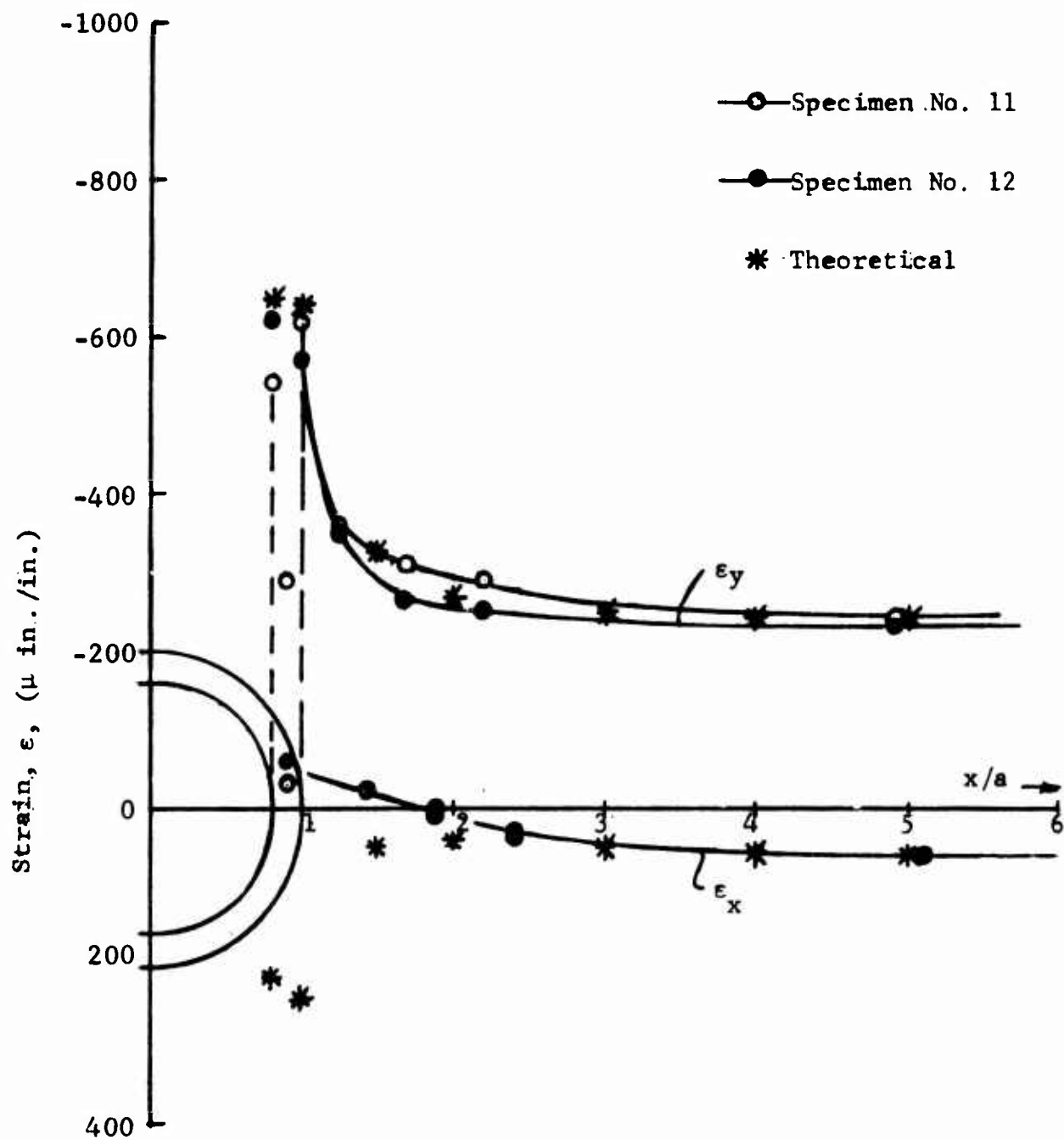
Fig. 165 STRAIN DISTRIBUTION ALONG X-AXIS FOR SPECIMENS NO. 11 AND 12 AT 2,000 PSI APPLIED STRESS (MARBLE WITH ALUMINUM LINER UNDER UNIAXIAL LOADING)
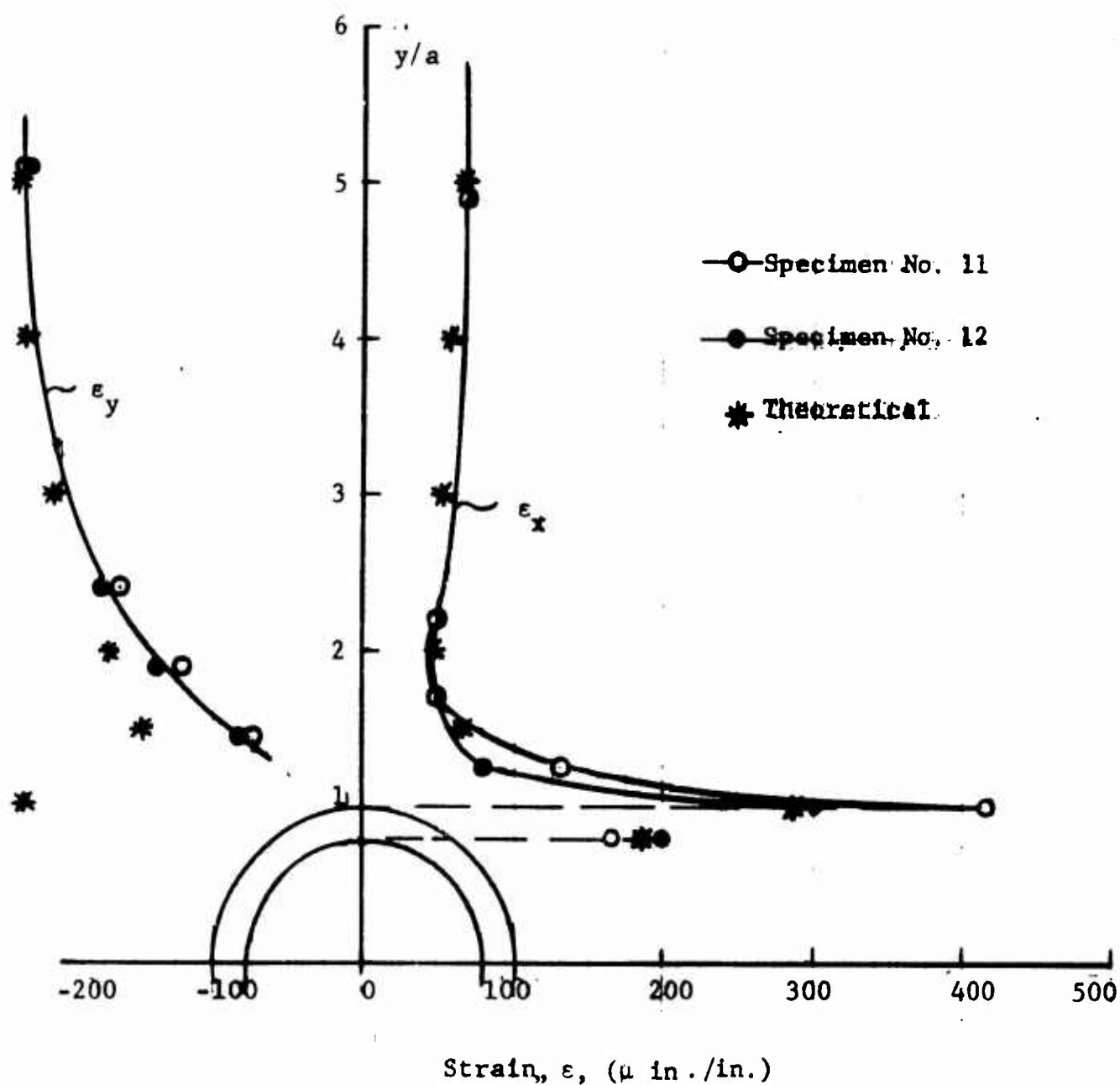
Fig. 166 STRAIN DISTRIBUTION ALONG Y-AXIS FOR SPECIMENS NO.
11 AND 12 AT 2,000 PIS APPLIED STRESS (MARBLE WITH
ALUMINUM LINER UNDER UNIAXIAL LOADING)

SECTION VII

STRESS DISTRIBUTION AND FRACTURE AROUND UNLINED CAVITIES
IN ROCK UNDER BIAXIAL LOADING

1. Specimens No. 13 and No. 14 - Unlined Limestone Under
   Biaxial Loading

   Two limestone plates of dimensions 36 in. x 24 in. x 3.08 in.,
and 36 in. x 24 in. x 2.55 in. with a 4 in. diameter hole were used.
Strain gages were applied along the horizontal and vertical axes of
symmetry and along a 45-degree radius as in previous specimens.
Diametral changes were monitored with two DCDTs inserted in the
cavity along the horizontal and vertical diameters. The overall
surface strain distribution was observed and recorded by means of
a photoelastic coating as described earlier.

   The instrumented specimens were tested in biaxial compression
with the applied horizontal stress equal to one-third the vertical.
The vertical load was applied by means of a 1,000,000 lb testing
machine as before in increments of 20,000 lb. The horizontal
pressure was applied in increments of 333 psi hydraulic pressure
or 10,000 lb lateral load by means of the hydraulic fixture describ-
ed earlier. Strain gage and DCDT readings were recorded with the
Digital Data Acquisition system at every load level. Photoelastic
patterns of the coating were photographed through the opening pro-
vided in the hydraulic fixture.

   Isochromatic fringe patterns for specimen No. 13 are shown
in Fig. 167 for various levels of loading. The applied vertical
and horizontal stresses are shown in each frame. The fringe pat-
terns show a high compressive strain increasing with load up to a
vertical stress of p = 3,220 psi and a horizontal stress of q = 1,100
psi. Failure occurred at a vertical stress of 3,550 psi and a hori-
zontal stress of 1,190 psi. Failure occurred by splitting of the
specimen along vertical planes parallel to the faces (Figs. 168 and
169). This failure is considered typical for materials like rock and

239
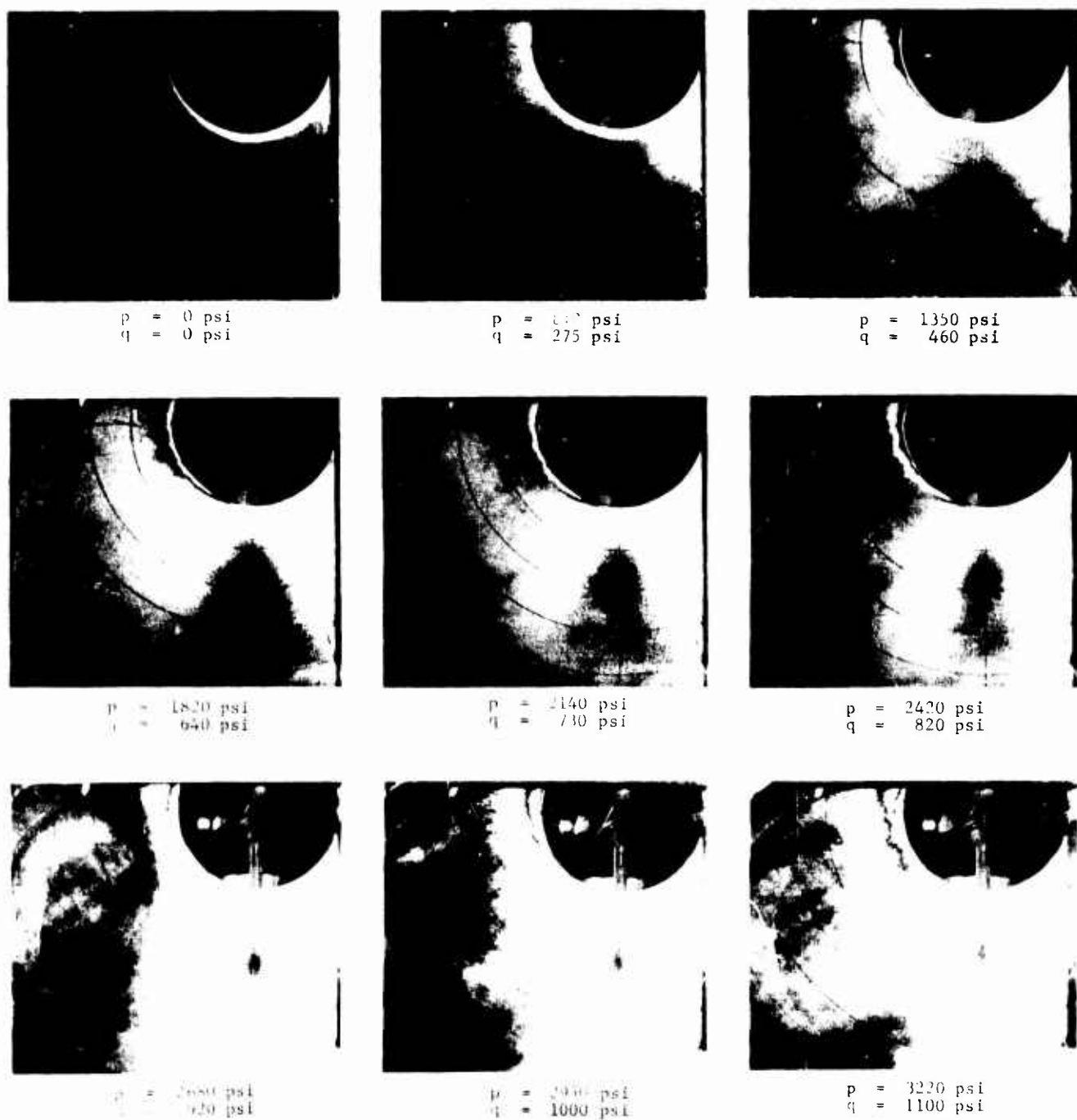
Fig. 167 ISOCHROMATIC FRINGE PATTERNS IN PHOTOELASTIC COATING
AROUND HOLE IN SPECIMEN NO. 13 (LIMESTONE UNLINED
UNDER BIAXIAL LOADING)

240

Fig. 168   TWO VIEWS OF SPECIMEN NO. 13 AFTER FAILURE
(LIMESTONE UNLINED UNDER BIAXIAL LOADING)
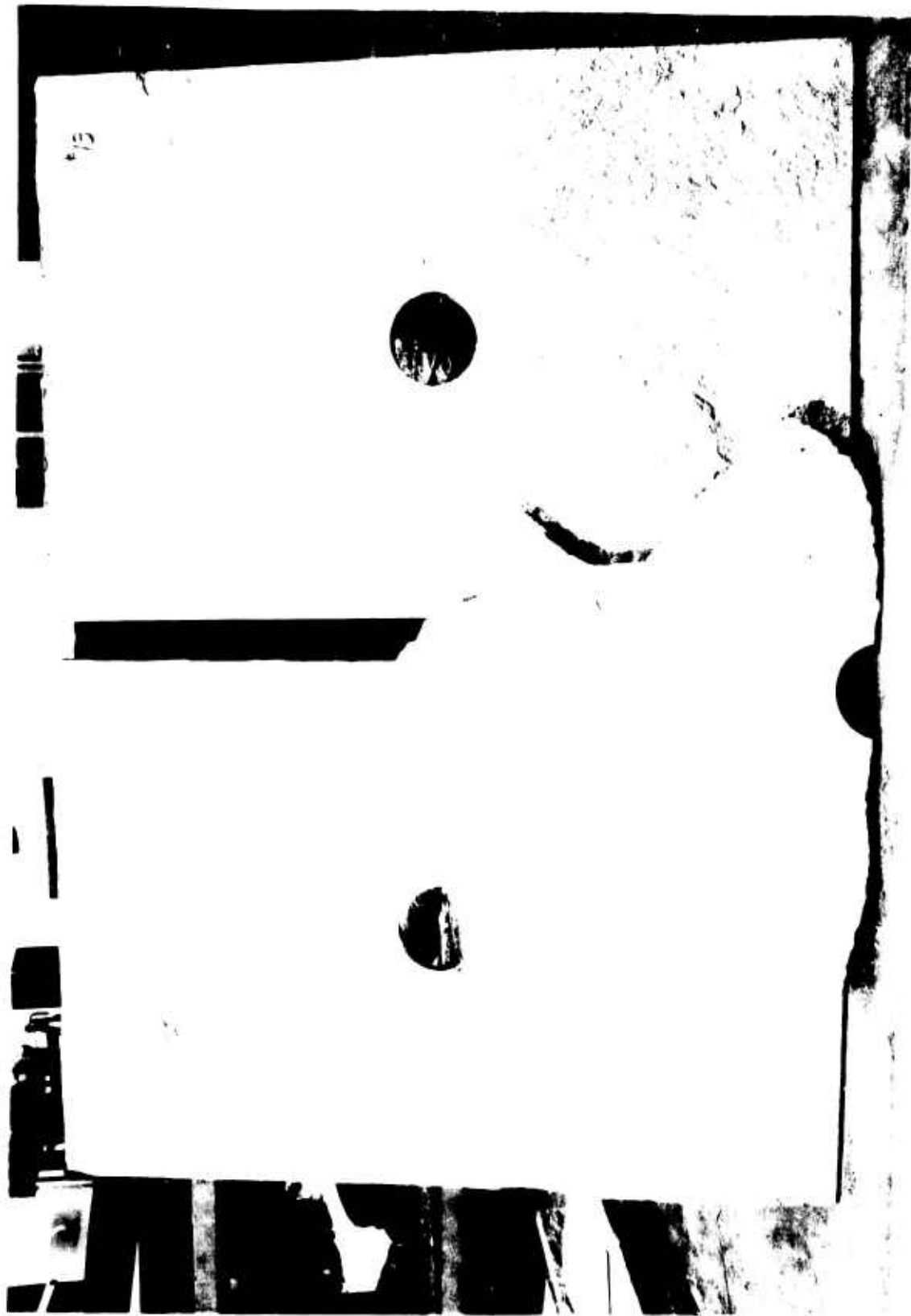
Fig. 169 FAILURE PATTERN OF SPECIMEN NO. 13 (LIMESTONE UNLINED UNDER BIAXIAL LOADING)

concrete. One possible reason for it is the inhomogeneity of the material with presence of higher modulus or lower Poisson's ratio inclusions. The tendency of the specimen under biaxial compression is to expand in the direction normal to the faces or along the axis of the hole (z-axis). The low Poisson's ratio inclusions restrain this lateral tensile strain and therefore are subjected to tensile stress which causes cracking along the x-y plane. The cracking usually occurs at the midplane where local lateral stresses would be higher. In this case, two crack surfaces were produced in one part of the specimen as seen by the splitting of the specimen into three pieces.

The maximum fringe order on the boundary of the hole on the horizontal axis was plotted versus applied vertical stress in Fig. 170. The variation is linear up to approximately 1,800 psi. The maximum compressive strain at p = 1,000 psi. computed from the photoelastic data is

$$(\varepsilon_1)_{p=1,000 \text{ psi}} = 900 \times \frac{1}{1.40} = 650 \, \mu\text{in./in.}$$

Isochromatic fringe patterns for specimen No. 14 are shown in Fig. 171. The last frame was taken after failure which occurred at a vertical stress of p = 4,460 psi and a horizontal stress of q = 1,460 psi. The failure seems to be in shear and it was explosive in nature with the specimen breaking into many fragments (Fig. 172). The fracture seems to have originated near the hole boundary at approximately the 45-degree location and is similar to that predicted by Hoek (Ref. 3). The fracture surfaces are inclined at angles of 30 degrees to 40 degrees from the faces of the specimen.

The maximum fringe order on the hole boundary along a horizontal axis is plotted versus applied vertical stress in Fig. 173. The curve is linear up to approximately 3,000 psi. The photoelastically computed maximum compressive strain at p = 1,000 psi is

$$(\varepsilon_1)_{p=1,000 \text{ psi}} = 900 \times \frac{0.95}{1.40} = 610 \, \mu\text{in./in.}$$

243
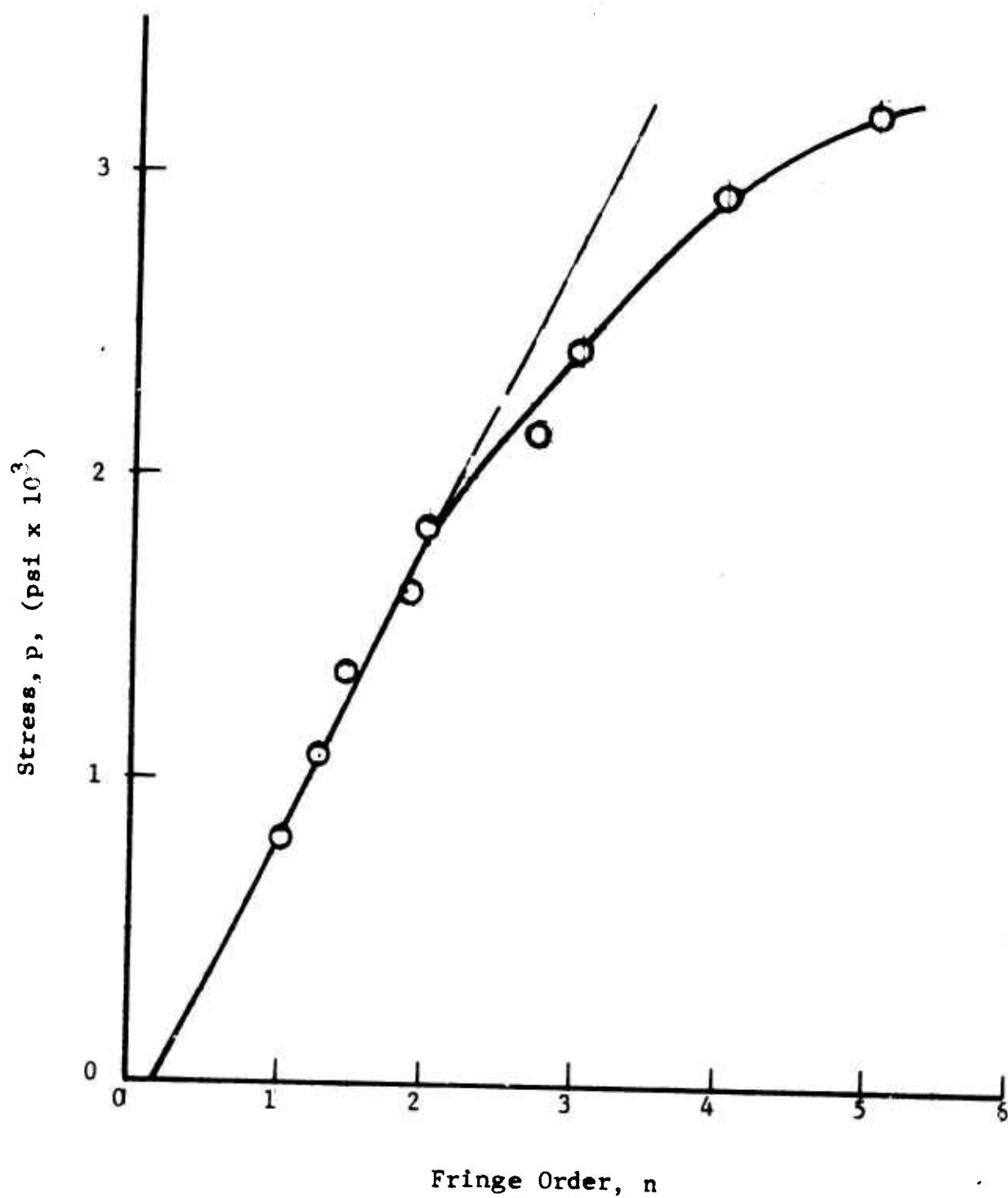
Fig. 170   FRINGE ORDER AT BOUNDARY OF HOLE ALONG HORIZONTAL
AXIS AS A FUNCTION OF APPLIED VERTICAL STRESS
FOR SPECIMEN NO. 13

244

p = 330 psi
q = 110 psi

p = 980 psi
q = 334 psi

p = 1640 psi
q = 560 psi

p = 2260 psi
q = 780 psi

p = 2580 psi
q = 890 psi

p = 2920 psi
q = 1000 psi

p = 3640 psi
q = 1220 psi

p = 3980 psi
q = 1330 psi

p = 4460 psi
q = 1460 psi

Fig. 171   ISOCHROMATIC FRINGE PATTERNS IN PHOTOELASTIC COATING
AROUND HOLE IN SPECIMEN NO. 14   (LIMESTONE UNLINED
UNDER BIAXIAL LOADING)

245

Fig. 172   FAILURE PATTERN IN SPECIMEN NO. 14 (LIMESTONE
UNLINED UNDER BIAXIAL LOADING)
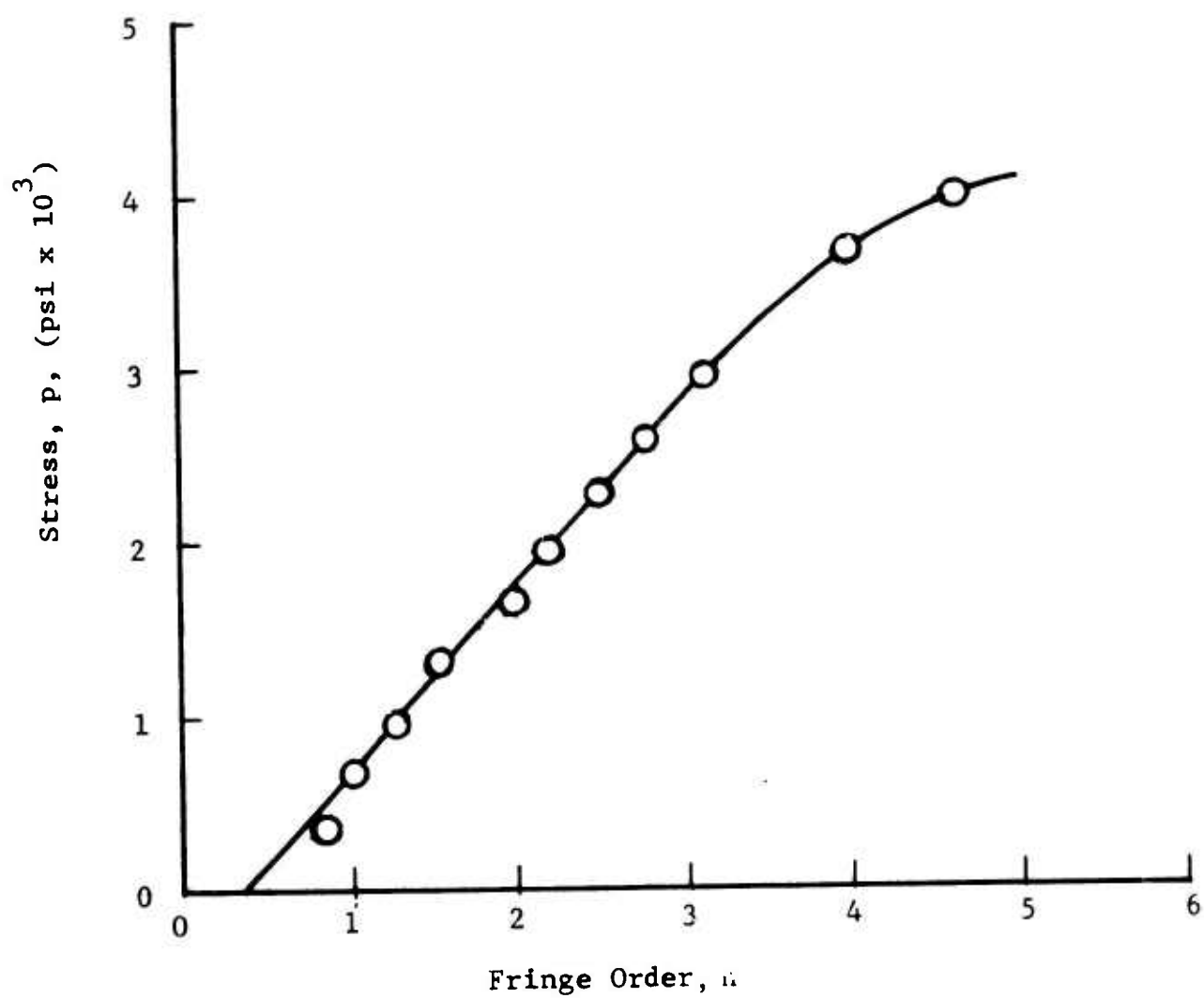
Fig. 173   FRINGE ORDER AT BOUNDARY OF HOLE ALONG HORIZONTAL AXIS
AS A FUNCTION OF APPLIED VERTICAL STRESS FOR SPECIMEN
NO. 14

247

Diametral changes computed from DCDT readings are plotted as a function of applied vertical stress for specimens No. 13 and No. 14 in Figs. 174 and 175. Deflections for specimen No. 13 are linear up to p = 1,700 psi. The deflections per unit vertical stress in the linear range are

$$\frac{\delta_h}{p} = 0.2 \times 10^{-6} \text{ in./psi}$$

$$\frac{\delta_v}{p} = -1.9 \times 10^{-6} \text{ in./psi}$$

In specimen No. 14, the diametral changes are linear up to approximately p = 2,700 psi. Thereafter, they become nonlinear with the horizontal deflection showing a sign reversal and high negative values prior to failure. The deflections per unit stress in the linear range are

$$\frac{\delta_h}{p} = 0.2 \times 10^{-6} \text{ in./psi}$$

$$\frac{\delta_v}{p} = -1.4 \times 10^{-6} \text{ in./psi}$$

The horizontal deflection is negligibly small due to the biaxiality ratio chosen (m = 1/3) which also tends to reduce to zero the stress at the crown and bottom points of the cavity. The vertical deflection under this biaxial loading is also reduced appreciably from the corresponding value under uniaxial loading.

Strains along the axes of symmetry and the 45-degree radius for specimen No. 13 were plotted as a function of applied vertical stress in Figs. 176 through 180. The vertical strains along the horizontal axis (Fig. 176) are linear up to approximately p = 1,600 psi. The ratio between the maximum compressive strain on the hole boundary and the free-field vertical strain is

$$k_\epsilon = 2.77$$

compared to the theoretical value of 2.67 for an infinite plate and a biaxiality ratio of m = 1/3. The maximum compressive strain at

248
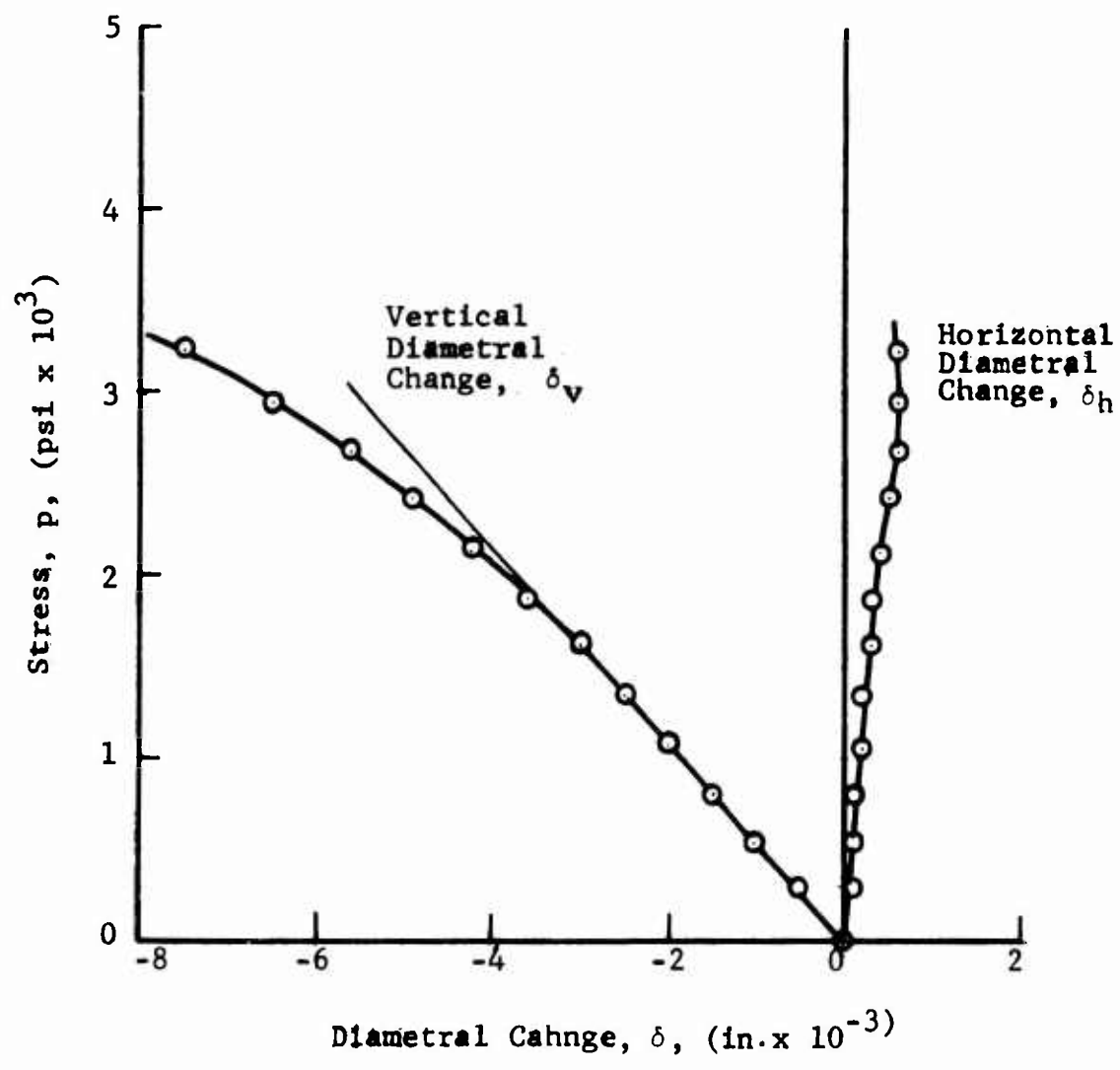
Fig. 174   DIAMETRAL CHANGES AS A FUNCTION OF APPLIED VERTICAL
STRESS FOR SPECIMEN NO. 13
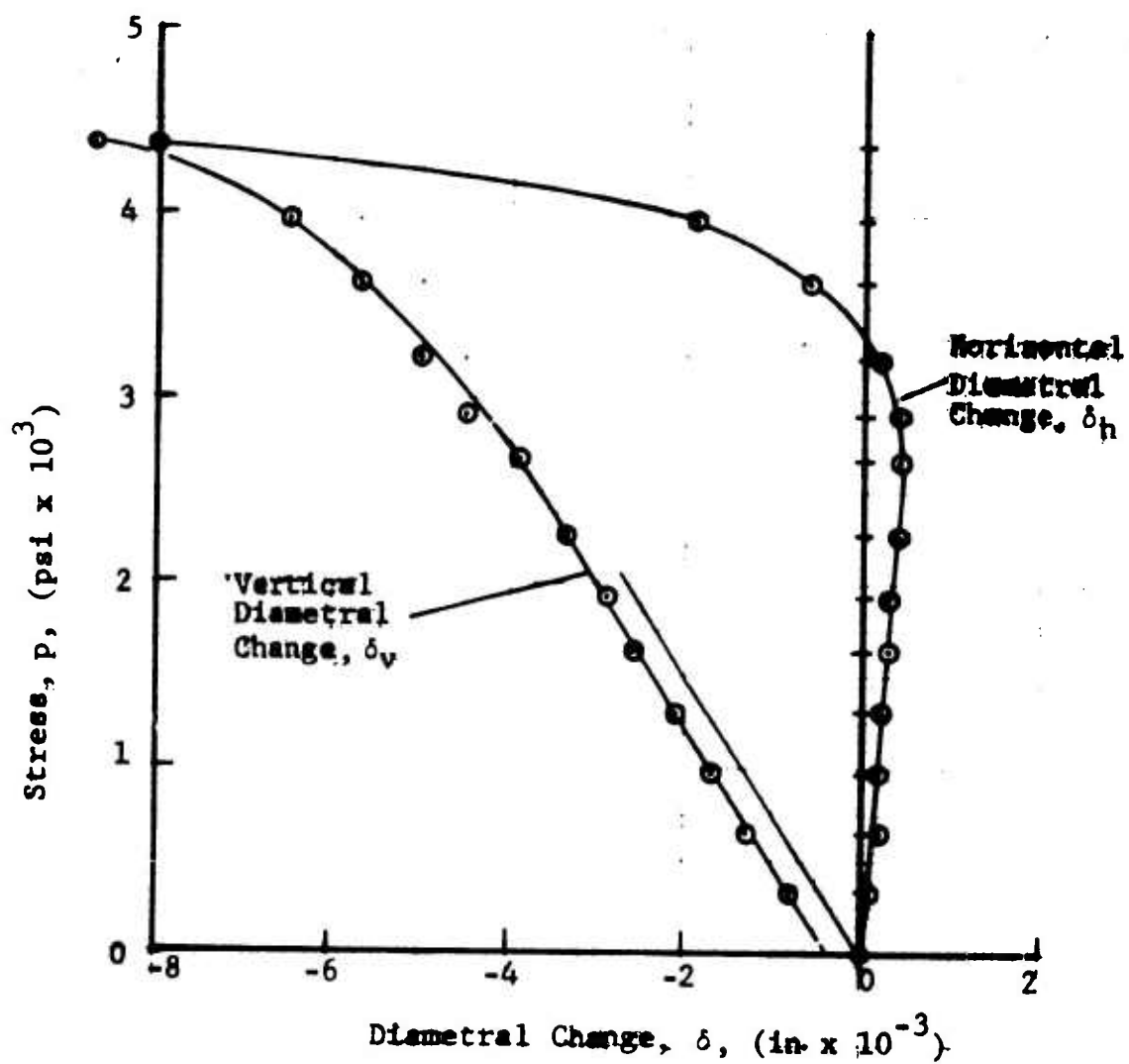
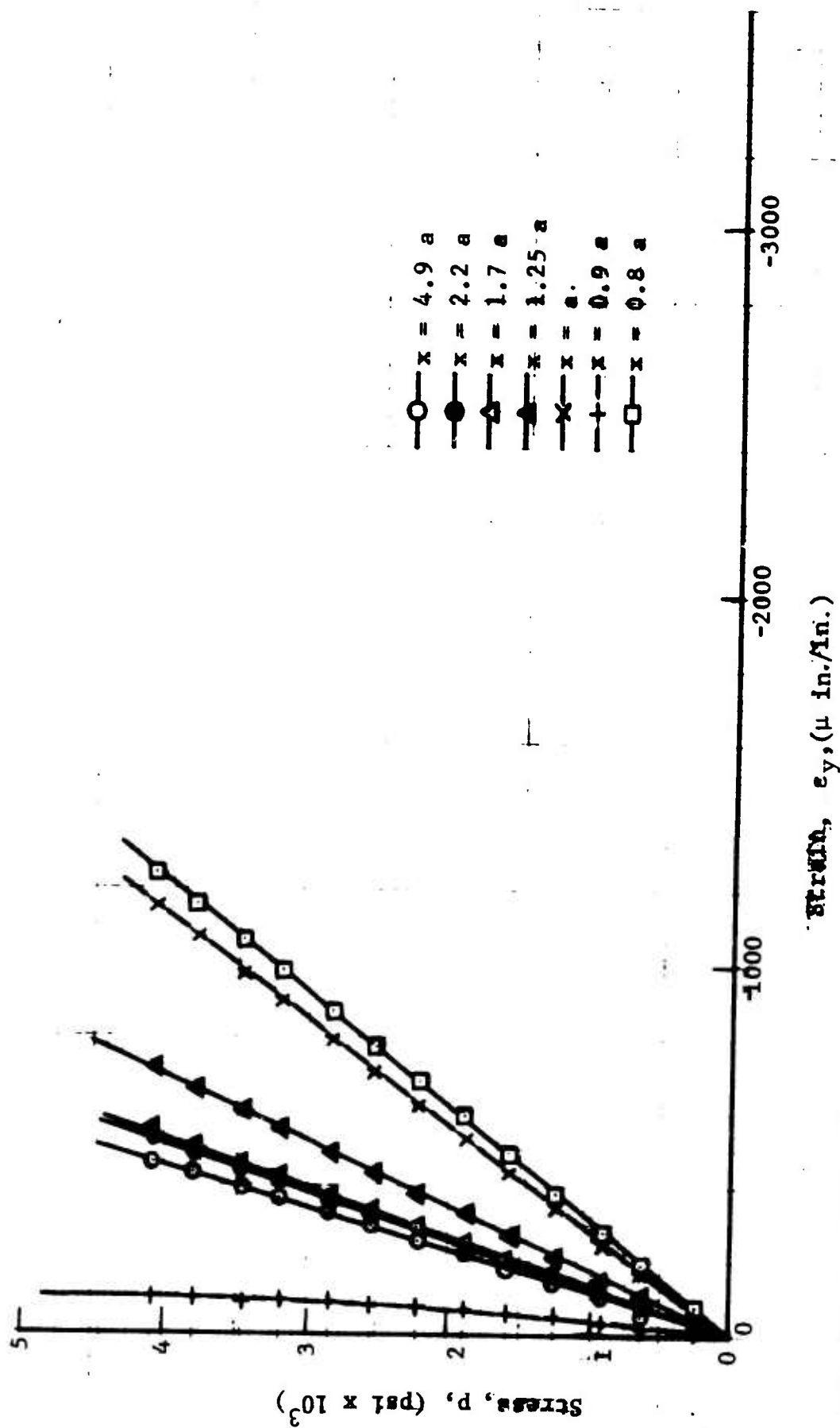Fig. 175 DIAMETRAL CHANGES AS A FUNCTION OF APPLIED VERTICAL
STRESS FOR SPECIMEN NO. 14
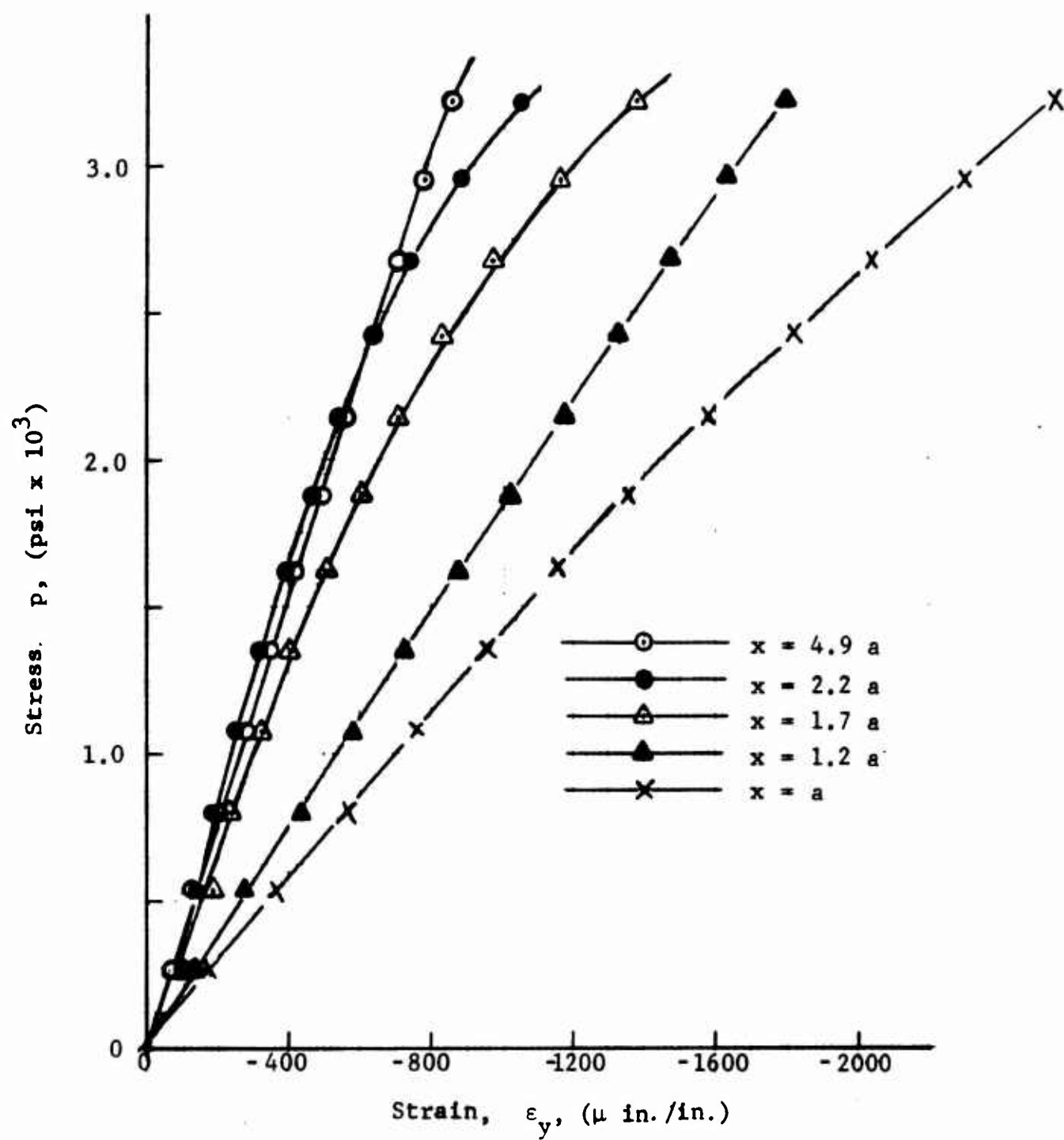
Fig. 176   VERTICAL STRAINS ALONG HORIZONTAL AXIS OF SYMMETRY
AS A FUNCTION OF APPLIED VERTICAL STRESS FOR SPECIMEN
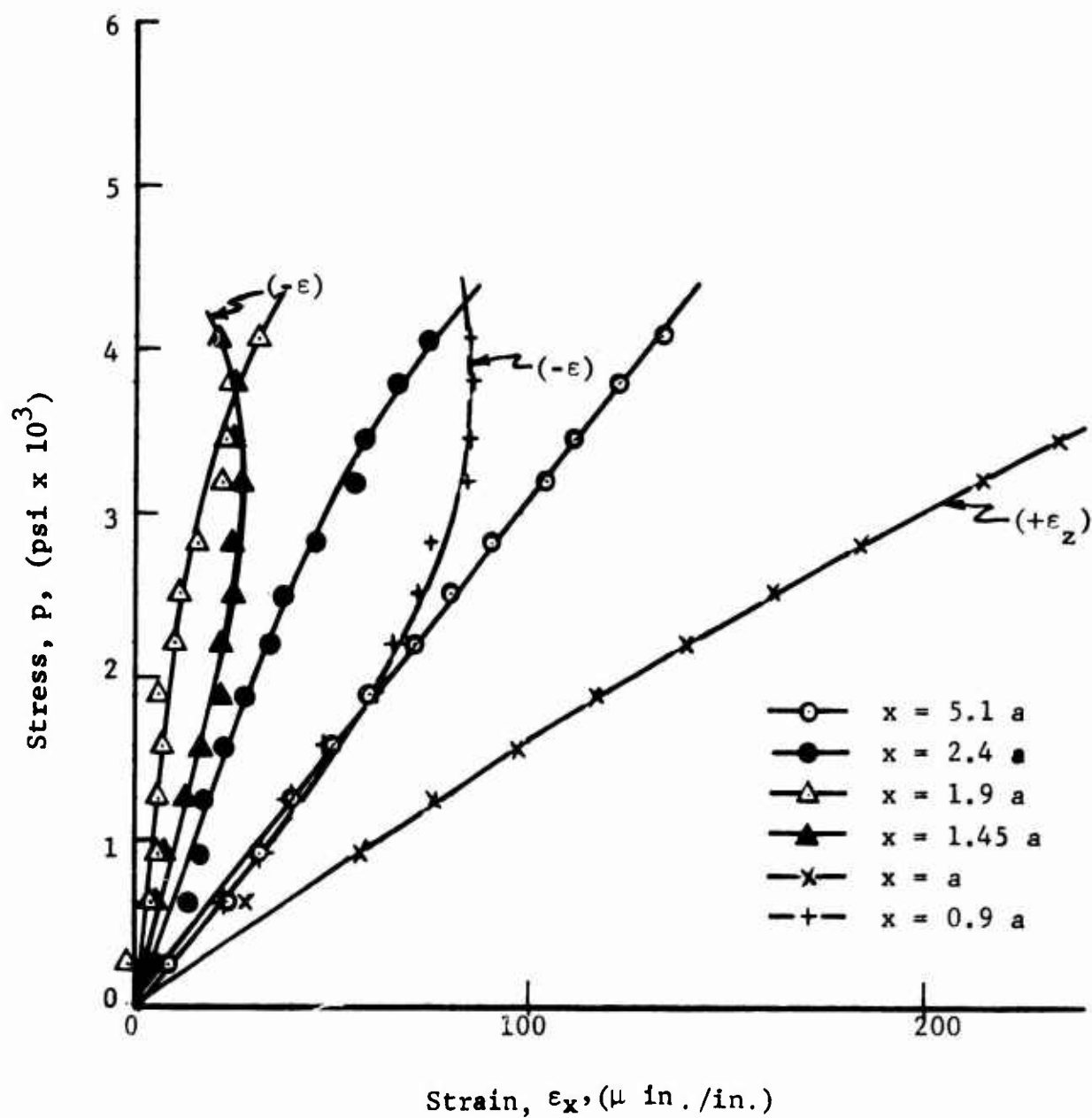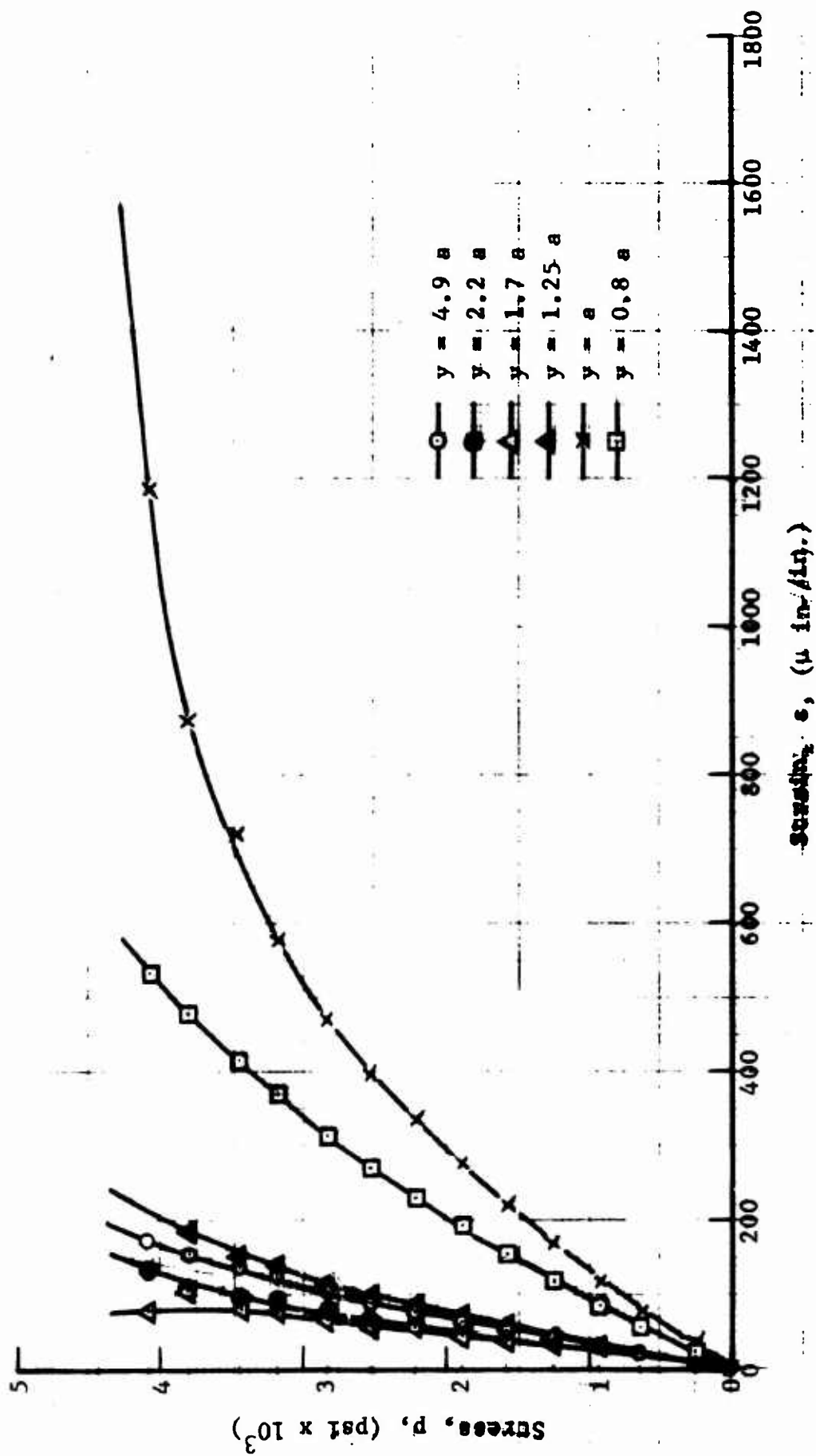NO. 13 (LIMESTONE UNLINED UNDER BIAXIAL LOADING)
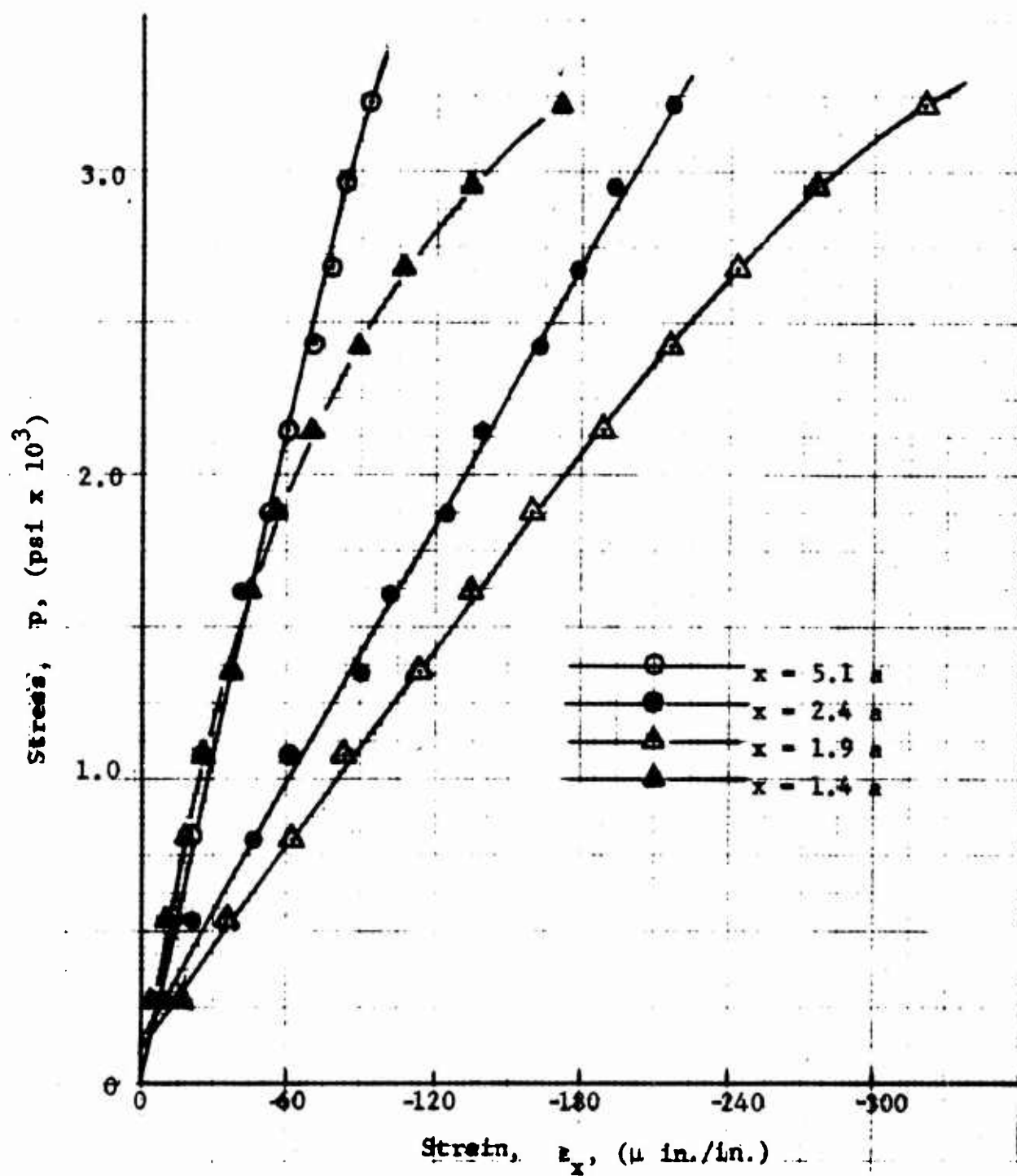
Fig. 177   HORIZONTAL STRAINS ALONG HORIZONTAL AXIS OF SYMMETRY
AS A FUNCTION OF APPLIED VERTICAL STRESS FOR SPECIMEN
NO. 13 (LIMESTONE UNLINED UNDER BIAXIAL LOADING)

2 ‒ 6 252
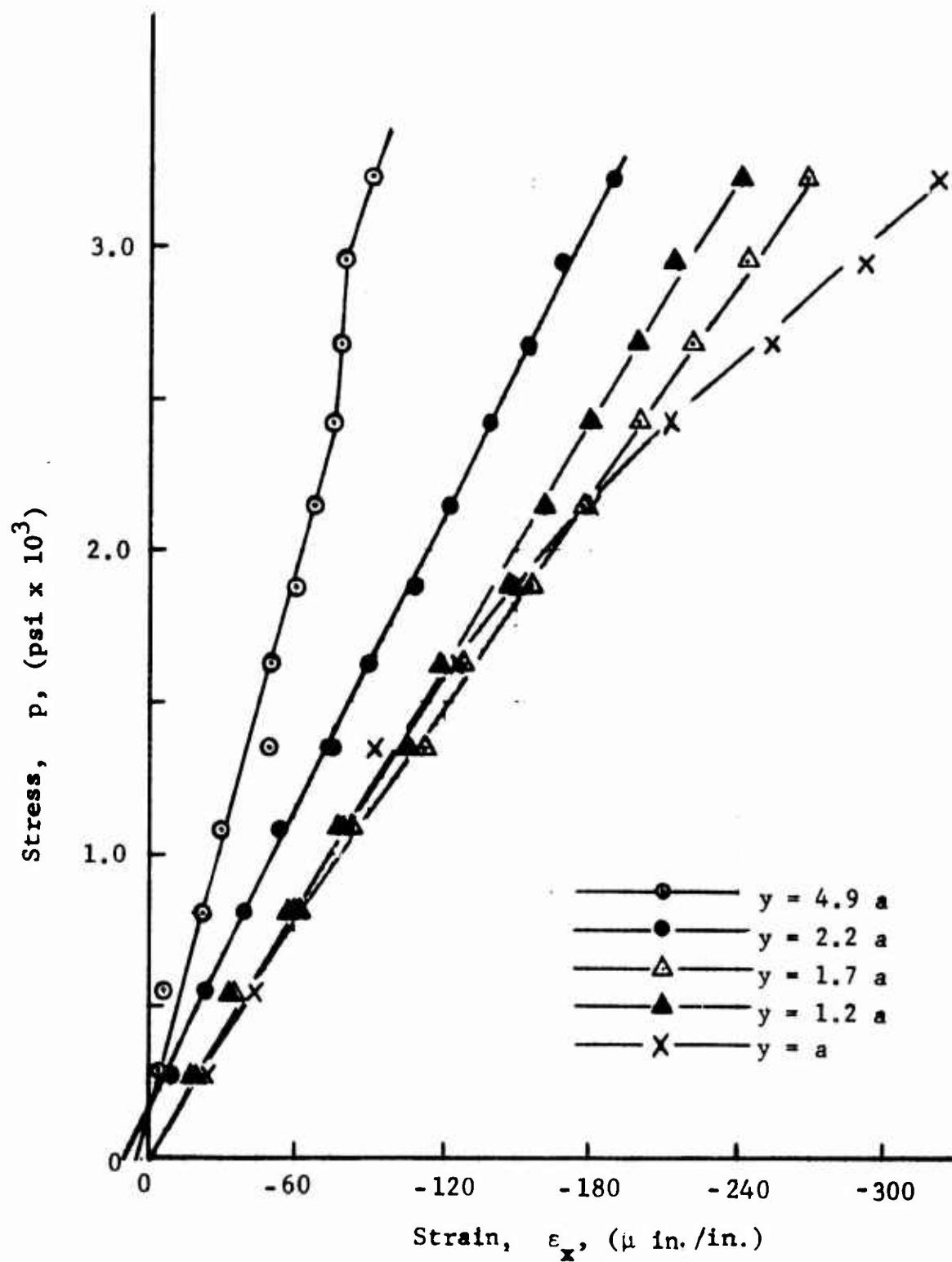
Fig. 178   HORIZONTAL STRAINS ALONG VERTICAL AXIS OF SYMMETRY
AS A FUNCTION OF APPLIED VERTICAL STRESS FOR SPECIMEN
NO. 13 (LIMESTONE UNLINED UNDER BIAXIAL LOADING)

253

Fig. 79 VERTICAL STRAINS ALONG VERTICAL AXIS OF SYMMETRY AS A FUNCTION OF APPLIED VERTICAL STRESS FOR SPECIMEN NO. 13 (LIMESTONE UNLINED UNDER BIAXIAL LOADING.

254

FIG. 180 STRAINS ALONG 45-DEGREE RADIUS FOR SPECIMEN NO.13
(LIMESTONE UNLINED UNDER BIAXIAL LOADING)

the hole boundary at p = 1,000 psi is 720 μin./in. which is slightly higher than the photoelastic result. The horizontal strains along the vertical axis are negative and fairly linear for the most part except for the strain at the hole boundary which is positive and becomes nonlinear at approximately p = 1,600 psi. Principal strains along the 45-degree radius were computed from the rosette readings and plotted in Fig. 181. The angle between the 45-degree radius and the principal direction of ε_1, measured clockwise, varies between 24 degrees and 27 degrees at r = 1.35a, and between 38 degrees and 39 degrees at r = 3.00a.

Strains along the axes of symmetry and the 45-degree radius for specimen No. 14 were plotted as a function of applied vertical stress in Figs. 182 through 186. The vertical strains along the horizontal axis are linear up to approximately p = 2,000 psi at the hole boundary and up to higher loads (p = 3,000 psi) away from the hole. The ratio between the maximum compressive strain on the hole boundary and the free-field vertical strain is

$$k_\varepsilon = 3.15$$

compared with the theoretical value of 2.67. The maximum compressive strain at the hole boundary at p = 1,000 psi is 700 μin./in. which is somewhat higher than the photoelastically computed strain. The horizontal strains along the vertical axis show some nonlinearities at low stresses, but they are not necessarily significant due to the low level of the strains. All of these strains are negative except for the ε_z strain on the boundary of the hole. Principal strains on the 45-degree radius were computed as before and plotted in Fig. 187. The angle between the 45-degree radius and the principal direction of ε_1, measured clockwise, varies between 22 degrees and 23 degrees at r = 1.35a.

The strain distribution along the x-axis at an applied vertical stress of 1,000 psi (within the linear range) for specimens No. 13 and No. 14 was plotted in Fig. 188. The theoretical distribution for an infinite plate under similar biaxial conditions and a modulus of 4×10^6 psi and a Poisson's ratio of 0.23 is also shown. The agreement between the two experiments and the theory is satisfactory.

256
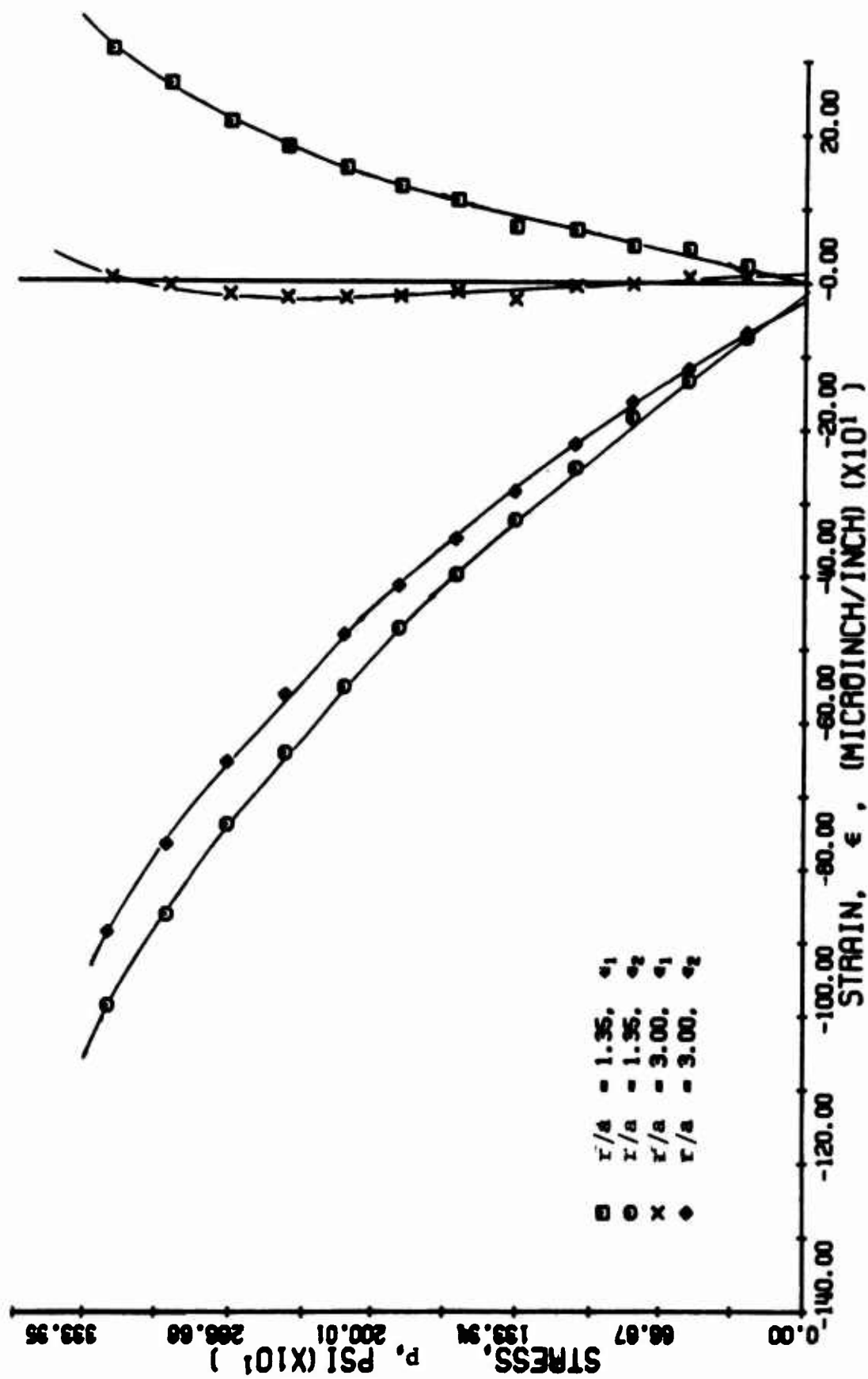
FIG. 181 PRINCIPAL STRAINS ALONG 45-DEGREE RADIUS FOR SPECIMEN NO. 13
(LIMESTONE UNLINED UNDER BIAXIAL LOADING)

257
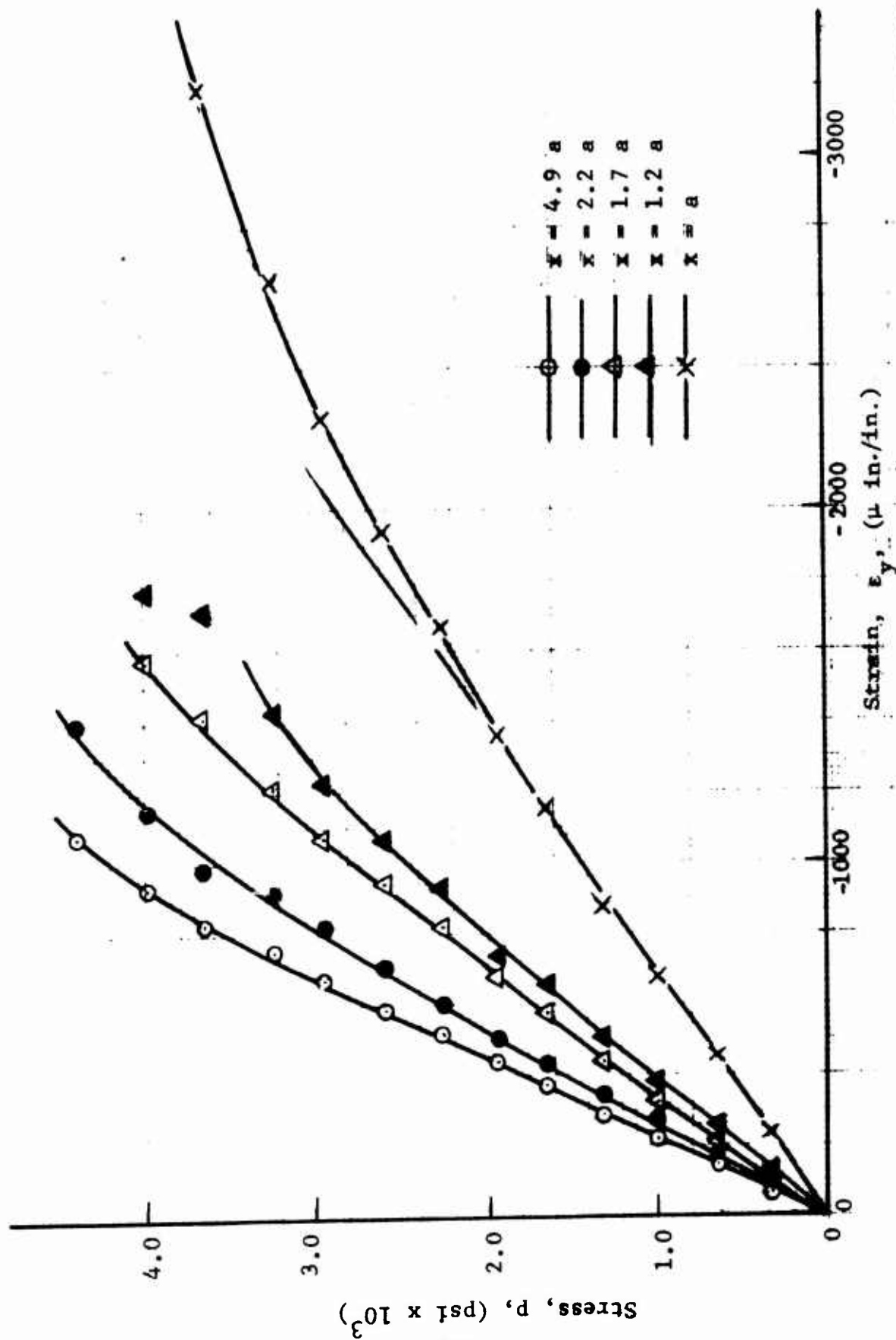
Fig. 182   VERTICAL STRAINS ALONG HORIZONTAL AXIS OF SYMMETRY AS A FUNCTION OF APPLIED VERTICAL STRESS FOR SPECIMEN NO. 14 (LIMESTONE UNLINED UNDER BIAXIAL LOADING)

Fig. 133   HORIZONTAL STRAINS ALONG HORIZONTAL AXIS OF SYMMETRY
AS A FUNCTION OF APPLIED VERTICAL STRESS FOR SPECIMEN
NO. 14 (LIMESTONE UNLINED UNDER BIAXIAL LOADING)

259
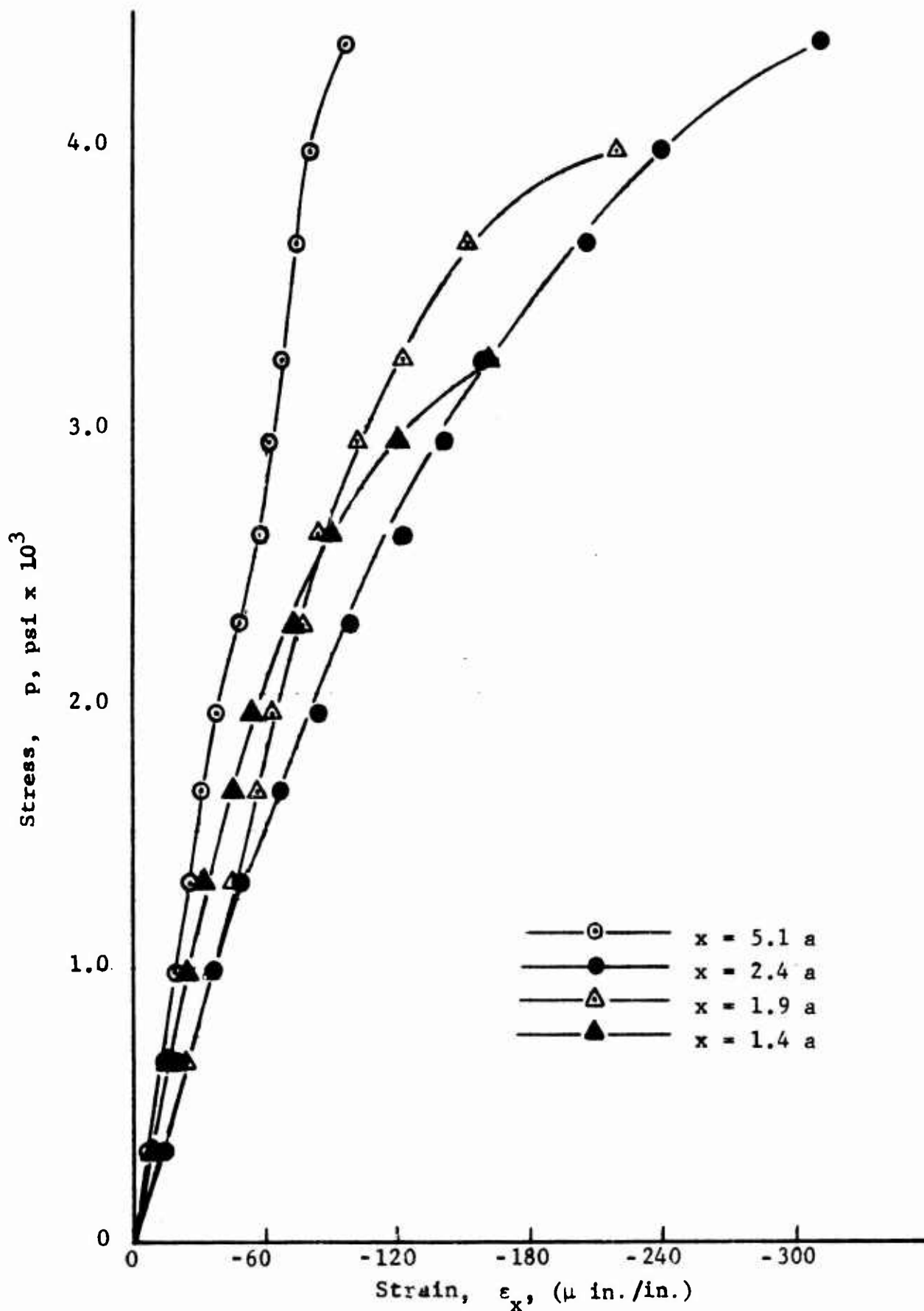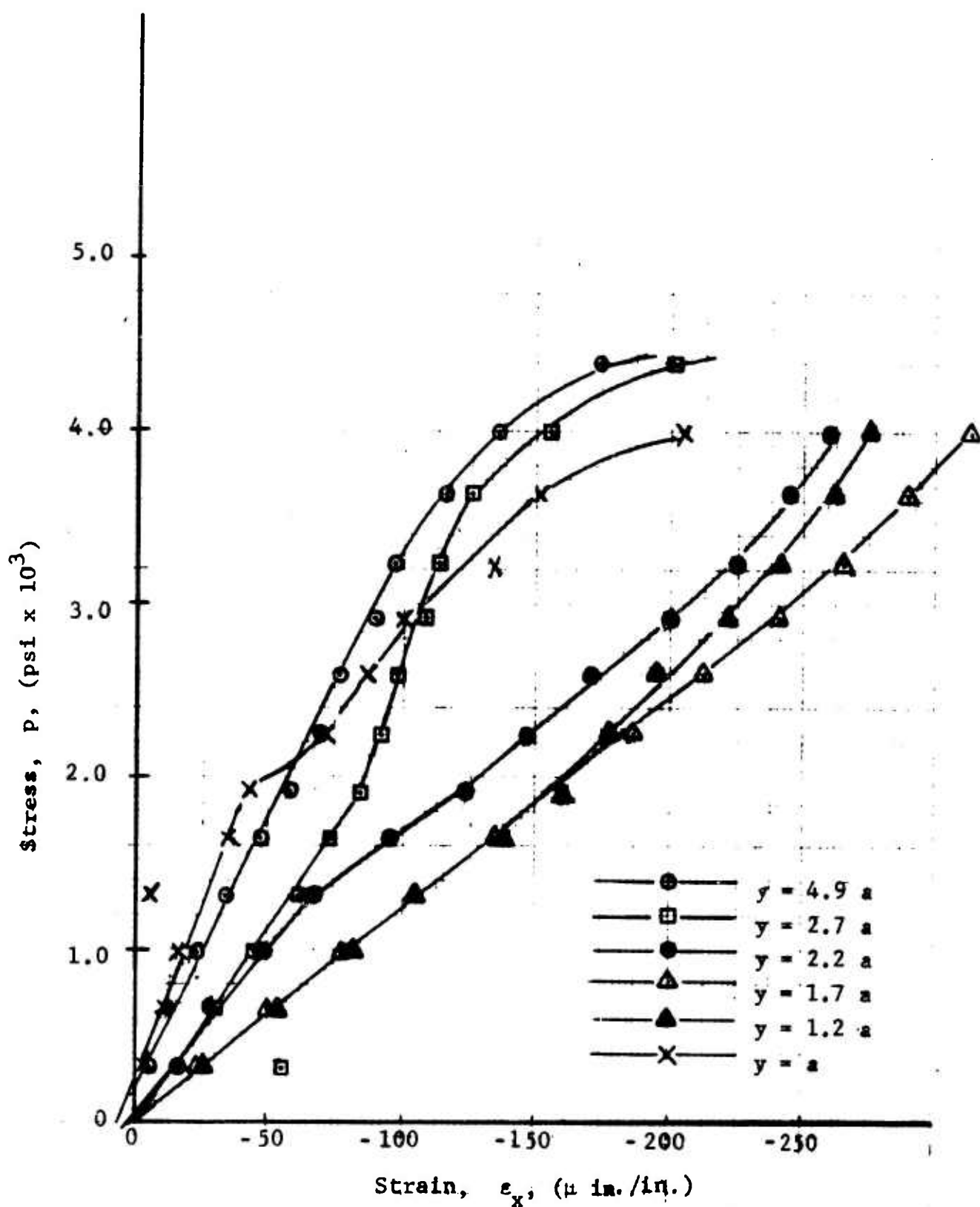
Fig. 184   HORIZONTAL STRAINS ALONG VERTICAL AXIS OF SYMMETRY
AS A FUNCTION OF APPLIED VERTICAL STRESS FOR SPECIMEN
NO. 14 (LIMESTONE UNLINED UNDER BIAXIAL LOADING)

260
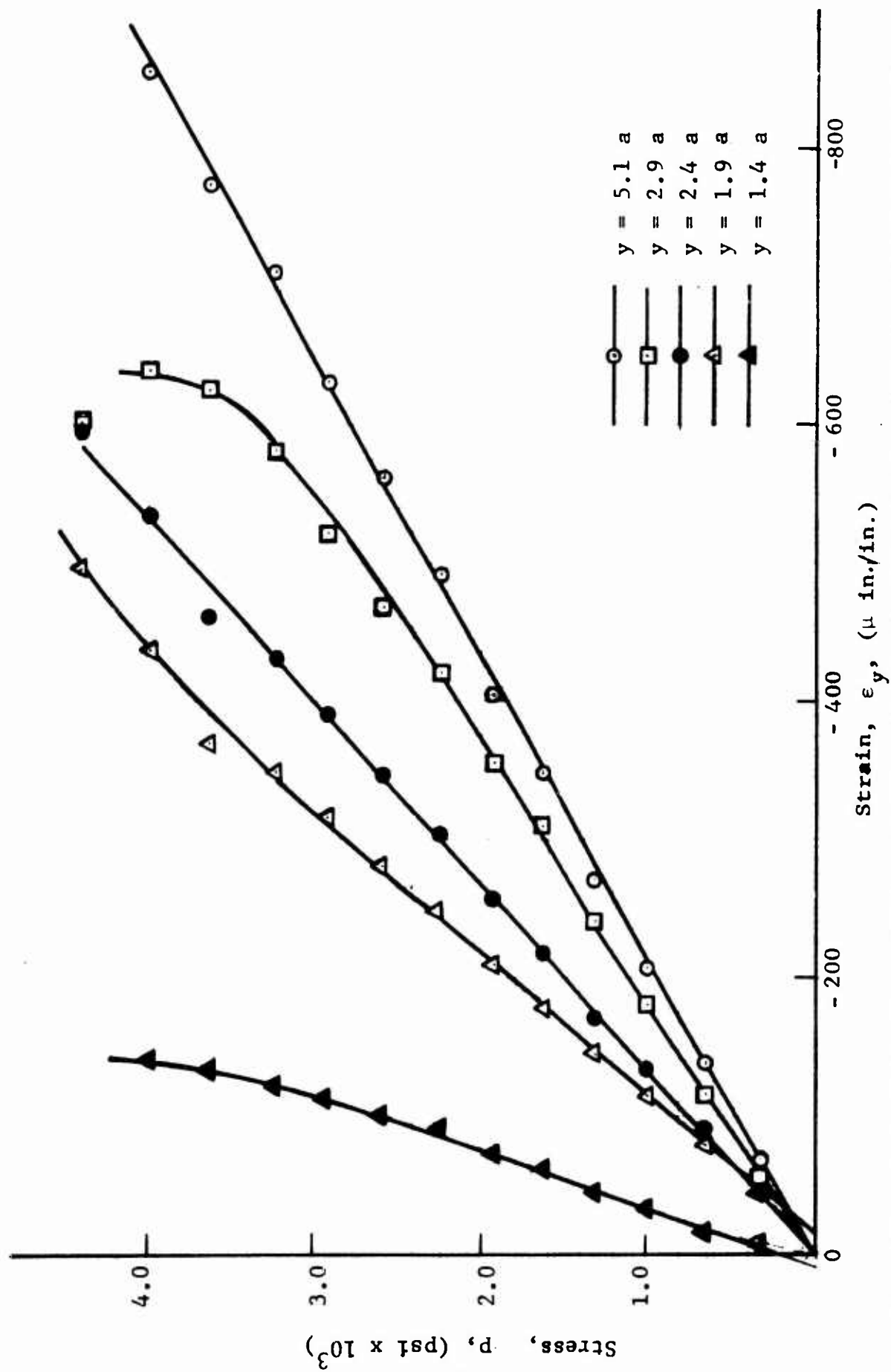
Fig. 185   VERTICAL STRAINS ALONG VERTICAL AXIS OF SYMMETRY AS A FUNCTION OF APPLIED VERTICAL
STRESS FOR SPECIMEN NO. 14 (LIMESTONE UNLINED UNDER BIAXIAL LOADING)

261
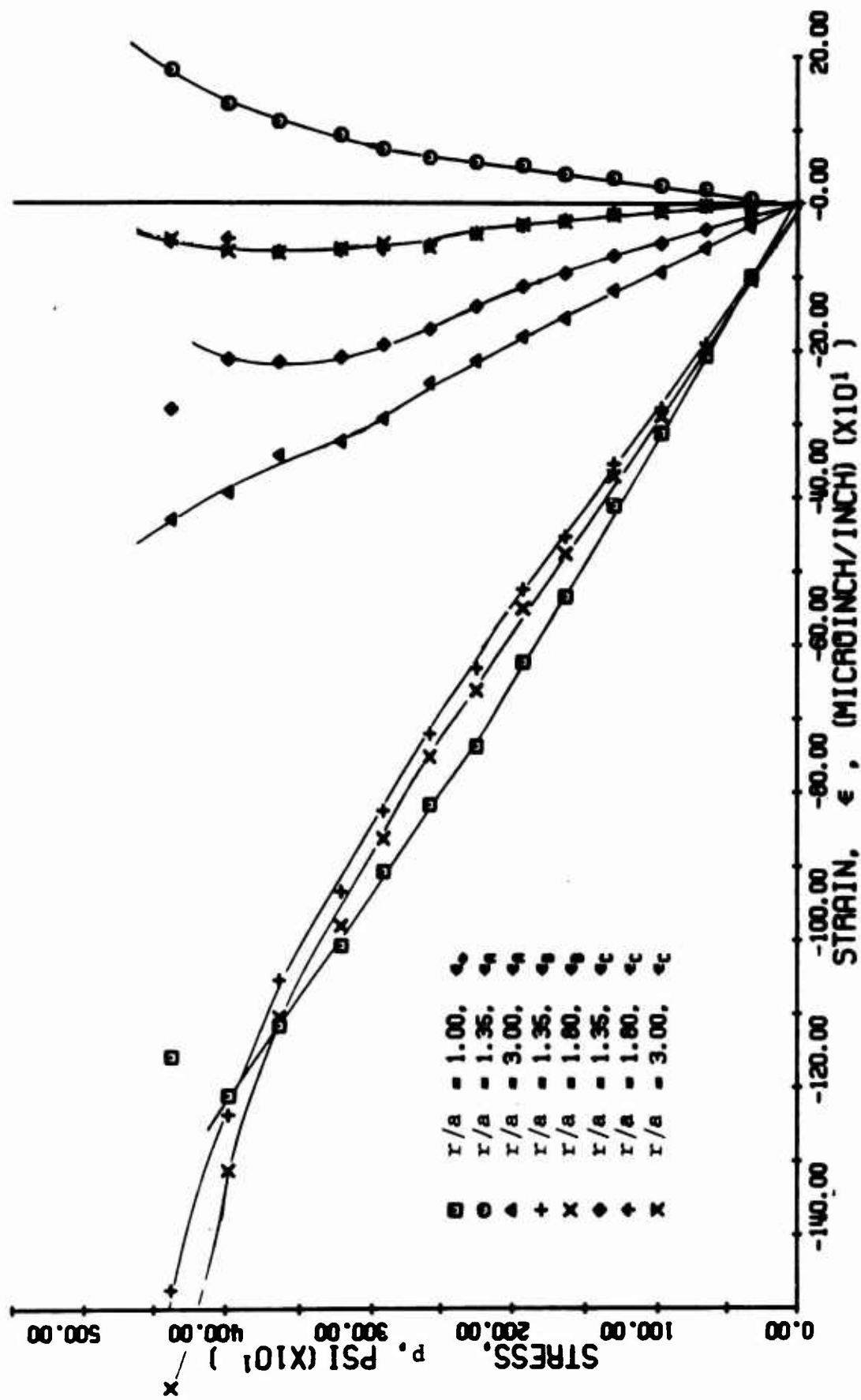
FIG. 186 STRAINS ALONG 45-DEGREE RADIUS FOR SPECIMEN NO.14
(LIMESTONE UNLINED UNDER BIAXIAL LOADING)

FIG. 187 PRINCIPAL STRAINS ALONG 45-DEGREE RADIUS FOR SPECIMEN NO. 14
(LIMESTONE UNLINED UNDER BIAXIAL LOADING)

263

Fig. 188 STRAIN DISTRIBUTION ALONG HORIZONTAL AXIS OF SYMMETRY
FOR SPECIMENS NO. 13 AND 14 AT 1,000 PSI APPLIED
VERTICAL STRESS (LIMESTONE UNLINED UNDER BIAXIAL LOADING)

264

2. Specimens No. 15 and 16 - Unlined Marble Under Biaxial Loading

Two marble specimens of dimensions 36 in. x 24 in. x 3.12 in. with a 4 in. diameter hole were instrumented and tested similarly as specimens No. 13 and 14. The vertical load was applied in increments of 30,000 lb and the hydraulic pressure for lateral load increments of 15,000 lb. Thus, a free-field horizontal stress equal to 0.34 of the vertical stress was obtained.

Specimen No. 15 was tested in the load increments mentioned above up to a vertical load of 272,000 lb and a hydraulic pressure of 4,500 psi when a connection in the fluid line failed. The sudden reduction in lateral pressure caused a small vertical crack to appear along the vertical axis, similar to that which occurred in unlined specimens under uniaxial loading. Subsequently, the test was rerun up to a vertical load of 410,000 lb and a lateral load of 210,000 lb when another hydraulic fitting failed resulting in sudden reduction of the lateral pressure and further cracking of the model. The hydraulic system was repaired and a third loading was carried to the rated capacity of the system, a vertical load of 600,000 lb and a lateral load of 300,000 lb. No additional failure of the specimen was observed.

Diametral changes are plotted in Fig. 189. The vertical deflection per unit vertical stress, linear up to approximately 3,300 psi, is

$$\frac{\delta_v}{p} = -0.82 \times 10^{-6} \text{ in./psi}$$

which is approximately half of that in the corresponding limestone specimen due to the fact that marble has twice as high a modulus. The horizontal deflection is almost zero throughout the test.

Strains along the axes of symmetry and the 45-degree radius for specimen No. 15 are plotted in Figs. 190 through 194. The vertical strains along the horizontal axis show some nonlinearity at a stress as low as $p = 1,100$ psi. The ratio of the maximum compressive strain on the hole boundary to the free-field strain is

$$k_\varepsilon = 2.74$$
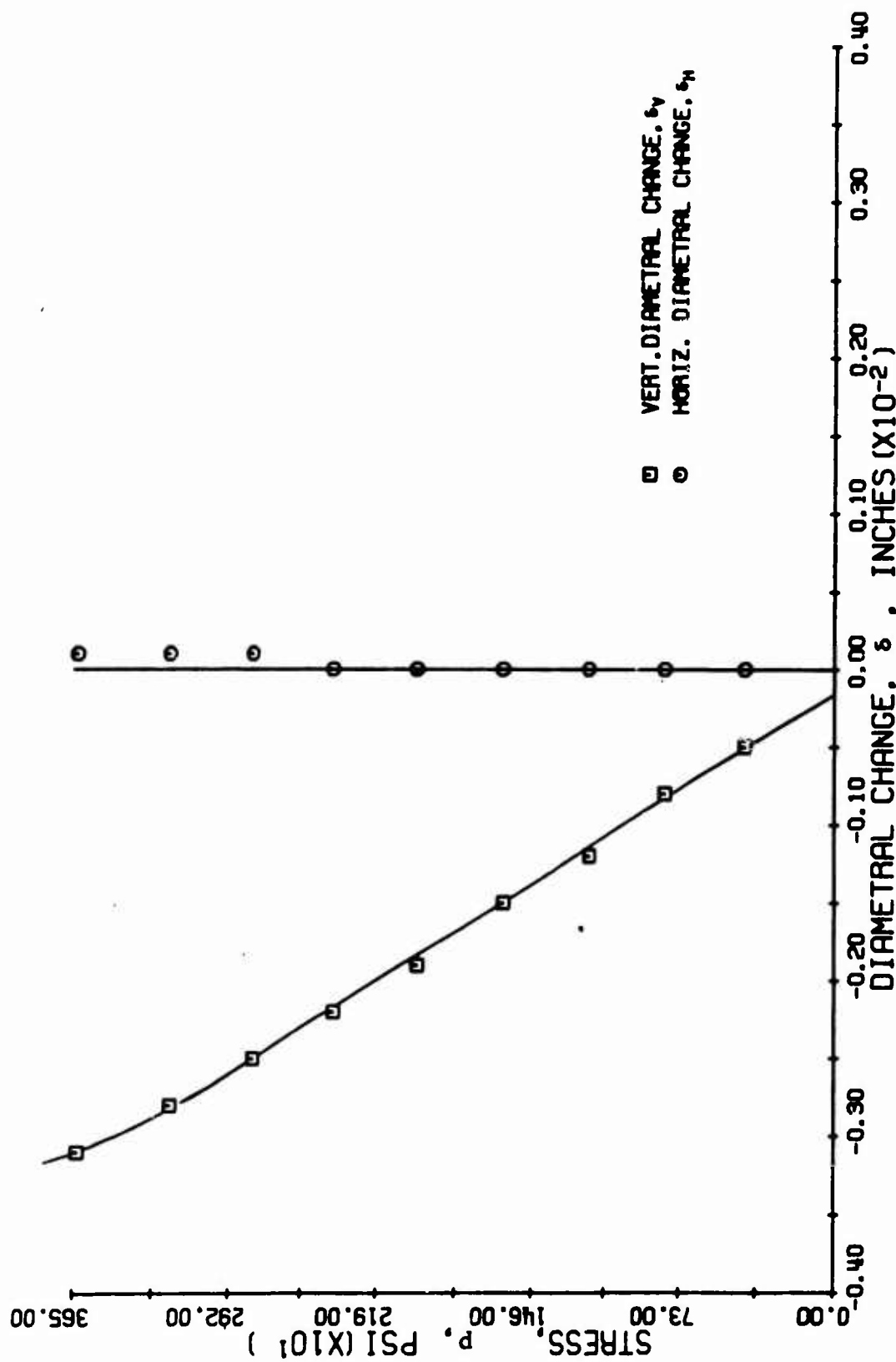
FIG. 189 DIAMETRAL CHANGES AS A FUNCTION OF APPLIED VERTICAL STRESS FOR SPECIMEN
NO.15 (MARBLE UNLINED UNDER BIAXIAL LOADING)

FIG. 190 VERTICAL STRAINS ALONG HORIZONTAL AXIS OF SYMMETRY AS A FUNCTION OF APPLIED VERTICAL STRESS FOR SPECIMEN NO.15 (MARBLE UNLINED UNDER BIAXIAL LOADING)

FIG. 191 HORIZONTAL STRAINS ALONG HORIZONTAL AXIS OF SYMMETRY AS A FUNCTION OF APPLIED VERTICAL
STRESS FOR SPECIMEN NO.15 UNMARBLE UNLINED UNDER BIAXIAL LOADING)

268

FIG. 192 HORIZONTAL STRAINS ALONG VERTICAL AXIS OF SYMMETRY AS A FUNCTION OF APPLIED VERTICAL STRESS FOR SPECIMEN NO.15 (MARBLE WITH NO LINER UNDER BIAXIAL LOADING)

269
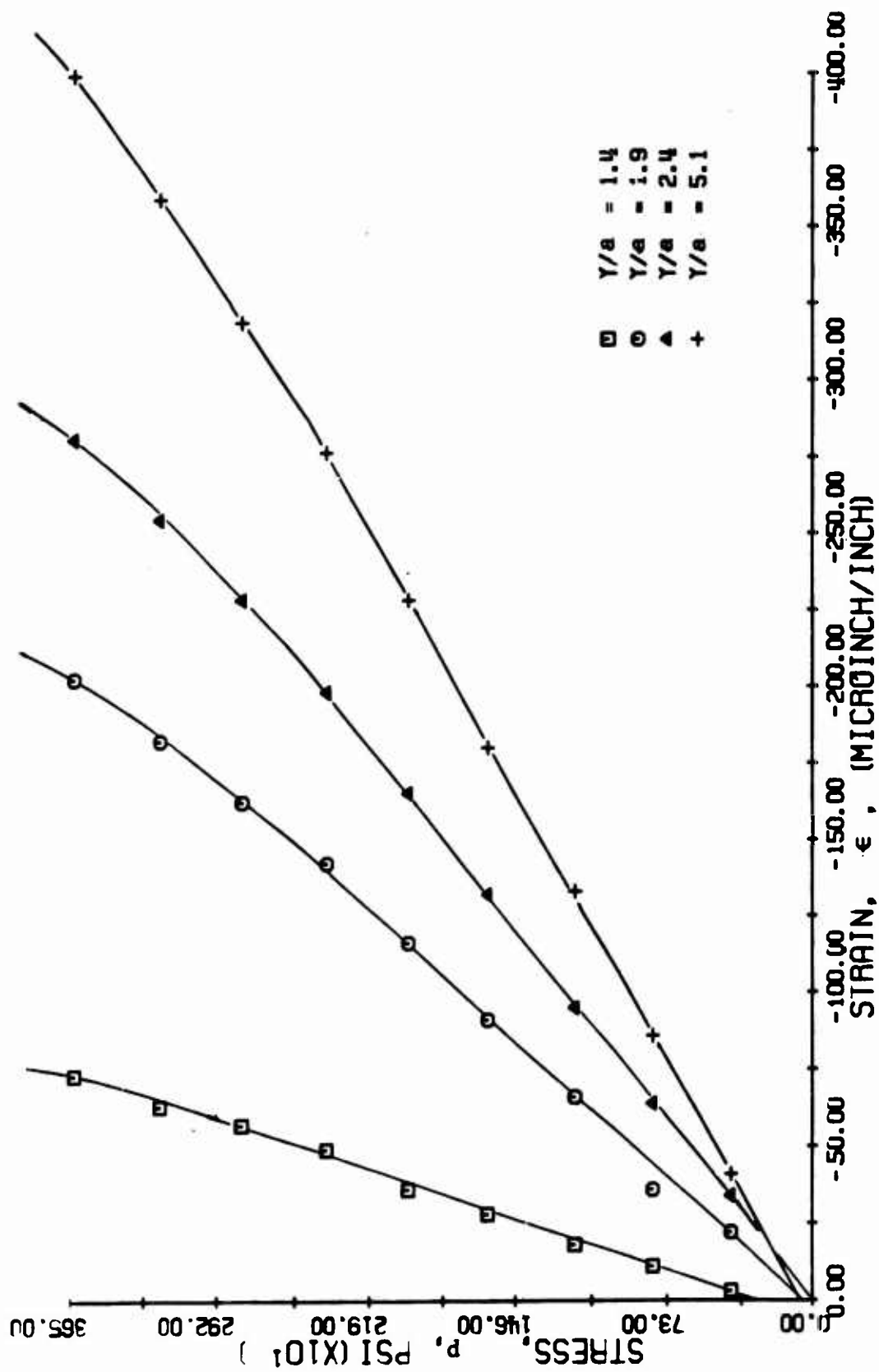
FIG. 193 VERTICAL STRAINS ALONG VERTICAL AXIS OF SYMMETRY AS A FUNCTION OF APPLIED VERTICAL STRESS FOR SPECIMEN NO.15 (MARBLE WITH NO LINER UNDER BIAXIAL LOADING)

270
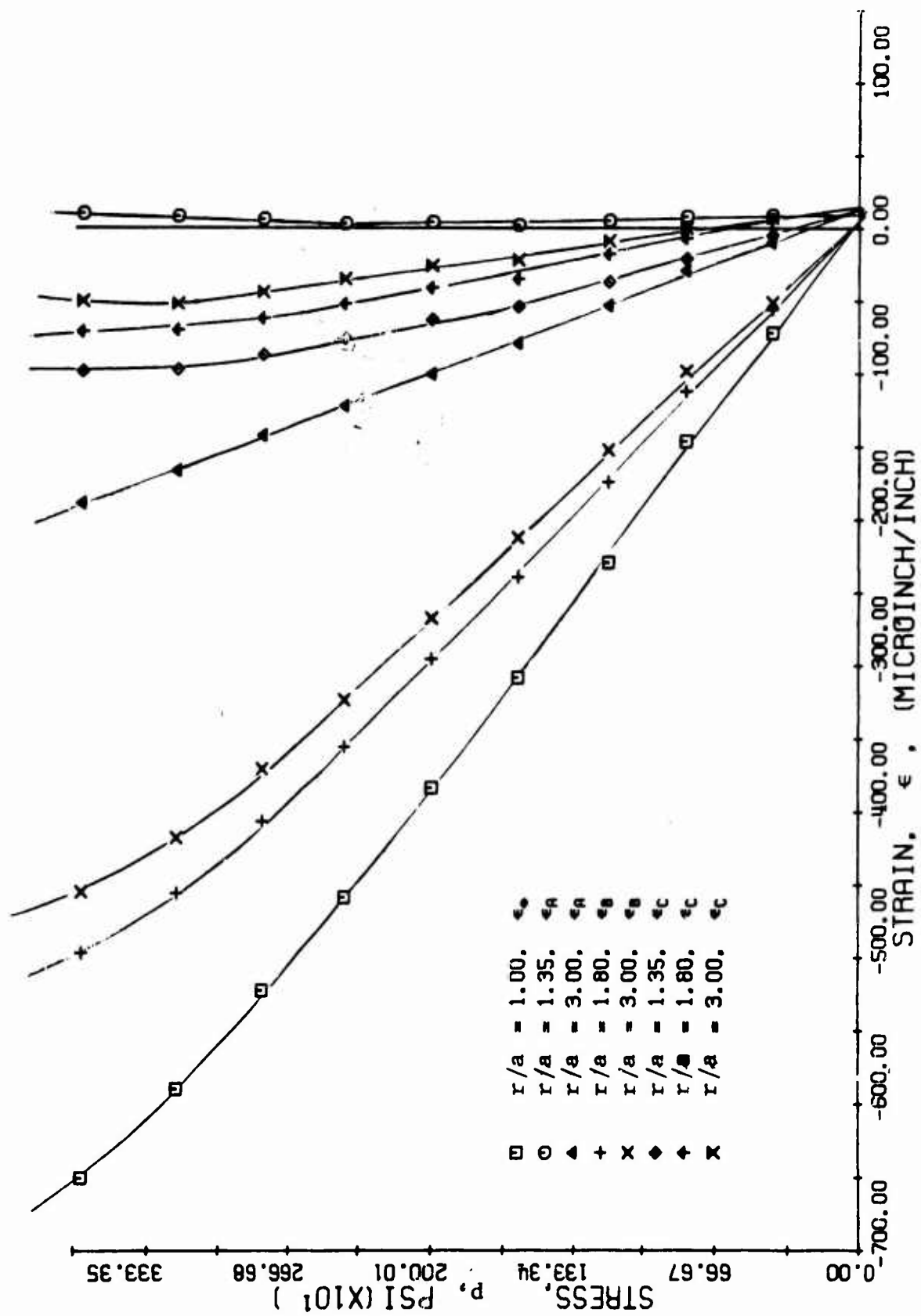
FIG. 194 STRAINS ALONG 45-DEGREE RADIUS FOR SPECIMEN NO.15
(MARBLE UNLINED UNDER BIAXIAL LOADING)

271

compared to the theoretical value of 2.67 for an infinite plate. The horizontal strains along the vertical axis are negative except for the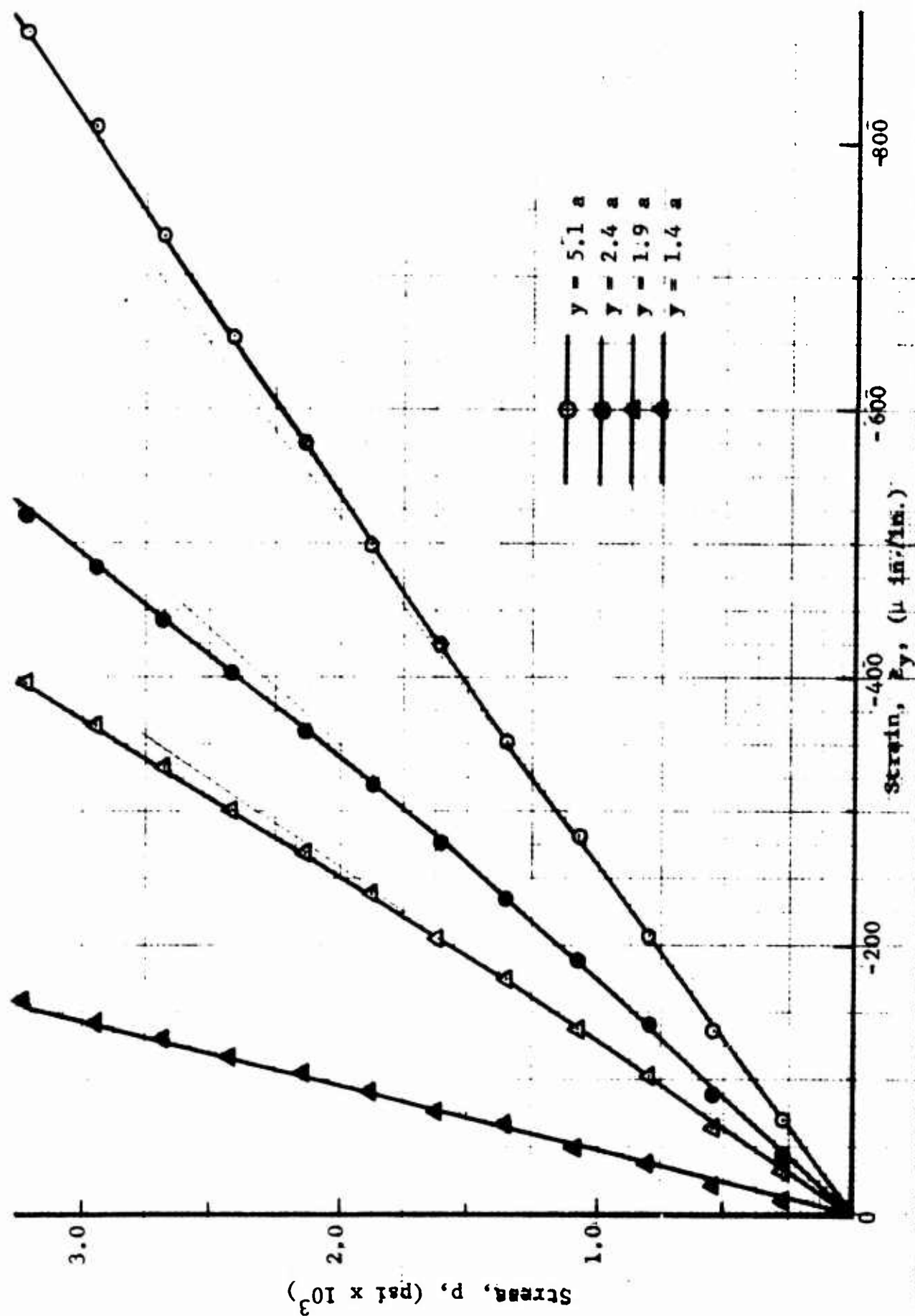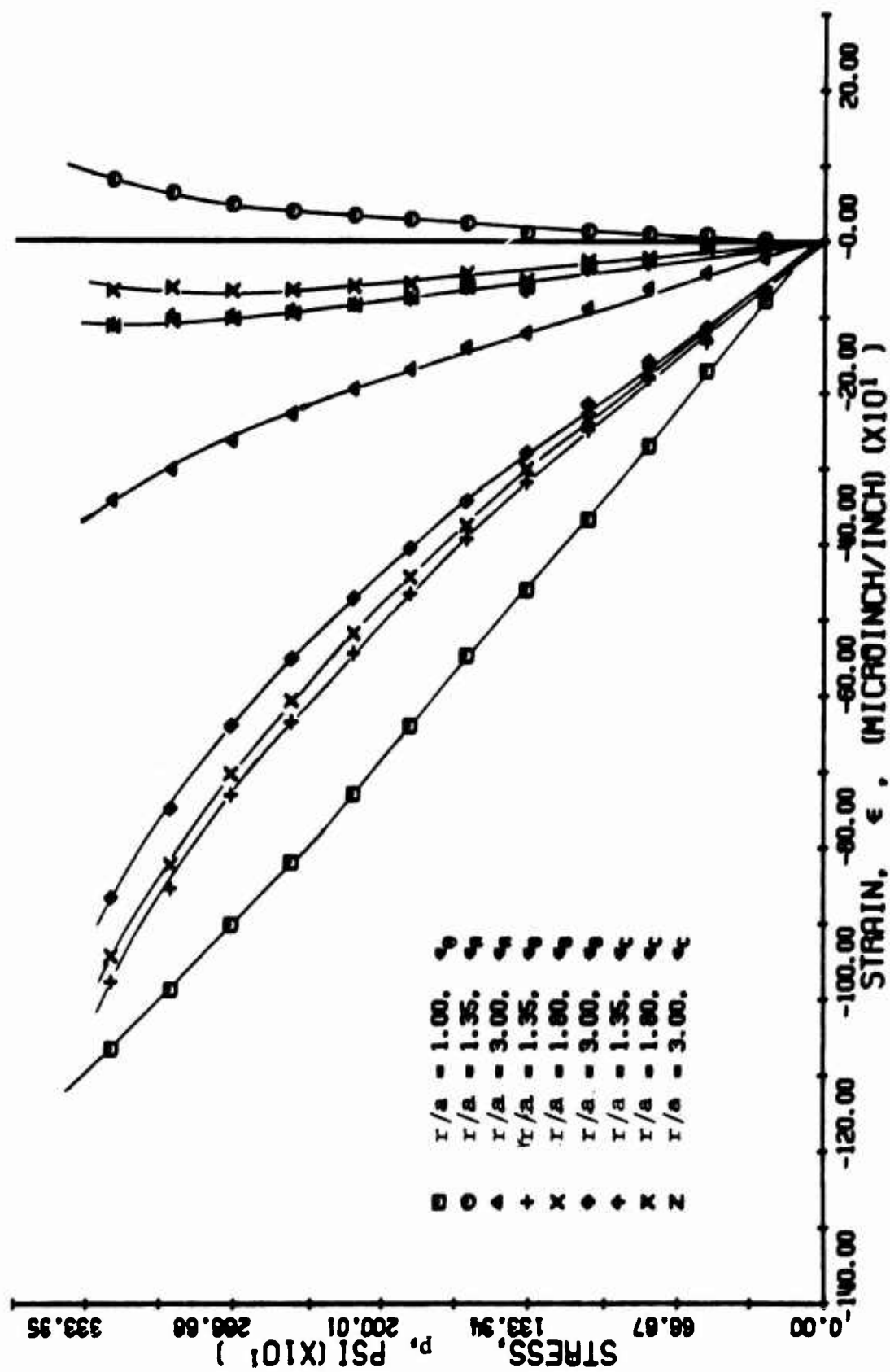 one on the hole boundary which is tensile but very small. Principal strains along the 45-degree radius at $r = 3.00a$ were computed from the rosette readings and plotted in Fig. 195. This computation was not possible at the other rosette locations due to lack of complete readings. The angle between the 45-degree radius and the principal direction of strain ε_1, measured clockwise varies between 38 degrees and 40 degrees.

Specimen No. 16 was loaded similarly as No. 15 in 30,000 lb and 15,000 lb psi increments up to a vertical load of 450,000 lb and a lateral load of 225,000 lb, when a piece of the specimen near the top loaded surface broke off. No failure around the hole was noticed during the loading. Isochromatic fringe patterns from the photoelastic coating around the hole are shown in Fig. 196 where both vertical and horizontal applied stresses are indicated in each frame.

Diametral changes are plotted in Fig. 197. The vertical deflection is linear and the horizontal is zero up to a vertical stress $p = 2,800$ psi, thereafter both become nonlinear. The vertical deflection per unit applied stress in the linear range is

$$\frac{\delta_v}{p} = -0.85 \times 10^{-6} \text{ in./psi}$$

which is very close to that in specimen No. 15.

Strains along the axis of symmetry and the 45-degree radius are plotted in Figs. 198 through 202. The vertical strains along the horizontal axis are linear up to approximately $p = 3,200$ psi. The ratio of the maximum compressive strain on the hole boundary to the free-field strain is

$$k_\varepsilon = 2.80$$

compared to the theoretical value of 2.67.

The strain distribution along the horizontal axis at an applied vertical stress of 2,000 psi is plotted in Fig. 203 for specimens No. 15 and 16. The theoretical distribution is also shown. The agreement between the two experiments and the theory is close.
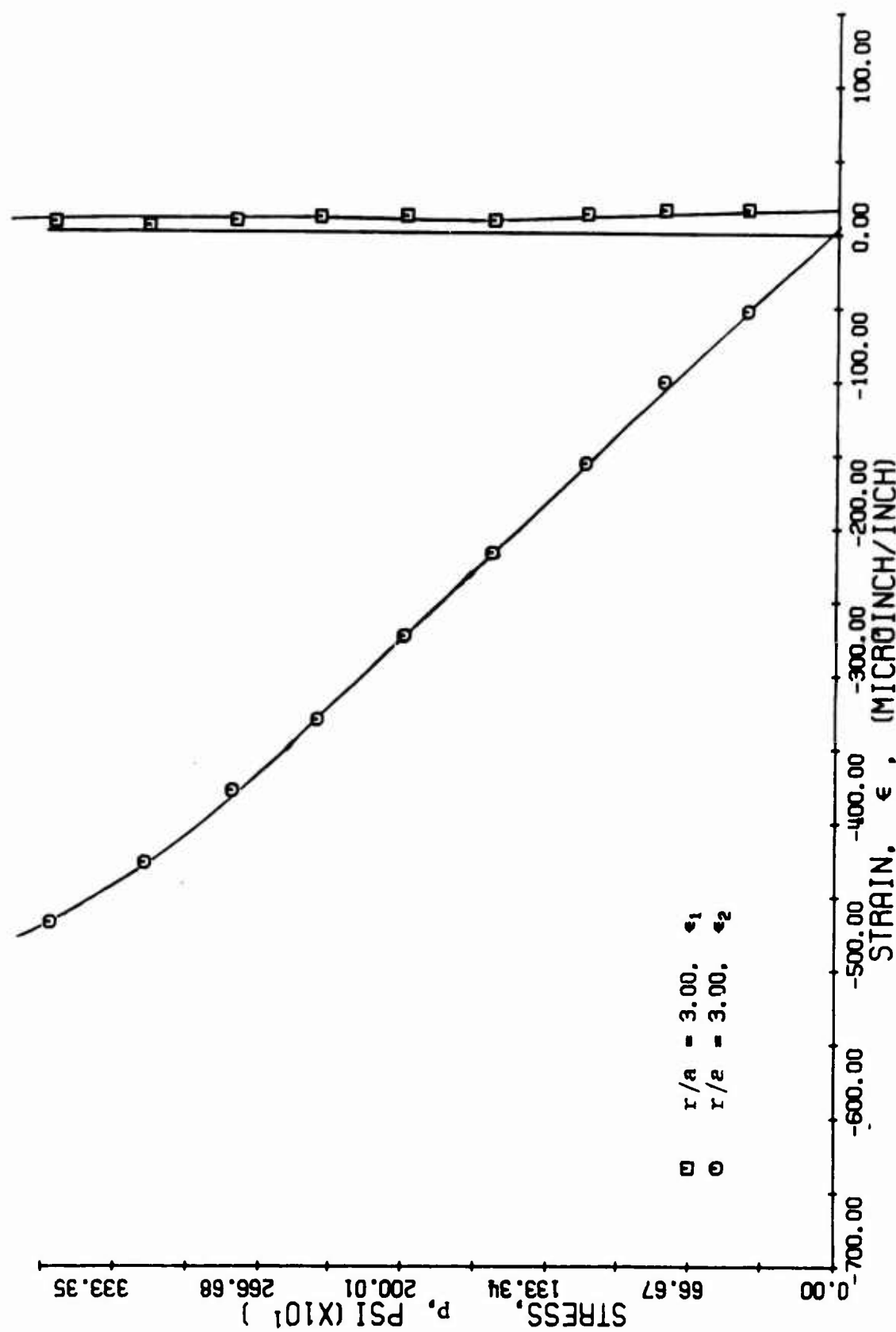
FIG. 195 PRINCIPAL STRAINS ALONG 45-DEGREE RADIUS FOR SPECIMEN NO.15
(MARBLE UNLINED UNDER BIAXIAL LOADING)

p = 400 psi
q = 135 psi

p = 1200 psi
q = 405 psi

p = 2000 psi
q = 680 psi

p = 2810 psi
q = 950 psi

p = 3610 psi
q = 1220 psi

p = 4420 psi
q = 1490 psi

p = 4820 psi
q = 1620 psi

p = 5220 psi
q = 1760 psi

p = 5550 psi
q = 1900 psi

Fig. 196   ISOCHROMATIC FRINGE PATTERNS IN PHOTOELASTIC COATING
AROUND HOLE IN SPECIMEN NO. 16 (MARBLE UNLINED UNDER
BIAXIAL LOADING)

274
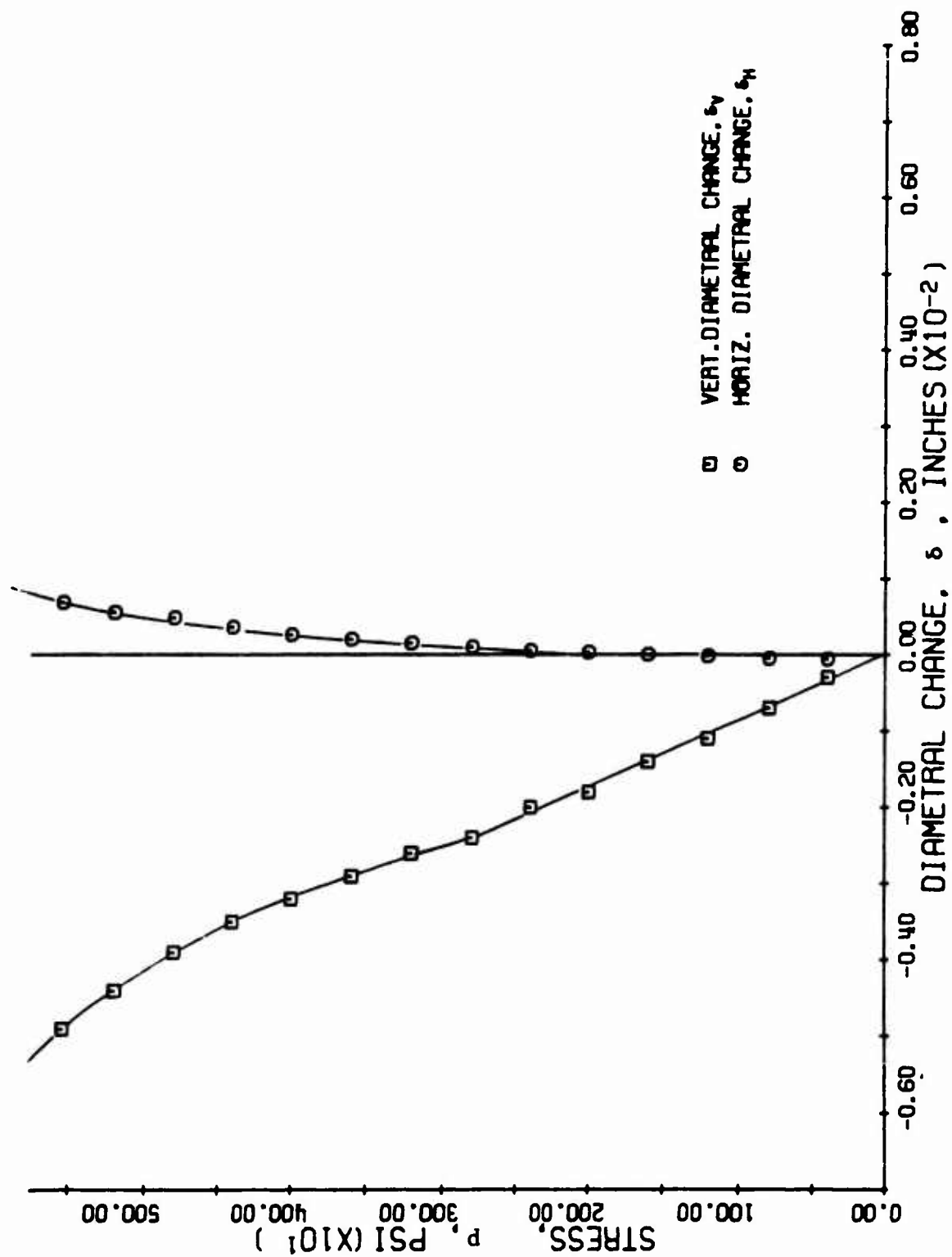
FIG. 197 DIAMETRAL CHANGES AS A FUNCTION OF APPLIED VERTICAL STRESS FOR SPECIMEN
NO.16 (MARBLE UNLINED UNDER BIAXIAL LOADING)

275
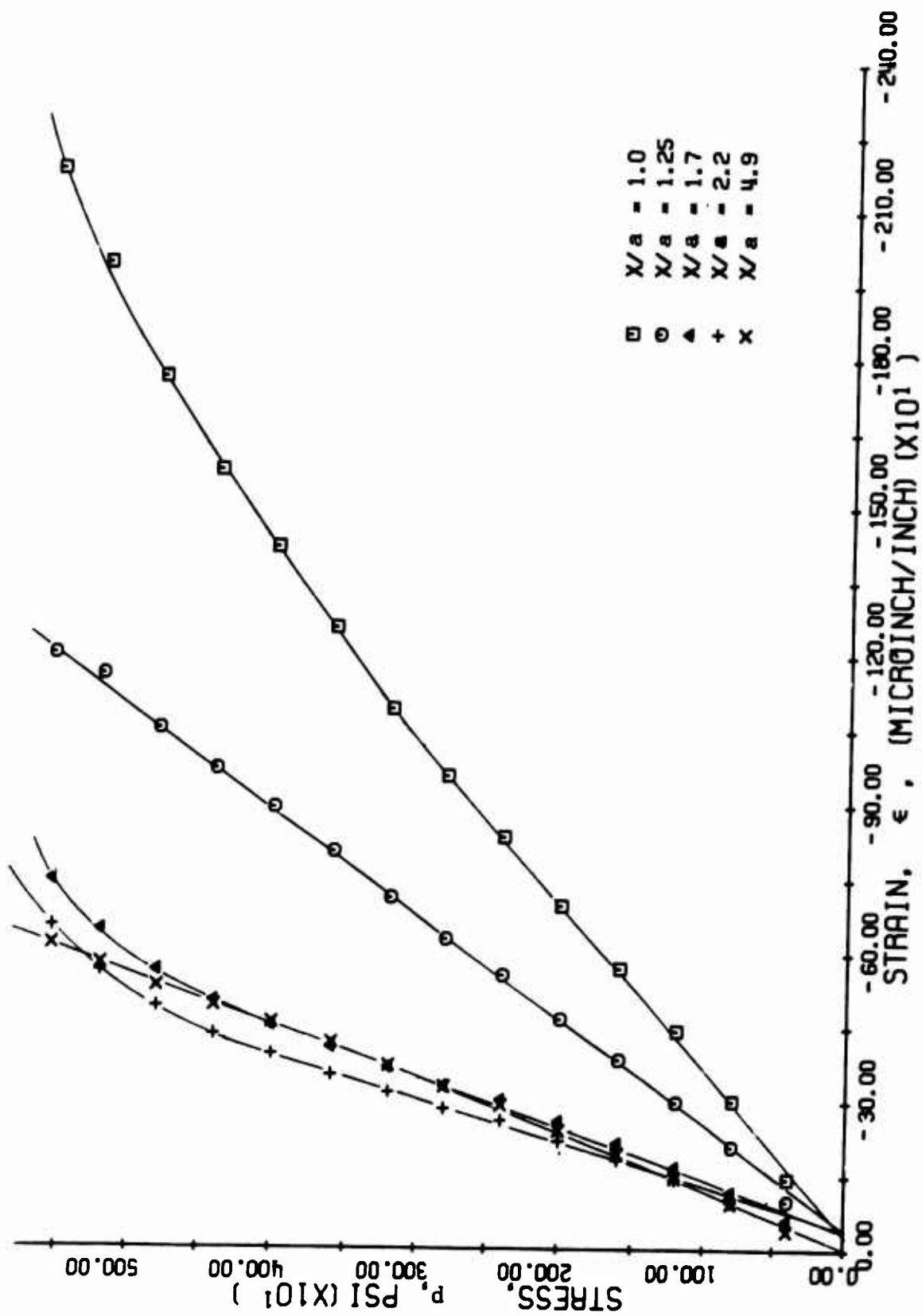
FIG. 198 VERTICAL STRAINS ALONG HORIZONTAL AXIS OF SYMMETRY AS A FUNCTION OF APPLIED VERTICAL STRESS FOR SPECIMEN NO.16 UNMARBLE UNLINED UNDER BIAXIAL LOADING)

276
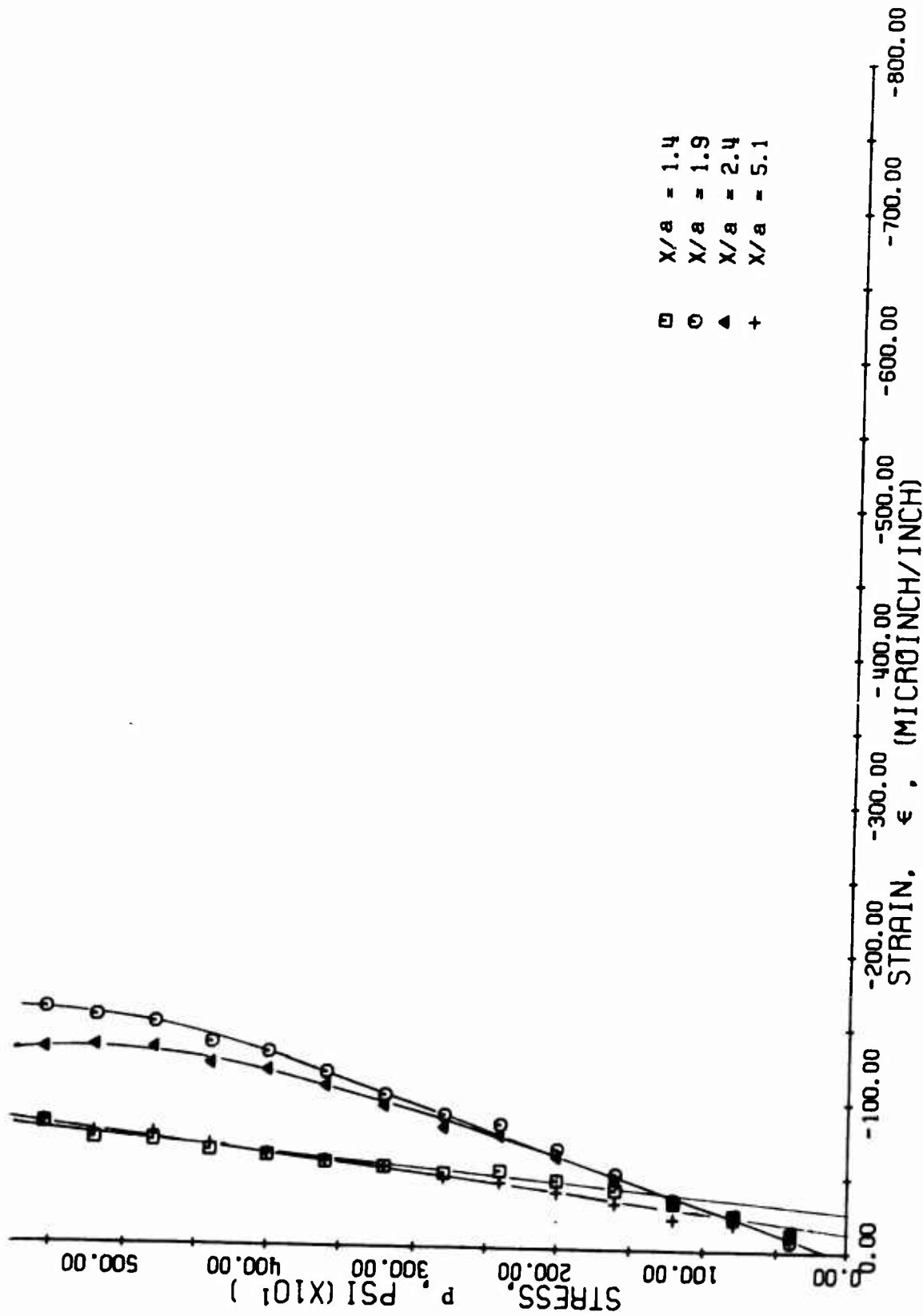
FIG. 199 HORIZONTAL STRAINS ALONG HORIZONTAL AXIS OF SYMMETRY AS A FUNCTION OF APPLIED VERTICAL
STRESS FOR SPECIMEN NO.16 (MARBLE UNLINED UNDER BIAXIAL LOADING)
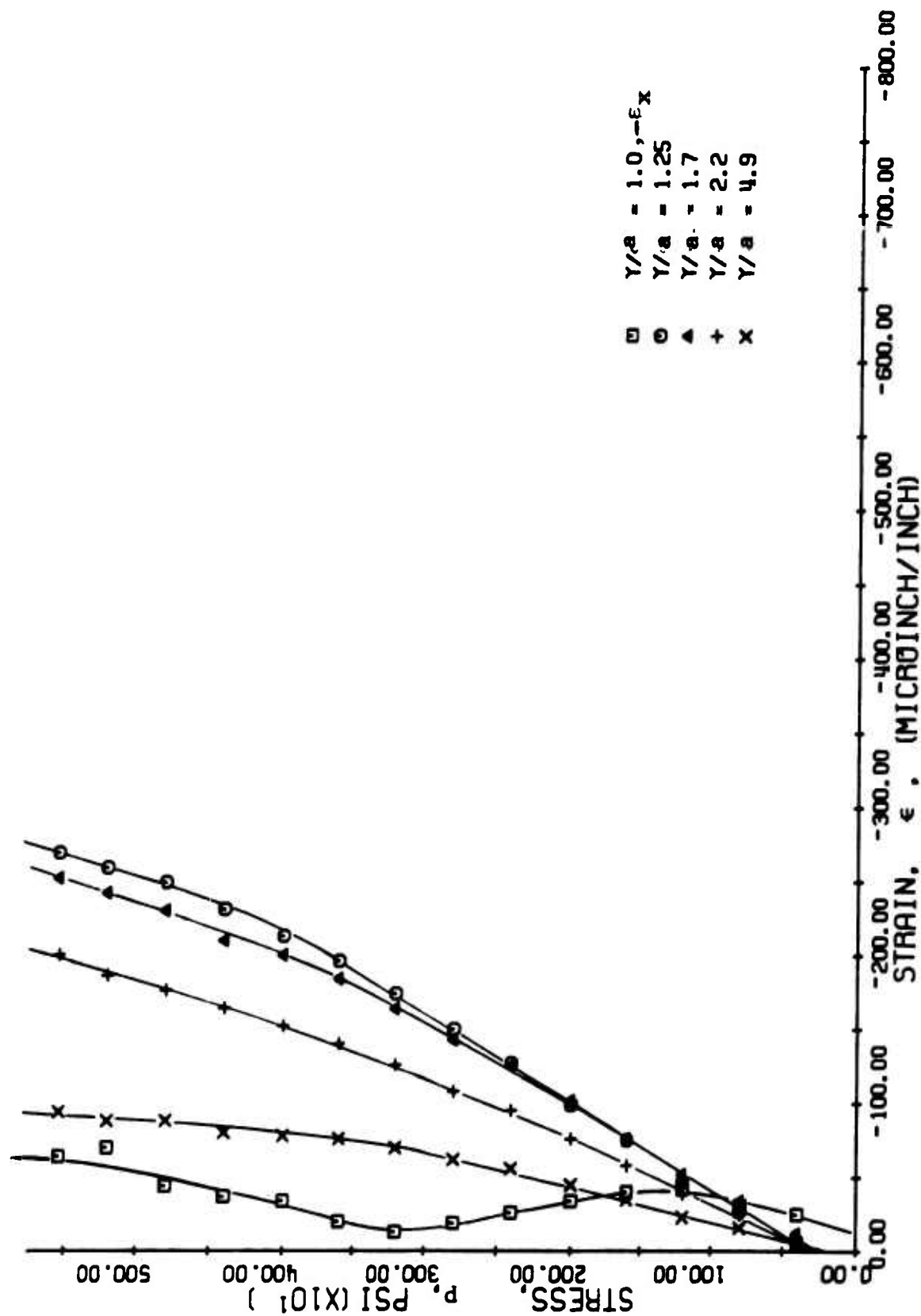
FIG. 200 HORIZONTAL STRAINS ALONG VERTICAL AXIS OF SYMMETRY AS A FUNCTION OF APPLIED VERTICAL STRESS FOR SPECIMEN NO. 16 UNMARBLE UNLINED UNDER BIAXIAL LOADING)

278
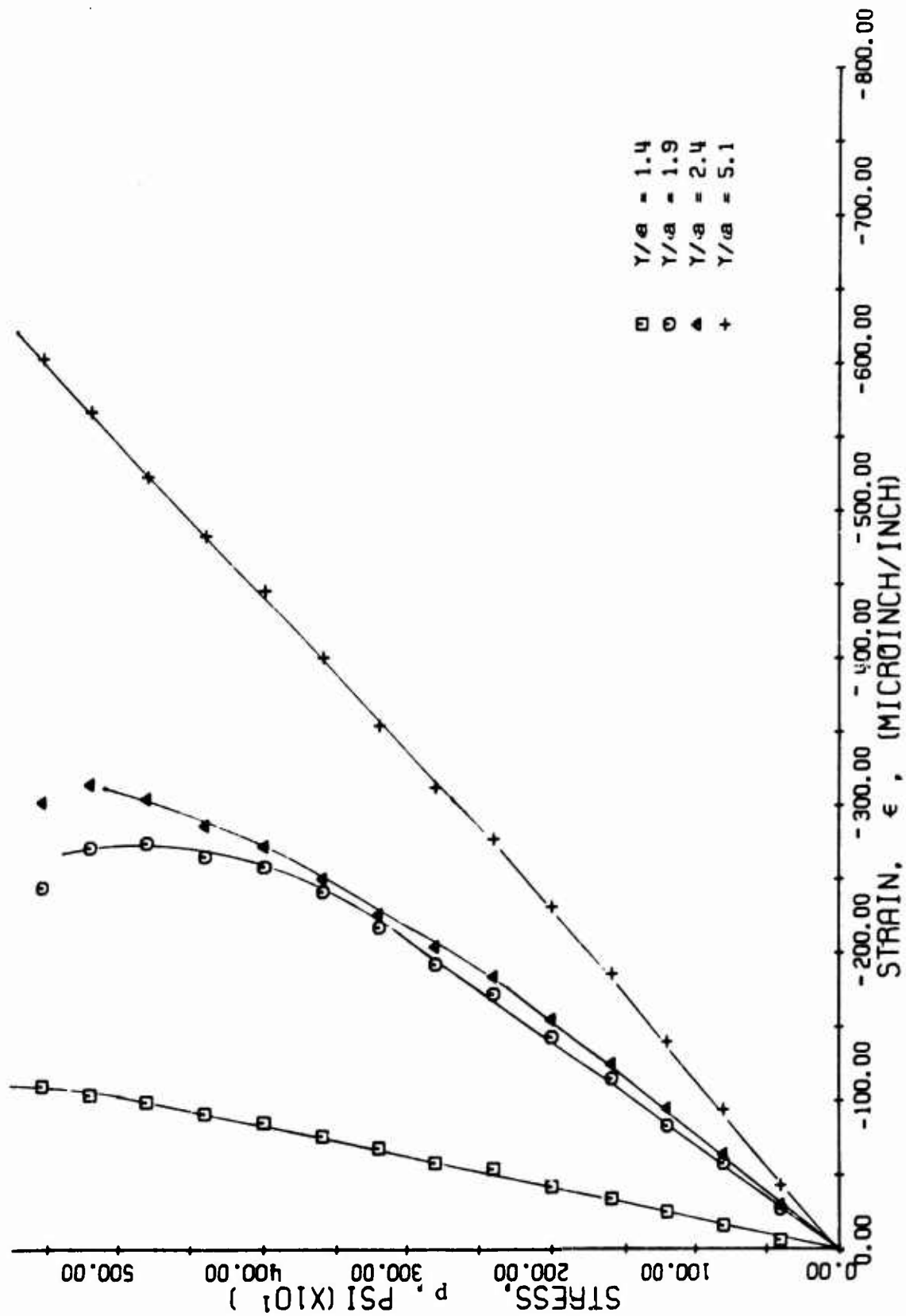
FIG. 201 VERTICAL STRAINS ALONG VERTICAL AXIS OF SYMMETRY AS A FUNCTION OF APPLIED VERTICAL STRESS FOR SPECIMEN NO.16 (MARBLE WITH NO LINER UNDER BIAXIAL LOADING)
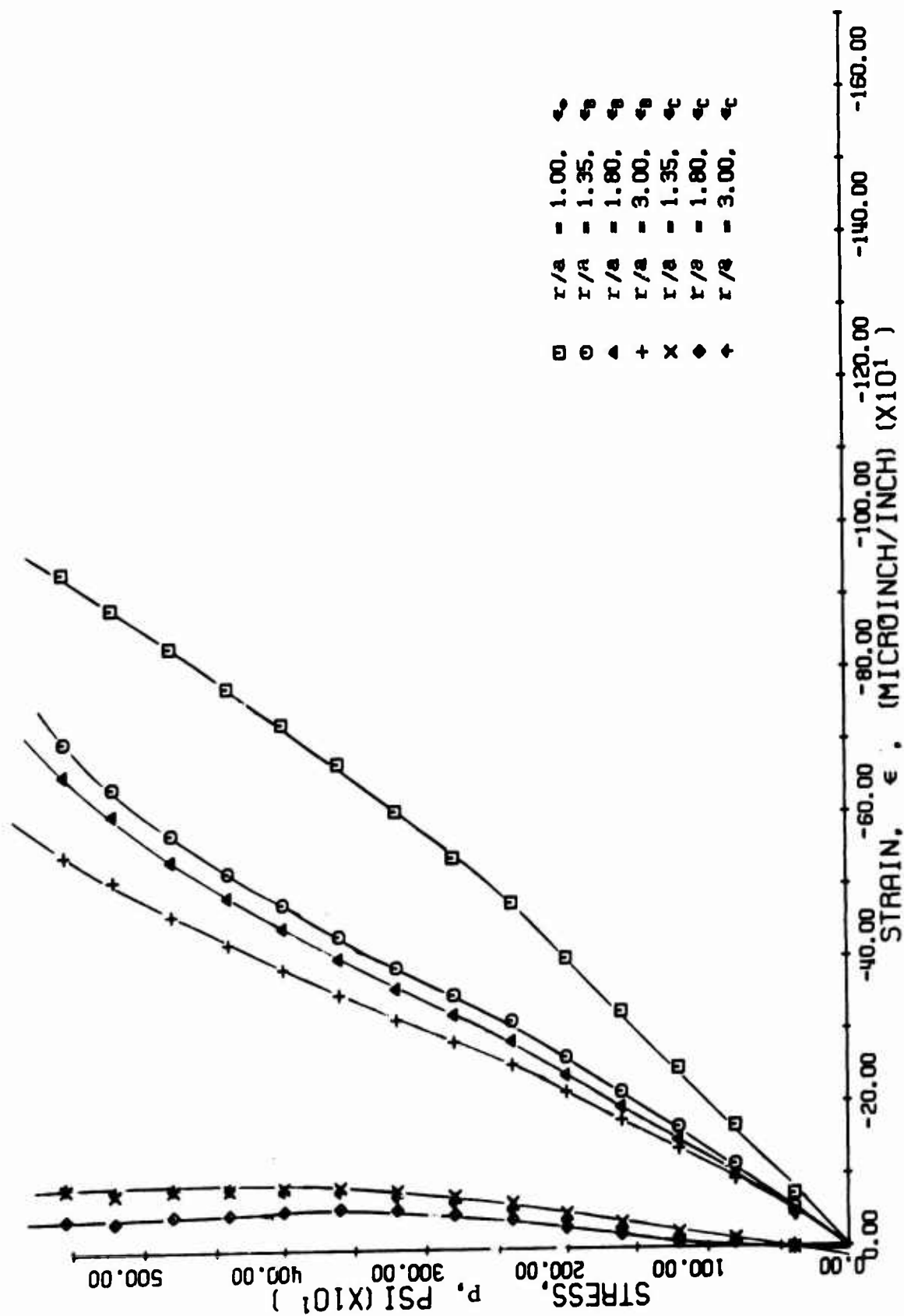
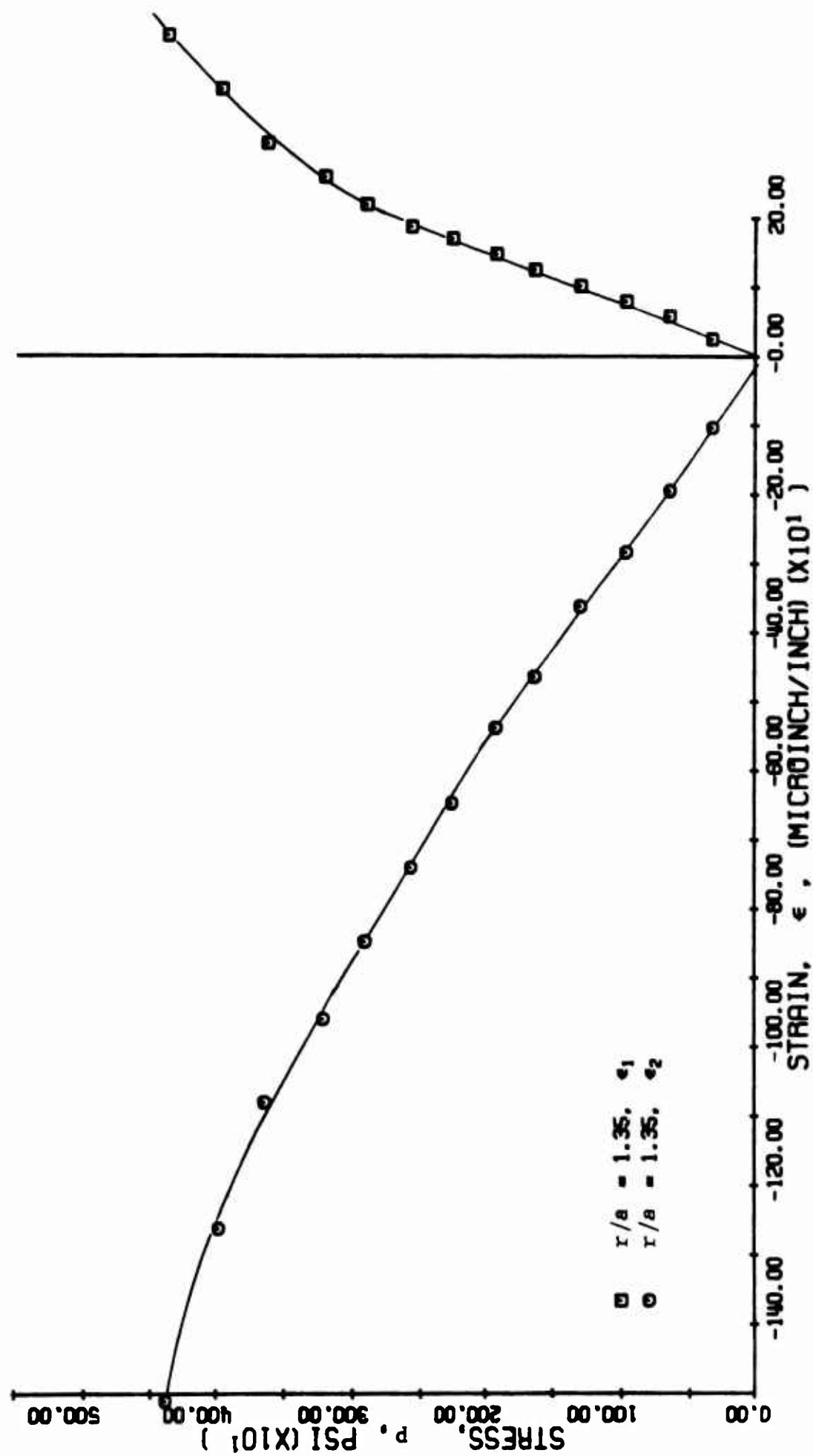FIG. 202 STRAINS ALONG 45-DEGREE RADIUS FOR SPECIMEN NO.16
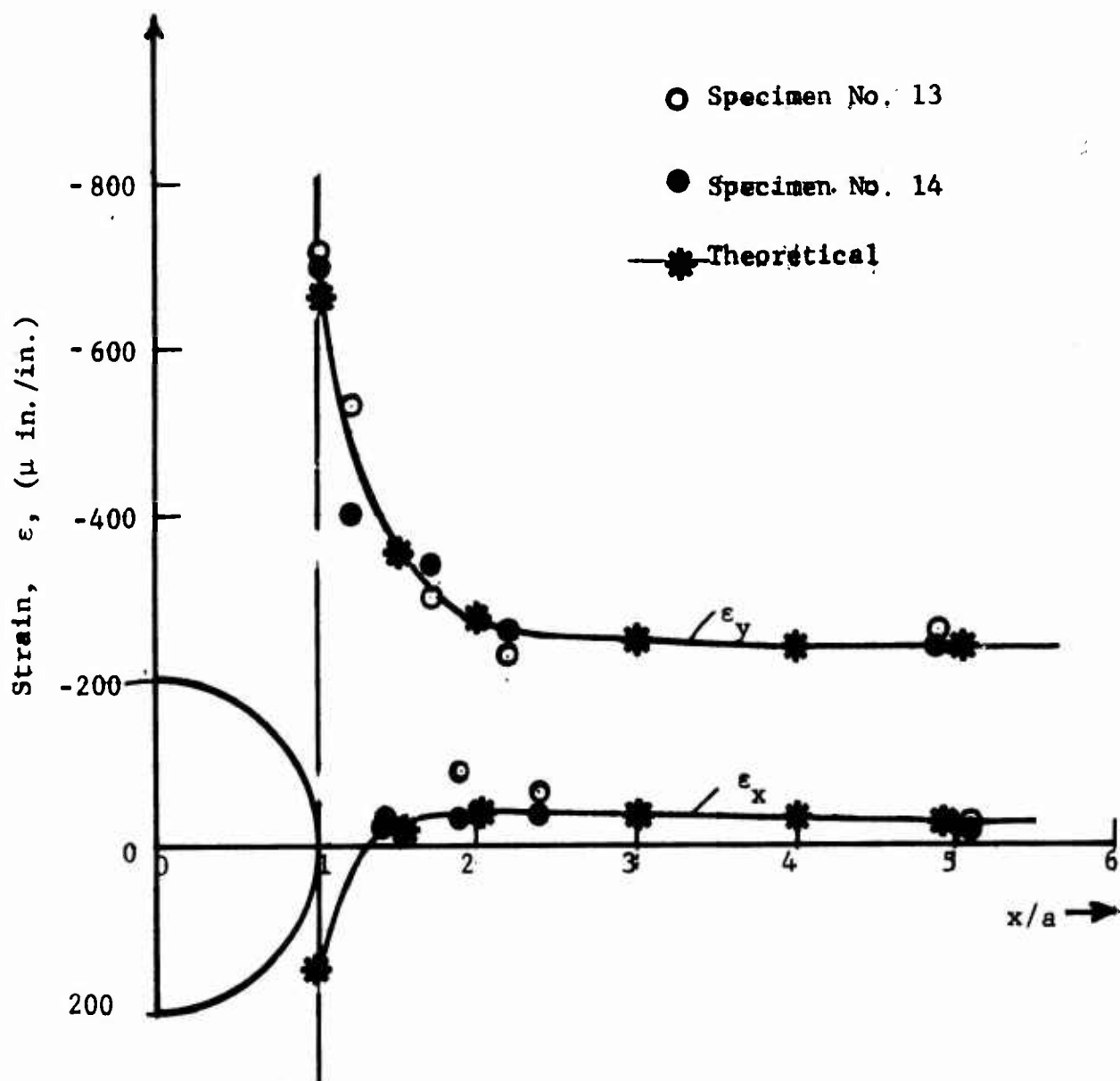(MARBLE UNLINED UNDER BIAXIAL LOADING)

280
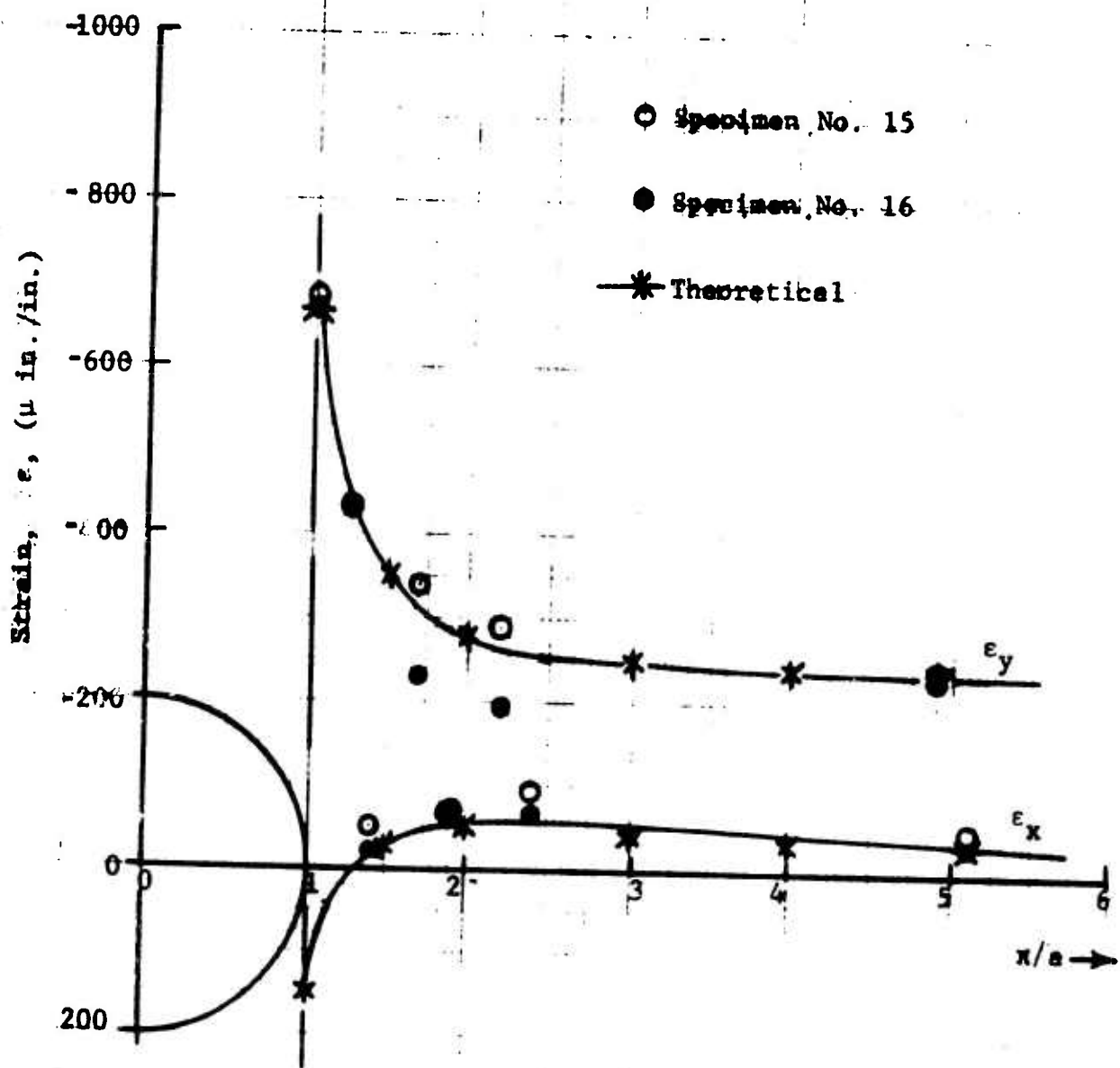
Fig. 203 STRAIN DISTRIBUTION ALONG HORIZONTAL AXIS OF SYMMETRY
FOR SPECIMENS NO. 15 AND NO. 16 AT 2,000 PSI APPLIED
VERTICAL STRESS (MARBLE UNLINED UNDER BIAXIAL LOADING)

SECTION VIII

STRESS DISTRIBUTION AND FRACTURE AROUND LINED CAVITIES
IN ROCK UNDER BIAXIAL LOADING

1. <u>Specimen No. 17 - Limestone Lined with Hydrostone Under
Biaxial Loading</u>

A limestone plate of dimensions 36 in. x 24 in. x 3.07 in.
with a 4 in. diameter hole lined with a 0.44 in. thick hydrostone
liner was loaded in biaxial compression. The vertical load was
applied in increments of 30,000 lb up to 120,000 lb and in 15,000
lb increments thereafter. The corresponding increments for the
lateral load were 15,000 lb and 7,500 lb.

Isochromatic fringe patterns are shown in Fig. 204 for
various levels of loading. The applied vertical and horizontal
stresses are shown in each frame. The patterns show a high com-
pressive strain on the inner surface of the liner along the hori-
zontal axis. The shear at the interface between the liner and the
rock seems to be more uniformly distributed than in the case of
uniaxial loading. The specimen was loaded up to a vertical load of
300,000 lb when it failed by splitting along a middle plane normal
to the axis of the hole. The corresponding vertical and horizontal
stresses were p = 4,080 psi and q = 1,380 psi. After this splitting,
both vertical and horizontal loads dropped abruptly and one of the
halves of the specimen cracked along the vertical axis of symmetry.
The failure pattern is shown in Fig. 205.

Diametral changes as a function of applied vertical stress
are plotted in Fig. 206. Both horizontal and vertical deflections
are negative, although the former is very small. They are both
linear up to a vertical stress of p = 2,700 psi. Deflections in
the linear range per unit of applied vertical stress are as follows:

$$\frac{\delta_h}{p} = -.08 \times 10^{-6} \text{ in./psi}$$

$$\frac{\delta_v}{p} = -2.6 \times 10^{-6} \text{ in./psi}$$

| p = 0 psi | p = 820 psi | p = 1630 psi |
| q = 0 psi | q = 280 psi | q = 550 psi |

| p = 2040 psi | p = 2450 psi | p = 2650 psi |
| q = 690 psi | q = 830 psi | q = 920 psi |

| p = 4260 psi | p = 4650 psi | p = 4850 psi |
| q = 1100 psi | q = 1240 psi | q = 1330 psi |
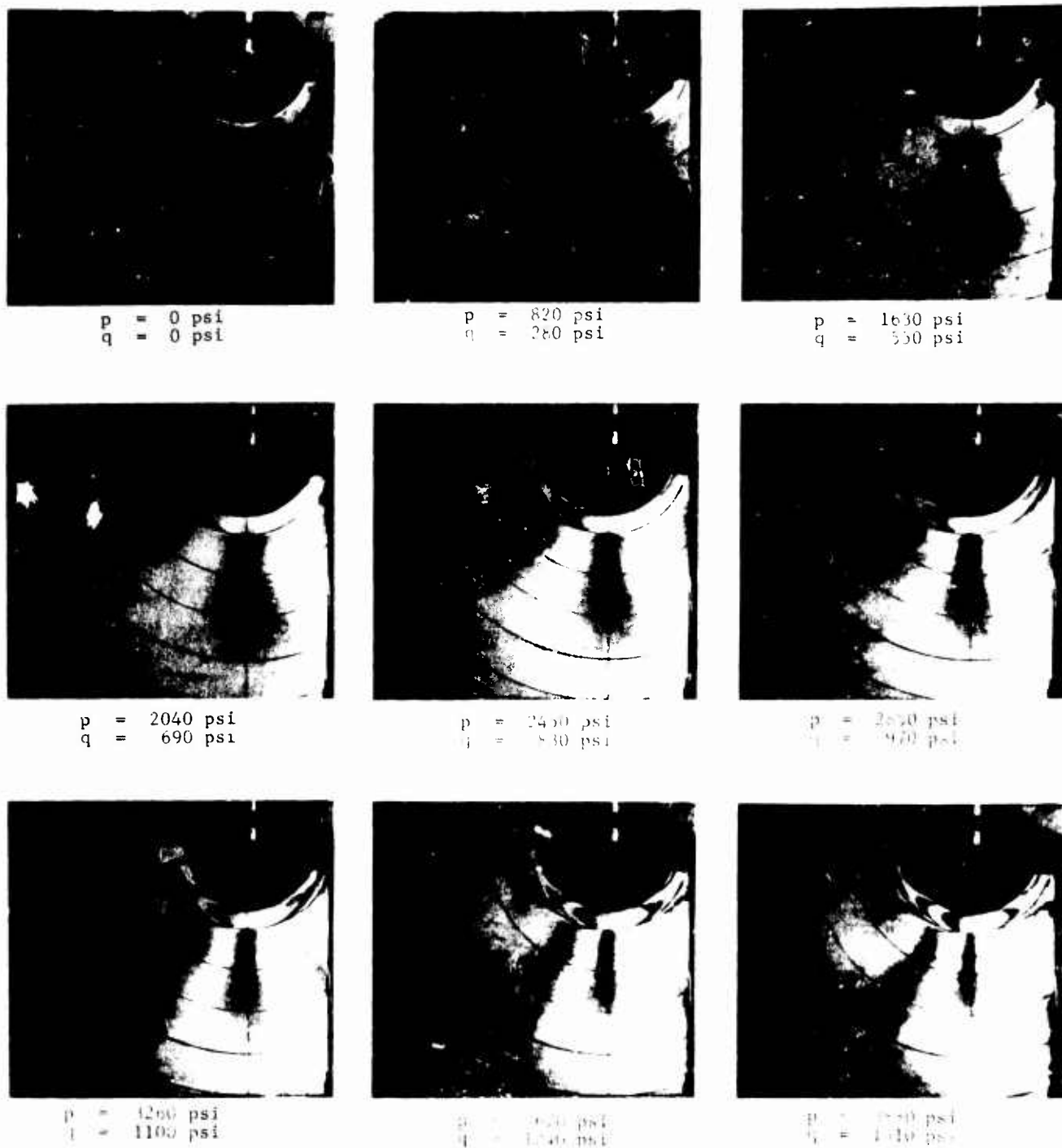
Fig. 204   ISOCHROMATIC FRINGE PATTERNS IN PHOTOELASTIC COATING
AROUND HOLE IN SPECIMEN NO. 17 (LIMESTONE LINED WITH
HYDROSTONE UNDER BIAXIAL LOADING)

283
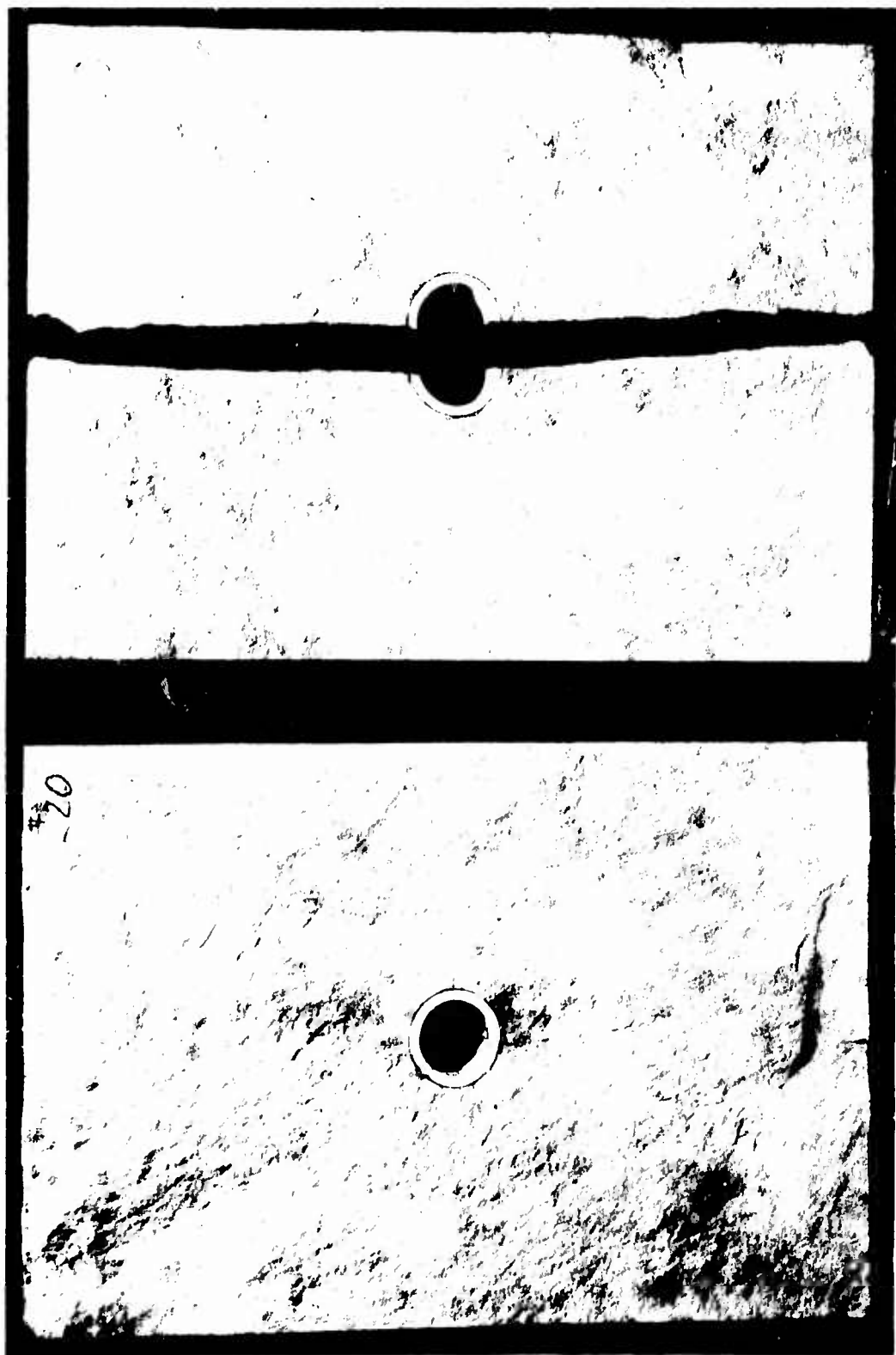
Fig. 205   FAILURE PATTERN OF SPECIMEN NO. 17 (LIMESTONE
LINED WITH HYDROSTONE UNDER BIAXIAL LOADING)

284
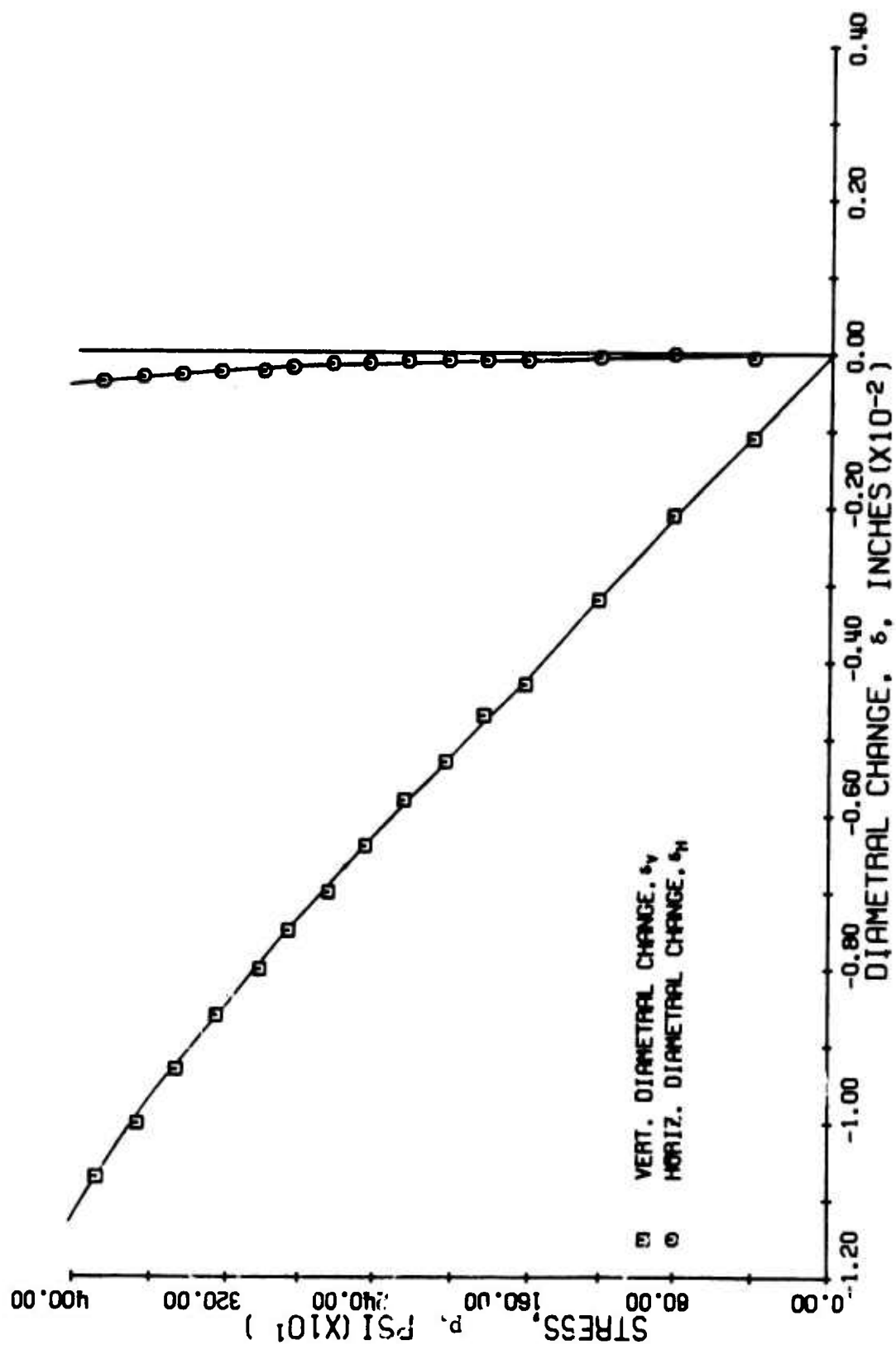
FIG. 206 DIAMETRAL CHANGES AS A FUNCTION OF APPLIED VERTICAL STRESS FOR SPECIMEN NO. 17 (LIMESTONE WITH HYDROSTONE LINER UNDER BIAXIAL LOADING)

285

Strains along the axes of symmetry and the 45-degree radius
are plotted as a function of applied vertical stress, with radial
distance as a parameter, in Figs. 207 through 211. The vertical
strains along the horizontal axis (Fig. 207) are linear up to at
least p = 2,400 psi. The ratio of the maximum compressive strain
at the interface to the far-field strain is

$$k_\varepsilon = 2.03$$

compared to the theoretically computed value of 2.19 (Eqs. 46 and 47).
On the basis of the far-field vertical strains a modulus of
$E = 3.7 \times 10^6$ psi was computed. The horizontal strains along the
horizontal axis near the cavity (x = 0.9a and x = a) are nonlinear
throughout. Those farther away from the hole are linear up to
approximately p = 2,400 psi. The horizontal strains along the
vertical axis show early nonlinearities. The vertical strains
along the same axis show similar behavior near the hole but they
are fairly linear farther away. Principal strains computed from
the rosette readings along the 45-degree radius are plotted in
Fig. 212. The strain ε_1 is positive but decreases with increasing
radial distance. It is almost zero at r = 3.00a. The angle between
the 45-degree radius and the direction of ε_1, measured clockwise,
is nearly constant with load; 29 degrees at r = 1.35a, 35 degrees
at r = 1.80a, and approximately 42 degrees at r = 3.00a.

The strain distribution along the horizontal axis at an
applied vertical stress of p = 1,200 psi is plotted in Fig. 213.
Theoretical points based on a value for Young's modulus equal to
3.7×10^6 psi have also been calculated for the inside of the liner
and the interface and are shown in the same figure. The agreement
with experimental results is very good.

2. Specimen No. 18 - Limestone Lined with Aluminum Under Biaxial
   Loading

A limestone plate of dimensions 36 in. x 24 in. x 3.04 in.
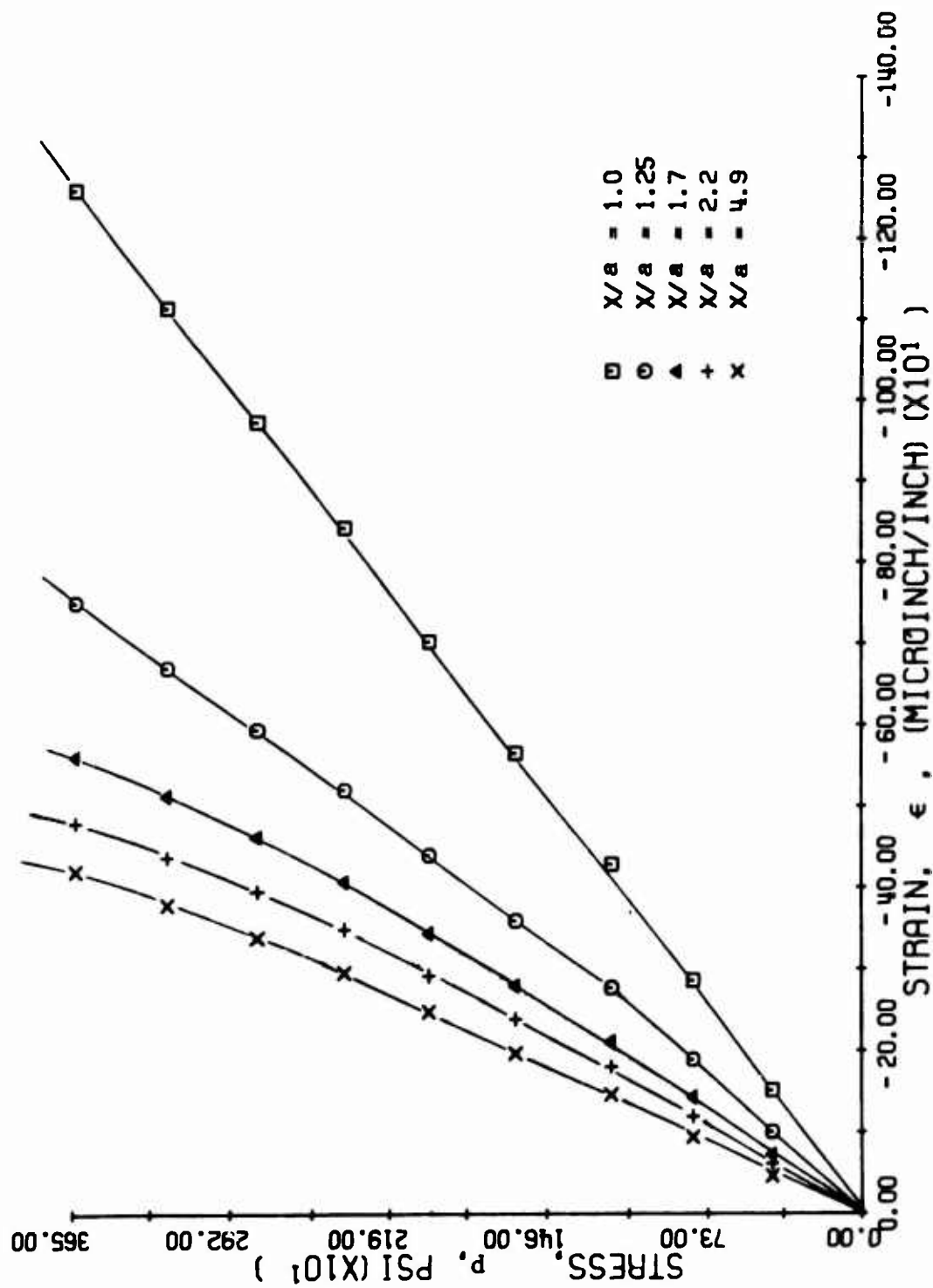with a 4 in. diameter hole lined with a 0.40 in. thick aluminum
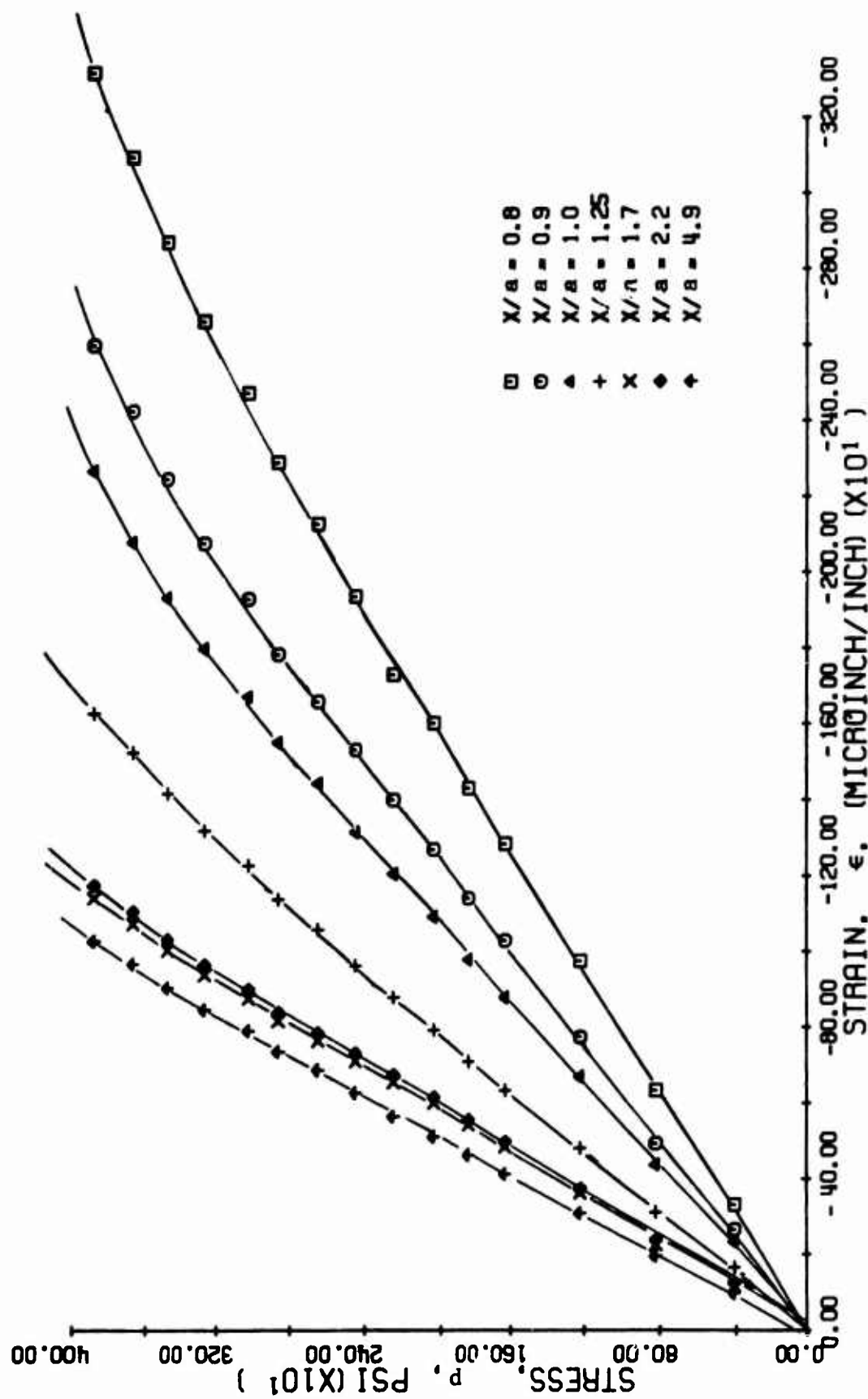
FIG. 207 VERTICAL STRAINS ALONG HORIZONTAL AXIS OF SYMMETRY AS A FUNCTION OF APPLIED VERTICAL STRESS FOR SPECIMEN NO. 17 (LIMESTONE WITH HYDROSTONE LINER UNDER BIAXIAL LOADING)
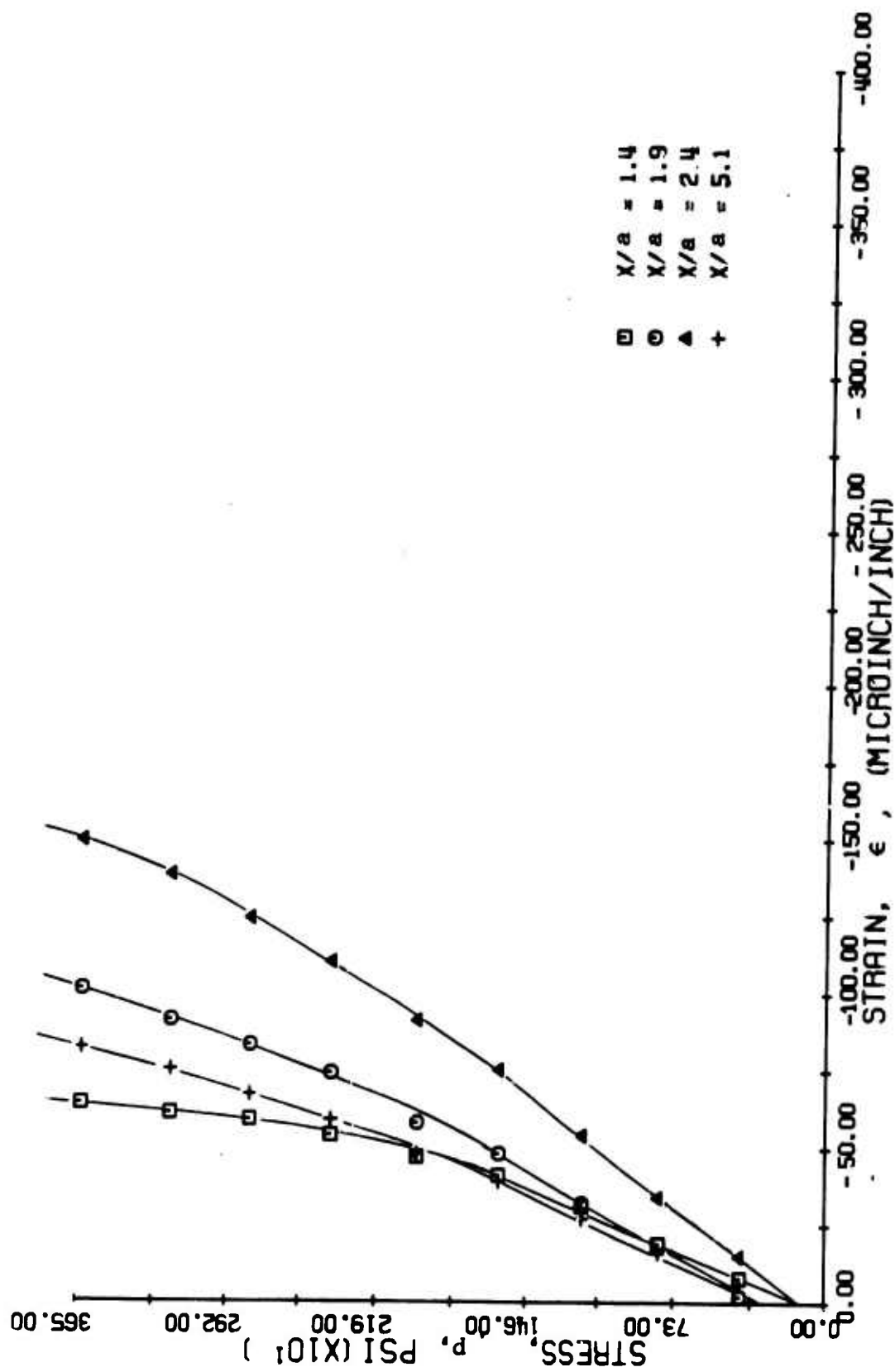
287
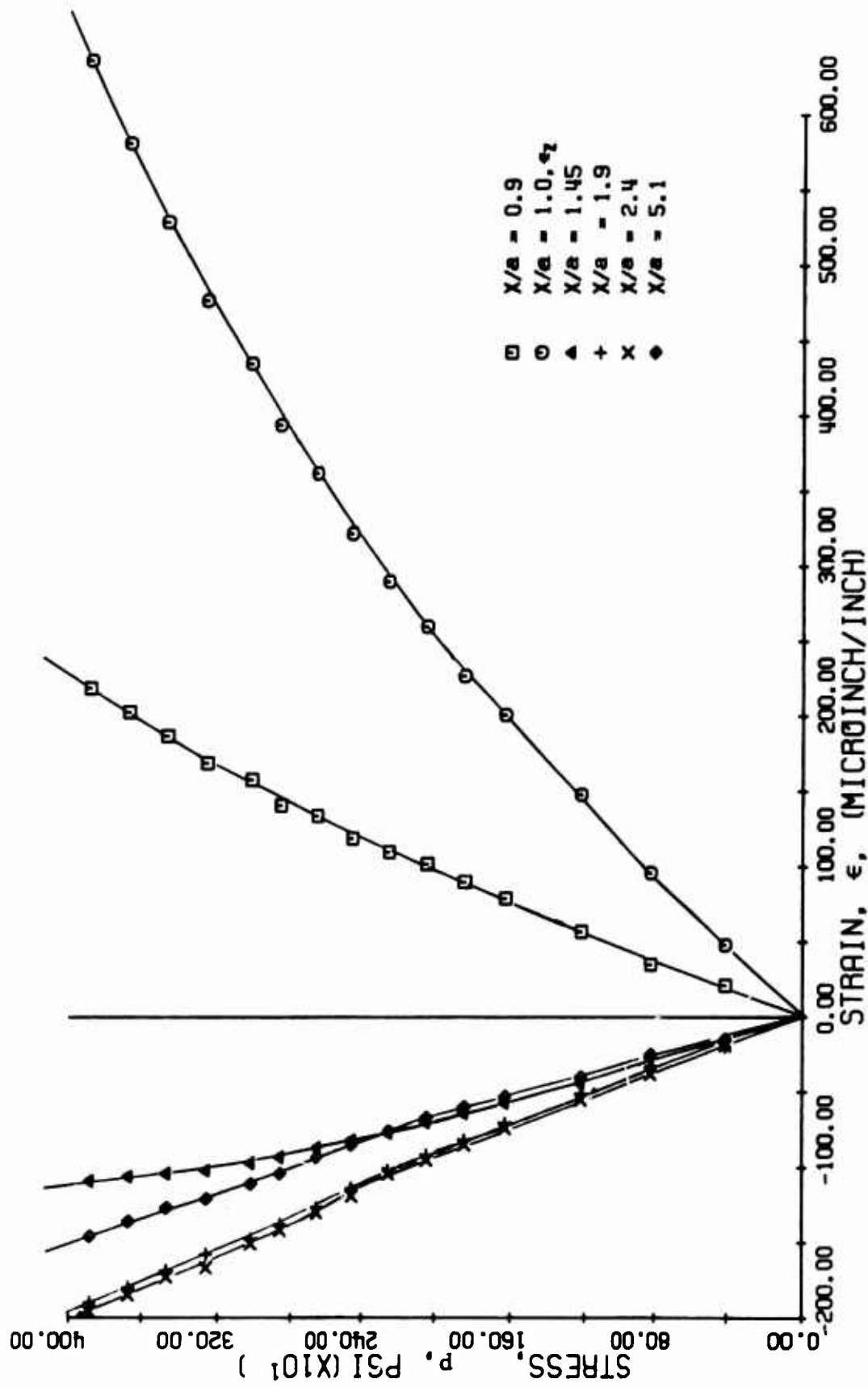
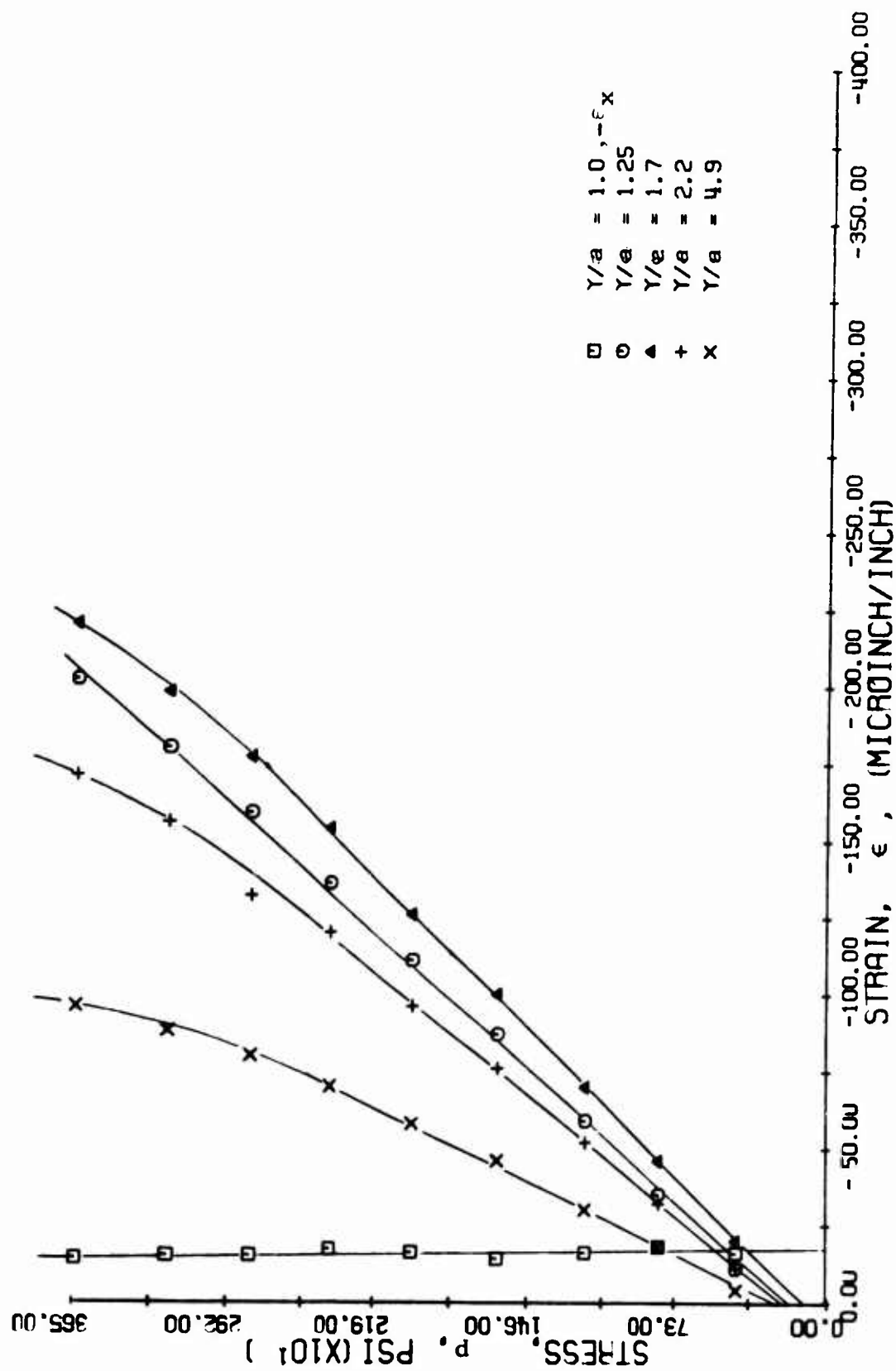FIG. 208 HORIZONTAL STRAINS ALONG HORIZONTAL AXIS OF SYMMETRY AS A FUNCTION OF APPLIED VERTICAL STRESS FOR SPECIMEN NO. 17 (LIMESTONE WITH HYDROSTONE LINER UNDER BIAXIAL LOADING)
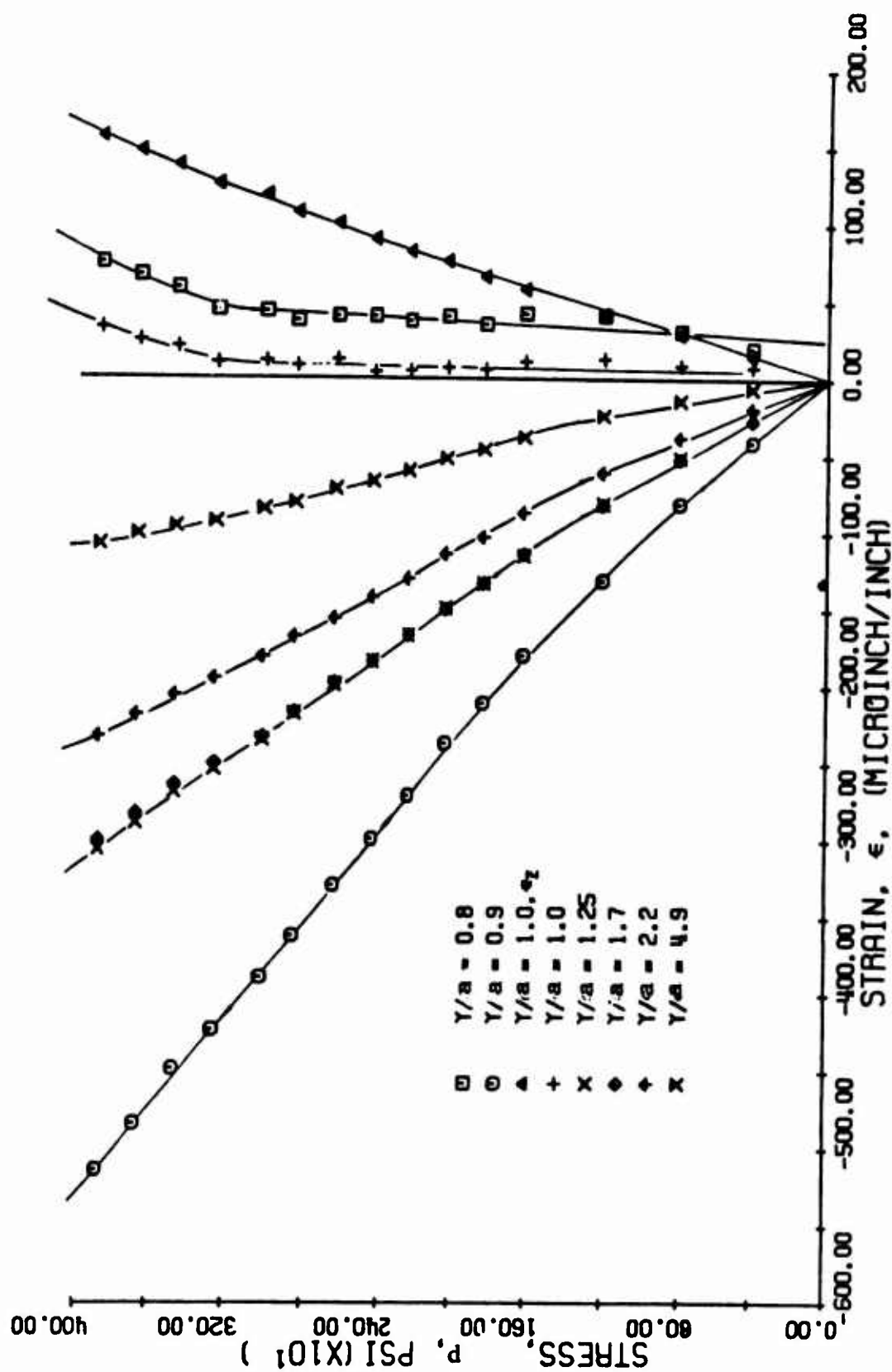
FIG. 209 HORIZONTAL STRAINS ALONG VERTICAL AXIS OF SYMMETRY AS A FUNCTION OF APPLIED VERTICAL STRESS FOR SPECIMEN NO. 17 (LIMESTONE WITH HYDROSTONE LINER UNDER BIAXIAL LOADING)

289
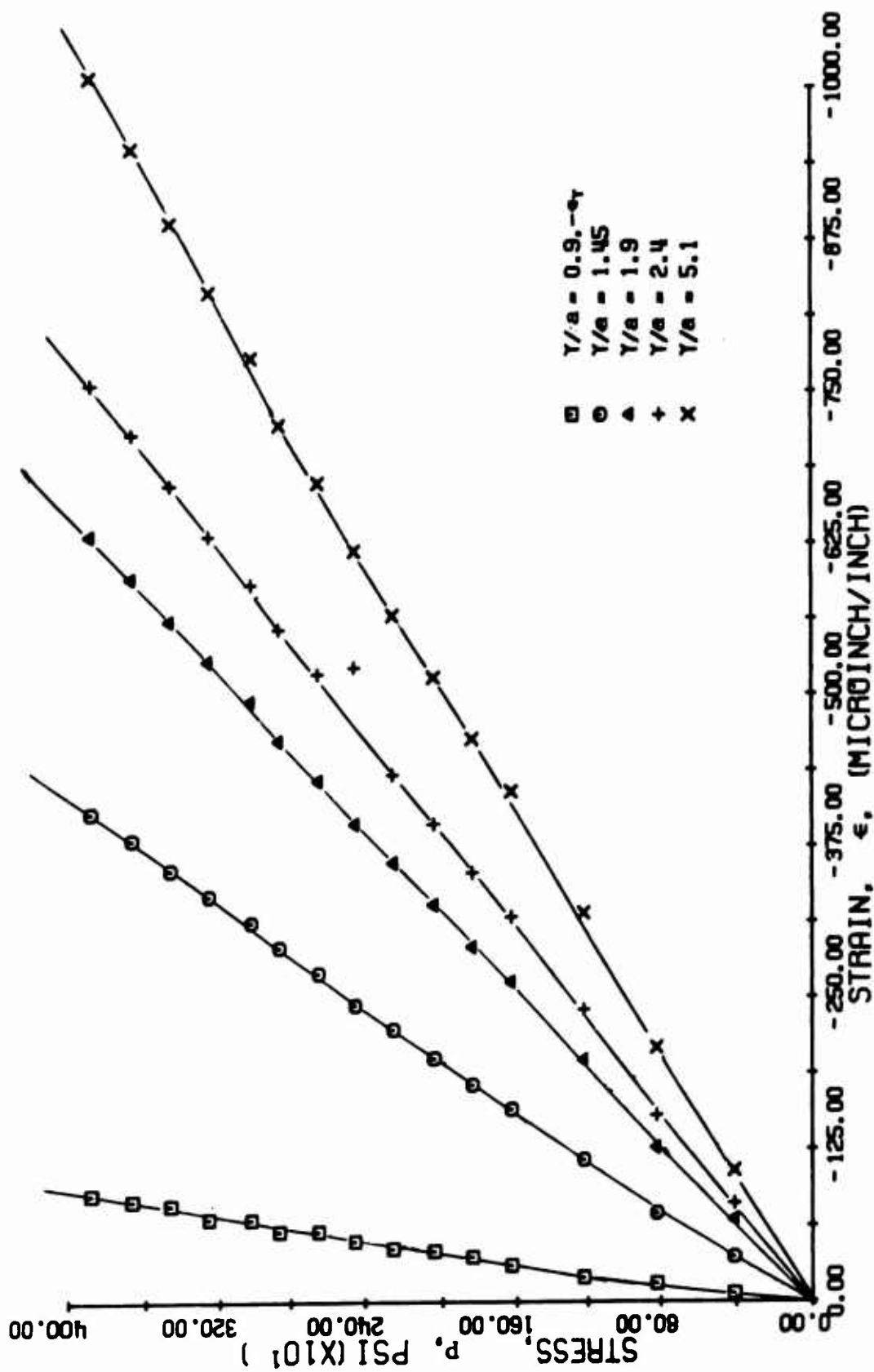
FIG. 210 VERTICAL STRAINS ALONG VERTICAL AXIS OF SYMMETRY AS A FUNCTION OF APPLIED VERTICAL STRESS FOR SPECIMEN NO. 17 (LIMESTONE WITH HYDROSTONE LINER UNDER BIAXIAL LOADING)
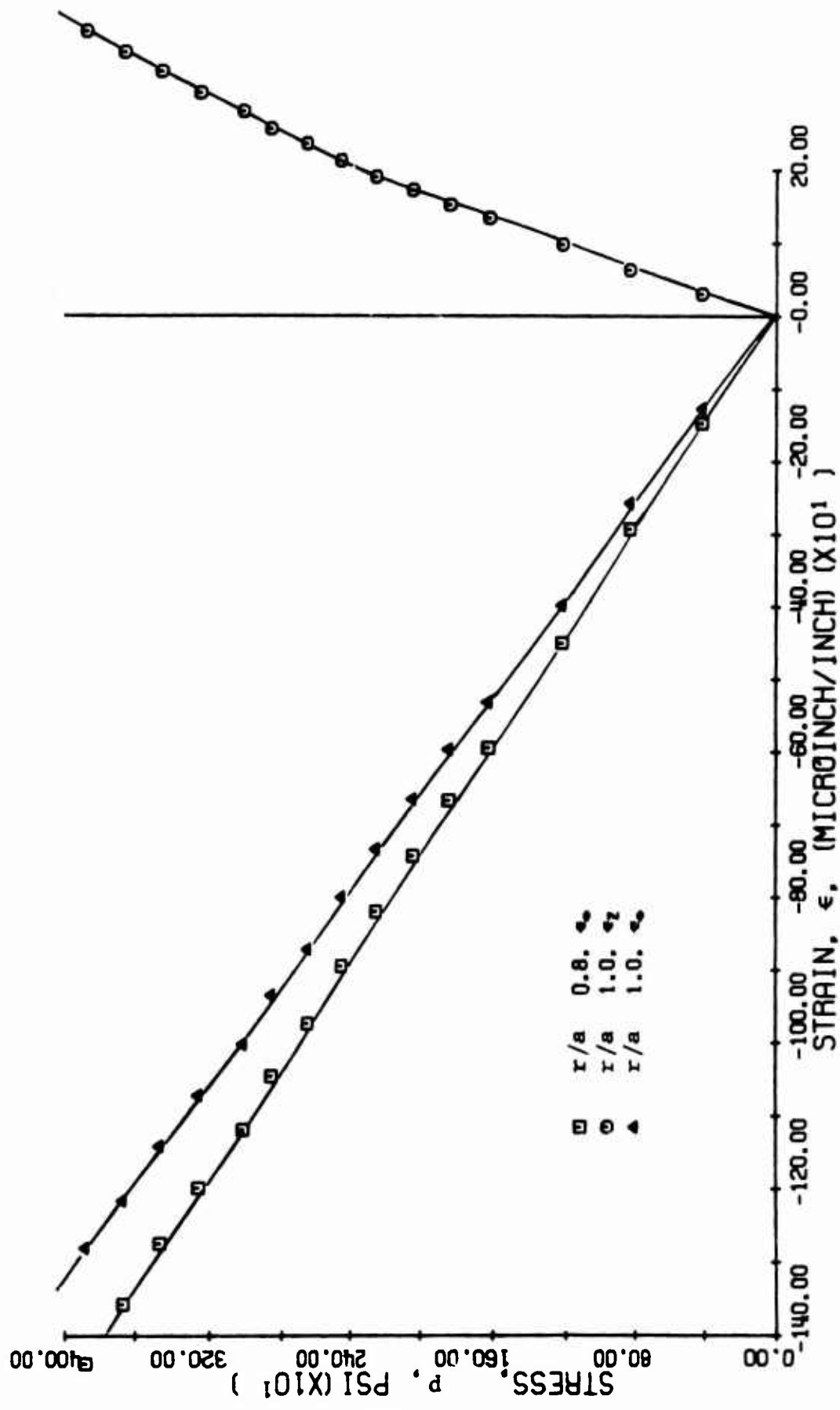
FIG. 211 STRAINS ALONG 45 DEGREE RADIUS FOR SPECIMEN NO. 17
(LIMESTONE WITH HYDROSTONE LINER UNDER BIAXIAL LOADING)

291
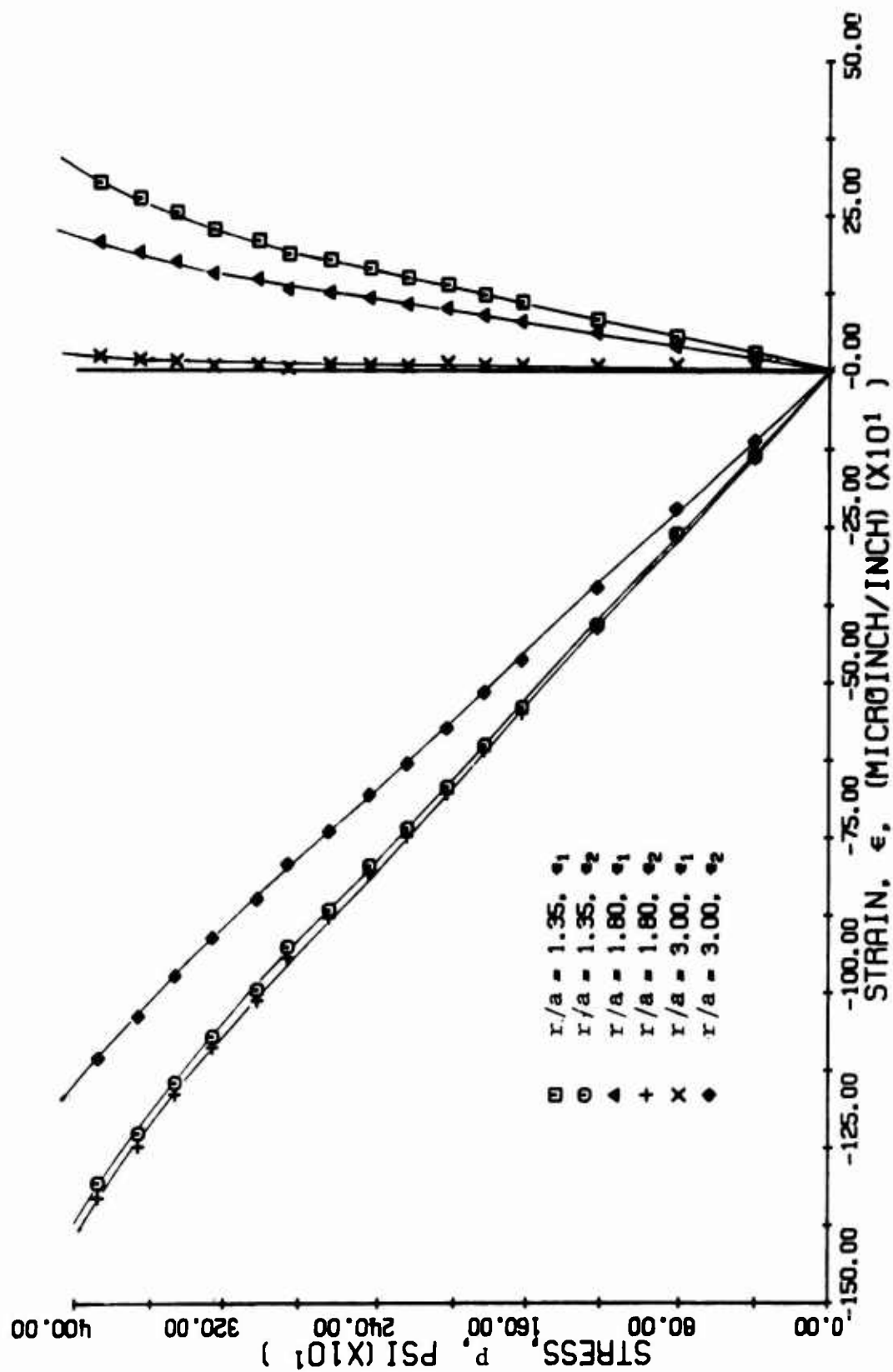
FIG. 212 PRINCIPAL STRAINS ALONG 45 DEGREE RADIUS FOR SPECIMEN NO. 17
(LIMESTONE WITH HYDROSTONE LINER UNDER BIAXIAL LOADING)
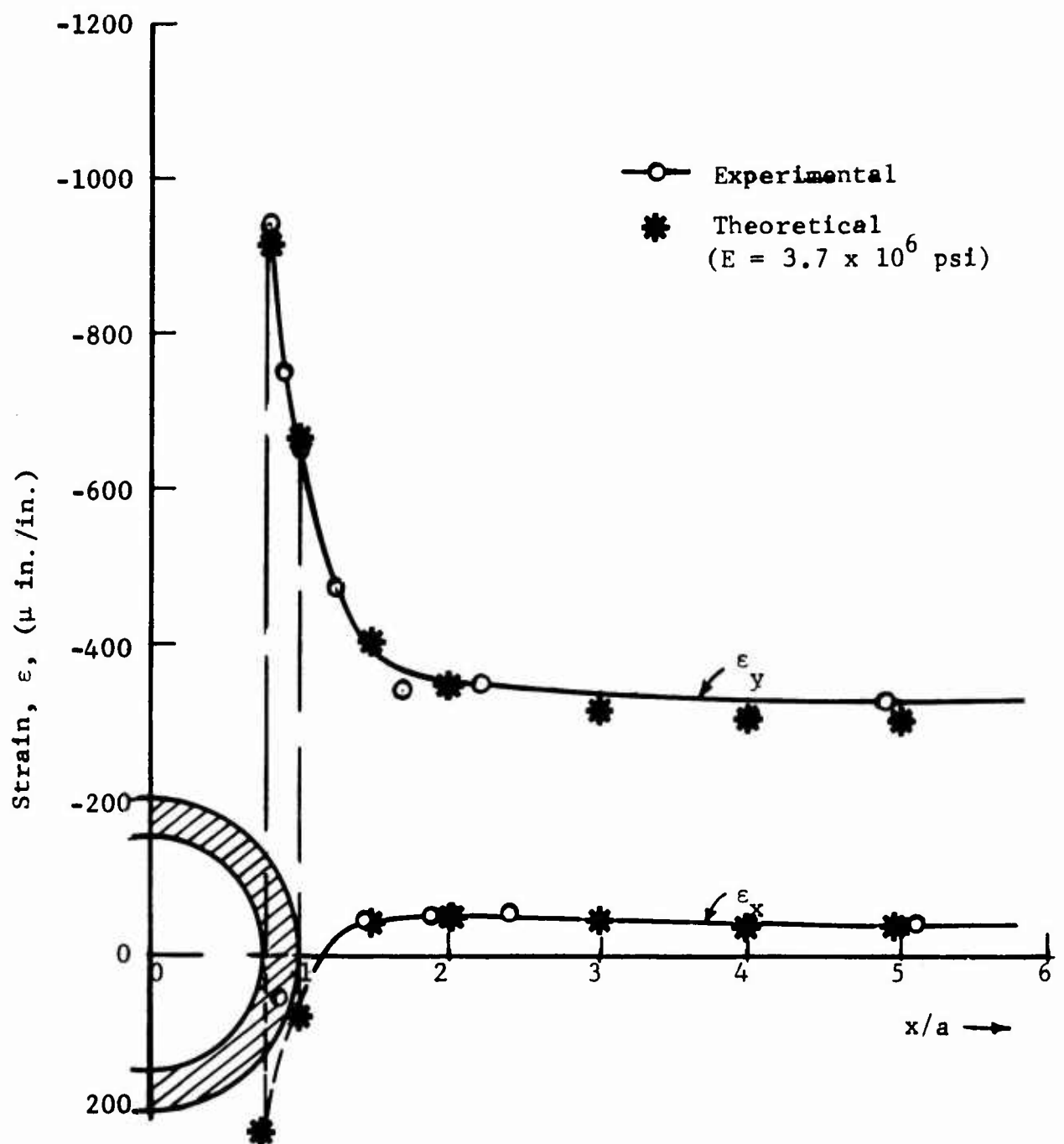
Fig. 213   STRAIN DISTRIBUTION ALONG HORIZONTAL AXIS AT APPLIED
VERTICAL STRESS OF p = 1,200 PSI FOR SPECIMEN NO. 17
(LIMESTONE LINED WITH HYDROSTONE UNDER BIAXIAL LOADING)

293

liner was loaded in biaxial compression. The vertical load was applied in 30,000 lb increments and the lateral load in increments of 15,000 lb.

Isochromatic fringe patterns are shown in Fig. 214 for various levels of loading including zero load after failure. The photoelastic pattern shows evidence of pronounced deformation in the 90-degree sector around the horizontal axis. The specimen failed at a vertical load of 300,000 lb. The corresponding vertical and horizontal stresses were 4,110 psi and 1,340 psi, respectively. The primary failure mode again was splitting along a vertical plane normal to the axis of the hole. One of the halves underwent further cracking in various radial directions around the hole (Fig. 215).

Diametral changes as a function of applied vertical stress are plotted in Fig. 216. Both horizontal and vertical deflections are negative with the former very small as expected. The vertical deflection is linear up to p = 3,300 psi. The horizontal deflection is linear throughout the recorded range. Deflections per unit vertical stress in the linear range are as follows:

$$\frac{\delta_h}{p} = -0.12 \times 10^{-6} \text{ in./psi}$$

$$\frac{\delta_v}{p} = -1.8 \times 10^{-6} \text{ in./psi}$$

Strains along the axes of symmetry and the 45-degree radius with radial distance as a parameter are plotted as a function of applied vertical stress in Figs. 217 through 221. The vertical strains along the horizontal axis are linear up to p = 3,000 psi. The ratio of the maximum compressive strain at the interface to the far-field vertical strain is

$$k_\varepsilon = 1.85$$

compared to the theoretical value of 1.25 (Eqs. 57, 58). A Young's modulus of $E = 4.0 \times 10^6$ psi was computed from the average of all

294

| p = 0 psi | p = 820 psi | p = 1650 psi |
| q = 0 psi | q = 280 psi | q = 560 psi |

| p = 2470 psi | p = 2880 psi | p = 3290 psi |
| q = 830 psi | q = 970 psi | q = 1110 psi |

| p = 3700 psi | p = 4110 psi | p = 0 psi |
| q = 1250 psi | q = 1440 psi | q = 0 psi |
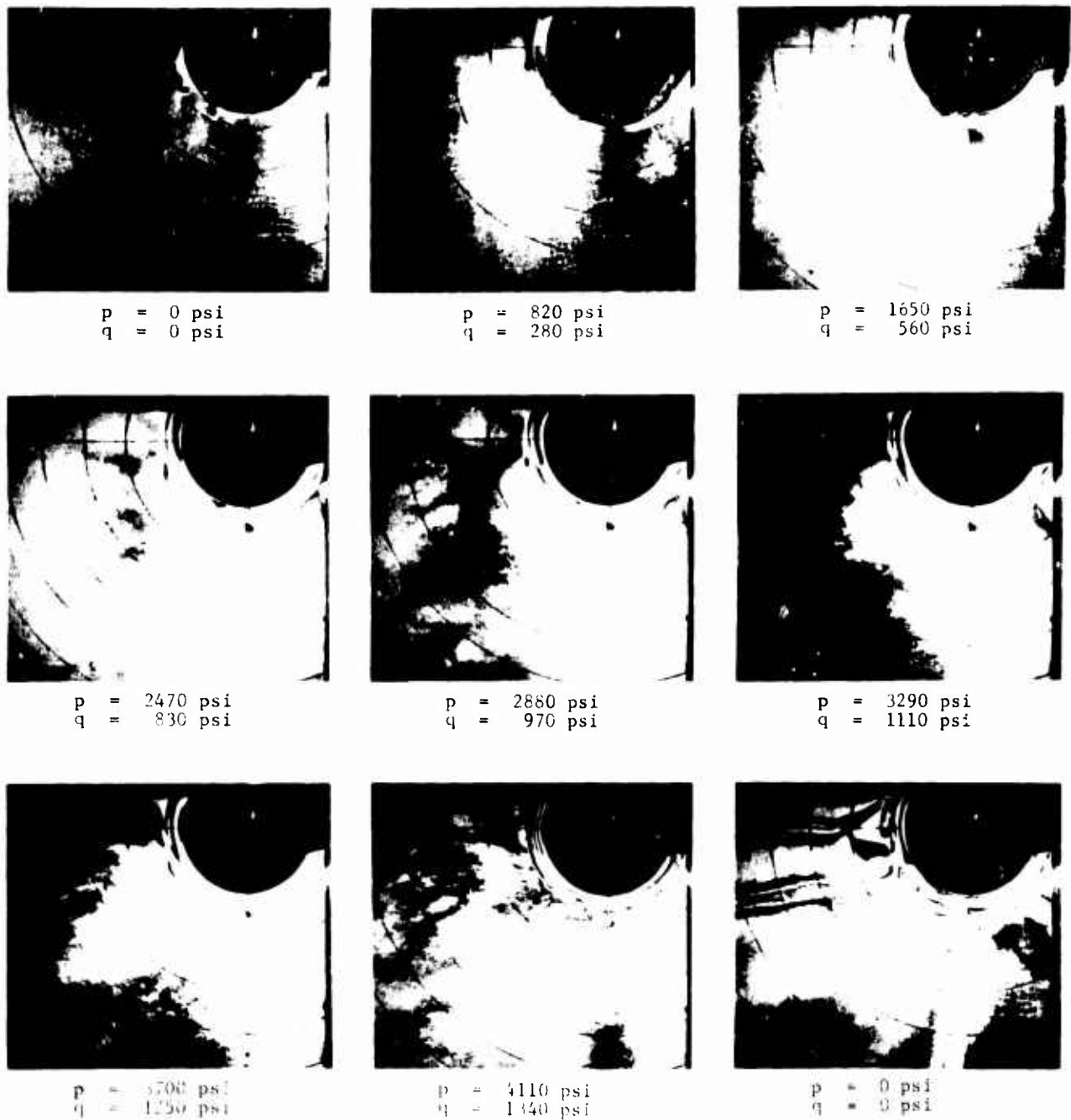
Fig. 214   ISOCHROMATIC FRINGE PATTERNS IN PHOTOELASTIC COATING
            AROUND HOLE IN SPECIMEN NO. 18 (LIMESTONE WITH ALUMINUM
            LINER UNDER BIAXIAL LOADING)

295

Fig. 215 FAILURE PATTERN OF SPECIMEN NO. 18 (LIMESTONE WITH ALUMINUM LINER UNDER BIAXIAL LOADING)

296
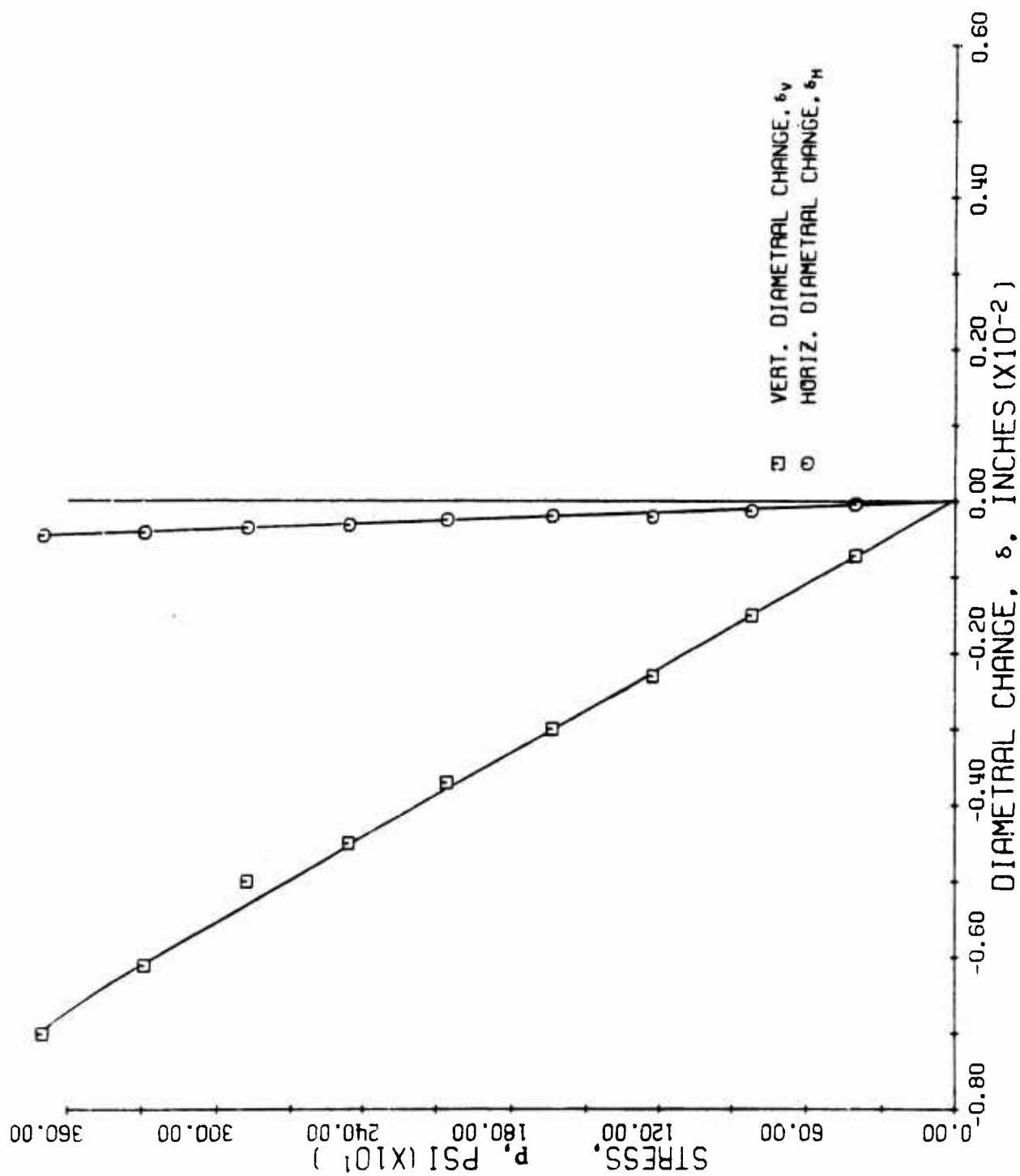
FIG. 216 DIAMETRAL CHANGES AS A FUNCTION OF APPLIED VERTICAL STRESS FOR SPECIMEN NO.18 (LIMESTONE WITH ALUMINUM LINER UNDER BIAXIAL LOADING)
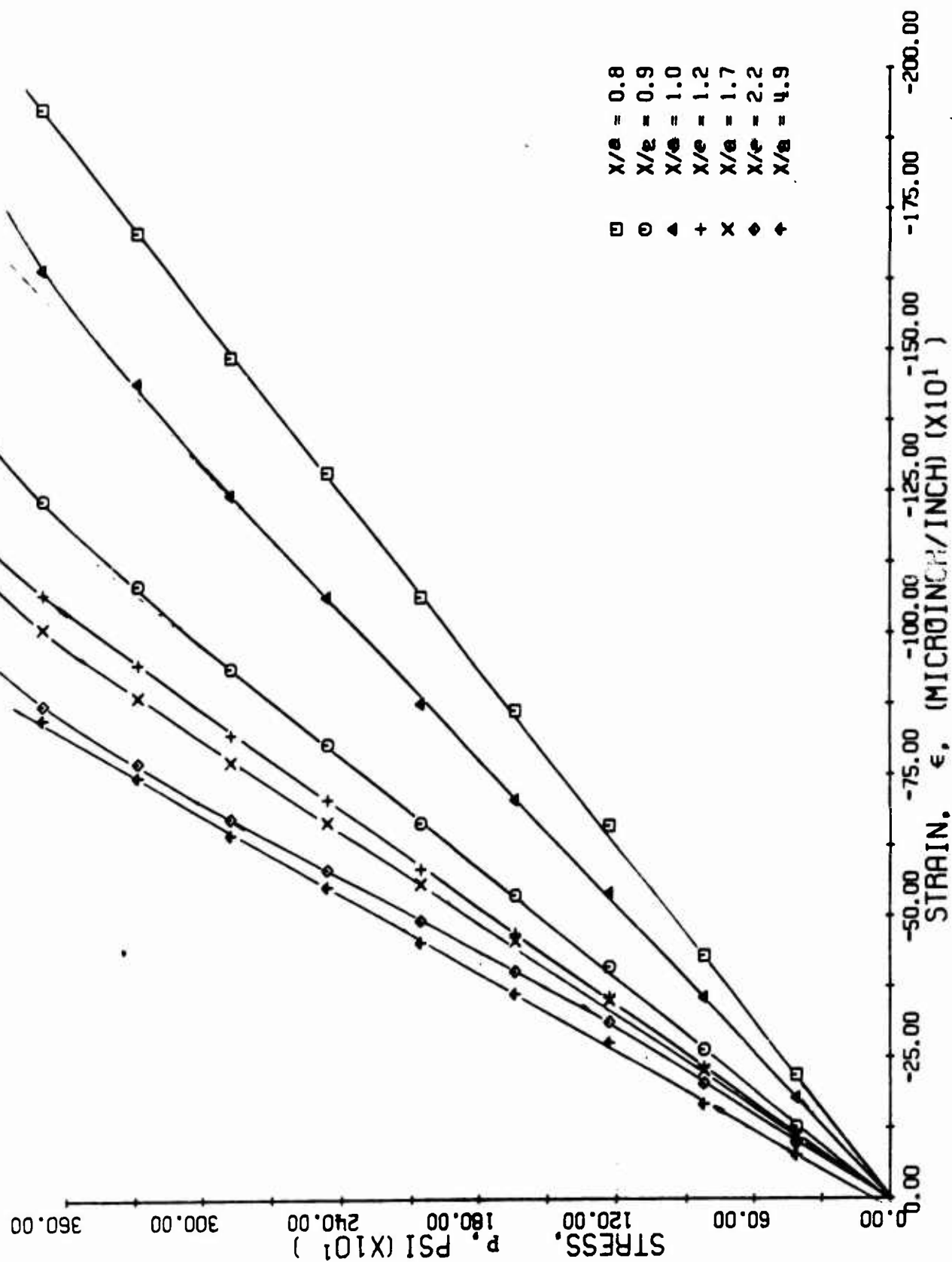
FIG. 217 VERTICAL STRAINS ALONG HORIZONTAL AXIS OF SYMMETRY AS A FUNCTION OF APPLIED VERTICAL STRESS FOR SPECIMEN NO. 18 (LIMESTONE WITH ALUMINUM LINER UNDER BIAXIAL LOADING)

298
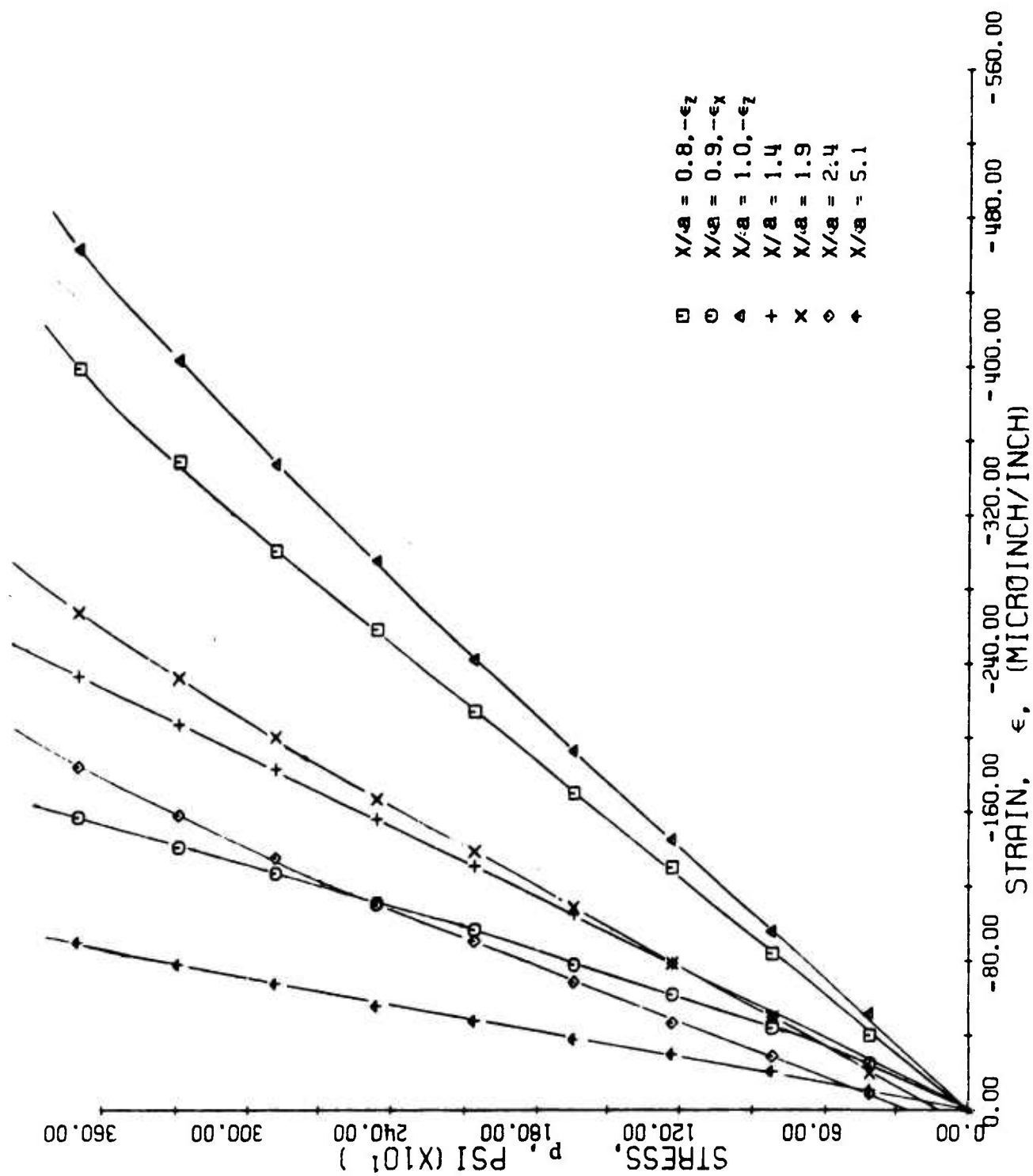
FIG. 218 HORIZONTAL STRAINS ALONG HORIZONTAL AXIS OF SYMMETRY AS A FUNCTION OF APPLIED VERTICAL
STRESS FOR SPECIMEN NO. 18 (LIMESTONE WITH ALUMINUM LINER UNDER BIAXIAL LOADING)

299
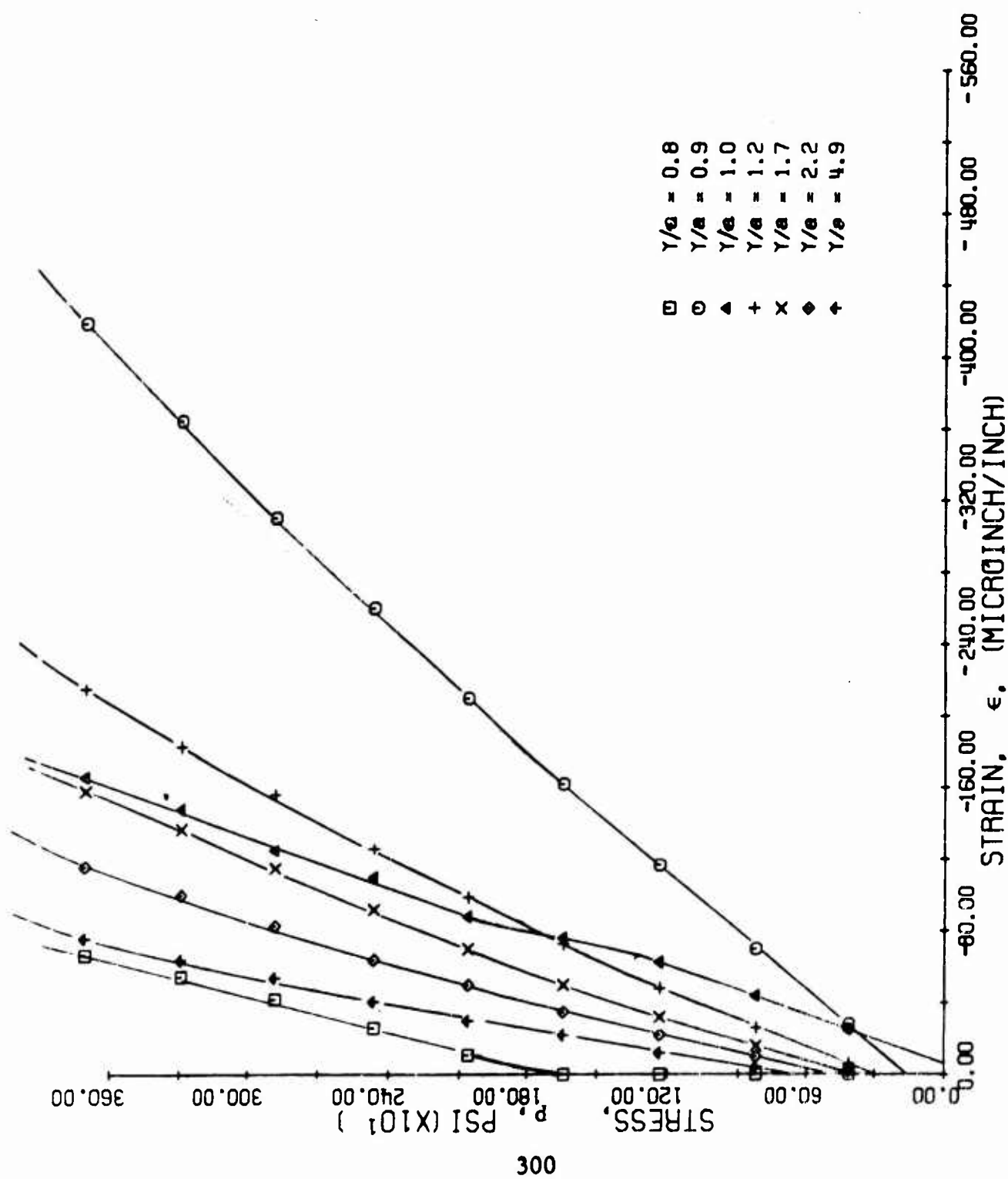
FIG. 219 HORIZONTAL STRAINS ALONG VERTICAL AXIS OF SYMMETRY AS A FUNCTION OF APPLIED VERTICAL STRESS FOR SPECIMEN NO. 18 (LIMESTONE WITH ALUMINUM LINER UNDER BIAXIAL LOADING)

300

FIG. 220   VERTICAL STRAINS ALONG VERTICAL AXIS OF SYMMETRY AS A FUNCTION OF APPLIED VERTICAL
STRESS FOR SPECIMEN NO. 18 (LIMESTONE WITH ALUMINUM LINER UNDER BIAXIAL LOADING)

301

FIG. 221 STRAINS ALONG 45 DEGREE RADIUS FOR SPECIMEN NO. 18 (LIMESTONE WITH ALUMINUM LINER UNDER BIAXIAL LOADING)

302

the vertical far-field strains. The horizontal strains along the horizontal axis, except for that on the edge of the liner, are linear up to at least p = 2,000 psi. The horizontal strains along the vertical axis show early nonlinearities, whereas the vertical strains along the same axis are linear throughout. Principal strains along the 45-degree radius were computed from the strain readings using the rosette equations and plotted in Fig. 222. The principal strain ε_1 is positive at r = 1.35a, decreases to nearly zero at r = 1.80a and becomes negative, although very small, at r = 3.00a. The angle between the 45-degree radius and the direction of ε_1, measured clockwise, remains nearly constant around 40.5 degrees at r = 1.35a, varies between 39 degrees and 40 degrees at r = 1.80a, and 39 degrees and 42 degrees at r = 3.00a.

Strains along the horizontal axis for an applied vertical stress of p = 1,800 psi were plotted in Fig. 223. Theoretical points for the inside of the liner and for the interface are also shown. The discrepancy in the strains at the interface between theory and experiment is apparent.

As discussed earlier, the failure of this specimen was rather complex, involving splitting along a vertical plane normal to the axis of the hole and radial cracking around the hole. The latter type of failure can be explained by calculating the principal stress distribution around the interface between liner and plate. Radial, circumferential and shear stresses were computed from Eqs. (57), (58), and (59) and principal stresses derived from these were plotted versus angular location in Fig. 224. It is seen that the tensile principal stress reaches a peak of 0.48p at θ = 38 degrees. Assuming elastic linear behavior, a maximum tensile stress of

$$\sigma_{max} = 0.48 \times 4110 = 1980 \text{ psi}$$

was reached when failure occurred.

FIG. 222 PRINCIPAL STRAINS ALONG 45 DEGREE RADIUS FOR SPECIMEN NO. 18
(LIMESTONE WITH ALUMINUM LINER UNDER BIAXIAL LOADING)

304

Fig. 223   STRAIN DISTRIBUTION ALONG HORIZONTAL AXIS AT APPLIED
VERTICAL STRESS OF p = 1,800 psi FOR SPECIMEN NO. 18
(LIMESTONE WITH ALUMINUM LINER UNDER BIAXIAL LOADING)

305

Fig. 224 VARIATION OF PRINCIPAL STRESSES AT INTERFACE BETWEEN ALUMINUM LINER AND LIMESTONE PLATE FOR BIAXIAL COMPRESSIVE LOADING (m = 0.34)

306

3. Specimen No. 19 - Marble Lined with Hydrostone Under Biaxial
   Loading

A marble plate of dimensions 36 in. x 24 in. x 3.03 in. with
a 4 in. diameter hole lined with a 0.44 in. thick hydrostone liner
was loaded in biaxial compression with a biaxiality ratio of m = 0.34.
The vertical load was applied in increments of 30,000 lb and the
corresponding hydraulic pressure for the lateral load in increments of
15,000 lb. At a vertical load level of 420,000 lb, a failure
occurred in one of the bolts of the hydraulic fixture and the lateral
load decreased abruptly. The specimen was retested up to the
capacity of the system, i.e., 600,000 lb vertical load, with no
apparent failure. However, the strain gage readings obtained from
the second test were erratic and were not used here.

A sequence of isochromatic fringe patterns is shown in Fig.225
for various levels of loading. The applied vertical and horizontal
stresses are shown with each frame. The last frame shows a high
compressive stress on the horizontal axis around the liner.

Diametral changes as a function of applied vertical stress
are plotted in Fig. 226. The horizontal deflection is essentially
zero throughout the test. The vertical deflection is linear for a
small portion of the loading range up to p = 1,750 psi. The curve
has a marked nonlinearity with a downward convexity, indicating some
stiffening around the cavity. The vertical deflection in the linear
range per unit of applied vertical stress is

$$\frac{\delta_v}{p} = -1.2 \times 10^{-6} \text{ in./psi}$$

This is approximately half the corresponding deflection for specimen
No. 17, since marble has a modulus twice as high as that of lime-
stone.

Strains along the axes of symmetry and the 45-degree radius
are plotted as a function of applied vertical stress in Figs. 227
through 231. The vertical strains along the horizontal axis are,

307

p = 0 psi
q = 0 psi
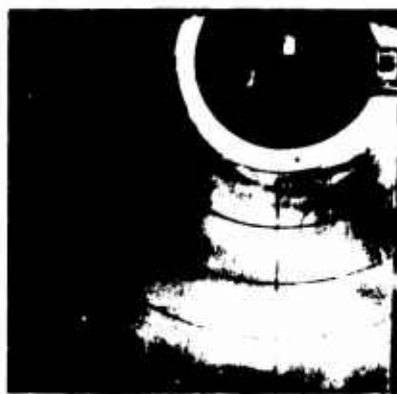
p = 820 psi
q = 280 psi
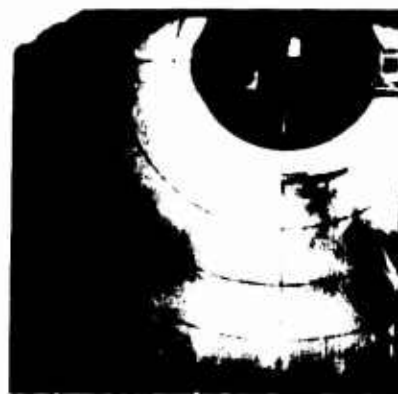
p = 1650 psi
q = 560 psi

p = 2470 psi
q = 840 psi

p = 3300 psi
q = 1120 psi

p = 3710 psi
q = 1260 psi

p = 4540 psi
q = 1540 psi

p = 5360 psi
q = 1820 psi

p = 8250 psi
q = 2800 psi

Fig. 225   ISOCHROMATIC FRINGE PATTERNS IN PHOTOELASTIC
COATING AROUND HOLE IN SPECIMEN NO. 19 (MARBLE
LINED WITH HYDROSTONE UNDER BIAXIAL LOADING)
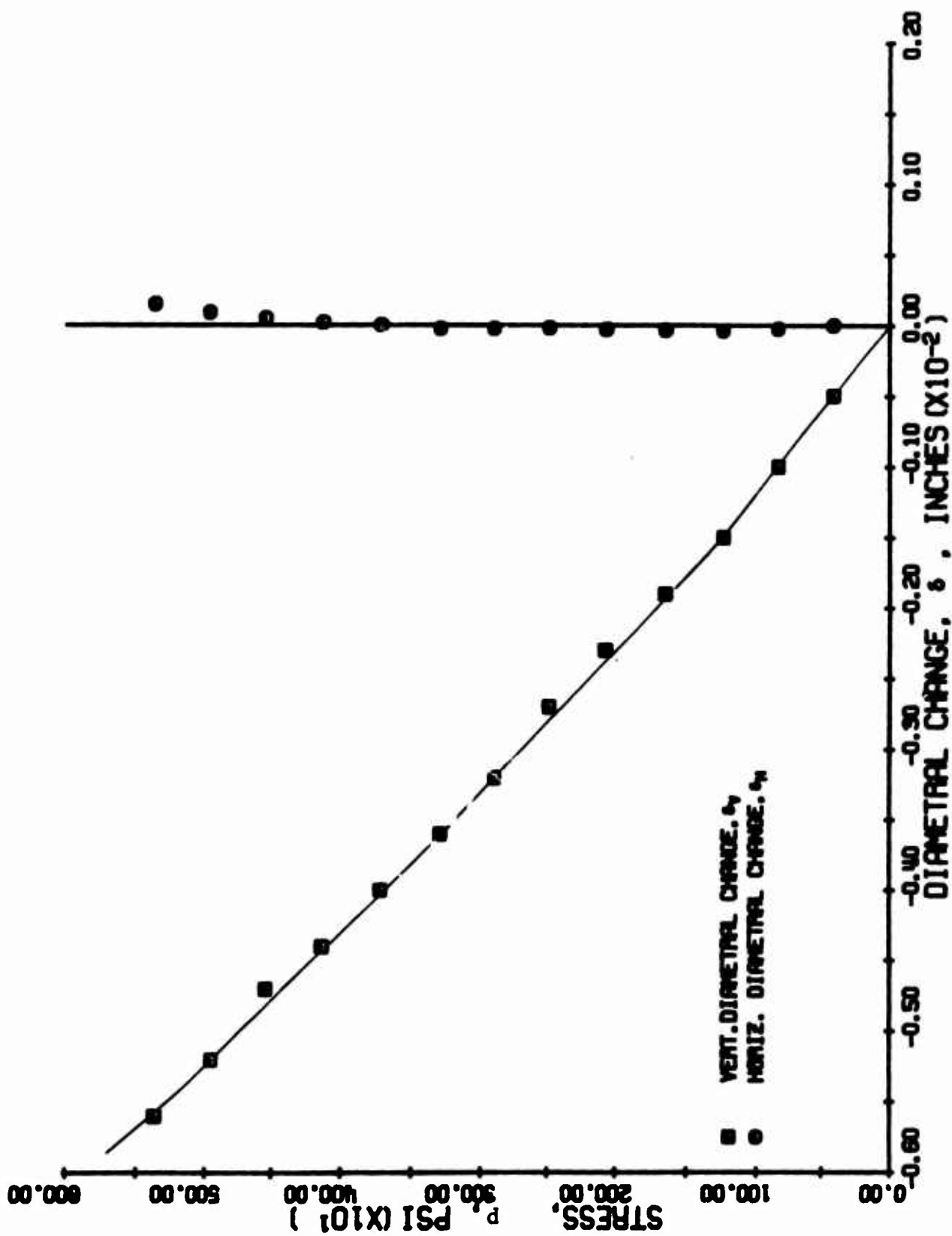
FIG. 226 DIAMETRAL CHANGES AS A FUNCTION OF APPLIED VERTICAL STRESS FOR SPECIMEN NO. 19 MARBLE WITH HYDROSTONE LINER UNDER BIAXIAL LOADING
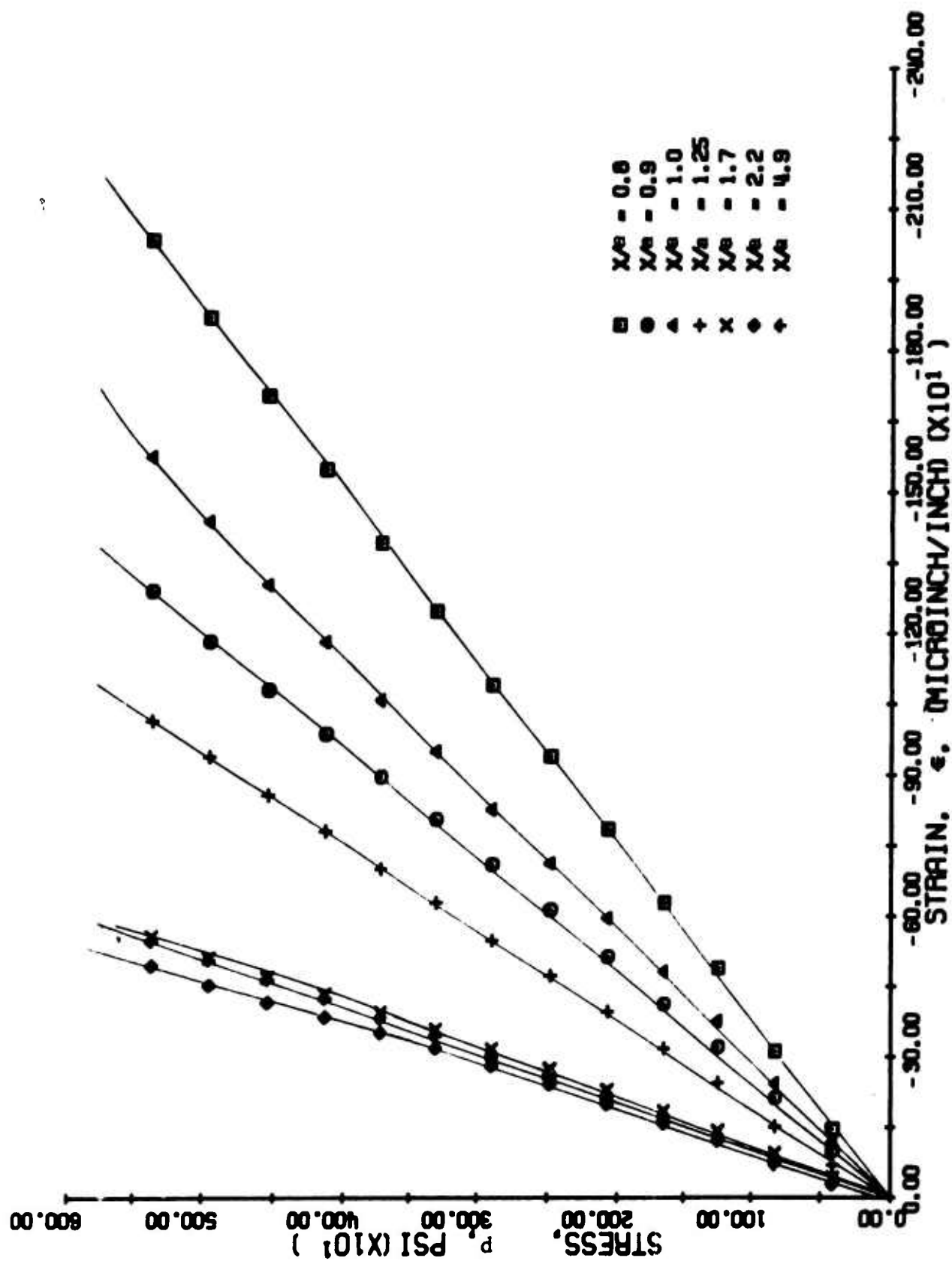
FIG. 227 VERTICAL STRAINS ALONG-HORIZONTAL AXIS OF SYMMETRY AS A FUNCTION OF APPLIED VERTICAL
STRESS FOR SPECIMEN NO. 19 MARBLE WITH HYDROSTONE LINER UNDER BIAXIAL LOADING
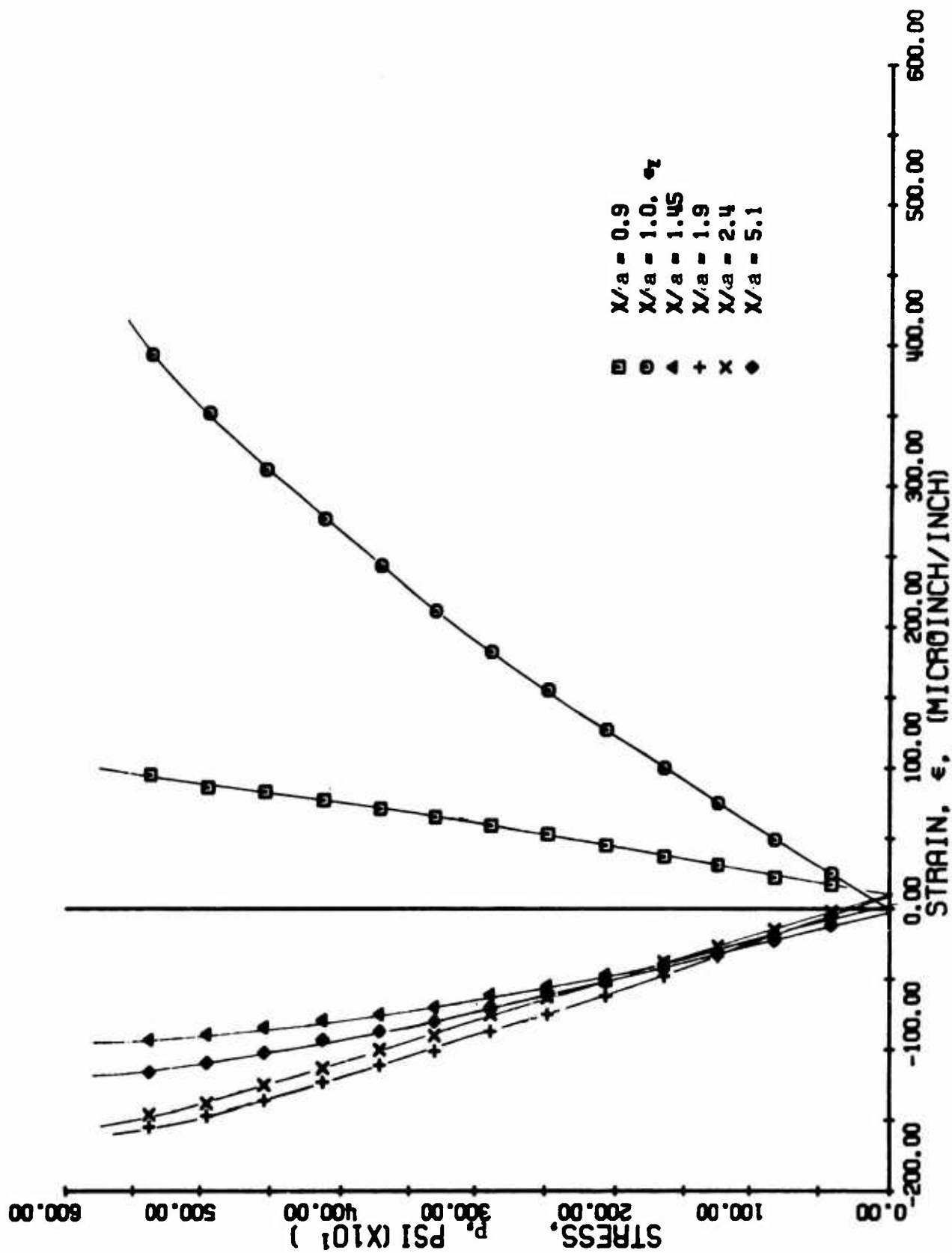
FIG. 228 HORIZONTAL STRAINS ALONG HORIZONTAL AXIS OF SYMMETRY AS A FUNCTION OF APPLIED VERTICAL STRESS FOR SPECIMEN NO. 19 (MARBLE WITH HYDROSTONE LINER UNDER BIAXIAL LOADING)
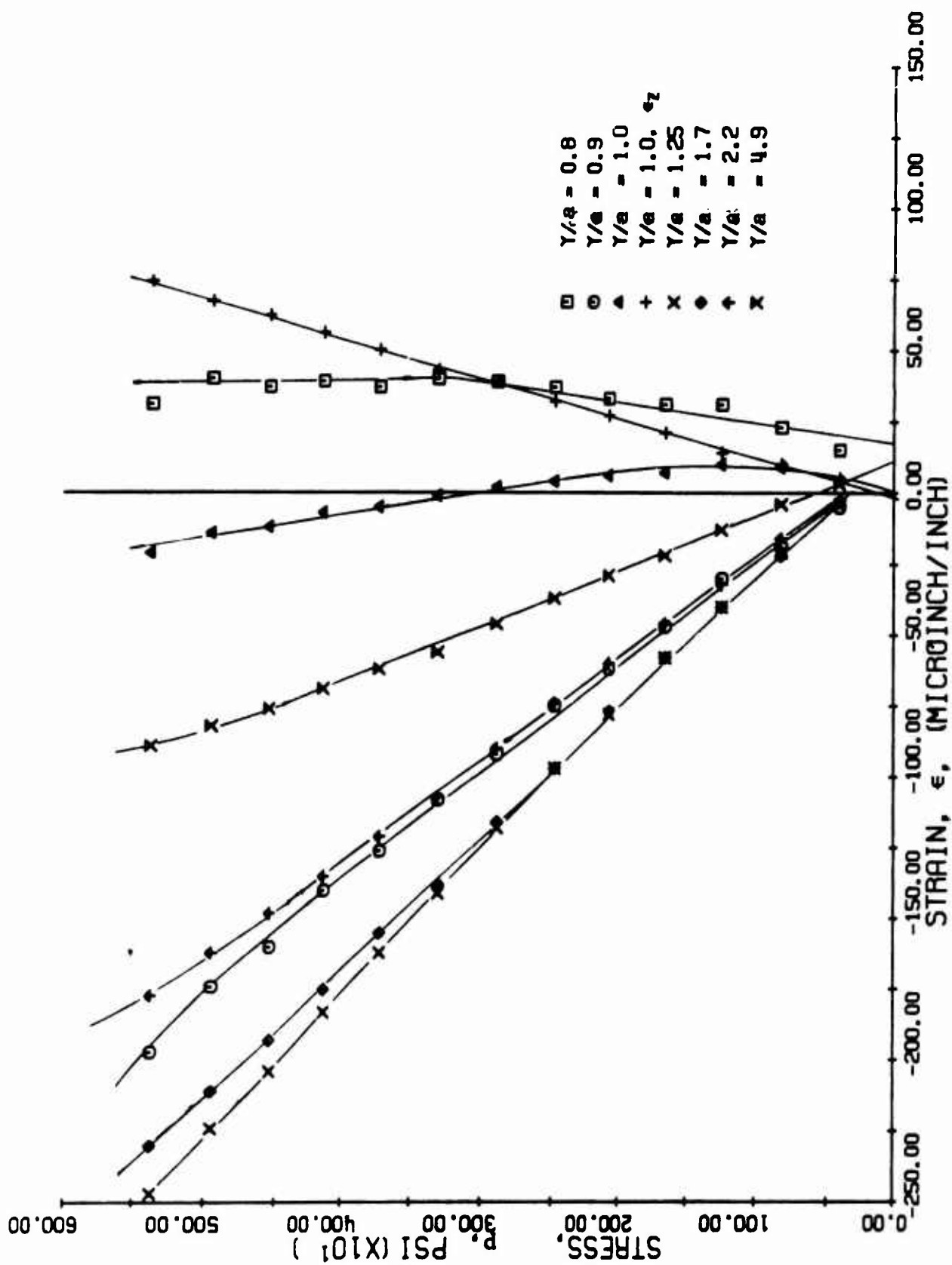
FIG. 229 HORIZONTAL STRAINS ALONG VERTICAL AXIS OF SYMMETRY AS A FUNCTION OF APPLIED VERTICAL STRESS FOR SPECIMEN NO. 19 (MARBLE WITH HYDROSTONE LINER UNDER BIAXIAL LOADING)
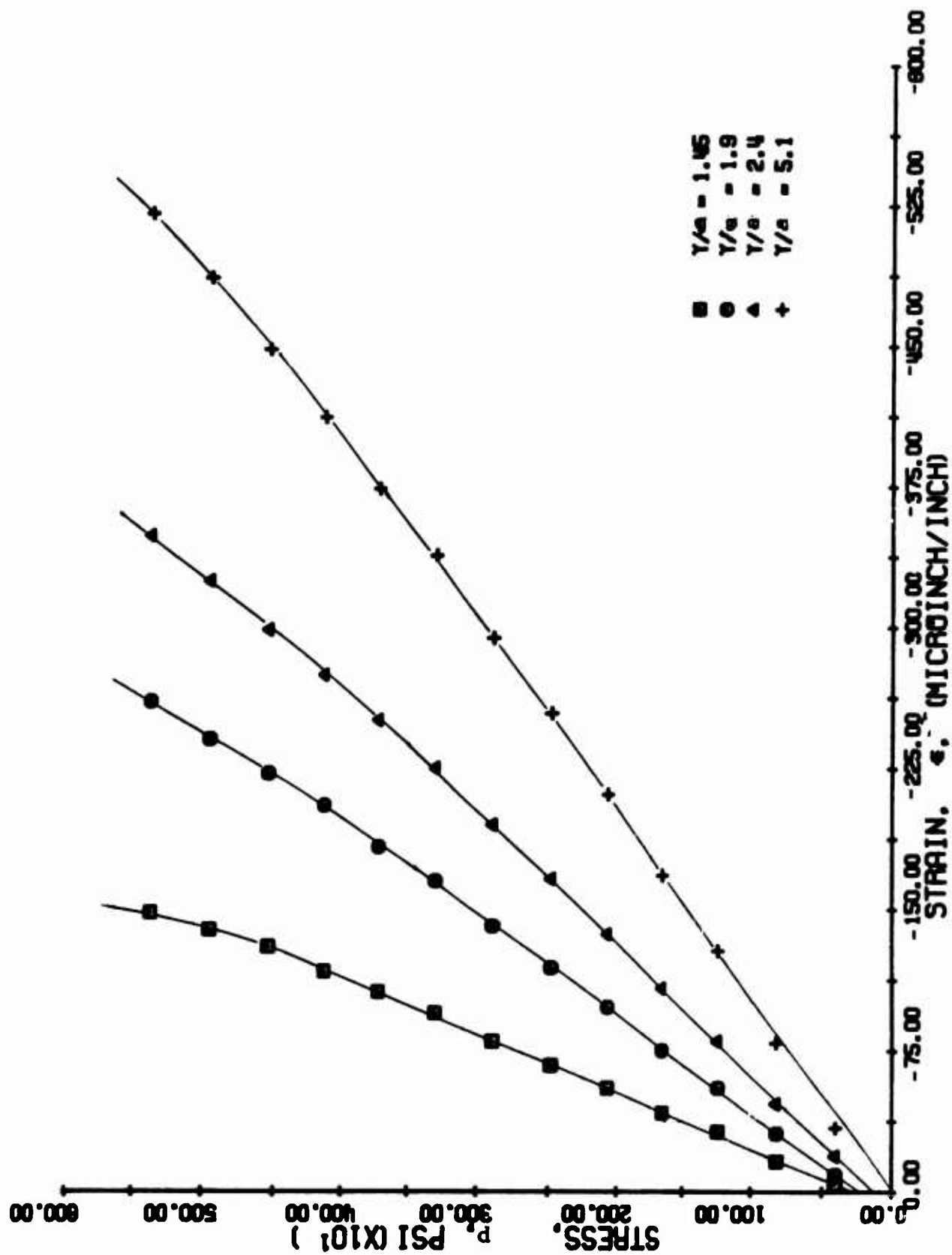
FIG. 230   VERTICAL STRAINS ALONG VERTICAL AXIS OF SYMMETRY AS A FUNCTION OF APPLIED VERTICAL
STRESS FOR SPECIMEN NO. 19 MARBLE WITH HYDROSTONE LINER UNDER BIAXIAL LOADING)

313
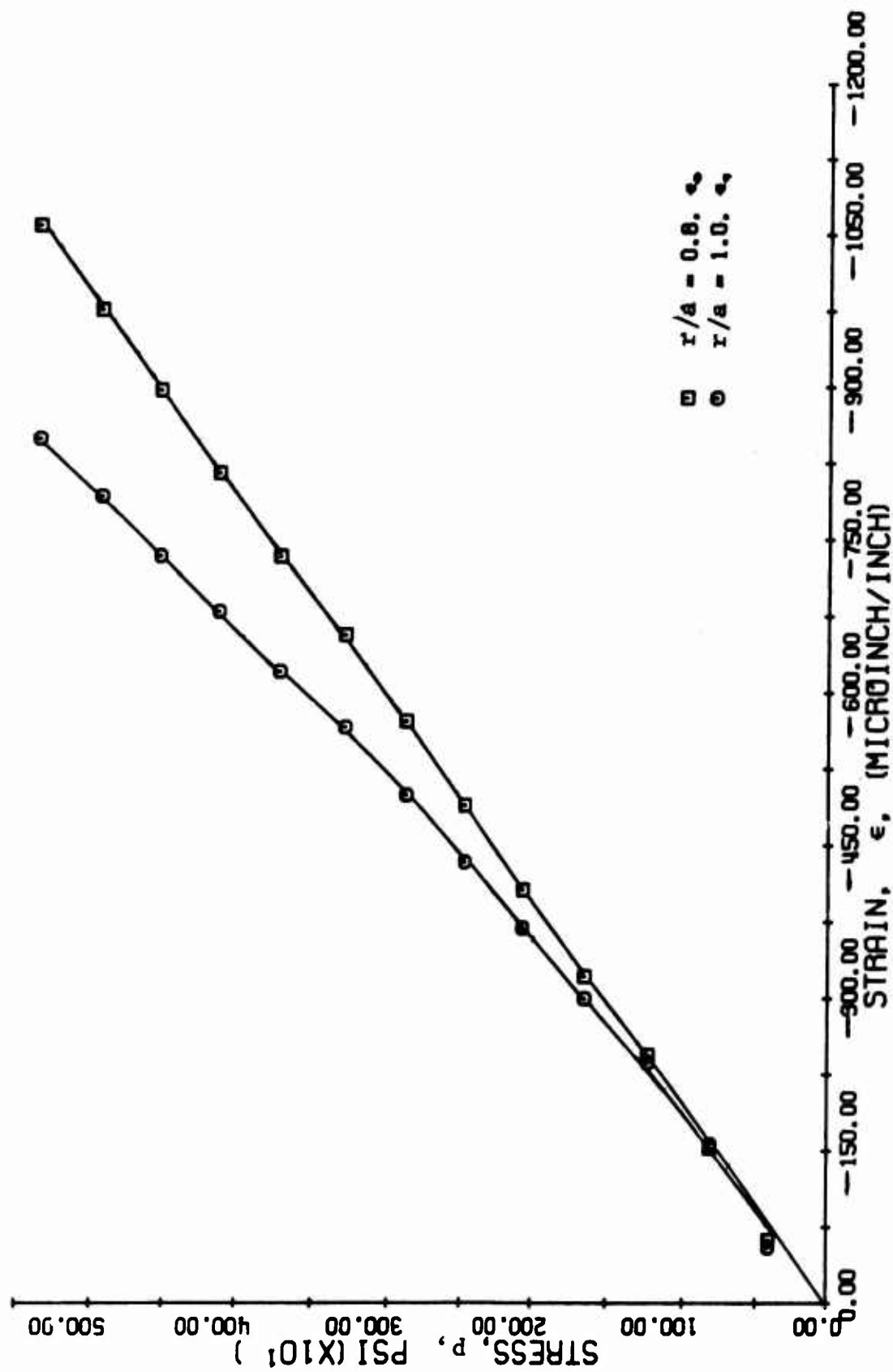
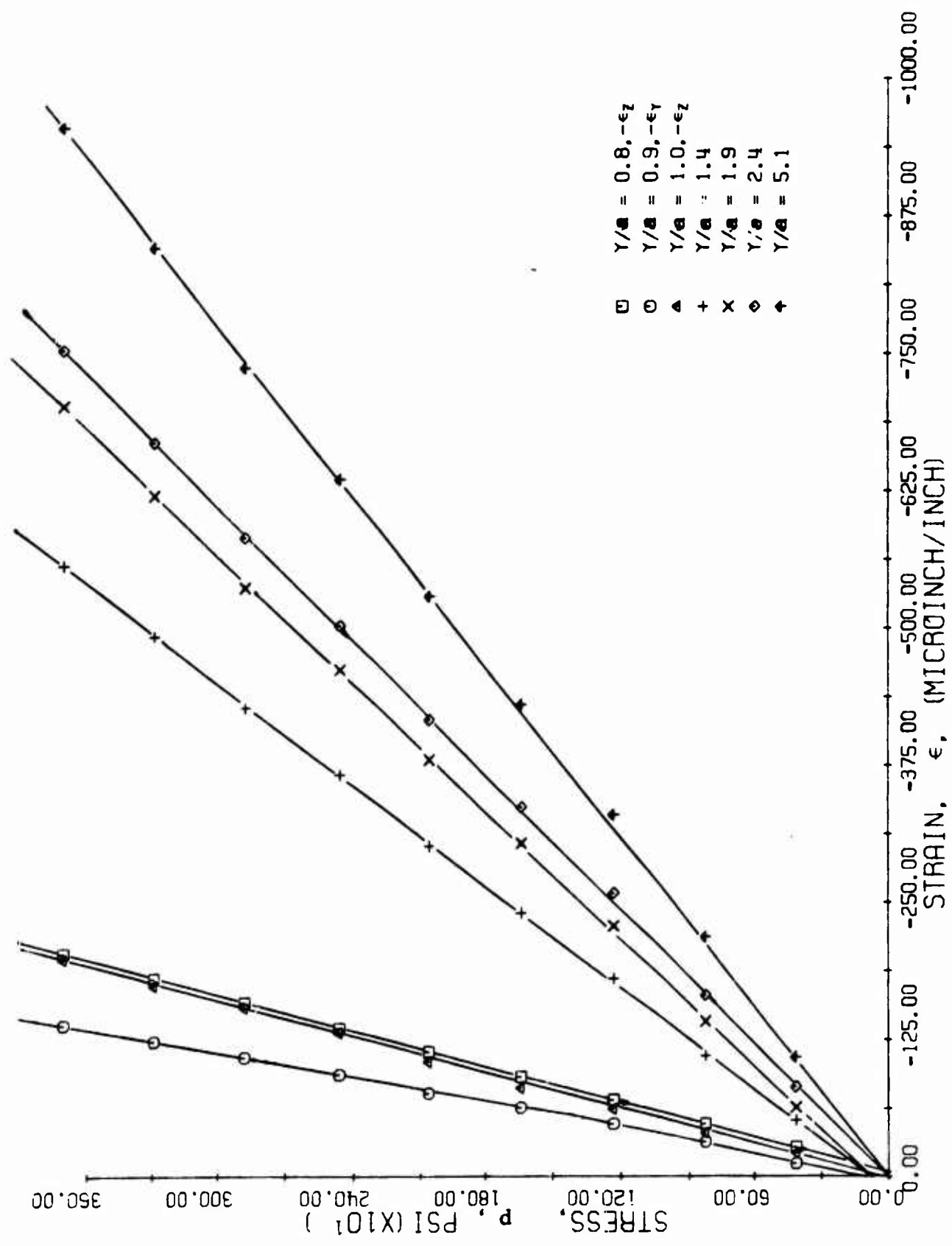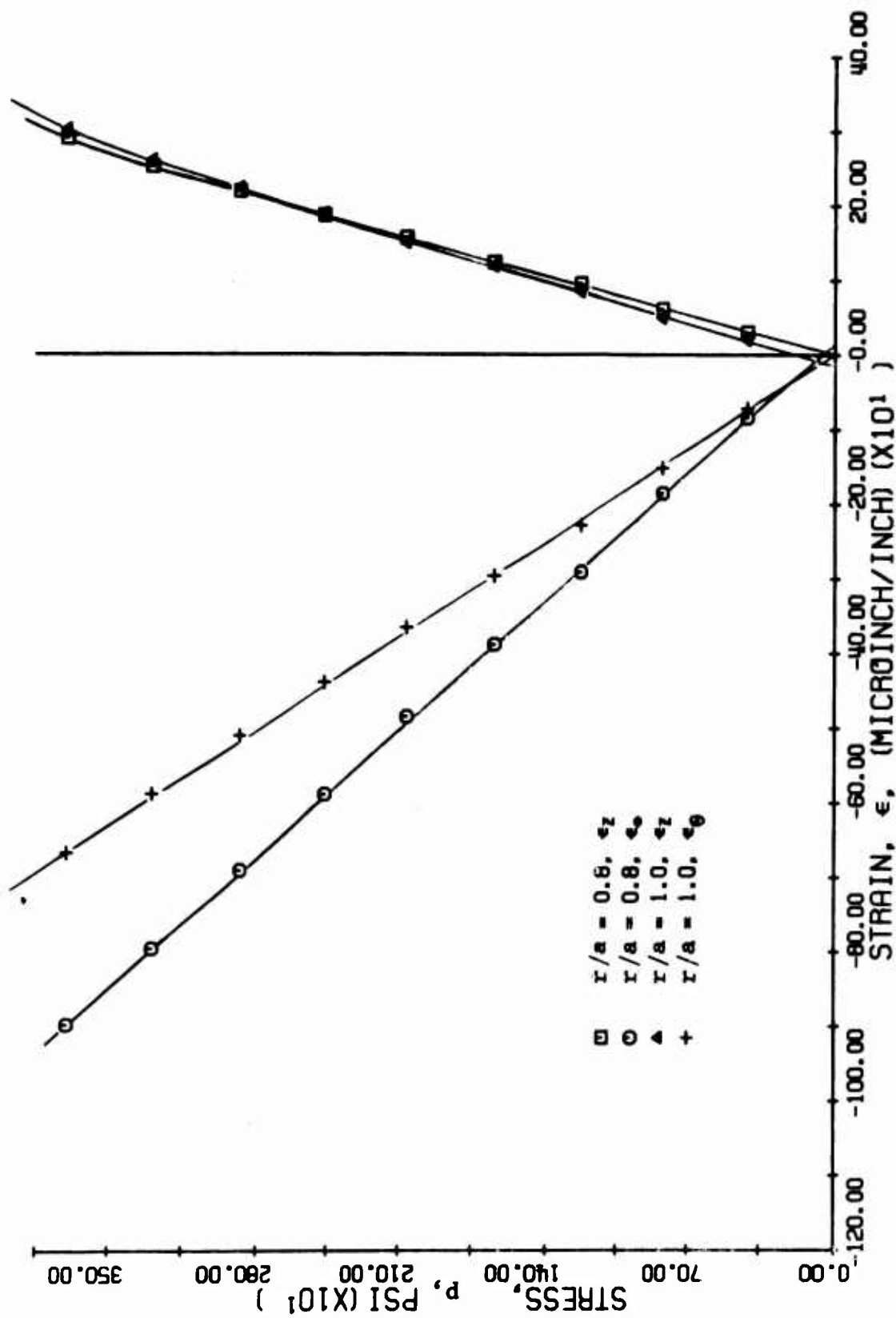FIG. 231 STRAINS ALONG 45 DEGREE RADIUS FOR SPECIMEN NO. 19 (MARBLE WITH HYDROSTONE LINER UNDER BIAXIAL LOADING)

with one exception, linear throughout (Fig. 227). The ratio of
the maximum compressive strain at the interface to the far-field
strain is

$$k_\varepsilon = 2.81$$

compared to the theoretical value of 2.63 (Eqs. 65 and 66). The
modulus computed from the far-field vertical strains is 8.8×10^6
psi. Principal strains computed from the rosette readings along
the 45-degree radius are plotted in Fig. 232. The principal strain
ε_1 decreases with increasing radial distance from positive values
at $r = 1.35a$ and $r = 1.80a$ to a slightly negative value at $r = 3.00a$.
The angle between the 45-degree radius and the direction of ε_1,
measured clockwise, varies between 25 degrees and 26 degrees at
$r = 1.35a$, 34 degrees and 36 degrees at $r = 1.80a$, and 39 degrees
and 39.5 degrees at $r = 3.00a$.

The strain distribution along the horizontal axis at an
applied vertical stress of $p = 3,000$ psi is plotted in Fig. 233.
The theoretical distribution is also shown. The agreement seems
to be satisfactory at the interface.

4. Specimen No. 20 - Marble Lined with Aluminum Under Biaxial
   Loading

A marble plate of dimensions 36 in. x 24 in. x 3.26 in.
with a 4 in. diameter hole lined with a 0.40 in. thick aluminum
liner was loaded in biaxial compression with a biaxiality ratio of
$m = 0.34$. The vertical load was applied in increments of 30,000 lb
and hydraulic pressure in increments of 15,000 lb. The specimen
was loaded to the full capacity of the system, i.e., a vertical
load of 600,000 lb and a hydraulic pressure of 10,000 psi, cor-
responding to a vertical stress of $p = 7,680$ and a horizontal stress
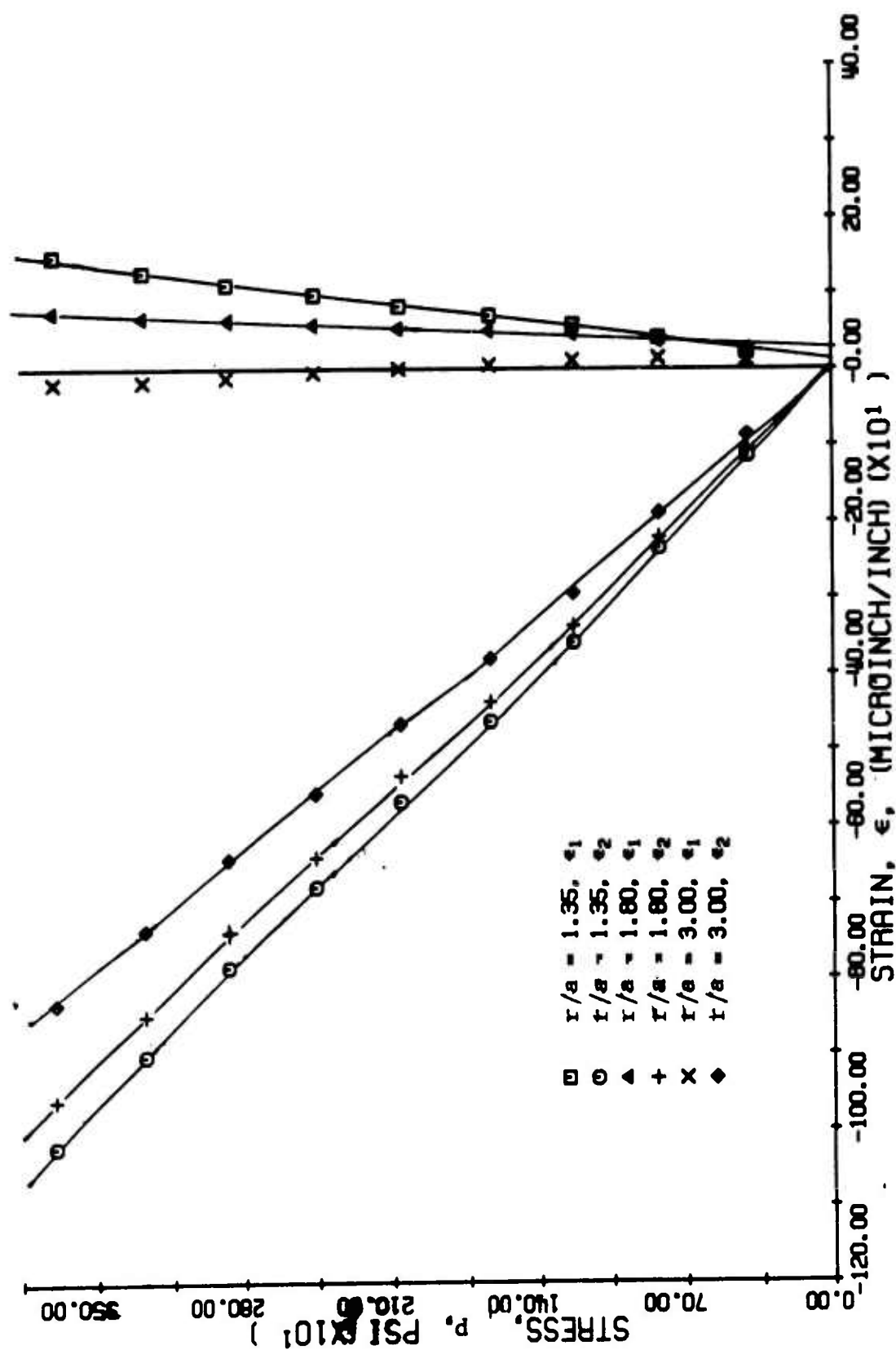of $q = 2,600$ psi. No failure was observed.
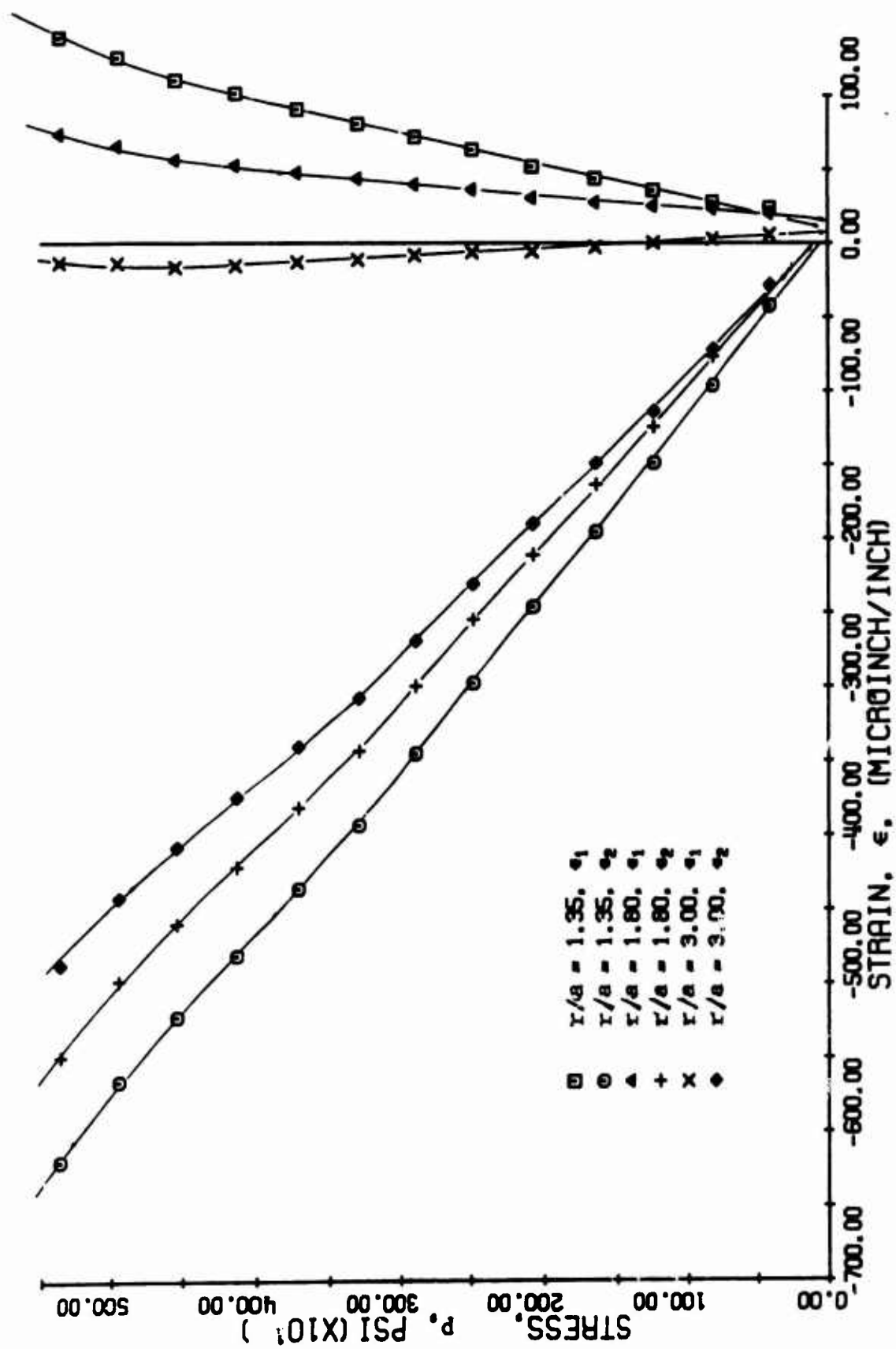
FIG. 232 PRINCIPAL STRAINS ALONG 45 DEGREE RADIUS FOR SPECIMEN NO. 19
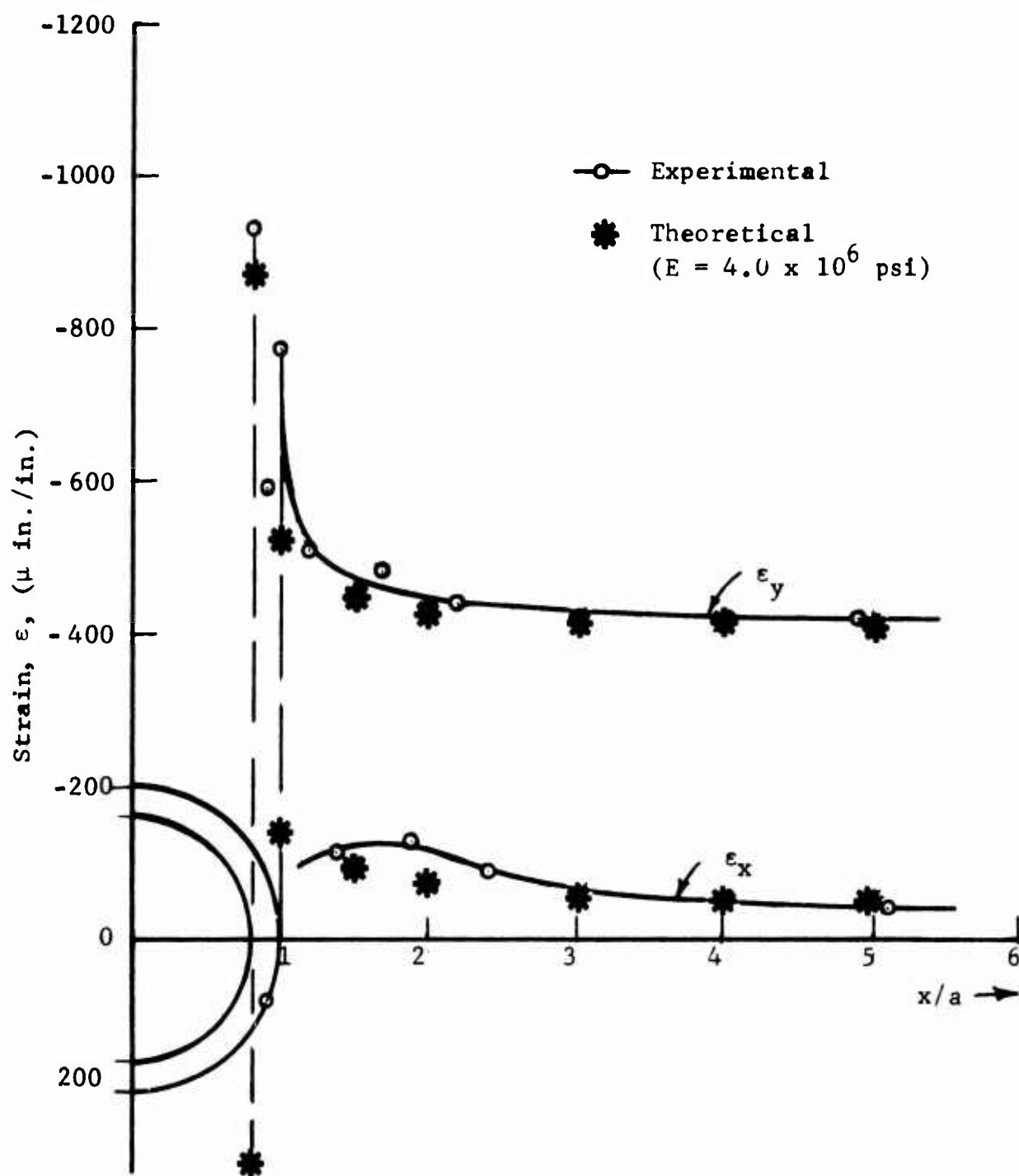(MARBLE WITH HYDROSTONE LINER UNDER BIAXIAL LOADING)

316
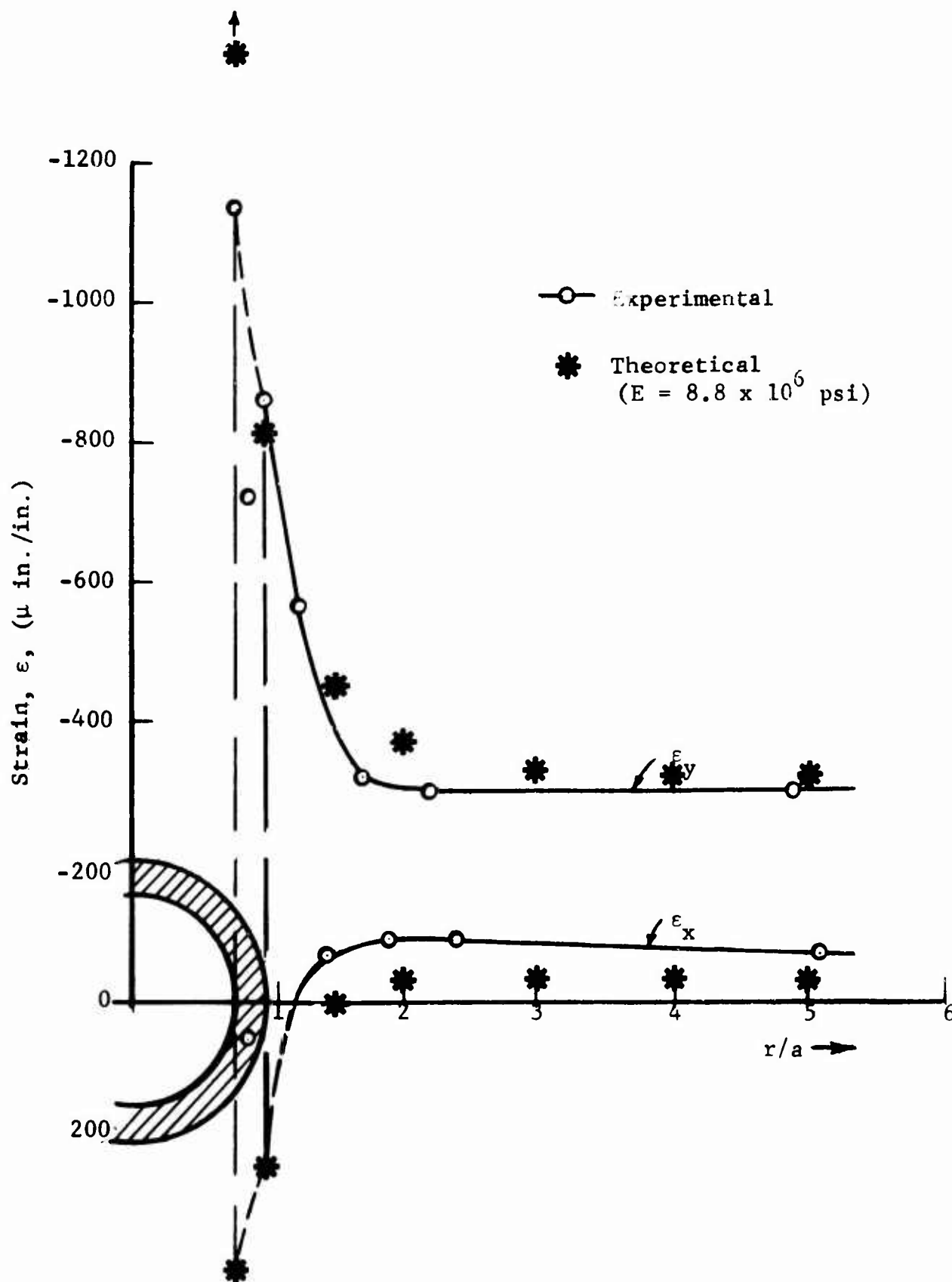
Fig. 233   STRAIN DISTRIBUTION ALONG HORIZONTAL AXIS AT APPLIED
VERTICAL STRESS OF p = 3,000 psi FOR SPECIMEN NO. 19
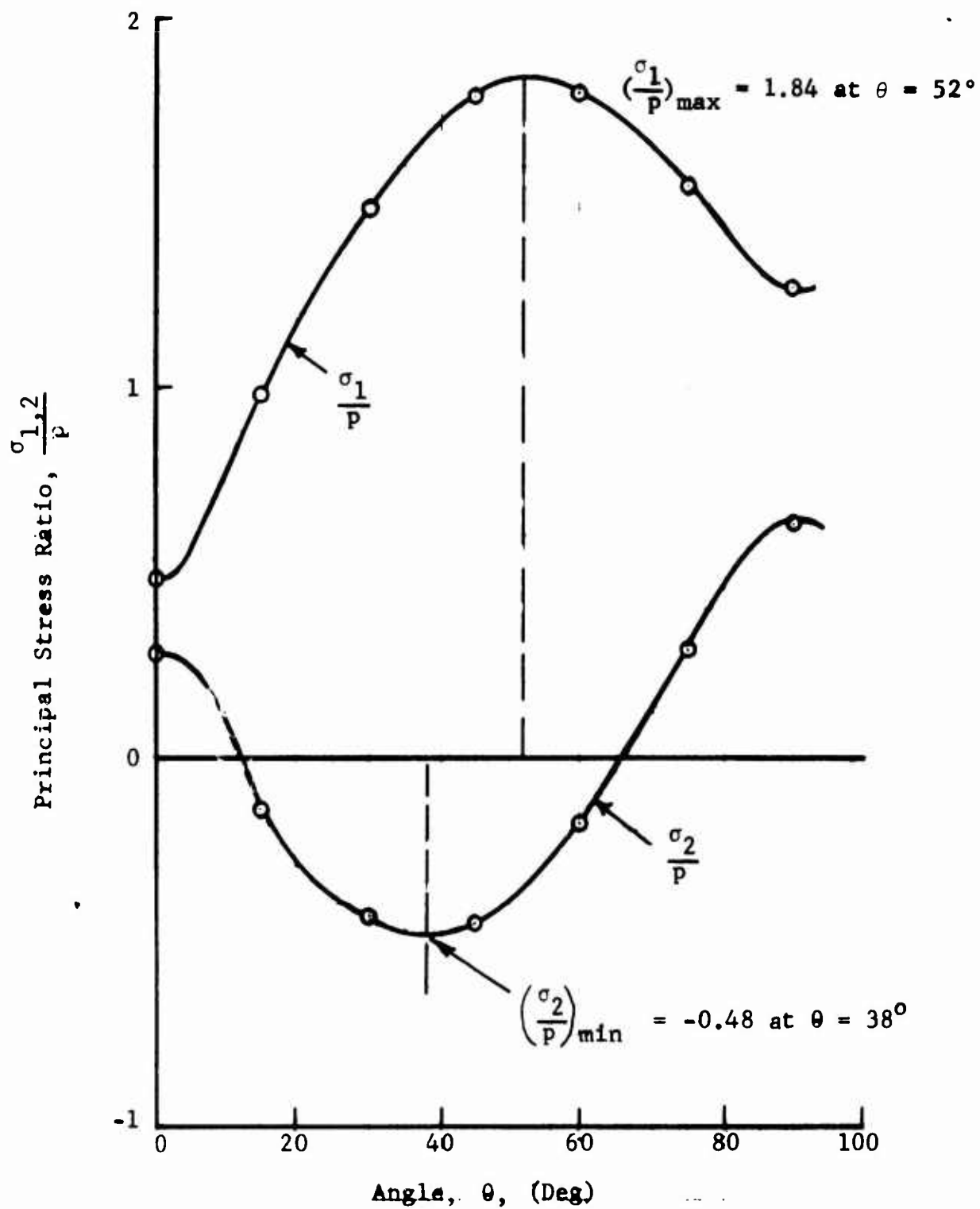(MARBLE LINED WITH HYDROSTONE UNDER BIAXIAL LOADING)

317

Isochromatic fringe patterns are shown in Fig. 234 for various levels of load. The fringe patterns show evidence of high compressive strains on the horizontal axis around the liner and high interfacial shear at the 45-degree locations.

Diametral changes as a function of applied vertical stress are plotted in Fig. 235. Both vertical and horizontal deflections are negative. They are linear up to approximately p = 4,200 psi. Deflections per unit of applied vertical stress are

$$\frac{\delta_h}{p} = -0.30 \times 10^{-6} \text{ in./psi}$$

$$\frac{\delta_v}{p} = -0.95 \times 10^{-6} \text{ in./psi}$$

The vertical deflection is approximately half the corresponding deflection in specimen No. 18, since the modulus of marble is approximately twice that of limestone. No reason is known for the discrepancy in the horizontal deflection.

Strains along the axes of symmetry and the 45-degree radius with radial distance as a parameter are plotted as a function of applied vertical stress in Figs. 236 through 240. The vertical strains along the horizontal axis become nonlinear at various stress levels with no discernible pattern. The lowest proportionality limit is at p = 3,200 psi. The ratio of the maximum compressive strain at the interface to the far-field vertical strain at this stress level is

$$k_\varepsilon = 1.95$$

compared to the theoretical value of 2.44 (Eqs. 73 and 74). A Young's modulus of $E = 8.6 \times 10^{-6}$ psi was computed from the average of all the vertical far-fiels strains. The lowest limit of linearity for the rest of the strains is p = 3,000 psi. Principal strains along the 45-degree radius were computed and plotted in Fig. 241. The

318

p = 5000 psi
q = 1690 psi

p = 7680 psi
q = 2600 psi

p = 1920 psi
q = 650 psi

p = 6530 psi
q = 2210 psi

p = 5760 psi
q = 1950 psi

Fig. 234 ISOCHROMATIC FRINGE PATTERNS IN PHOTOELASTIC COATING AROUND HOLE IN SPECIMEN NO. 20 (MARBLE WITH ALUMINUM LINER UNDER BIAXIAL LOADING)
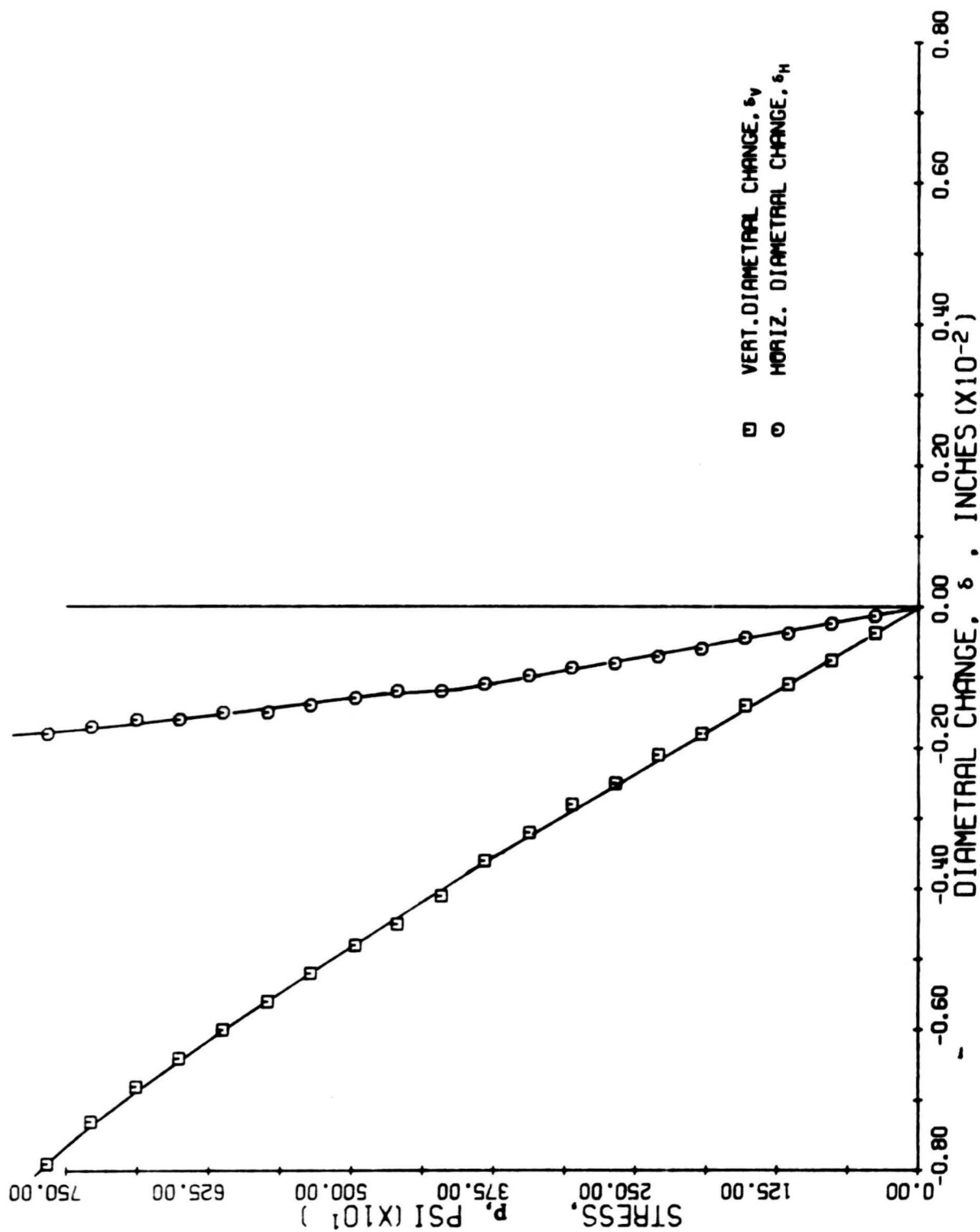
FIG. 235 DIAMETRAL CHANGES AS A FUNCTION OF APPLIED VERTICAL STRESS FOR SPECIMEN NO.20 (MARBLE WITH ALUMINUM LINER UNDER BIAXIAL LOADING)

320
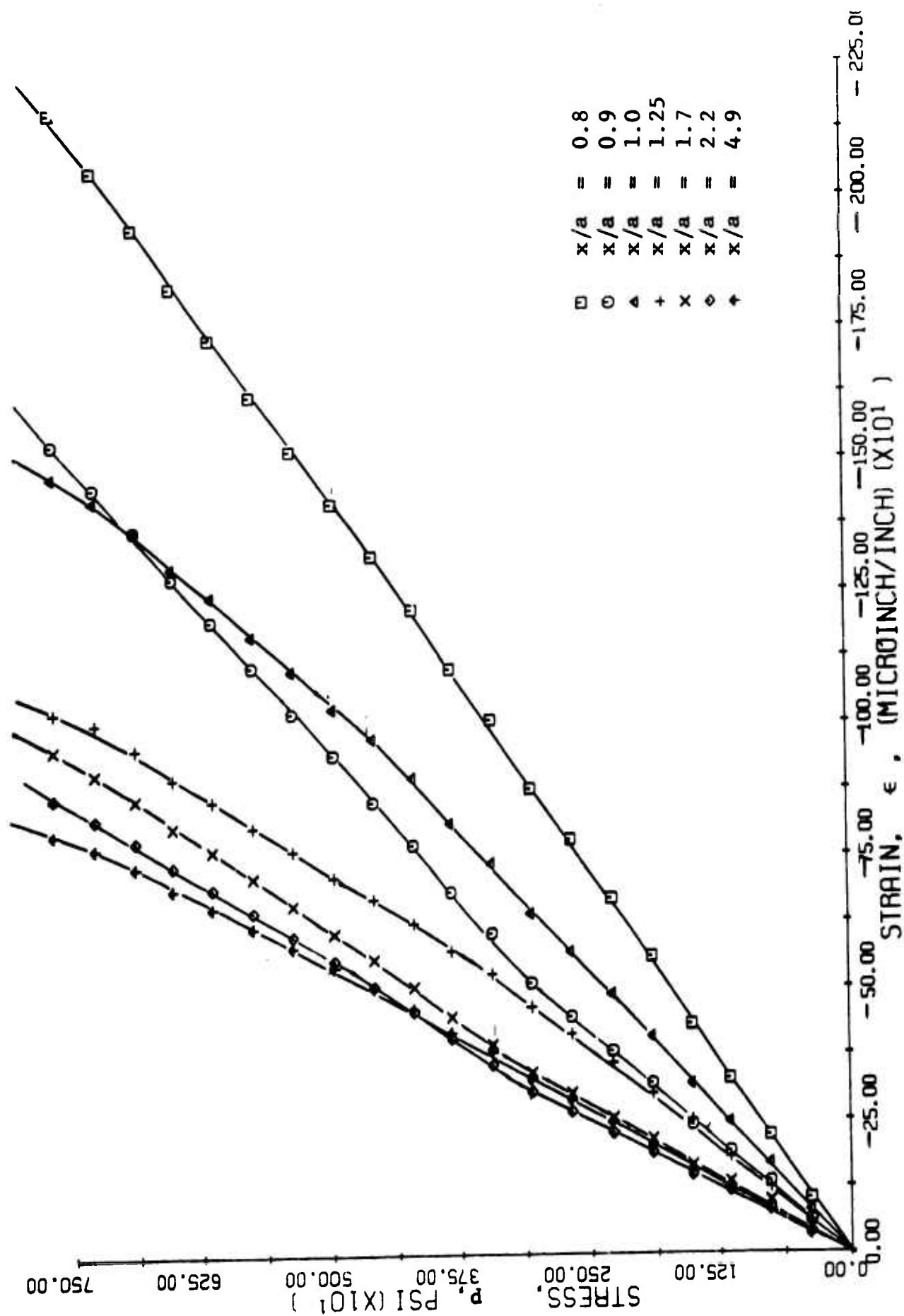
FIG. 236 VERTICAL STRAINS ALONG HORIZONTAL AXIS OF SYMMETRY AS A FUNCTION OF APPLIED VERTICAL STRESS FOR SPECIMEN NO.20 (MARBLE WITH ALUMINUM LINER UNDER BIAXIAL LOADING)
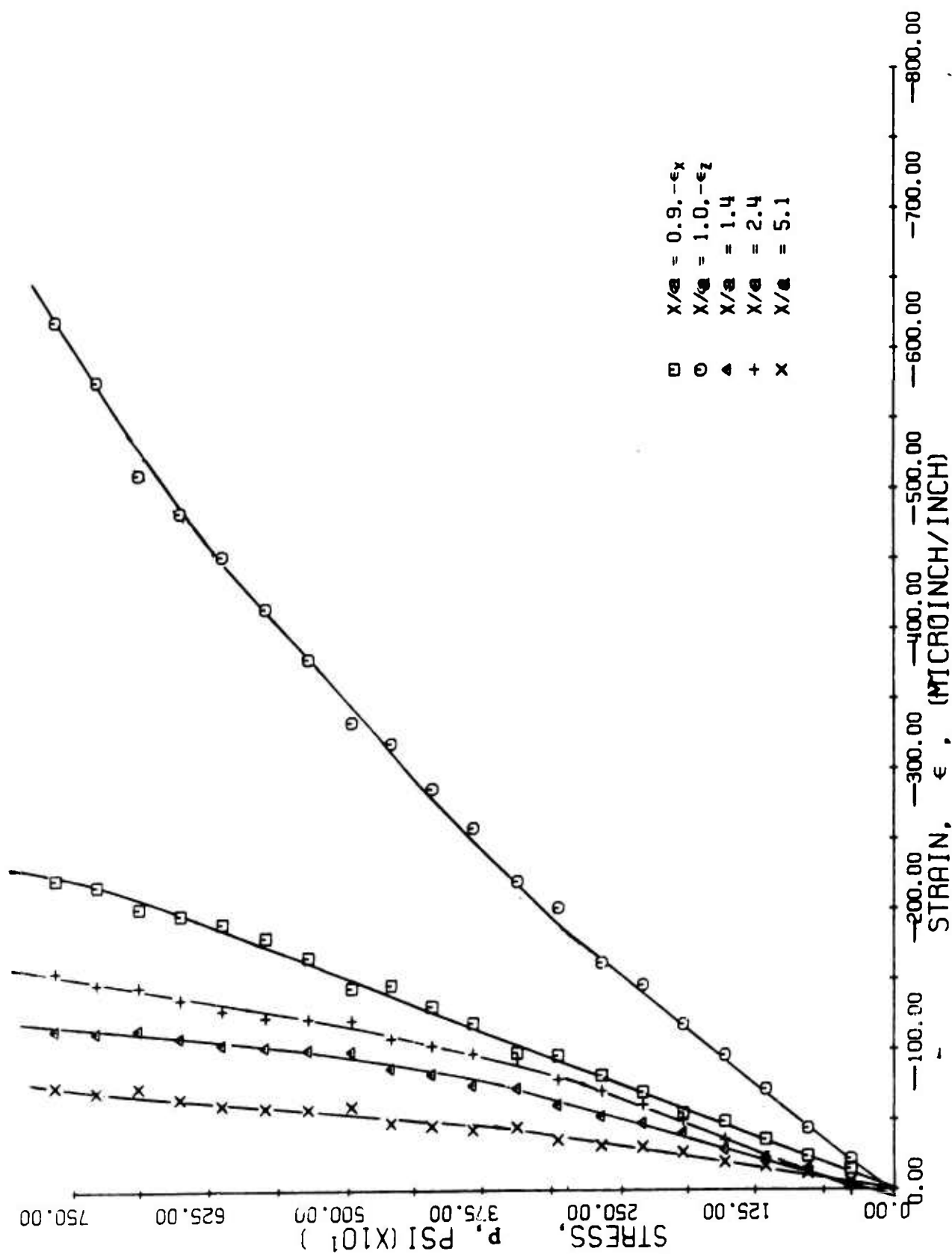
FIG. 237 HORIZONTAL STRAINS ALONG HORIZONTAL AXIS OF SYMMETRY AS A FUNCTION OF APPLIED VERTICAL
STRESS FOR SPECIMEN NO.20 (MARBLE WITH ALUMINUM LINER UNDER BIAXIAL LOADING)
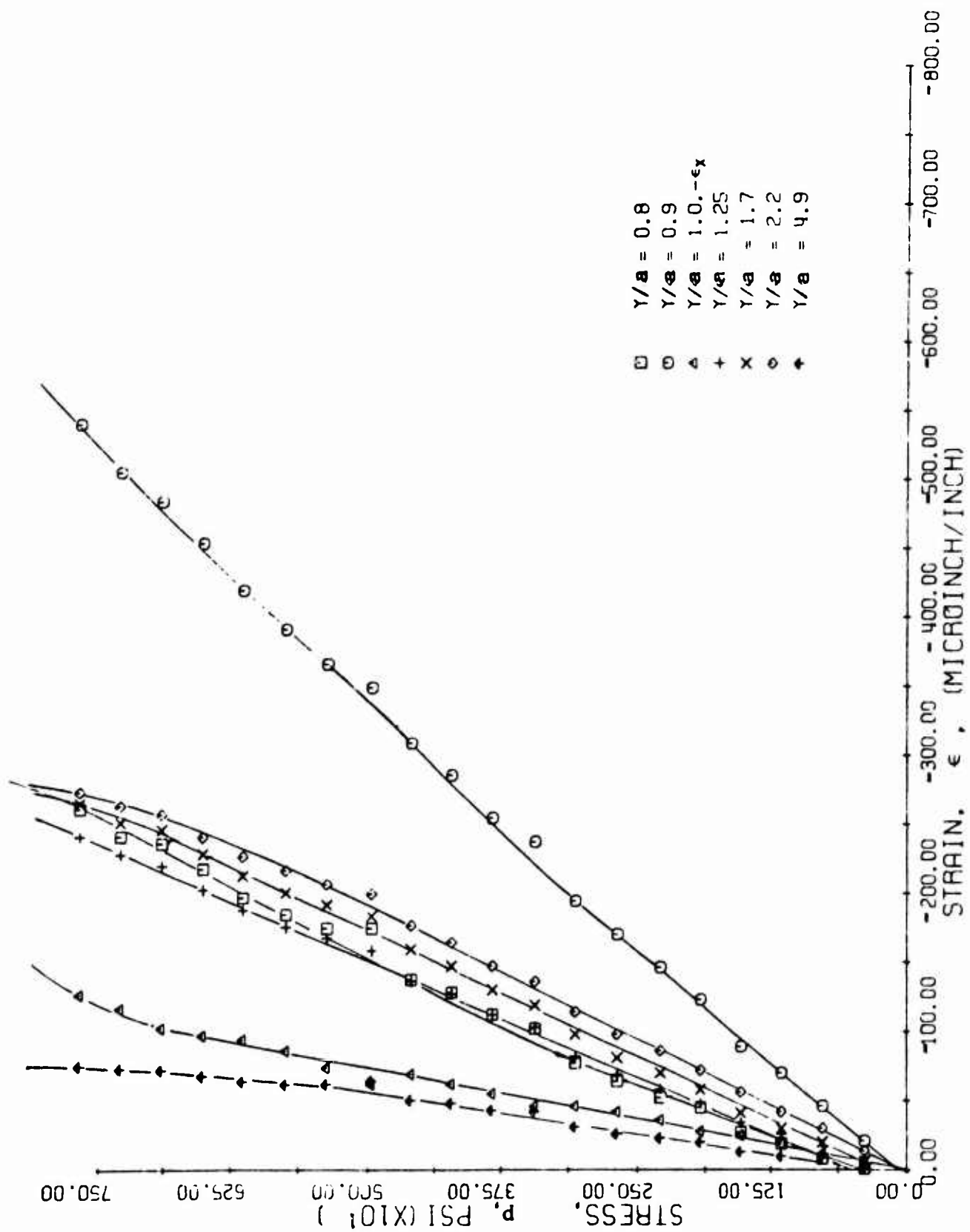
FIG. 238 HORIZONTAL STRAINS ALONG VERTICAL AXIS OF SYMMETRY AS A FUNCTION OF APPLIED VERTICAL STRESS FOR SPECIMEN NO.20 (MARBLE WITH ALUMINUM LINER UNDER BIAXIAL LOADING)
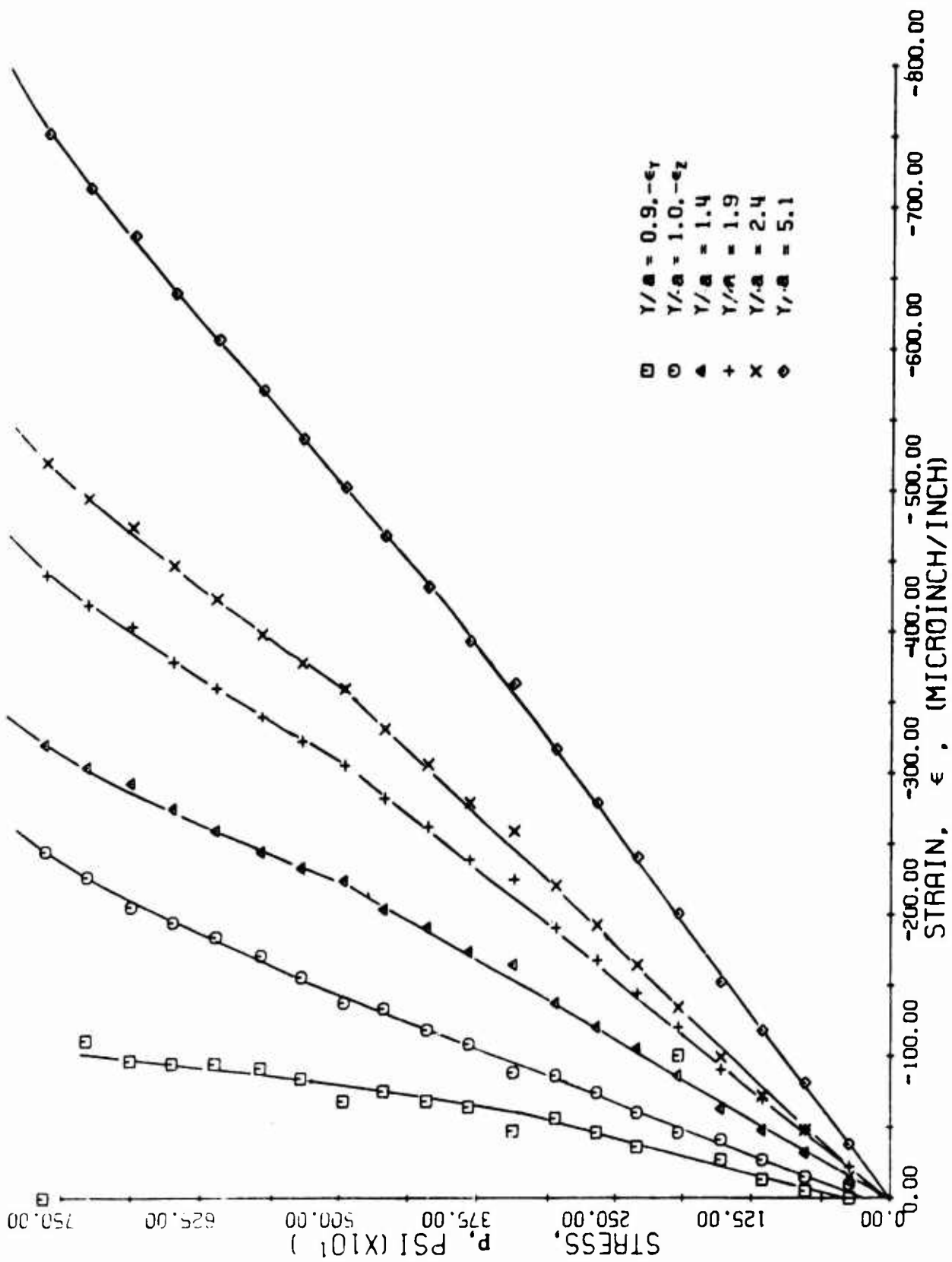
FIG. 239 VERTICAL STRAINS ALONG VERTICAL AXIS OF SYMMETRY AS A FUNCTION OF APPLIED VERTICAL STRESS FOR SPECIMEN NO.20 (MARBLE WITH ALUMINUM LINER UNDER BIAXIAL LOADING)
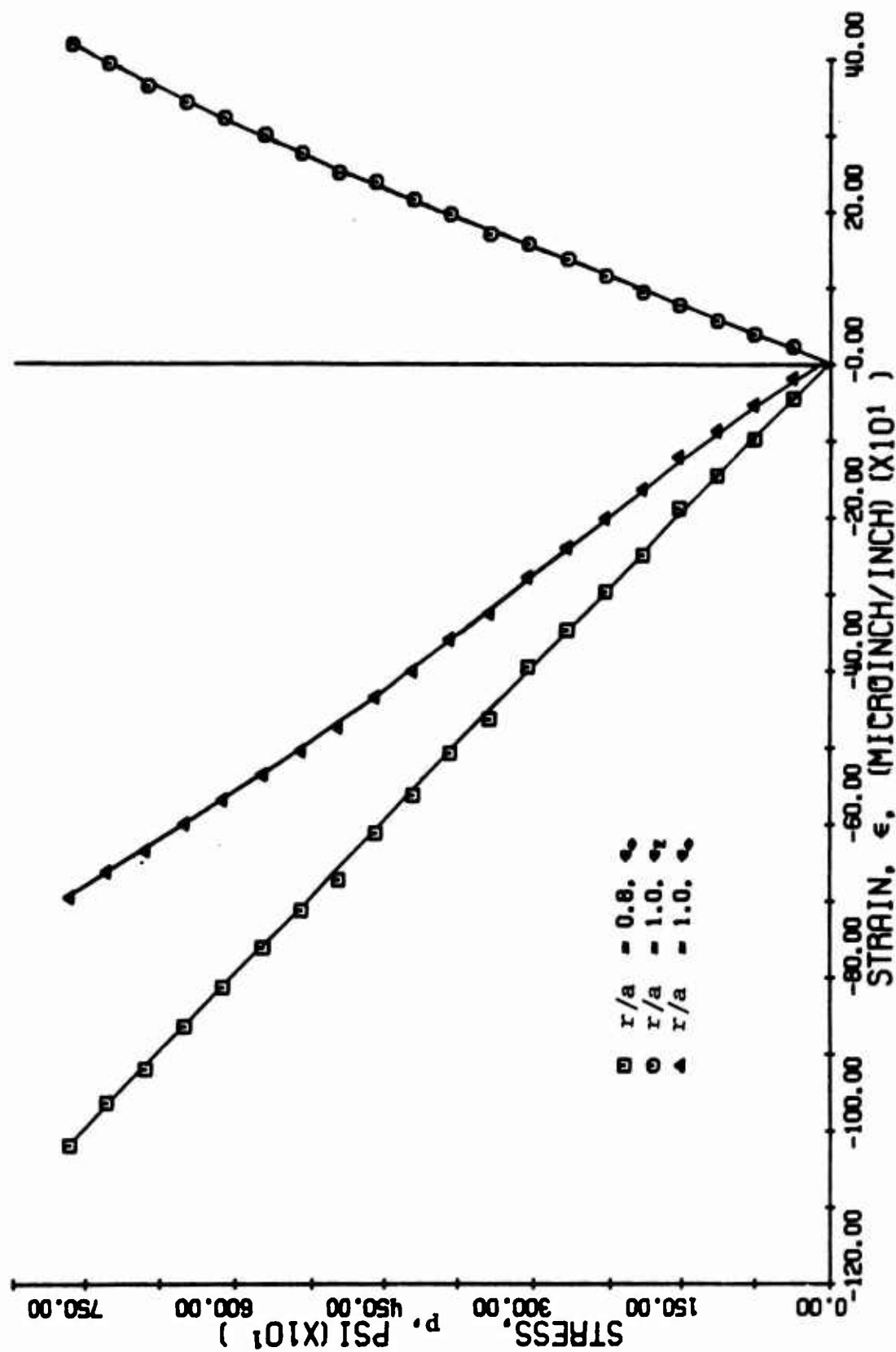
FIG. 240   STRAINS ALONG 45 DEGREE RADIUS FOR SPECIMEN NO. 20
(MARBLE WITH ALUMINUM LINER UNDER BIAXIAL LOADING)
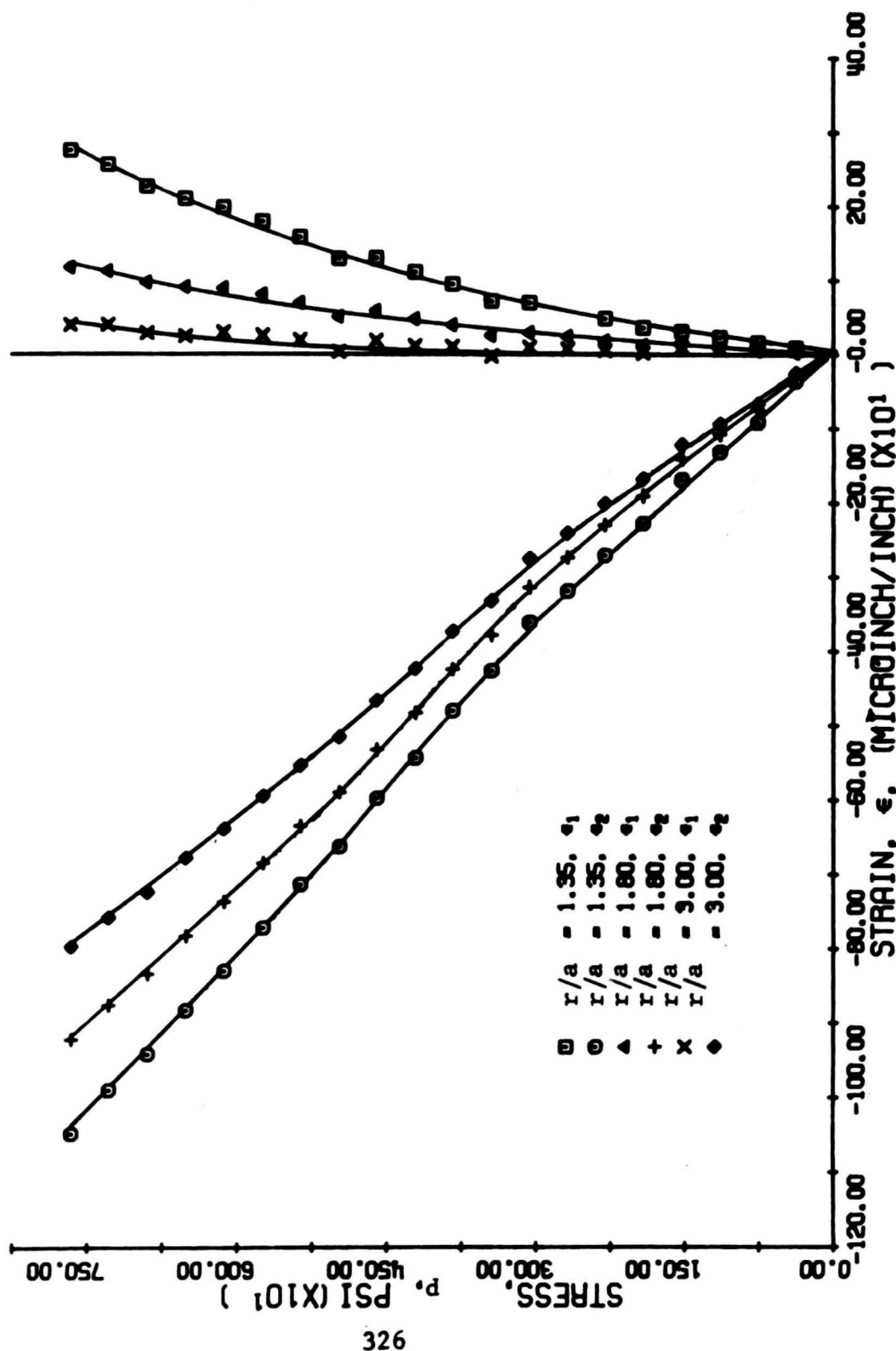
FIG. 241 PRINCIPAL STRAINS-ALONG 45 DEGREE RADIUS FOR SPECIMEN NO. 20 (MARBLE WITH ALUMINUM LINER UNDER BIAXIAL LOADING)

principal strain ε_1 is positive but decreases with increasing radial distance, becoming nearly zero at $r = 3.00a$. The angle between the 45-degree radius and the direction of ε_1, measured clockwise, remains nearly constant around 35 degrees at $r = 1.35a$, 37 degrees at $r = 1.80a$, and varies between 40 degrees and 42 degrees at $r = 3.00a$.

Strains along the horizontal axis for an applied vertical stress of $p = 3,000$ psi were plotted in Fig. 242. Theoretical points for the inside of the liner and for the interface are also shown.
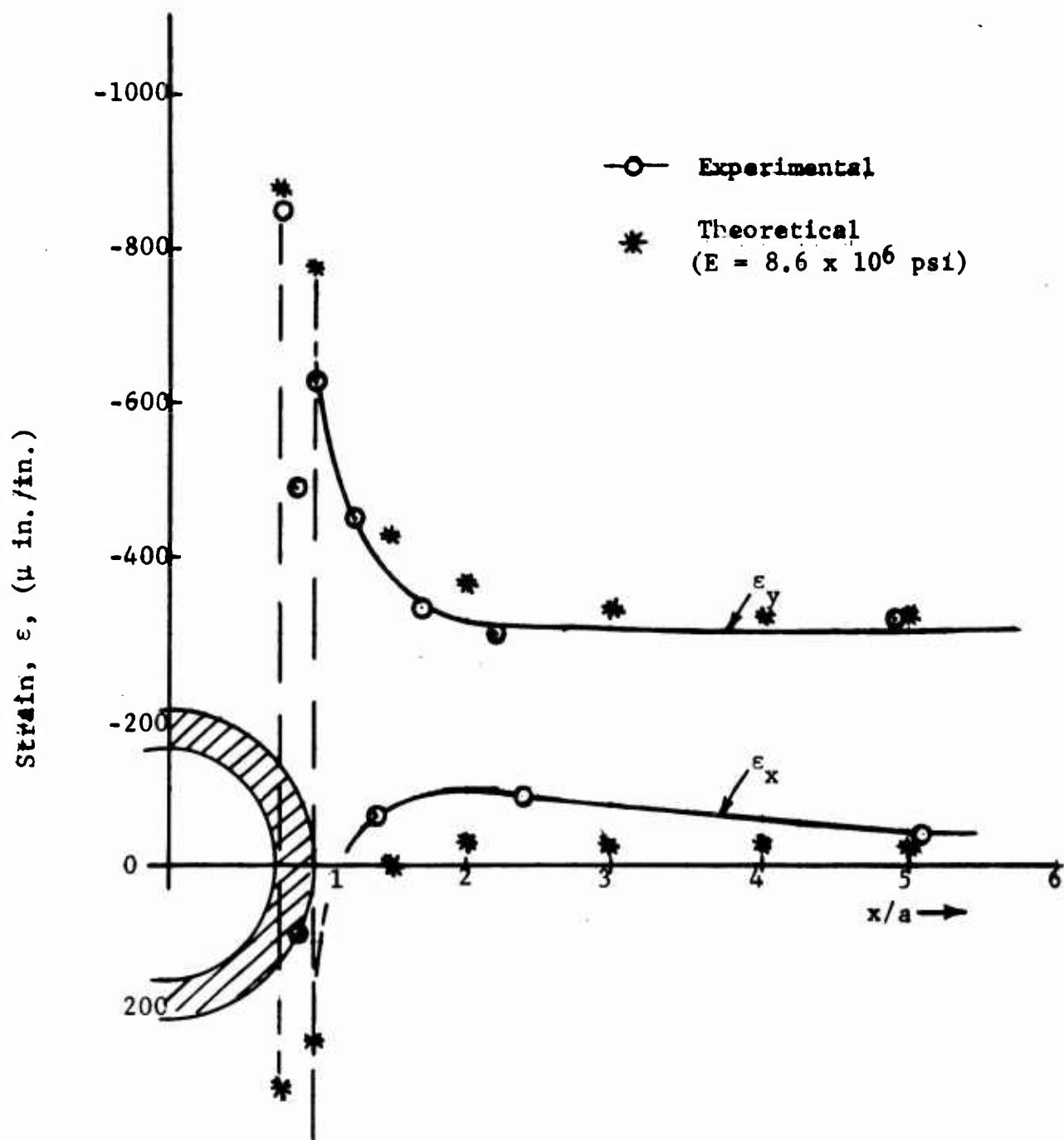
Fig. 242   STRAIN DISTRIBUTION ALONG HORIZONTAL AXIS AT APPLIED
VERTICAL STRESS OF p = 3,000 psi FOR SPECIMEN NO. 20
(MARBLE LINED WITH ALUMINUM UNDER BIAXIAL LOADING)

328

SECTION IX

SUMMARY, CONCLUSIONS AND RECOMMENDATIONS FOR FUTURE WORK

This report deals with an experimental study of the state of strain, deformati·n and fracture around lined and unlined cylindrical cavities in rock under uniaxial and biaxial static compressive loadings.

Two materials were investigated; Indiana limestone and Vermont marble. The specimens were typically 36 in. high x 24 in. wide x 3 in. thick with a 4 in. diameter cylindrical cavity. Two liner materials were used; hydrostone and aluminum. Liner thicknesses were 0.44 in. and 0.40 in. for the two liner materials, respectively. Ten specimens of each material with lined and unlined cavities were tested, six under uniaxial and four under biaxial compression. The applied lateral stress in the biaxial tests was one-third of the applied vertical stress to simulate conditions of lateral restraint of an infinite rock mass.

Each specimen was instrumented with strain gages along the horizontal, vertical and 45-degree radii. Strain gages were placed on the faces of the specimen, the inside of the cavity, on the liner and at the interface between the liner and the rock. Horizontal and vertical diametral changes were measured with differential trans-formers (DCDTs). Full-field strain distributions were measured on the face of the specimen near the cavity, and yielding and cracking were also monitored with a photoelastic coating.

Basic properties for each of the rock varieties used were determined by simple uniaxial tests. Properties determined were tensile strength, compressive strength, Young's modulus, Poisson's ratio, modulus of rigidity and bulk density. In addition, Mohr envelopes of failure were developed by means of triaxial testing.

Results were presented in the form of strain distributions as a function of applied stress (vertical) along the horizontal,

vertical and 45-degree radii, diametral changes as a function of
applied stress and isochromatic fringe patterns for various stress
levels. Whenever possible, specimens were loaded to failure. Crack
initiation and propagation were detected by the strain and diametral
variations with applied stress but were clearly manifested by the
isochromatic fringe patterns of the photoelastic coating. Some of
the numerical results obtained from each specimen were Young's
modulus and Poisson's ratio of the material determined from the
far-field strains, compressive strain concentration factor, diametral
changes per unit of applied vertical stress, applied stress at crack
initiation and maximum tensile stress at point and time of fracture.
All these results are tabulated in Tables 2 and 3 for all 20
specimens.

Young's modulus as determined from the far-field strains in
the limestone specimens varied between 3.6×10^6 and 5.5×10^6 psi
compared to the value of 3.8×10^6 determined from uniaxial tensile
tests. The two highest values obtained from specimens No. 1 and 2
may be due in part to some nonuniform load distribution. The average
value for the modulus, excluding the two highest values, is 4.0×10^6
psi. The value of Poisson's ratio of approximately 0.23 checks well
with the value of 0.22 determined from the uniaxial tests. For the
marble specimens, Young's modulus varied between 7.6×10^6 and
8.8×10^6 psi with an average value of 8.2×10^6 psi compared to
the value of 7.9×10^6 psi determined from uniaxial tests. The
average value for Poisson's ratio was 0.27 compared to the value of
0.24 obtained from the uniaxial tests.

The strain concentration factor in the unlined uniaxially
loaded specimens reached values of 3.40 and 4.00 for limestone and
3.40 and 3.50 for marble, appreciably higher than the theoretical
value of 3.00. No explanation is readily available for this discrep-
ancy. The variability in strain concentration factor is much greater
in limestone than in marble. In limestone, the experimentally determ-
ined strain concentration factor, with the exception of specimen No.
17, was appreciably higher than the theoretical value. In marble, the

330

Table 2

SUMMARY OF RESULTS FOR LIMESTONE

Specimen No.	Specimen Thickness (in.)	Liner	Liner Thickness (in.)	Loading	Young's Modulus E (psi x 10^6)	Poisson's Ratio	Strain Concentration k_t Experimental	Strain Concentration k_t Theoretical	Diametral Change Vertical ε_v/P (in./psi)x10^-6	Diametral Change Horizontal ε_h/P (in./psi)x10^-6	Applied Vertical Stress at Failure P_{cr} (psi)	Type of Failure	Maximum Tensile Stress at Failure σ_{max} (psi)
1	2.50	None	-	Uniaxial	4.8	0.22	3.40	3.00	-2.7	1.3	1,250	Cracking Along Vertical Axis	1,800°
2	16	None	-	Uniaxial	5.5	0.23	4.00	3.00	-2.7	1.5	640	Cracking Along Vertical Axis	1,650*
5	3.0	Hydrostone	0.44	Uniaxial	4.2	0.23	3.15	2.18	-2.5	1.1	1,100	Cracking Along Vertical Axis	1,450
6	3.06	Hydrostone	0.44	Uniaxial	3.7	0.23	2.45	2.18	-3.2	1.1	1,500	Cracking Along Vertical Axis	1,550
7	2.54	Aluminum	0.40	Uniaxial	4.3	0.22	3.13	1.14	-2.3	1.6	1,100	Cracking Near Vertical Axis and Near 45-Degree Location	2,260
8	2.53	Aluminum	0.40	Uniaxial	4.3	0.30	1.64	1.14	-2.5	0.9	2,050	Cracking Near 45-Degree Location	1,500
13	3.08	None	-	Biaxial	3.6	-	2.77	2.67	-1.9	0.2	3,550	Splitting	-
14	2.55	None	-	Biaxial	4.1	-	3.15	2.67	-1.4	0.2	4,460	Shear Type. Explosive	-
17	3.07	Hydrostone	0.44	Biaxial	5.7	-	2.03	2.19	-2.6	-0.08	4,080	Splitting	-
18	3.04	Aluminum	0.40	Biaxial	4.0	-	1.85	1.25	-1.8	-0.12	4,110	Splitting and Radial Cracking	1,980

* Approximate value computed from nonlinear strain curve.

Note: Uniaxial Tensile Tests: $E = 3.8 \times 10^6$ psi, $\nu = 0.22$, $\sigma_t = 630$ psi.

Table 3

SUMMARY OF RESULTS FOR MARBLE

Specimen No.	Specimen Thickness (in.)	Liner	Liner Thickness (in.)	Loading	Young's Modulus E (psi x 10^6)	Poisson's Ratio ν	Strain Concentration k_t Experimental	Strain Concentration k_t Theoretical	Diametral Change Vertical ε_v/P, (in./psi)x10^-6	Diametral Change Horizontal ε_h/P, (in./psi)x10^-6	Applied Vertical Stress at Failure P_{cr} (psi)	Type of Failure	Maximum Tensile Stress at Failure σ_{max} (psi)
3	3.25	None	-	Uniaxial	8.3	0.25	3.50	3.00	-1.5	0.6	1,606	Cracking Along Vertical Axis	3,800*
4	3.28	None	-	Uniaxial	8.0	0.28	3.40	3.00	-1.2	1.1	1,906	Cracking Along Vertical Axis	3,800*
9	3.42	Hydrostone	0.44	Uniaxial	8.1	0.26	2.92	2.66	-1.6	0.6	2,350	Cracking Along Vertical Axis	3,060
10	3.42	Hydrostone	0.44	Uniaxial	8.4	0.28	2.90	2.66	-1.5	0.6	2,100	Cracking Along Vertical Axis	3,500
11	3.32	Aluminum	0.40	Uniaxial	8.2	0.27	2.85	2.63	-1.7	0.6	2,500	Cracking Off Vertical Axis	4,500
12	3.30	Aluminum	0.40	Uniaxial	8.2	0.28	2.50	2.63	-1.6	0.5	4,000	Cracking Away from Interface	2,000-5,000**
15	3.13	None	-	Biaxial	7.6	-	2.74	2.67	-0.82	0	-	No Failure Observed	-
16	3.12	None	-	Biaxial	7.8	-	2.80	2.67	-0.85	0	-	No Failure Observed	-
19	3.03	Hydrostone	0.44	Biaxial	8.8	-	2.81	2.63	-1.2	0	-	No Failure Observed	-
20	3.26	Aluminum	0.40	Biaxial	8.6	-	1.95	2.44	-0.95	-0.30	-	No Failure Observed	-

*Approximate values computed from nonlinear strain curves.

**Maximum tensile stress at point of fracture approximately 2,000 psi, maximum stress at interface on vertical axis 5,000 psi.

Note: Uniaxial Tensile Tests: E = 7.9 x 10^6 psi, ν = 0.24, σ_t = 900 psi.

332

experimental values were, with the exception of specimens No. 12 and No. 20, only slightly higher than the theoretical values.

The diametral changes in limestone under uniaxial loading were roughly the same regardless of liner. The vertical deflections were 2-3 times higher than the horizontal deflections. Under biaxial conditions, the vertical deflections were approximately two-thirds of those under uniaxial loading, and the horizontal deflections were nearly zero. Diametral changes in the marble specimens have the same relative magnitudes to each other and are approximately half of the corresponding values in the limestone specimens. The latter is obviously due to the 2:1 ratio of moduli between marble and limestone. All diametral changes varied linearly with applied stress up to the crack initiation level.

The mode of failure in the uniaxially loaded unlined specimens (Nos. 1, 2, 3 and 4) was clearly tensile cracking along the vertical axis of symmetry. Cracking started on the boundary of the cavity on the vertical axis. In the limestone specimens, cracking started at sharply differing applied stress levels (1,250 psi and 640 psi). The maximum tensile stress at the crack initiation point, computed using the measured strain and Young's modulus, was 1600 psi and 1,650 psi, for specimens No. 1 and 2, respectively. This shows that an unusually high tensile strain existed in the second specimen, unexplained by any theory. The stress values above are appreciably higher than the tensile strength of 630 psi determined from uniaxial tests. The difference may be due to size effects and to nonlinearity and yielding in the rock specimen. The two marble specimens (No. 3 and 4) cracked at stress levels of 1,600 psi and 1,900 psi. The maximum tensile strain on the boundary of the hole shows appreciable nonlinearity and yielding prior to cracking. An approximate value for the local maximum tensile stress at fracture is 3,800 psi, roughly four times higher the tensile strength determined from uniaxial tensile tests. This is undoubtedly due to higher ductility and yielding in marble prior to fracture. The crack propagation in the marble tended to be slower and final fracture was appreciably less dramatic and violent than in the limestone. This is due in part to

333

lower elastic energy release in marble at fracture which is a result
of increased yielding prior to fracture.

The presence of a liner, even a weak liner, such as hydro-
stone, tends to strengthen the cavity, but the performance of the
liner and the strain distribution in the material around it depend
greatly on the condition of bonding. In the limestone specimens,
the hydrostone liner, having a modulus of approximately half of that
of limestone, increased the strength only slightly. Maximum tensile
stresses at failure were approximately 1,500 psi. The same liner
in marble increased the strength by approximately 27 percent.
Maximum tensile stresses at failure were 3,060 psi and 3,500 psi.
All of these specimens (Nos. 5, 6, 9, and 10) failed by cracking
along the vertical axis. In specimens No. 5 and No. 6, cracking
started in the limestone at the interface with the hydrostone liner.
The hydrostone liner itself cracked at higher applied stresses,
although the material has approximately the same strength as the
limestone. In the marble specimens, cracking initiated in the
hydrostone but it quickly propagated into the marble.

Specimens with aluminum liners produced the most divergent
results, probably due to higher sensitivity to bonding conditions.
One of the limestone specimens (No. 7) failed by cracking near the
vertical axis at a low applied stress of 1,100 psi. However, due
to a peculiar distribution of stresses around the hole, a maximum
tensile stress of 2,260 psi was reached at fracture. The second
limestone specimen (No. 8) showed much lower strain concentrations
and much higher strength. Cracking initiated at an applied stress
of 2,050 psi at the interface near the 45-degree location. This is
near the theoretically calculated location of the maximum tensile
stress. A tensile stress of 1,500 psi was computed at the point and
time of crack initiation. The first marble specimen (No. 11) cracked
near the vertical axis at the interface at an applied stress of
2,500 psi and reached a local tensile stress at the point of fracture
of 4,500 psi. This is approximately five times the tensile strength
of marble as determined from uniaxial tests. The second marble speci-
men (No. 12) showed a more than 100 percent increase in strength over

334

that of the unlined specimens. Cracking started off the vertical axis and possibly away from the interface at an applied stress of 4,000 psi. This peculiar type of fracture has been predicted theoretically by Hoek (Ref. 3) and confirmed experimentally. At the point of crack initiation, the maximum tensile stress was of the order of 2,000 psi, although a tensile stress of approximately 5,000 psi was reached at the interface on the vertical axis. This result points to the influence of size effect, inhomogeneity and stress biaxiality on fracture of this rock.

Under biaxial compressive loading, most of the stresses are compressive and no pure tensile failure results. The first unlined limestone failed by splitting into two halves along the middle plane parallel to the faces at an applied vertical stress of 3,550 psi. This failure which is typical of concrete and rocklike materials may be due to the inhomogeneity of the material. It is assumed that the material contains higher modulus or lower Poisson's ratio inclusions which tend to restrain the lateral tensile strain and therefore are subjected to local tensile stress which causes failure. The second limestone specimen (No. 14) failed in an explosive manner under shear around the 45-degree radius. Failure occurred at a vertical stress of 4,460 psi. The hydrostone-lined limestone specimen (No. 17) failed by vertical splitting at a vertical stress of 4,080 psi, approximately 10 percent higher than in the unlined specimen. The aluminum-lined limestone specimen (No. 18) failed at 4,110 psi vertical stress both by vertical splitting and radial cracking. A maximum tensile stress of 1,980 psi was calculated at the interface at the time of failure. None of the four marble specimens loaded in biaxial compression produced failure around the cavity when loaded to the capacity of the loading system.

The results above point out that the strength of a cavity, although definitely dependent on the type of liner, loading conditions and basic material properties, cannot always be predicted. Depending on the combination of materials, geometrical and loading parameters

several types of failure can be observed, tensile cracking along the vertical axis, tensile cracking off the vertical axis, splitting with or without radial cracking, fracture away from cavity boundary, and compressive (shear) failure. The tensile stresses computed at the point and time of fracture were much higher than the strengths determined from uniaxial tests. In limestone, maximum tensile stresses from 1.5 to 3.5 times the uniaxial tensile strength were computed. In marble such stresses were from 3.7 to 5.0 times the uniaxial tensile strength. Such factors can be taken into account in designing silos, provided the material properties (in situ) and loading conditions are known.

It has been clearly demonstrated that liners in general have a definitely strengthening effect. This effect depends on the relative modulus, thickness and strength of the liner.

The present work clearly demonstrates that small-scale experimental studies are very useful in determining the influence of various parameters on the structural response of silo structures. Such tests are necessary to fill the gap between theory and field testing. Although a great many cases were investigated in the present work, many more questions remain to be answered.

The influence of faults and layers in the rock medium around the cavity merits careful study. Experiments similar to those described in this report can be easily conducted with faulted and layered rocks. The influence of material and geometrical parameters of liners on the strength of the cavity merits further study. Given a medium and a loading environment, an optimum liner can be designed.

The static loading used here can be extended to a quasi-dynamic programmable biaxial loading. A biaxial loading simulating the given free-field radial and circumferential strain histories can be applied to a rock specimen containing a cavity by means of an electro-hydraulic system available at IITRI. Two-dimensional dynamic studies using explosive loadings and photoelastic and rock models would be useful in checking computer codes and the effects of liner rigidity and nature of bond between liner and medium.

336

The dynamic loading conditions and the three-dimensional aspects of the problem can be incorporated into a three-dimensional photoelastic study of a silo model subjected to explosive or air-blast loading. The medium around the silo can be simulated by as many layers of different photoelastic materials as desired. Experimental techniques and facilities for dynamic three-dimensional photoelastic studies are available at IITRI.

A similar study can be conducted using a model of a silo in rock loaded on the surface with explosive or other dynamic loading (small scale DIHEST test). The effects of cracks and faults can be incorporated in such a study.

REFERENCES

1. Hiramatsu, Y. and Oka, Y., "The Fracture of Rock Around Underground Openings," *Memoirs of Faculty of Engineering of Kyoto University*, Vol. XXI, part 2, April 1959.

2. Hoek, E., "Experimental Study of Rock Stress Problems in Deep-Level Mining," *Experimental Mech.*, Proc. 1st Intern. Congr., (edited by B. E. Rossi), The MacMillan Co., New York, 1963.

3. Hoek, E., "Rock Fracture Around Mine Excavations," *Proc. 4th International Conf. on Strata Control and Rock Mech.*, May 4-8, 1964, Henry Crumb School of Mines, Columbia Univ., New York, N. Y.

4. Hawkes, I. and Hollister, G. S., "Photoelastic Techniques Applied to Rock Mechanics Problems of Underground Excavations and Foundations," *Stress Analysis*, Ed. by O. C. Zienkiewicz and G. S. Hollister, John Wiley & Sons, 1965.

5. Kirsch, G., "Die Theorie der Elastizität und die Bedürfnisse der Festigkeitslehre," *Zeitschrift der Vereine deutscher Ingenieure*, Vol. 42, 1898, p. 113.

6. Howland, R. C. J., "On the Stresses in the Neighborhood of a Circular Hole in a Strip Under Tension," *Phil. Trans. of the Royal Soc. of London*, series A, Vol. 224, 1930, pp. 49-86.

7. Neuber, H., *Theory of Notch Stresses*, English Transl. AEC-tr-4547 (Kerbspannungslehre, Springer - Verlag, Berlin, 1958).

8. Savin, G. N., *Stress Concentration Around Holes*, Pergamon Press, 1961.

9. Baron, M. L. and Matthews, A. T., "Diffraction of Pressure Wave by a Cylindrical Cavity in an Elastic Medium," *Jour. Appl. Mech.*, Vol. 28, Sept. 1961, pp. 347-354.

10. Daniel, I. M. and Riley, W. F., "Stress Distribution on the Boundary of a Circular Hole in a Large Plate Due to an Air Shock Wave Traveling Along an Edge of the Plate." *J. Appl. Mech.*, Vol. 31, Sept. 1964, pp. 402-408.

11. Daniel, I. M., "Viscoelastic Wave Interaction with Cylindrical Cavity," *J. of Eng. Mech. Division* of ASCE, Vol. 92, Dec. 1966, pp. 25-42.

REFERENCES (Cont'd.)

12. Gettel, R. W., "Photoelastic Study of Crack Propagation from a Circular Opening in an Infinite Plate," Presented at Soc. for Exp. Stress Analysis Mtg., Oct. 14-17, 1969, Houston, Texas.

13. Griffith, A A., "The Phenomena of Rupture and Flow in Solids," Phil. Trans. of the Royal Soc. of London, series A, Vol. 221, 1921, pp. 163-197.

14. McClintock, F. A. and Walsh, J. B., "Friction on Griffith Cracks in Rock Under Pressure," Intern. Congress on Applied Mech., Berkeley, Calif. 1962.

15. Suzuki, Shin-inchi, "Stress Measurements in an Infinite Plate with a Hole Reinforced by Different Materials," Exper. Mech., Vol. 9, July 1969, pp. 332-336.

16. Dally, J. W. and Riley, W. F., Experimental Stress Analysis, McGraw-Hill, New York, 1965.

17. Weibull, W., "A Statistical Theory of the Strength of Materials," Ing. Vetenskaps Akad. Handl., Vol. 151 (1939); "The Phenomena of Rupture in Solids," Ibid., Vol. 153 (1939).

DOCUMENT CONTROL DATA - R & D

(Security classification of title, body of abstract and indexing annotation must be entered when the overall report is classified)

1. ORIGINATING ACTIVITY (Corporate author)	2a. REPORT SECURITY CLASSIFICATION
IIT Research Institute Chicago, Illinois 60616	UNCLASSIFIED
	2b. GROUP

3. REPORT TITLE

EXPERIMENTAL INVESTIGATION OF SMALL SCALE LINED AND UNLINED CYLINDRICAL CAVITIES IN ROCK

4. DESCRIPTIVE NOTES *(Type of report and inclusive dates)*
October 1968-December 1969

5. AUTHOR(S) *(First name, middle initial, last name)*

I. M. Daniel; R. E. Rowlands; M. M. Singh

6. REPORT DATE	7a. TOTAL NO. OF PAGES	7b. NO. OF REFS
November 1970	368	17

8a. CONTRACT OR GRANT NO. F29601-69-C-0016	9a. ORIGINATOR'S REPORT NUMBER(S)
b. PROJECT NO. 5710	AFWL-TR-70-55
c. Subtask No. SC 157	9b. OTHER REPORT NO(S) *(Any other numbers that may be assigned this report)* IITRI Project No. D6006
d.	

10. DISTRIBUTION STATEMENT This document is subject to special export controls and each transmittal to foreign governments or foreign nationals may be made only with prior approval of AFWL (DEV), Kirtland AFB, NM, 87117. Distribution is limited because of the technology discussed in the report.

11. SUPPLEMENTARY NOTES	12. SPONSORING MILITARY ACTIVITY
	AFWL (DEV) Kirtland AFB, NM 87117

13. ABSTRACT

(Distribution Limitation Statement No. 2)

An experimental study of the state of strain, deformation and fracture around lined and unlined cylindrical cavities in rock under uniaxial and biaxial static compressive loadings is discussed. Twenty limestone and marble specimens of typical dimensions 36 in. high, 24 in. wide and 3 in. thick with a 4 in. diameter cylindrical hole unlined or lined with hydrostone and aluminum liners were used. Deformation and fracture were monitored with strain gages, differential transformers and photoelastic coatings. Strain distributions and diametral changes as a function of applied load were obtained. Deviations from linear elastic theory were noted and discussed. Crack initiation and propagation were monitored with all three experimental means. Strain concentration factors were, with few exceptions, higher and in some instances appreciably higher than theoretical factors. The presence of the liner, even the weak hydrostone liner, had a strengthening influence, although not always predictable. Depending on the combination of material, geometrical and loading parameters, several types of failure were observed: tensile cracking along the vertical axis for the unlined specimens and those lined with hydrostone; tensile cracking off the axes of symmetry for specimens lined with aluminum; fracture away from cavity boundary for the aluminum-lined specimen; splitting along a vertical plane, or compressive (shear) failure, or combined splitting and radial cracking for biaxially compressed limestone specimens. The tensile stresses computed at the point and time of fracture were much higher than the tensile strengths determined from uniaxial tests. In limestone, maximum tensile stresses from 1.5 to 3.5 times the uniaxial tensile strength were computed. In marble, this factor varied from 3.7 to 5.0

DD FORM 1473
1 NOV 65

14. KEY WORDS	LINK A		LINK B		LINK C	
	ROLE	WT	ROLE	WT	ROLE	WT
Rock						
Rock mechanics						
Rock inclusions						
Lined rock inclusions						
Plane stress						
Plane strain						
Biaxial loading						
Uniaxial loading						
Tunnels						
Indiana limestone						
Vermont marble						